Ponnadurai Ramasami · Minu Gupta Bhowon ·
Sabina Jhaumeer Laulloo · Henri Li Kam Wah
Editors

Chemistry for a Clean and Healthy Planet

Springer

Chemistry for a Clean and Healthy Planet

Ponnadurai Ramasami · Minu Gupta Bhowon ·
Sabina Jhaumeer Laulloo · Henri Li Kam Wah
Editors

Chemistry for a Clean and Healthy Planet

Springer

Editors
Ponnadurai Ramasami
Department of Chemistry
Faculty of Science
University of Mauritius
Réduit, Moka, Mauritius

Minu Gupta Bhowon
Department of Chemistry
Faculty of Science
University of Mauritius
Réduit, Moka, Mauritius

Sabina Jhaumeer Laulloo
Department of Chemistry
Faculty of Science
University of Mauritius
Réduit, Moka, Mauritius

Henri Li Kam Wah
Department of Chemistry
Faculty of Science
University of Mauritius
Réduit, Moka, Mauritius

Preface

The fifth edition of the International Conference on Pure and Applied Chemistry (ICPAC 2018) was held from 2 to 6 July 2018 at Hotel Sofitel Mauritius L'Impérial Resort & Spa, Wolmar, Flic en Flac, Mauritius. The theme of the conference was "Chemistry for a Clean and Healthy Planet". ICPAC 2018 was attended by 160 participants coming from 30 countries. The conference featured 105 oral and 37 poster presentations. The keynote lecture was delivered by Ms. Veronika Stromsikova, Director, Office of Strategy and Policy, Organisation for the Prohibition of Chemical Weapons (OPCW). OPCW was the 2013 Nobel Peace Prize winner.

The participants of ICPAC 2018 were invited to submit full papers. The latter were subsequently peer-reviewed, and the selected papers are collected in this book of proceedings.

This book encloses 31 chapters covering a wide range of topics from nano-technology, natural product chemistry to analytical and environmental chemistry and applied chemistry. There are also two reviews among the chapters.

We would like to thank all those who submitted full manuscripts for consideration and the reviewers for their timely help in assessing these manuscripts for publication.

We would also like to pay a special tribute to all the sponsors of ICPAC 2018.

We hope that this collection of papers will serve as a useful resource for researchers.

Moka, Mauritius   Ponnadurai Ramasami
May 2019   Minu Gupta Bhowon
                                                     Sabina Jhaumeer Laulloo
                                                      Henri Li Kam Wah

Contents

Chapter 1
Controlled Microstructure of Ag/AgBr-AC Synergistic Enhancement on Photocatalytic Degradation of Tetracycline: A Synthesis Approach Comparison

Saheed Sanni, Elvera Viljoen and Augustine E. Ofomaja

Abstract The controlled microstructure of plasmonic Ag/AgBr has enormously influenced their potential application in environmental remediation. On this basis, Ag/AgBr-AC (activated carbon) nanocomposites were synthesized by thermal polyol and template assisted routes, and then their photocatalytic activities on the degradation of tetracycline under visible light were further investigated. The synthesized nanocomposites microstructure, structural, optical and electrochemical properties were determined using analytical techniques. From the analysis results, the Ag/AgBr nanoparticles were distributed evenly on the AC surface without agglomeration with an average particle size between 160 and 190 nm and possess {111} exposed facets of AgBr NPs. Due to the exceptional uniform nanospheres shape, smaller particle size, speedier interfacial separation of photogenerated charge carriers, the Ag/AgBr-AC nanocomposite from thermal polyol route displays superior catalytic performance on tetracycline as compared to the nanocomposite from template assisted route and Ag/AgBr alone. AC synergistic interaction with Ag/AgBr NPs in this study significantly enhances charge transfer, the creation of active sites for the generation of reactive species and boosts the stability of plasmon K1 in the photocatalytic process. A plausible photocatalytic mechanism on enhanced degradation of tetracycline is proposed.

Keywords Microstructure · Ag/AgBr-AC · Thermal polyol · Template assisted route · Tetracycline · Visible light

S. Sanni · E. Viljoen · A. E. Ofomaja (✉)
Biosorption and Wastewater Treatment Research Laboratory, Department of Chemistry, Faculty of Applied and Computer Sciences, Vaal University of Technology, P. Bag X021, Vanderbijlpark 1900, South Africa
e-mail: augustineo@vut.ac.za

S. Sanni
e-mail: mosqit.saheed@gmail.com

E. Viljoen
e-mail: elverav@vut.ac.za

1.1 Introduction

The prevalence of antibiotics in the surface and municipal water poses huge risks to our environment and human health at large. Trace level and long accumulation of these antibiotics in the environment have adverse effects towards both aquatic and terrestrial organisms [1]. Tetracycline is a commonly used antibiotic that has been detected in the ecosystem [2]. The complete removal of this antibiotic using conventional techniques still have their pitfalls, hence the need for effective treatment method that can be applied on a large scale is required [2]. Semiconductor photocatalysis under advanced oxidation processes (AOPs) has shown promising attributes for tetracycline removal [3]. However, the development of efficient and sustainable visible light driven photocatalysts that can fully explore the potential of the solar spectrum is considered as one of the promising strategies toward solving the future energy shortages. Huge attention is channeled towards the design of Ag-based photocatalysts (Ag/AgX, X = Cl, Br, I), which respond intensively to the visible light due to surface plasmon resonance (SPR) of Ag nanoparticles (NPs) anchored on the large band gap of the photocatalysts [4, 5].

Ag/AgBr is an important photocatalyst with exceptional attributes as compared to Ag/AgX (X = Cl, I) [6, 7], with less emphasis on the synthetic approach for well-defined Ag/AgBr nanostructures. The synthetic approach plays a huge role in the development of this highly efficient photocatalyst. However, the rapid reaction in the formation of AgBr nanospecies from conventional post-treatment route (photoinduced reduction) is still challenging for effective distribution and growth of the metallic silver nanoparticles (Ag NPs) [5]. The well tailor surface plasmon resonance properties (SPR) of Ag NPs are dependent on controlled microstructure (shape, size, and composition) of Ag/AgX nanocomposite. The controlled synthesis of Ag/AgBr nanospecies with different sizes and defined morphologies have been achieved through a host of approaches [7–9]. However, the SPR attributes of produced Ag NPs anchored on AgBr NPs from these preceding works [7–10] have limited significance on separation of charge carriers and as such high recombination rate of electron and holes is still evident. Therefore, there is need to disperse Ag/AgBr NPs on the clean surface material, which can participate in the controlled microstructure of Ag/AgBr NPs. This material should also boost the separation efficiency of charge carrier and behaves as a transport medium, and boosts their overall stability in the catalytic process.

The application of carbonaceous materials with abundant oxygenated functional groups as a template, promoter, and support in the dispersion of Ag/AgBr nanoparticles [6, 11–13], has shown exceptional attributes to overcome the challenges of previous works [7–9]. In view of the outstanding properties of these carbonaceous materials, this work focuses on the utilization of activated carbon as template and support in the controlled microstructure of Ag/AgBr nanoparticles. The Ag/AgBr-AC nanocomposites were prepared through two different approaches (thermal polyol and template-assisted method) for photocatalytic degradation of tetracycline antibiotics under visible light irradiation. Ag/AgBr-AC nanocomposite from thermal polyol

route displays higher photocatalytic activity on tetracycline than the nanocomposite from template assisted route and Ag/AgBr alone under visible light irradiation. The synergy of a well-controlled microstructure of Ag/AgBr NPs and the AC support acting as an acceptor of the photogenerated electrons from the Ag/AgBr, effectively enhanced the catalytic properties of the nanocomposite synthesized from thermal polyol route. A plausible reaction mechanism was proposed based on the scavenging experiment.

1.2 Experimental Section

1.2.1 Materials

$AgNO_3$ (99%) was purchased from Merck whereas hexadecyltrimethylammonium bromide (HTAB, 99%), polyvinyl-pyrolidine PVP (K29-32), ethylene glycol (EG, 99%) were purchased from Acros. Ethanol (98%), potassium hydroxide (KOH, 99%), hydrochloric acid, sodium hydroxide and tetracycline hydrochloride (99%) were bought from Sigma Aldrich. All the reagents were used as received and water used in all these experiments was purified with a Millipore system.

1.2.2 Activated Carbon Synthesis

The chemical activation of pine cone biomass (PCB, 5 g) was conducted by impregnating pine cone in 25 mL solution of 2 M KOH at a ratio of 2.24:1 (g KOH/g PCB). The prepared solution was impregnated for 24 h and the solution was later dried in the oven at 80 °C for 12 h to eliminate remaining moisture present in the material. A sample of KOH impregnated pine cone placed in a Duran bottle under nitrogen atmosphere flow was pyrolyzed in the microwave reactor (model LG MH8042GM), at a constant power of 400 W for 16 min. The pine cone activated carbon produced was cooled to room temperature, washed with 0.1 M HCl and hot distilled water to remove any impurities until the pH was between 6 and 7. Then the washed activated carbon obtained was dried at 105 °C overnight and then stored in an airtight container.

1.2.3 Preparation of Ag/AgBr-AC Through Thermal Polyol Route

The synthesis of Ag/AgBr-AC was carried out through a modified thermal polyol route [13]. 18 mL of ethylene glycol was poured into a round-bottom flask which was heated at 60 °C for 30 min. PVP (0.12 g) and 480 mg of HTAB were added to the

solution, then AC (0.06 g) was added to the stirred mixture. After proper mixing to completely dissolve the PVP and HTAB, 3 mL ethylene glycol solution containing silver nitrate was slowly added dropwise to the above mixture. The solution was maintained at 60 °C for an additional 30 min and the mixture was then heated to a temperature of 140 °C. After attainment of the desired temperature, the reaction was further allowed to proceed for 14 min. The reaction vessel was taken out and cooled down to room temperature in the air. The resulting solids were collected by centrifugation (REMI bench top centrifuge-R-8D), washed thoroughly with ethanol and dried in an oven for 12 h. The synthesized nanocomposite was coded as plasmon K1 and Ag–AgBr was synthesized through the same route described above without the addition of AC.

1.2.4 Preparation of Ag/AgBr-AC Through Template Assisted Route

The Ag/AgBr coupled AC nanocomposite was synthesized through a modified template-assisted method with respect to the literature [14]. Typically, 12 mL ethylene glycol solution (EG) was heated in a round-bottom flask for 30 min at a temperature of 65 °C. HTAB (0.26 g) and AC (0.09 g) were sequentially added to the EG stirred solution. After homogenization, 0.2 g of silver nitrate mixed with 1 M ammonium hydroxide solution (2.50 mL) was added dropwise to the stirred solution and further allowed to stir for 6 h under ambient light for formation of Ag^0 NPs on nucleated AgBr. The precipitated solution was allowed to cool down, separated by centrifugation (6000 rpm, 10 min), further washed with ethanol and deionized water repeatedly, then dried in an vacuum oven at 60 °C overnight. The synthesized nanocomposite was stored in an airtight container in the dark and denoted as plasmon K2.

1.2.5 Characterization of the Synthesized Materials

The morphology and composition properties of the nanocomposite materials were determined using scanning electron microscopy (SEM, Zeiss Leo 1430 VP) and energy dispersive X-ray spectrometer (EDS, INCA). Shimadzu X-ray 700 (XRD) with Cu Kα radiation was used to determine the crystal structure and phase data for the photocatalysts in the 2θ range of 20–80° at 40 kV and 40 mA. The crystallite size of the nanocomposites was estimated from the Scherrer equation by using the most intense reflection peak [15]. The functional groups on the prepared samples were investigated by Fourier transform infrared spectrometer (Perkin Elmer spectrum 400) within the range of 600–4000 cm^{-1}. The UV–visible spectra of the nanocomposites was recorded using Ocean Optics high-resolution spectrometer (Maya 2000) equipped with an integrating sphere accessory, using $BaSO_4$ as a reference. Elec-

trochemical impedance spectroscopy (EIS) was carried out in a three-way electrode system using a Biologic SP 240 potentiostat workstation. The working, reference and counter electrode were glassy carbon electrode, Ag/AgCl (in saturated KCl) and platinum wire respectively. The EIS experiments were carried out between frequency ranges of 100 kHz to 40 MHz with a perturbation amplitude of 5 mV in 5 mM ferrocyanide containing 0.1 M KCl solution.

1.2.6 Photocatalytic Activity Evaluation

The photocatalytic activity of the prepared samples was evaluated on the degradation of tetracycline (TC) in aqueous solution under the irradiation of 36 W white visible LED light strips. The initial TC concentration was 15 mg/L with a catalyst loading of 0.3 g/L in 150 mL of TC solution. Prior to irradiation, the mixed solution was ultra- sonicated, then stirred in the reactor for 1 h in the dark to reach the adsorption/desorption equilibrium of TC on the photocatalyst surface. The adsorbed solution was further subjected to degradation by switching on the LED light under stirring for 3 h, while 3 mL of the sample solution was withdrawn at given time intervals (30 min) and centrifuged to remove suspended particles. The concentration of TC left was determined by measuring the absorbance of the solution in a UV–visible spectrophotometer at 356 nm. The percentage degradation of tetracycline was calculated using the Eq. 1.1 below:

$$\%R = 1 - \frac{C_t}{C_o} \times 100\% \tag{1.1}$$

where C_o is denoted as the initial concentration of TC solution that reached adsorption-desorption equilibrium and C_t denoted as the concentration at reaction time t.

1.3 Characterization

1.3.1 Morphology, Size and Composition Analysis

The SEM micrographs of plasmon K1 and K2 are shown in Fig. 1.1a, b, where the formation of nanospheres morphology is well-defined in Fig. 1.1a for plasmon K1 with an average diameter of 162 nm. However, the morphologies of plasmon K2 are irregular spheres with an average particle size of 180 nm (Fig. 1.1b). The reduced particle size and uniform morphologies for plasmon K1 as compared to plasmon K2 are ascribed to moderate synthesis temperature and PVP influence, as these two parameters hamper irregular growth of Ag/AgBr nanoparticles that yield formation
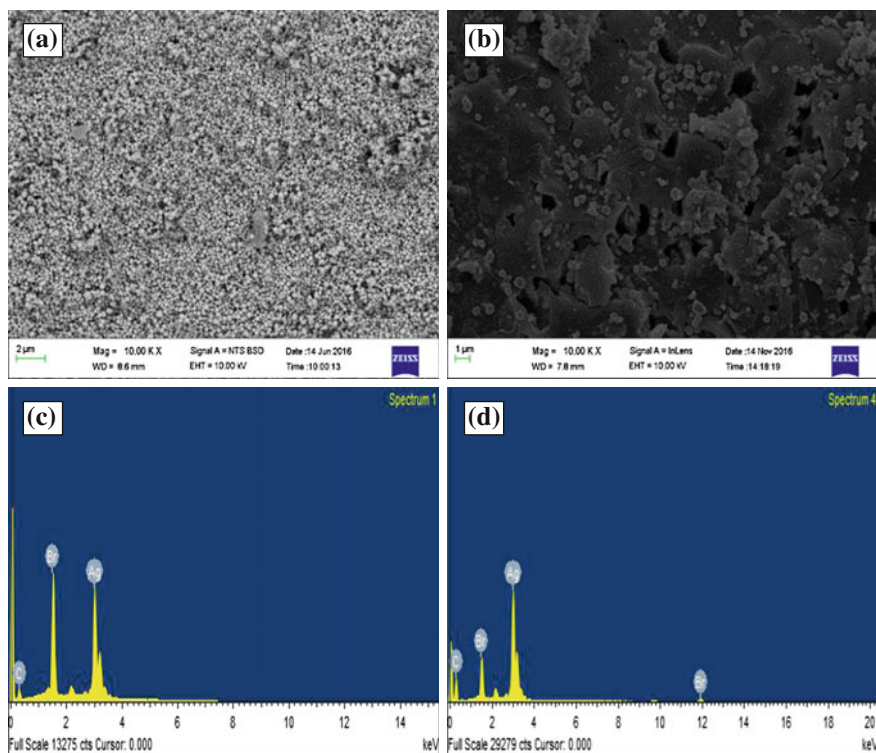
Fig. 1.1 SEM images and EDX spectrum of plasmon K1 (**a**, **c**) and plasmon K2 (**b**, **d**)

of uniform nanostructures. The moderate synthesis temperature from previous work has resulted in the formation of isotropically shaped Ag/AgBr nanoparticles [13, 16], whilst PVP acts as a capping agent [8] in particle size reduction and formation of well-defined shaped nanoparticles. Plasmon K1 with small particle size and uniform nanospheres morphology will have speedier charge transfer, facilitating adsorption of the pollutant on the surface of catalyst and creation of active sites in the catalytic system for enhanced degradation of tetracycline pollutant in this study.

The elemental components of the plasmon nanocomposites (K1 and K2) were investigated by energy dispersive X-ray spectroscopy (EDX) analysis. As depicted in Fig. 1.1c, d, Ag, Br and presence of C element from activated carbon are identified in the Ag/AgBr-AC nanocomposites. The elemental analysis also reveals no other elements in the prepared Ag/AgBr-AC photocatalyst, which confirms the high purity of the prepared products, while the atomic ratio between Ag and Br was more than 1:1 for the nanocomposite materials based on the semi-quantitative analysis (Table 1.1). This further confirms the formation of metallic Ag NPs anchored on AgBr in the nanocomposite. However, the plasmon K2 possesses more content of Ag NPs ratio and higher percentage reduction of Ag NPs as compared to plasmon K1. A few amounts of metallic Ag are formed from AgBr NPs under ambient light with plasmon

Table 1.1 Elemental composition of Ag/AgBr-AC nanocomposites synthesized from both methods

Sample	Atomic ratio (C)	Atomic ratio (Br)	Atomic ratio (Ag)	[a]Atomic ratio (Ag:AgBr)	[b]Reduction % of Ag
Plasmon K1	20.50	28.73	50.77	0.77:1	43.41
Plasmon K2	72.44	7.13	20.43	1.86:1	65.10

$a = \frac{A-B}{B}$; $b = \frac{A-B}{A}$ (A is atomic ratio of Ag and B is atomic ratio of Br) [17]

K1, while more Ag NPs from reduction of rich AgBr NPs are formed with plasmon K2. This is ascribed to ammonium hydroxide ionizing the carboxylic functional groups on AC surface leading to the formation of more carboxylate anions. The formed carboxylate anions act as additional capping sites for AgBr NPs dispersion and growth through electrostatic interactions between the carboxylate anions and silver cations [14].

1.3.2 Crystal Phase and Structures by X-Ray Diffraction

The crystal structures and the existence of metallic Ag in the nanocomposites were established with XRD investigation. As shown in Fig. 1.2, the XRD pattern of the Ag/AgBr-AC nanocomposites indicated distinct diffraction peaks that are ascribed to face centered cubic phase of AgBr (JPCDS 079-0148) and metallic Ag NPs (JCPDS 071-3762) [18]. These peaks at the 2θ include 26.6° (111), 31.1° (200), 44.3° (220), 54.8° (222), 64.8° (400), 73.4° (420) for AgBr and 38.0° (111), 44.2° (200), 64.4° (220) and 77.8° (311) all belong to Ag NPs [19]. The XRD results show that the
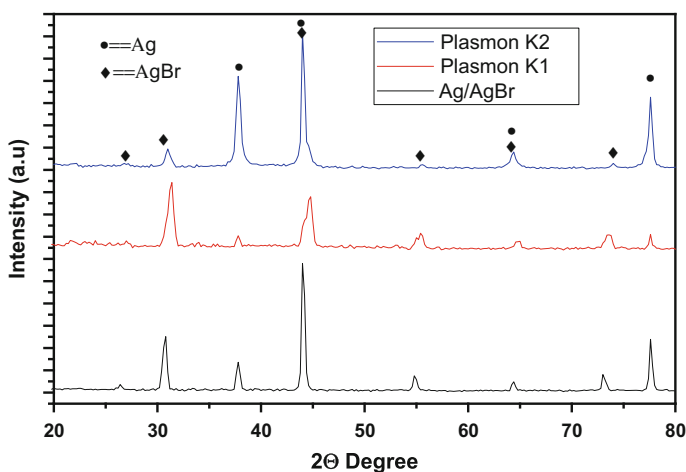
Fig. 1.2 XRD patterns of the synthesized Ag/AgBr-AC nanocomposites and Ag/AgBr

formed nanocomposites are composed of abundant Ag NPs based on the distinct peaks of Ag and AgBr nanoparticles. The intensity ratio of $I_{(200)}/I_{(220)}$ of AgBr peaks for plasmon K1 and K2 are about 1.06 and 0.68, which are higher than that of Ag/AgBr NPs at 0.42. This observation confirms that synthesized Ag/AgBr materials growth directions are <100> direction with high exposed facet of {111} AgBr NPs [20]. This {111} facets of AgBr from previous work describe the facets as possessing higher surface energy than facets of {100} and {110} with enhanced catalytic activities [21]. As a result, the plasmon K1 with a high ratio of the {111} facet AgBr NPs will exhibit higher catalytic activity as compared to plasmon K2 and Ag/AgBr with lower ratios.

1.3.3   Fourier-Transform Infrared (FTIR) Analysis

The FTIR analysis confirms the synergistic interaction between AC and Ag/AgBr NPs. The AC [22] displays a broad peak at 3333 cm^{-1} which corresponds to O–H stretching, while the carbonyl stretching peak is at 1706 cm^{-1} [23] and the peak at 1567 cm^{-1} is ascribed to the carboxylic (–COO) stretching vibration (Fig. 1.3). The characteristic peaks of C–OH and C–O–C are found at 1367 and 1227 cm^{-1} respectively. The carbonyl-stretching band shifted to high wavenumber in the Ag/AgBr-AC nanocomposites (Fig. 1.3), which confirms the formation of the nanocomposite as observed with other reports [24, 25] using carbonaceous material in hybridization of plasmonic materials.

Fig. 1.3 FTIR spectrum of AC, plasmon K1 and K2
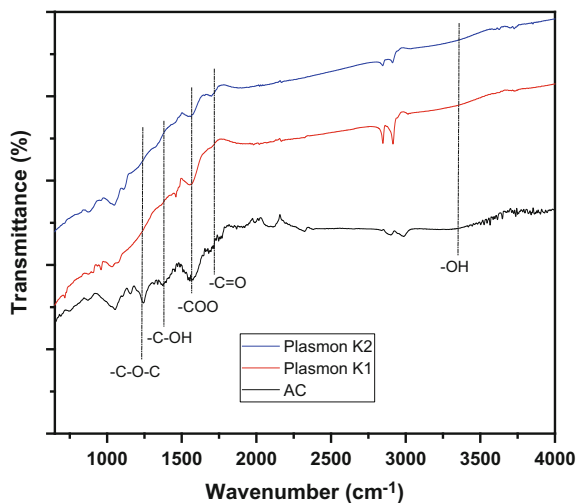
1.3.4 Optical Properties of Ag/AgBr-AC

The as-prepared nanocomposites (plasmon K1 and K2) display strong absorptions both in the UV and visible regions as shown in Fig. 1.4. This further confirms the presence of metallic Ag NPs in both nanocomposites, which generates surface plasmon resonance (SPR) absorption in the visible region [26]. As the tailored SPR properties of Ag NPs anchored on AgBr are influenced by controlled microstructure (size, morphology, and composition) [7], plasmon K1 nanocomposite exhibits more intense absorption in the visible region as compared with plasmon K2, which can be ascribed to oriented SPR properties of Ag NPs. The as-prepared plasmon K1 on the basis of controlled microstructures will possess higher photocatalytic activity than plasmon K2 in the whole solar spectrum region.

1.3.5 Electrochemical Properties

The electrochemical impedance spectra (EIS) Nyquist plots and equivalent circuit utilized in fitting the curve are shown in Fig. 1.5, where R_s denotes the series resistance of electrolyte, R_d is the diffusion resistance, R_{ct} is the charge transfer resistance, while CPE, C_f, and W_s are the constant phase element, chemical capacitance and Warburg resistance between the photoanode and electrolyte respectively. The plasmon K1 displays a smaller arc radius as compared to plasmon K2 and Ag/AgBr in the EIS Nyquist plots (Fig. 1.5), which signify a reduced charge transfer resistance with enhanced interfacial separation of charge carriers. The charge transfer resistance (R_{ct}) calculated from the equivalent circuit model values for plasmon K1, K2 and Ag/AgBr are given in Table 1.2. Plasmon K1 has least R_{ct} values with the highest efficiency for

Fig. 1.4 UV–Vis diffusive reflection spectra of plasmon K1 and plasmon K2
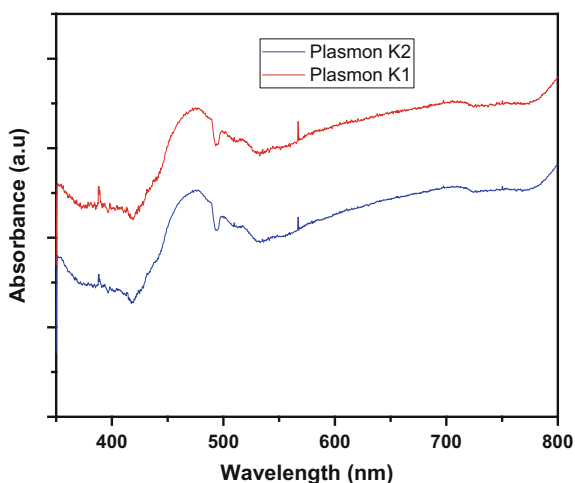
Fig. 1.5 EIS Nyquist plots of plasmon K1, plasmon K2 and Ag/AgBr with an equivalent circuit diagram
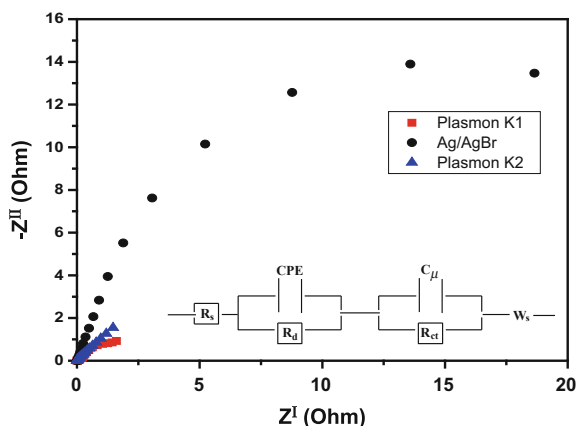
Table 1.2 The charge resistance values of different Ag/AgBr samples in accordance with a series circuit

Sample	R_s (Ω)	R_d (Ω)	R_{ct} (Ω)
Plasmon K1	126	7602	1266
Plasmon K2	140	21,061	3885
Ag/AgBr	173	257,075	4163

electron-hole separation for enhancing the generation of reactive active species for tetracycline (TC) degradation. This is ascribed to the well-controlled microstructure of Ag/AgBr nanoparticles with exposed active sites and also the synergetic coupling of Ag and AgBr with activated carbon. The carbon support behaves as a transport medium in the separation of charge carriers from the Ag/AgBr nanoparticles.

1.3.6 Photocatalytic Degradation of Tetracycline

The photocatalytic activities of the as-prepared samples were assessed by degradation of tetracycline (TC) under visible light irradiation. As shown in Fig. 1.6a, after 180 min of degradation of TC, only 24.66% removal was achieved in the absence of the photocatalyst, indicating that TC molecule is highly stable under visible light irradiation. However, with other photocatalysts prepared in this work, the decrease in concentration of TC as a function of time is evident in Fig. 1.6a. The Ag/AgBr showed visible light activity on the degradation of TC (59.82%), while the dispersion of Ag/AgBr on AC using above described synthetic route improves the degradation rate significantly. Plasmon K1 induces more degradation rate (92.08%) than plasmon K2 (81.12%) due to the tailored SPR properties of Ag NPs and also restrained recombination of photogenerated charge carriers by the activated carbon in transferring the photogenerated charge (e$^-$) away which enhances the charge separation efficiency.

Fig. 1.6 **a** Photocatalytic activity of as-prepared nanocomposites on TC degradation under visible light and **b** decrease in maximum absorption peak of TC at different irradiation times using plasmon K1 as a photocatalyst
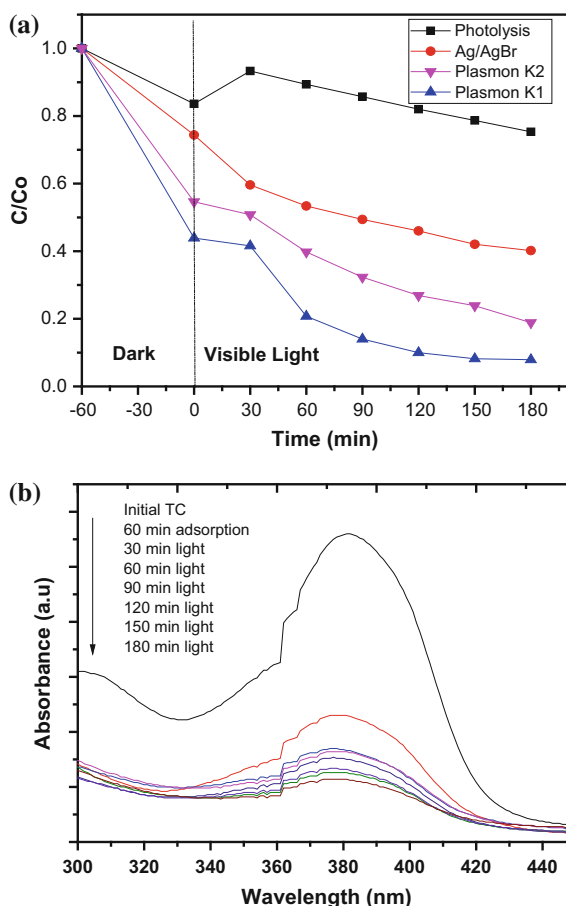
Overall, plasmon K1 photocatalytic performance was higher than that of plasmon K2, Ag/AgBr and photolysis in the degradation of TC.

Figure 1.6b shows the UV–Vis absorption plot of TC degradation in the presence of plasmon K1 under visible light irradiation. The characteristic maximum absorption peak of TC (376 nm) decreases rapidly as the degradation time increases. The catalytic degradation rates of TC over the as-prepared photocatalyst and photolysis all obey the pseudo-first-order kinetics [27] (Fig. 1.7a). The equation model is $\ln(C/C_o) = -kt$, where C_o is the initial concentration of TC, C is the concentration at the irradiation time t, and the slope (k) is the apparent first-order rate constant (min^{-1}). The k values for dispersion of Ag/AgBr on AC nanocomposites are higher than Ag/AgBr and photolysis (Fig. 1.7b). The k value for plasmon K1 is 2, 3 and 9 times faster than plasmon K2, Ag/AgBr and photolysis respectively in this work.

Fig. 1.7 **a** Pseudo-first-order
reaction kinetics and
b corresponding apparent
rate constants of as-prepared
nanocomposites for TC
degradation
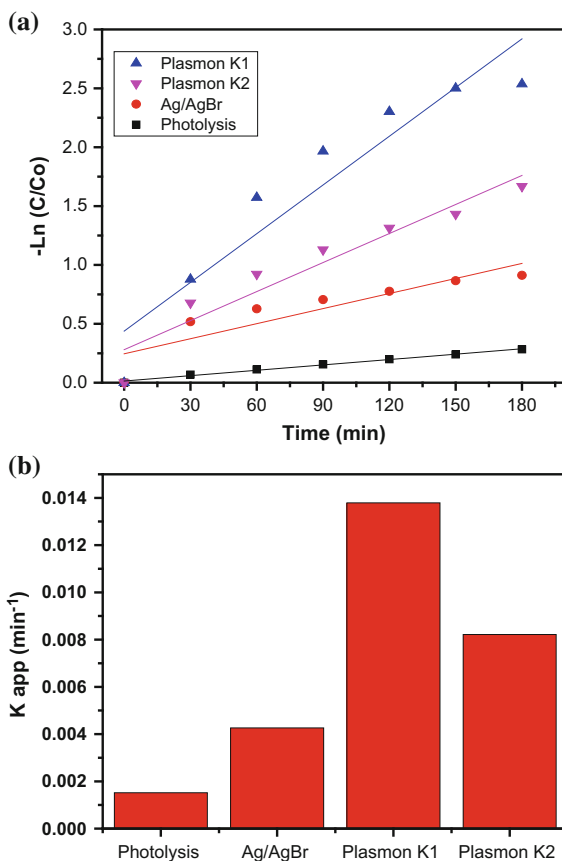
1.3.7 Photocatalytic Mechanism

For further confirmation of active reactive species responsible for enhanced pho-
todegradation of TC over plasmon K1 and plasmon K2 under visible light irradia-
tion, a host of different scavenger solutions (1 mmol) such as benzoquinone (BQ),
isopropanol (IPA) and ethylenediaminetetraacetic acid disodium (EDTA-Na$_2$) were
added to TC solution to quench $\cdot O_2{}^-$, $\cdot OH$, and h^+ in the degradation process. The
degradation rate of TC decreases significantly to 9–14% and 32–40% in the pres-
ence of BQ and EDTA-Na$_2$ respectively (Fig. 1.8a), which indicates $\cdot O_2{}^-$ and h^+
greater influence in the removal of TC. However, the degradation rate of TC was
not affected by the addition of IPA, indicating that $\cdot OH$ is not the major reactive
radical and combination of all the scavengers highlights their participation in TC
degradation. Overall, the $\cdot O_2{}^-$ is majorly responsible for enhanced TC degradation,
as its significant role is further explored in this study.

Fig. 1.8 **a** Photocatalytic
degradation of TC solution
over plasmon K1 and K2
with different scavengers and
b quantification of $^{\cdot}O_2{}^-$
reactive species using NBT
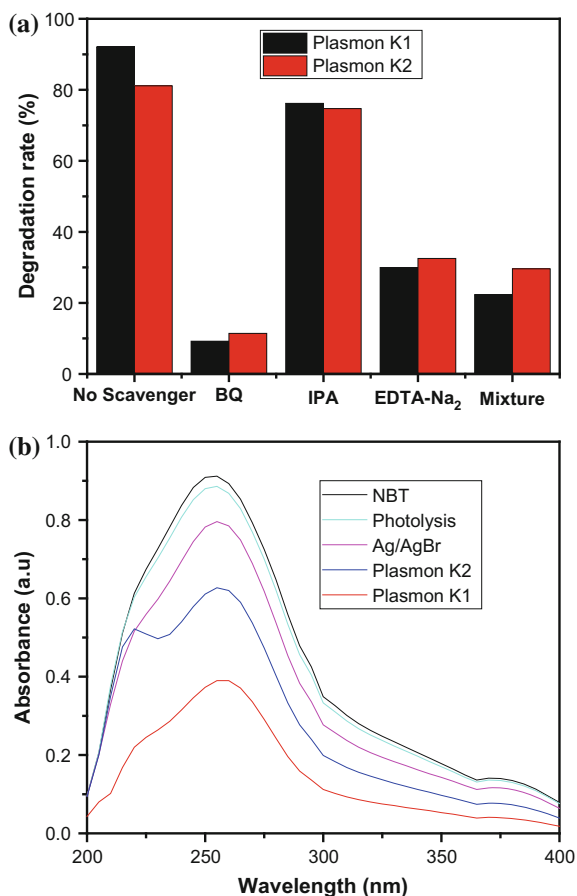
To confirm the rate of formation of $^{\cdot}O_2{}^-$ in this study, degradation of nitroblue tetrazolium (NBT) to diformazan [28] under visible light irradiation was carried out. The generation rate of $^{\cdot}O_2{}^-$ is measured by the decrease in absorbance peak of NBT (259 nm) with degradation time. A higher amount of reactive $^{\cdot}O_2{}^-$ is produced with plasmon K1 (Fig. 1.9b) with faster decline in absorbance peak, which is in tune with its enhanced degradation rate on TC as compared to plasmon K2, Ag/AgBr and photolysis.

Furthermore, the stability of plasmon K1 was evaluated. The nanocomposite still keeps its original catalytic performance after 5 cycle runs on TC degradation as shown in Fig. 1.9a under visible light irradiation. Our findings reveal that the plasmon K1 will have an extraordinary photocatalytic performance for a host of organic compounds elimination with good stability under visible light irradiation.

Figure 1.9b illustrates the plausible reaction mechanism of plasmon K1 on the degradation of TC under visible light irradiation. The TC solution was adsorbed on the surface of the AC through electrostatic adsorption [29]. The AC and the smaller
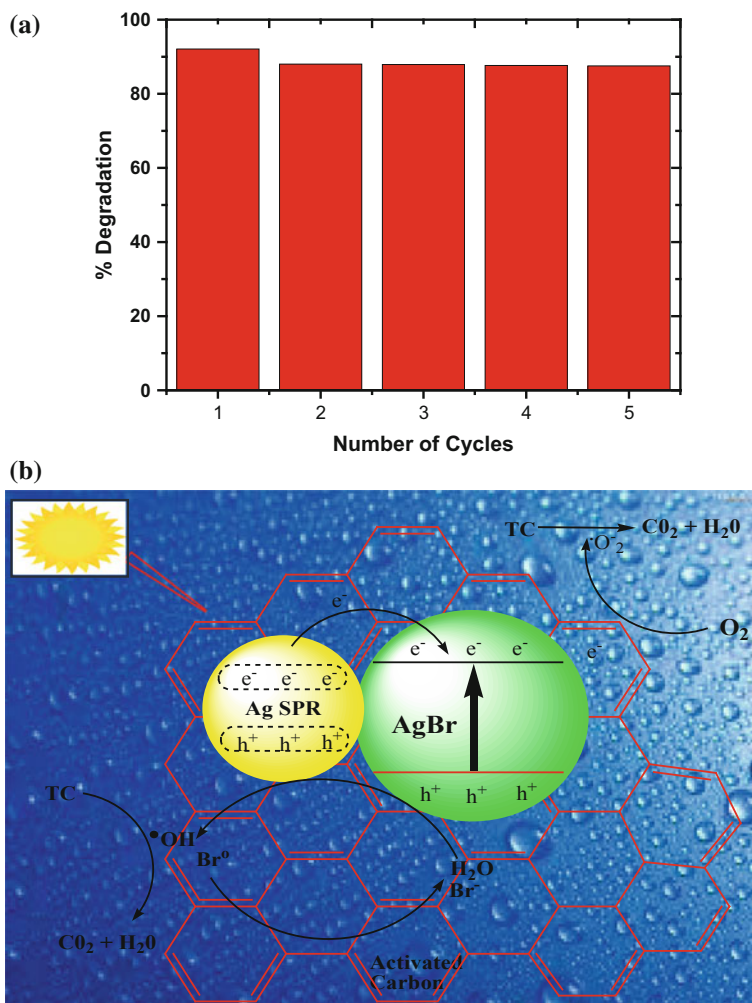
Fig. 1.9 The degradation rate of TC solution by plasmon K1 photocatalyst **a** five recycling runs and **b** plausible photocatalytic reaction mechanism

particle size of the overall nanocomposite increase the active sites between TC and photocatalyst, with the generation of reactive species for enhanced degradation of TC. Under visible light irradiation, both Ag and AgBr can generate photogenerated electron-hole pairs, while the controlled SPR attributes of Ag NPs result in efficient interfacial separation of photogenerated charge carriers [5]. There is first the transport of separated electrons from photoexcited Ag NPs into the conduction band (CB) of AgBr through the Schottky barrier. Then the AC further transfers the electron away from the CB of AgBr, which reacts with adsorbed oxygen to generate the reactive superoxide species, which is a strong oxidant species that degrades the adsorbed TC

effectively [30, 31]. The holes left behind on the surface of Ag and in the valence band (VB) of AgBr [32] react with H_2O to form $^{\cdot}OH$; this formed reactive species will also degrade TC effectively under visible light irradiation. The positively charged holes also oxidize Br^- to Br^0, a reactive species that can also oxidize TC and is reduced back to Br ions again [7].

From the analysis and discussion described above, the tailored SPR properties of Ag NPs from the controlled microstructure of Ag/AgBr-AC nanocomposite, speedier interfacial separation of photogenerated charge carriers and large generation of reactive superoxide species in plasmon K1 from thermal polyol route all resulted in higher photocatalytic activity on TC removal in this study.

1.4 Conclusion

In summary, the microstructure of Ag/AgBr-AC nanocomposites (plasmon K1 and K2) were effectively controlled in this study through two different synthetic approaches (thermal polyol and template-assisted method), then subsequently utilized in the degradation of tetracycline under visible light irradiation. Both plasmon K1 and K2 have spherical shape with the distribution of Ag/AgBr nanoparticles with an average particle size between 160 and 190 nm on the surface of activated carbon as support. However, based on uniform nanospheres morphology, smaller particle size, a more exposed facet of AgBr and restrained recombination of charge carriers in the generation of reactive species, plasmon K1 displays exceptional enhanced photocatalytic degradation of tetracycline as compared to plasmon K2 and Ag/AgBr under visible light. The activated carbon presence in the nanocomposite significantly boosted the transport and separation efficiency of charge carrier, and the overall stability in the catalytic process after several repetitive cycles.

References

1. Zhang H, Liu P, Feng Y, Yang F (2013) Fate of antibiotics during wastewater treatment and antibiotic distribution in the effluent-receiving waters of the Yellow Sea, northern China. Mar Pollut Bull 73:282–290
2. Chao Y, Zhu W, Yan B, Lin Y, Xun S, Ji H, Wu X, Li H, Han C (2014) Macroporous polystyrene resins as adsorbents for the removal of tetracycline antibiotics from an aquatic environment. J Appl Polym Sci 131:40561
3. Lu Z, Chen F, He M, Song M, Ma Z, Shi W, Yan Y, Lan J, Li F, Xiao P (2014) Microwave synthesis of a novel magnetic imprinted TiO$_2$ photocatalyst with excellent transparency for selective photodegradation of enrofloxacin hydrochloride residues solution. Chem Eng J 249:15–26

4. Xiao X, Ge L, Han C, Li Y, Zhao Z, Xin Y, Fang S, Wu L, Qiu P (2015) A facile way to synthesize Ag@ AgBr cubic cages with efficient visible-light-induced photocatalytic activity. Appl Catal B: Environ 163:564–572

5. Kuai L, Geng B, Chen X, Zhao Y, Luo Y (2010) Facile subsequently light-induced route to highly efficient and stable sunlight-driven Ag–AgBr plasmonic photocatalyst. Langmuir 26:18723–18727

6. Zhu M, Chen P, Liu M (2012) Ag/AgBr/graphene oxide nanocomposite synthesized via oil/water and water/oil microemulsions: a comparison of sunlight energized plasmonic photocatalytic activity. Langmuir 28:3385–3390

7. Wang P, Huang B, Zhang X, Qin X, Jin H, Dai Y, Wang Z, Wei J, Zhan J, Wang S (2009) Highly efficient visible-light plasmonic photocatalyst Ag@ AgBr. Chem-A Eur J 15:1821–1824

8. Yan T, Zhang H, Luo Q, Ma Y, Lin H, You J (2013) Controllable synthesis of plasmonic Ag/AgBr photocatalysts by a facile one-pot solvothermal route. Chem Eng J 232:564–572

9. Li B, Wang H, Zhang B, Hu P, Chen C, Guo L (2013) Facile synthesis of one-dimensional AgBr@ Ag nanostructures and their visible light photocatalytic properties. ACS Appl Mater Interfaces 5:12283–12287

10. Xu H, Song Y, Liu L, Li H, Xu Y, Xia J, Wu X, Zhao S (2012) Plasmonic-enhanced visible-light driven photocatalytic activity of Ag–AgBr synthesized in reactable ionic liquid. J Chem Technol Biotechnol 87:1626–1633

11. Esmaeili A, Entezari MH (2015) Cubic Ag/AgBr–graphene oxide nanocomposite: sono-synthesis and use as a solar photocatalyst for the degradation of DCF as a pharmaceutical pollutant. RSC Adv 5:97027–97035

12. Esmaeili A, Entezari MH (2016) Sonosynthesis of an Ag/AgBr/graphene-oxide nanocomposite as a solar photocatalyst for efficient degradation of methyl orange. J Coll Interface Sci 466:227–237

13. Chen G, Li F, Huang Z, Guo CY, Qiao H, Qiu X, Wang Z, Jiang W, Yuan G (2015) Facile synthesis of Ag/AgBr/RGO nanocomposite as a highly efficient sunlight plasmonic photocatalyst. Catal Commun 59:140–144

14. Zhu M, Chen P, Liu M (2013) High-performance visible-light-driven plasmonic photocatalysts Ag/AgCl with controlled size and shape using graphene oxide as capping agent and catalyst promoter. Langmuir 29:9259–9268

15. Amin SA, Pazouki M, Hosseinnia A (2009) Synthesis of TiO$_2$–Ag nanocomposite with sol–gel method and investigation of its antibacterial activity against *E. coli*. Powder Technol 196:241–245

16. Wu S, Shen X, Ji Z, Zhu G, Zhou H, Zang H, Yu T, Chen C, Song C, Feng L (2017) Morphological syntheses and photocatalytic properties of well-defined sub-100 nm Ag/AgCl nanocrystals by a facile solution approach. J Alloy Compd 693:132–140

17. Shahzad A, Yu T, Kim WS (2016) Controlling the morphology and composition of Ag/AgBr hybrid nanostructures and enhancing their visible light induced photocatalytic properties. RSC Adv 6:54709–54717

18. Zhu Q, Wang WS, Lin L, Gao GQ, Guo HL, Du H, Xu AW (2013) Facile synthesis of the novel Ag$_3$VO$_4$/AgBr/Ag plasmonic photocatalyst with enhanced photocatalytic activity and stability. J Phys Chem C 117:5894–5900

19. Lou Z, Huang B, Qin X, Zhang X, Cheng H, Liu Y, Wang S, Wang J, Dai Y (2012) One-step synthesis of AgCl concave cubes by preferential overgrowth along <111> and <110> directions. Chem Commun 48:3488–3490

20. Lin Z, Xiao J, Yan J, Liu P, Li L, Yang G (2015) Ag/AgCl plasmonic cubes with ultrahigh activity as advanced visible-light photocatalysts for photodegrading dyes. J Mater Chem A 3:7649–7658

21. Ma X, Dai Y, Lu J, Guo M, Huang B (2012) Tuning of the surface-exposing and photocatalytic activity for AgX (X = Cl and Br): a theoretical study. J Phys Chem C 116:19372–19378

22. López-Peñalver JJ, Sánchez-Polo M, Gómez-Pacheco CV, Rivera-Utrilla J (2010) Photodegradation of tetracyclines in aqueous solution by using UV and UV/H$_2$O$_2$ oxidation processes. J Chem Technol Biotechnol 85:1325–1333

23. Feng Y, Zhou H, Liu G, Qiao J, Wang J, Lu H, Yang L, Wu Y (2012) Methylene blue adsorption onto swede rape straw (*Brassica napus* L.) modified by tartaric acid: equilibrium, kinetic and adsorption mechanisms. Bioresour Technol 125:138–144
24. Petroski J, El-Sayed MA (2003) FTIR study of the adsorption of the capping material to different platinum nanoparticle shapes. J Phys Chem A 107:8371–8375
25. Zhu M, Chen P, Liu M (2011) Graphene oxide enwrapped Ag/AgX (X = Br, Cl) nanocomposite as a highly efficient visible-light plasmonic photocatalyst. ACS Nano 5:4529–4536
26. Jiang J, Li H, Zhang L (2012) New insight into daylight photocatalysis of AgBr@ Ag: synergistic effect between semiconductor photocatalysis and plasmonic photocatalysis. Chem-A Eur J 18:6360–6369
27. Xu J, Wang W, Shang M, Sun S, Ren J, Zhang L (2010) Efficient visible light induced degradation of organic contaminants by Bi_2WO_6 film on SiO_2 modified reticular substrate. Appl Catal B: Environ 93:227–232
28. Obregón S, Zhang Y, Colón G (2016) Cascade charge separation mechanism by ternary heterostructured $BiPO_4/TiO_2/gC_3N_4$ photocatalyst. Appl Catal B: Environ 184:96–103
29. Upadhyay RK, Soin N, Roy SS (2014) Role of graphene/metal oxide composites as photocatalysts, adsorbents, and disinfectants in water treatment: a review. RSC Adv 4:3823–3851
30. Hu C, Peng T, Hu X, Nie Y, Zhou X, Qu J, He H (2009) Plasmon-induced photodegradation of toxic pollutants with $Ag–AgI/Al_2O_3$ under visible-light irradiation. J Am Chem Soc 132:857–862
31. Hou J, Wang Z, Yang C, Zhou W, Jiao S, Zhu H (2013) Hierarchically plasmonic Z-scheme photocatalyst of Ag/AgCl nanocrystals decorated mesoporous single-crystalline metastable $Bi_{20}TiO_{32}$ nanosheets. J Phys Chem A 117:5132–5141
32. Zhang L, Wong KH, Chen Z, Jimmy CY, Zhao J, Hu C, Chan CY, Wong PK (2009) AgBr-Ag-Bi_2WO_6 nanojunction system: a novel and efficient photocatalyst with double visible-light active components. Appl Catal A: Gen 363:221–229

Chapter 2
Emerging Phytochemicals and Bioactive Compounds from a Desert Plant *Prosopis cineraria* (L.) Druce and Future Prospects

Mohammad W. Islam, Samir H. Bloukh, Zehra Edis and Richie R. Bhandare

Abstract *Prosopis cineraria* (L.) Druce (Family Leguminosae, subfamily Mimosoideae) has a number of uses in ethnomedicine. *P. cineraria* has social, ethnological, traditional and remedial effects on the lives of people. *P. cineraria* is an important herbal plant as mentioned in the ancient literature. It is used traditionally for treatment of various ailments like leprosy, dysentery, asthma, leukoderma, dyspepsia and earache. The objective is to review the phytochemicals and the bio potential of the plant. This paper includes an overview on the studies of different herbal extracts, metabolites and major classes of metabolites which are pharmacologically active, like alkaloids and flavonoids, which have anti-tumor, antioxidant, anti-diabetic, anti-nociceptive, estrogenic and antimicrobial activity. A comprehensive literature survey was performed on the phytochemicals present in the different parts of the plant *P. cineraria* and their pharmacological properties with chemical structures. This review was prepared with thorough advanced search by using key words *P. cineraria* (L.) Druce in Google, Google Scholar, PubMed, SciFinder, Scopus and ProQuest as well as from English language scientific journals, magazines and books. The phytochemicals discussed in the present review could be promising candidates to be utilized as bioactive compounds for direct use as drug or herbal extracts as botanical drugs.

Keywords *Prosopis cineraria* · Ghaf · Biopharmaceutical potential · Chemical structures · Phytochemicals · Bioactive compounds · Bioactivity

M. W. Islam · Z. Edis · R. R. Bhandare
Department of Pharmaceutical Sciences, College of Pharmacy and Health Sciences, Ajman University, Ajman, United Arab Emirates
e-mail: m.islam@ajman.ac.ae

Z. Edis
e-mail: z.edis@ajman.ac.ae

R. R. Bhandare
e-mail: r.bhandareh@ajman.ac.ae

S. H. Bloukh (✉)
Department of Clinical Sciences, College of Pharmacy and Health Sciences, Ajman University, Ajman, United Arab Emirates
e-mail: s.bloukh@ajman.ac.ae

2.1 Introduction

The plant *P. cineraria* (L.) Druce (Family Leguminosae, subfamily Mimosoideae) occurs in most of the world's hot arid and semi-arid regions as native or introduced species [1]. This promising multipurpose tree holds an important place in the rural economy [2]. The plants are found in the Thar desert of India and Pakistan, but smaller populations are available in Iran, Afghanistan and the Arabian Peninsula [3, 4].

The invasion of *Prosopis* sp. generates environmental, social and economic benefits worldwide [5–7]. *Prosopis* plays an important role in the rural economy in the northwest region of the Indian subcontinent [2] and has substantial impacts on biodiversity, ecosystem, and local and regional economies. It is used as fuel, fodder, windbreaks, shade, construction materials, and soil stabilization in Africa and Asia [1]. *P. cineraria* is an important native species to the northeastern United Arab Emirates (UAE), locally known as Ghaf tree. *Prosopis* sp. has been reported to be a plant with remarkable properties [8]. It is found on inland sand plains and low dunes of Abu Dhabi Emirate, and appears occasionally in Wadi beds of the Hajar mountain range [9]. *P. cineraria* are among the few trees growing in the arid deserts of the UAE and constitute a major ecological feature in the Northern Emirates of the UAE [10]. *P. cineraria* has been reported to be beneficial for the growth and development of other species [11]. High temperatures, high humidity and low rainfall, typical of this ecoregion, characterize the climate of the UAE [12]. Bedouin lifestyle has been very much associated with the *Prosopis* tree and its products [13]. As the country rapidly modernized due to a change in socioeconomic conditions, the dependency of Bedouins on the plant became less. Therefore, the plant has been badly neglected for scientific studies. Almost no scientific work has been carried out on the plants especially from the medicinal and nutritional potential point of view except in agroforestry related studies [14]. The *Prosopis* sp. has been given a status as one of the national symbols of UAE [15] and got an immense importance in preserving the country's heritage [16].

Literature research showed that almost all the work related to the exploration of medicinal properties of the plant has been carried out in Indian and Afghanistan desert conditions [17–22]. No scientific work has been carried out on the *Prosopis* sp. under Emirate environmental conditions. The plant is yet to be explored for its chemical and pharmaceutical properties [23]. In our laboratory, the chemical, pharmacological and safety studies aiming to explore the therapeutic potential of the plant are under way.

The objective of this article is to provide the emerging phytochemicals and metabolites from *P. cineraria* so that their biopotential could be assessed for possible biopharmaceutical application.

The emerging phytochemicals are the result of the research advancement in the purification and isolation of bioactive compounds from plants, which have undergone new developments in recent years [24–27]. The present review is a thorough compilation of the research data as an overview of the phytochemicals of the plant species

with their pharmacological properties. The reported data on chemical and pharmacological studies of *P. cineraria* could be useful as potential future applications in drug development.

2.2 Methods

For the present review, a systematic web search analysis was conducted from July 2018 until November 2018. The search included chemical, pharmacological and nutritional studies of the plant *P. cineraria*. The databases Scopus, ProQuest, PubMed, SciFinder, as well as Google and Google Scholar were searched by using the keywords "*P. cineraria* (L.) Druce", "Ghaf" and "*Prosopis* sp.". Only results in English language and scientific peer-reviewed journals, magazines and books were included.

2.3 Species

The genus *Prosopis* as described by Burkart [28] consists of 44 species. They have been introduced globally and have become naturalized or invasive in many places [29]. These species of *Prosopis* are present in most of the world's hot arid and semi-arid regions [30]. They can withstand climatic extremes [28], are able to withstand the hottest winds and the driest season, and yet remain alive when other plants would succumb [31].

2.4 Taxonomical Classification

The taxonomic position has been described by Khatri et al. [2].

Kingdom	*Plantae*—Plants
Subkingdom	*Tracheobionta*—Vascular plants
Super division	*Spermatophyta*—Seed plants
Division	*Magnoliophyta*—Flowering plants
Class	*Magnoliopsida*—Dicotyledons
Subclass	*Rosidae*
Order	*Fabales*
Species	*Prosopis cineraria* (L.) Druce
Common name	*Ghaf*

2.5 Distribution

Prosopis has been reported to occur in 129 countries globally while many more countries are climatically suitable [8]. *P. cineraria* is mainly distributed in the deserts of India and Pakistan, Afghanistan, Iran and the Arabian Peninsula [4]. In the Arabian Peninsula, *P. cineraria* exists mostly in the UAE and Oman [9], though it has also been reported as an infrequent species in the eastern and southern margins of Saudi Arabia [32].

2.6 Bioactivity of Extracts and Metabolites

Literature search revealed that most of the studies are carried out either on different extracts of the plant for their pharmacological properties or on isolation and characterization of metabolites. The studies carried out on the metabolites for pharmacological activity are comparatively less in number.

2.6.1 Studies on Extracts of P. cineraria

Various pharmacological studies (Table 2.1) have been reported on different plant extracts including antitumor/cytotoxic activity [33–39], antioxidant activity [37, 40–44] and antimicrobial activity [37, 41, 45–49]. The studies have shown that the cytotoxic, anti-tumor agents involve a free radical quenching mechanism (i.e. OH, ROO). Many plant extracts and natural products, especially phenols, with high antioxidant activity have shown cytotoxic effects in different cell lines [33, 34]. The other pharmacological properties include antidepressant activity [40, 50], analgesic/antipyretic activity [40, 51–53], antihyperlipidemic and antihyperglycemic activity [22, 44, 54–56], anticonvulsant activity [57], bronchodilator activity [58], nootropic activity [59, 60], estrogenic activity [61], muscle relaxing activity [43, 50], anthelmintic activity [62] and antivenom activity [63]. It was reported that the bioactivity of *P. cineraria* extracts showed a good correlation with the usages of the plant in indigenous systems as a folk medicine for various ailments [58]. The extracts are the essential source for metabolites and have therapeutic benefit for treating diseases. This knowledge opens up future perspectives in using active components for drug development [64].

Table 2.1   Bioactivity of different extracts of the plant *P. cineraria* (L.)

Experimental model	Extract	Parts used	Reported bioactivity	References
Antitumor studies/cytotoxic activity	Hydrochloric acid extract	Leaves	Exhibited significant cytotoxicity towards Ehrlich ascites carcinoma tumor model; assessed using survival time, peritoneal cells, haematolological studies, lipid peroxidation and antioxidant enzymes	[33]
	Hydrochloric acid extract	Leaves	Exhibited significant cytotoxicity. The extract was evaluated against *N*-nitrosodiethylamine induced experimental liver tumors in male Wistar rats	[34]
	Alcoholic extract	Leaves, stem, root and flowers	Exhibited weak cytotoxicity against laboratory cultured brine shrimp larva	[35]
	Alcoholic extract	Leaves	The lipid peroxide levels were significantly increased and mitochondrial antioxidant levels decreased in 7,12-dimethylbenzeneanthracene induced breast cancer in Sprague-Dawley rats	[36]
	Silver and copper nanoparticles (CuNPs; AgNPs)	Leaves	Assay results indicated that CuNPs show potential cytotoxic effect followed by AgNPs against MCF-7 cancer cell line	[37]
	Methanolic extract	Leaves	Inhibited the proliferation of MCF-7 breast cancer cells and non-cancerous cell line HBL 100; produced apoptosis	[38]
	Methanolic extract	Leaves	Showed hepatoprotective role by modulating the levels of membrane bound enzymes and suppressing glycoprotein levels against *N*-nitrosodiethylamine-induced phenobarbital promoted liver tumors in male Wistar rats	[39]

Table 2.1 (continued)

Experimental model	Extract	Parts used	Reported bioactivity	References
Antioxidant activity	Petroleum ether, benzene, chloroform, ethyl acetate, methanol and aqueous extracts	Leaves	All fractions of the plant showed scavenging activity. The ethyl acetate and methanolic extracts showed maximum scavenging activity while petroleum ether has minimum scavenging activity	[40]
	Ethanolic extract	Stem, leaves and bark	Exhibited antioxidant potential. The percentages of antioxidant activity are 82.19, 71.16 and 89.92% in stem, leaf and bark extract respectively against the standard, which was ascorbic acid with antioxidant activity of 96.00%, using the DPPH method	[41]
	Methanolic extract	Leaves	Exhibited improved antioxidant status in the homogenate of goat liver slices; protected against oxidative damage	[42]
	Methanolic extract	Pods	Exhibited high antioxidant activity using in vitro method	[43]
	50% Hydro-alcoholic extract	Stem bark	Have shown antioxidant efficacy of the extract	[44]
Antimicrobial activity/antiviral activity	Silver and copper nanoparticles	Leaves	Showed antimicrobial activity against Gram-positive and Gram-negative bacteria. MTT assay results indicated that both nanoparticles showed antimicrobial activity	[37]
	Methanolic and aqueous extracts	Stem bark	Exhibited moderate antibacterial activity using agar well diffusion method	[45]
	Acetone extract	Aerial parts	Exhibited moderate antibacterial activity against three bacterial strains *Staphylococcus aureus*, *Staphylococcus epidermidis* and *Escherichia coli* at the concentration of 175 μg/ml using agar disc diffusion assay	[46]

Table 2.1 (continued)

Experimental model	Extract	Parts used	Reported bioactivity	References
	Methanolic extract and aqueous extract	Stem bark	Methanolic extract showed significant antibacterial activity at 250 µg/ml on various pathogens, using agar disc diffusion method	[47]
	Ethyl acetate and hydro-alcoholic extracts	Stem bark	Exhibited dose dependent activity against two Gram positive (*Staphylococcus aureus*, *Staphylococcus epidermidis*), two Gram-negative (*Escherichia coli*, *Klebsiella pneumoniae*) bacterial strains and two fungal strains (*Aspergillus niger*, *Aspergillus fumigatus*) using agar disc diffusion method	[48]
	Ethyl ether and alcoholic extract	Leaves	Showed positive reactions against micro-organisms *Staphylococcus aureus* (Gram positive), *Escherichia coli* (Gram negative) and *Candida albicans*	[49]
	Various extracts	Stem bark	Moderate antibacterial activity was observed in the extract against *Salmonella*, *Staphylococcus*, *Bacillus*, *Escherichia*, *Pseudomonas* species using agar well diffusion method	[45]
	Methanolic extract	Leaves	Showed significant antimicrobial activity against several multidrug resistant bacterial and fungal strains	[72]
	Different extracts	Stem bark	Exhibited antihelmintic activity against *Pheretima posthuma* as compared to the standard drug piperazine citrate	[62]
Antidepressant	Aqueous extract	Leaves	The leaf extract significantly decreased the duration of immobility time in Forced swim test. The antidepressant effect of leaf extract was compared to that of standard imipramine	[50]
	Aqueous extract	Leaves	Significantly decreased the duration of immobility time in force swimming test	[62]

Table 2.1 (continued)

Experimental model	Extract	Parts used	Reported bioactivity	References
Analgesic/antipyretic activity	Petroleum ether; ethyl acetate and ethanol extracts	Stem bark and root	Showed a significant analgesic activity in rats, using Eddy's hot plate model	[51]
	Aqueous extract	Root	Significant analgesic activity in albino mice as compared to control, using acetic acid induced writhing test model	[52]
	Aqueous extract	Root	Exhibited a significant antipyretic activity at same dose using Brewer's yeast induced hyperpyrexia model	[52]
	Petroleum ether extract	–	Exhibited significant anti-pyretic activity, when compared with other extracts Brewer's yeast induced hyperpyrexia model	[53]
	Aqueous extract	Leaves	Exhibited a significant antipyretic activity using Brewer's yeast induced hyperpyrexia model	[51]
	Petroleum ether/ethyl acetate/ethanol extracts	Stem bark	Exhibited a significant antipyretic activity using Brewer's yeast induced hyperpyrexia model	[51]
Antihyperlipidemic/ antihyperglycemic activity	Methanolic extract	Leaves	Produced antidiabetic and antihyperlipidemic effect on *streptozotocin*-induced diabetic Wistar rats	[54]
	70% Ethanol extract	Stem bark	Significantly reduced serum total cholesterol, LDLC, triglyceride, VLDL-C and also ischemic indices in hyper-lipidemic rabbits model	[55]
	Aqueous extract	Leaves	Blood glucose levels were significantly decreased; significant increase in lipids level except HDL observed	[22]
	Hydrochloric acid extract	Leaves	Showed dose dependent effect on the lipid profile; higher dose shows significant action over triglyceride, cholesterol, and also increases the level of the HDL	[22]

Table 2.1 (continued)

Experimental model	Extract	Parts used	Reported bioactivity	References
	70% ethanol extract	Fruit	Showed anti-hyperlipidemia and antioxidant activities	[56]
	50% Hydro-alcoholic extract	Stem bark	Fasting blood glucose level decreased significantly, comparable to that of standard glibenclamide; reduction and liver glycogen content was significantly increased as compared to control group in hyperglycemic mice, orally administered once in a day for 45 days	[44]
Anticonvulsant activity	Methanolic extract	Plant	Showed significant anticonvulsant activity using maximal electroshock and *pentylenetetrazole* induced convulsions models	[57]
Bronchodilator activity	Methanolic extract	Stem bark	Produced bronchodilatory activity tested on carbachol-induced contractions in isolated rabbit tracheal preparations	[58]
Nootropic activity	Methanolic extract	Stem bark	Significantly improved both spatial reference and working memories in the spatial working memory using Morris water-maze test and spatial working memory models	[59, 60]
Estrogenic activity	Methanolic extract	Pods	Exhibited estrogenic activity in vitro using vaginal cornification assay, using an ovariectomized rat model	[61]
Muscle relaxing activity	Aqueous extract	Leaves	Exhibited muscle relaxing activity using rota rod test	[43]
	Aqueous extract	Leaves	Exhibited significant skeletal muscle relaxant activity using rota rod test. The extract produced a significant decrease in fall off time and its efficacy was found to be comparable with Diazepam	[50]
Anthelmintic activity	Different extracts	Stem bark	Exhibited anthelmintic activity	[57]
Antivenom activity	Aqueous extract	Bark	Used for identifying various protein toxins present in the venom of Indian cobra	[63]

2.6.2   Studies on Metabolites of P. cineraria

Various metabolites from *P. cineraria* have been mentioned in the literature
(Tables 2.2 and 2.3). Flavonoids reported from *P. cineraria* include quercetin,
rutin, luteolin, patuletin, patulitrin and prosogerin A, prosogerin B, prosogerin C,
prosogerin D and prosogerin E. Apigenin belongs to flavones isolated from aerial
part and exhibited antibacterial, antidermatitic and anti-inflammatory activity [65,
66]. Quercetin exhibited cytotoxicity [65, 67], patulitrin from flowers showed cyto-
toxicity against Lewis lung carcinoma in vivo and the luteolin inhibited skin cancer
[68]. The alkaloids found in the *Prosopis* extract showed broad-spectrum antibac-
terial activity against both Gram-positive and Gram-negative bacteria comparable
to penicillin, streptomycin, ampicillin, sulphamethoxazole and tetracyclin [19, 69].
Alkaloids exhibited anticonvulsant activity [70]; tannins from barks of *P. cineraria*
exhibited antibacterial and antiviral activity [66] and produce anthelmintic activity
[17]. Terpenoids from pods exhibited antioxidant activity [26]. Steroids reported
from *P. cineraria* are cholesterol, 7,24-tirucalladien-3-one, campesterol, stigmas-
terol, β-sitosterol, stigmasta-4,6-dien-3-one. Steroids like β-sitosterol, campesterol,
stigmasterol isolated from leaves caused reduction of cholesterol [44]. Tryptamine
from bark showed antibacterial and antiamoebic activity [65]. Hydroxycinnamic acid
and coumaric acid derivatives also exhibited antioxidant properties [71]. In the drug
discovery process, secondary metabolites play a major role and determine the fate
of the prospective drugs.

2.7   Nutrients

Various parts of the *P. cineraria* have nutritional phytoconstituents. It has been
reported that the dried pods of the plant are a good source against protein malnutri-
tion [74]. In another study, foliage and pods have been shown to be rich in protein,
carbohydrates, mineral matter and fiber content [75]. The dry pods also contained
good amount of iron, copper, manganese, and zinc contents [76]. Seeds contain fixed
oils, fatty acids such as gallic acid, palmitic acid, stearic acid, oleic acid and linoleic
acid [77, 78]. The seed alone contains 31–37% crude protein and 3.4–8.5% crude
fiber. The seed coat contains 60–69% crude protein [76]. Green leaves of *P. cineraria*
contain 14–18% crude protein, 13–22% crude fiber and about 6% ash, with a high
calorific value of 5000 kcal [76]. Calcium and phosphorus are important minerals
found in *P. cineraria* [79] and together with Zn contents showed antioxidant activity
in *diabetes mellitus* [75]. Amino acids isolated from leaves and pods are aspartic
acid, glutamic acid, serine, glycine, histidine, threonine, arginine, alanine, proline,
tyrosine, valine, methionine, cysteine, isoleucine, leucine, phenylalanine and lysine
[80].

Table 2.2 Bioactivity of metabolites isolated from the plant *P. cineraria* (L.)

Bioactivity	Metabolites	Parts used	Reported bioactivity	References
Antitumor/cytotoxic activity	Quercetin	Leaves	Exhibited cytotoxicity activity on human cancer cell lines viz. HeLa and MCF-7 using MTT assay	[67]
	Patulitrin	Flowers	Cytotoxic against Lewis lungs carcinoma in vivo	[73]
	Quercetin	Leaves	Cytotoxic activity	[65]
	Luteolin	Leaves	Inhibited skin cancer mechanisms in vitro and in vivo	[68]
Antioxidant activity	Terpenoids	Pods	Antioxidant activity	[26]
	Hydroxycinnamic acid and coumaric acid derivatives	Pods	Antioxidant activity	[71]
Antimicrobial/antiviral/antiamoebic activity	Tannin	Bark	Antibacterial and antiviral activity	[66, 65]
	Tryptamine	Bark	Antibacterial and anti-amoebic activity	[65]
	L-arabinose	Aerial parts	No activity reported	[66]
	Apigenin	Aerial parts	Antibacterial, antidermatitic, and anti-inflammatory activity	[66, 65]
Antidepressant activity	Saponins, flavonoids, alkaloids, glycosides, tannins and phenolics	Leaves	Antidepressant, anti-pyretic, and analgesic activity	[11]
	5-Hydroxytryptamine	Aerial parts	Antidepressant	[66, 65]
Antihyperlipidemic/antihyperglycemic activity	Steroids like β-sitosterol, campesterol, and stigmasterol	Leaves	Caused reduction in cholesterol level in blood; exhibited antioxidant, hypoglycemic and thyroid inhibiting properties	[44]

Table 2.2 (continued)

Bioactivity	Metabolites	Parts used	Reported bioactivity	References
Anticonvulsant activity	Alkaloids	Leaves	Anticonvulsant activity in pentylene tetrazole-induced convulsion method	[70]
Anti-inflammatory	Apigenin	Aerial parts	Antibacterial, antidermatitic, and anti-inflammatory activity	[66, 65]
Hepatoprotective activity	Isorhamnetin-3-diglucoside	Aerial parts	Hepatoprotective activity	[66, 65]

2.8 Discussion
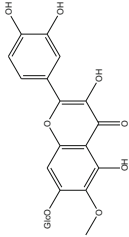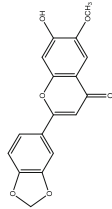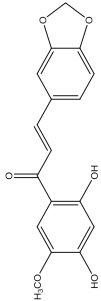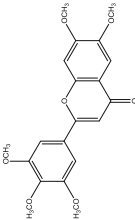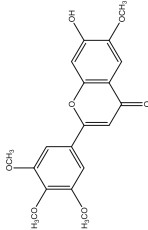
A considerable amount of work has been carried out on the genus *Prosopis*, mainly on chemical investigations and biological activity evaluation. *Prosopis* sp. have varied phytoconstituents, possess different kinds of biological activities and are used medicinally since ancient times. However, for the present review the focus is on the single species *P. cineraria.*

The studies of the *P. cineraria* using extracts (Table 2.1) showed strong antioxidant capacity, and the extracts can be considered as a good source of natural antioxidants and antimicrobials. Phenols are very important plant constituents because of their scavenging ability on free radicals due to their hydroxyl groups. Therefore, the phenolic content of plants may contribute directly to their antioxidant action [81]. It is interesting to note that measured bioactivities of *P. cineraria* reported are in agreement with the traditional usage for the treatment of various ailments [59].

Phytopharmacological studies on *P. cineraria* revealed the presence of valuable active compounds [82]. The presence of secondary metabolites in this plant ensure that this plant has medicinal uses against different human diseases [83]. The distribution of chemical constituents in various parts of the plant with respect to the role of the plant in ethnomedicine is an important aspect to correlate [84], urging further researches on chemical compounds and their interrelationship with impacts of climate change.

The literature review reveals that the majority of activity measurements have been carried out on various polar extracts and fewer studies have been done using aqueous extracts. However, the pharmacological properties reported are analgesic, anti-inflammatory, antimicrobial, antiviral, hypoglycemic activity and proved to be effective against cancer cells and the malignant growth when tested on several cell lines.

Table 2.3 Chemical constituents of *Prosopis cineraria* (L.)

Chemical group	Compounds	Structure	References
Flavonoids	Patulitrin		[84]
	Prosogerin A (6-methoxy-7-hydroxyl-3′4′-methylenedioxyflavone)		[85]
	Prosogerin B (2′,4′-dihydroxy-5′-methoxy-3,4-methylenedioxy chalcone (II))		[85]
	Prosogerin C (6,7,3′,4′,5′-pentamethoxyflavone)		[86]
	Prosogerin D (6′,3′,4′5′-tetramethoxy-7-hydroxylflavone)		[87]
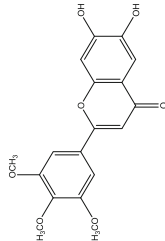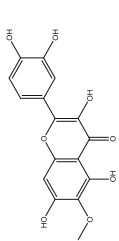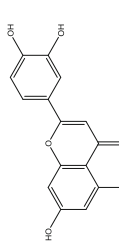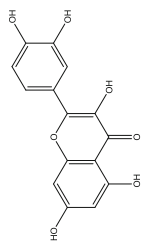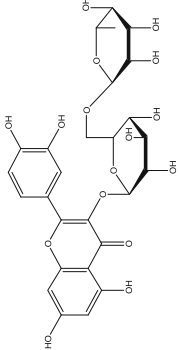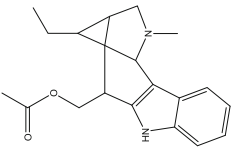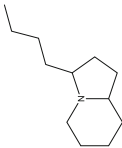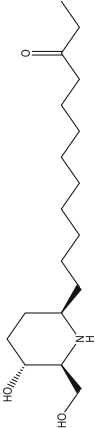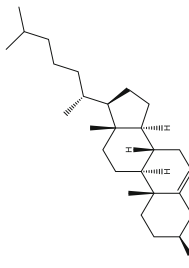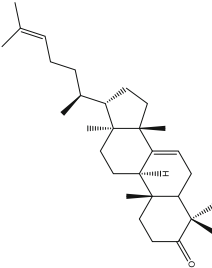
Table 2.3 (continued)

Chemical group	Compounds	Structure	References
	Prosogerin E (6,7-dihydroxy-3′,4′,5′-trimethoxyflavone)		[76]
	Patuletin		[76, 77]
	Luteolin		[76, 77]
	Quercetin		[73]

(continued)

Table 2.3 (continued)

Chemical group	Compounds	Structure	References
	Rutin		[73, 77]
Alkaloids	Spicigerine		[85]
	Dasycarpidan-1-methanol, acetate (ester)		[88]
	3-Butylindolizidine		[88]
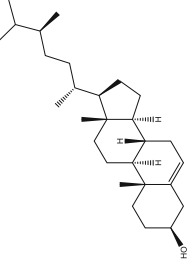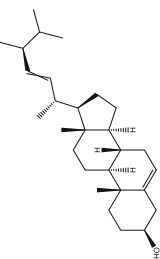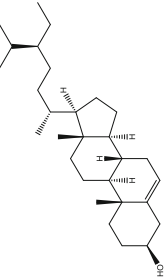
(continued)

Table 2.3 (continued)

Chemical group	Compounds	Structure	References
	Prosophylline		[88]
Steroids	Cholesterol		[84]
	7,24-Tirucalladien-3-one		[88]

(continued)

Table 2.3 (continued)

Chemical group	Compounds	Structure	References
	Campesterol		[76]
	Stigmasterol		[76]
	β-Sitosterol		[76]

(continued)

Table 2.3 (continued)
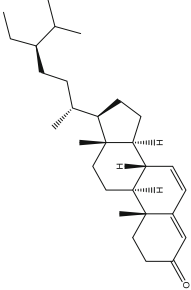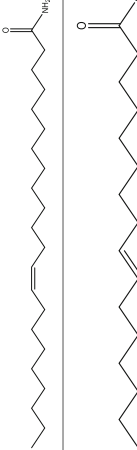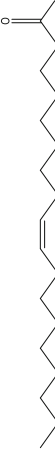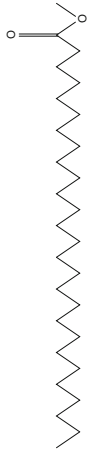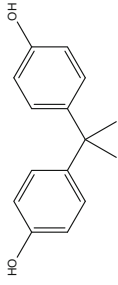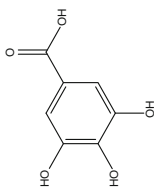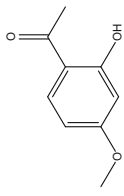
Chemical group	Compounds	Structure	References
	Stigmasta-4,6-dien-3-one		[76]
Fatty acids and derivatives	(Z)-13-Docosenamide		[88]
	9-Hexadecenoic acid		[88]
	Palmitic acid		[77]
	Stearic acid		[77]
	Oleic acid		[77]
	Linoleic acid		[77]

(continued)

Table 2.3 (continued)

Chemical group	Compounds	Structure	References
	Heneicosanoic acid		[89]
	Methyl heptacosanoate		[89]
Phenolic compounds	4,4′-(1-Methylethylidene) bis-phenol		[88]
	Gallic acid		[76, 77]
	Paeonol		[90]

(continued)

Table 2.3 (continued)
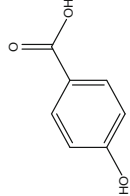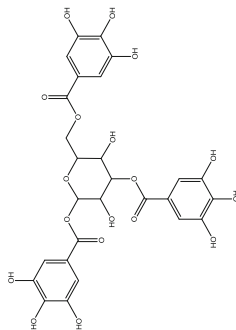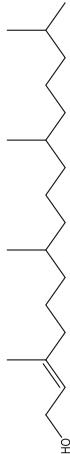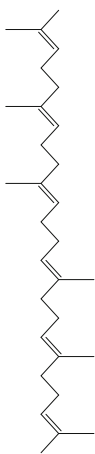
Chemical group	Compounds	Structure	References
	4-Hydroxybenzoic acid		[89]
Tannins	Tannin		[73]
Terpenoids	Phytol		
	Squalene		[88]

(continued)

Table 2.3 (continued)
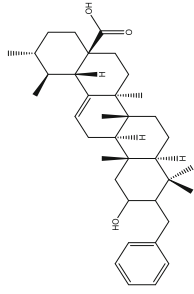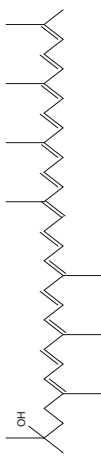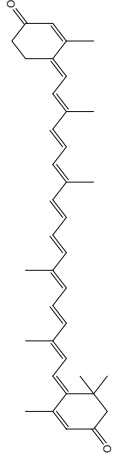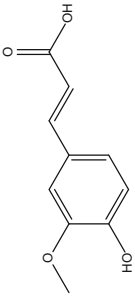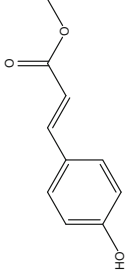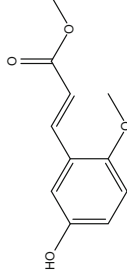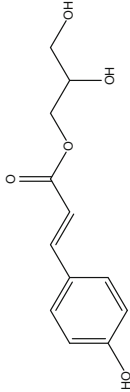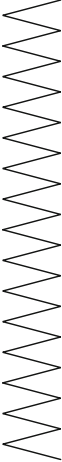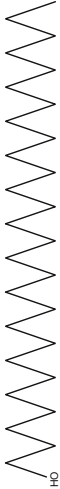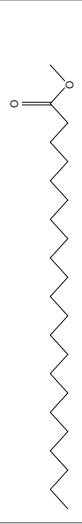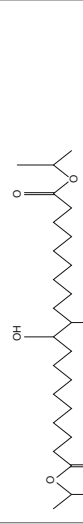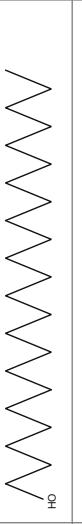
Chemical group	Compounds	Structure	References
	3-Benzyl-2-hydroxy-urs-12-en-28-oic acid		[88]
	Rhodopin		[91]
	Rhodoxanthin		[88]
Phenyl propanoids	Ferulic acid		[90]

(continued)

Table 2.3 (continued)

Chemical group	Compounds	Structure	References
	Methyl 4-hydroxycinnamate		[89]
	Methyl 2-methoxy-5-hydroxycinnamate		[89]
	O-Coumaroylglycerol		[89]
Others (alcohols, esters, diketones, alkanes)	Hentriacontane		[74, 92]
	Octacosanol		[74, 92]
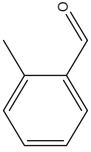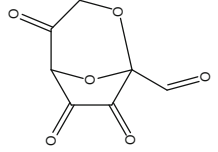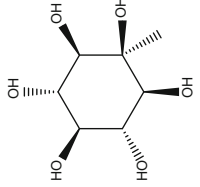
(continued)

Table 2.3 (continued)

Chemical group	Compounds	Structure	References
	Methyl docosanoate		[74, 92]
	Diisopropyl-10,11-dihydroxyicosane-1,20-dioate		[74, 92]
	Tricosan-1-ol		[74, 92]
	Dichloronitromethane		[88]
	Octamethylcyclotetrasiloxane[a]		[88]
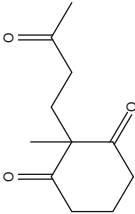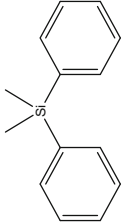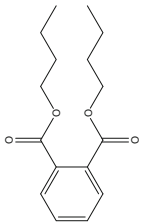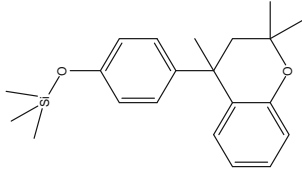
(continued)

Table 2.3 (continued)

Chemical group	Compounds	Structure	References
	2-Methylbenzaldehyde		[88]
	2,7-Anhydro-1-heptulofuranose		[88]
	2-[(9Z)-9-Octadecene-1-yloxy]ethanol		[88]
	2-C-Methyl myoinositol		[88]
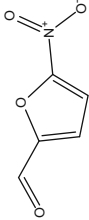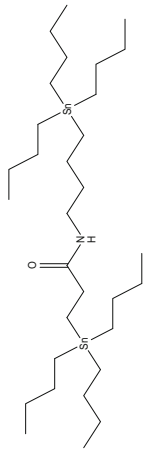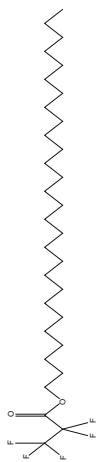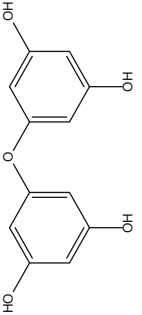
(continued)

Table 2.3 (continued)

Chemical group	Compounds	Structure	References
	2-Methyl-2-(3-oxobutyl)-1,3-cyclohexanedione		[88]
	Diphenyldimethylsilane[a]		[88]
	Dibutyl phthalate[a]		[88]
	2,2,4-Trimethyl-4-(4′-trimethylsilyloxyphenyl) chromane[a]		[88]
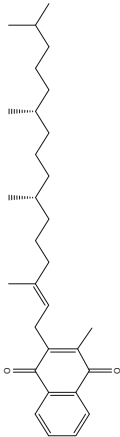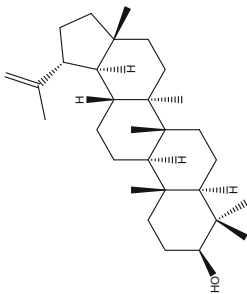
Table 2.3 (continued)

Chemical group	Compounds	Structure	References
	5-Nitro-2-furaldehyde		[88]
	N-[4-(Tributylstannyl)butyl]-3-tributylstannylpropionamide[a]		[88]
	17-Pentatriacontene		[88]
	Octacosyl pentafluoropropionate		[88]
	5,5′-Oxybis-1,3-benzendiol		[26]

(continued)

Table 2.3 (continued)

Chemical group	Compounds	Structure	References
	Vitamin K		[91]
	n-Octacosyl acetate		[91]
	Nonacosan-8-one		[93]
	Lupeol		[93]

[a] Artefact of isolation (no natural product)

2.9 Conclusions

P. cineraria is well-adapted to extreme environmental conditions and grows in a wide array of geographic areas. It can be concluded that *P. cineraria* is a promising medicinal plant with a wide range of pharmacological activities. It is used traditionally as an antioxidant, antimicrobial, anti-diabetic and against hypertension. It exhibits hepatotoxicity, lipid lowering activity, anti-inflammatory and anticancer potential. In addition to their medicinal importance, *P. cineraria* has significant nutritional importance. The present review is aimed to summarize the up-to-date information on the phytochemicals of *P. cineraria* and their bioactive importance.

Emerging phytochemicals and their pharmacological activity have paved the way to explore and find out the possibility for new and natural medication to be used safely and effectively by patients, especially in the field of carcinogenic disease prevention and in the ever-increasing global demand for food.

2.10 Future Prospects

In the recent past, much of the scientific attention has been drawn to the discovery of new and effective therapeutic agents from natural sources. Reports of *P. cineraria* and its activities have gained attention leading to the development of further medicinal uses. A multitude of phytoconstituents has been explored for their prospective use to prevent the occurrence of a number of ailments including carcinogenesis. A number of studies on anti-inflammatory, analgesic, antioxidant, antiviral, antibacterial, anti-diabetic, anticancer, antimicrobial, antifungal and plant defense activities have also reported the therapeutic efficacy of extracts and the plants secondary metabolites. The scientific information on *P. cineraria* includes various aspects of chemical and biological uses underlining the plants as potentially important. There is an ample scope for future research on *P. cineraria* in many important fields including cancer prevention and treatment, also as antimicrobial agents in the present critical era of emerging resistance towards classical antibiotics. Numerous chemical components of this plant are a rich source of nutrients providing useful future applications as phytochemicals and hence further pharmacological investigations are warranted.

References

1. Pasiecznik NM, Felker P, Harris PJ, Harsh L, Cruz G, Tewari J et al (2001) The '*Prosopis juliflora*' -'*Prosopis pallida*' complex: a monograph. HDRA Publishing, Coventry, UK, p 172
2. Khatri A, Rathore A, Patil U (2010) *Prosopis cineraria* (L.) Druce: a boon plant of desert-an overview. Int J Biomed Adv Res 1:141–149
3. Gallacher DJ, Hill JP (2005) Status of *Prosopis cineraria* (Ghaf) tree clusters in the Dubai Desert Conservation Reserve. Tibullus 15:3–9
4. Pasiecznik N, Harris P, Smith S (2004) Identifying tropical *Prosopis* species: a field guide. HDRA Publishing, Coventry, UK, p 29
5. Chikuni M, Dudley C, Sambo E (2005) *Prosopis glandulosa* Torrey (leguminosae-Mimosoidae) at Swang'oma, Lake Chilwa plain: a blessing in disguise? Malawi J Sci Technol 7:10–16
6. Geesing D, Al-Khawlani M, Abba ML (2004) Management of introduced *Prosopis* species: can economic exploitation control an invasive species? Unasylva 55:36–5544
7. Arshad M, Ashraf M, Arif N (2006) Morphological variability of *Prosopis cineraria* (L.) Druce, from the Cholistan desert, Pakistan. Genet Resour Crop Evol 53:89–96
8. Shackleton RT, Le Maitre DC, Pasiecznik NM, Richardson DM (2014) Prosopis: a global assessment of the biogeography, benefits, impacts and management of one of the world's worst woody invasive plant taxa. AoB Plants 6:1–18
9. Jongbloed MVD, Feulner GR, Böer B, Western AR, Environmental Research and Wildlife Development Agency (2003) The comprehensive guide to the wild flowers of the United Arab Emirates. Environmental Research and Wildlife Development Agency (ERWDA), Abu Dhabi, pp 1–574
10. Gallacher D, El-Keblawy A (2016) Macromorphology and recruitment of *Prosopis cineraria* in the United Arab Emirates. Ecol Environ Conserv 22:499–504
11. Abdel Bari E, Fahmy G, Al Thani N, Al Thani R, Abdel-Dayem M (2007) The Ghaf tree, *Prosopis cineraria* in Qatar. Environmental Studies Centre and National Council for Culture, Arts and Heritage, Doha, p 163
12. Böer B (1997) An introduction to the climate of the United Arab Emirates. J Arid Environ 35:3–16
13. Lemons J, Victor R, Schaffer D (2003) Conserving biodiversity in arid regions: best practices in developing nations. Springer Science & Business Media, The Netherlands
14. Orwa C, Mutua A, Kindt R, Jamadars R, Simons A (2009) Agroforestry database: a tree species reference and selection guide version 4.0. World Agroforestry Centre ICRAF, Nairobi, Kenya
15. Philp M (2013) UAE groups help to save Ghaf trees on UN 'Combat Desertification Day'. 7 DAYS in Dubai, Al Sidra Media. Retrieved 11 Sept 2013
16. Alam H, Khattak JZ, Ppoyil SB, Kurup SS, Ksiksi TS (2017) Landscaping with native plants in the UAE: a review. Emirates J Food Agric 6:729–74117
17. Pareek AK, Garg S, Kuma M (2015) *Prosopis cineraria*: a gift of nature for pharmacy. Int J Pharma Sci Res 6:958–964
18. Chaudhry P (2011) *Prosopis cineraria* (L) Druce a lifeline tree species of the Thar Desert in danger. Biodivers Ecol Sci 1:289–293
19. Mann H, Shankar Narayan K (1980) The role of *Prosopis cineraria* in an agropastoral system in Western Rajasthan. Africa International Livestock Centre for Africa, Addis Ababa, pp 437–442
20. Panwar D, Pareek K, Bharti CS (2014) Unripe pods of *Prosopis cineraria* used as a vegetable (Sangri) in Shekhawati region. Int J Sci Eng Res 5:2014
21. Rogers KE (2000) The magnificent mesquite, 1st edn. University of Texas Press, USA. ISBN-10:0292771
22. Sharma D, Singla YP (2013) Evaluation of antihyperglycemic and anti-hyperlipidemic activity of *Prosopis cineraria* (Linn.) in Wistar rats. J Sci Innov Res 2:751–758

23. Ghazanfar SA, Al-Al-Sabahi AM (1993) Medicinal plants of Northern and Central Oman (Arabia). Econ Bot 47:89–98

24. Altemimi A, Lakhssassi N, Baharlouei A, Watson DG, Lightfoot DA (2017) Phytochemicals: extraction, isolation, and identification of bioactive compounds from plant extracts. Plants (Basel) 6:42

25. Altemimi A, Lightfoot DA, Kinsel M, Watson DG (2015) Employing response surface methodology for the optimization of ultrasound assisted extraction of lutein and β-carotene from spinach. Molecules 20:6611–6625

26. Liu Y, Singh D, Nair MG (2012) Pods of Khejri (*Prosopis cineraria*) consumed as a vegetable showed functional food properties. J Funct Foods 4:116–121

27. Corrales M, Toepfl S, Butz P, Knorr D, Tauscher B (2008) Extraction of anthocyanins from grape by-products assisted by ultrasonic, high hydrostatic pressure or pulsed electric fields: a comparison. Innov Food Sci Emerg Technol 9:85–91

28. Burkart A (1976) A monograph of the genus *Prosopis* (Leguminosae subfam. Mimosoideae). J Arnold Arboretum 57:450–525

29. Gallacher D, Hill J (2005) Status of *Prosopis cineraria* (ghaf) tree clusters in the Dubai Desert Conservation Reserve. Tribulus 15:3–9

30. Shiferaw H, Teketay D, Nemomissa S, Assefa F (2004) Some biological characteristics that foster the invasion of *Prosopis juliflora* (Sw.) DC. at Middle Awash Rift Valley Area, northeastern Ethiopia. J Arid Environ 58:135–154

31. Felker P, Cannell G, Osborn J, Clark P, Nash P (1983) Effects of irrigation on biomass production of 32 *Prosopis* (mesquite) accessions. Exp Agric 19:187–198

32. Mandaville JP (1990) Flora of eastern Saudi Arabia. Kegan Paul International London and New York jointly with the National Commission for Wildlife Conservation and Development, Riyadh. ISBN 07103-0371-8

33. Robertson S, Narayanan N, Raj Kapoor B (2011) Antitumor activity of *Prosopis cineraria* (L.) Druce against Ehrlich ascites carcinoma-induced mice. Nat Prod Res 25:857–862

34. Maideen N, Velayutham R, Manavalan G (2011) Protective activity of *Prosopis cineraria* against N-nitrosodiethylamine induced liver tumors in accordance to mitochondrial lipid peroxidation, mitochondrial antioxidant and liver weight. Cont J Pharm Sci 5:1e6

35. Satish PV, Somaiah K, Brahmam P, Rekha NS, Sunita K (2015) Antimalarial activity of *Prosopis cineraria* (L) Druce against chloroquine sensitive *Plasmodium falciparum* 3D7 strain. Eur J Pharm Med Res 2:295–303

36. Ramakrishnan G, Raghavendran HR, Vinodhkumar R, Devaki T (2006) Suppression of N-nitrosodiethylamine induced hepatocarcinogenesis by silymarin in rats. Chem Biol Interact 161:104–114

37. Jinu U, Gomathi M, Saiqa I, Geetha N, Benelli G, Venkatachalam P (2017) Green engineered biomolecule-capped silver and copper nanohybrids using *Prosopis cineraria* leaf extract: enhanced antibacterial activity against microbial pathogens of public health relevance and cytotoxicity on human breast cancer cells (MCF-7). Microb Pathog 105:86–95

38. Sumathi S, Dharani B, Sivaprabha J, Raj KS, Padma P (2013) Cell death induced by methanolic extract of *Prosopis cineraria* leaves in MCF-7 breast cancer cell line. Int J Pharmacol Sci Invent 2:21–26

39. Maideen NM, Velayutham R, Manavalan G (2012) Protective effect of *Prosopis cineraria* against N-nitrosodiethylamine induced liver tumor by modulating membrane bound enzymes and glycoproteins. Adv Pharm Bull 2:179

40. Dharani B, Sumathi S, Sivaprabha J, Padma P (2011) *In vitro* antioxidant potential of *Prosopis cineraria* leaves. J Nat Prod Plant Resour 1:26–32

41. Mohammad IS, Haji Muhammad Shoaib Khan NA, Rasool F (2013) Biological potential and phytochemical evaluation of *Prosopis cineraria*. World Appl Sci J 27:1489–1494

42. Bangaruswamy D, Jambunathan S, Padma PR, Sundaravadivelu S (2015) *Prosopis cineraria* leaf extract protect H_2O_2 induced oxidative stress-induced cell death in *Saccharomyces cerevisiae*. Asian J Pharm Clin Res 8:311–315

43. Karim AA, Azlan A (2012) Fruit pod extracts as a source of nutraceuticals and pharmaceuticals. Molecules 17:11931–11946
44. Sharma N, Garg V, Paul A (2010) Antihyperglycemic, antihyperlipidemic and antioxidative potential of *Prosopis cineraria* bark. Indian J Clin Biochem 25:193–200
45. Velmurugan V, Arunachalam G, Ravichandran V (2010) Antibacterial activity of stem bark of *Prosopis cineraria* (Linn.) Druce. Arch App Sci Res 2:147–150
46. Salar RK, Dhall A (2010) Antimicrobial and free radical scavenging activity of extracts of some Indian medicinal plants. J Med Plants Res 4:2313–2320
47. Preeti K, Avatar SR, Mala A (2015) Pharmacology, phytochemistry and therapeutic application of *Prosopis cineraria* Linn: a review. J Plant Sci 3:33–39
48. Robertson S, Narayanan N (2009) Pharmacognostical and antimicrobial studies of the stem barks of *Prosopis cineraria* (L) Druce. Res J Pharmacognosy Phytochem 1:227–231
49. Kapoor BB, Bansal R (2013) Antimicrobial screening of some medicinal tree species of Nagaur District of Rajasthan. Int J Herbal Med 1:10–11
50. George M, Joseph L, Sharma A (2012) Antidepressant and skeletal muscle relaxant effects of the aqueous extract of the *Prosopis cineraria*. Braz J Pharm Sci 48:577–581
51. Manikandar RV, Rajesh V, Kumar RS, Perumal P, Raj CD (2009) Analgesic and anti-pyretic activity of stem bark of *Prosopis cineraria* (Linn) Druce. J Pharm Res 2:660–662
52. Kumar A, Yadav SK, Singh S, Pandeya S (2011) Analgesic activity of ethanolic extract of roots of *Prosopis cineraria* (L.) Druce. J App Pharm Sci 1:158
53. Gupta A, Verma S, Gupta AK, Jangra M, Pratap R (2015) Evaluation of *Prosopis cineraria* (Linn.) Druce leaves for wound healing activity in rats. Ann Pharm Res 3:70–74
54. Asija S, Jeyabalan G, Ahuja A, Asija R (2015) Formulation and evaluation of *Prosopis cineraria* (Linn.) Druce phospholipid complex. Asian J Chem Pharm Res 3301–3305
55. Purohit A, Ram H (2012) Hypolipidemic and antiatherosclerotic effects of *Prosopis cineraria* bark extract in experimentally induced hyperlipidemic rabbits. Asian J Pharm Clin Res 5:106–109
56. Jain PG, Surana SJ (2015) Hypolipidemic activity of *Prosopis cineraria* L (Druce) fruit extract and molecular modeling study with farnesoid X receptor (FXR). Trop J Pharm Res 14:1621–1628
57. Velmurugan V, Arunachalam G, Ravichandran V (2012) Anticonvulsant activity of methanolic extract of *Prosopis cineraria* (Linn) Druce stem barks. Int J PharmTech Res 4:89–92
58. Janbaz KH, Haider S, Imran I, Zia-ul-Haq M, De Martino L, De Feo V (2012) Pharmacological evaluation of *Prosopis cineraria* (L.) Druce in gastrointestinal, respiratory, and vascular disorders. Evid Based Complement Altern Med 212:7–12
59. Bithu BS, Reddy NR, Prasad SK, Sairam K, Hemalatha S (2012) *Prosopis cineraria*: a potential nootropic agent. Pharm Biol 50:1241
60. Gupta A, Sharma G, Pandey S, Verma B, Pal V, Agrawal SS (2014) *Prosopis cineraria* and its various therapeutic effects with special reference to diabetes: a novel approach. Int J Pharm Sci Rev Res 27:328–333
61. Marquez SR, Aguirre FG, Alcantara M, Diaz EG, Gutierrez MM, Silva MA, Lopez G, Romero C, Chemineau P, Keller M, Delgadillo JA (2012) Mesquite pod extract modifies the reproductive physiology and behavior of the female rat. Horm Behav 61:549–558
62. Velmurugan V, Arunachalam G, Ravichandran V (2011) Anthelmintic potential of *Prosopis cineraria* (Linn.) Druce stem barks. Asian J Plant Sci Res 1:88–91
63. Sivaraman T, Rajesh SS, Elango V (2013) *In vivo* studies on detoxifying actions of aqueous bark extract of *Prosopis cineraria* against crude venom from Indian cobra (*Naja naja*). Bangladesh J Pharmacol 8:395–400
64. Newman DJ, Cragg GM (2007) Natural products as sources of new drugs over the last 25 years. J Nat Prod 70:461–477
65. Prabha DS, Dahms HU, Malliga P (2014) Pharmacological potentials of phenolic compounds from *Prosopis* spp.-a. J Coast Life Med 2:918–924

66. Duke JA (2014) Dr. Duke's phytochemical and ethnobotanical databases. National Government Publication, Fulton, USA
67. Robertson S, Narayanan N (2014) Isolation and characterization of secondary metabolite from *Prosopis cineraria* (L.) Druce for anticancer activity. World J Pharm Res 3:876–884
68. López-Lázaro M (2009) Distribution and biological activities of the flavonoid luteolin. Mini Rev Med Chem 9:31–59
69. Leakey R (1980) Biology and potential of *Prosopis* species in arid environments, with particular reference to *P. cineraria*. J Arid Environ 3:9–24
70. Rahman AA, Samoylenko V, Jacob MR, Sahu R, Jain SK, Khan SI, Tekwani BL, Muhammad I (2011) Antiparasitic and antimicrobial indolizidines from the leaves of *Prosopis glandulosa* var. *glandulosa*. Planta Med 77:1639–1643
71. Ferguson LR, Zhu S-T, Harris PJ (2005) Antioxidant and antigenotoxic effects of plant cell wall hydroxycinnamic acids in cultured HT-29 cells. MN Food Res 49:585–593
72. Khan R, Zakir M, Afaq SH, Latif A, Khan AU (2010) Activity of solvent extracts of *Prosopis spicigera*, *Zingiber officinale* and *Trachyspermum ammi* against multidrug resistant bacterial and fungal strains. J Infect Dev Countries 4:292–300
73. Garg A, Mittal SK (2013) Review on *Prosopis cineraria*: a potential herb of Thar desert. Drug Invent Today 5:60–65
74. Malik S, Mann S, Gupta D, Gupta RK (2013) Nutraceutical properties of *Prosopis cineraria* (L.) Druce pods. J Pharmacognosy Phytochem 2:66–73
75. Rani B, Singh U, Sharma R, Gupta A, Dhawan NG, Sharma AK et al (2013) *Prosopis cineraria* (L) Druce: a desert tree to brace livelihood in Rajasthan. Asian J Pharm Res Health Care 5:58–64
76. Bhardwaj DK, Gupta AK, Jain RK, Sharma GC (1981) Chemical examination of *Prosopis spicigera* seeds. J Nat Prod 44:656–659
77. Ukani M, Limbani N, Mehta N (2000) A review on the Ayurvedic herb *Prosopis cineraria* (L) Druce. Anc Sci Life 20:58
78. Claude B, Paule S (1979) The manual of natural living, 1st edn. Biddles Limited Guildford, Surrey, UK, p 98
79. Tapia A, Feresin GE, Bustos D (2000) Biologically active alkaloids and a free radical scavenger from *Prosopis* species. J Ethnopharmacol 71:241–246
80. Mason TL, Wasserman BP (1987) Inactivation of red beet *beta glucan synthase* by native and oxidized phenolic compounds. Phytochem 26:2197–2202
81. Chandrakala S, Mallikarjuna K, Reddy C (2013) *In vitro* pharmacological investigations of *Biophytum sensitivum* callus extract: lack of potent activities. J Pharm Negat Results 4:60–62
82. Wild S, Roglic G, Green A, Sicree R, King H (2004) Global prevalence of diabetes: estimates for the year 2000 and projections for 2030. Diabetes Care 27:1047–1053
83. Edeoga HO, Okwu DE, Mbaebie BO (2005) Phytochemical constituents of some Nigerian medicinal plants. Afr J Biotechnol 4:685–688
84. Pal D, Chancha MK (2015) *Prosopis cineraria* (L.) Druce: a boon plant of desert—an overview. Int J Sci Eng Res 6:112–114
85. Bhardwaj DK, Bisht MS, Mehta CK, Sharma GC (1979) Flavonoids of *Prosopis spicigera* flowers. Phytochem 18:355–366
86. Bhardwaj DK, Jain RK, Sharma GC, Mehta CK (1978) Prosogerin-C, a new flavone from *Prosopis spicigera* seeds. Indian J Chem B16:1133–1134
87. Bhardwaj DK, Bisht MS, Jain RK (1980) Prosogerin-D, a new flavone of *Prosopis spicigera* seeds. Phytochem 19:1269–1270
88. Aneela S, Dey A, De S (2014) GC-MS analysis of methanolic extract of *Prosopis spicigera*. Int J Phytopharmacol 5:168–171
89. Khan S, Riaz N, Afza N, Nelofar A, Malik A, Ahmed E et al (2006) Studies on the chemical constituents of *Prosopis cineraria*. J Chem Soc Pakistan 28:619–622
90. Singh S, Naresh V, Sharma SK (2013) Pharmacognostic studies on the leaves of *Prosopis cineraria* (L) Druce growing in South Haryana, India. J Pharmacognosy Phytochem 2:320–325
91. Gangal S, Sharma S, Rauf A (2009) Fatty acid composition of *Prosopis cineraria* seeds. Chem Nat Compd 45:705

92. Jewers K, Nagler MJ, Zirvi KA, Amir F (1976) Lipids, sterols, and a piperidine alkaloid from *Prosopis spicigera* leaves. Phytochem 15:238–240
93. Soni LK, Dobhal S, Parasher P, Dobhal MP (2018) Phytochemicals from *Prosopis* sp. Int J Environ Sci Technol 4:9–32

Chapter 3
Conductimetric Analysis and Preliminary Evaluation of Phytochemical Constituents of *Sporobolus spicatus* (Vahl) Kunth [Family: Poaceae] by FTIR and UV–Vis Spectroscopic Techniques

Adewale Olufunsho Adeloye

Abstract FTIR and UV–Vis techniques, being essential tools for analytical and research applications, were used to provide first-hand spectroscopic information on the phytochemical constituents present in *Sporobolus spicatus*, a halophytic plant commonly referred to as salt grass. The plant sample used in the analysis was collected from the Okavango Delta area, Republic of Botswana. Preliminary phytochemical screening on the whole plant parts shows positive tests for flavonoid and phenolic compounds but absence of saponins. FTIR method in the mid-infrared region 4000–400 cm^{-1} revealed the characteristic peak values, intensity and functional groups present in the plant. The FTIR wavenumber frequencies of the crude aqueous-ethanolic extracts of the leaves, stem bark and root compared to corresponding raw dry plant parts confirmed the presence of alcohols, phenols, alkanes, esters, carboxylic acids, aromatics and possibly aliphatic amine compounds as major phytochemical constituents in the plant. The transmission, reflection and absorption data as a function of wavelength and absorption coefficient were determined by UV–Vis spectroscopy in solution and solid states ranging from 200–800 nm on a double beam Perkin Elmer spectrophotometer. Well resolved and separated characteristic broad absorption band peaks at the wavelength λ_{max} 280–450 nm mostly associated with flavonoid and other phenolic compounds were obtained. In addition, a preliminary investigation into salt uptakes ability of the plant in predetermined concentrations of sodium chloride solution was carried out by pH and conductimetry methods. The report in this paper is the first communication on spectroscopic analysis of *Sporobolus spicatus* which is intended to provide useful information for further research on the value-added applications in biotechnology for the development of salt-tolerant crops for use in salt-afflicted agro-ecosystems or as a natural agent for wastewater purification and desalination.

A. O. Adeloye (✉)
Faculty of Applied Sciences, Department of Chemistry, Cape Peninsula University of Technology, Bellville Campus, 7535 Cape Town, Republic of South Africa
e-mail: aowale@gmail.com

3.1 Introduction

Over 831 million hectares which include 397 and 434 million hectares of saline and sodic soil respectively have been reported as total areas of salt-affected soils worldwide [1, 2]. The detrimental effects of the increased salinity on the soil as well as ground water relate to the decreased agricultural land use, strains in sustainable farming practices which are attributed to constant increase in factors such as population pressure, adverse environmental condition, climate change, natural calamities and food shortage [3]. To recover substantial parts of these salt-affected land and ground water for useful applications require large investment to maintain advanced water desalination technologies which include reverse osmosis and membrane filtrations [4]. Many research groups have intensified studies towards the identification of less costly and economically viable alternative technologies of which the use of natural plants for the removal of salts from contaminated soils or water have been put forward especially in the removal of salts in agronomic practices and wastewaters [5–8].

Among the plants so far examined though with scarce information available till date based on their phytodesalination activity potentials, phytochemical constituents and isolation as well as the understanding of the molecular mechanisms used in adaptation and removal of salts are the halophytes. Many authors have reported that most halophytes either excrete or accumulate salts in their morphological, anatomical, physiological parts and/or been involved in biochemical processes [2, 9, 10]. The understanding of the coordination chemistry of metals within plant tissues has been recommended as one of the means to fine-tune the process of phytoremediation in spite of the many challenges facing phytoremediation as a green remediation technology with great potentials [10].

Halophytes have been described as those group of plants that have superior adaptation to live in an extreme saline environment such as seawater, a salt water marsh or a salt desert using certain forms of mechanisms such as osmotic adjustment and ion compartmentalization in their vacuoles to survive the conditions [11]. There is no universally-agreed definition for these plants but, it is clear that the high tolerance of halophytes to salinity is recognized as the common characteristic of these group of plants [7, 12]. It has been reported that based on definition, some plants are categorized as halophytes for their ability to complete the life cycle in a rather high salinity level of about 11.7 g NaCl L^{-1} (200 mM NaCl) [7], and on a broader list in a recent database include certain species of plant that can tolerate a minimum salinity of 4.7 g NaCl L^{-1} (80 mM NaCl) as halophytes [13, 14].

With the growing body of information about molecular markers, genomics and post-genomics, the significant knowledge about the mechanism and control of salinity tolerance at molecular level is appraised. Over two decades, in spite of the few

studies that have been performed on the molecular mechanism of salt tolerance as exhibited by halophytes unlike those studies on concentration on glycophytes, studies involving the understanding of how plants respond to salt stress have been carried out on various halophytes with the findings based on unique genetic makeup that allow them to grow and survive under salt stress conditions [15–24]. Among other studies is that which involved the sodium compartmentation in the vacuolar Na^+/H^+ antiporter (NHX) which explains the move of potentially harmful ions from cytosol into large, internally acidic, tonoplast-bound vacuoles and the mechanism or regulation of the chloride ions [25, 26].

In spite of previous research and reports on halophytic plants so far, little information on the phytochemistry and spectroscopic characterization of compounds present are found in the literature. The focus of the present study is limited to an attempt to report through the use of FTIR, UV-V is spectroscopy, pH and conductimetric properties, of the inherent phytochemical functional groups present in the leaf, stem and root extracts of *Sporobolus spicatus*. The plant (Family: Poaceae), commonly known as salt grass grows near water, has short-tufted perennial stoloniferous, flat blade leaves and is of maximum height of 40 cm [27].

3.2 Materials and Methods

3.2.1 Plant Material

The plant sample used for this study (Fig. 3.1) was collected in the month of February, 2016 from Okavango Delta area of Botswana. The plant was identified and authenticated botanically at the Okavango Research Institute, Maun, Botswana.

Fig. 3.1 *Sporobolus spicatus* growing along water stream and dried ground samples of the leaf, stem and root in bottles

3.2.2   Plant Sample Preparation and Extraction

3.2.2.1   Aqueous Ethanol Extraction

The fresh plant was prepared and separated into various parts (leaf, stem and root) and air-dried at room temperature, and finely cut into pieces before extraction. The three different sectional parts (0.200 g) were extracted with 50% aqueous-ethanol (200 mL) in the cold for 72 h, filtered and concentrated to dryness using a rotary evaporator to obtain ethanolic extracts of the leaf, stem and root. Each dry extract was kept in refrigerator until use.

3.2.2.2   Sodium Chloride Solution Extraction

Sodium chloride solutions with concentration of 1.00 and 0.40 M were prepared respectively by dissolving 58.44 and 23.38 g of NaCl salt in 1000 mL deionized water. Sodium chloride solution extracts of the *S. spicatus* of the leaf and stem were then prepared by weighing 0.20 g dry weight of the leaf and stem in 200 mL, and 0.10 g of the root in 100 mL (based on quantity available). Equivalent amount of the leaf, stem and root were also added to deionized water. The plant materials soaked in salt solutions were left under agitation for 24 h. The extracts were thereafter filtered to measure the pH and conductivity of the filtrates.

3.3   Phytochemical Screening

Preliminary phytochemical screening was carried out on the aqueous-ethanolic (1:1, v/v) extracts of *Sporobulus spicatus* (leaves, stem bark and root) using the standard procedures as reported by Odebiyi and Sofowora [28] to identify the phytochemicals present in the extracts. The tests carried out were for the flavonoids, phenols, and saponins.

3.3.1   Determination of Flavonoids

The ethanolic extract of the leaf, stem and root was each added to a small piece of magnesium ribbon, followed by dropwise addition of concentrated hydrochloric acid. Changes of colours observation from red to crimson and to magenta were taken as positive results for the presence of flavonoid compounds.

3.3.2 Determination of Phenolic Compounds

Each of the plant part ethanolic extracts (leaf, stem and root) was separately stirred in 10 mL of distilled water and then filtered. To the filtrate was added two drops of 5% iron(III) chloride reagent. Blue—black colouration or precipitate was taken as positive result of the presence of phenolic compounds.

3.3.3 Determination of Saponins

Each of the plant parts (leaf, stem and root) was separately stirred in a test tube vigorously; absence of foaming was taken as negative result and absence of saponins.

3.4 Spectroscopic Analysis, pH and Conductivity

FTIR and UV–Vis absorption spectra of the raw dry leaf, stem and root of *Sporobolus spicatus* and the corresponding 50% crude aqueous-ethanol extracts were obtained using FTIR (IRTracer-100) SHIMADZU, MIRacle 10 with Single Reflection ATR Accessory analysis in vibrational frequency range 4000–600 cm^{-1}, at resolution of 8 cm^{-1} with 64 co-added scans. All spectra were subtracted against a background of air spectrum. After every scan, a new reference of air background spectrum was taken. The ATR plate was carefully cleaned by gentle scrub with methanol soaked in soft tissue paper before taking another sample for analysis. During acquisition, room temperature and humidity were maintained at 22 °C and 40% respectively. The Ultraviolet-Visible and UV–Vis reflection spectroscopy were performed in a double beam diode array UV-2600 SHIMADZU spectrophotometer. The spectra were collected from 250–500 nm using a slit width of 10 mm. The pH and conductivity were obtained for each sample's filtrate using InoLab pH 7110 and Thermo scientific conductivity meter (P00187) respectively.

3.5 Results and Discussion

3.5.1 Infrared Spectral Studies of the Dry and Aq. Ethanolic Extracts of Sporobolus Spicatus

The FTIR spectra of each studied *Sporobolus spicatus* leaf, stem and root sample are as shown in Figs. 3.2, 3.3 and 3.4 respectively. The bands identified in each sample are displayed in Table 3.1.
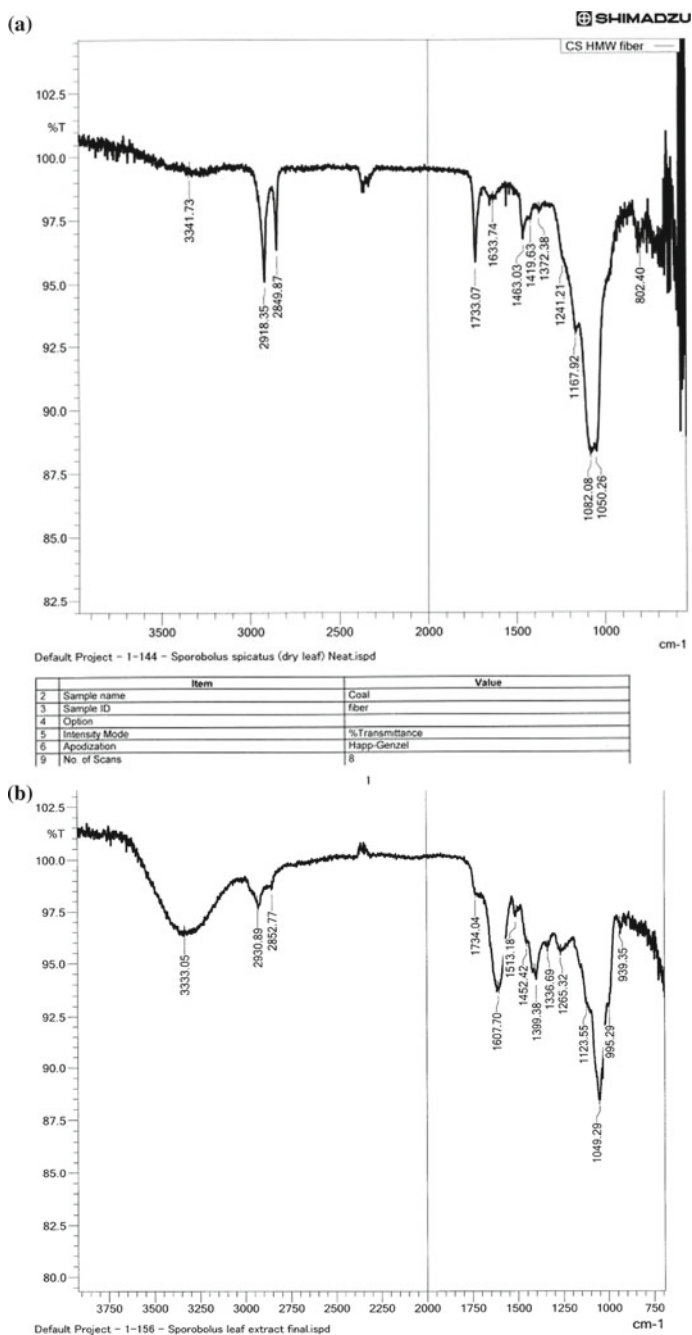
Fig. 3.2 a FTIR spectrum of the dry raw leaf of *Sporobolus spicatus*, b FTIR spectrum of aq. ethanol extract of *Sporobolus spicatus* leaf
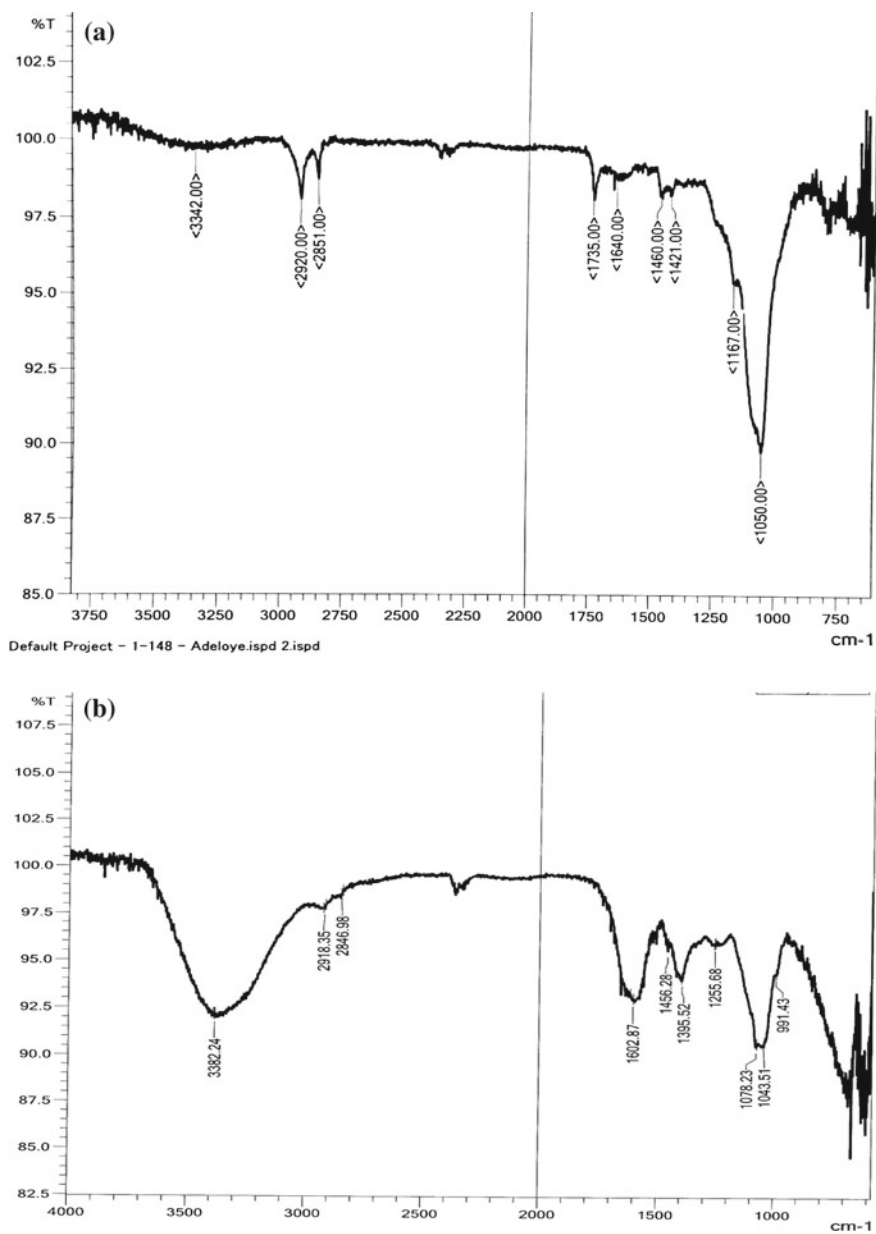
Fig. 3.3 a FTIR spectrum of the dry raw stem of *Sporobolus spicatus*, b FTIR spectrum of aq. ethanol extract of *Sporobolus spicatus* stem

Default Project – 1-146 – Sporobolus spicatus (dry root) Neat.ispd
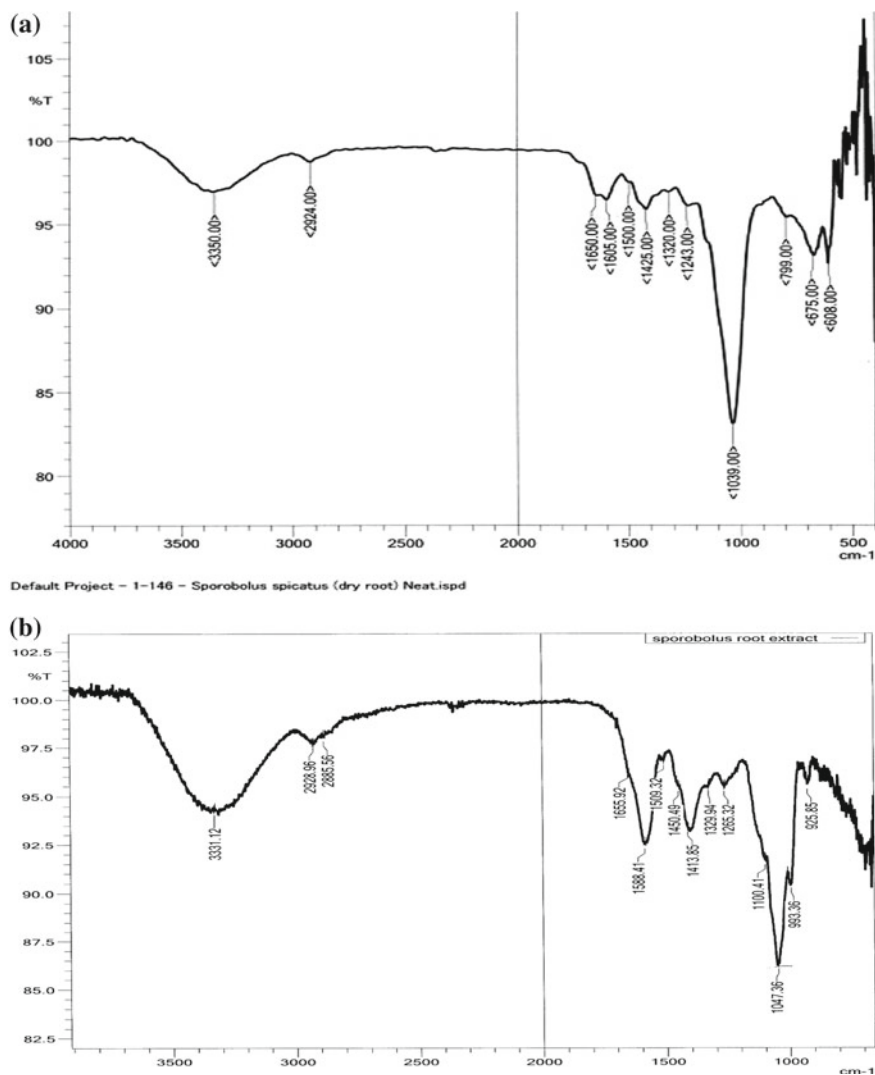
Fig. 3.4 **a** FTIR spectrum of the dry raw root of *Sporobolus spicatus*, **b** FTIR spectrum of aq. ethanol extract of *Sporobolus spicatus* root

3.5.1.1 Discussion on FTIR Spectra

It is possible to relate the specific vibrational frequencies to the functional groups present in the phytochemicals as contained in the three sections of the sample plant. From the spectra, common frequency band peaks are found in all the sample extracts (dry and ethanolic) with slight shifts of ± 5 cm^{-1}. The significant broad frequency band peaks between 3382–3331 cm^{-1} and 2930–2846 cm^{-1} are specific to the OH

Table 3.1 ATR-FTIR wavenumber frequency (cm^{-1}) in *Sporobolus spicatus* plant

Leaf		Stem		Root	
Raw (Dry)	Aq. EtOH	Raw (Dry)	Aq. EtOH	Raw (Dry)	Aq. EtOH
3341	3333	3342	3382	3350	3331
2918	2930	2920	2918	2924	2928
2849	2852	2851	2846	–	2885
1733	1734	1735	–	1650	1666
1633	1604	1640	1602	1605	1588
1463	1513	1460	1456	1500	1509
1419	1452	1421	1395	1425	1420
1372	1399	1167	1255	–	1413
1241	1336	1050	1078	1320	1359
1167	1265	–	1043	–	1266
1082	1123	–	991	–	1100
1050	1049			1039	1047
–	995			799	993
–	939			675	852
802	–			608	–

group and to the C–H stretch vibrations for methyl and methylene groups. The peaks having the values of 1733–1735 cm^{-1} are assigned to the carbonyl υ(C = O) group possibly of the 4-position of ring C of the C6–C3–C6 flavonoid structure, an ester, or carboxylic acid. This band is considerably lower in the root extracts, being observed at 1650 and 1666 cm^{-1}, which may be due to factors associated with the presence of extended π-conjugation and/or hydrogen bonding which lower frequencies. The 1640–1588 cm^{-1} represent the υ(C = C)$_{str.}$; 1463–1419 cm^{-1} peaks correspond to the υ(C–H) bending of alkane; 1399–1336 cm^{-1} peaks are assigned to the carboxylate symmetric υ(–COO^{-}) of the carboxylic acid group; the peaks at 1266–1241 cm^{-1} indicate (C = C) aromatic bending and 1123 cm^{-1} peak is assigned to the υ(C–O–C)$_{str}$ of ethereal group. The strong intense peaks at 1082–1039 cm^{-1} are characteristic of C–C stretching, while bands at 608, 675, 799, 802, 852, 939, 991, 993 and 995 cm^{-1} correspond to the in-plane deformation vibrations of C–H bonds which support the different aromatic substitution patterns in the molecules [29, 30].

3.5.2 UV–Vis Absorption and Reflectance Spectra Studies

The UV–Vis spectra of the *Sporobolus spicatus* extracts obtained in solution of methanol are as shown in Fig. 3.5 and 3.6 respectively for the aq. ethanolic extracts
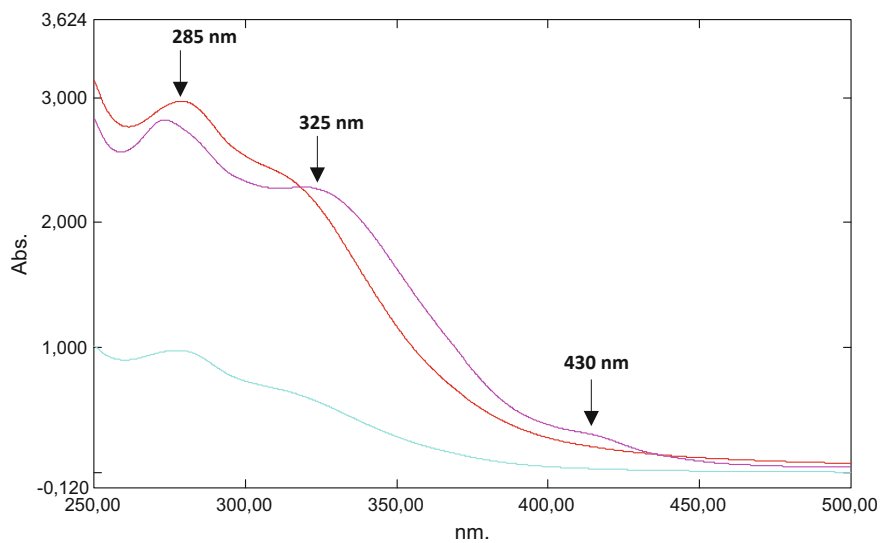
Fig. 3.5 Overlay of UV–Vis spectra of *S. spicatus* (Aq. EtOH extracts) (**Leaf** = pink, **Stem** = red, **Root** = grey)
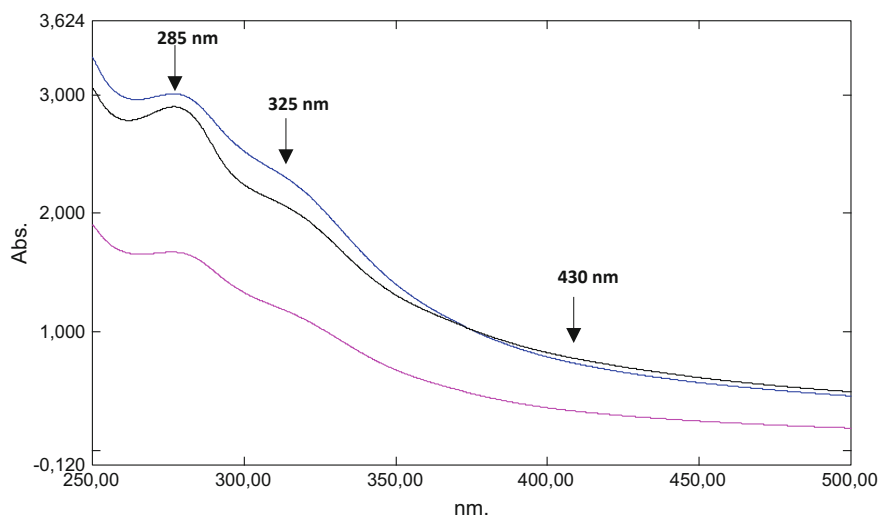
Fig. 3.6 Overlay of UV–Vis spectra of dry *S. spicatus* in NaCl solution (**Leaf** = black, **Stem** = blue, **Root** = pink)

and sodium chloride solution. Non-destructive UV–Vis reflectance spectra for the dry raw leaf, stem and root plant samples are depicted in Fig. 3.7a–c.

The absorption wavelengths of the aqueous ethanolic extracts and dry samples recorded in the range 250–500 nm show for the aqueous extracts of the leaf (λ_{max} 275, 322, and 412 nm), stem (λ_{max} 280, 323 nm), and root (λ_{max} 278 and 320 nm). Similar absorption wavelengths are recorded for the dry samples soaked in NaCl solution with the leaf: λ_{max} 277 and 323 nm; stem: λ_{max} 280 and 320 nm and root: λ_{max} 279 and 311 nm. A common trend in the absorption bands in the crude ethanolic extracts and dry samples was observed with the root having lowest values as when compared to the leaf and stem respectively. It is well known that ultraviolet and visible spectroscopy was one of the earliest techniques routinely used for flavonoid analysis due to the existence of two characteristic UV/Vis bands: band I in the 300 to 550 nm range, arising from the B ring, and band II in the 240–285 nm range, arising from the A ring. Literature shows that while the band I of flavones and flavonols lies in the 240-285 nm range, that of flavanone (no C ring unsaturation) lies in the 270–295 nm range; and conversely, the band II of flavones and flavanones (no 3-OH group) lies around 303–304 nm, and that of 3-hydroxylated flavonols is centered around 352 nm [31, 32]. The similarity in the UV–Vis absorption spectra as recorded for both crude ethanolic extract and dry sample depicts the presence of varied flavonoid compounds in the plant. The presence of hydroxyl group in the structure of flavonoids makes them a hydrogen and/or electron donor(s). The non-destructive reflection spectra of the plant samples were obtained with wavelength scans between 250–500 nm to support the characteristic absorption bands of the aqueous ethanol extracts. It was observed that the root sample showed highest reflective property of 131.72% at λ_{max} 338 nm, followed by the stem, 6.78, 6.59 and 6.21% at relatively close λ_{max} at 335 nm and lower contents at λ_{max} 421 and 449 nm, while for the leaf, percentage reflection was lowered to ~1.19% at λ_{max} 275, 377 and 450 nm. UV–Vis reflectance spectroscopy has been used for proving in situ the organization of chemical constituents in materials and employed in the study of plant surfaces [33, 34]. This is supported by the thin layer chromatography (TLC) in dichloromethane-methanol (9:1) showing the number of spots in the leaf, stem and root extracts as shown in Fig. 3.8. The TLC plate showed two prominent fluorescent (reflective) spots (marked with bar lines) on the stem (S) and root (R) at R_f ~ 0.85 observed under UV lamp at long wavelength of 366 nm. The non-reflective spots are marked with circles. The reflective spots are conspicuously absent at same wavelength in the leaf (L) extract on the TLC plate which is also confirmed by the low percentage in the spectra.

3.5.3 pH and Conductimetric Analysis Determination

3.5.3.1 pH Measurement and Analysis

Solution pH is a critical parameter that governs the biosorption process. The pH measurement of salt solutions prepared in concentration of 400 mM and 1.0 M NaCl

Active Spectrum Graph Report 2016-02-05 04:31:22 PM

Data Set: File_160205_155932 - RawData

(a)
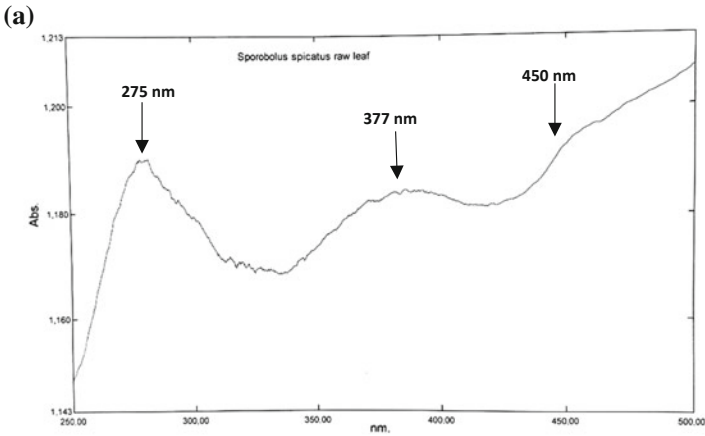
Spectrum Point Pick Report 2016-02-05 04:58:45 PM

Data Set: File_160205_161330 - RawData

(b)
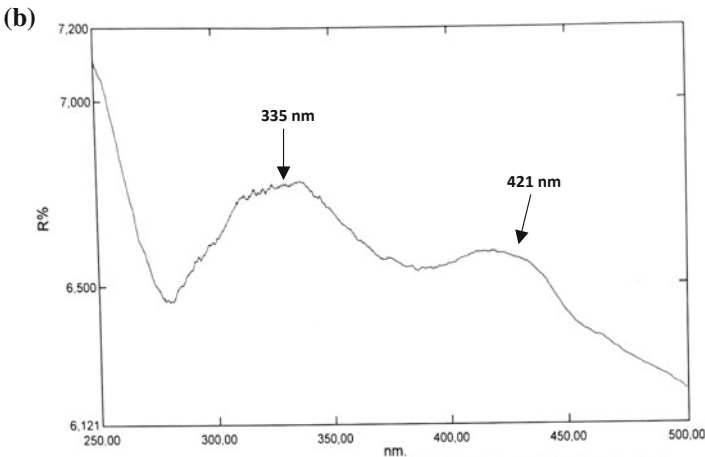
[Measurement Properties]
Wavelength Range (nm.): 250.00 to 500.00
Scan Speed: Fast
Sampling Interval: 0.2
Auto Sampling Interval: Disabled
Scan Mode: Single

[Instrument Properties]
Instrument Type: UV-2600 Series
Measuring Mode: Reflectance
Slit Width: 5.0
Accumulation time: 0.2 sec.

No.	Wavelength	Reflectance	Description
1	421.80	6.587	
2	335.20	6.782	
3	499.60	6.212	
4			

Fig. 3.7 **a** Non-destructive UV–Vis reflection spectrum of dry raw leaf of *Sporobolus spicatus*, **b** non-destructive UV–Vis reflection spectrum of dry raw stem of *Sporobolus spicatus*, **c** non-destructive UV–Vis reflection spectrum of dry raw root of *Sporobolus spicatus*
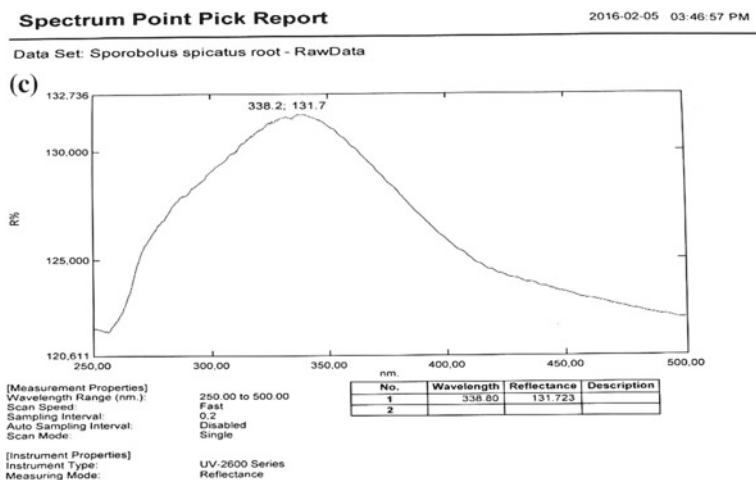
Fig. 3.7 (continued)
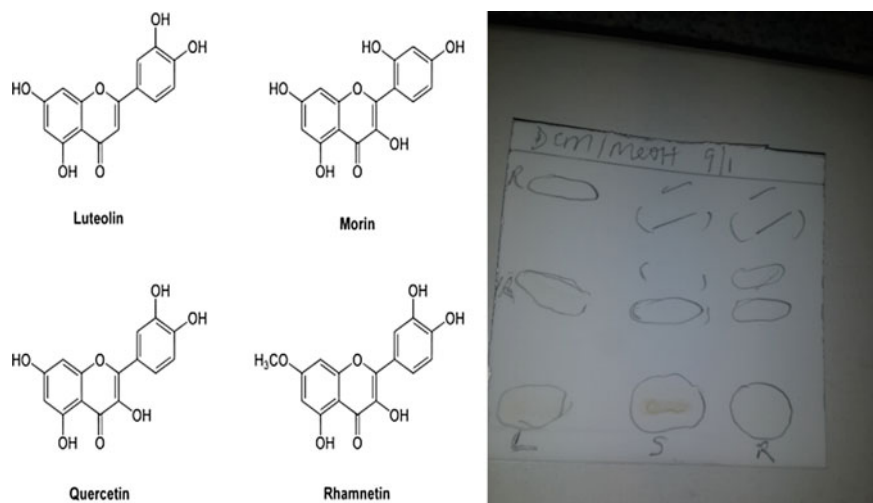
Fig. 3.8 Structures of some flavonoids and TLC plate of *Sporobolus spicatus* extracts (L = leaf, S = stem and R = root)

of sample extracts of the leaf, stem and root of *Sporobolus spicatus* are monitored and compared in triplicates to extracts in ordinary deionized water. The average pH values were monitored on a 3 day interval for a total of 9 days. All measurements are taken at room average temperature of 22.6 °C.

The experiment was carried out at two extreme salt concentrations for comparison. The results show a steady increase in average pH values for deionized water and 1.0 M NaCl solution extracts of the leaf, stem and root, but with corresponding

significant decreased pH values in 400 mM NaCl solution as shown in Table 3.2 and in Figs. 3.9 and 3.10. Metal bioaccumulation efficiency has been found to be controlled by different factors such as surrounding pH and metal concentration [35]. A low pH value indicates that hydrogen ions in aqueous solution compete with metal ions which result in protonation of the active sites. The decreased pH values in the 400 mM NaCl are therefore assumed to indicate lower H^+ released into the system relative to higher salt concentration. However, at the higher pH, more negatively charged surfaces are available resulting in high salt uptake. Since ionic interaction is the main mechanism contributing to biosorption of metals on the biosorbent [36, 37], it is invariably possible that the hydrogen bond dissociation originates from the phenolic OH groups of the flavonoids. The variations in pH values from different parts of the plant are thought to be related to the numbers of -OH groups on the phenyl rings A and B of flavonoids. It is expected that NaCl behaves as ionic species (Na^+ and Cl^-) when dissolved in water, therefore, the formation of negative phenoxide ions after H-bond dissociation is possibly expected to form a monovalent complex with sodium ions with the release of H^+ which increases the acidity of the solution (See flavonoid structures in Fig. 3.8). It is also not unlikely that the presence of Cl^- ions in the solution may form chlorine gas relating to bubble formation and slight exothermic reaction on reaction vessel. On the other hand, at higher pH, more

Table 3.2 pH of the filtrate of the dry leaf, stem and root extracts of the *S. spicatus* in 40 mM, 1.0 M NaCl solutions and deionized water

	pH (deionized water extract) Control	pH (400 mM NaCl)	pH (1.0 M NaCl)
Blank	6.870	6.787	6.470
Leaf	6.975	6.037	7.005
Stem	7.263	6.625	7.100
Root	7.656	6.326	6.903
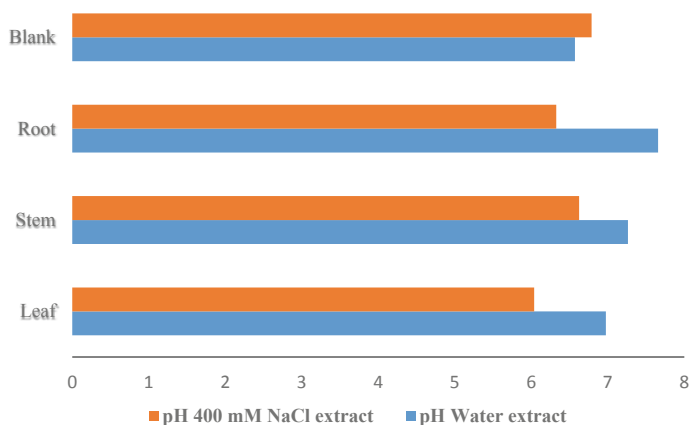
Fig. 3.9 pH values of 400 mM NaCl versus deionized water
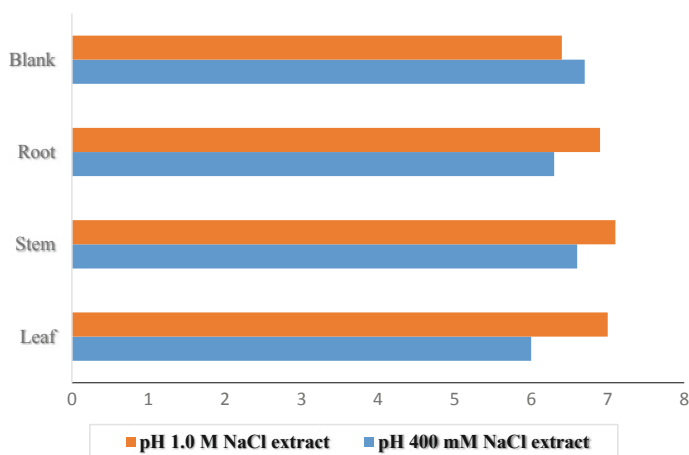
Fig. 3.10 pH values of NaCl extracts in two different concentrations
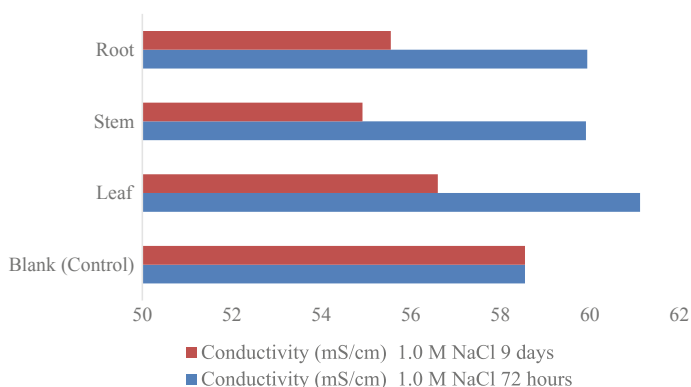
Fig. 3.11 Time change of conductivity of *S. spicatus* (leaf, stem and root) extracts

negatively charged surfaces are available resulting in high sodium ion uptake or removal (Fig. 3.11).

3.5.3.2 Conductimetric Analysis Determination

Electrical conductivity (EC) measures the ability of a solution to conduct electricity and is expressed in deciSiemens per meter (dS/m, which is equivalent to mmhos/cm). The result obtained from the UV–Vis absorption spectroscopy also provided a direct correlation between absorbance values and the electrical conductivity of the plant extracts [25, 26]. The results of conductivity measurement of the leaf, stem and root sample extracts of *Sporobolus spicatus* are as shown in Table 3.3; low electrical

Table 3.3 Time change conductivity measurement of the filtrate of the leaf, stem and root of *S. spicatus* in 400 mM, 1.0 M NaCl solutions and deionized water

	Conductivity (μS/cm) deionized water 72 h	Conductivity (mS/cm) 400 mM NaCl 72 h	Conductivity (mS/cm) 1.0 M NaCl		
			72 h	9 days	% Reduction
Blank (control)	94.8	4.82	58.55	58.55	NA
Leaf	746	5.34	61.12	56.60	7.40
Stem	303	6.43	59.91	54.92	8.33
Root	510	5.30	59.94	55.55	7.33

conductivity values were obtained in the unit μS/cm concentration for all extracts soaked for 72 h in deionized water. This could be explained in terms of number of possible number of charges available in the solution to conduct electricity. It is however not a clear proper explanation to the observed variants in the values obtained for the 400 mM NaCl solution. The blank solution measurement gave 4.82 mS/cm with corresponding increase in conductivity at 5.34, 6.43 and 5.30 mS/cm for the leaf, stem and root respectively. A similar trend was found in the 1.0 M NaCl solution, where 58.55 mS/cm was being recorded for a blank salt solution and 61.12, 59.91 and 59.94 mS/cm respectively for the leaf, stem and root.

The conductivity measurement of same salt solution containing plant materials monitored on a three day interval for nine days was carried out. A significant reduction in conductivity values was obtained for the leaf, stem and root extracts at 56.60 (<7.40%), 54.92 (<8.33%) and 55.55 (<7.33%) mS/cm respectively. This possibly implies that lower NaCl ions concentration in solution are available for electrical conductivity owing to electrostatic binding formation of sodium-flavonoid complex or other phytochemicals present in plant samples. The electrical conductivity values for the plant samples in deionized water are found to be 746, 303 and 510 μS/cm respectively for the leaf, stem and root. The low values may reasonably imply that little or insignificant chemical compounds interaction occur with the plant parts in ordinary deionized water.

3.6 Conclusion

Preliminary phytochemical screening, spectroscopic characterization, pH and conductimetric analysis of various sectional parts (leaf, stem and root) of *Sporobolus spicatus* were undertaken in this study. The functional groups, wavelengths and band intensity peaks confirm the characteristic features of phytochemicals present, which may include: flavonoids, lignins, lignocellulose, hemicellulose, tannins, and possibly other phenolic acid compounds. The types of secondary metabolites provide useful information on chelation and/or metal adsorption mechanisms by which *Sporobolus spicatus* survive in saline soil or salty water ecosystem. Further research work how-

ever is needed to support the development, uses and biotechnological applications most especially in the phytoremediation and phytodesalination.

References

1. FAO (2000) Global Network on Integrated Soil Management for Sustainable Use of Salt–Affected Soils. Rome, Italy. http://www.fao.org/ag/agl/agll/spush
2. Hasanuzzaman M, Nahar K, Alam Md M, Bhowmik PC, Hossain Md A, Rahman MM, Prasad MNV, Ozturk M, Fujita M (2014) Potential use of halophytes to remediate saline soils. BioMed Res Int. Article ID 589341
3. Hasanuzzaman M, Nahar K, Fujita M (2013) Plant response to salt stress and role of exogenous protectants to mitigate salt-induced damages. In: Ahmad P, Azooz MM, Prasad MNV (eds) Eco physiology and responses of plants under salt stress, Springer, New York, USA, pp 25–87
4. Freedman A, Gross A, Shelef O, Rachmilevitch S, Arnon S (2014) Salt uptake and evapotranspiration under arid conditions in horizontal subsurface flow constructed wetland planted with halophytes. Ecol Eng 70:282–286
5. Ashraf MY, Ashraf M, Sarwar G (2005) Physiological approaches to improving plant salt tolerance. In: Dris R (ed) Crops: growth, quality and biotechnology. WFL Publisher, Helsinki, Finland, pp 1206–1227
6. Rabhi M, Hafsi C, Lakhdar A (2009) Evaluation of the capacity of three halophytes to desalinize their rhizosphere as grown on saline soils under non-leaching conditions. Afr J Ecol 47:463–468
7. Flowers TJ, Colmer TD (2008) Salinity tolerance in halophytes. New Phytol 179:945–963
8. Dracup MNH, Greenway H (1985) A procedure for isolating vacuoles from leaves of the halophyte *Suaeda maritime*. Plant, Cell Environ 8:149–154
9. Naz N, Hameed M, Wahid A, Arshad M, Ahmad MSA (2009) Patterns of ion excretion and survival in two stoloniferous arid zone grasses. Physiol Plantarum 135:185–195
10. Hameed A, Hussain T, Gulzar S, Aziz I, Gul B, Khan MA (2012) Salt tolerance of a cash crop halophyte *Suaeda fruticosa*: biochemical responses to salt and exogenous chemical treatments. Acta Physiol Plant 34:2331–2340
11. Flower TJ, Hajibagheri MA, Clipson NJW (1986) Halophytes. Q Rev Biol 61:313–337
12. Grigore MN, Ivanescu L, Toma C (2014) Halophytes: an integrative anatomical study. Springer International Publishing, Switzerland
13. Santos J, Al-azzawi M, Aronson J, Flower TJ (2015) eHALOPH a database of salt-tolerant plants: helping put halophytes to work. Plant Cell Physiol https://doi.org/10.1093/pcp/pcv155
14. Pouladi SF, Anderson BC, Wootton B, Rozema L (2016) Evaluation of phytodesalination potential of vegetated bioreactors treating greenhouse effluent. Water 8:233. https://doi.org/10.3390/w8060233
15. Bartels D, Sukur R (2005) Drought and salt tolerance in plants. Crit Rev Plant Sci 24:23–58
16. Bohnert HJ, Cushman JC (2000) The ice plant cometh: lessons in abiotic stress tolerance. J Plant Growth Regul 19:334–346
17. Bohnert HJ, Nelson DE, Jensen RG (1995) Adaptations to environmental stresses. Plant Cell 7:1099–1111
18. Rajalakshmi S, Parida A (2012) Halophytes as a source of genes for abiotic stress tolerance. J Plant Biochem Biotechnol 21:S63–S67
19. Kane NC, Rieseberg LH (2007) Selective sweeps reveal candidate genes for adaptation to drought and salt tolerance in common sunflower *Helianthus annuus*. Genetics 175:1823–1834

20. Lowry DB, Hall MC, Salt DE, Willis JH (2009) Genetic and physiological basis of adaptive salt tolerance divergence between coastal and inland *Mimulus guttatus*. New Phytol 183:776–788
21. Agarwal PK, Shukla PS, Gupta K, Jha B (2013) Bioengineering for salinity tolerance in plants: state of the art. Mol Biotechnol 54:102–123
22. Shabala S, Mackay A (2011) Ion transport in halophytes. Adv Bot Res 57:151–199
23. Flowers TJ, Troke PF, Yeo AR (1977) The mechanism of salt tolerance in halophytes. Ann Rev Plant Physio 28:89–121
24. Teakle NL, Tyerman SD (2010) Mechanisms of Cl^- transport contributing to salt tolerance. Plant, Cell Environ 33:566–589
25. Apse MP, Blumwald E (2007) Na^+ transport in plants. FEBS Lett 581:2247–2254
26. Rodriguez-Rosales MP, Galvez FJ, Huertas R, Aranda MN, Baghour M, Cagnac O, Venema K (2009) Plant NHX cation/proton antiporters. Plant Signaling and Behaviour 4:265–276
27. Burkill HM (1985) The useful plants of west tropical Africa. Royal Botanic Gardens Kew, vol 2
28. Odebiyi OO, Sofowora EA (1978) Phytochemical screening of Nigeria medical plants II. Lloydia 41:234–246
29. Coates J (2000) Interpretation of infrared spectra, a practical approach. In: Meyers RA (ed) Encyclopedia of analytical chemistry. Wiley, Chichester, UK, pp 10815–10837
30. Adeloye AO (2011) Synthesis, photophysical and electrochemical properties of a mixed bipyridyl-phenanthrolyl ligand Ru(II) heteroleptic complex having trans-2-methyl-2-butenoic acid functionalities. Molecules 16:8353–8367
31. Markham KR (1982) Techniques of flavonoid identification (1st edn). Academic Press, UK, ISBN 978-0124726802
32. Petro FP, Goncalo CJ (2012) Structural analysis of flavonoids and related compounds—a review of spectroscopic applications. Centro de Quimica Estrutural 2:33–54
33. Cea P, Martin S, Villares A, Mobius D, Carmen Lopez M (2005) Use of UV–Vis reflection spectroscopy for determining the organization of viologen and viologen tetracyanoquinodimethanide monolayers. J Phys Chem B 110:963–970
34. Upasani SM, Kotkar HM, Mendki PS, Maheshwari VL (2003) Partial characterization and insecticidal properties of *Ricinus communis* L foliage flavonoids. Pest Manag Sci 59:1349–1354
35. Ponce SC, Prado C, Pagano E, Prado FE, Rosa M (2015) Effect of solution pH on the dynamic of biosorption of Cr(VI) by living plants of *Salvinia minima*. Ecol Eng 74:33–41
36. Kulkarni RM, Shetty KV, Srinikethan G (2013) Cd(II) and Ni(II) biosorption by *Basillus katerosporus* (MTCC 1628). J Taiwan Inst Chem E 45:1628–1635
37. Prabhu SG, Salian CS, Kiran SK, Naik MM, Srinikethan G (2016) Studies on the potential of *Adiantum philippense* L. as a biosorbent for nickel removal. Res J Chem Environ Sci 4:31–39

Chapter 4
The Molecular Dynamics Simulation of a Multi-domain Outer Membrane Protein A (OmpA) from *Shigella flexneri* in POPE Lipid Bilayer

Roy Lee Yung-Hung, Theam Soon Lim, Asma Ismail and Yee Siew Choong

Abstract *Shigella flexneri* serotype 2a is a major public health concern in the developing and under-developed countries as it contributes to the endemic shigellosis (also known as bacillus dysentery) as well as shigellosis mortality. A 35 kDa antigenic protein from *S. flexneri* has been shown to be a potential biomarker and the predictive model from earlier studies showed that this protein is a variant of outer membrane protein A (OmpA) that consists of OmpA domain and OmpA-like domain. This study was conducted to further sample and explore the conformation of the OmpA of *S. flexneri* in POPE lipid bilayer. The trajectories data from molecular dynamics (MD) simulation showed that the OmpA secondary structure is retained and the protein integrity is not impaired. The four extracellular loops are flexible and similar observation was noted for the linker of the two domains. The conformation of the extracellular loops could be useful for possible future development for diagnostics or vaccine of shigellosis.

Keywords *Shigella flexneri* · Outer membrane protein A (OmpA) · Molecular dynamics (MD) simulation

R. L. Yung-Hung · T. S. Lim · Y. S. Choong (✉)
Institute for Research in Molecular Medicine, Universiti Sains Malaysia, 11800 Penang, Malaysia
e-mail: yeesiew@usm.my

R. L. Yung-Hung
e-mail: royleeyh@gmail.com

T. S. Lim
e-mail: theamsoon@usm.my

A. Ismail
Institute for Research in Molecular Medicine, Health Campus, Universiti Sains Malaysia, 16150 Kubang Kerian, Malaysia
e-mail: asma@usm.my

© Springer Nature Switzerland AG 2019

4.1   Introduction

S. flexneri is a rod-shaped entero-invasive, non-motile and non-spore forming Gram-negative bacteria. It is physiologically similar to *Shigella dysenteriae*, *Shigella boydii*, and *Escherichia coli*. Statistics showed that the annual number of shigellosis cases throughout the world was about 164.7 million, with 99% occurring in developing and under-developed countries. The estimated number of deaths is 1.1 million. Children under the age of 5 are the main target of the disease, representing 69 and 61% of cases and deaths, respectively [1–5]. In developing and under-developed countries, *S. flexneri* is the main shigellosis serogroup (60%), followed by *S. sonnei* (15%), while *S. dysenteriae* and *S. boydii* occur at the same frequency of 6% [6].

Studies showed that the outer membrane protein A (OmpA) of *S. flexneri* is involved in the bacterial pathogenesis, protrusion and inter-cellular spreading and induces immune response [7–9]. Despite the biological importance, membrane proteins are difficult to be expressed and crystallised. Therefore, in silico studies can at least provide some information to understand the dynamics of membrane proteins. Molecular dynamics (MD) simulation would be one of the most abundant and widely computer modelling used techniques to embed a membrane protein whose structure is obtained from crystal or a predictive model into a lipid bilayer to study in atomic detail, yielding the dynamic behaviour within the membrane protein's native environment. Recent advances in computational software and hardware have enabled longer time and length scales to be reached for simulation systems made up of many thousands and even millions of atoms. MD simulations have provided insights into many other aspects of membrane proteins biophysics [10–14]. Among these are simulations which have been employed to explore the structure-function relationship of bacterial outer membrane proteins [15–17], mechanism of transporters [18–20] and water permeation through aquaporins [21–23].

In this paper, a relatively short (30 ns) MD simulation was utilised in order to give insights to the conformations of *S. flexneri* OmpA from the homology model that we built earlier [24]. Results showed that the secondary structure and protein integrity of OmpA was not impaired. Flexibility of the extracellular loops could suggest the possibility of interactions searching with benevolent partners, e.g. bacterial conjugation or molecules intake/expelled. The linker flexibility also suggested that the OmpA-like region is ready to interact with e.g. peptidoglycan for bacteria cell wall formation as reported in some other studies [24–29].

4.2   Methods

4.2.1   *Preparation of the System*

The starting structure of *S. flexneri* OmpA is a predictive homology structure obtained from our previous study [24]. It was then embedded in a pre-equilibrated

1-palmitoyl-2-oleoyl-sn-glycero-3-phosphoethanolamine (POPE; http://terpconnect.umd.edu/~jbklauda/research/download.html) lipid bilayer that was duplicated in box size dimension x-axis and y-axis of 15 nm × 15 nm, respectively. The duplication of membrane patch was performed by GROMACS 4.5.4 simulation package [30]. The protein was then oriented with its principal axis perpendicular to the bilayer planar [31]. Overlapping lipid molecules with the protein were removed. The system was solvated with TIP3P water model [32] and overlapping water molecules in the lipid bilayer region were also removed. Neutralising chloride ions were added by replacing randomly chosen water molecules.

4.2.2 Simulation Protocol

All simulations were performed using GROMACS 4.5.4 package [30]. Energy minimisation was performed with steepest descents to relax any steric conflicts generated during the setup. Short-range electrostatic interactions were treated using the particle mesh Ewald method [33] with a 1.2 nm cut-off for the real space calculation. Same cut-off value was also used for the van der Waals interactions. A total of 50,000 steps of minimisation were performed. The system was subjected to equilibration in two phases. The first stage of NVT was to equilibrate the temperature of the entire system using Berendsen temperature coupling [34] for 200 ps at 310 K, whereby the protein complex was under position restraint condition. NPT equilibration of the system on the protein complex was done for a length of 2 ns under restraint condition. Nose-Hoover thermostat [35] was used to produce a kinetic ensemble and to allow molecular fluctuations within the system for dynamics simulation. Production stage, 30 ns, was performed under NPT ensemble at a pressure of 1 bar and temperature of 300 K. The CHARMM36 force field [36, 37] was used for both built model and lipid bilayer system. All bond lengths were constrained to their equilibrium value using LINCS algorithm for the bonds between heavy atom and hydrogen atoms in protein and lipids [38] and SETTLE algorithm [39] for water molecules. Integration time step of 2 fs was used and the neighbour list to calculate non-bonded interactions was updated every 10 time steps during the entire simulation time. Periodic boundary condition in all directions was applied in the simulation.

4.3 Results

The OmpA-like domain is located at the intra-cellular region, covering a larger area compared to the extra-cellular region. The overall structure of the protein is relatively stable throughout the 30 ns simulation (Fig. 4.1). The OmpA protein also retained its secondary structure, specifically the beta sheets and alpha helix throughout the simulation.
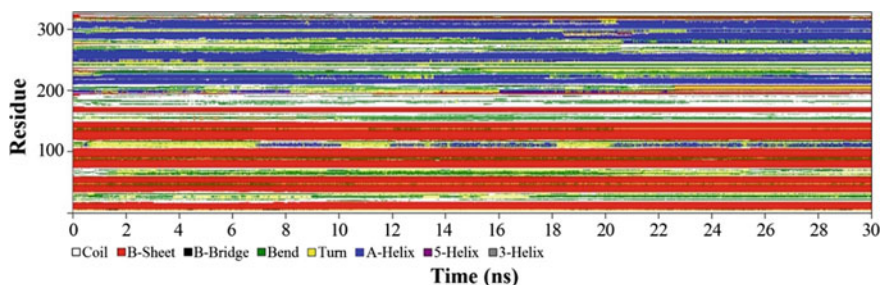
Fig. 4.1 The secondary structure calculation of *S. flexneri* OmpA from 30 ns of MD simulation

Conformational drift of the system was evaluated by calculating the root mean square deviation (RMSD) of the OmpA Cα atoms. Fig. 4.2a shows the RMSD of the overall structure deviated within 0.75–1.5 nm. This provided the evidence of relatively small overall conformational drift simulation for the OmpA. Root mean square fluctuation (RMSF) is a measure of the average atomic mobility of backbone atoms (N, Cα and C atoms) during MD simulations. The time-averaged RMSF of Cα atoms in OmpA showed that the greatest flexibility was exhibited by the extracellular loops, followed by intra-cellular turns, with the β-barrel residues being the least mobile (Fig. 4.2b).

OmpA structure was further evaluated by clustering analysis whereby similar conformations will be grouped into a cluster. This allows a coherent analysis to be formed concerning the number of clusters present in the respective region in the MD trajectory data [40]. The clustering analysis was sub-divided into the extracellular loops, OmpA-like domain, β-barrel and also OmpA as a whole. From the clustering analysis, it can be concluded that the extracellular loops and the OmpA-like domain were dynamically mobile during the simulation while the β-barrel is fairly
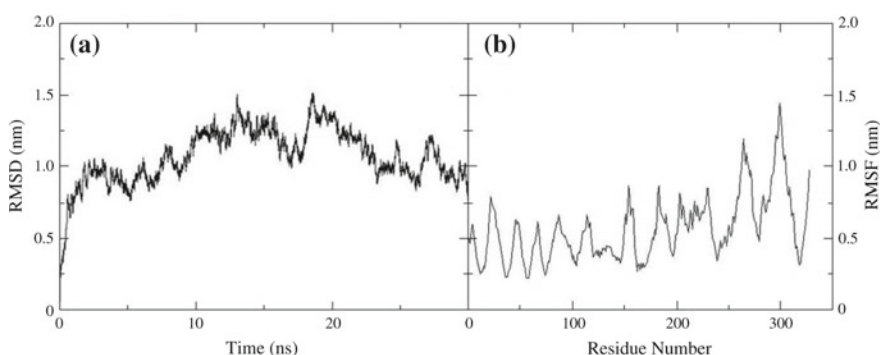
Fig. 4.2 **a** Conformational drift (root mean square deviation; RMSD) and **b** the time-averaged root mean square fluctuation (RMSF) of *S. flexneri* OmpA Cα atom from MD simulation

less flexible. The representative structure of the 35 kDa protein was obtained from the dominant cluster of OmpA (Fig. 4.3).

Pore-like regions in the β-barrel were analysed using HOLE [41]. The analysis showed that the diameter decreased from 0.3 to 0.1 nm towards the middle of the β-barrel (Fig. 4.4a). A steady increase in diameter of a conical shaped-like structure can be observed at the end of the β-barrel (Fig. 4.4b). The maximum width of 1.1 nm can be observed at the opening of the β-barrel, near to the extra-cellular loops.

Hydrogen bonding analysis was also performed for the extracellular loops and β-barrel of OmpA. The extracellular loops regions (Fig. 4.5a) showed the fluctuation of ~5 to ~21 hydrogen bonds along the simulation time. However, results from the β-barrel analysis showed that the number of hydrogen bonds was at the plateau (~120 to ~150 hydrogen bonds) after 18 ns, indicating that the mobility of the β-barrel is less pronounced (Fig. 4.5b).

In addition, the radius of gyration for the β-barrel region of OmpA was also studied. A compact packing of amino acid residues is known to affect the folding rate and stability of the protein [42]. The degree of stability of the β-barrel which is inferred from the calculated radius of gyration showed the fluctuation around 1.8 nm and only deviated around 0.09 nm (Fig. 4.6). Therefore, no significant drift was observed indicating that the β-barrel is tightly packed and rigid, consistent with the analysis revealed from the hydrogen bonding analysis.
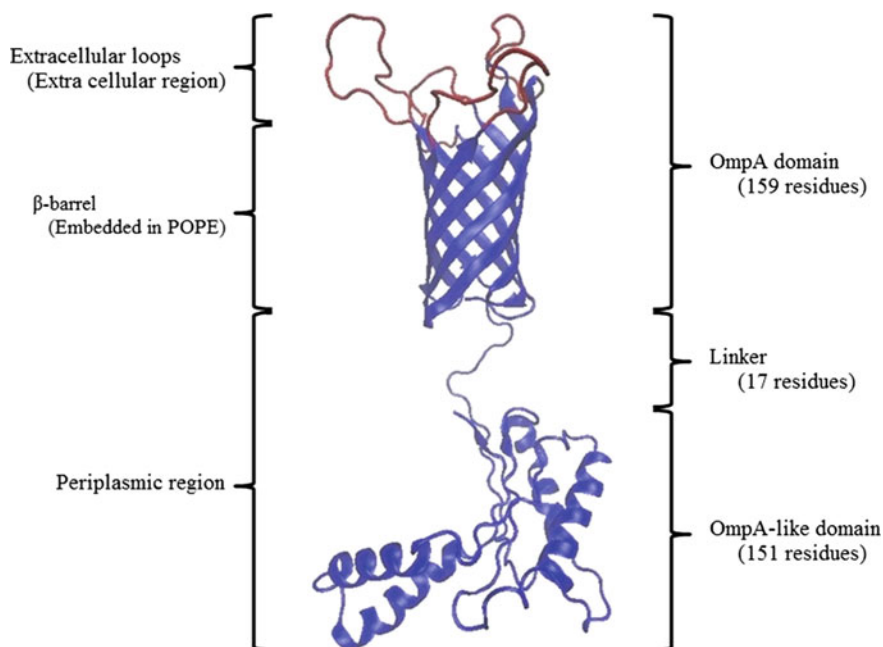
Fig. 4.3 The ribbon representation of average MD structure of OmpA from *S. flexneri*. Red coils are the predicted epitopes. The POPE lipid bilayer is not shown for clarity purpose
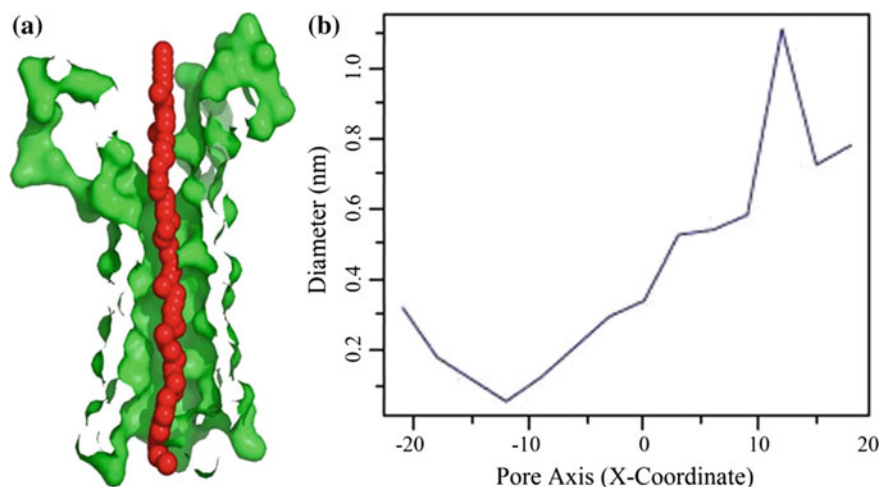
Fig. 4.4 OmpA domain of *S. flexneri* from **a** pore analysis, and **b** pore diameter profile. Red spheres representing pore centre at 0.1 nm step along the pore axis. The "pore" is located at the β-barrel region with ~35Å in length

4.4 Discussion

The function of a protein always involves conformational changes. Hence, a molecular understanding of its mechanism requires a detailed description of the different functional states the structure can explore dynamically. A small change in protein sequence could have significant effects on its biophysical properties. However, experimental determination of protein is laborious and often an unpredictable task [43]. Therefore, in this work, we performed molecular simulations in order to obtain the structural details of OmpA from *S. flexneri* in the lipid environment. As phosphoethanolamine was the main lipid found in Gram negative bacteria [44, 45], thus the POPE model was used in the system setup to study OmpA of *S. flexneri*. Conformational drift analysis of the OmpA has provided the insights into the stability of the component domains and also their movements relative to each other. The root mean-squared deviation (RMSD) provided a simple but direct measurement of the structural drift of OmpA from its initial conformation over the course of 30 ns MD simulation (Fig. 4.2a). The results indicated that the overall conformational dynamics properties are stable specifically the β-barrel and without significant fluctuation. The N-terminal β-barrel domain of the OmpA exhibited similar conformational dynamics to N-terminal of *Pasteurella multocida* OmpA-like (PmOmpA) [46]. This suggested that the overall OmpA conformational dynamic properties might be similar with other 8-stranded outer membrane protein domains such as PagP [47] and OmpX [48].

The degree of stability of the β-barrel can also be inferred from the radius of gyration (Fig. 4.6). No obvious significant drift was observed for the β-barrel. This

Fig. 4.5 The number of hydrogen bonds in OmpA of *S. flexneri* at the **a** extracellular loops, and **b** β-barrel region
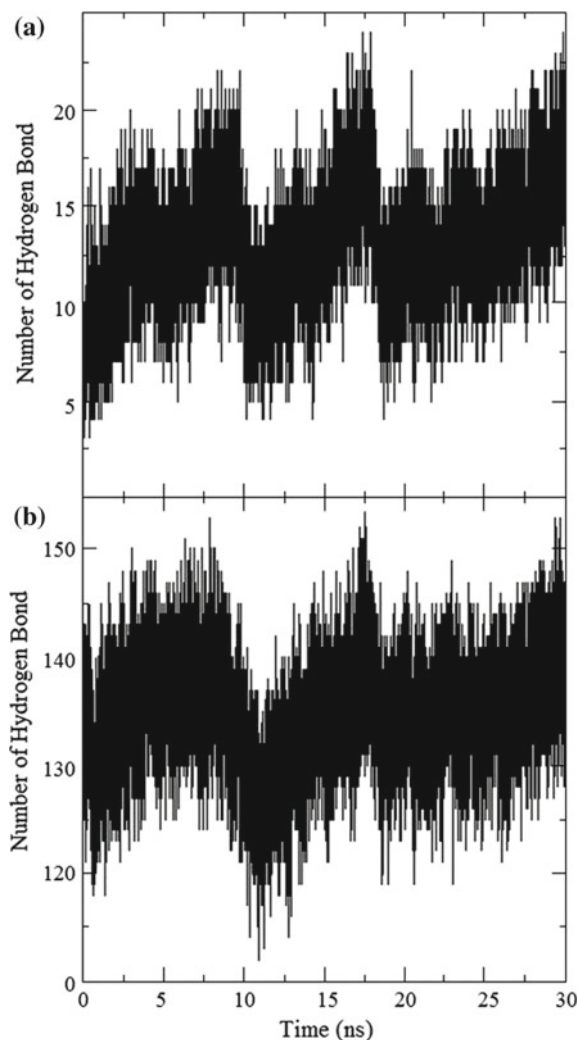
showed that the structure was stable and no secondary structure changed during the simulation (Fig. 4.2a). RMSF calculation indicated the flexibility of the large extracellular loops (Fig. 4.2b). Overall, the predictive model of the OmpA retained the secondary structure throughout the simulation (Fig. 4.1). The obtained averaged structure (Fig. 4.3) showed that the OmpA maintained its β-sheets on the β-barrel and α-helix of the OmpA-like domain. The extracellular loops, postulated to be the predicted epitopes, serve as antibody recognition site also at its random coil conformation.

In addition, the linker (residues 174–189) also retained a "random coil" conformation throughout simulation. The C-terminal domain showed some movement

Fig. 4.6 Radius of gyration of OmpA β-barrel from *S. flexneri*
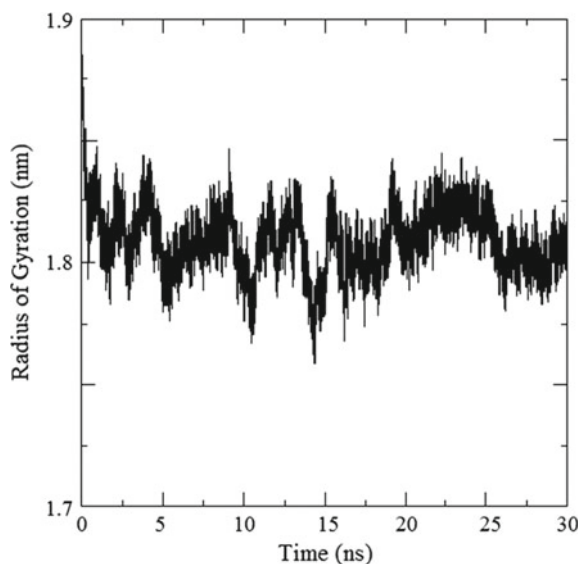
towards the β-barrel. This linker may function in enabling coupling or anchorage of the outer membrane to the peptidoglycan matrix. This finding is similar to the results from *E. coli* OmpA where the movement of the linker suggested possible mechanical stability of the cell [28]. The peptidoglycan forms the bacterial cell wall which is important to prevent the bacteria from lysis, essential for cell division and giving structural shape and strength to bacteria [26]. Besides, the folding of the periplasmic C-terminal domain of OmpA from *Acinetobacter baumannii* is ligand mediated [49], thus further supporting the simulation result of only slight movement towards the β-barrel.

A more detailed picture of the conformational dynamics of the OmpA can also be obtained by the analysis of the hydrogen bonds. Analysis of the total numbers of hydrogen bonds indicated that the loops showed a conformational open/closed pattern on every ~9–10 ns (Fig. 4.5a). The pattern of increase and then decrease in the number of hydrogen bonds could be due to the opening and closing of the loops or constant fluctuation of the loops. On the other hand, the number of hydrogen bonds after ~18 ns for the β-barrel region (Fig. 4.5b) indicates that the integrity of the β-barrel is strong and packing the secondary structure tightly as a rigid core for the OmpA.

OmpA is known as an integral outer membrane protein which consists of four surfaces exposed loops in which peptides can be inserted and subsequently displayed on the cell surface [50]. Reports have indicated that OmpA protein can be used for bacterial surface display system for application such as peptide library screening [51, 52], live vaccines [53], bioremediation [54] or as positive selection strategy for epitopes enrichment [55]. Therefore, we postulated that this OmpA with its large flexible loops is also important as a potent immunogen and is vital in antibody

mediated immune response. Similarly, the experimental data from Pore et al. also suggested the possible usage of OmpA from *S. flexneri* 2a as a promising subunit vaccine candidate [9].

There are not many experimental studies to suggest the pore activities of the β-barrel domain of the OmpA. Thus it is interesting to examine the dimensions of any interior pore during the course of MD simulation. An analysis of the internal β-barrel pore size was carried out by calculation of the pore radius profile (Fig. 4.4a). Significant differences in pore radius profile were observed. Therefore, this suggests that formation of water filled pores is likely to occur in the β-barrel of the OmpA. However, no salt-bridge was detected in the OmpA β-barrel throughout this simulation although there were reports which showed gating formation in EcOmpA [56, 57]. The absence of formation barrier in this OmpA β-barrel might be due to a larger channel, ~1.1 nm, at the periplasmic end with no salt-bridge formation in that region [58].

The pore diameter profile of the β-barrel (Fig. 4.4b) also showed a diameter of at least ~0.15 nm (approximate van der Waals radius of a water molecule) through the entire β-barrel. Moreover, there is a clear increase in pore radius from the OmpA-like region of the β-barrel towards the extracellular loops of the β-barrel suggesting the opening of the pore to enable the passage of water molecules through the OmpA. Some degree of pore expansion occurring especially at the β-barrel mouth are expected, consistent with the observation from NMR [59]. This indicated that the β-barrel not only allows water permeation into the β-barrel but could also transport important solutes for the survival of the bacteria [44, 60]. The interactions of *N*-glycans in FcγRIa with *E. coli* K1 OmpA for entry into macrophages also suggested the importance of the β-barrel in the inducement of disease pathogenesis [61].

4.5 Conclusions

This study extended the use of a predictive model combined with MD simulations to explore the conformation of the OmpA from *S. flexneri*. Throughout the simulation, OmpA showed slightly less conformational drift especially at the β-barrel region. However, the four large extracellular loops showed flexibility in the form of random coils. As for the C-terminal OmpA-like domain, the degree of flexibility can also be observed from the movement of the OmpA-like domain towards the β-barrel. The representative structure of the OmpA had its secondary structure retained which showed that the protein integrity is not impaired. This observation might indicate the possibility of coupling with peptidoglycan matrix for bacterial cell wall formation. In conclusion, the current study is encouraging in that computational approaches using MD simulation have provided some structural insight of the OmpA that could be useful in future design for a specific binder against OmpA for diagnostic application or vaccine development.

References

1. Camacho AI, Irache JM, de Souza J, Sanchez-Gomez S, Gamazo C (2013) Nanoparticle-based vaccine for mucosal protection against *Shigella flexneri* in mice. Vaccine 31:3288–3294
2. Kotloff KL, Winickoff JP, Ivanoff B, Clemens JD, Swerdlow DL, Sansonetti PJ, Adak GK, Levine MM (1999) Global burden of *Shigella* infections: implications for vaccine development and implementation of control strategies. Bull World Health Organ 77:651–666
3. Jennison AV, Verma NK (2004) *Shigella flexneri* infection: pathogenesis and vaccine development. FEMS Microbiol Rev 28:43–58
4. Liu J, Platts-Mills JA, Juma J, Kabir F, Nkeze J, Okoi C, Operario DJ, Uddin J, Ahmed S, Alonso PL, Antonio M, Becker SM, Blackwelder WC, Breiman RF, Faruque AS, Fields B, Gratz J, Haque R, Hossain A, Hossain MJ, Jarju S, Qamar F, Iqbal NT, Kwambana B, Mandomando I, McMurry TL, Ochieng C, Ochieng JB, Ochieng M, Onyango C, Panchalingam S, Kalam A, Aziz F, Qureshi S, Ramamurthy T, Roberts JH, Saha D, Sow SO, Stroup SE, Sur D, Tamboura B, Taniuchi M, Tennant SM, Toema D, Wu Y, Zaidi A, Nataro JP, Kotloff KL, Levine MM, Houpt ER (2016) Use of quantitative molecular diagnostic methods to identify causes of diarrhoea in children: a reanalysis of the GEMS case-control study. Lancet 388:1291–1301
5. Pires SM, Fischer-Walker CL, Lanata CF, Devleesschauwer B, Hall AJ, Kirk MD, Duarte AS, Black RE, Angulo FJ (2015) Aetiology-specific estimates of the global and regional incidence and mortality of diarrhoeal diseases commonly transmitted through food. PLoS ONE 10:e0142927
6. Zaidi MB, Estrada-Garcia T (2014) *Shigella*: a highly virulent and elusive pathogen. Curr Trop Med Rep 1:81–87
7. Ambrosi C, Pompili M, Scribano D, Zagaglia C, Ripa S, Nicoletti M (2012) Outer membrane protein A (OmpA): a new player in *Shigella flexneri* protrusion formation and inter-cellular spreading. PLoS ONE 7:e49625
8. Confer AW, Ayalew S (2013) The OmpA family of proteins: roles in bacterial pathogenesis and immunity. Vet Microbiol 163:207–222
9. Pore D, Chakrabarti MK (2013) Outer membrane protein A (OmpA) from *Shigella flexneri* 2a: a promising subunit vaccine candidate. Vaccine 31:3644–3650
10. Biggin PC, Bond PJ (2008) Molecular dynamics simulations of membrane proteins. Methods Mol Biol 443:147–160
11. Domene C, Bond PJ, Sansom MS (2003) Membrane protein simulations: ion channels and bacterial outer membrane proteins. Adv Protein Chem 66:159–193
12. Dror RO, Jensen MO, Shaw DE (2009) Elucidating membrane protein function through long-timescale molecular dynamics simulation. Conf Proc IEEE Eng Med Biol Soc 2009:2340–2342
13. Gumbart J, Wang Y, Aksimentiev A, Tajkhorshid E, Schulten K (2005) Molecular dynamics simulations of proteins in lipid bilayers. Curr Opin Struct Biol 15:423–431
14. Lindahl E, Sansom MS (2008) Membrane proteins: molecular dynamics simulations. Curr Opin Struct Biol 18:425–431

15. Khalid S, Bond PJ, Carpenter T, Sansom MS (2008) OmpA: gating and dynamics *via* molecular dynamics simulations. Biochim Biophys Acta 1778:1871–1880
16. Straatsma TP, Soares TA (2009) Characterization of the outer membrane protein OprF of *Pseudomonas aeruginosa* in a lipopolysaccharide membrane by computer simulation. Proteins 74:475–488
17. Tieleman DP, Berendsen HJ (1998) A molecular dynamics study of the pores formed by *Escherichia coli* OmpF porin in a fully hydrated palmitoyl oleoyl phosphatidylcholine bilayer. Biophys J 74:2786–2801
18. DeChancie J, Shrivastava IH, Bahar I (2011) The mechanism of substrate release by the aspartate transporter GltPh: insights from simulations. Mol BioSyst 7:832–842
19. Khalili-Araghi F, Gumbart J, Wen PC, Sotomayor M, Tajkhorshid E, Schulten K (2009) Molecular dynamics simulations of membrane channels and transporters. Curr Opin Struct Biol 19:128–137
20. Shi L, Weinstein H (2010) Conformational rearrangements to the intracellular open states of the LeuT and ApcT transporters are modulated by common mechanisms. Biophys J 99:L103–L105
21. Hub JS, Grubmuller H, de Groot BL (2009) Dynamics and energetics of permeation through aquaporins. What do we learn from molecular dynamics simulations? Handb Exp Pharmacol 57–76
22. Qiu H, Ma S, Shen R, Guo W (2010) Dynamic and energetic mechanisms for the distinct permeation rate in AQP1 and AQP0. Biochim Biophys Acta 1798:318–326
23. Wang Y, Schulten K, Tajkhorshid E (2005) What makes an aquaporin a glycerol channel? A comparative study of AqpZ and GlpF. Structure 13:1107–1118
24. Yung-Hung RL, Ismail A, Lim TS, Choong YS (2011) A 35 kDa antigenic protein from *Shigella flexneri*: in silico structural and functional studies. Biochem Biophys Res Commun 415:229–234
25. De Mot R, Vanderleyden J (1994) The C-terminal sequence conservation between OmpA-related outer membrane proteins and MotB suggests a common function in both gram-positive and gram-negative bacteria, possibly in the interaction of these domains with peptidoglycan. Mol Microbiol 12:333–334
26. Holtje JV (1998) Growth of the stress-bearing and shape-maintaining murein sacculus of *Escherichia coli*. Microbiol Mol Biol Rev 62:181–203
27. Koebnik R (1995) Proposal for a peptidoglycan-associating alpha-helical motif in the C-terminal regions of some bacterial cell-surface proteins. Mol Microbiol 16:1269–1270
28. Ortiz-Suarez ML, Samsudin F, Piggot TJ, Bond PJ, Khalid S (2016) Full-length OmpA: structure, function, and membrane interactions predicted by molecular dynamics simulations. Biophys J 111:1692–1702
29. Schiffrin B, Brockwell DJ, Radford SE (2017) Outer membrane protein folding from an energy landscape perspective. BMC Biol 15:123
30. Hess B, Kutzner C, van der Spoel D, Lindahl E (2008) GROMACS 4: algorithms for highly efficient, load-balanced, and scalable molecular simulation. J Chem Theory Comput 4:435–447
31. Stansfeld PJ, Sansom MS (2011) Molecular simulation approaches to membrane proteins. Structure 19:1562–1572
32. Jorgensen WL, Chandrasekhar J, Madura JD, Impey RW, Klein ML (1983) Comparison of simple potential functions for simulating liquid water. J Chem Phys 79:926–935
33. Darden T, York D, Pedersen L (1993) Particle mesh Ewald: An N⟨…log(N) method for Ewald sums in large systems. J Chem Phys 98:10089–10092
34. Berendsen HJC, Postma JPM, Vangunsteren WF, Dinola A, Haak JR (1984) Molecular-dynamics with coupling to an external bath. J Chem Phys 81:3684–3690
35. Hoover WG (1985) Canonical dynamics: equilibrium phase-space distributions. Phys Rev A 31:1695–1697

36. Best RB, Zhu X, Shim J, Lopes PE, Mittal J, Feig M, MacKerell AD Jr (2012) Optimization of the additive CHARMM all-atom protein force field targeting improved sampling of the backbone phi, psi and side-chain chi(1) and chi(2) dihedral angles. J Chem Theory Comput 8:3257–3273
37. Huang J, MacKerell AD Jr (2013) CHARMM36 all-atom additive protein force field: validation based on comparison to NMR data. J Comput Chem 34:2135–2145
38. Hess B, Bekker H, Berendsen HJC, Fraaije JGEM (1997) LINCS: a linear constraint solver for molecular simulations. J Comput Chem 18:1463–1472
39. Miyamoto S, Kollman PA (1992) SETTLE: an analytical version of the SHAKE and RATTLE algorithm for rigid water models. J Comput Chem 13:952–962
40. Wolf A, Kirschner KN (2013) Principal component and clustering analysis on molecular dynamics data of the ribosomal L11.23S subdomain. J Mol Model 19:539–549
41. Smart OS, Neduvelil JG, Wang X, Wallace BA, Sansom MS (1996) HOLE: a program for the analysis of the pore dimensions of ion channel structural models. J Mol Graph 14:354–360
42. Lobanov M, Bogatyreva NS, Galzitskaia OV (2008) Radius of gyration is indicator of compactness of protein structure. Mol Biol 42:701–706
43. Schwede T (2013) Protein modeling: what happened to the "protein structure gap"? Structure 21:1531–1540
44. Roux B (2005) Ion conduction and selectivity in K(+) channels. Annu Rev Biophys Biomol Struct 34:153–171
45. Ruiz N, Kahne D, Silhavy TJ (2006) Advances in understanding bacterial outer-membrane biogenesis. Nature Rev Microbiol 4:57–66
46. Carpenter T, Khalid S, Sansom MS (2007) A multidomain outer membrane protein from *Pasteurella multocida*: modelling and simulation studies of PmOmpA. Biochim Biophys Acta 1768:2831–2840
47. Hwang PM, Choy WY, Lo EI, Chen L, Forman-Kay JD, Raetz CR, Prive GG, Bishop RE, Kay LE (2002) Solution structure and dynamics of the outer membrane enzyme PagP by NMR. Proc Natl Acad Sci USA 99:13560–13565
48. Fernandez C, Hilty C, Wider G, Guntert P, Wuthrich K (2004) NMR structure of the integral membrane protein OmpX. J Mol Biol 336:1211–1221
49. Mushtaq AU, Park JS, Bae SH, Kim HY, Yeo KJ, Hwang E, Lee KY, Jee JG, Cheong HK, Jeon YH (2017) Ligand-mediated folding of the OmpA periplasmic domain from *Acinetobacter baumannii*. Biophys J 112:2089–2098
50. Freudl R (1989) Insertion of peptides into cell-surface-exposed areas of the *Escherichia coli* OmpA protein does not interfere with export and membrane assembly. Gene 82:229–236
51. Bessette PH, Hu X, Soh HT, Daugherty PS (2007) Microfluidic library screening for mapping antibody epitopes. Anal Chem 79:2174–2178
52. Bessette PH, Rice JJ, Daugherty PS (2004) Rapid isolation of high-affinity protein binding peptides using bacterial display. Protein Eng Des Sel 17:731–739
53. Ruppert A, Arnold N, Hobom G (1994) OmpA-FMDV VP1 fusion proteins: production, cell surface exposure and immune responses to the major antigenic domain of foot-and-mouth disease virus. Vaccine 12:492–498
54. Mejare M, Ljung S, Bulow L (1998) Selection of cadmium specific hexapeptides and their expression as OmpA fusion proteins in *Escherichia coli*. Protein Eng 11:489–494
55. Camaj P, Hirsh AE, Schmidt W, Meinke A, von Gabain A (2001) Ligand-mediated protection against phage lysis as a positive selection strategy for the enrichment of epitopes displayed on the surface of *E. coli* cells. Biol Chem 382:1669–1677
56. Bond PJ, Faraldo-Gomez JD, Sansom MS (2002) OmpA: a pore or not a pore? Simulation and modeling studies. Biophys J 83:763–775
57. Hong H, Szabo G, Tamm LK (2006) Electrostatic couplings in OmpA ion-channel gating suggest a mechanism for pore opening. Nat Chem Biol 2:627–635
58. Brinkman FS, Bains M, Hancock RE (2000) The amino terminus of *Pseudomonas aeruginosa* outer membrane protein OprF forms channels in lipid bilayer membranes: correlation with a three-dimensional model. J Bacteriol 182:5251–5255

59. Arora A, Abildgaard F, Bushweller JH, Tamm LK (2001) Structure of outer membrane protein A transmembrane domain by NMR spectroscopy. Nat Struct Biol 8:334–338
60. Hub JS, de Groot BL (2008) Mechanism of selectivity in aquaporins and aquaglyceroporins. Proc Natl Acad Sci USA 105:1198–1203
61. Krishnan S, Liu F, Abrol R, Hodges J, Goddard WA 3rd, Prasadarao NV (2014) The interaction of *N*-glycans in Fcgamma receptor I alpha-chain with *Escherichia coli* K1 outer membrane protein A for entry into macrophages: experimental and computational analysis. J Biol Chem 289:30937–30949

Chapter 5
In Vitro Comparative Quality Attributes of Selected Brands of Fexofenadine Hydrochloride Tablets Marketed in UAE and India

Akram Ashames, Richie R. Bhandare, Sham Zain AlAbdin, Amna Aljashamy, Aya Atfeh, Abir Elwaer and Noura Fakhry

Abstract The quality of pharmaceutical formulations has become a global concern due to the widespread counterfeit and substandard products that are available in the global market. Therefore, it is mandatory for the drug manufacturers to assess the quality standards of their formulations. Fexofenadine hydrochloride is a piperidine derivative indicated for various seasonal allergic rhinitis conditions such as rhinorrhea, sneezing nose, throat and itchy eyes. The aim of the present work was to evaluate the quality attributes of different brands of fexofenadine hydrochloride tablets having a strength of 180 mg using pharmacopeial and non-pharmacopeial methods. Two brands were bought from a retail pharmacy in India and the remaining two were bought from a local pharmacy in the Emirate of Ajman, UAE. The results of physical and chemical analyses were statistically evaluated using one tail *t*-test, when appropriate, to compare between different fexofenadine hydrochloride products with the innovator product. Identification, weight variation, disintegration and friability results were met by all the brands as per the British Pharmacopoeia

A. Ashames (✉) · R. R. Bhandare · S. Zain AlAbdin · A. Aljashamy · A. Atfeh · A. Elwaer ·
N. Fakhry
Department of Pharmaceutical Sciences, College of Pharmacy and Health Sciences, Ajman
University, PO Box 346, Ajman, UAE
e-mail: a.ashames@ajman.ac.ae

R. R. Bhandare
e-mail: r.bhandareh@ajman.ac.ae

S. Zain AlAbdin
e-mail: shamo.95@hotmail.com

A. Aljashamy
e-mail: amna-ahmed96@hotmail.com

A. Atfeh
e-mail: a.g.a.1112@hotmail.com

A. Elwaer
e-mail: abeer.elwaer@hotmail.com

N. Fakhry
e-mail: nourafakhry510@yahoo.com

2018 specifications. However, brands from Indian market showed percentages of dissolved fexofenadine hydrochloride less than the allowed pharmacopeial lower limit of 80.0% after 45 min, while brands from UAE market represented dissolved concentrations laid within the acceptable range ($\geq$80.0%). Additionally, brands from Indian market showed percentage contents of active ingredient range from 75.1 to 80.5% for brand I and 91.4–97.8% for brand II. Brands from UAE market showed percentages of fexofenadine hydrochloride ranges from 93.2 to 100.0% for brand III and from 96.5 to 102.3% for brand IV. Brand I and II showed significant differences with the originator brand IV.

Keywords Fexofenadine hydrochloride · Quality control · Counterfeit · UV–Vis spectrophotometer · British pharmacopeia (BP)

5.1 Introduction

Fexofenadine is a second-generation, H1-receptor antagonist (antihistamine) with a selective and peripheral H1-antagonist action [1]. Fexofenadine hydrochloride is a non-sedating anti-histamine drug used for the symptomatic relief of symptoms associated with rhinitis, urticarial and allergic skin conditions [2]. It is used to relieve the allergy symptoms of seasonal allergic rhinitis (hay fever), including sneezing, red, itchy, or watery eyes, or itching of the nose, throat, or roof of the mouth in adults [3]. Unlike most other antihistamines, fexofenadine hydrochloride does not cross the blood brain barrier and, therefore, does not cause drowsiness. Fexofenadine hydrochloride also lacks cardiotoxic potential of its predecessor terfenadine, since it does not block the potassium channel involved in repolarization of cardiac cells [1]. Fexofenadine is proved to be a safe choice in the treatment of asthma and atopic dermatitis. Fexofenadine is also rapidly absorbed with a long duration of action, making it suitable for once daily administration as it has a long half-life [4]. Literature survey reveals that fexofenadine hydrochloride tablets are estimated individually or in combination with other drugs by different methods including UV spectrophotometry and RP-HPLC [5–11]. In vitro equivalence studies have been reported in literature for fexofenadine hydrochloride 60 and 120 mg tablets [12, 13]. Literature review has not revealed any study related to fexofenadine hydrochloride 180 mg strength for brands that are already in the market.

The purpose of the present study is to assess the quality control parameters of different brands of fexofenadine hydrochloride tablets having a strength of 180 mg available in the Indian and UAE markets. For the present study, we selected two brands from India and two brands from UAE and assessed the tablets in terms of key physical and chemical parameters using the British Pharmacopeia 2018 [14] and non-pharmacopeial methods.

Table 5.1 Information on fexofenadine hydrochloride tablet samples

Brand	Country of origin	Market	Strength (mg)	Expiry date	Shape
I	India	India	180	Aug 2017	Elliptical
II	India	India		Jun 2019	Oval
III	Saudi Arabia	UAE		Apr 2020	Oval
IV	France	UAE		Mar 2019	Elliptical

5.2 Materials and Methods

Four brands of fexofenadine hydrochloride tablets from different manufacturers from India, France, and Saudi Arabia that are marketed in UAE and India were studied. The products were given names of brand I and brand II for products from Indian market, and brand III and IV for those from UAE market. Brands I and II of fexofenadine hydrochloride 180 mg tablets were purchased from a local pharmacy in Mumbai, India, while brands III and IV of the same strength were bought from a local pharmacy in Ajman, UAE (Table 5.1). All the purchased tablets were stored at room temperature away from direct sunlight. All the chemicals required for the study were of AR grade and bought commercially. Fexofenadine hydrochloride certified reference material and HPLC grade methanol and ethanol solvents were purchased from Sigma-Aldrich (USA). Water used for dilution and solution preparations was prepared by Milli-Q reverse osmosis Millipore. A sensitive digital analytical balance (OHAUS, USA), UV–Visible spectrophotometer, model UV-1800 from Shimadzu (Japan), and Fourier transform infrared (FTIR) spectrophotometer, model IRAffinity from Shimadzu (Japan) were used in the experiments.

   All the physical and chemical testing were carried out before the expired dates stated by the manufacturers.

5.3 Physical Testing

All physical test parameters for the tablets were performed according to BP 2018 [14].

5.3.1 Uniformity of Weight

Weight variation test was carried out in order to ensure uniformity in the weight of tablets. The samples of the tablets of each brand were weighed using an electronic weighing balance, and the average weight was determined. The weight variation of the 20 tablets was conducted for each brand as per the BP 2018 specification [14].

5.3.2   Thickness

Ten tablets from each brand were subjected to tablet thickness test, and the average thickness of tablets of each brand was determined using a Vernier caliper. Thickness should be controlled within ±5.0% variation of a standard value.

5.3.3   Disintegration

The disintegration test was performed on 6 tablets from individual brand as per BP 2018 procedures and specifications [14]. The disintegration time of six (6) tablets of each brand was determined at 37 °C in distilled water using a tablet disintegrator.

5.3.4   Friability

Friability is the loss of weight of a tablet in the container due to removal of fine particles from the surface during transportation or handling. This test was performed using an Erweka friabilator where ten (10) tablets from each brand were weighed before performing the test to determine their initial weight. Then, they were placed in the friabilator at 25 rpm for 4 min. After that, the tablets were cleaned from any fragments and re-weighed to determine their final weight for calculating the percentage friability using the following equation:

$$\%\text{Friability} = ((\text{Initial weight} - \text{Final weight})/(\text{Initial weight})) \times 100$$

Friability (% loss) must be less than or equal to 1.0%. This is a non-official test [14].

5.3.5   Dissolution

The dissolution test was conducted using a basket apparatus as per procedure specified in BP 2018 on tablets from individual brands [14]. This was determined by using a Tablet Dissolution Apparatus II Paddle Type. Six (6) tablets were taken randomly from each brand, and one tablet at a time was placed in each of the six vessels of the apparatus. A volume of 900 mL 0.1 N hydrochloric acid was poured in each vessel, and the system was maintained at 37 °C with a speed of 50 rpm. 5 mL of sample was withdrawn from each of the vessels at time intervals of 10, 15, 30, and 45 min. The absorbance of each of the withdrawn samples at λ_{max} 219 nm was determined using an UV-visible spectrophotometer. The concentrations of dissolved

fexofenadine hydrochloride present in the samples were determined by referring to the calibration curve of standard fexofenadine hydrochloride. To pass the test, not less than 80.0% of the labeled amount of fexofenadine hydrochloride should be dissolved within 45 min [14].

5.4 Chemical Testing

5.4.1 FTIR Spectroscopy

The samples from the four brands were subjected to FTIR spectroscopic analysis to examine the presence of fexofenadine hydrochloride in the formulations. The spectra of the samples were compared to the spectrum of the standard fexofenadine hydrochloride. The FTIR scanning range was from 400 to 2000 cm^{-1}.

5.4.2 UV–Vis Spectrophotometric Assay

The UV–Vis spectrophotometric assay of fexofenadine hydrochloride used in this work was reported in the literature [12]. A solution with a concentration of 0.00015% w/v of standard fexofenadine was scanned for confirming the wavelength of maximum absorbance (λ_{max}). For each brand, 10 tablets were powdered and an amount equivalent to 0.003 g of fexofenadine hydrochloride was taken for the assay. Since fexofenadine is freely soluble in methanol and ethanol, the powder from each brand was dissolved in 25 mL methanol and sonicated for 10 min, then made up to 100 mL with ethanol [12]. 5 mL from the resulting solution were diluted with the same mixture of methanol and ethanol (25:75) to make a 100 mL solution with a concentration of 0.00015% w/v solution. This procedure was repeated for all the brands. Then, the absorbance of the resulting solutions of different brands was measured at 219 nm. Same procedures were performed for the fexofenadine hydrochloride certified reference standard using different concentrations to construct the calibration curve. The percentage contents of fexofenadine hydrochloride in each brand were then calculated using the calibration curve and the following formula:

%Content = (Absorbance of Sample)/(Absorbance of Standard) × 100

Ten (10) measurements of the absorbance for each brand were carried out, and the average values of percentage drug contents were compared to the main brand of fexofenadine (brand IV) by *t*-test one tail.

Table 5.2 Weight uniformity of different brands

Brand	Average weight ± SD (mg)	Minimum weight (mg)	Maximum weight (mg)	% Deviation (±mg)	Range allowed (mg)
I	376.5 ± 1.1	374.5	378.5	5.0% (±18.8)	357.7–395.3
II	610.0 ± 1.5	608.0	612.0	5.0% (±30.5)	579.5–640.5
III	608.0 ± 2.2	605.0	611.0	5.0% (±30.4)	577.6–638.4
IV	630.0 ± 2.0	627.0	632.0	5.0% (±31.5)	598.5–661.5

5.5 Results and Discussion

5.5.1 Weight Uniformity Test

The weight uniformity test is a method of establishing the drug content uniformity in tablets. According to the BP 2018 specifications [14], if the average mass of the tablets is 250 mg or more, the percent deviation should not be more than 5.0%. In general, the tablet passes the BP 2018 test if no more than two tablets are outside the percentage limit and if no tablet differs by more than two times the percentage limit. Twenty tablets for the four brands were individually weighed (Table 5.2) and the average weight was calculated for each brand. Brands I-IV had the percentage deviation values within the range specified by BP 2018 specifications and hence passed the test.

5.5.2 Thickness Test

The thickness for brand I was found to be 6.5 ± 0.1 mm whereas brands II-IV had the same thickness of 7.7 ± 0.0 mm (Table 5.3). This shows that there is a consistency in the thickness of fexofenadine tablets from the four brands.

Table 5.3 Thickness of different brands

Brand	Thickness Mean ± SD (mm)
I	6.5 ± 0.1
II	7.7 ± 0.0
III	7.7 ± 0.0
IV	7.7 ± 0.0

Table 5.4 Disintegration time of different brands

Brand	Average disintegration time (s) $\pm$ SD
I	16.0 $\pm$ 1.8
II	13.0 $\pm$ 1.9
III	59.0 $\pm$ 1.4
IV	24.0 $\pm$ 1.4

5.5.3 Disintegration Test

Disintegration test is an important experiment to estimate the drug release from immediate release type of dosage forms. Table 5.4 shows the results of disintegration test performed for the four brands using six tablets in each brand. Brand II had the fastest disintegration time with an average disintegration time of 13 s, whereas brand III had the slowest average disintegration time of 59 s. The order of increasing average disintegration time of fexofenadine brands was brand II, brand I, brand IV and then brand III. The disintegration values lied in the range of 13–59 s. All brands passed the test, where BP 2018 specifications state that the time should not exceed 30 min for film-coated tablets [14].

5.5.4 Friability Test

Friability test is conducted to assess the ability of the tablet to withstand abrasion during packaging, shipping and handling. The specification for friability test for tablets in BP 2018 states that the percentage weight loss from each tablet after tumbling should not exceed 1.0% [14]. The percent friability for the four brands was found to be less than 1%, which indicates that the four brands passed the friability test as shown in Table 5.5.

Table 5.5 Percent friability of different brands

Brand	% Friability
I	0.3
II	0.2
III	0.0
IV	0.0

5.5.5 Dissolution Test

The dissolution study was conducted on the four brands using BP type II dissolution apparatus. According to the BP 2018, for a drug to pass the test, a minimum of 80% of the drug must be completely dissolved after 45 min, i.e. the quantity (Q) + 5.0% or 80.0% of the drug, where the term Q is the quantity of active substance dissolved in a specified time [14]. Dissolution test results are shown in Table 5.6 and Fig. 5.1. Each run was repeated 6 times, and the results are expressed as average values ± standard deviation (SD). It can be seen that the average percentage dissolved amount of fexofenadine hydrochloride of brands I and II failed to reach 80% after 45 min. Brands III and IV showed better dissolution of above 80.0% (81.8 ± 0.8% and 83.1 ± 2.8%, respectively) after 45 min.

Table 5.6 Dissolution test for different brands

Time (min)	Average dissolved concentration (% w/v) ± SD			
	Brand I	Brand II	Brand III	Brand IV
0	0.0 ± 0.0	0.0 ± 0.0	0.0 ± 0.0	0.0 ± 0.0
15	80.2 ± 3.9	74.9 ± 4.4	74.4 ± 2.4	76.4 ± 5.1
30	82.5 ± 4.4	77.0 ± 3.2	75.5 ± 1.3	81.8 ± 4.0
45	79.3 ± 3.4	75.3 ± 1.7	81.8 ± 0.8	83.1 ± 2.8
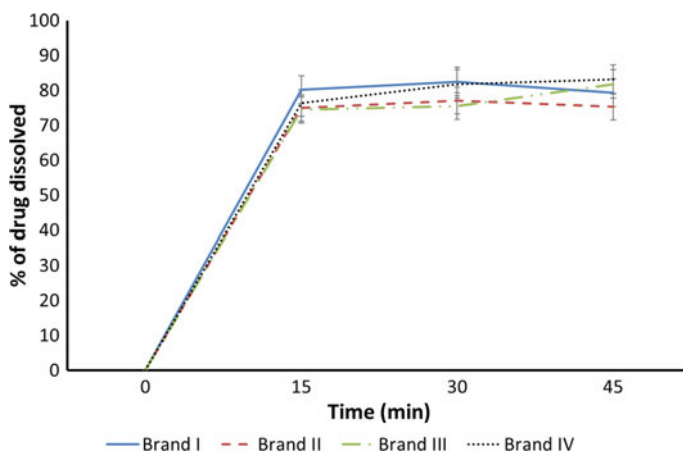
Fig. 5.1 Dissolution study of different brands

5.5.6 FTIR Test

From the FTIR study, it can be inferred that the spectra of the four brands matched with the spectrum of the fexofenadine hydrochloride standard (Figs. 5.2, 5.3, 5.4, 5.5 and 5.6).
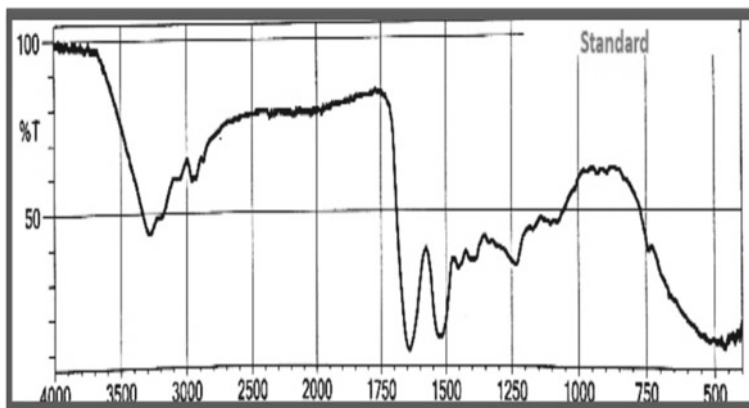
Fig. 5.2 FTIR spectrum of fexofenadine hydrochloride reference standard
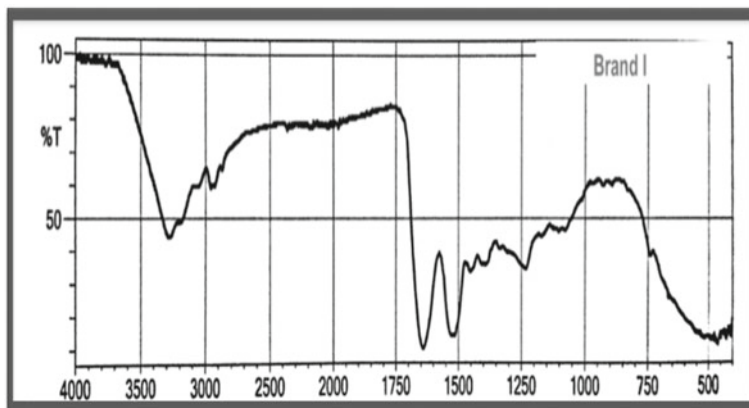
Fig. 5.3 FTIR spectrum of brand I tablets
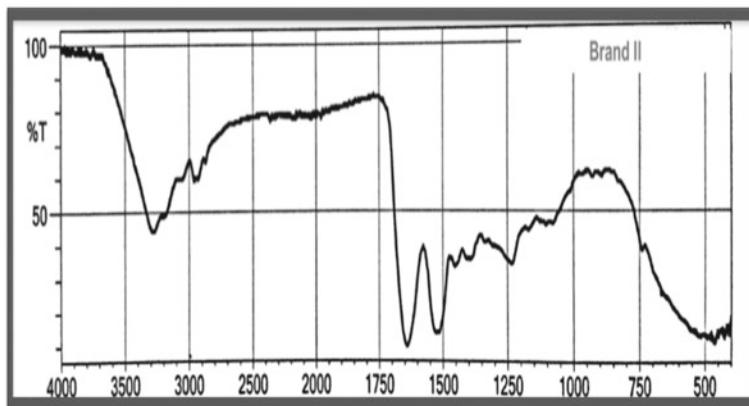
Fig. 5.4 FTIR spectrum of brand II tablets
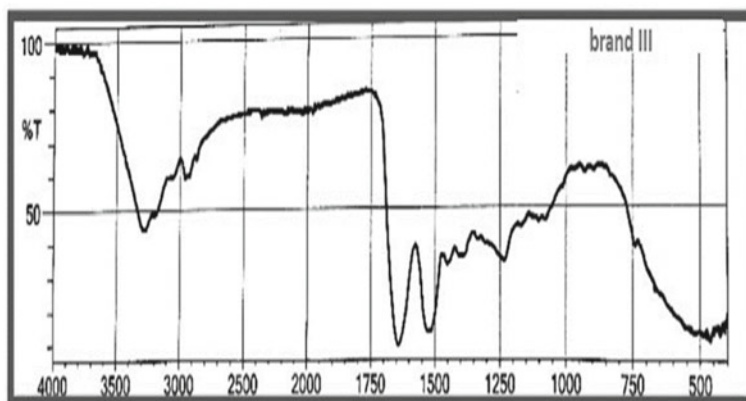
Fig. 5.5 FTIR spectrum of brand III tablets

5.5.7 Assay of Fexofenadine Hydrochloride

The percent content of fexofenadine hydrochloride was determined using UV–Vis spectrophotometry at 219 nm. Table 5.7 shows the average percent contents of fexofenadine hydrochloride per tablet for all the studied brands. The brands from Indian market showed percentage contents of active ingredient range from 75.1 to 80.5% for brand I and 91.4–97.8% for brand II. Brands from UAE market showed percentages of fexofenadine hydrochloride range from 93.2 to 100.0% for brand III and from 96.5 to 102.3% for brand IV. Moreover, there was a significant difference ($p <$ 0.05) between the originator brand IV and brands I and II. However, no significant difference was shown between brands III and IV as can be seen in Table 5.7.
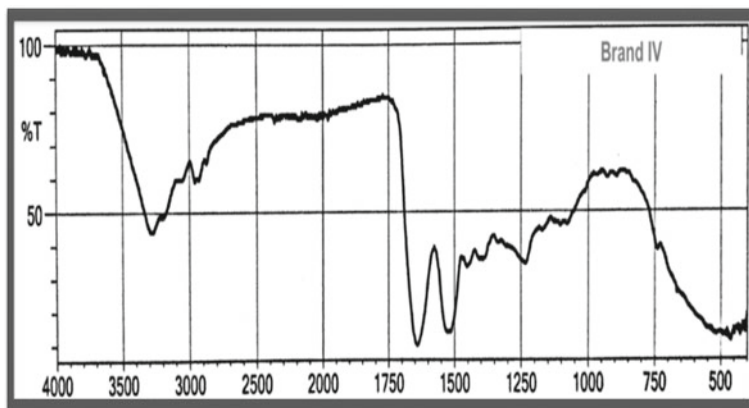
Fig. 5.6 FTIR spectrum of brand IV tablets

Table 5.7 Assay of fexofenadine hydrochloride in different brands

Brand	Average % content ± SD	Significant difference compared to brand IV ($P(T <= t)$ one-tail)
I	77.8 ± 2.7 (75.1–80.5)	0.0002
II	94.6 ± 3.2 (91.4–97.8)	0.0312
III	96.6 ± 3.4 (93.2–100.0)	0.2280
IV	99.4 ± 2.9 (96.5–102.3)	–

5.6   Conclusion

Fexofenadine hydrochloride manufactured in generic form is one of the most popular choices of antihistamine products used for the treatment of allergy symptoms such as hay fever, nasal congestion, and urticarial. Two brands from Indian market and two brands from UAE market having a strength of 180 mg were evaluated for their quality control parameters using the methodologies from BP 2018 and a developed non-pharmacopeial assay method. It was found that all the four brands passed the tests for weight variation, disintegration, FTIR, and friability. However, significant difference was observed between brands I and II compared to the innovator brand (brand IV) for the other quality control tests such as dissolution and content uniformity. More work is in progress to assess more brands of fexofenadine hydrochloride 180 mg tablets from these two markets using pharmacopeial methods.

References

1. Markham A, Wagstaff AJ (1998) Fexofenadine. Drugs 55:269–276
2. Sakairi T, Suzuki K, Makita S, Wajima T, Shakuto S, Yoshida Y et al (2005) Effects of fexofenadine hydrochloride in a guinea pig model of antigen-induced rhinitis. Pharmacology 75:76–86
3. Seidman MD, Gurgel RK, Lin SY, Schwartz SR, Baroody FM, Bonner JR et al (2015) Clinical practice guideline: allergic rhinitis. Otolaryngol-Head Neck Surg 152:S1–S43
4. Simpson K, Jarvis B (2000) Fexofenadine: a review of its use in the management of seasonal allergic rhinitis and chronic idiopathic urticaria. Drugs 59:301–321
5. Hofmann U, Seiler M, Drescher S, Fromm MF (2002) Determination of fexofenadine in human plasma and urine by liquid chromatography–mass spectrometry. J Chromatogr B 766:227–233
6. Polawar PV, Shivhare UD, Bhusari KP, Mathur VB (2008) Development and validation of spectrophotometric method of analysis for fexofenadine HCl. Res J Pharm Technol 1:539–554
7. Kumar KS, RavichandranV Mohan Maruga, Raja MK, Thyagu R, Dharamsi A (2006) Spectrophotometric determination of fexofenadine hydrochloride. Indian J Pharm Sci 73:300–302
8. Narayan B, Veena K (2010) A new method for the spectrophotometric determination of fexofenadine hydrochloride. Indian J Chem Tech 17:386–390
9. Karakuş S, Küçükgüzel İ, Küçükgüzel ŞG (2008) Development and validation of a rapid RP-HPLC method for the determination of cetirizine or fexofenadine with pseudoephedrine in binary pharmaceutical dosage forms. J Pharm Biomed Anal 46:295–302
10. Maggio RM, Castellano PM, Vignaduzzo SE, Kaufman TS (2007) Alternative and improved method for the simultaneous determination of fexofenadine and pseudoephedrine in their combined tablet formulation. J Pharm Biomed Anal 45:804–810
11. Radhakrishna T, Om Reddy G (2002) Simultaneous determination of fexofenadine and its related compounds by HPLC. J Pharm Biomed Anal 29:681–690
12. Khan MN, Naveed S, Dilshad H, Ayub M (2016) Pharmaceutical equivalent dissertation of fexofenadine hydrochloride brands. Bull Env Pharmacol Life Sci 5:21–27
13. Raka SC, Rahman A, Bodiuzzaman B (2017) Comparative in-vitro equivalence evaluation of fexofenadine hydrochloride 120 mg generic tablets marketed in Bangladesh. Glob J Pharmaceu Sci 3:555602
14. British Pharmacopoeia Commission (2018) British Pharmacopoeia. TSO, London, UK

Chapter 6
The Cytotoxicity of *Mimusops Caffra*-Derived Ursolic Acid and Its Three Triterpenoid Semi-synthesized Derivatives on HEK293 and HepG2 Cells

Senabello T. Mngomezulu, Adebola O. Oyedeji, Francis O. Shode, Opeoluwa O. Oyedeji, Andy R. Opoku and Moganavelli Singh

Abstract The isolation of pure ursolic acid (UA) from most plants presents a problem because it often comes as a mixture with its isomer, oleanolic acid (OA). In this study the separation of UA from OA/UA mixture obtained from *Mimusops caffra* was achieved through acetylation to give the acetate of UA and OA respectively. Pure UA (90%) was then obtained by simple de-acetylation of the UA acetate. The resulting UA was used as template for the semi-synthesis of three triterpenoids derivatives. This study confirmed the various reports in literature that UA is always accompanied by its isomer oleanolic acid (OA). This article further reports for the first time the synthesis of 3-acetyl-UA-28-cinnamate. The cytotoxicity of all compounds was evaluated on human embryonic cells (HEK293) and human hepatocellular carcinoma cells (HepG2) by MTT assay. All the compounds studied exhibited low toxicity levels with $IC_{50} > 300$ μg/ml.

S. T. Mngomezulu · A. O. Oyedeji (✉)
Department of Chemical and Physical Sciences, Walter Sisulu University, Mthatha 5099, South Africa
e-mail: aoyedeji@wsu.ac.za

S. T. Mngomezulu
e-mail: sennychiliza@gmail.com

F. O. Shode
Department of Chemistry, Cape Peninsula University of Technology, Cape Town 8000, South Africa
e-mail: francisshode@yahoo.com

O. O. Oyedeji
Department of Chemistry, University of Fort Hare, Alice 5700, South Africa
e-mail: ooyedeji@ufh.ac.za

A. R. Opoku
Department of Biochemistry and Microbiology, University of Zululand, KwaDlangezwa, Empangeni 3886, South Africa
e-mail: opokua@unizulu.ac.za

M. Singh
Department of Biochemistry, University of KwaZulu-Natal, Durban 4001, South Africa
e-mail: singhm1@ukzn.ac.za

6.1 Introduction

The search for isolated or semi-synthesised compounds that can be used in drug
formulation, which are non-toxic but more active and having fewer side-effects than
synthetic drugs, is on the increase. The use of natural products as templates for
the semi-synthetic derivatives with more potency [1], is the alternative route. Penta-
cyclic triterpenes and their derivatives are widely reported for their diverse biological
activities potentials based on different chemical structure modification [2–4].

Compound **1** (Fig. 6.1), known as ursolic acid, the pentacyclic triterpene of inter-
est, obtained in large amounts from certain plants, can be used as a starting material
for the synthesis of other biologically active compounds. However, it is generally
accompanied by its isomer (oleanolic acid) compound **2** (Fig. 6.1) and the close-
ness of their chemical structures makes their separation by simple chromatographic
methods very difficult; hence, researchers have relied on derivatization as alternative
means of separation [5, 6].

Secondly, despite the biological potential of ursolic acid (**1**), unfortunately, it
is only slightly soluble in water preventing its direct use for the pre-clinical and
clinical evaluation. The need of synthesizing soluble derivatives as template for
clinical drug evaluation and formulations is therefore necessary. Some derivatives of
compound **1** have been reported to have a variety of biological activities based on the
different chemical structure modifications [7]. Studies reported by Yu et al. [8] and
Sun et al. [9] reveal C3 derivatives of compound **1** being active against HIV-1-infected
H9 lymphocytes. Cinnamic acid and its synthetic derivatives of compound **1** have
drawn interest over the years due to the antibacterial and antifungal effects [10, 11].
However, a combination of these functional groups in compound **1** at position C3 and
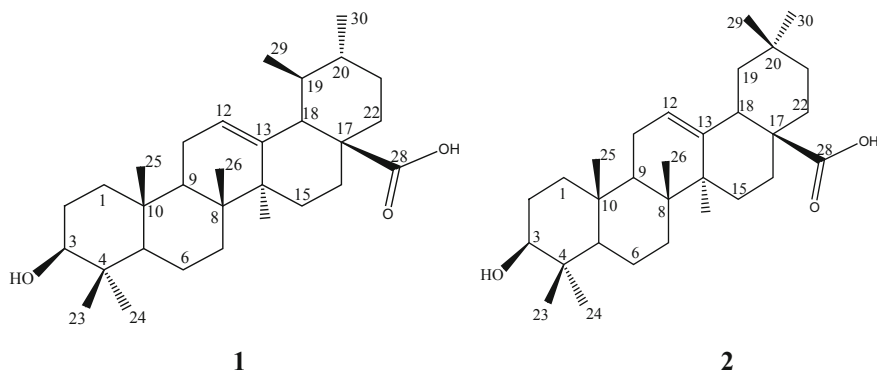
Fig. 6.1 The carbon numbered structures of ursolic acid (**1**), and oleanolic acid (**2**)

C28 have not been reported. Tanachatchairatana et al. [12] reported the biological activity of the cinnamate-based esters of closely related triterpenes at position C3. Baglin et al. [13] reported the anti-tumour and anti-HIV activity of UA linked at C3 with the substituted cinnamic acid. Our interest in structure-activity relationship (SAR) studies prompted the introduction of different functional groups at C3- and C28-position of compound **1** with the aim of enhancing their biological activity. The main aim of the study is to obtain pure UA, to increase the solubility of the parental compound by synthesizing C3- and C28-modified derivatives, and to evaluate the antineoplastic activity of the spectrum of **1** derivatives.

6.2 Experimental

6.2.1 Preparation and Extraction of Plant Material

The leaves of *Mimusops caffra* were collected from the Durban Botanic Gardens and authenticated. The voucher number of the specimen was FOS005. The dried leaves of the plant were pulverised and stored at room temperature. Approximately 1 kg of the powder was macerated twice in 5 litres of ethyl acetate for 48 h with constant shaking. Crude extract solution was concentrated using a rotary evaporator under reduced pressure to obtain ethyl acetate crude extract of yield 87.24 g.

6.2.2 Purification and Separation of Ursolic Acid (1) and Oleanolic Acid (2) from Crude Extract

Ethyl acetate extract (87.0 g) was washed twice with hexane at room temperature to remove the non-polar components followed by an acetone wash to yield the residue (61.48 g) and the combined filtrate (25.41 g). The ^{1}H NMR analysis of residue reveals that it was a mixture of compounds **1** and **2**. Separation of **1** and **2** was achieved by acetylating the mixture of the two isomers followed by fractionation on column chromatography and finally, hydrolysis of the acetates gave back the free acids as indicated in Scheme 6.1.

6.2.3 Derivatization of 1

6.2.3.1 Acetylation Procedure for the Preparation of 3

Mixture of compounds **1** and **2** (10 mmol) was dissolved in 40 ml pyridine. While stirring, 9.45 ml of acetic anhydride was added to the mixture in an ice bath. DMAP
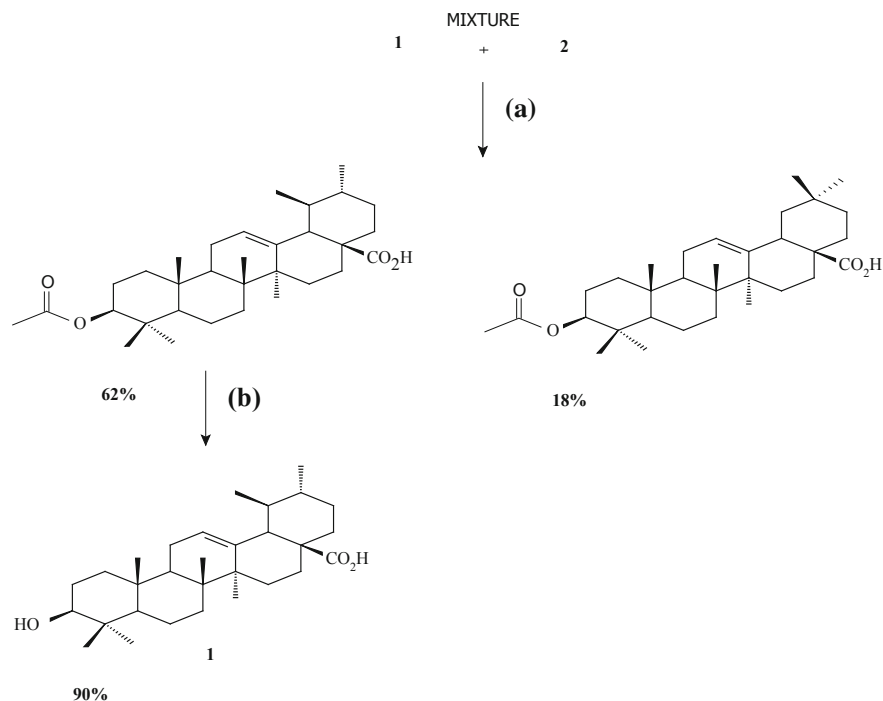
Scheme 6.1 Separation of ursolic and oleanolic acids; reagents and conditions: **a** acetic anhydride, pyridine, DMAP, 24 h, r.t. [6]; **b** 10% aqueous K_2CO_3, MeOH, 30 min, r.t. [12]

(4-dimethylaminopyridine) (1.22 g, 10 mmol) was added and the mixture was further stirred at room temperature for 24 h. The reaction mixture was poured into distilled ice water and stirred for an hour. The solid product was filtered and washed with 2 M HCl to remove unreacted pyridine and DMAP. The product was recrystallized in methanol, air dried and subjected to column chromatography (**3:** 3.087 g and **4:** 0.896 g) using Hex/EtOAc (9:1).

6.2.3.2 De-Acetylation Procedure for the Preparation of 1

6 mmol of **3** was added to 10 ml of MeOH and stirred. Excess solution of 10% aqueous K_2CO_3 (5 ml) was added with continuous stirring at ambient temperature for 30 min. Water (20 ml) was added and the solution mixture was acidified with 5% aqueous HCl and extracted three times with ethyl acetate (3 × 40 ml). The combined organic phase was then washed with water (2 × 40 ml) and dried over anhydrous sodium sulphate (Na_2SO_4); the solvent was evaporated and the residue recrystallized in methanol (**1**: 2.472 g) (Scheme 6.1).

6.2.3.3   Preparation of 5

Modified Wen et al. procedure [14] was adapted in which 3-acetyl-UA (**3**) (0.5 g; 0.001 mol) was treated with excess CH_3I (2 g) in the presence of Na_2CO_3 (2–3 g) in 40 ml DMF at 20 °C for 24 h while stirring. Afterwards, the content was decanted into 100 ml water and stirred again for about 2 h before filtering. The desired compound **5** (3-acetyl-UA-28-methylate) was formed as indicated by TLC; purification by column chromatography eluting with Hex/EtOAc (9:1) gave **5** as pure white crystals (0.4805 g).

6.2.3.4   Preparation of 6

Modified procedure of Cativela and Diaz-de-Villegas [15] was used for preparation of **6**. A mixture of **3** (0.5 g, 0.001 mol) and K_2CO_3 (0.3 g) in DMF (40 ml) was heated to 50 °C and excess benzyl chloride (10 ml) was added. After 2 h, the temperature was raised to 60 °C for another 2 h, and finally to 70 °C for a total of 24 h without letting air into the reaction. The hot reaction mixture was quenched with distilled water and stirred for a few minutes, allowing the oily product to settle at the bottom of the flask. A creamy layer of water (with a pleasant smell) was filtered by gravity. Crystals were observed within four days. The product was recrystallized in ethanol. Product **6** (3-acetyl-UA-28-benzylate) was obtained as pure white shiny needles (0.31 g) (Scheme 6.2).

6.2.3.5   Preparation of 7

Modified procedure of Tanachatchairatana et al. [12] was employed in which $SOCl_2$ (3 ml) was added to cinnamic acid (0.15 g, 1 mmol) in a 500 ml round bottom flask and refluxed for two hours without letting air into the reaction. Excess $SOCl_2$ was removed after which CCl_4 (1.0 ml) was then added to the mixture and concentrated under vacuo at 40 °C to remove any traces of $SOCl_2$. Compound **3** (0.4 g, 0.8 mmol) was placed in another beaker containing a mixture of 7 ml of DCM and 1.0 ml of triethylamine (TEA). This mixture was stirred and transferred into the round-bottom flask. The combined mixture was stirred at room temperature for 24 h after which it was diluted with 4 ml CCl_4 and washed three times with distilled water (3 × 50 ml). The organic layer was separated and dried over anhydrous Na_2SO_4 and concentrated under pressure at 40 °C. Compound **7** (3-acetyl-UA-28-cinnamate) (0.025 g) was purified by column chromatography using Hex/EtOAc (9:1) and was obtained as a creamy white powder (Scheme 6.2).
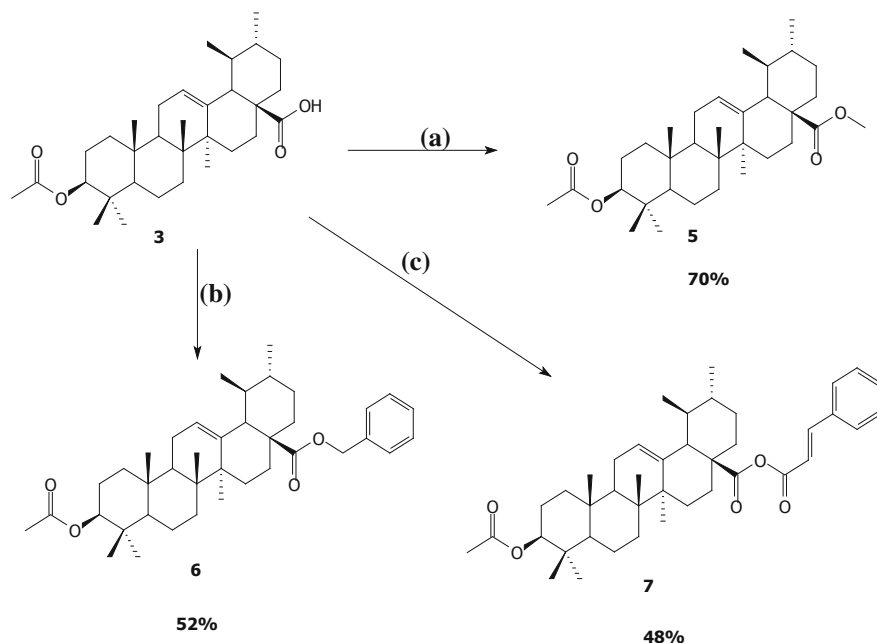
Scheme 6.2 Semi-synthesis of 28-UA-analogues, reagents and conditions: **a** DMF, Na$_2$CO$_3$, iodomethane, r.t., 24 h [14]; **b** DMF, K$_2$CO$_3$, benzyl chloride, 70 °C, 24 h [15]; **c** SOCl$_2$, cinnamic acid, CHCl$_3$, TEA, 24 h, r.t. [12]

6.2.4 Cytotoxic Bioassay—The MTT Assay

Slightly modified method of Mosmann [16] was used to test for the cytotoxicity of the drugs. Human embryonic kidney (HEK293) and hepatocellular carcinoma (HepG2) cells were grown to confluence in 25 ml flasks. These were then trypsinized and placed in 96-well plates at specific speed densities. The cells were incubated for 24 h at 37 °C. Thereafter, the medium was removed and a fresh medium mixture of minimal essential medium (MEM + Glutamax + antibiotics + 10% foetal bovine serum) was added. The compounds were added in triplicate for each concentration and incubated for 48 h and the cells were subjected to MTT assay as described by Nanyonga et al. [17]. The medium was removed from the cells in a multiwell plate, and 100 µl of 5 mg/ml MTT solution in phosphate buffer saline (PBS pH 7.4) and 100 µl of medium were added and the plate was incubated again for 4 h at 37 °C. Thereafter, the medium and MTT solution were removed from the wells and 100 µl of dimethyl sulfoxide (DMSO) were added to each well to stop the reaction and dissolve the insoluble formazan crystals. For the control, no compound was added to the reacting solutions. The plate was read using the Mindray plate reader. The percentage mortality was calculated for all measurements using the following formula:

$$\% \, \text{Cell Mortality} = \left(1 - \frac{A_{\text{test}}}{A_{\text{blank}}}\right) \times 100$$

where A_{test} is the absorbance of the tested sample and A_{blank} is the absorbance of the control or blank. The concentration range of the semi-synthesised compounds was 50–300 µg/ml. The graphs are plotted as the cell mortality (%) against concentration of extract used.

Statistical analysis calculated the percentage of cell mortality based on the average absorbance of the triplicate samples; standard deviation was calculated as a percentage of each measurement using 2010 Microsoft Excel.

6.3 Results and Discussion

Direct ethyl acetate extraction of the *M. caffra* leaves afforded OA and UA as a mixture. De-fatting of the ethyl acetate extract followed by acetone washing gave purified ethyl acetate extract (61.48 g). TLC of the purified extract gave one spot at R_f value of 0.49. However, NMR analysis of the purified extract confirms the presence of compounds **1** and **2** in the mixture. Separation of these isomers was achieved by the acetylation reaction (Scheme 6.1).

The acetylated products OA acetate (**4**) and UA-acetate (**3**) (Fig. 6.2) were isolated by column chromatography. Structural elucidation was established with the help of 2D NMR and comparison with data from the literature [18–20]. The carbon numbered structures of ursolic acid derivatives and oleanolic acetyl derivative (**4**) are given in Fig. 6.2. Compounds **3** and **4** were obtained as white amorphous powders.

6.3.1 Ursolic Acid (1)

Hydrolysis of **3** yielded pure compound **1** (90%, R_f 0.49, pink spot) as white powder melting at 286–288 °C which was correlated with the report of Deri et al. [21]. The structure of compound **1**, which is the backbone of all the other semi-synthesized compounds reported in this article, was confirmed by the appearance of 30 peaks in ^{13}C NMR. The DEPT 90 experiment showed seven peaks (CH), whilst DEPT 135 showed a total of 14 peaks (CH and CH_3) and nine CH_2 peaks (Table 6.1). Furthermore, HMBC was used to assign the protons to each carbon in accordance with the literature [18, 21]. The most notable carbons were C-3, C-12, C-13 and C28, which were distinctly separated from the rest of the carbons. The C-28 resonated at the highest frequency δ 183.2 ppm which is a carboxylic acid carbon. The C-13 quaternary carbon was downfield at δ 143.6 ppm due to the carbon double bond while the vinyl C-12 was deshielded to the frequency of δ 122.6 ppm. C-3 was easily recognised at δ 79.03 ppm due to the C–O bond, which causes it to be deshielded.
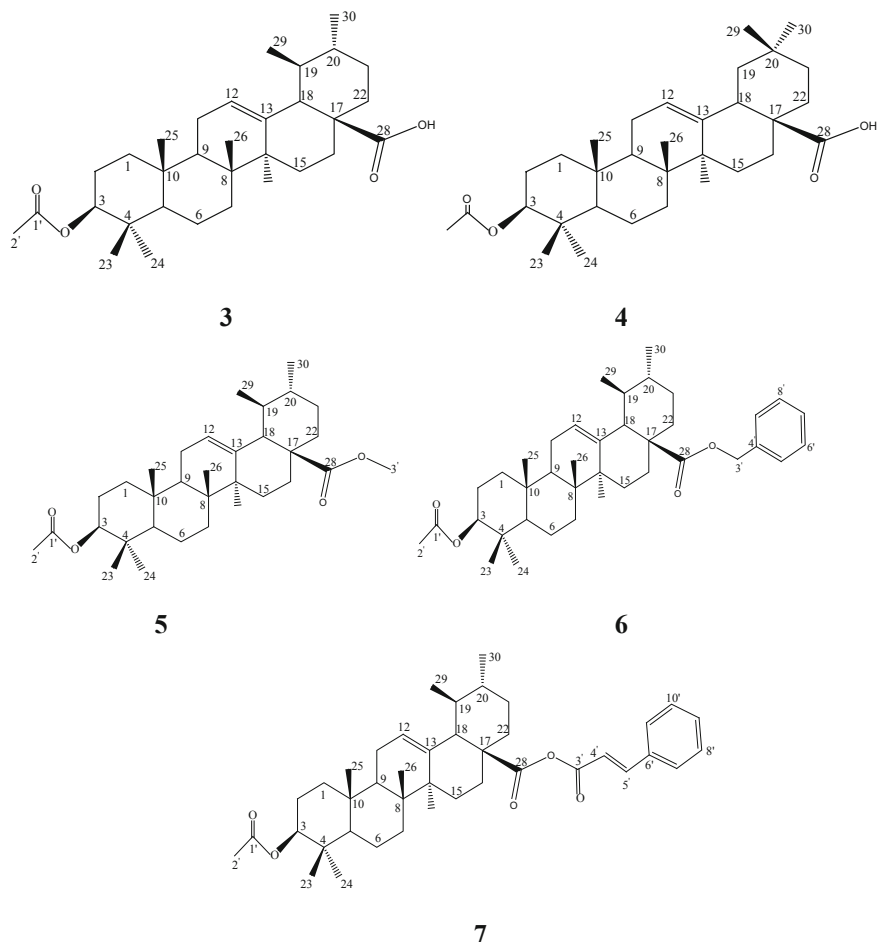
Fig. 6.2 The carbon numbered structures of ursolic acid derivatives and oleanolic acetyl derivative (**4**)

The remaining carbons that fall under the methylene envelope were assigned their position using the 2D NMR and reference data in literature [18].

6.3.2 3-Acetyl-UA (3)

After the acetylation of the mixture of the isomers **1** and **2**, 3-acetyl-UA (Scheme 6.2) was obtained as a white amorphous powder, with a melting point of 279 °C, yield 62% with R_f 0.89, a pinkish spot (while OA-acetate had a melting point range of 231–234 °C as compared to 230–233 °C reported in the literature by Habila et al.

Table 6.1 ^{1}H and ^{13}C NMR data (δ ppm) of compounds **1–7**

^{13}C	^{13}C DEPT	1	3	OA[a]	2		4		UA[b]	5		6		7	
		δC	δC	δC	δH	δC	δH	δC	δC	δH	δC	δH	δC	δH	δC
1	CH2	38.8	39.0	39.0	1.26, t	31.9	1.25, t	37.0	38.8	1.27, t	38.3	1.25, t	38.3	1.26, t	38.3
2	CH2	28.1	23.6	28.1	1.60, q	27.2	1.60, m	28.1	27.3	1.62, q	23.6	1.60, m	23.5	1.62, q	23.5
3	CH	79.0	80.9	78.2	3.20, dd	79.1	4.50, dd	81.0	78.8	4.50, dd	80.9	4.50, dd	80.9	4.30, dd	81.0
4	C	38.4	37.7	39.4	—	38.7	—	37.7	38.8	—	39.5	—	39.5	—	39.7
5	CH	55.2	55.3	55.9	1.35, m	55.2	1.34, m	55.3	55.5	1.35, m	55.3	1.34, m	55.3	1.40, m	55.3
6	CH2	18.3	18.2	18.8	1.53, m	16.9	1.53, m	16.9	18.4	1.53, m	18.2	1.53, m	18.2	1.53, m	18.9
7	CH2	33.1	33.7	33.4	1.33, t	29.7	1.34, t	32.9	33.0	1.32, t	30.7	1.34, t	30.7	1.32, t	30.7
8	C	39.3	39.0	39.8	—	39.5	—	40.0	39.6	—	37.7	—	37.7	—	37.7
9	CH	47.6	52.1	48.2	1.50, dd	47.5	1.50, dd	47.6	47.5	1.49, dd	47.5	1.50, dd	47.5	1.49, d	47.5
10	C	37.1	36.9	37.4	—	36.9	—	36.7	37.0	—	36.7	—	36.6	—	37.8
11	CH2	23.4	23.3	23.8	1.92, m	22.7	1.92, m	23.6	23.3	1.95, m	23.3	1.92, m	23.3	1.95, m	23.3
12	CH	122.6	125.7	122.6	5.20, t	125.9	5.20, t	124.3	125.5	5.20, t	125.5	5.20, t	125.6	5.20, t	125.6
13	C	143.6	137.9	144.8	—	138.9	—	139.6	138.0	—	138.2	—	138.1	—	137.9
14	C	41.6	41.9	42.2	—	41.9	—	41.5	42.0	—	41.9	—	41.0	—	42.5
15	CH2	27.7	28.0	28.4	0.99, d	28.1	0.98, d	28.7	28.2	0.92, d	28.0	0.98, d	27.9	0.92, d	27.8
16	CH2	23.6	23.6	23.8	1.08, d	23.6	1.07, d	23.4	24.3	1.03, d	24.2	1.07, d	24.2	1.03, d	24.2
17	C	46.5	47.5	46.7	—	47.9	—	42.1	48.1	—	47.1	—	48.1	—	49.8
18	CH	41.0	39.5	42.1	2.19, d	52.7	2.00, d	59.1	52.8	2.20, d	52.9	2.00, d	52.9	2.20, d	52.6
19	CH2	45.9	48.0	46.6	1.32, s	39.1	1.30, s	39.7	39.1	1.29, s	39.0	1.30, s	39.1	1.29, s	39.1
20	C	30.7	32.8	31.0	1.32, d	38.8	1.33, d	39.6	38.8	1.32, d	38.9	1.33, d	38.8	1.32, d	39.5
21	CH2	33.8	30.6	34.3	1.26, m	29.4	1.25, m	31.2	30.7	1.26, m	32.9	1.25, m	33.0	1.26, m	33.0
22	CH2	32.6	28.1	33.2	0.99, m	38.6	1.70, m	38.5	36.7	0.99, m	36.9	1.70, m	36.9	0.99, m	36.9
23	CH3	22.9	23.6	28.8	1.25, s	29.1	0.98, s	29.7	28.2	1.23, s	28.1	0.98, s	28.1	1.23, s	28.1
24	CH3	15.6	16.7	16.5	0.85, s	14.0	0.83, s	14.1	15.5	0.85, s	15.5	0.83, s	15.5	0.85, s	15.5
25	CH3	15.3	15.5	15.6	0.77, s	15.5	0.78, s	15.7	15.7	0.78, s	16.7	0.78, s	16.7	0.78, s	16.7
26	CH3	17.1	17.1	17.5	0.86, s	15.6	0.82, s	18.2	16.9	0.86, s	16.9	0.82, s	17.0	0.85, s	17.1
27	CH3	25.9	24.0	26.2	1.08, s	23.4	1.07, s	23.2	23.6	1.10, s	23.3	1.07, s	23.6	1.10, s	23.6
28	C	183.2	183.7	180.0	—	178.8	—	195.0	177.7	—	178.1	—	177.3	—	172.6
29	CH3	27.2	38.8	33.4	0.87, d	14.1	0.88, d	18.2	16.9	0.87, d	17.1	0.88, d	17.0	0.87, d	17.3
30	CH3	23.9	21.2	23.8	0.85, s	17.1	0.84, s	17.5	21.2	0.84, s	21.3	0.84, s	21.3	0.84, s	21.3
1'	C		171.1			171.0	—			—	171.0		171.0	—	171.0
2'	CH3		21.3			21.4	1.90, s			2.00, s	21.2	1.90, s	21.2		
3'										3.50, s	51.5	5.00, dd	66.0	2.00, s	21.1
4'											—		136.4	—	172.6
5'												7.30, d	128.4	6.50, s	117.5
6'												7.30, dd	128.1	7.80, s	145.2
7'												7.20, dd	127.9	—	137.8
8'														7.50, d	128.0
9'														7.40, d	128.0

[a]Kontogianni et al. [19], Uddin et al. [20]
[b]Mohato and Kundu [18]

[22]). The MS of **3** indicated *m/z* = 497.35, which is M-H for [$C_{32}H_{49}O_4$]. The NMR analysis of compound **3** had two additional signals due to methyl and carboxy carbons of the acetoxy group in the ^{13}C NMR spectrum and a high intense singlet, which was due to the methyl protons in the ^{1}H NMR spectrum. The ^{1}H NMR spectrum further indicated that the proton at C-3 had deshielded from δ 3.2 ppm to a notable δ 4.5 ppm, and the slight difference in chemical shifts of the nearby carbons as indicated in Table 6.1, was due to the added acetyl group at C-3.

6.3.3   *3-Acetyl-UA-28-Methylate (5)*

The methylation of compound **3** gave 70% of **5** as pure white crystals (Scheme 6.2). The melting point of **5** was found to be 219–220 °C with R_f 0.92, a dark purplish spot. The MS *m/z* = 513.39, which is M + H for [$C_{33}H_{52}O_4$]. On NMR analysis, an

additional signal in ^{13}C spectrum at δ 51.5 ppm, the C-3′ carbon, correlating to the singlet in proton NMR spectrum at δ 3.5 ppm that is due to the added methyl group, was observed (Table 6.1).

6.3.4 3-Acetyl-UA-28-Benzylate (6)

The benzylation of compound **3** gave 52% of **6** as pure white shiny needles (Scheme 6.2). The melting point was 190–191 °C with R_f 0.94, a dark pink spot. The MS $m/z = 589.42$, which is M + H for [$C_{39}H_{56}O_4$]. The NMR analysis showed additional signals on the ^{13}C spectrum for the added benzyl group. Notably also was the CH$_2$ signal at C-3′ at δ 66.0 ppm with the corresponding protons in ^{1}H NMR spectrum at δ 5.0 ppm (Table 6.1).

6.3.5 3-Acetyl-UA-28-Cinnamate (7)

The reaction of compound **3** and cinnamic acid chloride gave 48% of **7** as a creamy white powder (Scheme 6.2). The melting point of **7** was found to be 163–165 °C with R_f 0.94, a dark bluish spot. The MS $m/z = 629.85$, which is M + H for [$C_{41}H_{56}O_5$]. Analysis of the ^{13}C NMR spectrum revealed additional distinct carbon signals at 117.5, 128.0, 137.8, 145.2 and 172.6 ppm for the added cinnamic group. The rest of the backbone structure of the parent compound was not affected as indicated by the chemical shifts in Table 6.1.

6.3.6 Cytotoxicity Activity

The effect of the anti-cancer activity of compounds **1**–**7** was determined by measuring the cell viability using the 3-(4,5-dimethylthiazolyl-2)2,5-diphenyltetrazolium bromide MTT technique. The results of the cytotoxicity/anti-proliferative activity of the drugs are summarised in Tables 6.2 and 6.3 and presented in Fig. 6.3. It is apparent that ursolic acid and its derivatives exhibit a dose-dependent cytotoxicity in both HEK293 and HepG2 cells; the response of the two cell lines was almost the same towards the drugs. In cytotoxic evaluations a compound is significantly active if it has an IC$_{50}$ less than 30 μg/ml [23]. The observed IC$_{50}$ values indicate that the drugs do not exhibit any appreciable antineoplastic activity. It is apparent also that the chemical modification of ursolic acid rather renders it less toxic. This result is in line with the report of Yin et al. [24] in which ursolic acid and its derivatives exhibited anticancer activity against breast cancer cells. In our report, the modified derivatives of ursolic acid were observed to be less toxic than the parent compound although still potent.

Table 6.2 Cytotoxicity in HEK293 (human embryonic kidney) cells

Conc. (μg/ml)	1	3	5	6	7
	Percentage of cell mortality (% ± SD)				
0	0.0	0.0	0.0	0.0	0.0
50	10.0 ± 5.8	17.3 ± 2.7	9.0 ± 0.6	3.2 ± 2.9	4.6 ± 1.5
100	29.8 ± 3.8	27.0 ± 1.7	15.2 ± 3.2	9.0 ± 8.1	13.4 ± 5.3
150	28.0 ± 5.8	32.0 ± 4.8	22.2 ± 4.7	13.0 ± 5.2	17.8 ± 5.5
200	35.2 ± 1.6	37.2 ± 5.1	29.3 ± 6.4	24.4 ± 4.7	25.4 ± 3.4
250	37.1 ± 6.1	40.7 ± 5.3	39.3 ± 1.2	31.5 ± 7.5	25.4 ± 2.7
300	43.0 ± 4.2	46.6 ± 2.4	42.6 ± 4.5	34.3 ± 6.4	32.2 ± 6.9
IC_{50} (μg/ml)	820	770	880	<1000	<1000

% = Percentage of cell mortality calculated on the average absorbance of the triplicate samples; standard deviation (SD) calculated as a percentage of each measurement using 2010 Microsoft Excel. The IC_{50} values were calculated using the Cheburator version 1.2.0 easy-to-use software

Table 6.3 Cytotoxicity in HepG2 (human hepatocellular carcinoma) cells

Conc. (μg/ml)	1	3	5	6	7
	Percentage of cell mortality (% ± SD)				
0.0	0.0	0.0	0.0	7.4 ± 5.5	7.6 ± 6.6
50.0	16.2 ± 8.8	5.2 ± 4.9	11.3 ± 8.0	7.9 ± 6.8	9.4 ± 4.1
100.0	23.6 ± 3.6	11.7 ± 3.4	13.4 ± 5.3	20.1 ± 7.0	14.4 ± 6.0
150.0	28.1 ± 0.8	15.6 ± 6.0	20.7 ± 7.0	22.4 ± 4.4	22.1 ± 1.5
200.0	36.3 ± 1.3	26.6 ± 23.8	23.9 ± 2.3	28.7 ± 6.7	28.1 ± 6.9
250.0	39.2 ± 2.4	20.5 ± 10.0	28.8 ± 3.8	39.5 ± 0.6	36.6 ± 2.0
300.0	46.8 ± 6.2	33.0 ± 4.6	33.0 ± 5.9	7.4 ± 5.5	7.6 ± 6.6
IC_{50} (μg/ml)	790	<1000	<1000	<1000	<1000

% = Percentage of cell mortality calculated on the average absorbance of the triplicate samples; standard deviation (SD) calculated as a percentage of each measurement using 2010 Microsoft Excel. The IC_{50} values were calculated using the Cheburator version 1.2.0 easy-to-use software

6.4 Conclusion

Mimusops caffra has been shown to be a good source of ursolic acid while ethyl acetate was found to be the best solvent to get good yields of **1** and **2** by extraction from the leaves of this plant. Acetylation of the mixture enabled separation of both compounds **1** and **2** with high recovery percentages. This semi-synthetic isolation route was found to be faster and easier and it gave a high product yield when compared to other methods described in the literature. The semi-synthesis of ursolic acid derivatives was achieved, and oleanolic analogues could be promising prosperous drugs for other human infectious diseases which need to be studied further.

Fig. 6.3 Cytotoxicity
activity of **a** compound 2
(OA), **b** compound 3
(3-acetyl-OA), **c** compound
1 (UA), **d** compound 4
(3-acetyl-UA), **e** compound 5
(3-acetyl-UA-28-methylate),
f compound 6
(3-acetyl-UA-28-benzylate)
and **g** compound 7
(3-acetyl-UA-28-cinnamate)
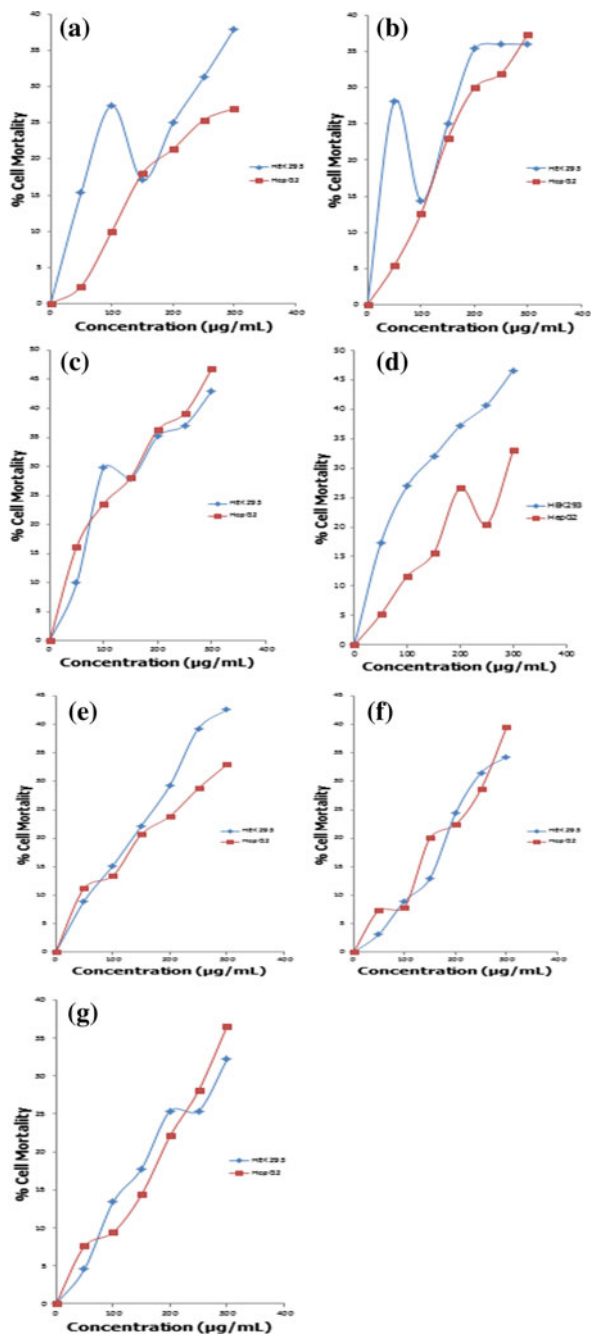
References

1. Young-Won C, Balunas MJ, Chai HB, Kinghorn AD (2006) Drug discovery from natural sources. AAPS J 2:8 Article 28
2. Chen Y, Liu J, Zhao XL, Xu HB (2005) Oleanolic acid nanosuspensions: preparation, *in-vitro* characterization and enhanced hepatoprotective effect. J Pharm Pharmacol 57:259–264
3. Dzubak P, Hajduch M, Vydra D, Hustova A, Kvasnica M, Biedermann D, Markova L, Urban M, Sarek J (2006) Pharmacological activities of natural triterpenoids and their therapeutic implications. Nat Prod Rep 23:394–411
4. Habila JD, Ndukwe GI, Amupitan JO, Nok AJ, Shode FO (2010) Synthesis, characterization and candidosis inhibition of hybrid molecule: 3β-cinnamyl oleanolic acid. J Appl Sci Res 8:1077–1085
5. Bannon C, Eade R, Saaan H, Simes J (1975) The chlorination of olean-12-enes. Aust J Chem 28:2649–2654
6. Kashiwada Y, Wang HK, Nagao T, Kitanaka S, Yasuda I, Fujioka T, Yamagishi T, Lewis KG (1983) The separation of substituted olean-12-en-28-oic acids from the corresponding urs-12-en-28-oic acid isomers. Aust J Chem 36:2297–2305
7. Sun H, Fang W, Wang W, Hu C (2006) Structure-activity relationships of oleanane- and ursane-type triterpenoids. Bot Stud 47:339–368
8. Yu D, Sakurai Y, Chen C, Chang F, Huang L, Kashiwadia Y, Lee K (2006) Anti-AIDS agents 69. Moronic acid and other triterpene derivatives as novel potent anti-HIV agents. J Med Chem 49:5462–5469
9. Sun I, Kashiwada Y, Morris-Natschke L, Lee KH (2003) Plant derived terpenoids and analogues as anti-HIV agents. Curr Top Med Chem 3:155–169
10. Tawata S, Taira S, Kobamoto N, Zhu J, Ishihara M, Toyama S (1996) Synthesis and fungal activity of cinnamic esters. Biosci Biotech Bioch 5:909–910
11. Tonari K, Mitsiu K, Yonemoto K (2002) Structure and activity of cinnamic acid related compounds. J Olea Sci 51:271–273
12. Tanachatchairatana T, Bremner J, Chokchaisiri R, Suksamrarn A (2008) Antimycobacterial activity of cinnamate-based esters of triterpenes betulinic, oleanolic and ursolic acids. Chem Pharm Bull 56:197–198
13. Baglin I, Mitaine-Offer A, Nour M, Tan K, Cave C, Lacaille-Dubois M (2003) A review of natural and modified betulinic, ursolic and echinocystic acid derivatives as potent antitumor and anti-HIV agents. Mini Rev Med Chem 3:525–539
14. Wen X, Zhang P, Liu J, Zhang L, Wu X, Ni P, Sun H (2006) Pentacyclic triterpenes. Part 2: synthesis and biological evaluation of maslinic acid derivatives as glycogen phosphorylase inhibitors. Bioorg Med Chem Lett 16:722–726
15. Cativela C, Díaz-de-Villegas MD (1998) Stereoselective synthesis of quaternary α-amino acids. Part 1: acyclic compounds. Tetrahedron-Asymmetr 9:3517–3599
16. Mosmann T (1983) Rapid colorimetric assay for cellular growth and survival: application to proliferation and cytotoxicity assays. J Immunol Meth 65:55–63
17. Nanyonga S, Opoku A, Lewu F, Oyedeji O, Singh M, Oyedeji A (2013) Antioxidant activity and cytotoxicity of the leaf and bark extracts of *Tarchonanthus camphorates*. Trop J Pharm Res 12:377–383
18. Mohato SB, Kundu AP (1994) ^{13}C NMR spectra of pentacyclic triterpenoids—a compilation and some salient features. Phytochemistry 37:1517–1575

19. Kontogianni VG, Axarchou V, Troganis A, Gerothanassis IP (2009) Rapid and novel discrimination and quantification of oleanolic and ursolic acids in complex plant extracts using two-dimensional nuclear magnetic resonance spectroscopy-comparison with HPLC methods. Anal Chim Acta 635:188–195
20. Uddin G, Siddiqui B, Alam M, Sadat A, Ahmad A, Uddin A (2011) Chemical constituents and phytotoxicity of solvent extracted fractions of stem bark of *Grewia optiva* Drummond ex Burret. J Sci Res 8:85–91
21. Deri VG, Vijayan C, John A, Gopakumar K (2012) Pharmacognostic and antioxidant studies on *Clerodendrum inerme* and identification of ursolic acid as a marker compound. Int J Pharm Sci 4:145–148
22. Habila JD, Shode FO, Ndukwe GI, Amupitan JO, Nok AJ (2012) Effect of C-3 modification of oleanolic acid on *Candida* spp. Trichophytontonsurans and Microsporumcanis inhibition. Pharmacologia 3:313–324
23. Suffness M, Pezzuto JM (1990) Assays related to cancer drug discovery. In: Methods in plant biochemistry: assays for bioactivity, Hostettmann K (ed) vol 6. Academic Press, London, pp 71–133. ISBN-10: 0124610161
24. Yin R, Li T, Tian JX, Xi P, Liu RH (2018) Ursolic acid, a potential anticancer compound for breast cancer therapy. Crit Rev Food Sci 58:568–574

Chapter 7
Chemical Composition of *Hypoxis hemerocallidea* Fisch. & C.A. Mey from Eastern Cape, South Africa

Pamela Rungqu, Opeoluwa O. Oyedeji and Adebola O. Oyedeji

Abstract The present study describes the chemical composition of *Hypoxis hemerocallidea*. The essential oil was obtained by hydrodistilling the leaves and corms (fresh and dry) of *H. hemerocallidea*. The percentage yield of the oil was 2.0% in fresh leaves, 2.2% in dry leaves, 2.8% in fresh corms and 2.5% (v/w) in dry corms; the colour of the oils were pale yellow. The essential oil profile was determined by GC and GC-MS. Twenty two components out of the fifty-one components detected by the GC and GC-MS in the fresh leaves essential oil of *H. hemerocallidea* accounted for 97.3%, 27 components in the dry leaves oil accounted for 96.7%, 27 components in the fresh corms oil accounted for 95.8% and 26 components in the dry corms accounted for 93.0% of the total oil composition. The major compounds in the essential oils of *H. hemerocallidea* are sabinene (0.9–27.6%), linalool (15.3–25.4%), α-terpineol (3.5–13.8%), β-caryophyllene (2.2–11.5%), α-terpinolene (0.4–9.8%), β-terpineol (2.1–9.2%), terpinene-4-ol (6.6–8.6%), hexadecane (2.7–8.1%), *cis*-nerolidol (6.8–7.7%), myrcene (4.1–7.5%), β-phellandrene (1.3–7.5%), n-hexadecanoic acid (6.6–6.9%), γ-terpinene (2.6–6.5%), linoleic acid (3.2–6.5%), *trans*-β-ocimene (0.4–6.4%), δ-3-carene (0.5–6.4%), octadecane (2.0–6.4%), β-bourbonene (3.0–6.2%), α-ionone (1.5–5.3%), β-selinene (2.4–5.2%), α-caryophyllene (1.8–4.8%), *trans*-isolimonene (0.1–4.6%), limonene (1.1–4.3%), ethyl linoleate (1.5–4.3%) and δ-cadinene (3.2–4.2%). Non-terpenic groups such as aliphatic carboxylic acids, saturated hydrocarbons and aromatics were significantly present in essential oils of *H. hemerocallidea*. Additionally, other chemical groups such as esters, ketones, and alcohols were present in the oils but their percentages

---

P. Rungqu · O. O. Oyedeji (✉)
Department of Chemistry, Faculty of Science and Agriculture, University of Fort Hare, Alice 5700, South Africa
e-mail: ooyedeji@ufh.ac.za

P. Rungqu
e-mail: prungqu@gmail.com

A. O. Oyedeji
Department of Chemistry, Faculty of Natural Sciences, Walter Sisulu University, Mthatha 5117, South Africa
e-mail: aoyedeji@gmail.com

were low. This is the first time the essential oils of *H. hemerocallidea* from South Africa have been investigated and reported despite its use in traditional medicine.

Keywords *Hypoxis hemerocallidea* · Essential oil · Sabinene · Linalool · α-terpineol · β-caryophyllene

7.1 Introduction

Hypoxis is a well-known genus of the family Hypoxidaceae [1, 2] and its species are monocotyledons that are commonly distributed in the Southern Hemisphere including sub-Saharan Africa, America, south-east Asia and Australia [3, 4]. The genus *Hypoxis* is reported to have its centre of variation in South Africa [5, 6] where it occurs in open undisturbed grasslands [7]. There are 96 known species of *Hypoxis* in Africa, out of which 30 *Hypoxis* species are found in southern Africa [8], eleven species of which are used for medicinal purposes with *H. hemerocallidea* and *H. colchicifolia* reported to be the most popular [2, 9]. *Hypoxis* genus has generated pharmaceutical interest based on its use as a traditional medicine by indigenous people of eastern and southern Africa [10]. The *Hypoxis* corm has a catalogue of medicinal uses and also serves as a source of food; it is among the commonly prescribed medicines by traditional healers [11]. *Hypoxis* species have been used in South Africa as umuthi for hundreds of years by different tribes to treat various ailments [12]. In Zulu traditional medicine, *Hypoxis* roots or corms are used for treating infertility, urinary infections, intestinal parasites, heart weakness, nausea, cough, palpitations, nervous disorder and vomiting. An infusion made from the tuber of *H. colchicifolia* is taken as an emetic against fearful dreams. *H. rigula* and *H. hemerocallidea* leaves are used as ropes in KwaZulu-Natal. Corms from *H. obtuse* are used to make black polish which is then applied to the floors of the huts. In the midst of starvation the Xhosa and the Sotho people roast or boil the corms of some *Hypoxis* species so that they can eat them [9, 13, 14]. Extracts from the corms of *Hypoxis* are used as ingredients in a wide range of products such as anti-oxidants, anti-inflammatories, anti-diabetics and anti-convulsants [15]. Some of the species, such as *H. hemerocallidea*, *H. stellipilis*, *H. sobolifera* var. sobolifera [16] and *H. obtusa* [17, 18] to name a few, have been scientifically proven to contain hypoxoside, a phytochemical that has immune regulatory properties and its extracts are now widely used in the pharmaceutical industry [19].

Hypoxis hemerocallidea Fisch. & C.A. Mey (Hypoxidaceae) was previously known as *H. rooperi*; however nowadays it is commonly known as the African potato, yellow star flower (English), inongwe (isiXhosa), ilabatheka, zifozonke (isiSwati) and Inkomfe (isiZulu). It is a stemless, geophytic, perennial herb with large corms (tubers) which are dark brown or black on the outside and bright yellow inside [20]; this type of *Hypoxis* species occurs in open grassland and woodland. It is widespread in South Africa in provinces like Eastern Cape, Free State, KwaZulu-Natal, Mpumalanga, Gauteng and Limpopo; *H. hemerocallidea* is also found in open

grass of Botswana and Lesotho and in savanna regions of Swaziland and Zimbabwe. Studies on the medicinal properties of *H. hemerocallidea* dated back to 1982 when unknowingly the corms were simultaneously studied for the first time in two countries by scientists in Italy and South Africa [21]. *H. hemerocallidea*, or African potato, is counted amongst the special indigenous medicinal species of commercial importance in southern Africa [6]. The corm of the *H. hemerocallidea* has been used in folk medicine to treat a variety of diseases, such as the common cold, flu, hypertension, adult-onset diabetes mellitus, psoriasis, urinary infections, testicular tumours, prostate hypertrophy and internal cancer, HIV/AIDS and some central nervous system disorders [22].

A hydroalcoholic extract of *H. rooperi* was patented with a long list of beneficial properties such as anti-inflammatory, antibiotic, antiarthritic, antiatherosclerotic, diuretic and stimulant of muscular and hormonal activities [23]. Some biomedical evidence suggests that *H. hemerocallidea* corm extract may be useful in the management of type 2 diabetes mellitus [9]. Previous studies have shown that crude aqueous and methanolic extracts of *H. hemerocallidea* exhibited good antibacterial activity against a number of bacteria strains including *Escherichia coli* and *Staphylococcus aureus* [13, 24]. The demand for *H. hemerocallidea* has intensified in recent years, following the isolation and elucidation of a phytosterol diglucoside, hypoxoside, which has various pharmacological activities [22, 25]. Bayley and Van Staden showed that the corms of *H. hemerocallidea* are the major site of biosynthesis of hypoxoside [26]. Some of the compounds isolated from *H. hemerocallidea* are desmosterol, β-sitosterol, campesterol, stigmastanol, stigmasterol and β-sitosterol glucoside [27–29]. The glucoside hypoxoside was first isolated and characterized from *H. obtusa* by Marini-Betolo et al. in 1982 four years before the findings by Drewes et al. (1984), and Vinesi et al., in 1990 [27, 28, 30]. Drewes et al., in 1984 reported the presence of hypoxoside in *H. acuminata*, *H. nitida*, *H. obtusa*, *H. rigidula*, and *H. latifolia* [27, 29]. The phytosterols including their main constituents, hypoxoside and its active derivative rooperol are now being used in fields of anti-oxidants, anti-inflammatories, anti-diabetes, anti-convulsants, inhibitors of drug marker substances, anti-cancerous and premalignant cancer cells [25]. Furthermore, the pharmacological properties of rooperol in studies conducted by several scientists have demonstrated its potency towards cancer, inflammation, and HIV [21, 26].

To the best of our knowledge no work has been reported on the essential oil chemical composition of *H. hemerocallidea*, Therefore, this study is aimed at extracting essential oils from both (fresh and dry) parts of *Hypoxis hemerocallidea* leaves and corms, to determine the chemical profile and then evaluate the medicinal potential of the essential oils. We therefore report the chemical composition of *H. hemerocallidea* essential oils from this study for the first time.

7.2   Materials and Methods

7.2.1   Plant Material

H. hemerocallidea plants were collected in the fields of Bathurst location near Grahamstown in the Eastern Cape Province. The plant samples were then sent to Rhodes University for identification; they were taxonomically identified by Mr. T. Dold and the voucher specimen was deposited in Selmar Schonland Herbarium Grahamstown (GRA) at Rhodes University; the collection number was PR/PL03.

7.2.2   Extraction of Essential Oils

600 g of fresh or dry (leaves and corms) of *H. hemerocallidea* were subjected to a hydro-distillation method for approximately 5 h using the Clevenger apparatus [31]. The extracted essential oils were then collected and stored in airtight amber glass bottles in a refrigerator at 4 °C until the time of analysis [32].

7.2.3   Analysis of Essential Oils

GC-FID was performed on a HP5890-II instrument, equipped with a DB-5MS (30 m × 0.25 mm; 0.25 µm film thickness) fused silica capillary column. Hydrogen was used as carrier gas adjusted to a linear velocity of 32 cm/s (measured at 100 °C). Split flow was adjusted to give a 20:1 ratio and septum sweep was a constant 10 mL/min. The oven was programmed as follows: 60–240 °C at 3 °C/min. The samples were injected using the splitless technique using 2 µL of oil in hexane (2:1000). Injector and detector were set at 250 °C. The GC was equipped with FID and connected to an electronic integrator HP 5896 Series II. The percentage yield of the samples was computed from the GC peak areas without using correction for response factors.

GC-MS was performed on a HP-6890 GC system equipped with a HP-5MS fused capillary column (30 m × 0.25 mm; 0.25 µm film thickness), coupled to a selective mass detector HP-5973. Helium (1 mL/min) was used as carrier gas; oven temperature program: 60–240 °C at 3 °C/min; splitless during 1.50 min; sample volume 2 µL of the oil solution in hexane (2:1000). Injector and detector temperature was 250 °C. EIMS: electron energy, 70 eV; ion source temperature and connection parts: 180 °C.

7.2.4   Identification of Essential Oils

Identification of compounds was done by matching their mass spectra and retention indices with those recorded in NIST08 library and by comparison of retention indices and mass spectra with literature values [33–35].

7.3   Results

7.3.1   Chemical Composition of Essential Oils

The essential oils extracted from the leaves and corms (fresh and dry) of *H. hemerocallidea* were pale yellow in color with an unpleasant odor; the percentage yields of the oils are as follows: 2.0% for fresh leaves, 2.2% for dry leaves, 2.8% for fresh corms and 2.5% for dry corms. Constituents identified in the leaves and corms (fresh and dry) of *H. hemerocallidea* together with their Kovat indices and percentage composition are listed in Table 7.1. A total of 51 components were identified in the fresh leaves GC-MS chromatogram of the essential oil of *H. hemerocallidea* with 22 components accounting for 97.3%, 27 components accounting for 96.7% in dry leaves, 27 components accounting for 95.8% in fresh corms and 26 components accounting for 93.0% in dry corms. The fresh leaves essential oil had the following main components: sabinene (27.6%), linalool (15.3%), terpinene-4-ol (8.6%), δ-3-carene (6.4%) and *trans*-β-ocimene (5.3%), while in dry leaves essential oil the main components were β-terpineol (9.2%), β-caryophyllene (11.5%), myrcene (7.5%), terpinen-4-ol (6.6%), γ-terpinene (6.5%), linoleic acid (6.5%), and β-selinene (5.2%). Hexadecane (8.1%), *cis*-nerolidol (7.7%), β-phellandrene (7.5%), *n*-hexadecanoic acid (6.9%), *trans*-β-ocimene (6.4%), octadecane (6.4%), β-bourbonene (6.2%) and α-terpinolene (5.1%) were the major components in the essential oil of fresh corms. In the essential oil of the dry corms, linalool (25.4%), α-terpineol (13.8%), α-terpinolene (9.8%), *cis*-nerolidol (6.8%) and *n*-hexadecanoic acid (6.6%) were the major components. The GC-MS analysis of the fresh leaves essential oil also showed that there was the presence of monoterpenes (55.6%), oxygenated monoterpenes (26.5%), sesquiterpenes (9.6%), aromatics (2.7%), esters (1.5%) and alcohols (1.4%), while in the essential oil of dry leaves monoterpenes (29.8%), oxygenated monoterpenes (23.1%), sesquiterpenes (28.7%), aromatics (4.0%), alcohols (0.3%), esters (4.3%) and carboxylic acids (6.5%) were found to be present. The essential oil of fresh corms was composed of monoterpenes (19.0%), sesquiterpenes (6.2%), oxygenated sesquiterpenes (7.7%), saturated hydrocarbons (22.4%), aromatics (28.3%), ketones (2.1%) and carboxylic acids (10.1%) while in the essential oil of dry corms the detected chemical classes of compounds were monoterpenes (10.7%), oxygenated monoterpenes (39.2%), oxygenated sesquiterpenes (6.8%), saturated hydrocarbons (10.4%), aromatics (13.1%),

Table 7.1 Chemical constituents from the different parts of *H. hemerocallidea* essential oils

No.	Components	KI[a]	KI[b]	H.H.F.L	H.H.D.L	H.H.F.C	H.H.D.C	I.M
1	Butan-2-one	601	605	–	–	0.6	0.9	MS[c], RI[d]
2	2,4-Dimethylbenzene	822	825	–	–	0.5	0.7	MS[c], RI[d]
4	*m*-Xylene	866	906	–	–	0.2	0.2	MS[c], RI[d]
5	2-Ethylthiophene	874	877	0.4	3.2	–	–	MS[c], RI[d]
6	1,2,3-Trimethylcyclohexane	883	890	–	–	–	0.2	MS[c], RI[d]
7	*p*-Xylene	883	888	–	–	0.2	0.3	MS[c], RI[d]
8	Santolinatriene	908	909	–	–	–	0.2	MS[c], RI[d]
9	Cumene	926	912	–	–	0.2	1.1	MS[c], RI[d]
10	Camphene	953	954	–	1.4	–	–	MS[c], RI[d]
11	Sabinene	976	973	27.6	0.9	–	–	MS[c], RI[d]
12	β-Pinene	980	978	2.3	1.7	–	–	MS[c], RI[d]
13	*trans*-Isolimonene	983	989	1.5	4.6	–	–	MS[c], RI[d]
14	Myrcene	991	988	4.1	7.5	–	–	MS[c], RI[d]
15	1,3,5-Trimethylbenzene	994	992	–	–	2.4	2.8	MS[c], RI[d]
16	δ-3-Carene	1011	1004	6.4	0.5	–	–	MS[c], RI[d]
17	α-Terpinene	1018	1017	1.3	3.5	–	–	MS[c], RI[d]
18	1,2,4-Trimethylbenzene	1023	1021	–	–	2.9	0.4	MS[c], RI[d]
19	*o*-Cymene	1020	1022	–	–	3.7	0.6	MS[c], RI[d]
20	*p*-Cymene	1026	1028	2.3	–	2.9	–	MS[c], RI[d]
21	Limonene	1031	1029	4.3	1.1	–	–	MS[c], RI[d]
22	β-Phellandrene	1031	1030	–	1.3	7.5	–	MS[c], RI[d]
23	2-Phenylacetaldehyde	1043	1039	–	0.8	3.1	–	MS[c], RI[d]
24	*trans*-β-Ocimene	1050	1052	5.3	0.7	6.4	0.9	MS[c], RI[d]
25	*trans*-Decahydronaphthalene	1057	1062	–	–	2.6	1.0	MS[c], RI[d]
26	1,2-Diethylbenzene	1057	1055	–	–	2.9	2.2	MS[c], RI[d]
27	1-Methyl-3-propylbenzene	1058	1060	–	–	2.1	2.4	MS[c], RI[d]
28	4-Methyldecane	1059	1063	–	–	3.1	2.0	MS[c], RI[d]
29	γ-Terpinene	1062	1059	2.6	6.5	–	–	MS[c], RI[d]
30	*trans*-Sabinene hydrate	1068	1066	0.5	3.4	–	–	MS[c], RI[d]
31	*cis*-Linalool oxide	1074	1077	–	0.4	–	–	MS[c], RI[d]
32	*m*-Cymene	1082	1085	–	–	3.7	2.2	MS[c], RI[d]
33	α-Terpinolene	1088	1079	1.6	0.4	5.1	9.8	MS[c], RI[d]

(continued)

Table 7.1   (continued)

No.	Components	KI[a]	KI[b]	H.H.F.L	H.H.D.L	H.H.F.C	H.H.D.C	I.M
34	4-Ethyl-1,2-dimethylbenzene	1093	1095	–	–	3.5	0.2	MS[c], RI[d]
35	Linalool	1098	1095	15.3	–	–	25.4	MS[c], RI[d]
36	β-Terpineol	1159	1163	2.1	9.2	–	–	MS[c], RI[d]
37	Ethyl linoleate	1159	1205	1.5	4.3	–	–	MS[c], RI[d]
38	Terpinen-4-ol	1177	1174	8.6	6.6	–	–	MS[c], RI[d]
39	α-Terpineol	1189	1188	–	3.5	–	13.8	MS[c], RI[d]
40	Tridecane	1299	1300	–	–	2.2	2.3	MS[c], RI[d]
41	β-Bourbonene	1384	1388	–	3.0	6.2	–	MS[c], RI[d]
42	β-Caryophyllene	1418	1419	2.2	11.5	–	–	MS[c], RI[d]
43	α-Ionone	1426	1426	–	–	1.5	5.3	MS[c], RI[d]
44	α-Caryophyllene	1454	1478	1.8	4.8	–	–	MS[c], RI[d]
45	β-Selinene	1485	1490	2.4	5.2	–	–	MS[c], RI[d]
46	δ-Cadinene	1524	1522	3.2	4.2	–	–	MS[c], RI[d]
47	*cis*-Nerolidol	1534	1565	–	–	7.7	6.8	MS[c], RI[d]
48	Hexadecane	1600	1600	–	–	8.1	2.7	MS[c], RI[d]
49	Octadecane	1800	1800	–	–	6.4	2.0	MS[c], RI[d]
50	*n*-Hexadecanoic acid	1984	1984	–	–	6.9	6.6	MS[c], RI[d]
51	Linoleic acid	2130	2134	–	6.5	3.2	–	MS[c], RI[d]

H.H.F.L—*H. hemerocallidea* fresh leaves; H.H.D.L—*H. hemerocallidea* dry leaves
H.H.F.C—*H. hemerocallidea* fresh corms; H.H.D.C—*H. hemerocallidea* dry corms
I.M—identification method
[a]KI: Kovat indices on HP-5MS capillary column
[b]KI: Literature Kovat indices [33–35]
[c]MS: Identification based on mass spectral data
[d]RI: Identification on the basis of NIST11 library and comparison with literature data

ketones (6.2%) and carboxylic acids (6.6%) as displayed in Table 7.2. Some of the major components identified in the essential oils of *H. hemerocallidea* are shown in Fig. 7.1.

7.4   Discussion

7.4.1   *Chemical Composition of Essential Oils*

The present study is the first report on essential oil composition of *H. hemero-callidea*. Monoterpenes, oxygenated monoterpenes, sesquiterpenes and oxygenated sesquiterpenes were the dominating groups in the oil profiles of the leaves and corms

Table 7.2 Chemical classes of compounds identified in the essential oils of *H. hemerocallidea*

Chemical classes of compounds	Fresh leaves (%)	Dry leaves (%)	Fresh corms (%)	Dry corms (%)
Terpenes				
Monoterpenes	55.6	29.8	19.0	10.7
Oxygenated monoterpenes	26.5	23.1	–	39.2
Sesquiterpenes	9.6	28.7	6.2	–
Oxygenated sesquiterpenes	–	–	7.7	6.8
Total	91.7	81.6	32.9	56.7
Non-terpenic compounds				
Saturated hydrocarbons	–	–	22.4	10.4
Aromatics	2.7	4.0	28.3	13.1
Alcohols	1.4	0.3	–	–
Ketones	–	–	2.1	6.2
Carboxylic acids	–	6.5	10.1	6.6
Esters	1.5	4.3	–	–
Total	5.6	15.1	62.9	36.3
Total of identified compounds	97.3	96.7	95.8	93.0

(i.e. fresh and dry) of *H. hemerocallidea* contributing in a total of 10.7–55.6%, 23.1–39.2%, 6.2–28.7% and 6.8–7.7% respectively. These figures were largely due to sabinene (0.9–27.6%), myrcene (4.1–7.5%), δ-3-carene (0.5–6.4), *trans*-isolimonene (1.5–4.6%), limonene (1.1–4.3%), β-phellandrene (1.3–7.5%), *trans*-β-ocimene (0.7–6.4), γ-terpinene (2.6–6.5%), α-terpinolene (0.4–9.8%), linalool (15.3–25.4%), β-terpineol (2.1–9.2%), terpinen-4-ol (6.6–8.6%), α-terpineol (3.5–13.8%), β-bourbonene (3.0–6.2%), β-caryophyllene (2.2–11.5%), α-caryophyllene (1.8–4.8%), β-selinene (2.4–5.2%), δ-cadinene (3.2–4.2%) and *cis*-nerolidol (6.8–7.7%). Non-terpinic aliphatic carboxylic acids, saturated hydrocarbons and aromatics accounted for 6.5–10.1%, 10.4–22.4% and 2.7–28.3% respectively, with the main representatives being α-ionone (1.5–5.3%), hexadecane (2.7–8.1%), octadecane (2.0–6.4%), *n*-hexadecanoic acid (6.6–6.9%) and linoleic acid (3.2–6.5%). Additionally, there were also other chemical groups which were present in the essential oil of *H. hemerocallidea* such as esters, ketones and alcohols, their percentages being 1.5–4.3, 2.1–6.2 and 0.3–1.4% respectively.
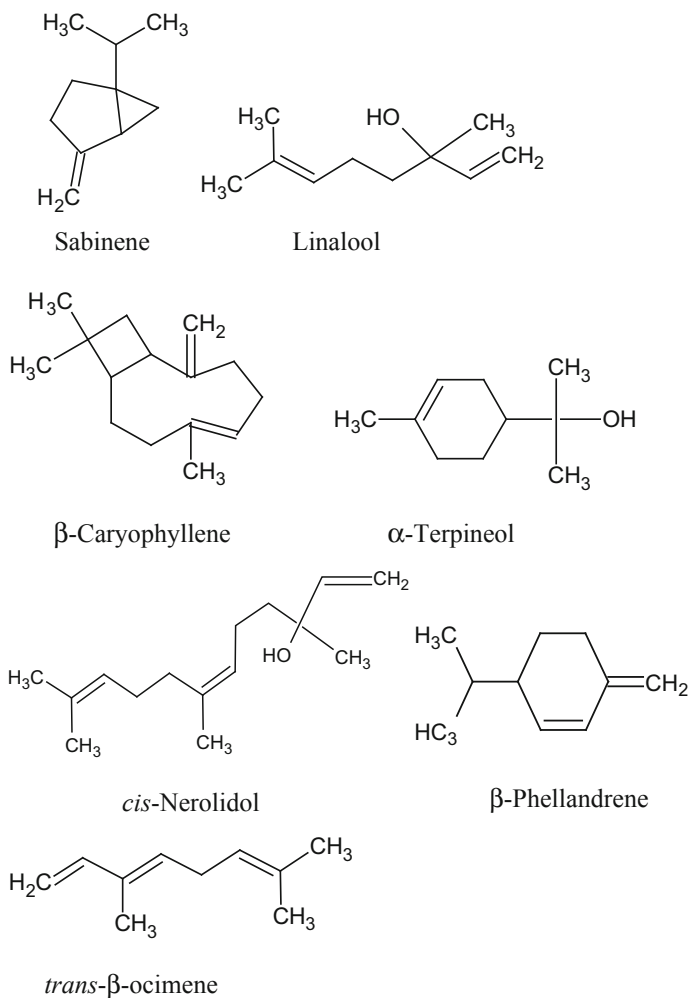
Fig. 7.1 Some of the major components identified in the essential oils of *H. hemerocallidea*

7.5 Conclusion

The findings of this study show that the *H. hemerocallidea* fresh/dry leaves and corms contain essential oils which varied in yields and chemical composition. The most abundant components identified in the essential oils were sabinene, linalool, α-terpineol and β-caryophyllene. The essential oils also had monoterpenes, monoterpenoids and sesquiterpenes as the most dominant chemical classes of compounds.

References

1. Laporta O, Perez-Fons L, Mallavia R, Caturla N (2007) Isolation, characterization and antioxidant capacity assessment of the bioactive compounds derived from *Hypoxis rooperi* corm extract (African potato). Food Chem 101:1425–1437

2. Nair VDP, Kanfer I (2007) A capillary zone electrophoresis method for the quantitative determination of hypoxoside in commercial formulations of African Potato (*Hypoxis hemerocallidea*). Phytochem Anal 18:475–483

3. Masubayane CT, Xozwa K, Ojewole AO (2005) Effects of *Hypoxis hemerocallidea* (Fisch. & C.A Mey.) [Hypoxidaceae] corm (African Potato) aqueous extract on renal electrolyte and fluid handling in the rat. J Ren Fail 27:763–770

4. Okem A, Stirk WA, Street RA, Southway C, Finnie JF, Van Staden J (2015) Effects of Cd and Al stress on secondary metabolites, antioxidant and antibacterial activity of *Hypoxis hemerocallidea* Fisch. & C.A Mey. Plant Physiol Biochem 97:147–155

5. Kennedy DO, Wightman EL (2011) Herbal extracts and phytochemicals: plant secondary metabolites and the enhancement of human brain function. Adv Nutr 2:32–50

6. Jian Z (2007) Nutraceuticals, nutritional therapy, phytonutrients, and phytotherapy for improvement of human health: a perspective on plant biotechnology application. Recent Pat Biotechnol 1:75–97

7. Groppa MD, Tomaro ML, Benavides MP (2001) Polyamines as protectors against cadmium or copper-induced oxidative damage in sunflower leaf discs. Plant Sci 161:481–488

8. Michalak A (2006) Phenolic compounds and their antioxidant activity in plants growing under heavy metal stress. J Environ Stud 15:523–530

9. Albrecht CF (1995) Hypoxoside: a putative, non-toxic prodrug for the possible treatment of certain malignancies, HIV-infections and inflammatory conditions. S Afr Med J 85:302–307

10. Katerere DR, Eloff JN (2008) Anti-bacterial and anti-oxidant activity of *Hypoxis hemerocallidea* (Hypoxidaceae): can leaves be substituted for corms as a conservation strategy? J Ethnopharmacol 74:613–616

11. Ramakrishna A, Ravishankar GA (2011) Influence of abiotic stress signals on secondary metabolites in plants. Plant Signal Behav 611:1720–1731

12. Sandhar HK, Kumar B, Prasher S, Tiwari P, Salhan M, Sharma P (2011) A review of phytochemistry and pharmacology of flavonoids. Int J Pharm Sci 1:25–41

13. Geerinck D (1968) Considérations taxonomiques au sujet des Haemodoraceae et des Hypoxidaceae (Monocotylédones). Bull Soc Roy Bot Belg 101:265–278

14. Keirungi J, Fabricius C (2005) Selecting medicinal plants for cultivation at Nqabara on the Eastern Cape Wild Coast, South Africa. S Afr J Sci 101:497–501

15. Selmar D, Kleinwachter M (2013) Influencing the product quality by deliberately applying drought stress during the cultivation of medicinal plants. Ind Crops Prod 42:558–566

16. Boukes GJ, Van de Venter M, Oosthuizen V (2008) Quantitative and qualitative analysis of sterols/sterolins and hypoxoside contents of three *Hypoxis* (African potato) spp. Afr J Biotechnol 7:1624–1629

17. Msonthi JD, Toyota M, Marston A, Hostettmann K (1990) A phenolic glycoside from *Hypoxis obtusa*. Phytochem 29:3977–3979

18. Vinesi P, Serafini M, Nicoletti M, Spano L, Betto P (1990) Plant regeneration and hypoxoside content in *Hypoxis obtusa*. J Nat Prod 53:196–199

19. Appleton MR, Ascough GD, Van Staden J (2012) *In vitro* regeneration of *Hypoxis colchicifolia* plantlets. S Afr J Bot 80:25–35

20. Van Wyk BE, Van Oudtshoorn B, Gericke N (1997) Medicinal plants of South Africa, 2nd improved impression (2000). Briza Publications, Pretoria, South Africa, p 188

21. Drewes SE, Kahn F (2004) The African potato (*Hypoxis hemerocallidea*): a chemical-historical perspective. S Afr J Sci 100:425–430

22. Albrecht CF, Kruger PB, Smit B, Freestone M, Gouws L, Koch HP, Miller R, Van Jaarsveld PP (1995) The pharmacokinetic behaviour of hypoxoside taken orally by patients with lung cancer in a phase 1 trial. S Afr Med J 85:861–865

23. Liebenberg RW (1969) Pharmaceutical corm extract of *Hypoxis*, anti-inflammatory and for the treatment of prostate gland hypertrophy. German Offenlegungsschrift, Patent, p 2015877
24. Ncube B, Finnie JF, Van Staden J (2011) Seasonal variation in antimicrobial and phytochemical properties of frequently used medicinal bulbous plants from South Africa. S Afr J Bot 77:387–396
25. Steenkamp V, Gouws MC, Gulumian M, Elgorashi EE, Van Staden J (2006) Studies on antibacterial, anti-inflammatory and antioxidant activity of herbal remedies used in the treatment of *benign prostate hyperplasia* and *prostatitis*. J Ethnopharmacol 103:71–75
26. Bayley AD, Van Staden J (1990) Is the corm the site of hypoxoside biosynthesis in *Hypoxis hemerocallidea*? Plant Physiol Biochem 28:691–695
27. Marini-Betolo GB, Patamia M, Nicoletti M, Galeffi C, Messana I (1982) Research on African medicinal plants-II: hypoxoside, a new glycoside of uncommon structure from *Hypoxis obtusa* Busch. Tetrahedron 38:1683–1687
28. Drewes SE, Hall AJ, Learmonth RA, Upfold UJ (1984) Isolation of hypoxoside from *Hypoxis rooperi* and synthesis of (E)-1,5-bis(30,40-dimethoxy phenyl) pent- 4-en-1-yne. Phytochem 23:1313–1316
29. Drewes SE, Elliot E, Dhlamini JTB, Gcumisa MSS (2008) *Hypoxis hemerocallidea*—not merely a cure for benign prostate hyperplasia. J Ethnopharmacol 119:593–598
30. Vinesi P, Serafini M, Nicoletti M, Spano L, Betto P (1990) Plant regeneration and hypoxoside content in *Hypoxis obtusa*. J Nat Prod 53:196–199
31. Meyer-Warnod B (1984) Natural essential oils extraction process and application to some major oils. Perfume Flav 9:93–104
32. Nyalambisa M, Oyemitan IA, Matewu R, Oyedeji OO, Oluwafemi OS, Nkeh-Chungag BN, Oyedeji AO (2017) Volatile constituents and biological activities of the leaf and root of *Echinacea* species from South Africa. Saudi Pharm J 25:381–386
33. Adams RP (2012) Identification of essential oil components by ion trap mass spectroscopy. Academic Press, New York, USA
34. Joulain D, Koenig AW (1998) The atlas of spectral data of sesquiterpene hydrocarbons. E.B.-Verlag, Hamburg, Germany
35. Adams RP (2007) Identification of essential oil components by gas chromatography/mass spectrometry. Allured Publishing Corporation Carol Stream, USA

Chapter 8
Photodegradation of Phenol by Silver Doped TiO$_2$; A Comparative Study of the Efficiency of HPLC and UV-Vis Analyses

Benton Otieno [ORCID]**, Nomalungelo Matjokana, Seth Apollo, Bobby Naidoo and Aoyi Ochieng**

Abstract The formation of colored intermediate compounds during photocatalytic degradation of phenol represents the risk of single-handedly employing ultraviolet visible (UV-Vis) spectrophotometry for the determination of residual phenol concentration. Moreover, the widely used titania (TiO$_2$) photocatalyst is hindered by the high recombination rate of electron-hole pairs. In this study, phenol was photodegraded in the presence of sol gel synthesized TiO$_2$ and silver doped titania (Ag-TiO$_2$), under UV illumination. Spectrophotometric determination of residual phenol concentration was done using high performance liquid chromatography (HPLC) and UV-Vis spectrophotometry. Scanning electron microscopy-energy-dispersive X-ray (SEM-EDX) and Fourier transform infrared (FTIR) spectroscopies revealed the successful introduction of the Ag dopant into the TiO$_2$ lattice. The UV-Vis and photoluminescence (PL) spectroscopic analyses revealed restrained electron hole-pair recombination and reduced energy bandgap in Ag-TiO$_2$. Ag-TiO$_2$ showed better photocatalytic efficiency than TiO$_2$, in line with the observed optical properties. Optimal conditions of 3% dopant loading, initial pH of 4 and catalyst loading of 1 g/L were determined for the degradation process. Formation of colored intermediates resulted in higher analytical values for residual phenol obtained from UV-Vis as compared to

B. Otieno (✉) · N. Matjokana · S. Apollo
Centre for Renewable Energy and Water, Vaal University of Technology, Private Bag X021, Vanderbijlpark 1900, South Africa
e-mail: bentononyango@gmail.com

N. Matjokana
e-mail: lungimatjokana@gmail.com

S. Apollo
e-mail: sethapollo@gmail.com

B. Otieno · B. Naidoo
Department of Chemistry, Vaal University of Technology, Private Bag X021, Vanderbijlpark, South Africa
e-mail: bobby@vut.ac.za

A. Ochieng
Botswana International University of Science and Technology, Private Bag 16, Palapye, Botswana
e-mail: aoyio@biust.ac.bw

those obtained from HPLC analyses. For high affirmation of the reproducibility of photodegradation results, UV-Vis spectrophotometry should, therefore, be employed alongside other analytical techniques.

8.1 Introduction

Phenol and its derivatives are some of the most encountered organic pollutants in industrial wastewaters generated from paint, pesticide, coal conversion, polymeric resin, petrochemical and pharmaceutical industries [1]. The phenolic compounds which can remain in the environment for longer periods given their stability, are toxic and carcinogenic, hence posing danger to water ecosystem and human health [2, 3]. Conventional wastewater treatment methods used for phenol removal include activated carbon adsorption, chemical oxidation, and biological degradation [1, 4, 5]. Due to the cost involved in some of these treatment methods, their inability to fully mineralize phenol into less harmful products and their inherent shortcomings of secondary pollution [2, 6], an effective alternative treatment method is highly desired [7].

Photocatalytic degradation processes have the ability to mineralize organic pollutants into less harmful and low molecular weight (LMW) products, particularly CO_2 and H_2O [8, 9], and can, therefore, be an effective alternative for the treatment of recalcitrant compounds including phenols. Titania (TiO_2), an effective and widely used photocatalyst for water treatment, suffers from high energy requirement given its wide bandgap and high recombination rate which lowers its overall quantum efficiency [10–14]. The wide bandgap can only be activated by UV light which accounts for about 4% of the solar energy [2], thereby hindering the application of TiO_2 based photocatalytic processes. For photocatalysis to be efficient for large-scale applications, a visible light responsive photocatalyst with low electron-hole pair recombination needs to be developed. Doping titania with silver (Ag) can reduce both the high recombination rate and large energy bandgap. Silver doped titania (Ag-TiO_2) has shown remarkable efficiency during photocatalytic processes under both solar and UV irradiations [2, 15, 16].

Chromatographic techniques such as gas chromatography (GC) and high performance liquid chromatography (HPLC) are commonly used for the determination of reaction intermediates and residual concentration during the degradation of phenol [1, 17]. Also, widely used for determination of residual phenol concentration is the simple, and fast UV-Visible (UV-Vis) spectrophotometric technique [18, 19]. Photocatalytic degradation of phenol yields numerous intermediates and by-products that may cause the phenol solution to develop color. Grabowska et al. [1] reported the photocatalytic oxidation of phenol to three main reaction intermediates: catechol, hydroquinone, and p-benzoquinone. These compounds were found to be persistent

as shown by their quantitative detectability even after three hours of illumination. When the phenol analyte of interest is accompanied by the stable intermediates which absorb in the same spectral region as the parent compound, a separation step or spectral overlap resolution is necessary [20]. Such a separation step is not possible with the widely used UV-Vis spectrophotometers, hence the need for an analytical technique with spectrophotometric detection such as HPLC.

Several studies on the photodegradation of phenol by TiO_2 based photocatalysts have been conducted and the concentration of residual phenol determined using UV-Vis spectrophotometry [2, 21–25]. The sole use of UV-Vis spectrophotometry has the potential for interference by intermediates and products leading to inconclusive findings. Moreover, there is very little literature reporting the analysis of phenol photodegradation by both HPLC and UV-Vis spectrophotometry or determination of the correlation between HPLC and UV-Vis analyses. The aim of this study, therefore, was to photodegrade phenol in the presence of synthesized Ag-TiO_2 under UV irradiation and monitor phenol reduction using UV-Vis spectrophotometry and HPLC analytical methods. Of special interest was the study of the analytical characteristics and the bias error for the UV-Visible method. Effects of initial pH, initial concentration and catalyst loading on the degradation process were also monitored.

8.2 Methodology

8.2.1 Materials, Equipment and Chemicals

All the chemicals listed herein were used as received without further purification. Titanium tetraisopropoxide (TTIP, 97%) and methanol used as a precursor source of titanium and an organic solvent, respectively, were obtained from Sigma Aldrich. Phenol used for making synthetic wastewater solution and silver nitrate, the source of the silver dopant, were obtained from ACE Chemicals, South Africa. A photoreactor with 250 ml capacity was sourced from Puritech, South Africa. The reactor had a 12 W UVC lamp with short wavelength range concentrated at around 254 nm, an important property for the production of hydroxyl radicals needed for the degradation of phenolic organic compounds [10].

8.2.2 Catalyst Synthesis

The sol-gel method modified from our previous studies was used to synthesize TiO_2 and Ag-TiO_2 [10, 26]. In brief, the titanium precursor (TTIP) was dissolved in methanol and ultra-sonicated to achieve a homogeneous solution. Deionized water was then introduced dropwise to the titanium solution for hydrolysis purposes. TTIP, methanol and deionized water were mixed in a molar ratio of 1:1:65 [27]. The result-

ing titanium sol was heated under reflux at 80 °C for 3 h. Afterwards, the sol was centrifuged to separate the solvent from TiO_2. The obtained wet TiO_2 powder was then dried for 12 h at 80 °C before undergoing calcination at 500 °C for three hours. To synthesize Ag-doped TiO_2, a similar method was used except for dissolving $AgNO_3$ in the deionised water used for hydrolysis. The amount of $AgNO_3$ dissolved in the water for hydrolysis was dependent on the percentage of Ag content required in the Ag-TiO_2.

8.2.3   Catalyst Characterization

Scanning electron microscopy-energy-dispersive X-ray spectroscopy (SEM-EDX, FEI Quanta 250 FEG ESEM with integrated Oxford X-Max 20 EDX system) analysis was carried out to determine the particle sizes and distribution, and compositions of the synthesized TiO_2 and Ag-TiO_2 photocatalysts. The composition and presence of functional groups were further investigated using Fourier transform infrared spectroscopy (FTIR, PerkinElmer FT-IR/NIR spectrometer). The optical properties of the photocatalysts were determined from photoluminescence (PL, Jasco spectrofluorometer FP-8600) and UV-Vis (T80+ UV/VIS Spectrometer, PG Instruments Ltd.) spectroscopies.

8.2.4   Photodegradation Experiments and Chemical Analysis

Photocatalytic studies were carried out in the 12 W UVC reactor by monitoring the reduction in phenol concentration with irradiation time. The catalyst, before irradiation, was added to 250 ml of phenol solution and stirred for 30 min in the dark to obtain adsorption-desorption equilibrium. The solution was then transferred to the photoreactor via a peristaltic pump, to be irradiated, and samples were taken at predetermined time intervals. Continuous pumping of air was maintained to keep the catalyst uniformly suspended in the solution and to provide oxygen necessary for electron scavenging during the degradation process. Samples were filtered using 0.45 μm membrane filters before determining the phenol concentration. For the effect of operational factors, only the fast UV-Vis analysis method was employed for the determination of residual phenol concentration, while for comparison of the analytical techniques, UV-vis and HPLC were employed.

8.3 Results and Discussion

8.3.1 Catalyst Characterization

The synthesized TiO_2 and Ag-TiO_2 were characterized by various techniques such as SEM-EDX, FTIR, UV-Vis, and PL to determine their morphological and optical properties, elemental composition and the presence of functional groups.

8.3.1.1 SEM-EDX Analysis

The SEM images of TiO_2 and Ag-TiO_2 (Fig. 8.1) show the successful introduction of the Ag dopant into TiO_2. Both the TiO_2 and Ag-TiO_2 photocatalysts obtained are in the nano range signifying the successful synthesis of nano-sized particles. The elemental composition of TiO_2 and Ag-TiO_2 was determined by EDX. From Table 8.1, the only elements found in Ag-TiO_2 were Ti, O and Ag, indicating the successful doping of TiO_2 with Ag. It is also shown by the EDX analysis that TiO_2 was only composed of Ti and O. The Ag composition by weight in the Ag-TiO_2 was found to be 3.17%. This is in close agreement with the catalyst synthesis conditions in which 3% Ag composition was required.
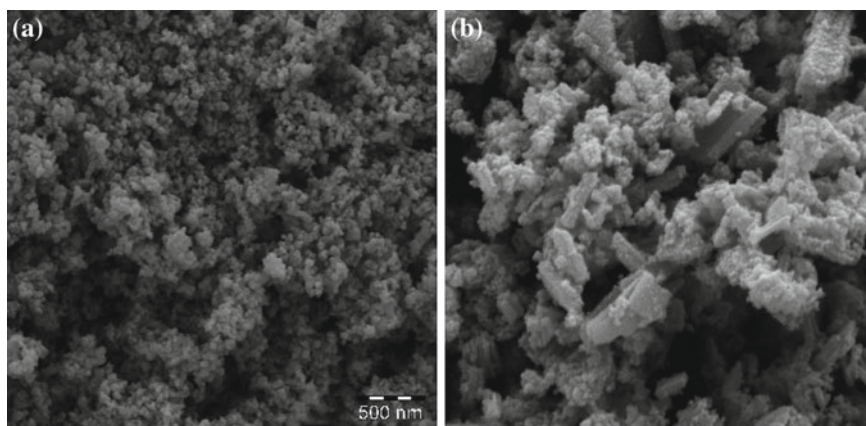
Fig. 8.1 SEM images of **a** TiO_2 and **b** Ag-TiO_2

Table 8.1 EDX spectra elemental composition (%) of TiO_2 and Ag-TiO_2

Spectrum	Ti	Ag	O	Total
TiO_2	59.85		40.15	100
Ag-TiO_2	57.89	3.17	38.94	100
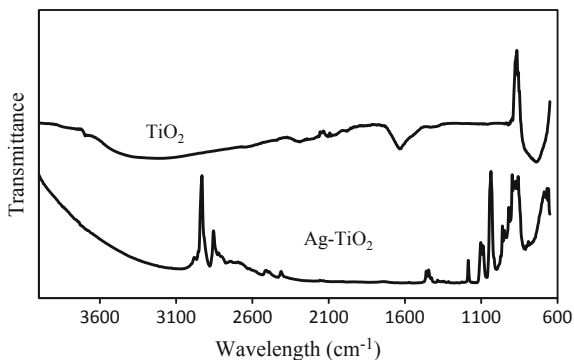
8.3.1.2   FTIR Results

The elemental composition and presence of functional groups were further ana-
lyzed by FTIR spectroscopy. The FTIR spectra of TiO$_2$ and Ag-TiO$_2$ (Fig. 8.2) were
obtained in the range of 600–4000 cm^{-1}. The peaks at 3400 and 1650 cm^{-1} for
the undoped TiO$_2$ could be due to OH stretching and water bending, respectively
[10]. The H–O–H bonds could have resulted from moisture adsorption during sample
preparation. The band at around 1400 cm^{-1} is attributable to the vibration mode of
the Ti–O bond [28], confirming that TiO$_2$ was formed. Compared to the spectrum
of TiO$_2$, the peaks are significantly broadened when Ag was introduced. The peaks
around 1090 cm^{-1} in the Ag-TiO$_2$ could be ascribed to the new substance formed by
the decomposition of AgNO$_3$, confirming the presence of Ag ions in Ag-TiO$_2$ [16].

8.3.1.3   UV-Vis and PL Analyses

The visible light-responsiveness of a photocatalyst and its electron-hole pair recom-
bination rate can be determined by both UV-Vis and PL spectroscopies, respectively
[10, 11, 26]. UV-Vis can be used to sight the interactions between photon energies
and a photocatalyst [26]. Change in energy bandgap due to doping is depicted by the
UV-Vis absorption spectrum. Figure 8.3 shows the absorbance spectra of TiO$_2$ and
Ag-TiO$_2$. It is observed from the spectra that a significant red shift resulted from the
introduction of the Ag dopant. The shift which can be related to the energy require-
ments of the two catalysts shows that Ag-TiO$_2$ needed less energy to be excited as
compared to TiO$_2$ [29, 30]. The direct bandgaps (E_g) of Ag-TiO$_2$ and TiO$_2$ were
calculated as:

$$E_g = 1240/\lambda \tag{8.1}$$

where λ is the wavelength of the exciting light [29]. The obtained bandgaps
(Table 8.2) show a reduction in the energy bandgap of Ag-TiO$_2$ as compared to
TiO$_2$.

Fig. 8.3 UV-Vis absorption spectra of Ag-TiO$_2$ and TiO$_2$
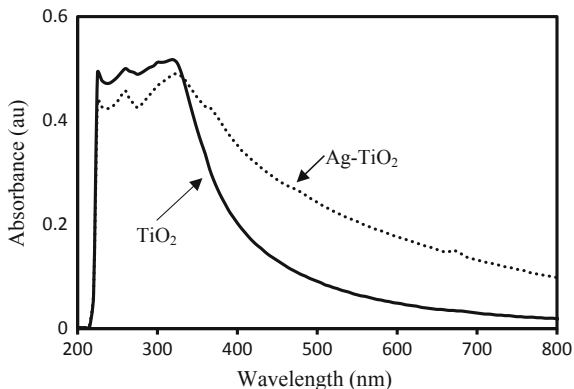
Table 8.2 Calculated bandgaps of Ag-TiO$_2$ and TiO$_2$

Catalyst	Wavelength (nm)	Bandgap (eV)
Ag-TiO$_2$	370	3.4
TiO$_2$	320	3.9

The separation efficiency of photogenerated species plays an important role in photocatalysis, as a high recombination rate results in low quantum efficiency while a low recombination rate results in high quantum efficiency [31]. Photoluminescence, which is caused by the emission of photons resulting from electron-hole pair recombination, can be used to investigate the efficiency of charge carrier trapping, migration, and transfer [32]. High and low recombination rates will result in high and low PL intensities, respectively. To obtain the PL spectra, equal amounts of TiO$_2$ and Ag-TiO$_2$ were uniformly dispersed in equal amounts of methanol before carrying out the PL measurements at an excitation wavelength of 425 nm. From the PL spectra shown in Fig. 8.4, Ag-doped TiO$_2$ had a reduced intensity as compared to the undoped TiO$_2$. The low intensity signifying the desirable reduced recombination rate is attributable to the introduction of the Ag dopant.

Fig. 8.4 PL spectra of Ag-TiO$_2$ and TiO$_2$
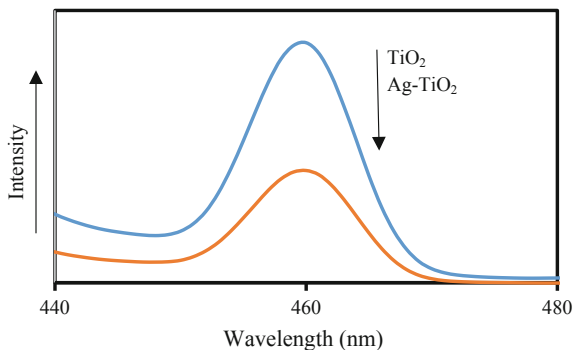
Fig. 8.5 Percentage removal
of phenol (25 ppm) after
50 min of irradiation in the
presence of undoped TiO_2
and Ag-TiO_2 doped at
various Ag content by
weight at pH 4 with 1 g/L
catalyst loading
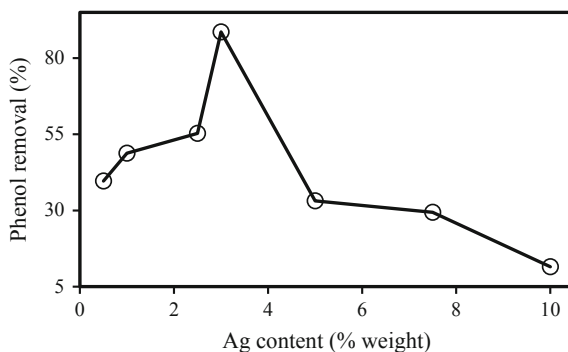
8.3.2 Photodegradation Studies

Photodegradation experiments were carried out to investigate the effect of Ag content, initial pH and concentration, and catalyst loading on the activity of Ag-TiO_2 for phenol removal.

8.3.2.1 Effect of Ag Weight Percentage Content

It is observed from Fig. 8.5 that phenol removal increased with increasing Ag content in the doped catalyst up to an optimum value of 3%. Above the optimum Ag content, phenol removal started to decline. A higher Ag content is undesirable due to its effect on photonic efficiency. At an optimum loading, Ag particles introduced into the TiO_2 structure act as centers for electron-hole separation. Due to the Fermi level of TiO_2 which is higher than that of silver, electron transfer from the conduction band (CB) of TiO_2 to metallic silver particles located at the interface is thermodynamically favorable. A resultant Schottky barrier at the metal-semiconductor contact region is, therefore, formed leading to improved charge separation observed with the reduced PL intensity (see Fig. 8.4), and enhanced photocatalytic activity as observed with the increased phenol removal [2, 16]. In contrast, above the optimum dopant loading, Ag particles can act as centers for recombination, hence decreasing the activity of the Ag-TiO_2 by increasing the recombination rate of the much needed photogenerated species [33].

8.3.2.2 Effect of Initial pH

The effect of initial pH on the removal of phenol (Fig. 8.6) was investigated by varying the initial pH from 4 to 10. The pH of an aqueous solution influences the surface-charge properties of the photocatalyst. Moreover, organic species such as phenol differ in several parameters including hydrophobicity, solubility, and speciation under

Fig. 8.6 Effect of pH on photodegradation efficiency on 25 ppm phenol in the presence of 3% Ag-TiO$_2$ loaded at 1 g/L after 50 min of irradiation
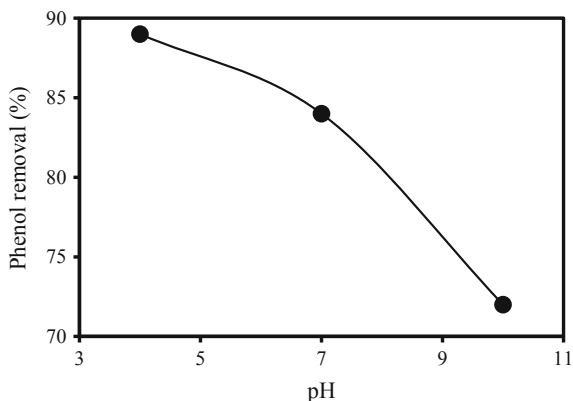
different pH conditions [34]. The acidic pH of 4 resulted in the highest phenol removal, with the lowest removal observed at pH 10. The Ag-TiO$_2$ photocatalyst, given its 97% composition by TiO$_2$ with a point of zero charge (pH$_{pzc}$) of 6.8 [23], can deprotonate under basic solutions as:

$$pH > pH_{pzc} \ TiOH + OH^- \rightarrow TiO^- + H_2O \tag{8.2}$$
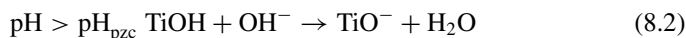
and protonate under acidic solutions as [34]:

$$pH > pH_{pzc} \ TiOH + H^+ \rightarrow TiOH_2^+ \tag{8.3}$$
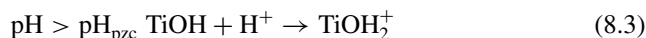
The surface of Ag-TiO$_2$ is negatively charged under basic conditions (pH > 6.8) while positively charged under acidic conditions (pH < 6.8) as per Eqs. (8.2) and (8.3), respectively. A decrease in initial pH will, therefore, lead to increased positively charged photocatalyst surface resulting in more adsorption of phenol, which exists as negatively charged phenolate compounds at higher pH [23]. The degradation of phenol is thus enhanced under acidic rather than basic conditions.

8.3.2.3 Effect of Initial Concentration

Change in rate of degradation due to change in concentration was investigated by varying the initial phenol concentration. The removal was decreased from 88 to 22%, as shown in Fig. 8.7, with increasing the initial phenol concentration from 25 to 75 ppm. Intramolecular competition by the phenolic organic compounds to reach the surface of Ag-TiO$_2$ is enhanced with increasing initial concentration. This leads to a higher number of movement of molecules to the active sites of Ag-TiO$_2$ in each unit time for a fixed catalyst loading. The active sites, therefore, become saturated by the target phenolic organic compounds, causing an inhibitive effect on further degradation [35].

Fig. 8.7 Percentage removal of phenol at different initial concentration after 50 min of irradiation at pH 4
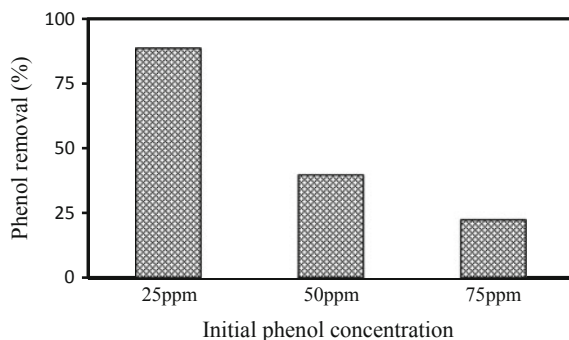
Table 8.3 Kinetic data of phenol photodegradation at various initial concentrations

Initial concentration (ppm)	k_{app} (min^{-1})	$1/k_{app}$ (min)	R^2
25	0.0188	53.19	0.9548
50	0.0115	86.96	0.9768
75	0.0084	119.05	0.9637

The initial concentration is one of the factors affecting degradation reaction kinetics. The photocatalytic process can best be described by the Langmuir-Hinshelwood model, which is normally reduced to pseudo-first-order kinetic model, Eq. (8.4), at a low initial concentration of substrate [35].

$$ln\frac{C_o}{C} = k_{app}t \tag{8.4}$$

Kinetic data shown in Table 8.3, were obtained from the plots of $ln\frac{C_o}{C_t}$ against t, for the three different initial concentrations, where k_{app} is the apparent reaction rate constant (min^{-1}), C_o and C_t are the initial concentration and concentration at time t, respectively. Just as observed with the reduced phenol removal with increasing initial concentration, the apparent initial rate constant was also significantly reduced.

8.3.2.4 Effect of Catalyst Loading

Effect of catalyst loading, which plays an important role in photocatalysis, was investigated by varying the loading from 0 to 2.5 g/L. At 0 g/L, only 16% of phenol removal was achieved due to photolysis (Fig. 8.8). The low removal due to photolysis alone is an indication of the stability of phenol to UVC irradiation, thereby necessitating the need for the introduction of a catalyst to speed up the process. On introducing Ag-TiO$_2$ photocatalyst, phenol removal was increased with increasing catalyst loading up to an optimum of 1 g/L. Above the optimum loading, the removal was gradually decreased. The increased amount of catalyst results in an increased num-

Fig. 8.8 Effect of catalyst loading on the removal of 25 ppm phenol in the presence of Ag-TiO$_2$ after 50 min of irradiation at pH 4
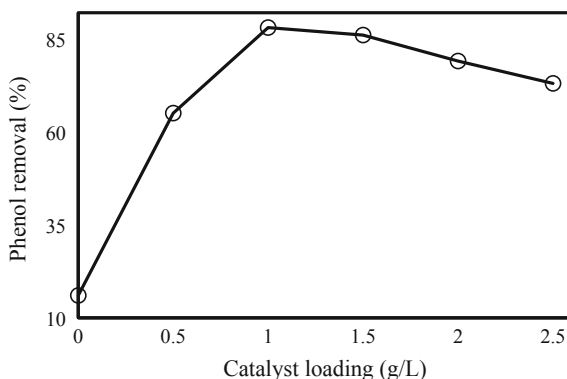
ber of active sites, which in turn increases the number of hydroxyl and superoxide radicals. In contrast, above the optimum loading, the degradation rate decreased due to increased turbidity, which is due to scattering and reduced light penetration [10]. Moreover, high catalyst loading may result in catalyst agglomeration, hence limiting the catalyst surface that is available for photon absorption.

8.3.2.5 Comparison of TiO$_2$ and Ag-TiO$_2$

The effect of Ag doping on Ag-TiO$_2$ photocatalytic activity under UV irradiation was evaluated. Phenol solutions of same initial concentration at same catalyst loading for both Ag-TiO$_2$ and TiO$_2$ were irradiated with UV light, and the extent of removal monitored. From Fig. 8.8, it was observed that UV photolysis alone resulted in 16% phenol removal. The direct photolysis can be attributed to the UVC lamp used which had a wave range concentrated at around 254 nm with a reported corresponding energy of 472 kJ/mol, which is higher as compared to the bond energies of C–O (357.7 kJ/mol), C-H (413 kJ/mol) and H–O (462.8 kJ/mol) [36]. Under a photocatalyzed process (Fig. 8.9), Ag-TiO$_2$ exhibited higher phenol removal than TiO$_2$. The higher activity could be as a result of the electron trapping Ag particles doped into TiO$_2$ lattice, enhancing the electron-hole separation as depicted with the

Fig. 8.9 A comparative study to determine the effect of Ag doping on the degradation of phenol (25 ppm) after 50 min of UV irradiation
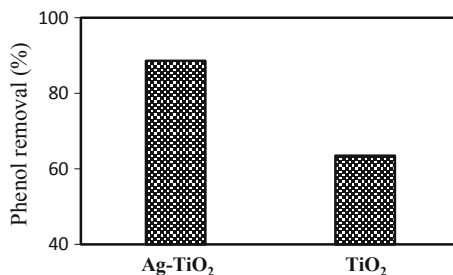
PL intensity (see Fig. 8.4), and subsequently transferring the trapped electron to the adsorbed electron accepting O_2 [16].

Irradiation by UV light excites valence electrons to the conduction band leading to the generation of a large number of photogenerated species. After varigated events, molecular oxygen scavenges the electrons on the catalyst surface, producing reactive oxygen radicals. The valence holes, on the other hand, are trapped in a similar manner as the surface-bound $OH^\bullet$ radicals that result from the oxidation of surface-bound OH or H_2O molecules. Charge separation, enhanced by the Ag particles, therefore plays an important part in the photocatalytic efficiency of the catalyst under UV irradiation [15]. From the UV-Vis absorbance spectra of TiO_2 and Ag-TiO_2 (see Fig. 8.3), the introduction of the Ag dopant shifted the absorption into the visible region. A similar observation of higher removal was made by Shet and Vidya [2]. A contrary observation made by Khanna and Shetty [37] in the photodegradation of an azo dye using Ag-TiO_2 nanoparticles, indicates that the photocatalytic efficiency is also dependent on the organic substrate.

8.3.3 Comparison Between UV-Vis and HPLC Analysis

Phenol degradation under UV irradiation on TiO_2 leads to the formation of intermediate compounds such as hydroquinone, benzoquinone, and ring opening products [1]. Some of these intermediates like benzoquinone are stable and are also colored, thereby making the phenol solution to develop color which can sometimes appear during the initial stages or for the entire degradation period, as was observed in the experiments. Due to the high rate of degradation observed under UV irradiation, the brown color was expected to rapidly disappear with increased irradiation time as a result of breaking down of the colored intermediate compounds formed. However, this was not the case given the high initial concentration of phenol solution undergoing degradation. UV-Vis and HPLC measurements of the phenol reduction process (Fig. 8.10) were done to determine the effect of the intermediates on the analytical methods used. The HPLC chromatograms of the phenol solution at different periods of irradiation are given in Fig. 8.11.

UV-Vis spectroscopy, a simple and fast technique which gives results that are close to those obtained from reference methods (Fig. 8.10), is applicable for both qualitative and quantitative analyses. For a fixed wavelength, from the Beer-Lambert law, Eq. (8.5), a UV-Vis spectrometer can determine the concentration of the absorbing solution.

$$A = \log_{10}(I_0/I) = \varepsilon.c.L \tag{8.5}$$

where A is the absorbance, I_0 and I are the intensities of the incident and transmitted lights, respectively, c is the concentration of the absorbing solution, L is the path length, and ε is the molar absorptivity of the solution. UV-Vis spectrometry, which depends on light, gave higher values as compared to the HPLC, which uses retention
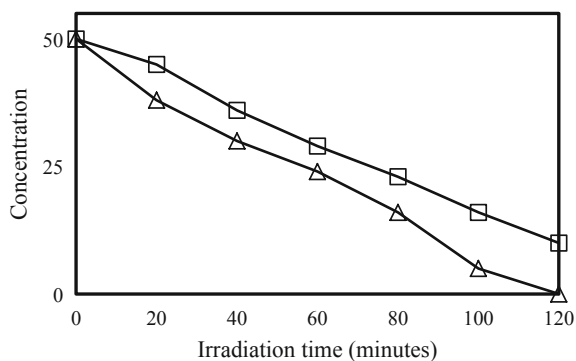
Fig. 8.10 Comparison of HPLC (△) and UV-Vis (□) measurement of phenol concentration under UV irradiation at pH 4 with 1 g/L Ag-TiO$_2$ loading
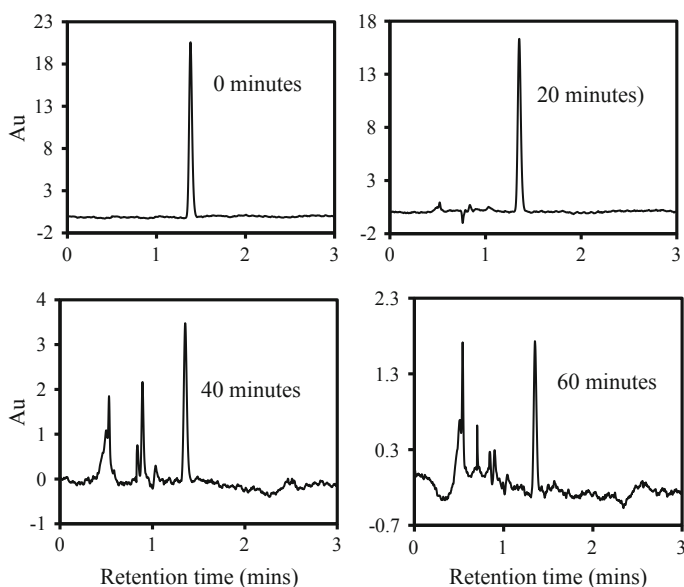
Fig. 8.11 HPLC chromatograms of phenol solution at different minutes of irradiation

time and therefore can detect both the parent compound and intermediates, and analyse them qualitatively and quantitatively [36]. From Fig. 8.11, the phenol solution at 0 min had only one peak, but on continued irradiation, several other peaks representing the intermediates were observed. The higher values observed for UV-Vis (Fig. 8.10) are attributable to the formation of coloured intermediates with maximum absorption similar or close to that of the parent phenolic compounds.

8.4   Conclusion

The introduction of Ag dopant into the TiO_2 lattice reduced both the bandgap and the recombination rate of photogenerated species of the resultant Ag-TiO_2. The reduced bandgap resulted from a red shift which extended the absorption range of the Ag-TiO_2 catalyst into the visible region. The Ag-doped titania catalyst had an improved efficiency under UV irradiation as compared to pure titania. Due to the formation of intermediate compounds during phenol degradation, UV-Vis spectrophotometric analysis alone was found to be inefficient for monitoring the degradation process. The degradation of phenol is, therefore, best monitored by UV-Vis alongside other analytical methods such as HPLC.

References

1. Grabowska E, Reszczyńska J, Zaleska A (2012) Mechanism of phenol photodegradation in the presence of pure and modified-TiO_2: a review. Water Res 46:5453–5471
2. Shet A, Vidya SK (2015) Solar light mediated photocatalytic degradation of phenol using Ag core—TiO_2 shell (Ag@TiO_2) nanoparticles in batch and fluidized bed reactor. Sol Energy 127:67–78
3. Mecha AC, Onyango MS, Ochieng A, Fourie CJS, Momba MNB (2016) Synergistic effect of UV-vis and solar photocatalytic ozonation on the degradation of phenol in municipal wastewater: a comparative study. J Catal 341:116–125
4. Soto ML, Moure A, Domínguez H, Parajó JC (2016) Batch and fixed bed column studies on phenolic adsorption from wine vinasses by polymeric resins. J Food Eng 209:52–60
5. Firozjaee TT, Najafpour GD, Khavarpour M, Bakhshi Z, Pishgar R, Mousavi N (2011) Phenol biodegradation kinetics in an anaerobic batch reactor. Iran J Energy Environ 2:68–73
6. Apollo S, Onyango MS, Ochieng A (2016) Modelling energy efficiency of an integrated anaerobic digestion and photodegradation of distillery effluent using response surface methodology. Environ Technol 3330:1–12
7. Akach J, Ochieng A (2018) Monte Carlo simulation of the light distribution in an annular slurry bubble column photocatalytic reactor. Chem Eng Res Des 129:248–258
8. Apollo S, Aoyi O (2016) Combined anaerobic digestion and photocatalytic treatment of distillery effluent in fluidized bed reactors focusing on energy conservation. Environ Technol 37:2243–2251
9. Titouhi H, Belgaied J (2016) Heterogeneous Fenton oxidation of ofloxacin drug by iron alginate support. Environ Technol 37:2003–2015
10. Otieno B, Apollo S, Naidoo B, Ochieng A (2016) Photodegradation of molasses wastewater using TiO_2-ZnO nanohybrid photocatalyst supported on activated carbon. Chem Eng Commun 6445:1443–1454
11. Mabuza J, Otieno B, Apollo S, Matshediso B, Ochieng A (2017) Investigating the synergy of integrated anaerobic digestion and photodegradation using hybrid photocatalyst for molasses wastewater treatment. Euro-Mediterranean J Environ Integr 2:17
12. Kotlhao K, Madiseng MDT, Mtunzi FM, Pakade VE, Modise SJ, Laloo N et al (2017) The synthesis of silver, zinc oxide and titanium dioxide nanoparticles and their antimicrobial activity. Adv Mater Proc 2:479–484

13. Brooms TJ, Otieno B, Onyango MS, Ochieng A (2018) Photocatalytic degradation of *p*-cresol using TiO$_2$/ZnO hybrid surface capped with polyaniline. J Environ Sci Heal—Part A Toxic/Hazard Subst Environ Eng 53:99–107

14. Otieno B, Apollo S, Aoyi O (2018) Application of natural zeolite in textile wastewater treatment: integrated photodegradation and anaerobic digestion system. In: Iqbal MJ, Thokozani M, Mutiu KA (eds) Water management; social and technological perspectives. CRC Press Taylor and Francis Group, London, pp 369–380

15. Seery MK, George R, Floris P, Pillai SC (2007) Silver doped titanium dioxide nanomaterials for enhanced visible light photocatalysis. J Photochem Photobiol A Chem 189:258–263

16. Sobana N, Muruganadham M, Swaminathan M (2006) Nano-Ag particles doped TiO$_2$ for efficient photodegradation of direct azo dyes. J Mol Catal A: Chem 258:124–132

17. Matos J, Quintana K, García A (2012) Influence of H-type and L-type activated carbon in the photodegradation of methylene blue and phenol under UV and visible light irradiated TiO$_2$. Mod Res Catal 1:1–9

18. Vaiano V, Matarangolo M, Murcia JJ, Rojas H, Navío JA, Hidalgo MC (2018) Enhanced photocatalytic removal of phenol from aqueous solutions using ZnO modified with Ag. Appl Catal B Environ 225:197–206

19. Duan L, Wang H, Sun Y, Xie X (2015) Biodegradation of phenol from wastewater by microorganism immobilized in bentonite and carboxymethyl cellulose gel. Chem Eng Commun 203:948–956

20. Campins-Falco P, Sevillano-Cabeza A, Gallo-Martinez L, Bosch-Reig F, Monzr-Mansanet I (1997) Comparative study on the determination of cephalexin in its dosage forms by spectrophotometry and HPLC with UV-vis detection. Mikrochim Acta 126:207–215

21. Borji SH, Nasseri S, Mahvi AH, Nabizadeh R, Javadi AH (2014) Investigation of photocatalytic degradation of phenol by Fe(III)-doped TiO$_2$ and TiO$_2$ nanoparticles. J Environ Heal Sci Eng 1–10

22. Ngamsopasiriskun C, Charnsethikul S, Thachepan S, Songsasen A (2010) Removal of phenol in aqueous solution by nanocrystalline TiO$_2$/activated carbon composite catalyst. Nat Sci 1182:1176–1182

23. Prabha I, Lathasree S (2014) Photodegradation of phenol by zinc oxide, titania and zinc oxide–titania composites: nanoparticle synthesis, characterization and comparative photocatalytic efficiencies. Mater Sci Semicond Process 26:603–613

24. Asiri AM, Al-Amoudi MS, Al-Talhi TA, Al-Talhi AD (2011) Photodegradation of rhodamine 6G and phenol red by nanosized TiO$_2$ under solar irradiation. J Saudi Chem Soc 15:121–128

25. Renuka MK, Gayathri V (2017) UV/solar light induced photocatalytic degradation of phenols and dyes by Fe(PS-BBP)Cl$_3$. J Photochem Photobiol A Chem 353:477–487

26. Otieno BO, Apollo SO, Naidoo BE, Ochieng A (2017) Photodecolorisation of melanoidins in vinasse with illuminated TiO$_2$-ZnO/activated carbon composite. J Environ Sci Heal Part A 52:1–8

27. Behnajady MA, Eskandarloo H, Modirshahla N, Shokri M (2011) Investigation of the effect of sol–gel synthesis variables on structural and photocatalytic properties of TiO$_2$ nanoparticles. Desalination 278:10–17

28. Bahadur NM, Furusawa T, Sato M, Kurayama F, Suzuki N (2010) Rapid synthesis, characterization and optical properties of TiO$_2$ coated ZnO nanocomposite particles by a novel microwave irradiation method. Mater Res Bull 45:1383–1388

29. Hamal DB, Klabunde KJ (2007) Synthesis, characterization, and visible light activity of new nanoparticle photocatalysts based on silver, carbon, and sulfur-doped TiO$_2$. J Colloid Interface Sci 311:514–522

30. Zhang Z, Yuan Y, Fang Y, Liang L, Ding H, Jin L (2007) Preparation of photocatalytic nano-ZnO/TiO$_2$ film and application for determination of chemical oxygen demand. Talanta 73:523–528

31. Ohtani B (2010) Photocatalysis A to Z—what we know and what we do not know in a scientific sense. J Photochem Photobiol C Photochem Rev 11:157–178

32. Naraginti S, Thejaswini TVL, Prabhakaran D, Sivakumar A, Satyanarayana VS, Arun Prasad AS (2015) Enhanced photo-catalytic activity of Sr and Ag co-doped TiO_2 nanoparticles for the degradation of Direct Green-6 and Reactive Blue-160 under UV & visible light. Spectrochim Acta—Part A Mol Biomol Spectrosc 149:571–579

33. Bechambi O, Chalbi M, Najjar W, Sayadi S (2015) Photocatalytic activity of ZnO doped with Ag on the degradation of endocrine disrupting under UV irradiation and the investigation of its antibacterial activity. Appl Surf Sci 347:414–420

34. Ahmed S, Rasul MG, Martens WN, Brown R, Hashib MA (2011) Advances in heterogeneous photocatalytic degradation of phenols and dyes in wastewater: a review. Water Air Soil Pollut 215:3–29

35. Li Y, Zhou X, Chen W, Li L, Zen M, Qin S et al (2015) Degradation of methyl orange by composite photocatalysts nano-TiO_2 immobilized on activated carbons of different porosities. J Hazard Mater 40:25–33

36. Guo Z, Ma R, Li G (2006) Degradation of phenol by nanomaterial TiO_2 in wastewater. Chem Eng J 119:55–59

37. Khanna A, Shetty VK (2014) Solar light induced photocatalytic degradation of Reactive Blue 220 (RB-220) dye with highly efficient Ag@TiO_2 core-shell nanoparticles: a comparison with UV photocatalysis. Sol Energy 99:67–76

Chapter 9
A Chemotaxonomic Study of 11 Species of the Genus *Psiadia* Endemic to La Reunion by ^{1}H NMR and GC-MS Based Metabolomic Approach

Keshika Mahadeo, Isabelle Grondin, Hippolyte Kodja, Hermann Thomas, Patricia Clerc, Michel Frederich and Anne Gauvin-Bialecki

Abstract The genus *Psiadia* Jacq. Ex. Willd. belongs to the Asteraceae family and includes more than 60 species, which are well represented in Madagascar and the Mascarene islands (La Réunion, Mauritius and Rodrigues). Several *Psiadia* species are used traditionally to treat various ailments such as expectorant for treatment of bronchitis and asthma, colds and abdominal pains. According to the literature, only a few species have been studied for their chemical composition. In order to make a comprehensive study of the genus *Psiadia* in the Mascarene islands, a chemotaxonomic study was conducted on 11 species endemic to La Réunion. The aim was to

---

K. Mahadeo · I. Grondin · P. Clerc · A. Gauvin-Bialecki (✉)
Laboratoire de Chimie des Substances Naturelles et des Sciences des Aliments, Faculté des Sciences et Technologies, Université de La Réunion, 15 Avenue René Cassin, CS 92 003, 97 744 St. Denis Cedex 9, La Réunion, France
e-mail: anne.bialecki@univ-reunion.fr

K. Mahadeo
e-mail: keshika.mahadeo@univ-reunion.fr

I. Grondin
e-mail: isabelle.grondin@univ-reunion.fr

P. Clerc
e-mail: patricia.clerc@univ-reunion.fr

H. Kodja
UMR Qualisud, Université de La Réunion, 15 Avenue René Cassin, CS 92 003, 97 744 St. Denis Cedex 9, La Réunion, France
e-mail: hippolyte.kodja@univ-reunion.fr

H. Thomas
Parc National de La Réunion, Secteur Nord, 165 Allée des Spinelles Bellepierre, 97 400 St. Denis, La Réunion, France
e-mail: hermann.thomas@reunion-parcnational.fr

M. Frederich
Laboratoire de Pharmacognosie, Département de Pharmacie, Centre Interfacultaire de Recherche sur le Médicament (CIRM), Université de Liège, Campus du Sart-Tilman, Quartier Hôpital, Avenue Hippocrate, 15 B36, 4000 Liège, Belgium
e-mail: M.Frederich@uliege.be

identify chemical markers by a metabolomic approach using GC-MS and GC-FID for volatile compounds and ^{1}H NMR for non-volatile compounds. The 11 studied species were collected from different locations and seasons in order to analyze the geographical or seasonal variability of the chemical profile of each species. This study led to two different classifications of the 11 species in terms of composition of volatile and non-volatile compounds.

Keywords Psiadia · Chemotaxonomy · GC-MS · GC-FID · Volatile compounds

9.1   Introduction

The genus *Psiadia* Jacq. Ex. Willd. (Asteraceae) includes more than 60 species mainly found in Madagascar (28 species) and the Mascarene Islands (La Réunion, Mauritius and Rodrigues, 26 species) [1]. Despite their uses in the traditional pharmacopoeia, only a small number of studies have been conducted on *Psiadia* species. Amongst all *Psiadia* species only a few species have been investigated for their phytochemical composition and pharmacological activities [2]. Sixteen species of the genus *Psiadia* are found in La Réunion and they occupy a diverse range of habitats from sea level up to 3000 m. According to the literature, a taxonomic study has been conducted on *Psiadia* species from La Réunion by Jacob de Cordemoy in 1895 and four groups of species have been defined based on morphological characteristics [3]. In 1993, A. J. Scott modified this classification and distinguished five main groupings of species within the Mascarene Islands, Madagascar and Sri Lanka [1]. In 2012, Strijk et al. [4] focused on the evolutionary and biogeographical history of this genus based on molecular phylogenetic. In this study, two clades containing *Psiadia* species were recognised. Those studies have defined two different groupings of species based on morphological and genetic aspects. In 2005, Gauvin and Smadja [5] attempted a first chemotaxonomic study on four *Psiadia* species (*P. anchusifolia*, *P. argentea, P. boivinii* and *P. salaziana)* from La Réunion based on their essential oil composition. In order to complete their study and to allow the comparison with the classifications reported previously, here we provide a chemotaxonomic study on 11 *Psiadia* species from La Réunion. To achieve this goal, the volatile and non-volatile composition of all studied species was investigated. The aims were to classify these species according to their composition and identify chemical markers. Thus, a metabolomic approach using GC-MS and GC-FID for the volatile compounds and ^{1}H NMR for the non-volatile compounds was carried out. The data obtained using these techniques were investigated using various chemometric tools.

9.2 Materials and Methods

9.2.1 Plant Material

Psiadia species leaves were collected in La Réunion Island in 2015 in several locations. Besides, each species was also collected in summer and winter to analyse the seasonal variability. A voucher specimen was deposited at the Herbarium of the University of Reunion Island for identification. The locations of collect and voucher numbers of all species are reported in Table 9.1 and Fig. 9.1.

9.2.2 GC Analysis

Hydrodistillation. Fresh leaves of each *Psiadia* species were subjected to hydrodistillation for 3 h using a modified Clevenger-type apparatus. The collected oils were taken up in dichloromethane (>99.5%, Carlo-Erba), dried over anhydrous sodium sulfate and stored in amber glass vials at 4 °C.

GC-MS and GC-FID. The GC-MS analyses were performed using a Hewlett Packard 6890-5973 instrument coupled with an HP 6890 mass selective detector. The data were obtained on a non-polar SPB-5 capillary column (60 m × 0.32 mm i.d.; film thickness: 0.25 μm). Operation conditions were: carrier gas He, flow of 0.7 mL/min, oven temperature program 60 °C rising at 4 °C/min to 250 °C and maintained at 250 °C for 50 min, sample injection port temperature 250 °C, detector temperature 250 °C, ionization mode EI, ionization voltage 70 eV, scanning over *m/z* 20–400 amu range, split ratio 1/50. The retention indices were calculated for all components using the Kovats method and *n*-alkanes as standards. A mixture of *n*-alkanes (C8–C22) was prepared from the pure chemicals at a 5% concentration in pentane. The components were identified on the basis of their retention indices and their mass spectral fragmentation pattern compared with those reported in the literature [6] and on MS libraries (Wiley 7 and NIST 02). The quantification of all components was performed using a Varian CP-3800 gas chromatograph coupled with a flame ionization detector and mounted with the same capillary column. The same temperature program was used for GC-FID. The qualitative and quantitative compositions of all essential oils were reported in a matrix for the multivariate data analysis. This matrix size consisted of 65 variables and was composed of compounds whose quantification were more than 5%.

9.2.3 NMR Analysis

Sample preparation. Freeze-dried leaves of each species were powdered and 50.0 mg were transferred to a 2 mL Eppendorf tube. A volume of 1.5 mL of a solution (1:1)

Table 9.1 Area of collects and voucher number of each *Psiadia* species

Psiadia species	Area of collect	Voucher number (summer)	Voucher number (winter)	GPS point	Altitude (m)
P. amygdalina	Salazie	REU13109	REU13488	21°S 4′ 19.9″/55°E 26′ 51.5″	2030
	Maïdo	REU13115	REU13494	21°S 4′ 49″/55°E 21′ 32.4″	1750
	Volcan	REU13130	REU13502	21°S 12′ 27.9″/55°E 36′ 59.7″	2080
P. anchusifolia	Salazie	REU13111	REU13489	21°S 4′ 19.9″/55°E 26′ 51.5″	2030
	Maïdo	REU13117	REU13495	21°S 3′ 48.8″/55°E 21′ 56.9″	1750
	Volcan	REU13130	REU13503	21°S 12′ 43.9″/55°E 36′ 49.0″	2050
	Roche-Ecrite	REU13131	REU13512	21°S 00′ 12.4″/55°E 27′ 40.4″	2050
P. argentea	Salazie	REU13112	REU13493	21°S 4′ 15.7″/55°E 26′ 52.9″	2015
	Volcan	REU13143	REU13504	21°S 12′ 25.8″/55°E 38′ 33.5″	2330
	Roche-Ecrite	REU13135	REU13513	21°S 00′ 12.9″/55°E 27′ 40.0″	2050
P. boivinii	Salazie	REU13113	REU13492	21°S 03′ 37.5″/55°E 27′ 9.4″	1828
	Maïdo	REU13116	REU13496	21°S 2′ 19.1″/55°E 21′ 15.9″	1350
	Volcan	REU13142	REU13505	21°S 09′ 56.5″/55°E 35′ 25.1″	1610
	Roche-Ecrite	REU13133	REU13510	20°S 58′ 04.2″/55°E 26′ 24.7″	1500

Table 9.1 (continued)

Psiadia species	Area of collect	Voucher number (summer)	Voucher number (winter)	GPS point	Altitude (m)
P. callocephala	Volcan	REU13140	REU13506	21°S 13′ 48.7″/55°E 39′ 03.6″	2330
P. dentata	Maïdo	REU13119	REU13497	21°S 1′ 14.1″/55°E 21′ 55.6″	1375
	Colorado	REU13139	REU13501	20°S 54′ 57.7″/55°E 25′ 00.0″	750
	Dos d'Ane	REU13128	REU13480	20°S 58′ 32.8″/55°E 23′ 21.5″	1320
	Montauban	REU13487	REU13500	20°S 56′ 57.6″/55°E 29′ 38.3″	580
P. insignis	Maïdo	REU13484	REU13499	21°S 4′ 49″/55°E 21′ 32.4″	1720
	Volcan	REU13483	REU13507	21°S 11′ 53.1″/55°E 36′ 9.6″	1805
	Dos d'Ane	REU13125	REU13481	20°S 58′ 31.6″/55°E 23′ 23″	1179
P. laurifolia	Salazie	REU13114	REU13491	21°S 3′ 19.6″/55°E 27′ 17.3″	1660
	Maïdo	REU13118	REU13498	21°S 1′ 16″/55°E 21′ 52.5″	1350
	Volcan	REU13141	REU13508	21°S 11′ 53.1″/55°E 36′ 9.6″	1805
	Roche-Ecrite	REU13132	REU13511	20°S 58′ 03″/55°E 26′ 24″	1475
P. melastom-atoides	Salazie	REU13110	REU13490	21°S 4′ 19.9″/55°E 26′ 51.5″	2030
	Roche-Ecrite	REU13134	REU13509	21°S 00′ 12.9″/55°E 27′ 40.0″	2052

Table 9.1 (continued)

Psiadia species	Area of collect	Voucher number (summer)	Voucher number (winter)	GPS point	Altitude (m)
P. montana	Dos d'Ane	REU13127	REU13479	20°S 59′ 32.3″/55°E 23′ 19.7″	1243
P. retusa	Cap Jaune	REU13129	REU13477	21°S 22′ 56.7″/55°E 39′ 50.6″	32
	Cap Méchant	REU13486	REU13476	21°S 22′ 28.7″/55°E 42′ 41.5″	0
	Piton Grande Anse	REU13485	REU13478	21°S 22′ 15.9″/55°E 33′ 14.8″	65
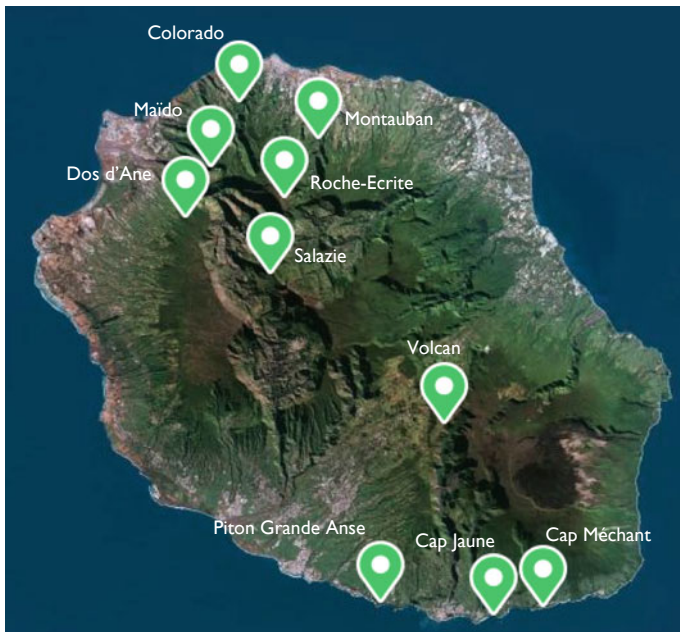
Fig. 9.1 Area of collects of *Psiadia* species in La Réunion Island

of KH$_2$PO$_4$ buffer (pH 6.0) in D$_2$O containing 0.05% trimethylsilylpropionic acid sodium salt-d_4 (TMSP, w/w) and methanol-d_4 (Eurisotop) was added to each sample. The mixture was vortexed at room temperature for 1 min, ultrasonicated for 20 min and centrifuged at 13,000 rpm for 10 min. An aliquot of 0.6 mL was transferred in 5 mm-NMR tubes for NMR analysis.

^{1}H NMR analysis. ^{1}H NMR spectra were recorded at 25 °C on a 600 MHz Bruker Ultrashield Avance spectrometer operating at a proton NMR frequency of 600.18 MHz. MeOH-d_4 was used as the internal lock. Each ^{1}H-NMR spectrum consisting of 256 scans was recorded with the following parameters: pulse width (PW) = 30° and relaxation delay (RD) = 1.0 s. A presaturation sequence was used to suppress the H$_2$O signal. Free induction decays (FIDs) were Fourier-transformed with LB = 0.3 Hz. The resulting spectra were manually phased, baseline-corrected and calibrated to TMS at 0.0 ppm using MestReNova 10.0 (Mestrelab Research S.L.). Spectral intensities were scaled to total intensity and reduced to integrated regions of equal width (0.04 ppm) corresponding to the region of δ 0.32–10.02 ppm. The regions of δ 3.25–3.34 and δ 4.78–4.86 ppm were excluded from the analysis because of the residual signals of H$_2$O and CH$_3$OH, respectively. The ^{1}H NMR matrix size consisted of 239 variables.

9.2.4   Multivariate Data Analysis

The SIMCA-P software version 12.0 (Umetrics, Umea, Sweden) was used for Principal Component Analysis (PCA), Orthogonal Partial Least Square Discriminant Analysis (OPLS-DA) and Hierarchical Clustering Analysis (HCA). HCA was performed using Euclidean distances and Ward's aggregation method. The scaling was based on Pareto method for the NMR dataset and a unit variance scaling was applied on the GC dataset. R^2X, R^2Y and Q^2 values described the quality of the model. R^2X indicated goodness of fit for PCA and R^2Y for OPLS-DA and they are defined as the proportion of the variance in the data observed in the model. Q^2 is defined as the proportion of variance in the data that was predictable by the model.

9.3   Results and Discussion

9.3.1   The Volatile Compounds Analysis

Data obtained by GC-MS and GC-FID consisted of a 62 × 65 data matrix, which was subjected to a supervised multivariate analysis. Among these 65 variables, only 6 remained unknown. OPLS-DA was performed with unit variance scaling. The model set of 10 principal components was highly significant (R^2Y(cum) = 83.8% and Q^2(cum) = 68.6%). Based on these results, a HCA dendrogram was built (Fig. 9.2a).
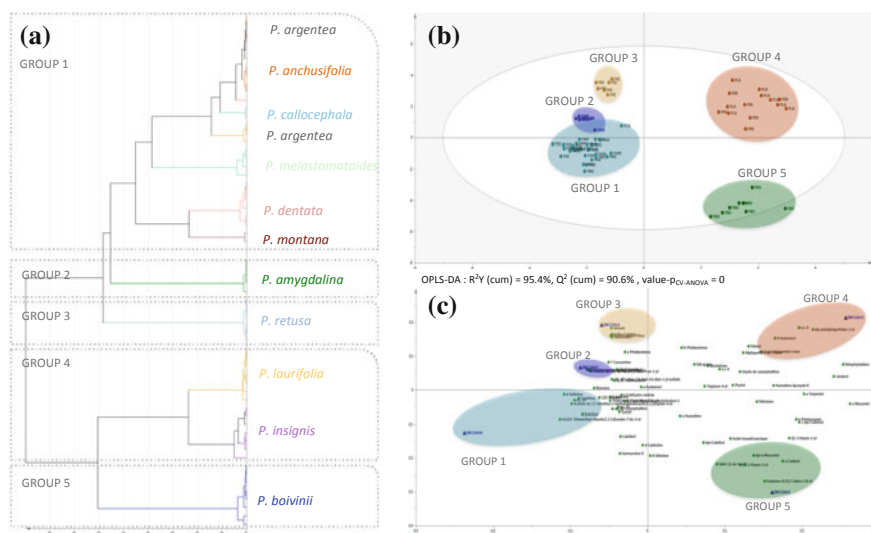
Fig. 9.2 HCA (**a**), score plot (**b**) and loading plot (**c**) of OPLS-DA results obtained from GC-MS and GC-FID data of *Psiadia* species essential oils

Five groups have been defined according to the OPLS-DA and HCA dendrogram obtained: a first large group containing species *P. argentea*, *P. anchusifolia*, *P. callocephala*, *P. melastomatoides*, *P. dentata* and *P. montana*; a second and third group with respectively *P. amygdalina* and *P. retusa*, a fourth group containing *P. laurifolia* and *P. insignis* and the last group comprising *P. boivinii*. A second OPLS-DA model was then built to provide deeper insight into the source of variability between these five groups and to identify chemical markers. Thus, a five component model explaining 95.4% of the variance was obtained and the five groups were well discriminated on the score plot (Fig. 9.2b). The loadings plot (Fig. 9.2c) analysis revealed compounds responsible for the groups' separation; these are listed in Table 9.2. The comparison of our results to those reported by Gauvin and Smadja [5] allowed confirming the essential oil composition of *P. anchusifolia* and *P. argentea* and their belonging to the same group. Indeed, Gauvin and Smadja [5] have defined one group containing species *P. anchusifolia*, *P. argentea*, *P. boivinii* and *P. salaziana* based on their essential oil composition. In contrast, *P. boivinii* belongs to another group in the present study. The analysis of the essential oil composition has shown differences particularly in terms of compounds anchusifolate and anchusifolol, which are completely absent in our results. These differences between both essential oil compositions can be explained by the influence of biotic and abiotic factors. However, the classification obtained has been able to enlarge the group obtained by Gauvin and Smadja [5] to species *P. callocephala*, *P. dentata*, *P. melastomatoides* and *P. montana*.

Table 9.2 Chemical markers in essential oil composition of *Psiadia* species from La Réunion

Classification	Species	Chemical markers
Group 1	*P. anchusifolia* *P. argentea* *P. callocephala* *P. dentata* *P. melastomatoides* *P. montana*	Anchusifolate *(oxygenated monoterpene)* Anchusifolol *(oxygenated sesquiterpene)* Cyperene *(sesquiterpene hydrocarbon)* δ-Selinene *(sesquiterpene hydrocarbon)*
Group 2	*P. amygdalina*	Isomers 1, 2 and 3 of 10-hydroxymatricariate *(polyynes)* (2*E*, 6*E*)-deca-2,6-dien-4-yn-1-yle acetate *(polyyne)*
Group 3	*P. retusa*	*ortho*-Cymene *(monoterpene hydrocarbon)* Anisole *(oxygenated monoterpene)* Thymol methyl ether *(oxygenated monoterpene)* Himachalol *(oxygenated sesquiterpene)*
Group 4	*P. insignis* *P. laurifolia*	7-*epi*-Silphiperfol-5-ene *(sesquiterpene hydrocarbon)* *epi*-Presilphiperfolan-1-ol *(oxygenated sesquiterpene)* Elemol *(oxygenated sesquiterpene)* β-Eudesmol *(oxygenated sesquiterpene)* Unknown compound
Group 5	*P. boivinii*	(2*E*)-Hexenol *(alcohol)* *epi*-α-Muurolol *(oxygenated sesquiterpene)* α-Cadinol *(oxygenated sesquiterpene)* Eudesma-4,(15),7-dien-1-β-ol *(oxygenated sesquiterpene)* Selin-11-en-4-α-ol *(oxygenated sesquiterpene)*

Anchusifolol 6,6,8,9-tetramethyltricyclo[3.3.3.0]undec-2-en-1-ol
Anchusifolate 7,7-dimethyl-2-methylidenebicyclo[3.1.1]heptan-6-ol acetate

9.3.2   The Non-volatile Compounds Analysis

The ^{1}H NMR data matrix consisted of 189 samples and 239 variables. PCA were performed with Pareto scaling for each species and the results showed a differentiation according to the geographic origin for *P. dentata* and *P. melastomatoides*. In addition, samples of *P. amygdalina*, *P. argentea* and *P. retusa* were also separated according to seasonal variation (Fig. 9.3). The other species have not displayed any specific clustering based on these two factors.
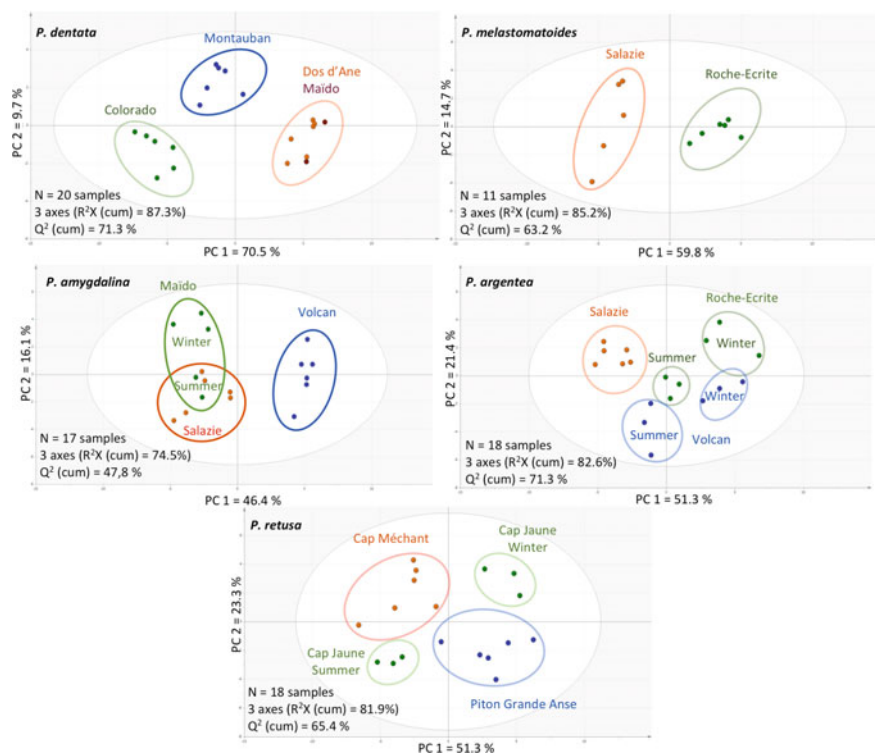
Fig. 9.3 PCA score plot generated from ^{1}H NMR spectra (600 MHz) of *P. dentata*, *P. melastomatoides*, *P. amygdalina*, *P. argentea* and *P. retusa* samples

In order to analyse the chemical variation between the 11 studied species and to differentiate them according to their metabolomic fingerprint, an OPLS-DA and a HCA dendrogram were generated. Three groups of species have been defined on the HCA dendrogram (Fig. 9.4a). The first group is a large one containing *P. argentea*, *P. callocephala*, *P. insignis*, *P. montana*, *P. melastomatoides* and *P. retusa*. The second group comprised *P. boivinii* and *P. anchusifolia* and the third one is composed of *P. dentata*, *P. amygdalina* and *P. laurifolia*. Chemical markers of these groups were investigated by means of a new OPLS-DA applied on all species spectral data (Fig. 9.4b). The discriminating chemical shifts are listed in Fig. 9.4c.

The discrimination of group 1 was based on chemical shifts located between δ_H 3.20 and 4.28 ppm. However, the multiplicity of all signals could not be determined due to overlapping with others. Thus, chemical markers of this group have not been identified. The other groups are characterised by a wide range of chemical shifts. Those located between δ_H 6.30 and 7.70 ppm might be attributed to phenolic compounds. The latter appeared to be different in both groups due to varied signals. Indeed, signals at 6.71 (d, $J = 1.9$ Hz), 6.75 (s), 6.79 (s) and 7.51 (d, $J = 15.9$ Hz) ppm in group 2 can be related to cinnamic acids derivatives [7] and signals at 6.36
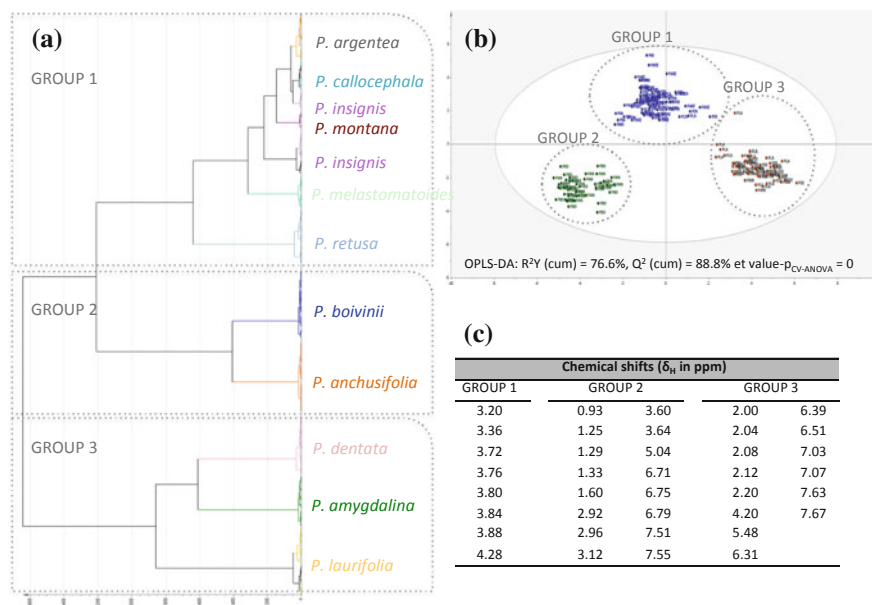
Fig. 9.4 HCA (**a**) and score plot (**b**) of OPLS-DA results obtained from ^{1}H NMR spectral data (600 MHz) of *Psiadia* species, (**c**) discriminating chemical shifts of *Psiadia* species

(d, $J = 15.9$ Hz), 6.47 (d, $J = 15.9$ Hz) and 7.63 (d, $J = 15.9$ Hz) ppm in group 3 can be attributed to caffeoyl or feruloyl acid derivatives [8, 9]. To our knowledge, this is the first report of a chemotaxonomic study of *Psiadia* species based on the non-volatile composition.

Two different classifications of *Psiadia* species have been obtained based on the volatile and non-volatile compounds composition. This information reflected the intervention of two different metabolic pathways for their biosynthesis. In the literature, two other classifications are reported based on morphological aspects [1] and molecular phylogenetics [4]. The four classifications including only studied species are represented in Fig. 9.5.

Their analysis showed for all of them five groups of *Psiadia* species. However, the composition of the groups is different in each classification except for the one comprising *P. callocephala* and *P. argentea*, which can be found in all classifications. No correlation was found between the morphological traits, the phylogenetics and the chemical composition of the studied species. Several authors have investigated the association of morphological, molecular phylogenetics and chemical diversity [10–13]. For example, Liu et al. [14] have found a correlation between morphological aspects and the genetic variability of *Heptacodium miconioides* Rehd. (Caprofiliaceae). In contrast, no correlation was found between agromorphological diversity and molecular diversity for *Carthamus tinctorius* L. (Asteraceae) [4]. Moreover, no correlation was observed between scent compounds and genetic variability for *Ophrys* species [13]. According to Persson and Gustavsson [15], the lack of cor-
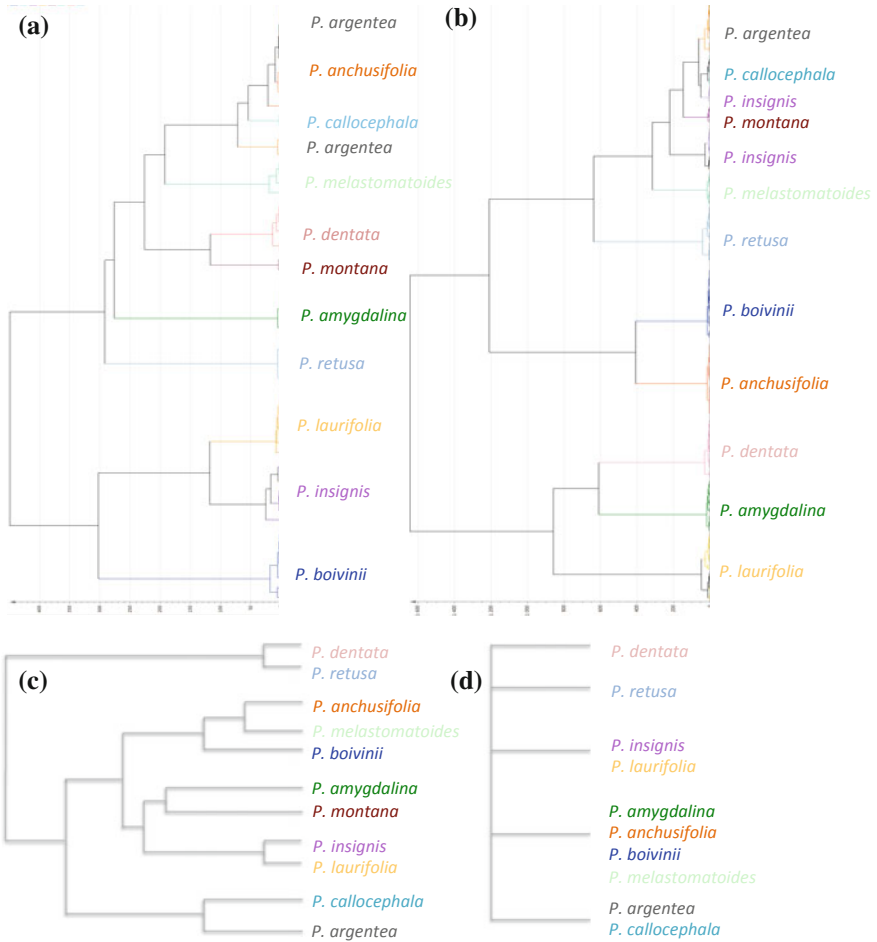
(a) classification based on volatile compounds composition (this study)
(b) classification based on non-volatile compounds composition (this study)
(c) classification based on molecular phylogenetics (Strijk *et al.*, 2012)
(d) classification based on morphological traits (Bosser *et al.*, 1993)

Fig. 9.5 Classifications of eleven *Psiadia* species from La Réunion

relation could be explained by the absence of relationship between the molecular markers and the morphological traits or the chemical composition. Another reason for this explanation might be a different regulation of genes according to species.

9.4 Conclusion

In this study, the essential oil profile and the non-volatile composition of eleven *Psiadia* species from La Réunion were analysed. The classification obtained for the volatile compounds separated all studied species in five groups whereas the non-volatile ones in three groups. Two distinct classifications were obtained. Based on the data presented here and in the literature, it could be concluded that no correlation was found between the morphological traits, the genetic aspect and the chemical composition of *Psiadia* species. However, both classifications obtained in this study are helpful for research of species containing bioactive compounds. In order to make a comprehensive chemotaxonomic study on the genus *Psiadia* it would be interesting to include species from Mauritius and Madagascar.

References

1. Bosser J, Guého J, Jeffrey C (1993) 109. Composées. In: Flore des Mascareignes. La Réunion, Maurice, Rodrigues, The Sugar Industry Research Institute, Mauritius, L'Institut Français de Recherche Scientifique pour le Développement en Coopération (ORSTOM), Paris, The Royal Botanic Gardens, Kew
2. Mahadeo K, Grondin I, Kodja H et al (2018) The genus *Psiadia*: review of traditional uses, phytochemistry and pharmacology. J Ethnopharmacol 210:48–68
3. Jacob de Cordemoy E (1895) Flore de l'île de la Réunion (phanérogames, cryptogames, vasculaires, muscinées) avec l'indication des propriétés économiques & industrielles des plantes. P. Klinsksieck, Paris, France
4. Strijk JS, Noyes RD, Strasberg D et al (2012) In and out of Madagascar: dispersal to peripheral islands, insular speciation and diversification of Indian Ocean daisy trees (*Psiadia*, Asteraceae). PLoS ONE 7:e42932
5. Gauvin A, Smadja J (2005) Essential oil composition of four *Psiadia* species from Reunion Island: a chemotaxonomic study. Biochem Syst Ecol 33:705–714
6. Adams RP (2001) Identification of essential oil components by gas chromatography/quadrupole mass spectrometry. Allured Publishing Corporation, Illinois, USA
7. Wang Y, Wray V, Tsevegsuren N et al (2012) Phenolic compounds from the Mongolian medicinal plant *Scorzonera radiata*. Z Naturforsch 67C:135–143
8. Lee SY, Moon E, Kim SY, Lee KR (2013) Quinic acid derivatives from *Pimpinella brachycarpa* exert anti-neuroinflammatory activity in lipopolysaccharide-induced microglia. Bioorg Med Chem Lett 23:2140–2144
9. Leiss KA, Maltese F, Choi YH et al (2009) Identification of chlorogenic acid as a resistance factor for thrips in chrysanthemum. Plant Physiol 150:1567–1575
10. Bahman P, Rahim A, Mahmoud GN et al (2013) Relationship among AFLP, RAPD marker diversity and agromorphological traits in safflower (*Carthamus tinctorius* L.). Prog Biol Sci 3:90–99
11. Kremer D, Bolarić S, Ballian D et al (2015) Morphological, genetic and phytochemical variation of the endemic *Teucrium arduini* L. (Lamiaceae). Phytochemistry 116:111–119

12. López PA, Widrlechner MP, Simon PW et al (2008) Assessing phenotypic, biochemical, and molecular diversity in coriander (*Coriandrum sativum* L.) germplasm. Genet Resour Crop Evol 55:247–275
13. Stökl J, Schlüter PM, Stuessy TF et al (2008) Scent variation and hybridization cause the displacement of a sexually deceptive orchid species. Am J Bot 95:472–481
14. Liu P, Yang YS, Hao CY, Guo WD (2007) Ecological risk assessment using RAPD and distribution pattern of a rare and endangered species. Chemosphere 68:1497–1505
15. Persson HA, Gustavsson BA (2001) The extent of clonality and genetic diversity in lingonberry (*Vaccinium vitis-idaea* L.) revealed by RAPDs and leaf-shape analysis. Mol Ecol 10:1385–1397

Chapter 10
Trace Metals Charaterisation of Soils in the Vicinity of a Major Active Dumpsite in Lagos: An Integrative Multivariate Indices Approach

Adeyi Adebola, Majolagbe Abdulrafiu and Osibanjo Oladele

Abstract The use of non-sanitary landfill facilities in refuse disposal process put much burden on the soils around the dumpsite, thereby portending health risk to man (soil-plant-man). However, the paucity of data on quality of soils around dumpsite necessitates this study using multivariate indices approach to assess the quality status of soils in and around dumpsite area. Forty (40) top and subsoil samples were collected around Olususon dumpsite in Lagos, and analysed for heavy metals and organic carbon using standard methods. The pH and particle size distribution of the soils were also investigated. The data obtained were analysed using descriptive statistics, correlation coefficient and multivariate indices: enrichment factor (EF), contamination factor (CF), geo accumulation index (I_{geo}) and pollution load index (PLI). The order of I_{geo} of metal pollution was $Zn > Cd > Ni > Fe > Cu > Pb$. The CF revealed low index for Pb, considerable index for Ni and very high index for Fe, Cu, Zn and Cd. The PLI confirmed deterioration of the soil in and around the dumpsite. Measures are urgently necessary to mitigate further accumulation of heavy metals which should include upgrading existing dumpsites to landfill and employing global refuse disposal standards of 3-Rs (Reduce-Recycle-Reuse).

Keywords Olususon dumpsite · Multivariate indices · Geo accumulation index · Pollution load index · Reduce-Recycle-Reuse

A. Adebola · O. Oladele
Department of Chemistry, University of Ibadan, Ibadan, Nigeria
e-mail: adebolaoketola@gmail.com

O. Oladele
e-mail: oosibanjo@yahoo.com

M. Abdulrafiu (✉)
Department of Chemistry, Lagos State University, P.M.B. 0001, LASU Post Office, Lagos, Nigeria
e-mail: abdulrafiu.majolagbe@lasu.edu.ng

10.1   Introduction

Dumpsite activities are known to be a major source of heavy trace metals pollution in an environment. The waste disposal process in Nigeria raises so many questions because of the low standard practice being employed. Non availability of sanitary landfill system makes the environment not isolated from the leachate generated from waste, hence, putting heavy environmental burden on the soil. The waste disposal activities, therefore, have deleterious impact on all components of environment including surface water, groundwater, air and soils. Soils have been described as reservoir of water and nutrients of terrestrial ecosystems and irreplaceable source of food production [1]. Topsoil (0–15 cm depth) is worst affected, i.e. most loaded with pollutants due to its proximity to refuse dumped and unfortunately it is the root zone of most of the vegetables and cereals regularly consumed. Hence, it has health consequence on man (soil–plant–man). The increase in level of industrialization and urbanization in an area affects the volume and nature of the wastes generated as well as the type of pollutants released into the environment. The chemical pollutants released into the environment range from organics, inorganics, heavy metals, carcinogenic to toxic, etc.

Trace and heavy metal pollution in the environment have been receiving extensive attention [2–6]. The attention becomes worrisome, considering the non-degrading nature of metals in the environment as well as the facts that various health situations have been linked to heavy metals. Some heavy metals including Cu, Zn, Co, Ca, Fe, and Mg contribute to functionality of metabolic processes in human systems while some elements such as Pb, Cd and Hg are toxic to living cells even at low concentrations [7]. Heavy metals accumulation in an environment have also been implicated in making land not suitable for agricultural production, thereby causing food insecurity and land tenure problems [8].

Though studies on several sources of heavy metals accumulation in soils are well documented, the paucity of data on heavy metals in soils in the vicinities of dumpsites is conspicuous. Therefore, this study aims at assessing the concentration of heavy metals in soils around a major dumpsite in Lagos thereby revealing the quality status of the soil.

10.2   Materials and Methods

10.2.1   Olososun Refuse Dumpsite

The Olususun refuse dumpsite is located within the longitude 3° 37′E and latitude 6° 59′N to 6° 60′N in Ojota, Kosofe Local Government Area of Lagos state (Fig. 10.1). It is the largest dumpsite facility in Nigeria and West Africa established in the year 1992 with a life span of 30 years. It occupies 45 hectars and is about 18 m deep. It is surrounded by Oregun industrial layout, Olususun compound, Shangisa residential
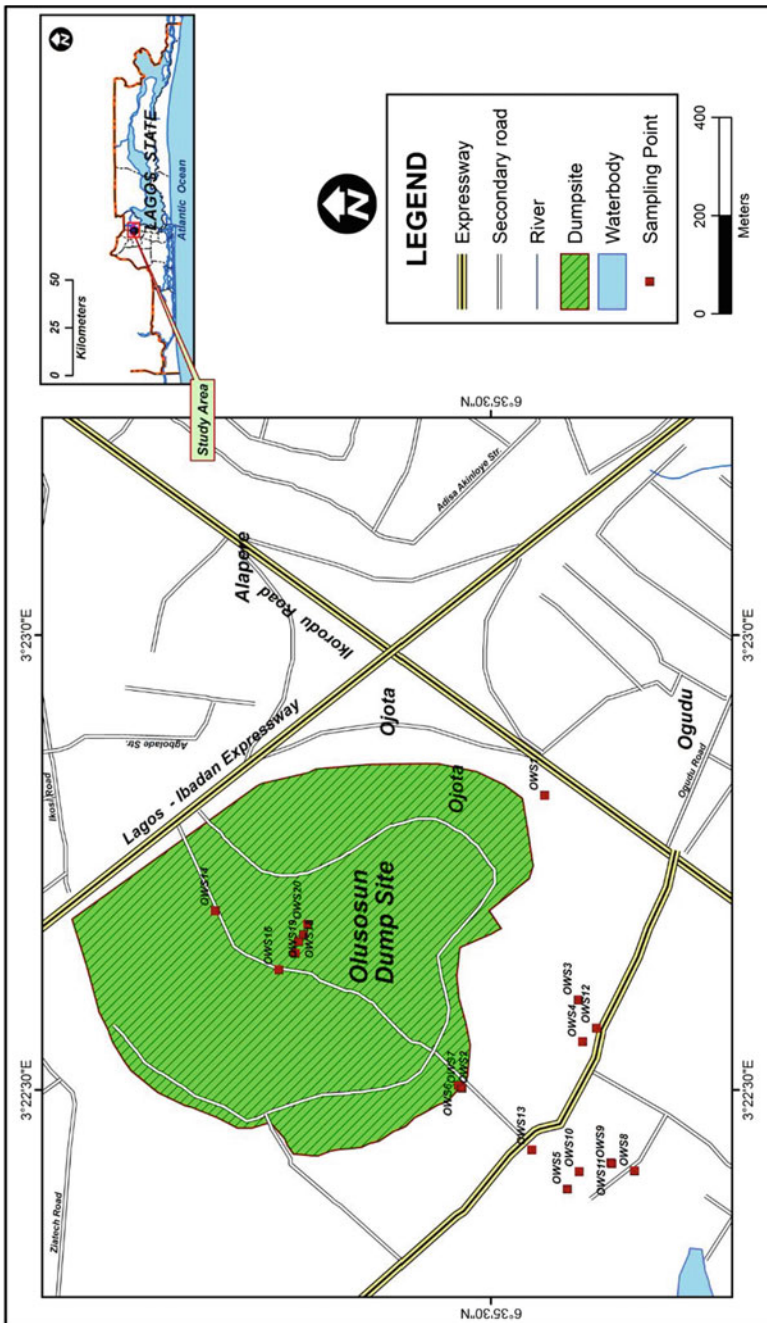
Fig. 10.1 Sampling locations around Olusosun dumpsite, Ojota, Lagos

area and commercial neighborhoods. It is owned and operated by the Lagos State Waste Management Authority (LAWMA) and receives about 485 daily truck trips amounting to 2650 tons of waste per day i.e. about 66% of the waste generated in the metropolis [9]. It receives an average of 1.9 million tons of wastes annually, and is currently serving as a pilot project for biogas production in Nigeria.

10.2.2 Soil Samples Collection

Representative soil samples were collected randomly between 0–15 cm (topsoil) and 15–30 cm (subsoil) from twenty (20) different locations around the dumpsite using a stainless soil auger. At each location, a composite sample was made from the pool of random soils collected, stored in clean polyethylene bags, labeled and transported to the laboratory for analyses. A representative sample was also collected from Palm Grove Estate, Onipanu, Lagos, about six (6) km from Olususun dumpsite as control sample.

10.2.3 Chemical Analyses

The pH of top and subsoil, soil particle size distribution, heavy metal load and total organic carbon were investigated, employing standard procedures.

10.2.3.1 Soil Sample Preparation and Treatment

The soil samples were air dried and pulverized using pre-cleaned mill (mortar and pestle), sieved through 2 mm aperture. The mill was further cleaned after each soil to avoid cross contamination.

10.2.3.2 pH Determination

About 20.0 g each of the soil samples were weighed into a clean beaker; 20 mL deionized water was added and the mixture was allowed to stand for 30 min with occasional stirring using a glass rod. The pH was then measured using a pH meter (pHep HANNA HI 98107) already calibrated with buffer solutions of pH 7 and 9.

10.2.3.3 Soils Particle Size Distribution by Hydrometer Method

50.0 g of sieved soil samples were weighed into a conical flask, 50 mL of 5.0% sodium hexametaphosphate (dispersing agent) was added along with 60 mL deionized water.

It was stirred with a stirring rod and left to settle for 30 min. The soil suspension was stirred for 15 min with the aid of a shaker, after which the suspension was transferred into a 1000 mL measuring glass cylinder. The hydrometer was introduced into the suspension and distilled water was added to the lower blue line until the volume was about 1130 mL The top of the measuring cylinder was covered with hand (with gloves) and inverted six (6) times until the soil was in the suspension. The measuring cylinder was made to stand and time was noted. The hydrometer was placed back into the suspension until it was floating. The first reading of the hydrometer was taken 40 s after the hydrometer settled down as H_1 and temperature taken as T_1. The second reading of hydrometer was taken 3 h after the hydrometer settled down as H_2 and temperature taken as T_2. A value of 2.0 was subtracted from every hydrometer reading to compensate for the addition of dispersing agent.

Calculation

a. % SAND $= 100.0 - (H_1 + T_1 - 2.0)\ 2$
b. % CLAY $= (H_2 + T_2 - 2.0)\ 2$
c. % SILT $= 100.0 - (\% \text{ SAND} + \% \text{ CLAY})$

where: hydrometer reading at 40 s $= H_1$, temperature at 40 s $= T_1$, hydrometer reading at 3 h $= H_2$ and temperature at 3 h $= T_2$.

10.2.3.4 Heavy Metal Determination by Spectrophotometric Method

About 2.0 g each of the sieved soil samples were weighed into a 250 mL beaker and moistened with drops of deionized water to prevent loss by spattering during digestion. The sample was digested with 10 mL of concentrated HNO_3 on a hot plate in a fume cupboard until the volume was about 3 mL. The residues obtained were further digested with a mixture of concentrated acids containing 5 mL each of HCl, HNO_3 and $HClO_4$ at room temperature for 10 min until the solution was brought to a final volume of about 5 mL on a hot plate in the fume cupboard. The digest was cooled and filtered into a 100 mL volumetric flask using Whatman No. 1 filter paper and made up to mark with the deionized water. The digest was analysed using model 210 VGP flame atomic absorption spectrophotometer. A standard addition technique was introduced to compensate for the usual variation caused by interferences in the sample solution. Standard solution of each pure metal was prepared in 10% of 5 M HNO_3. The blank samples were similarly analysed. Each analysis was duplicated, so as to ascertain the validity of the method. The control samples were also treated as field samples.

10.2.3.5   Total Organic Carbon Determination (Walkley-Black Chromic Acid Oxidation Method)

2.0 g of sieved soil sample was accurately weighed into a 250 mL conical flask. 10 mL of 1 M $K_2Cr_2O_7$ was added and swirled, followed by 20 mL of concentrated H_2SO_4. The conical flask was swirled continuously on a hot plate until the reagents were properly mixed and reached 135 °C, after which it was set aside to cool for about 30 min. The solution was transferred into a 250 mL standard flask and made up with double distilled water. The solution was then titrated against 0.4 N ferrous sulphate using ferroin indicator. The colour initially changed from greenish to dark green, but with additional two drops of ferroin, the colour changed from blue green to reddish grey which is the end point of titration.

Calculation

From the equation: $2Cr_2O_7^{2-} + 3C + 16H^+ \rightarrow 4Cr^{3+} + 8H_2O + 3CO_2 \uparrow$

$$Organic\ Carbon\ (\%) = \frac{0.003\,\text{g} \times \text{N} \times 10\,\text{mL} \times (1 - \text{T/S}) \times 100}{\text{W}}$$

where: N = normality of $K_2Cr_2O_7$ solution, T = volume of $FeSO_4$ used in sample titration (mL), S = volume of $FeSO_4$ used in blank titration (mL) and W = weight of the sieved soil (g).

10.2.4   Data Analysis

The data generated from soil chemical analyses were analysed using Graph Pad Prism (version 5.00). For all metal concentrations, descriptive analysis was also carried out. Correlations were performed in a pairwise fashion employing Pearson correlation procedure. Various multivariate statistical indices were also applied to assess potential ecological risks. These indices are Enrichment Factor (EF), Contamination Factor (CF), Geo accumulation Index (I_{geo}) and Pollution Load Index (PLI).

10.2.4.1   Enrichment Factor (EF)

The EF of heavy metals in the soil can be calculated through the mathematical relationship:

$$EF = \frac{[Cmetal/Cnormalizer]sample}{[Cmetal/Cnormalizer]control}$$

where C_{metal} and $C_{normalizer}$ are the concentrations of heavy metals and normalizer in soil samples and unpolluted control. Sutherland and Tolosa [10] listed five categories of metal contamination: EF < 2 is deficient mineral enrichment; EF 2–5 is moderate enrichment; EF 5–20 is significant enrichment; EF 20–40 is very high enrichment and EF > 40 is extremely high enrichment.

10.2.4.2 Contamination Factor (CF)

This expresses the contamination of soil and is calculated as:

$$CF = \frac{C_{metal\ sample}}{C_{metal\ control}}$$

where $C_{metal\ sample}$ and $C_{metal\ control}$ is the concentration of the heavy metal in the study sample and unpolluted control sample respectively. Contamination categories known are as follows: CF < 1 means low contamination; $1 \leq CF < 3$ means moderate contamination; $3 \leq CF < 6$ means considerable contamination and CF > 6 means very high contamination.

10.2.4.3 Geoaccumulation Index (I_{geo})

The I_{geo} of heavy metals in the soil can be calculated through the mathematical relationship:

$$I_{geo} = \log_2 \frac{C_{metal\ sample}}{1.5 \times C_{metal\ control}}$$

where $C_{metal\ sample}$ and $C_{metal\ control}$ is the concentration of the heavy metal in the study sample and unpolluted control sample respectively. The factor 1.5 is introduced to minimize the effect of the possible variations in the background or control which may be attributed to lithogenic variations in the soil [11]. The degree of metal pollution is assessed in terms of seven contaminant categories based on increasing value of the index as follows: $I_{geo} < 0$ means unpolluted; $0 \leq I_{geo} < 1$ means unpolluted to moderately polluted; $1 \leq I_{geo} < 2$ means moderately polluted; $2 \leq I_{geo} < 3$ means moderately to strongly polluted; $3 \leq I_{geo} < 4$ means strongly polluted; $4 \leq I_{geo} < 5$ means strongly to very strongly polluted and $I_{geo} > 5$ means very strongly polluted.

10.2.4.4 Pollution Load Index (PLI)

The PLI helps to evaluate the extent to which a site under investigation is polluted by metals. It is calculated as follows:

$$PLI = (CF_1 \times CF_2 \times CF_3 \times \cdots CF_n)^{1/n}$$

where n is the number of metals studied and CF is the contamination factor. The degree of site deterioration is categorized into the following: PLI < 1 means perfect site; PLI = 1 means baseline pollution; PLI > 1 means deterioration.

10.3 Results and Discussion

The results of soil chemical analysis and heavy metal load in both topsoil (0–15 cm) and subsoil (15–30 cm) from Olusosun dumpsite are presented in Table 10.1, while the correlation coefficients between various metals in the soil samples around the dumpsite are presented in Table 10.2. The pH value of soils under investigation range from 7.12 to 7.37 and from 7.10 to 7.24 for topsoil and subsoil, respectively. The mobility of metals in the alkaline region is impaired by the pH of the soil and this possibly accounts for low metal concentration in the surrounding aquifer. The pH of the soil also influences the activities of microorganisms which thrive best in soil with pH between 6.0 and 7.5. The acidity level of the soil from the studied site is lower compared to the control samples. This suggests the possible influence of organic matter in refuse dumpsites. In Olusosun dumpsite, the pH of the topsoil is

Table 10.1 Descriptive statistics of soil from Olusosun dumpsite

Parameter	Depth (cm)	Minimum n = 20	Maximum n = 20	Mean n = 20	S.D.	Control (Mean) n = 4	USEPA [12]
pH	0–15	7.12	7.37	7.20	0.63	6.90	
	15–30	7.10	7.24	7.17	0.80	6.80	
Organic carbon %	0–15	2.21	2.24	2.22	0.79	1.88	
	15–30	2.10	2.18	2.15	0.84	1.60	
Ni (mg/kg)	0–15	18.7	87.4	37.5	33.5	18.4	75
	15–30	12.5	100	44.8	40.4	20.1	
Cu (mg/kg)	0–15	25.6	45.0	38.2	8.1	0.53	4300
	15–30	9.54	27.4	22.0	8.3	0.18	
Cd (mg/kg)	0–15	0.24	4.44	1.77	1.9	0.20	85
	15–30	0.34	2.80	1.45	1.17	0.21	
Fe (mg/kg)	0–15	12,800	19,800	17,900	1930	3910	
	15–30	16,500	21,600	19,200	2290	2270	
Zn (mg/kg)	0–15	200	285	260	40.1	58.9	7500
	15–30	138	290	239	68.9	9.80	
Pb (mg/kg)	0–15	17.5	124.9	53.1	23.1	49.63	420
	15–30	2.2	125.0	46.3	26.3	55.70	

NB 0–15 cm = Topsoil, 15–30 cm = Subsoil

Table 10.2 The Pearson correlation coefficient of heavy metals in Olusosun dumpsite soil

	Fe	Cu	Cd	Pb	Zn	Ni
Fe						
Cu	−0.155					
Cd	0.543	0.349				
Pb	−0.596	−0.271	−0.318			
Zn	0.571	0.481	0.577	−0.843		
Ni	0.509	0.051	0.820	−0.079	0.473	

more alkaline than the subsoil, an observation that is opposite to the trend reported for another dumpsite in Lagos (Solous dumpsite) i.e., from 7.90 to 8.15 and from 7.90 to 8.33 for topsoil and subsoil, respectively.

The observation was similar to the results reported by Oluyemi et al. [13]. They proffered the reason to be the presence of substances in the dumpsite such as broken blocks and other materials that act as source of calcium carbonate ($CaCO_3$) buffer, and rainfall diluting the soil solution, thus leading to an increase in pH value. At low pH, metals are more soluble and available to plants. Hence, toxicity problems are more pronounced in acidic soil [14]. The higher the depth of soil level, the lower the organic carbon content, which implies that mobility of carbon down the soil was minimal.

The organic carbon content of the site under investigation was higher compared to the control site, indicating a lower chemical activity in the control site. The percentage composition of organic waste on the Olusosun dumpsite (57%) influences the level of organic carbon content of the soil. Organic matter plays an important role in soil structure, water retention, and carbon exchange as well as in the formation of complexes [15]. The mean organic carbon content is lower in the study area: 0–15 cm (2.22%), 15–30 cm (2.15%). This could be attributed to incessant burning in the dumpsite, leading to oxidation of organic carbon, thereby altering the organic colloids. The topsoil is the first part of the ecosystem that is exposed to contaminants and the concentration of some pollutants is usually greater than other parts of the ecosystem of sub-urban or rural areas. The contamination is often as a result of the level of human activities of urban settlement [16]. Therefore, soil is an important sink for contaminants [17].

The soil type classification was done employing United States Department of Agriculture (USDA) soil texture triangle or ternary [12]. The soil ternary plot for Olusosun dumpsite area is presented in Fig. 10.2 and shows also the distribution of soil samples in terms of sand-clay-silt. The plot revealed the soils around Olusosun to be more in clay form which is corroborated by particle size distribution analysis. The particle size distribution of soil from Olusosun dumpsite was conducted. The clay fraction was dominant in both refuse dumpsite soils, the immediate environment as well as in the control.

The clay-silt-sand texture for Olusosun dumpsite was 61–13–26 (%). The clay plays a very important role in the mobility of many inorganic elements. Apart from the
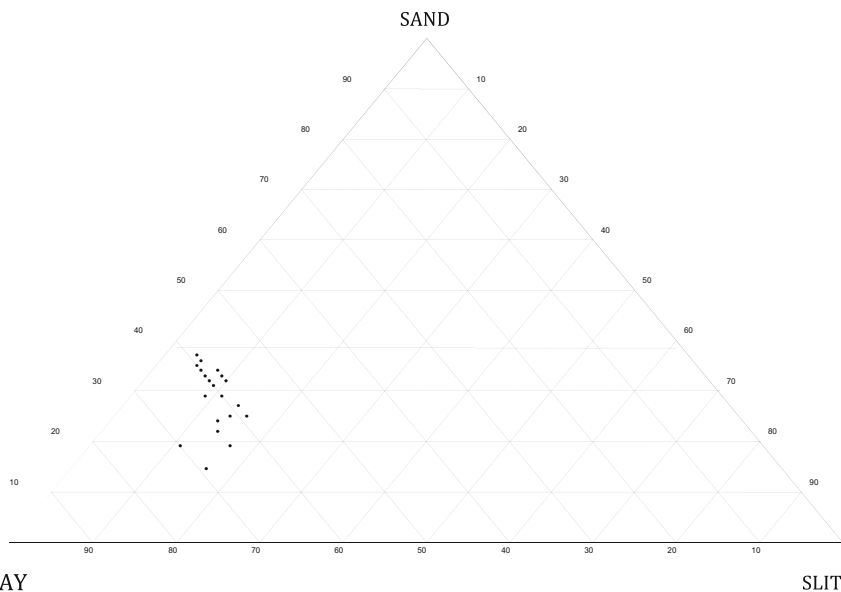
Fig. 10.2 Ternary plot of soil composition of Olususun dumpsite

fact that clay acts as a sealant, slowing down the dispersion of trace metals by retaining them, it also absorbs many of the cations. A low permeability clay-rich geological unit (hydraulic conductivity $< 10.5 \text{ ms}^{-1}$) can perform the function of an attenuating layer, enabling leachate to percolate slowly downwards, simultaneously undergoing attenuation by biodegradation, sorption, filtration, and ion exchange processes with the clays in the unit.

The report of soil study in Maiduguri by Uwah [17], revealed that loamy sandy soil did not only contribute to extremely low level of heavy metal contamination but more importantly led to low retention of anthropogenically introduced metals [18]. The high clay content of the soil from the dumpsite is further shown in the ternary plot in Fig. 10.2. Metals associated with the aqueous phase of soils are subjected to movement with soil water, and may be transported through to groundwater. Some metals, such as Cr, As, Se, and Hg can be transformed to other oxidation states in soil, thereby reducing their mobility and toxicity. Immobilization of metals by mechanisms of adsorption and precipitation will prevent movement of the metals to groundwater [19].

Metal-soil interaction is such that, when metals are introduced at the soil surface, downward transportation does not occur to any great extent unless the metal retention capacity of the soil is overstretched, or the clay content is too low and metal interaction with the associated waste matrix enhances its mobility [20]. Changes in soil environmental conditions over time, such as the degradation of organic waste matrix, changes in pH, redox potential, or soil composition can also enhance metal mobility. The extent of vertical contamination is intimately related to the soil composition and

surface chemistry of the soil matrix with reference to the metal and waste matrix in question [21].

The mean concentration of heavy metals in the soil (0–15 cm) and (15–30 cm) are shown in Table 10.1. The levels of all heavy metals analysed in the soils around the dumpsite were high, an indication of the influence of pollutants from municipal solid waste. The order of concentrations of metals in the topsoil analysed was Fe >> Zn >> Pb > Cu > Ni > Cd while that of subsoil was Fe >> Zn >> Pb > Ni > Cu > Cd. The concentrations of all the metals analysed were higher in the topsoil (0–15 cm) than in the sub soil (15–30 cm) except for nickel and iron.

This could be attributed to the high level of Fe in the geological composition of the area and the contributions from various anthropogenic activities also influenced the relative high level of other metals in the site. The high level of zinc and copper could indicate that wastes laden with copper and zinc are frequently deposited in the dumpsite. Though the mean values reported in this study are below the allowable limits of some countries as shown in Table 10.3, the zinc and copper levels are still much higher than the values observed in the control samples. This is an indication of possible buildup of the trace metals in the lithosphere.

The concentrations of Ni, Cd, and Pb were also high in Olususun dumpsite soils. This can be attributed to the possible dumping of industrial wastes laden with lead and nickel as well as cadmium such as waste from battery companies, automobile waste smelting and aluminum industries. The observed mean value of cadmium and nickel in the soil samples have exceeded the maximum allowable limits of many countries (Table 10.3), thus portending disaster. The soil in the dumpsite is still seen as fertile and can increase crop productivity. Hence, according to Amusan et al. [22], local farmers from nearby areas often come to collect "soils" (due to its high organic component) from dumpsite to be used as compost on their farms. This practice is potentially harmful to the health and wellbeing of the populace [16].

Human exposure to heavy metals occurs via three primary routes: inhalation, ingestion and skin absorption. Nickel concentration was observed to increase with depth in the study area. Geochemical properties of component parent soil or rock could be responsible for this trend. The nickel values in this study ranged between 18.7 and 87.4 mg/kg for topsoil and 12.5–100 mg/kg for subsoil from Olususun dumpsite. These values observed were lower than what were reported by Awokunmi et al. [23], with a Ni concentration range of 18–335 mg/kg at the surface layer in a

Table 10.3 Maximum allowable limits of heavy metals in soil from various countries (mg/kg)

Heavy metal	Austria	Germany	France	Sweden	Spain	Canada	Great Britain	USEPA [12]
Cd	1.0	2.0	2.0	0.4	1	5	3	85
Cu	100	50	–	–	–	100	100	4300
Ni	50–70	100	50	30	30	–	50	75
Pb	100	70	100	40	40	200	100	420
Zn	300	300	–	–	–	–	300	7500

dumpsite. Nickel is known to accumulate in plants. Intake of high level of Ni can cause cancer of lung, nose larynx and prostrate as well as respiratory failure [24, 25].

The deposition of industrial wastes, mining activities, atmospheric deposition and agricultural waste deposition are some of the sources of cadmium in the environment [26]. Human diseases have been linked to consumption of Cd contaminated food even at low concentration.

Inter-elemental association was also evaluated by employing Pearson correlation coefficient. The results for correlation coefficient of heavy metals in soil around Olusosun dumpsite are represented in Table 10.2. Some elemental pairs like Cd/Ni, Cd/Fe, Zn/Fe and Cd/Zn had strong correlation; Zn/Cu and Ni/Zn had weak correlation while others did not correlate at all.

The results of the enrichment factor (EF) and geochemical factor (I_{geo}) are presented in Table 10.4 for Olusosun refuse dumpsite soil. Fe was taken in this study as a normalizing element because of its natural abundance in Nigerian soil. Fagbote and Edward [27] also used Fe as normalizing element because according to them, it has low occurrence variability. The EF value of heavy metals investigated showed Fe (1.00), Pb (0.14) and Ni (0.55) had no enrichment. Cd (1.22) and Zn (1.32) had minimized enrichment while Cu (5.63) has significant enrichment at Olusosun dumpsite. The Olusosun dumpsite may have problem of pollutants from natural origin.

The results of geochemical factor (I_{geo}) are shown in Table 10.4. The negative value for Pb (-0.68) indicates that the soils around Olusosun dumpsite were not polluted by Pb, whereas the I_{geo} value of 1.17 for copper classifies it as a zone of unpolluted to moderately polluted. The I_{geo} values of the remaining heavy metals (Fe, Cd, Zn and Ni) ranging from 2.01 and 2.40 revealed that the dumpsite is moderately to strongly polluted by the metals. The order of pollution of metals is therefore Zn > Cd > Ni > Fe > Cu > Pb in Olusosun dumpsite.

The results of assessment by contamination factor (CF) are presented in Table 10.5. The contamination factors for Olusosun dumpsite soil revealed low contamination by Pb with 0.94 index value, considerable contamination by Ni with 3.29 index value

Table 10.4 Enrichment factor (EF) and Geochemical index (I_{geo}) of heavy metals in soil of Olusosun dumpsite

	Fe	Cu	Cd	Pb	Zn	Ni
C (Ms)/mg/kg	18,600	30.1	1.54	49.7	250	41.2
C (Fes)/mg/kg	18,600	18,600	18,600	18,600	18,600	18,600
C (Mc)/mg/kg	3090	0.89	0.21	52.6	34.3	12.5
C (Fec)/mg/kg	3090	3090	3090	3090	3090	3090
EF	1.00	5.56	1.22	0.16	1.20	0.55
I_{geo}	2.01	1.17	2.30	-0.68	2.40	2.19

Note C (Ms)—concentration of metal in the sample, C (Fes)—concentration of iron (normalizer) in the sample, C (Mc)—concentration of metal in the control sample, C (Fec)—concentration of iron (normalizer) in the control sample

Table 10.5 Contamination factor of heavy metals in Olususun dumpsite soil

	Fe	Cu	Cd	Pb	Zn	Ni
C (Ms)/mg/kg	18,600	30.1	1.54	49.7	271	41.1
C (Mc)/mg.kg	3090	0.89	0.21	52.6	34.3	12.5
CF	6.02	33.8	7.33	0.94	7.92	3.29

Note C (Ms)—concentration of metal in the sample, C (Mc)—concentration of metal in the control sample

and high contamination by Fe, Cu, Zn and Cd in Olususun dumpsite (CF > 6). It is an indication that copper and zinc laden solid wastes are substantial in the dumpsite.

The pollution load index (PLI) is another important tool, often employed to further reveal certain trends on the nature of pollutants in soil or sediments and its origin. It also helps to show the extent of the deterioration of a study site [11]. This type of measurement, however has been defined with different names, for example, as the numerical sum of contamination factor (CF) [28], and as arithmetic of mean of analysed pollutants by Abrahim and Parker [29]. The calculated PLI gave a value of Olususun dumpsite to be 5.78. This shows that the study area is highly polluted or deteriorated. It further suggests the input from anthropogenic sources.

10.4 Conclusions

This study assessed the quality of top and subsoil in the vicinity of Olususun dumpsite, Lagos, using various multivariate indices which include enrichment factor, contamination factor and geoaccumulation factors. This integrative approach reveals deleterious impact of dumpsite activities as well as buildup of trace metals in the lithosphere. The pH value of the soil samples analysed (top and subsoil) ranged from neutral to slightly alkaline. The enrichment factor (EF) value of heavy metals investigated showed no enrichment by Fe (1.00), Pb (0.14) and Ni (0.55). There was minimal enrichment by Cd (1.22) and Zn (1.32) while there was significant enrichment by Cu (5.63) at Olususun dumpsite. The I_{geo} showed the order of pollution of metals analysed as Zn > Cd > Ni > Fe > Cu > Pb in Olususun dumpsite. The pollution load index value of 5.78 indicates a strong deterioration of the dumpsite through anthropogenic sourced pollutants. There is need for stakeholders in wastes disposal activities to step up measures to mitigate further deterioration of the soils around the dumpsite. These steps should include the implementation of global standards of 3-Rs (Reduce–Recycle–Reuse), as well as upgrading the present dumpsite to landfill, thereby saving our environment from the deleterious impacts of leachates.

References

1. Sardans J, Montes F, Peñuelas J (2011) Electrothermal atomic absorption spectrometry to determine As, Cd, Cr, Cu, Hg, and Pb in soils and sediments: a review and perspectives. Soil Sediment Contam 20:447–491

2. Nwachukwu MA, Feng H, Alinnor J (2010) Trace metal dispersion in soil from auto-mechanic village to urban residential areas in Owerri, Nigeria. Afr J Environ Sci Technol 4:310–322

3. Tchounwou PB, Yedjou CG, Patlolla AK, Sutton DJ (2012) Heavy metals toxicity and the environment. EXS 101:133–164

4. Najib NWZ, Mohammed SA, Ismail HS, Wan Ahmad A (2012) Assessment of heavy metals in soil due to human activities in Kangar, Perlis, Malaysia. Int J Civ Environ Eng 12:28–33

5. Majolagbe AO, Alkali II, Onwordi CT (2014) Ecological risk assessment of soil metallic pollution in mechanic villages, Abeokuta, Nigeria. J Environ 3:1–9

6. Cortez LS, Ching JA (2014) Heavy metal concentration of dumpsite soil and accumulation in *Zea mays* (corn) growing in a closed dumpsite in Manila, Philippines. Int J Environ Sci Dev 5:77–80

7. Manahan SE (2001) Fundamentals of environmental chemistry, 2nd edn. CRC Press, Florida, USA

8. McLaughlin MJ, Hamon RE, McLaren RG, Speir TW, Rogers SL (2000) Review: a bioavailability-based rationale for controlling metal and metalloid contamination of agricultural land in Australia and New Zealand. Aust J Soil Res 38:1037–1086

9. Lagos State Waste Management Authority (LAWMA) (2011) Integrated waste management: shifting the paradigm. In: Proceedings of the 47th Annual International Conference of the Nigerian Mining and Geosciences Society (NMGS). (www.lawma.gov.ng)

10. Sutherland RA, Tolosa CA (2000) Multi-element analysis of road-deposited sediment in an urban drainage basin, Honolulu, Hawaii. Environ Pollut 110:483–495

11. AL-Jibury DA, Essa KS (2016) Using pollution indexes to assessment of heavy metals pollution in highway–side soils around Baghdad City. J Environ Earth Sci 10:161–175

12. United States Department of Agriculture (USDA) (2000) Urban Technical Note No. 3. Soil Quality Institute, USA

13. Oluyemi EA, Feuyit G, Oyekunle JAO, Ogunfowokan AO (2008) Seasonal variations in heavy metal concentration in soil and some selected crops at a landfill in Nigeria. Afr J Environ Sci Technol 2:89–96

14. Butterly CR, Baldock JA, Tang C (2013) The contribution of crop residues to changes in soil pH under field conditions. Plant Soil 366:185–198

15. Alloway BJ, Ayres DC (1997) Chemical principles of environmental pollution, in wastes and their disposal, 2nd edn. Blackie Academics Professional, London

16. Adelekan BA, Alawode AO (2011) Contributions of municipal refuse dumpsites to heavy metals concentrations in soil profile and groundwater in Ibadan, Nigeria. J Appl Biosci 40:2727–2737

17. Uwah EI (2009) Concentration levels of some heavy metal pollutants in soils, and carrot (*Daucus Carota*) obtained in Maiduguri, Nigeria. Cont J Appl Sci 4:76–88

18. Fonge BA, Nkoleka EN, Asong FZ, Ajonina SA, Che VB (2017) Heavy metal contamination in soils from a municipal landfill, surrounded by banana plantation in the eastern flank of Mount Cameroon. Afr J Biotechnol 16:1391–1399

19. Othman AF, Ghandour MA (2005) Square-wave stripping voltammetry direct determination of eight heavy metals in soil and indoor airborne particulate matter. Environ Res 97:229–235

20. Lee SCL, Li XD, Shi WZ, Cheing SC, Thorton I (2006) Metal concentration in urban, sub urban and country parks soil of Hong Kong: a study based on GIS and multivariate analysis statistics. Sci Total Environ 4:45–61

21. EPA (2002) Guidance for comparing background and chemical concentrations in soil for EPA/600/P-95/002Fc. Office of Research and Development, U.S. EPA, Washington, DC

22. Amusan AA, Ige DV, Olawale R (2005) Characteristics of soils and crops uptake of metals in municipal waste landfill in Nigeria. J Human Ecol 17:167–171

23. Awokunmi EE, Asaolu SS, Ipinmoroti KO (2010) Effect of leaching on heavy metals concentration of soil in some dumpsites. Afr J Environ Sci Technol 4:495–499
24. Duda-Chodak A, Blaszczyk U (2008) The impact of nickel on human health. J Elementol 13:685–696
25. Lenntech Water Treatment (2009) Chemical properties, health and environmental effects of copper. Lenntech water treatment and purification holding B V. http://www.Lenntech.com/periodic/element
26. Ferguson C, Kasamas H (1999) Risk assessment for contaminated sites in Europe. Policy framework, vol 2. LQM Press, Nottingham
27. Fagbote EO, Edward OO (2010) Evaluation of the status of heavy metal pollution of soil and plant (*Chromolaena odorata*) of Agbabu bitumen deposit area, Nigeria. Am-Eurasian J Sci Res 5:241–248
28. Hakanson L (1980) Ecological risk index for aquatic pollution control, a sediment logical approach. Water Res 14:975–1001
29. Abrahim GMS, Parker RJ (2008) Assessment of heavy metals enrichment factors and the degree of contamination in marinesediments from Tamaki Estuary, Auckland, New Zealand. Environ Monit Assess 136:227–238

Chapter 11
Parasitic Plants of Namibia

Check for updates

Muvari Connie Tjiurutue, Ezekeil G. Kwembeya and Erika Maass

Abstract Parasitic plants are common in many ecological and agricultural settings, and often play major roles in structuring ecosystems. Over 4,100 species in approximately 19 families of the world's angiosperms are parasitic plants. In sub-Saharan Africa, parasitic plants such as *Striga* (Witchweed) can lead to millions of dollars of losses in crop yields, devastating livelihoods. In spite of the important economic roles that parasitic plants play in both natural and agricultural systems, many aspects of parasitic plants remain unknown including host-plant interactions, pollination biology, chemical ecology and ethnobotanical uses, especially in Namibia. Here, we explore and describe the known medicinal parasitic plants that occur in Namibia. Based on literature search and herbarium studies we recorded 8 families, 16 genera and 52 species of parasitic plants in Namibia, of which two are endemic namely: *Agelanthus discolor* (Schinz) Balle and *Thesium xerophyticum* A. W. Hill. Additionally, most species of parasitic plants belong to the Family Loranthaceae (28.8%). Of the 52 species of parasitic plants in Namibia only 14 have documented uses, namely *Cuscuta planiflora* Ten. var. *planiflora*, *Cassytha filiformis* L., *Oncocalyx welwitschii* (Engl.) Polhill & Wiens, *Plicosepalus undulatus* (E. Mey. ex Harv.) Tiegh., *Plicosepalus kalachariensis* (Schinz) Danser, *Tapinanthus oleifolius* (J. C. Wendl.) Danser, *Ximenia americana* L. var. *americana*, *Ximenia caffra* Sond. var. *caffra*, *Striga asiatica* (L.) Kuntze, *Striga gesnerioides* (Willd.) Vatke, *Thesium lacinulatum* A. W. Hill, *Thesium lineatum* L.f., *Viscum capense* L.f. and *Viscum rotundifolium* L.f. The genus *Ximenia* had the most medicinal applications (27%) with all plant parts used. A sig-

M. C. Tjiurutue (✉)
Department of Chemistry & Biochemistry, University of Namibia, 340 Mandume Ndemufayo Avenue, Pionierspark, Windhoek, Namibia
e-mail: mctjiurutue@unam.na

E. G. Kwembeya
Department of Biological Sciences, University of Namibia, 340 Mandume Ndemufayo Avenue, Pionierspark, Windhoek, Namibia
e-mail: ekwembeya@unam.na

E. Maass
Office of Academic Affairs, University of Namibia, 340 Mandume Ndemufayo Avenue, Pionierspark, Windhoek, Namibia
e-mail: emaass@unam.na

nificant association was established between the plant parts used and plant genera (Chi-square = 58.380, $P = 0.008 < 0.05$). This current review has identified gaps in ethnobotanical knowledge, especially that the majority of parasitic plant species in Namibia are understudied. Expanding our knowledge on parasitic plants may open avenues to conserve parasitic plant biodiversity, contribute to effective management efforts of problematic parasites and to investigate their medicinal value while integrating Indigenous Knowledge Systems into mainstream knowledge systems.

Keywords Ethnobotany · Mistletoes · Medicinal plants · Namibia · Parasitic plants

11.1 Introduction

Parasitic plants occur in many ecosystems and are integral in structuring and functioning of their ecosystems [1, 2]. Approximately 4,100 species in approximately 19 families are parasitic plants amounting to more than 1% of the flowering plants [3]. While extensive research has focused on the ecology, biology and physiology of parasitic plants, ethnobotanical uses of parasitic plants are lacking, especially in the African context including Namibia. Information on ethnobotanical studies of parasitic plants will not only shed light on the benefits of parasitic plants but also expand our knowledge on the medicinal applications of parasitic plants. Parasitic plants are often viewed negatively due to the devastations that some of them may pose to important crops [4] and thereby negatively impacting the livelihoods of people that who depend on such crops [5]. However, parasitic plants do offer several benefits such as the maintenance of a healthy ecosystem by suppressing dominant species and allowing less dominant species to thrive [2, 6], nutrient cycling [2], provision of shelter and food to other species [7], and less commonly known their medicinal applications that need further exploration.

Depending on the extent to which parasites are autotrophic, parasitic plants can be classified as either holoparasites or hemiparasites. Holoparasitic plants depend entirely on their hosts and lack chlorophyll [1, 8] while hemiparasitic plants contain chlorophyll and can make their own food. Additionally, hemiparasites can further be classified as facultative or obligate hemiparasites. Facultative hemiparasites are often opportunistic parasites that may require host only at certain life cycle stages or may complete their life cycles without the host [1, 8]. On the other hand, obligate hemiparasites require a host to complete their life cycles even though they may be capable of photosynthesis [1]. For example, *Striga* species require host stimulants for seed germination [1] and haustorial formation. On the basis of haustorial connection to the host, parasites can be divided into stem or root parasites. Stem parasites form haustorial connections on the stem of the host and roots parasites form connections with host roots [1, 3].

The purpose of this review is to synthesize literature on the families, genera, and species of parasitic plants with important medicinal uses in Namibia and suggest

areas for future research. We confine our review to medicinal uses of parasitic plants to highlight the various medicinal benefits that parasitic plants offer arising from the use of different plant parts, mixtures and mode of parasitism. Our intent is to stimulate new interest in the critical roles that parasitic plants play in offering alternatives to medicinal applications and thus promote and preserve indigenous knowledge.

11.2   Methods

We collected all available data on the status of parasitic plants in Namibia. First, we reviewed authoritative botanical texts to glean details on medicinal uses of parasitic plants. We then cross-referenced these data against the Botanical Research and Herbarium Management System (BRAHMS) database, and compared these data against herbaria records at the National Herbarium of Namibia (WIND). Ethnobotanical data were obtained from the Survey of Economic Plants for Arid and Semi-Arid Lands (SEPASSAL) database.

11.3   Results and Discussion

We found that Namibian parasites spanned across 8 families, 16 genera and 52 species, of which two are endemic namely: *Agelanthus discolor* (Schinz) Balle and *Thesium xerophyticum* A. W. Hill (Table 11.1). More specifically, we found that most species of parasitic plants belong to the Family Loranthaceae at 28.8%, followed by Santalaceae at 19.2% and Orobanchaceae at 17.3%. The family with the least species was Lauraceae representing 1.9% of all species followed by species belonging to Olacaceae comprising of 3.8% of all parasitic species in Namibia (Fig. 11.1).

Although the family Loranthaceae had the most species, the genus that had the most parasitic plants was *Thesium* (19.2%), followed by the genus *Viscum* (13.5%) belonging to the Viscaceae family (Fig. 11.2).

Of the 52 species of parasitic plants in Namibia only 14 have documented uses, namely *Cuscuta planiflora* Ten. var. *planiflora*, *Cassytha filiformis* L., *Plicosepalus undulatus* (E. Mey. ex Harv.) Tiegh., *Plicosepalus kalachariensis* (Schinz) Danser, *Tapinanthus oleifolius* (J. C. Wendl.) Danser, *Oncocalyx welwitschii* (Engl.) Polhill & Wiens, *Ximenia americana* L. var. *americana, Ximenia caffra* Sond. var. *caffra*, *Striga asiatica* (L.) Kuntze, *Striga gesnerioides* (Willd.) Vatke, *Thesium lacinulatum* A. W. Hill, *Thesium lineatum* L.f., *Viscum capense* L.f. and *Viscum rotundifolium* L.f. (Table 11.2). Although five of the seven species of *Hydnora* found in the old world [9] occur in Namibia, there are no documented uses so far. However, uses of *Hydnora* have been reported elsewhere [10–12]. *Hydnora* species are subterranean in nature and only emerge above ground when flowering [10, 11, 13] and it is possible that their uses are not documented because they are not easily observable. Additionally, some *Hydnora* species occur in the drier parts of the country such as the succulent Karoo

Table 11.1 Parasitic plant families represented in Namibia

Plant family	Genus	Number of species
Convolvulaceae	*Cuscuta*	3
Aristolochiaceae	*Hydnora*	5
Lauraceae	*Cassytha*	1
Loranthaceae	*Agelanthus*	4
Loranthaceae	*Erianthemum*	1
Loranthaceae	*Plicosepalus*	2
Loranthaceae	*Septulina*	2
Loranthaceae	*Phragmanthera*	3
Loranthaceae	*Tapinanthus*	2
Loranthaceae	*Oncocalyx*	1
Olacaceae	*Ximenia*	2
Orobanchaceae	*Cycnium*	2
Orobanchaceae	*Rhamphicarpa*	1
Orobanchaceae	*Striga*	6
Santalaceae	*Thesium*	10
Viscaceae	*Viscum*	7
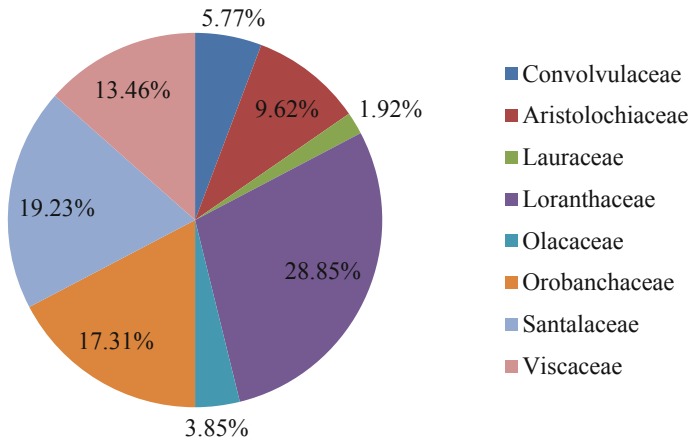
Fig. 11.1 Percentage of Namibian parasitic plants by family
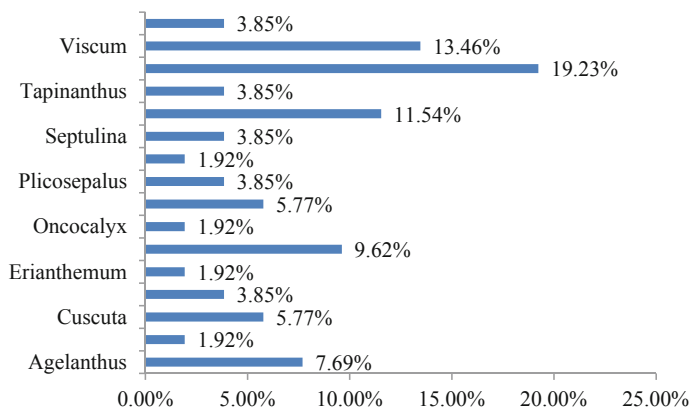
Fig. 11.2 Percentage of Namibian parasitic plants by genus

[13–16] where there are fewer inhabitants. In any case, this review has identified ethnobotanical knowledge gaps in the medicinal uses of *Hydnora* species in Namibia requiring further studies.

Interestingly, despite having the second lowest number of species, Olacaceae species had the most medicinal applications (Table 11.2 and Fig. 11.3). Fruits of *Ximenia* can be consumed while leaves and roots have been used traditionally for treatment of multiple ailments. Chi-square tests of association were conducted at 5% level to establish whether significant relationships existed between genera, family and category of use. There was no significant relationship between either genera or family and category of use ($P > 0.05$). However, a significant association was established between the plant parts used and plant genera (Chi-square $= 58.380$, $P = 0.008 < 0.05$) (Table 11.3). The significant association between plant parts is partly due to the fact that some parasitic plants do not have leaves or roots and therefore, only the parts that are present will most likely be used. This significant association might also explain why *Ximenia* species had the most medicinal applications compared to other parasitic plants because all the plant parts are used in processing traditional medicines.

11.4   Conclusions

This study has provided insight into how parasitic plants are used in Namibia. Information on how indigenous people manage and perceive natural resources can provide crucial details on the population ecology and economic importance of many species, and are thus crucial when developing environmental management or designing conservation projects. Our review revealed that there is urgent need for a full scale medicinal and ethnobotanical survey of parasitic plants in Namibia since there is not much information documented on this subject.

Table 11.2 Medicinal uses of parasitic plants in Namibia

Plant family	Species name	Vernacular name	Medicinal use(s)	Part(s) used	Reference(s)	Notes on medicinal use(s)
Convolvulaceae	*Cuscuta planiflora* Ten. var. *planiflora*	Ongongoro, omongorwa (Otjiherero)	Treat both humans and livestock with diarrhoea	Stem	[17]	Extract from stem
		Kao (Damara)				
Lauraceae	*Cassytha filiformis* L.	False Dodder (English); Vrouehaar (Afrikaans)	Treatment of vermin	Stem	[18, 19]	Juice of plant
			Treatment of inflamed eyes, snake bites, gonorrhea, dysentery, diuretic, increase semen secretion, and hemorrhoids	Stem		Sap from plant used as eye drops. Plant pulp rubbed in wound for snake bites
Loranthaceae	*Plicosepalus kalachariensis* (Schinz) Danser	Dai ʻgu.b (Damara); Oviraura (Otjiherero)	Treatment of gonorrhea	Stem	[20]	Decoction of stems. Half a cup is drunk 2–3 times a day
Loranthaceae	*Plicosepalus undulatus* (E. Mey. ex Harv.) Tiegh.	Mistletoe, lighted candles, lighted matches, (English); Vuurhooutjiesvoelent (Afrikaans); Oviraura (Otjiherero); Oshilunda (Kwanyama); Máiǃkhuis, Mäias (Damara/Nama)	Treatment of menopausal problems	Swellings on stem	[18–21]	Water is extracted from the tumor like swellings found on the stem

Table 11.2 (continued)

Plant family	Species name	Vernacular name	Medicinal use(s)	Part(s) used	Reference(s)	Notes on medicinal use(s)
			Expulsion of afterbirth in cattle	Leaves		Extract from leaves is used in expelling after-birth
Loranthaceae	*Tapinanthus oleifolius* (J. C. Wendl.) Danser	Mistletoe, lighted candles, lighted matches, (English); Vuurhooutjiesvoelent (Afrikaans); Otjiraura (Otjiherero); Oshilunda (Kwanyama); Mâi!khuis, Mäias (Damara/Nama)	Treatment of menopausal problems	Swellings on stem	[18–21]	Water is extracted from the tumor like swellings found on the stem
			Expulsion of afterbirth in cattle	Leaves		Extract from leaves is used in expelling after-birth
			Treatment of lumbago	Infusion of plant		
			Treatment of gonorrhea	Branches and leaves		Decoction from branches and leaves

(continued)

Table 11.2 (continued)

Plant family	Species name	Vernacular name	Medicinal use(s)	Part(s) used	Reference(s)	Notes on medicinal use(s)
Loranthaceae	*Oncocalyx welwitschii* (Engl.) Polhill & Wiens		Expulsion of afterbirth in cattle	Leaves	[20]	Extract from leaves is used in expelling after-birth
Olacaceae	*Ximenia americana* L. var. americana	Sour Plum (English); Kleinsuurpruim, doring pruim (Afrikaans); Omuninga (Otjiherero); ‡ēros (Nama)	Treatment for dry skin, increasing skin elasticity and increases blood flow to the skin	Seed kernel (pit)	[17, 18, 20, 22]	Oil extract from seed kernel
			Remedy for fever	Leaves and barks		Powdered leaves and fresh bark applied to skin
			Treatment of venereal diseases	Leaves		Chewed leaves
			Treatment of gonorrhea	Roots		Decoction from roots
			Treatment of dysentery, diarrhoea, abdominal pain, mental illness, fever and bilharzia	Roots		Potion made from roots

Table 11.2 (continued)

Plant family	Species name	Vernacular name	Medicinal use(s)	Part(s) used	Reference(s)	Notes on medicinal use(s)
			Treatment of sores and wounds	Roots		Powdered roots
			Treatment of animal sores	Barks and fruits		Crushed bark and rind of fruit
			Treatment of burns and cuts	Seeds		Burned seeds are ground into a powder and applied to burns and cuts
			Treatment of ulcers and ringworms	Barks and root mixture		Mixture of ground bark and roots
			Treatment of burns and boils	Root barks		Powder from dried or roasted root-bark is applied to burns and boils
			Used as a 'douche'	Roots		Powder from soft roots used as a douche by women

(continued)

Table 11.2 (continued)

Plant family	Species name	Vernacular name	Medicinal use(s)	Part(s) used	Reference(s)	Notes on medicinal use(s)
Olacaceae	*Ximenia caffra* Sond. var. *caffra*	Large Sour Plum (English); Grootsuurpruim, suurpruim (Afrikaans); Omuninga, Omumbeke (Otjiherero); ǂēros (Nama); Oshipeke oshimbyu (Kwanyama); Sipeke (Kwangali)	Treatment for dry skin, increasing skin elasticity and increases blood flow to the skin	Seed kernel (pit)	[17, 20, 22, 23]	Oil extract from seed kernel
			Remedy for fever	Leaves and barks		Powdered leaves and fresh bark applied to skin
			Treatment of venereal diseases	Leaves		Chewed leaves
			Treatment of gonorrhea	Roots		Decoction from roots

Table 11.2 (continued)

Plant family	Species name	Vernacular name	Medicinal use(s)	Part(s) used	Reference(s)	Notes on medicinal use(s)
			Treatment of dysentery, diarrhoea, abdominal pain, mental illness, fever and bilharzia	Roots		Potion made from roots
			Treatment of sores and wounds	Roots		Powdered roots
			Treatment of animal sores	Barks and fruits		Crushed bark and rind of fruit
			Treatment of burns and cuts	Seeds		Burned seeds are ground into a powder and applied to burns and cuts
			Treatment of ulcers and ringworms	Barks and root mixture		Mixture of ground bark and roots
			Treatment of burns and boils	Root barks		Powder from dried or roasted root-bark is applied to burns and boils

(continued)

Table 11.2 (continued)

Plant family	Species name	Vernacular name	Medicinal use(s)	Part(s) used	Reference(s)	Notes on medicinal use(s)
			Used as a 'douche'	Roots		Powder from soft roots used as a douche by women
Orobanchaceae	*Striga asiatica* (L.) Kuntze		Treatment of gout		[18]	Ash of plant is mixed with cow and sheep and applied as anointment
Orobanchaceae	*Striga gesnerioides* (Willd.) Vatke	Purple witchweed (English); blou-rooiblommetjie, rooiblom (Afrikaans); Onime (Kwanyama); Kakadona (Rukwangali)	Treatment of swollen neck glands and wound healing	Plant and roots	[19, 23]	Plant and roots roasted together, pulverize and ointment is made from the powder
			Healing of painful body parts	Roots		Roots are pounded and burned on glowing embers and used for smoking painful body parts
			Treatment for head and stomach aches	Plant		Plant boiled in bit of water and extract is obtained. Extract is cooled before use

(continued)

Table 11.2 (continued)

Plant family	Species name	Vernacular name	Medicinal use(s)	Part(s) used	Reference(s)	Notes on medicinal use(s)
Santalaceae	*Thesium lacinulatum* A. W. Hill		Remedy for uterine problems	Roots	[19]	Roots are crushed and boiled
Santalaceae	*Thesium lineatum* L.f.	Besembos (Afrikaans)	Treatment of venereal diseases	Roots	[19, 23]	Root are boiled
Viscaceae	*Viscum capense* L.f.	Cape Mistletoe, mistletoe (English); Voelent (Afrikaans); Mâi!khuis, Mâias (Damara/Nama)	Removal of warts, treatment for bronchitis and bronchial asthma	Leaves	[19, 23, 24]	Leaf sap is drunk as a remedy
			Treatment of nosebleeds and menorrhagia	Leaves or fruits		Infusion of the leaves or fruits
			Remedy for epilepsy	Plant (stems)		
			Herbal tonic and general health	Stems		
Viscaceae	*Viscum rotundifolium* L.f.	Red-berried mistletoe, round-leaved mistletoe (English); Voelent (Afrikaans); Oviraura (Otjiherero); Mâi!khuis, Mâias (Damara/Nama)	Removal of warts and as astringent	Plant	[19, 23]	Plant sap
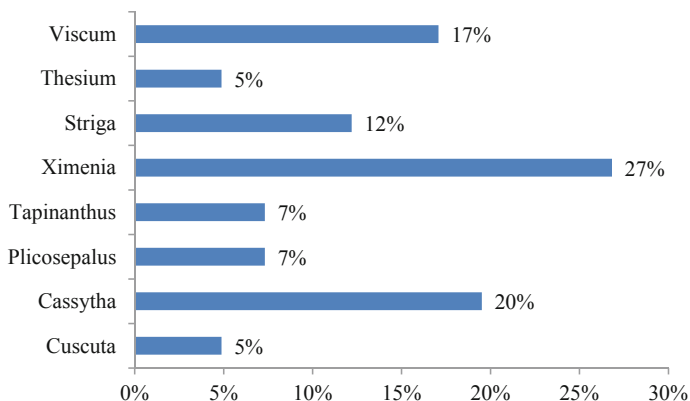
Fig. 11.3 Medicinal uses of Namibian parasitic plants by genus

Table 11.3 Genus* plant parts used for cross tabulation

Genus	Plant parts used						
	Stem	Roots	Leaves	Seeds	Bark	Fruits	Total
Cuscuta	2	0	0	0	0	0	2
Cassytha	8	0	0	0	0	0	8
Plicosepalus	2	0	1	0	0	0	3
Tapinanthus	3	0	1	0	0	0	4
Ximenia	0	3	2	3	1	2	11
Striga	0	5	0	0	0	0	5
Thesium	0	2	0	0	0	0	2
Viscum	5	0	1	0	0	1	7
Total	20	10	5	3	1	3	42

*Represents a significant association between the plant parts used and plant genera (Chi-square = 58.380, P = 0.008 < 0.05)

Furthermore, this current review has identified gaps in knowledge about various parasitic plant species and their uses. We recommend that future studies conduct interviews with communities where parasitic plants commonly occur to better understand the biocultural context of these species, with emphasis on ethnobotanical uses.

References

1. Press MC, Graves JD (1995) Parasitic plants, 1st edn. Chapman & Hall, London, UK
2. Press MC, Phoenix GK (2005) Impacts of parasitic plants on natural communities. New Phytol 166:737–751
3. Kuijt J (1969) The biology of parasitic flowering plants, Illustrated edn. University of California Press, Berkeley, USA, p 246
4. Kokla A, Melnyk CW (2018) Developing a thief: haustoria formation in parasitic plants. Dev Biol 442:53–59
5. Runyon JB, Tooker JF, Mescher MC, de Moraes CM (2009) Parasitic plants in agriculture: chemical ecology of germination and host-plant location as targets for sustainable control. Sustain Agric Rev 1:813–822
6. Pennings SC, Callaway RM (1996) Impact of a parasitic plant on the structure and dynamics of salt marsh vegetation. Ecology 77:1410–1419
7. Pennings SC, Callaway RM (2002) Parasitic plants: parallels and contrasts with herbivores. Oecologia 131:479–489
8. Kaiser B, Vogg G, Furst UB, Albert M (2015) Parasitic plants of the genus *Cuscuta* and their interaction with susceptible and resistant host plants. Front Plant Sci 6:1–9
9. Bolin JF, Lupton D, Musselman LJ (2018) *Hydnora arabica* (Aristolochiaceae), a new species from the Arabian Peninsula and a key to *Hydnora*. Phytotaxa 338:99–108
10. Musselman LJ (1991) The genus *Hydnora (Hydnoraceae)*. In: 5. International symposium of parasitic weeds, Nairobi (Kenya), 24–30 Jun 1991
11. Musselman LJ, Visser JH (1986) The strangest plant in the world. Veld Flora 71:109–111
12. Musselman LJ, Visser JH (1989) Taxonomy and natural history of *Hydnora* (*Hydnoraceae*). Aliso 12:317–326
13. Maass E, Musselman LJ (2004) *Hydnora triceps* (*Hydnoraceae*)-first record in Namibia and first description of fruits. Dinteria 29:1–10
14. Bolin JF, Maass E, Musselman LJ (2009) Pollination biology of Hydnora africana Thunb. (*Hydnoraceae*) in Namibia: brood-site mimicry with insect imprisonment. Int J Plant Sci 170:157–163
15. Seymour RS, Maass E, Bolin JF (2009) Floral thermogenesis of three species of *Hydnora* (*Hydnoraceae*) in Africa. Ann Bot 104:823–832
16. Tennakoon KU, Bolin JF, Musselman LJ, Maass E (2007) Structural attributes of the hypogeous holoparasite *Hydnora triceps* Drege & Meyer (*Hydnoraceae*). Am J Bot 94:1439–1449
17. Malan J, Owen-Smith G (1974) The ethnobotany of Kaokoland. Cimbebasia 2:131–178
18. Watt J, Breyer-Brandwikj M (1962) The medicinal and poisonous plants of Southern and Eastern Africa, 2nd edn. E & S Livingstone LTD., Edinburgh and London, UK
19. von Koenen E (2001) Medicinal, poisonous, and edible plants in Namibia, vol 4. Klaus Hess Publishers, Windhoek, Namibia
20. Sullivan S (1998) People, plants and practice in drylands: socio-political and ecological dimensions of resource-use by Damara farmers in north-west Namibia. Doctoral thesis, University College London, UK p 89
21. Rodin RJ (1985) The Ethnobotany of the Kwanyama Ovambos, vol 9. Allen Press, Kansas, United States
22. Van den Eynden V, Vernemmen P, Van Damme P (1992) The Ethnobotany of the Topnaar. The Commission of the European Community
23. National Herbarium of Namibia (Undated) Specimen Collection (WIND) National Botanical Research Institute of Namibia, Windhoek, Namibia
24. van Wyk B, Gericke N (2000) People's plants: a guide to useful plants of Southern Africa, 1st edn. Briza Publications, Pretoria, South Africa

Chapter 12
An Insight into the Adsorption Mechanism of Hexavalent Chromium onto Magnetic Pine Cone Powder

Immaculate L. A. Ouma, Eliazer B. Naidoo and Augustine E. Ofomaja

Abstract The remediation of hexavalent chromium [Cr(VI)] contaminated water has been a challenge due to its high toxicity and mobility in the environment. Adsorption has so far been the most promising method for the treatment of chromium containing water due to the availability of low cost materials capable of chromium sequestration. The mechanism for hexavalent chromium removal has however not been fully understood with many studies pointing to a reduction-coupled mechanism. In this study, a composite material consisting of agricultural waste material (pine cone) and magnetite nanoparticles was used for the remediation of hexavalent chromium contaminated water with a focus on the removal mechanism and adsorbent regeneration studies. The mechanism was identified to be adsorption-coupled reduction where Cr(VI) was reduced on the adsorbent surface to the less toxic trivalent chromium [Cr(III)] before being adsorbed. The adsorbed chromium was successfully desorbed using NaOH allowing for concentration and chromium recovery. The adsorbent material was applied in three adsorption-desorption cycles without a significant loss in adsorption capacity.

Keywords Adsorption · Chromium · Magnetite · Mechanism · Pine cone · Regeneration

12.1 Introduction

Among the pollutants found in water, heavy metals are of concern because they are non-biodegradable, hence leading to accumulation in the environment. Even at low concentrations these metals may interfere with normal biological processes, hence

I. L. A. Ouma · E. B. Naidoo · A. E. Ofomaja (✉)
Biosorption and Wastewater Treatment Research Laboratory, Vaal University of Technology, Private Bag X021, Vanderbijlpark 1900, South Africa
e-mail: augustineo@vut.ac.za

I. L. A. Ouma
e-mail: oumachieng@gmail.com

E. B. Naidoo
e-mail: bobby@vut.ac.za

becoming toxic resulting in either heavy metal poisoning or genetic disorders. The removal of these metal species from water is therefore critical to the general availability of clean water for human and animal consumption. Chromium is a highly soluble metal pollutant with strong oxidizing properties which can cause irritation in plant and animal tissues [1–3]. It has several uses including metal plating, leather processing, surface treatments and in refractories [3, 4]. It exists in six oxidation states with the trivalent [Cr(III)] and hexavalent [Cr(VI)] states being the most prevalent in water [5]. Trivalent chromium is an essential nutrient while the hexavalent form is toxic, carcinogenic, teratogenic and mutagenic to living organisms [1, 6]. The maximum levels permitted for chromium in water are 5 mg L^{-1} and 0.05 mg L^{-1} for Cr(III) and Cr(VI)respectively [5, 6]. The removal of chromium from contaminated water has been investigated over the years with different methods being reported for water treatment. All these methods are aimed at reducing the level of pollutants to produce water suitable for human consumption or agricultural use. The methods for remediation of Cr(VI) contaminated water include oxidation, coagulation-flocculation, ion exchange, membrane separation and adsorption among others [7, 8]. Among these methods, adsorption has been considered the most favorable due to its low operation cost and versatility. However, the mechanism of hexavalent chromium adsorption is still not well documented. In our previous work we described the adsorption of Cr(VI) onto FTP-MNP, a composite biosorbent made from pine cone powder and magnetite nanoparticles with detailed characterization of the prepared adsorbent and analysis of the adsorption parameters [9]. This study therefore proceeds by providing an insight into the adsorption mechanism of Cr(VI) remediation using FTP-MNP and the regeneration efficiency of the adsorbent material.

12.2 Experimental

12.2.1 Materials

Sodium hydroxide (NaOH, >98%) and potassium dichromate ($K_2Cr_2O_7$, >99%) were purchased from Associated Chemical Enterprises (South Africa). Ammonium hydroxide (NH_4OH, 25%) was supplied by Labchem (South Africa). Hydrochloric acid (32%) and ferrous sulphate ($FeSO_4 \cdot 7H_2O$, >98%) were supplied by Merck. Ferric chloride ($FeCl_3 \cdot 6H_2O$, >99%) and sodium arsenite ($NaAsO_2$, >90%) were purchased from Sigma-Aldrich. All chemicals were used without any further purification. All syntheses were carried out under nitrogen atmosphere with vigorous stirring to ensure uniform dispersions.

12.2.2 Methods

The synthesis of the composite material is described in detail in our previous work [10]. Briefly, the material was prepared in a single step co-precipitation method where 1.5 g of Fenton's treated pine cone powder was added to degassed water followed by the addition of ferrous and ferric salts and precipitation with ammonium hydroxide at 60 °C under nitrogen atmosphere.

12.2.2.1 Determination of Cr(VI) Adsorption Mechanism

To determine the effect of solution pH, solutions of 100 mg L^{-1} Cr(VI) were prepared in separate volumetric flasks and the solution pH in each flask was varied between 2 and 12 using 0.01 HCl and 0.01 M NaOH. 0.5 g of the adsorbent was introduced into a separate sealable flask containing 100 cm^3 of each solution and agitated for 2 h. The solution pH and redox potential before and after adsorption were determined on a Crison Basic 20 pH meter.

12.2.2.2 Desorption and Regeneration

To determine the most appropriate solvent for desorption, 0.1 L of 200 mg L^{-1} solution of Cr(VI) was contacted with 1 g of the adsorbent material for 2 h. After adsorption, the adsorbent was filtered, washed with deionised water and dried overnight. The chromium loaded adsorbent was then shaken in either deionised water (H$_2$O), 0.1 M acetic acid (AA), 0.1 M hydrochloric acid (HCl) or 0.1 M sodium hydroxide (NaOH) for 2 h and filtered to obtain the supernatant solution while the spent adsorbent was washed and dried for reuse. The residual solutions after adsorption and desorption were both analysed for Cr(VI) content.

Cr(VI) concentration was determined spectrophotometrically following the diphenyl-carbazide method at a wavelength of 540 nm [11]. Total chromium concentration was determined on a Shimadzu AA 7000 Atomic Absorption Spectrophotometer with an air/acetylene flame and wavelength of 357.9 nm. Cr(III) concentration was determined as the difference between total chromium and Cr(VI) concentrations. X-ray photoelectron spectroscopy (XPS) studies were performed using XPS microprobe (PHI 5000 Scanning ESCA Microprobe ULVAC-PHI Inc) with Al Kα radiation (hν = 1486.6 eV).

12.3 Results and Discussion

During the removal of hexavalent chromium from solution, mechanistic pathways have been proposed based on two principles namely: (i) electrostatic attraction of negatively charged Cr(VI) ions in solutions to the adsorbent surface, and (ii) reduc-

tion of Cr(VI) to Cr(III) followed either by adsorption or repulsion by the adsorbent surface. The mechanism for chromium removal from aqueous solutions by biomaterials has been determined to be by direct and indirect reduction [12]. In the direct reduction mechanism, Cr(VI) is reduced to Cr(III) by the electron donating groups of the biomaterial. The indirect reduction mechanism is a three step process in which anionic Cr(VI) ions bind to cationic groups on the biomaterial surface, Cr(VI) ions are then reduced to Cr(III) by adjacent electron donating groups followed by either the release of Cr(III) into the solution due to repulsion or complexation with adjacent groups [12]. The proposed mechanisms each lead to the consumption of hydrogen ions therefore raising the solution pH during adsorption. Both mechanisms have been shown to describe the adsorption of Cr(VI) on lignocellulosic biosorbents and iron oxide nanoparticles [13, 14]. To determine which of the mechanisms was responsible for the removal of Cr(VI) from solution, the parameters associated with each mechanism were considered. These parameters include the change in hydrogen ion (H^+) concentration, change in the oxidation-reduction potential (ORP) of the solution and the total amount of chromium ions (total Cr) left in the solution after adsorption.

12.3.1 Change in H^+ Concentration

The adsorption of hexavalent chromium is highly dependent on solution pH and has been reported to be favoured by its high redox potential (+1.3 V) at acidic pH [5]. The optimum pH for Cr(VI) adsorption was found to be pH 2 where $HCrO_4^-$ is predominant [9]. This species has low adsorption free energy and is therefore favourably adsorbed at low pH when the adsorbent surface is positively charged allowing for electrostatic attraction with the anionic species [15]. Reduction of Cr(VI) to Cr(III) in the presence of organic matter and magnetite results in the consumption of hydrogen ions as shown in Eqs. 12.1 and 12.2 [16, 17]. Cr(VI) can be reduced by electron donor groups on the biomass which have a lower reduction potential than that of Cr(VI) (1.3 V) [13].

$$HCrO_4^- + Organic\ matter + H_3O^+ \rightarrow Cr^{3+} + H_2O + CO_2 \qquad (12.1)$$

$$6Fe_3O_4 + 8H^+ + 2HCrO_4^- \rightarrow 9\gamma - Fe_2O_3 + 2Cr^{3+} + 5H_2O \qquad (12.2)$$
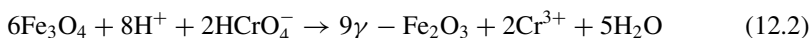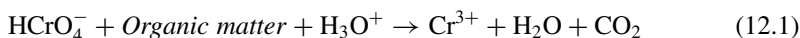
At low solution pH the change in hydrogen ion concentration was high due to large amounts of Cr(VI) being either bound or reduced by the adsorbent (Fig. 12.1). As the solution pH was raised the change in H^+ was reduced and the amount of Cr(VI) removed was lowered.

In both the electrostatic attraction and adsorption coupled reduction mechanisms, removal of Cr(VI) is favoured at lower solution pH due to the presence of high concentrations of hydrogen ions. The consumption of hydrogen ions also causes the solution pH to increase during the reduction of Cr(VI) to Cr(III) [18]. The change
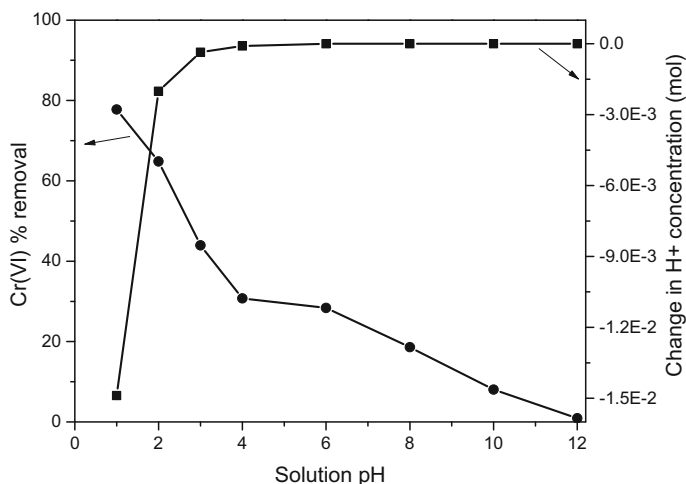
Fig. 12.1 Effect of solution pH on Cr(VI) removal and change in H$^+$ concentration

in H$^+$ concentration was therefore not sufficient in determining whether the adsorption of Cr(VI) onto FTP-MNP proceeded through either electrostatic attraction or reduction to Cr(III).

12.3.2 Cr(III) Concentration After Adsorption

The amount of Cr(III) ions in solutions was determined to confirm whether the reduction in Cr(VI) concentration was due to electrostatic attraction or conversion to Cr(III). In the electrostatic attraction mechanism, only Cr(VI) ions are expected to be present in solution since there is no reduction expected to take place. In the reduction coupled adsorption however, Cr(III) ions are present in the solution. This is a result of the reduction process which may be followed by some of the formed Cr(III) ions being adsorbed while others are repelled back into the solution by positive charges on the adsorbent surface. Therefore, the total amount of chromium in solution is the sum of Cr(VI) and Cr(III) in the solution. In the case of complete reduction from Cr(VI) to Cr(III) as reported by Sanghi et al., the chromium left in solution only consist of Cr(III) ions [19].

Throughout the studied pH range there was some amount of Cr(III) ions remaining in the solution after adsorption (Fig. 12.2). The highest amount of Cr(III) was observed at lower solution pH due to the presence of high amounts of H$^+$ ions aiding in the reduction of Cr(VI) to Cr(III). However, at high solution pH the amount of Cr(III) was lower due to repulsion of Cr(VI) anions from the negatively charged adsorbent surface, therefore resulting in low reduction. Some of the formed Cr(III) ions were not adsorbed due to repulsion of the cations by the positively charged
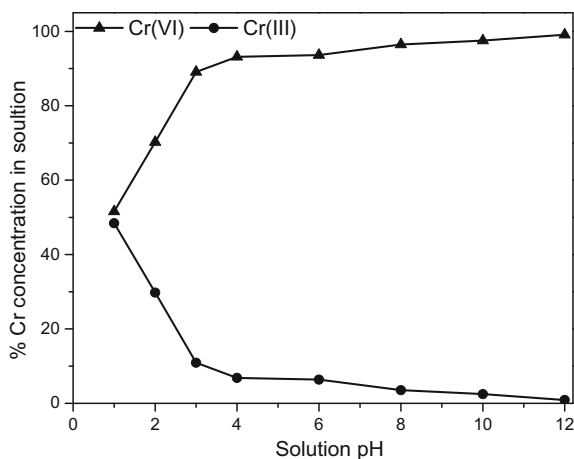
Fig. 12.2 Cr(VI) and Cr(III) concentration in solution after adsorption

adsorbent surface, leading to higher amounts of Cr(III) in solution at low solution pH since there was maximum reduction at low pH following higher redox potentials.

12.3.3 Change in Redox Potential

The difference in oxidation reduction potential (ORP) of the solution before and after adsorption was determined in order to confirm Cr(VI) reduction to Cr(III). A reduction in ORP indicates Cr(VI) reduction as observed by Yu et al., when nanoscale zero-valent iron particles which have a strong reductive capacity were introduced into Cr(VI) wastewater [18]. During Cr(VI) adsorption onto FTP-MNP the difference between the final and initial ORP of the solution increased with increasing pH (Fig. 12.3). This was because of decreased Cr(VI) reduction as the pH of the solution increased with greater decreases in ORP being observed at lower pH where higher Cr(VI) reduction was expected. Similar trends have been reported for Cr(VI) reduction by magnetite indicating that reduction to Cr(III) decreases as pH increases [20, 21].

12.3.4 XPS Analysis

The XPS spectra of FTP-MNP before and after Cr(VI) adsorption were studied to determine the changes in surface states resulting from the adsorption process. The survey spectrum of the chromium loaded adsorbent showed that all peaks from the

Fig. 12.3 Change on redox potential with solution pH
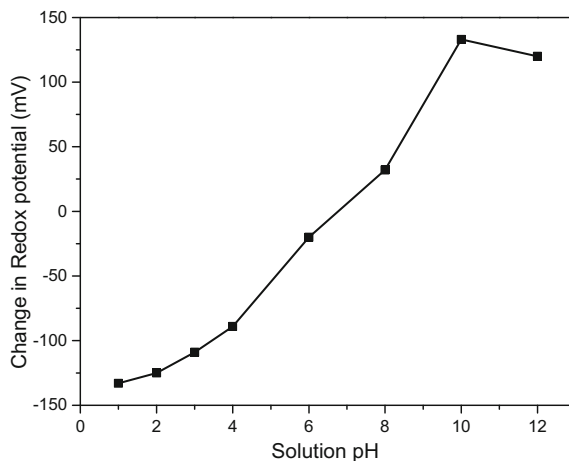
pristine adsorbent were retained with the introduction of a new peak at approximately 580 eV assigned to Cr2p (Fig. 12.4) [15].

The O1 s peak in Fig. 12.5a was slightly shifted from 529.4 to 529.9 eV after Cr(VI) adsorption indicating that oxygen containing groups were involved in the binding of Cr(VI) to the FTP-MNP surface. The Cr2p band (Fig. 12.5b) consisted of two peaks at 587 and 575 eV which were assigned to $Cr2p_{1/2}$ and $Cr2p_{3/2}$ representing Cr(VI) and Cr(III) respectively [15]. The presence of both peaks suggested that Cr(VI) was
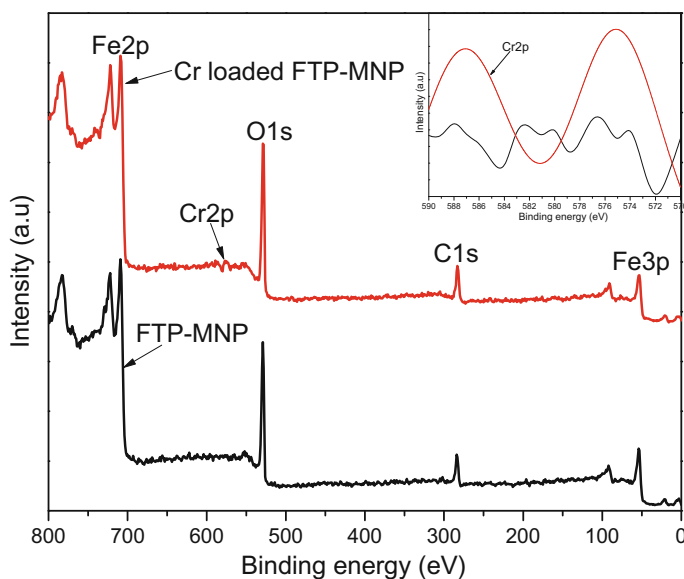
Fig. 12.4 XPS full spectra before and after Cr(VI) adsorption (Inset: Cr2p peak comparison)
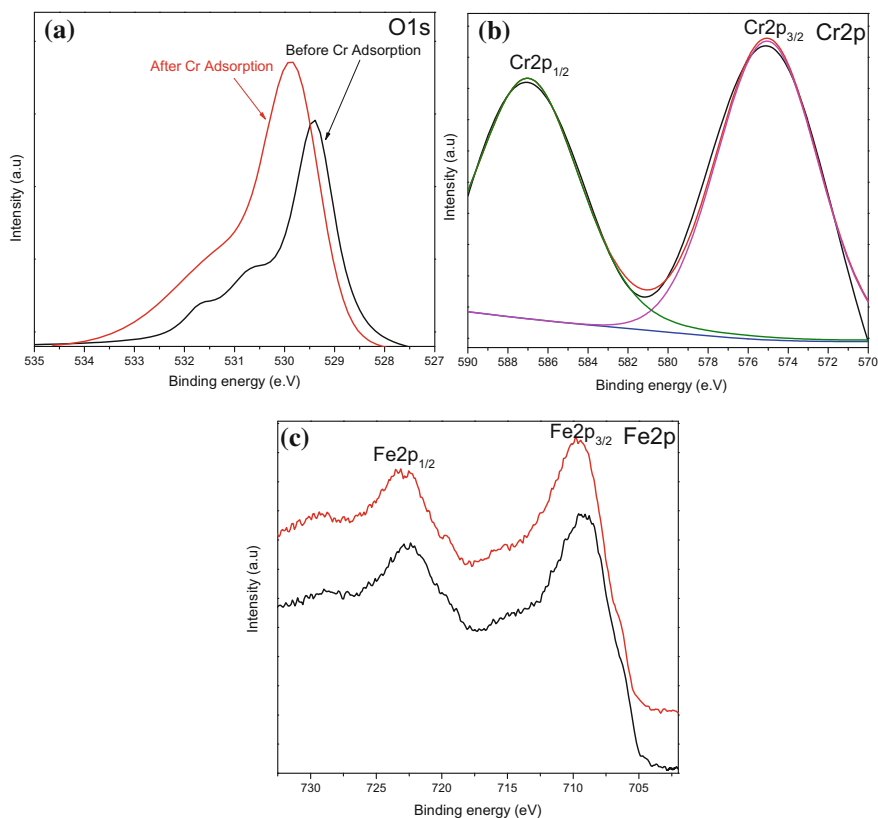
Fig. 12.5 XPS spectral comparisons of FTP-MNP before and after Cr(VI) adsorption

adsorbed and later reduced to Cr(III) on the adsorbent surface [22]. The reduction of Cr(VI) to Cr(III) at acidic pH or in the presence of organic matter follows a redox reaction (Eq. 12.3) [15]:

$$HCrO_4^- + 7H^+ + 3e^- \rightarrow Cr^{3+} + 4H_2O \tag{12.3}$$
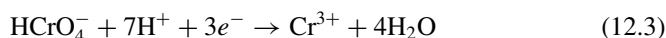
The binding energies for $Fe2p_{1/2}$ and $Fe2p_{3/2}$ showed no significant shift after chromium adsorption at energies of 722.6 and 709.3 eV in the pristine adsorbent and 722.9 and 709.6 eV in the chromium loaded adsorbent (Fig. 12.5c). The constant binding energies for Fe2p indicate that there was no Cr substitution in the iron phase of the adsorbent and the magnetite phase was retained throughout the adsorption process [14, 22].

12.3.5   Desorption and Adsorbent Regeneration

Regeneration of spent adsorbents is important in making the adsorption process more economical [23]. In order to determine the reusability of the adsorbent it is important to establish the most suitable eluent solution to desorb the bound adsorbate from the adsorbent surface. Desorption studies are important in the practical considerations of adsorbents for water treatment [24]. Desorption of Cr(VI) was tested using four eluents namely deionised water (H_2O), 0.1 M acetic acid (AA), 0.1 M hydrochloric acid (HCl) and 0.1 M sodium hydroxide (NaOH). The adsorption of Cr(VI) was pH dependent, therefore desorption was also affected by the pH of the eluent solution. The percentage efficiency of desorption was calculated using Eq. 12.4 and the results are presented in Fig. 12.6a [25]. The efficiency of the eluents was in the order H_2O < AA < HCl < NaOH and NaOH was therefore considered the best eluent and was used in the determination of adsorbent reusability. The presence of OH^- ions from NaOH led to the formation of soluble sodiumchromate which was released into the solution [26].

$$Desorption\ (\%) = \frac{amount\ desorbed}{amount\ adsorbed} \times 100 \qquad (12.4)$$

The reusability of the adsorbent was studied by consecutive adsorption-desorption cycles (Fig. 12.6b). After each adsorption, the loaded adsorbent was shaken with the eluent solution, then filtered and washed with deionised water and dried before being contacted with the adsorbate solution. After three cycles the adsorbent retained >85% of its initial adsorption capacity. FTP-MNP was therefore favourable for Cr(VI)
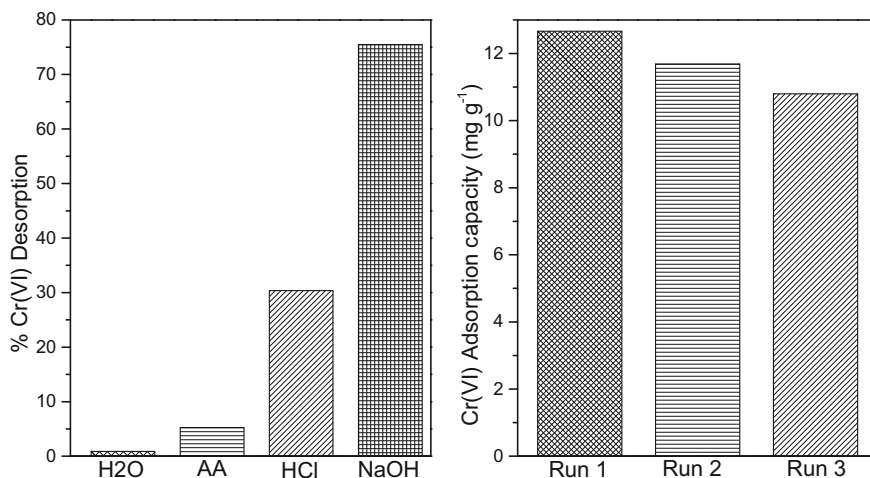
Fig. 12.6   a Desorption efficiency using different solvents and **b** reusability of FTP-MNP for Cr(VI) adsorption

adsorption and can be applied in up to three cycles therefore increasing its cost efficiency.

12.4 Conclusion

The adsorption of hexavalent chromium was optimum at low solution pH where electrostatic attraction was responsible for the binding of anionic chromium species to the adsorbent surface. Hydrogen ions were used up during both Cr(VI) binding and reduction to Cr(III) resulting in an increase in solution pH after adsorption. The presence of Cr(III) ions after adsorption and a change in redox potential further confirmed that Cr(VI) was reduced to Cr(III) during the adsorption process. XPS analysis further indicated that Cr(VI) ions were bound to the adsorbent surface as well as Cr(III) therefore confirming that the mechanism of Cr(VI) adsorption onto FTP-MNP was via adsorption coupled reduction. The adsorbed Cr(VI) was successfully desorbed using 0.1 M sodium hydroxide and the adsorbent was reused twice, losing less than 15% of its initial capacity.

References

1. Das AP, Mishra S (2008) Hexavalent chromium(VI): environment pollutant and health hazard. J Environ Res Dev 2:386–392
2. López-Téllez G, Barrera-Díaz CE, Balderas-Hernández P et al (2011) Removal of hexavalent chromium in aquatic solutions by iron nanoparticles embedded in orange peel pith. Chem Eng J 173:480–485
3. Yuan P, Liu D, Fan M et al (2010) Removal of hexavalent chromium [Cr(VI)] from aqueous solutions by the diatomite-supported/unsupported magnetite nanoparticles. J Hazard Mater 173:614–621
4. Cheung KH, Gu J-D (2007) Mechanism of hexavalent chromium detoxification by microorganisms and bioremediation application potential: a review. Int Biodeterior Biodegradation 59:8–15
5. Miretzky P, Cirelli AF (2010) Cr(VI) and Cr(III) removal from aqueous solution by raw and modified lignocellulosic materials: a review. J Hazard Mater 180:1–19
6. Garg UK, Kaur MP, Garg VK, Sud D (2007) Removal of hexavalent chromium from aqueous solution by agricultural waste biomass. J Hazard Mater 140:60–68
7. Mondal P, Bhowmick S, Chatterjee D et al (2013) Remediation of inorganic arsenic in groundwater for safe water supply: a critical assessment of technological solutions. Chemosphere 92:157–170
8. Baskan MB, Pala A (2011) Removal of arsenic from drinking water using modified natural zeolite. Desalination 281:396–403
9. Ouma ILA, Naidoo EB, Ofomaja AE (2017) Iron oxide nanoparticles stabilized by lignocellulosic waste as green adsorbent for Cr(VI) removal from wastewater. Eur Phys J Appl Phys 79:30401
10. Ouma ILA, Naidoo EB, Ofomaja AE (2018) Thermodynamic, kinetic and spectroscopic investigation of arsenite adsorption mechanism on pine cone-magnetite composite. J Environ Chem Eng 6:5409–5419

11. Bishop ME, Glasser P, Dong H et al (2014) Reduction and immobilization of hexavalent chromium by microbially reduced Fe-bearing clay minerals. Geochim Cosmochim Acta 133:186–203
12. Park D, Yun Y-S, Lee HW, Park JM (2008) Advanced kinetic model of the Cr(VI) removal by biomaterials at various pHs and temperatures. Bioresour Technol 99:1141–1147
13. Joutey NT, Sayel H, Bahafid W, El Ghachtouli N (2015) Mechanisms of hexavalent chromium resistance and removal by microorganisms. Rev Environ Contam Toxicol 233:45–69
14. Poulin S, França R, Moreau-Bélanger L, Sacher E (2010) Confirmation of X-ray photoelectron spectroscopy peak attributions of nanoparticulate iron oxides, using symmetric peak component line shapes. J Phys Chem C 114:10711–10718
15. Zhao Z, Wei J, Li F et al (2017) Synthesis, characterization and hexavalent chromium adsorption characteristics of aluminum- and sucrose-incorporated tobermorite. Materials (Basel) 10:597
16. Villacís-García M, Villalobos M, Gutiérrez-Ruiz M (2015) Optimizing the use of natural and synthetic magnetites with very small amounts of coarse Fe(0) particles for reduction of aqueous Cr(VI). J Hazard Mater 281:77–86
17. Namasivayam C, Sureshkumar MV (2008) Removal of chromium(VI) from water and wastewater using surfactant modified coconut coir pith as a biosorbent. BioresourTechnol 99:2218–2225
18. Yu R-F, Chi F-H, Cheng W-P, Chang J-C (2014) Application of pH, ORP, and DO monitoring to evaluate chromium(VI) removal from wastewater by the nanoscale zero-valent iron (nZVI) process. Chem Eng J 255:568–576
19. Sanghi R, Sankararamakrishnan N, Dave BC (2009) Fungal bioremediation of chromates: conformational changes of biomass during sequestration, binding, and reduction of hexavalent chromium ions. J Hazard Mater 169:1074–1080
20. Kendelewicz T, Liu P, Doyle C, Brown G (2000) Spectroscopic study of the reaction of aqueous Cr(VI) with Fe_3O_4 (111) surfaces. Surf Sci 469:144–163
21. He YT, Traina SJ (2005) Cr(VI) reduction and immobilization by magnetite under alkaline pH conditions: the role of passivation. Environ Sci Technol 39:4499–4504
22. Yuan P, Fan M, Yang D et al (2009) Montmorillonite-supported magnetite nanoparticles for the removal of hexavalent chromium [Cr(VI)] from aqueous solutions. J Hazard Mater 166:821–829
23. Argun ME, Dursun S (2008) A new approach to modification of natural adsorbent for heavy metal adsorption. Bioresour Technol 99:2516–2527
24. Liu Y, Chen M, Yongmei H (2013) Study on the adsorption of Cu(II) by EDTA functionalized Fe_3O_4 magnetic nano-particles. Chem Eng J 218:46–54
25. Aryal M, Liakopoulou-Kyriakides M (2011) Equilibrium, kinetics and thermodynamic studies on phosphate biosorption from aqueous solutions by Fe(III)-treated *Staphylococcus xylosus* biomass: common ion effect. Colloid Surf A 387:43–49
26. Ghosh A, Pal M, Biswas K et al (2015) Manganese oxide incorporated ferric oxide nanocomposites (MIFN): a novel adsorbent for effective removal of Cr(VI) from contaminated water. J Water Process Eng 7:176–186

Chapter 13
Review on Tuberculosis: Trends in the Discovery of New and Efficient Chemotherapeutic Agents

Tozama Qwebani-Ogunleye, Ikechukwu P. Ejidike and Fanyana M. Mtunzi

Abstract Bacterial infections are one of the world's most pressing public health problems. The major challenge in anti-bacterial treatment is the transformation in bacteria strains leading to antibiotics resistant. Each year over 1 million people die from major infections associated with MDR tuberculosis. This review gives the synopsis of tuberculosis, first-line TB drugs and their mode of action, second-line TB drugs, challenges faced with drug discovery of new TB entities and medicinal plant species. The first-line anti-TB drugs act as bacteriostatic or as bactericidal. Isoniazid and ethambutol are both bacteriostatic. They act by inhibiting mycolic acid synthesis that is required for the mycobacterial cell wall. Rifampicin is bactericidal. It inhibits DNA-dependent RNA polymerase in the bacterial cells by binding its beta-subunit, thus preventing transcription to RNA and subsequent translation to proteins. Pyrazinamide, also a prodrug, is only active in acidic conditions. It disrupts the energy-dependent pathway. Streptomycin is a protein synthesis inhibitor. It binds to the S12 protein of the 30S subunit of the bacterial ribosome, thereby allowing the selectivity of this antibiotic for bacteria. Despite the challenges faced with the development of new drug candidates, the government and non-governmental organizations have started to invest in TB drug research and development. Potential drug candidates are discussed in this review.

T. Qwebani-Ogunleye · I. P. Ejidike (✉) · F. M. Mtunzi
Institute of Traditional Knowledge and Traditional Medicine, Faculty of Applied and Computer Sciences, Vaal University of Technology, Southern Guateng Science and Technology Park, 5 Moshoeshoe Road, Sebokeng 1911, South Africa
e-mail: destinedchild12@gmail.com; ikechukwue@vut.ac.za

T. Qwebani-Ogunleye
e-mail: QwebaniO@dihlare.com; olathozie@gmail.com

F. M. Mtunzi
e-mail: fanyana@vut.ac.za

I. P. Ejidike · F. M. Mtunzi
Department of Chemistry, Faculty of Applied and Computer Sciences, Vaal University of Technology, Vanderbijlpark 1911, South Africa

I. P. Ejidike
Department of Chemical Sciences, Faculty of Science and Science Education, Anchor University, P.M.B. 001, Ipaja, Lagos, Nigeria

Keywords TB-drugs · Respiratory infection · *Mycobacterium tuberculosis* · Drug resistance · Mechanisms · Medicinal plants

13.1 Introduction

In the past, tuberculosis (TB) was well known as Consumption because of the way it will consume from within anyone infected by the disease. Other names of TB include phthisis, King's evil and lupus vulgaris. In 1882, Robert Koch made the landmark discovery that TB is caused by an infectious agent called *Mycobacterium tuberculosis* (*M.tb.*). Koch's findings welcomed opportunities that antibiotics can be developed to combat this disease [1]. The latter is one of the most common contagious diseases known to mankind. It is caused by a respiratory infection and primarily affects the lungs, but it can also affect organs in the central nervous system, lymphatic system, and circulatory system. In 1993, WHO declared TB as the global health emergency [2]. Although there has been major progress in subsequent years, more than 60 million people have been documented as treated and cured since 2000 and death rates have fallen steadily [3].

According to the World Health Organisation, TB is one of the top 10 causes of death worldwide, ranking above HIV [AIDS] as the leading cause of death from an infectious disease [3]. In 2017, TB caused an estimated 1.3 million deaths (range, 1.2–1.4 million) [4].

Every 2 sec one TB patient dies and about 30 million people will be infected by *M.tb.* within the next 20 years [5]. Globally it has been estimated that 10.0 million people developed TB disease in 2017: 5.8 million men, 3.2 million women, and 1.0 million children. Worldwide 6.4 million new cases of TB were officially notified to national authorities and then reported to WHO [3]. The 6.4 million represent 64% of the estimated 10.0 million new cases that occurred in 2017. Ten countries accounted for 80% of the 3.6 million global gaps, the top three being India (26%), Indonesia (11%) and Nigeria (9%). This is due to the mixture of underreporting of detected cases and underdiagnoses, either people do not access health care, or they are not diagnosed when they do [3]. In 2015, 6.1 million new TB cases were notified to authorities and reported by WHO [6]. The same year there were about 1.4 million TB deaths and an additional of 0.4 million deaths resulting from TB disease among HIV positive people [6]. In 2011, 8.7 million people fell ill with TB and 1.4 million died from the disease [7]. In 2010 there were about 10 million orphan children because of the TB deaths among parents [7].

Reports on TB reveal that about one-third of the world population carry a latent TB infection and it is the leading infectious cause of death in people infected with HIV and it is a disease of poverty [7].

The global incidence of TB cases is skewed heavily toward low income and emerging economies [5]. Africa, and more specifically sub-Saharan Africa have the highest incident rate of TB, with approximately 83 and 290 per 100,000 respectively [5]. The highest prevalence of cases is in Asia, where China, India, Bangladesh,

Indonesia, and Pakistan collectively make up to 50% of the global burden [5]. Despite the availability of antibiotics for over 50 years, TB remains a major global health problem. One can get TB by breathing in air droplets from a cough or sneeze of an infected person. The resulting lung infection is called primary TB.

Most people recover from primary TB infection without further evidence of the disease. The infection may stay inactive (dormant) for years. However, in some people, it can reactivate. Most people who develop symptoms of a TB infection first became infected in the past. In some cases, the disease becomes active within weeks after the primary infection to a drug-sensitive TB. Drug-sensitive TB means that all the TB drugs will be effective so long as they are taken properly. It still means that several drugs need to be taken together to provide effective TB treatment. The Sustainable Development Goals (SDGs) for 2030 were adopted by the United Nations in 2015 [6]. One of the objectives is to end the global TB epidemic. All member States of WHO and the UN have committed to this goal. The target set in the End TB Strategy include a 90% reduction in TB deaths and in 80% reduction in TB incidence by 2030, compared to 2015.

13.2 Materials and Methods

Scopus and journals' databases were accessed for data/information collection, and snowball sampling method was used in this study.

13.3 Results and Discussion

13.3.1 First-Line TB Drugs

The first-line anti-TB drugs that have been used for TB treatment include: isoniazid (INH) **1**, pyrazinamide (PZA) **2**, streptomycin (STR) **3**, ethambutol (ETH) **4**, and rifampicin (RIF) **5** (Fig. 13.1) [8].

No sooner were the first anti-tuberculosis agents introduced to humans than the emergence of drug-resistant isolates of *M.tb.* were observed [9–11]. Since the early 1990s, there has been a great concern in public health due to the emergence of resistance to multiple drugs (MDR-TB). This is caused by *M.tb.* strains which are resistant to at least two first-line anti-TB drugs INH **1** and rifampicin RIF **5**. MDR-TB develops during treatment of drug-sensitive TB when the course of antibiotics regime is interrupted and the levels of the drug in the body are insufficient to kill 100% of the bacteria [12].

In vitro studies showed that spontaneous mutations in *M.tb.* can be associated with drug resistance, while selective (antibiotic) pressure can lead to enhanced accumulation of these drug resistant mutants [13, 14]. The efficient selection of drug resistance
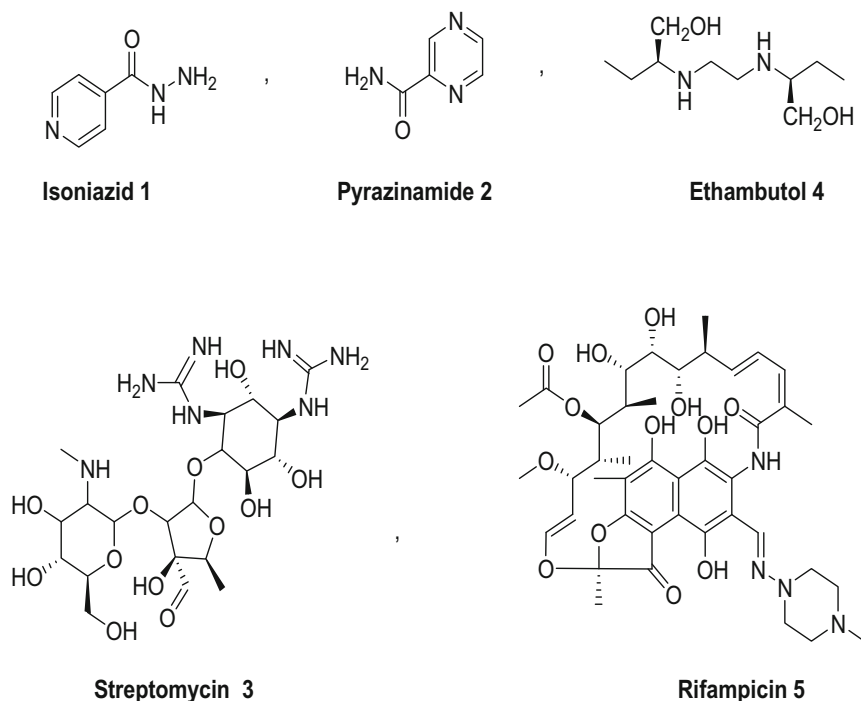
Fig. 13.1 First-line TB drugs [8]

in the presence of a single antibiotic led investigators to recommend combination therapy, using more than one antibiotic to reduce the emergence of drug-resistance during treatment [15–17]. Combination treatment is properly managed and TB control has been effective [17–19]. Drug-resistant TB continues to be a public health crisis. The best estimate is that, worldwide in 2017, 558,000 people developed TB that was resistant to rifampicin (RR-TB), the most effective first-line drug and of this 82% had multidrug-resistant TB (MDR-TB) [2]. Among cases of MDR-TB in 2017, 8.5% were estimated to have extensively drug-resistant TB (XDR).

13.3.2 Mode of Action of First-Line Anti-TB Drugs

Understanding the mechanisms of mycobacterial action to the anti-tuberculosis drugs not only enables the development of more rapid molecular diagnostic tests and furnishes implications for designing new anti-tuberculosis drugs, but it also helps to implement measures to prevent the development resistance [20]. The mechanisms of first-line TB drugs on *M.tb.* are further exemplified and described below.
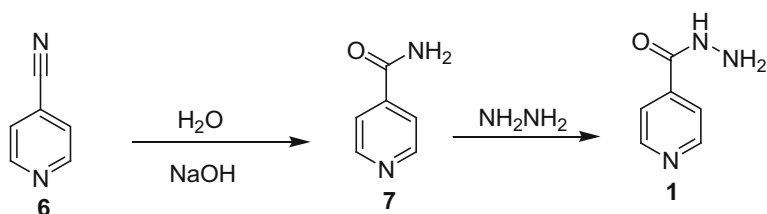
Scheme 13.1 Synthesis of isoniazid [16]

13.3.2.1 Isoniazid

Synthesis

Isoniazid **1** was first made in 1952 and may be prepared by the base hydrolysis of 4-cyanopyridine **6** to give the amide **7**, followed by displacement of ammonia by hydrazine as shown in Scheme 13.1 [20].

Mode of Action

Isoniazid, also known as isonicotinylhydrazide which a pro-drug, is a pharmacological substance that is administered in an inactive or significantly less active form. It is activated by a bacterial catalase-peroxidase enzyme called KAtG or by Mn^{2+} [21]. Mycolic acid synthesis is the primary pathway inhibited by the action of isoniazid [22–28].

Mycolic acids are fatty acids containing up to 90 carbons and are the major components of the mycobacterial cell wall. Two enzymes involved in this synthesis have shown to be targets of isoniazid and they are NADH-dependent *enoyl-acyl carrier* protein and *β-ketoacyl* carrier protein synthase designated KasA [29]. KatG couples the isonicotinic acyl with NADH to form isonicotinic acyl-NADH complex **14** as displayed in Scheme 13.2.

This complex binds tightly to ketoenoylreductase known as inhA, thereby blocking the natural enoyl-AcpM substrate and the action of fatty acid synthase. Isoniazid **1**, therefore, acts by inhibiting an oxygen-sensitive pathway in the mycolic acid biosynthesis required for the mycobacterial cell wall.

Mechanism of Resistance

Mutations in INH-resistant clinical isolates are most commonly detected in the katG gene, occurring in 50–80% of cases, thus reducing the ability of the catalase-peroxidase to activate the INH pro-drug [30]. The katG gene is in a highly variable and unstable region of the *M. tuberculosis* genome [30]. Point mutations in katG are
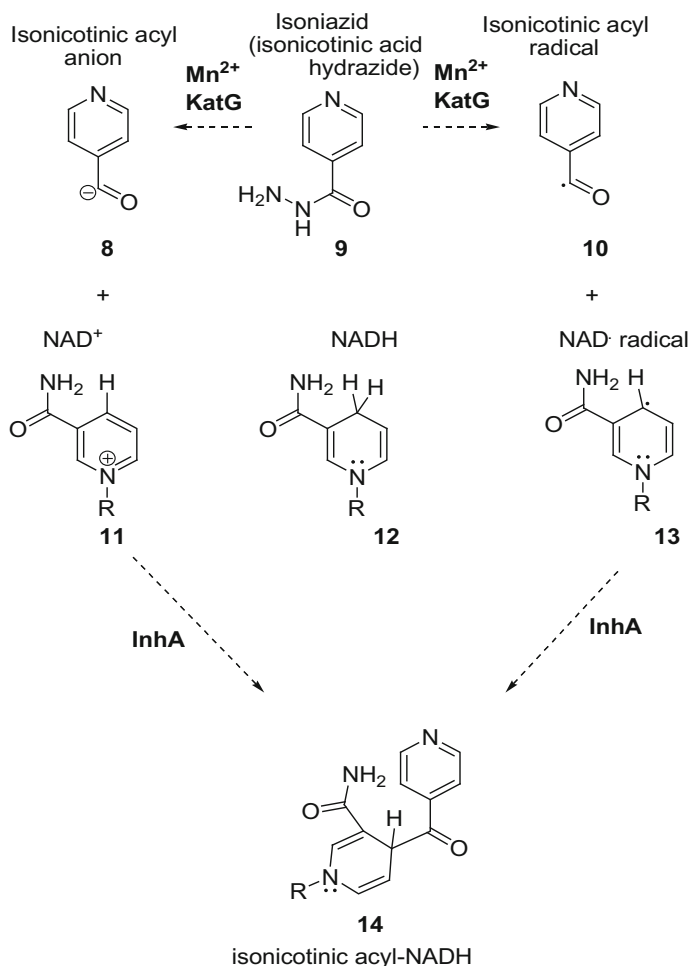
Scheme 13.2 Formation of the isonicotinic acyl-NADH [20]

more commonly observed than other types of mutations, and a single point mutation resulting in the substitution of threonine for serine at residue 315 (S315T) accounts for the majority of INH resistance among clinical isolates [31].

The S315T mutation results in a significant reduction in catalase and peroxidase activity and is associated with high-level INH resistance (MIC = 5–10 μg/mL) [32]. INH resistance may also arise from mutations in inhA, resulting in reduced affinity of the enzyme for NADH without affecting its enoyl reductase activity [33]. Generally, mutations in inhA or in the promoter region of its operon usually confer low-level resistance (MIC = 0.2–1 mg/L) [33]. Mutations in inhA also cause resistance to the structurally related second-line drug ethionamide [33].

13.3.2.2 Pyrazinamide

Synthesis

Pyrazinamide **2** was first used against tuberculosis in 1952 and can be synthesized by oxidation of quinoxaline **15** to form pyrazine-2,3-dicarboxylic acid **16**. The latter undergoes esterification in the presence of the acid to form ethyl pyrazine-2-carboxylate **17**. This is then followed by amination of **17** to form compound **2** as shown in Scheme 13.3.

Mode of Action

Pyrazinamide **2** is also a pro-drug like isoniazid **1**. *M.tb.* has the *pyrazinamidase* enzyme which is only active in acidic conditions as depicted in Scheme 13.4 [34]. Pyrazinamidase converts pyrazinamide to the active form, pyrazinoic acid which accumulates in the bacilli. Accumulation of pyrazinoic acid disrupts membrane potential and interferes with energy production that is necessary for the survival of *M.tb.* at an acidic site of infection.

Mechanism of Resistance

PZA resistance has been attributed primarily to mutations in the pncA gene encoding PZase [35]. Most mutations, including point mutations, deletions, and insertions, have been reported in a 561-bp region of the open reading frame or in an 82-bp region of its putative promoter [36, 37]. The relatively high degree of diversity in pncA mutations among PZA-resistant clinical isolates has complicated the development of molecular assays for the rapid and economical detection of PZA resistance.

A small percentage of isolates with high-level PZA resistance contain no mutations in pncA or its promoter, suggesting alternative mechanisms of resistance such as deficient uptake enhanced efflux, or altered pncA regulation [38]. The high specificity of PZA for *M.tb.*, with little or no activity against *M. bovis* and other mycobacteria, is attributable to pncA mutations, which render PZase inactive in the latter mycobacterial species.

13.3.2.3 Streptomycin

Synthesis

Though streptomycin was first reported in 1944, its total synthesis has not yet been achieved. However, it has been reported that it can be made from dihydrostreptomycin (DSM) **19** trihydrochloride which has the structure shown in Scheme 13.5 [39, 40] using the following steps:
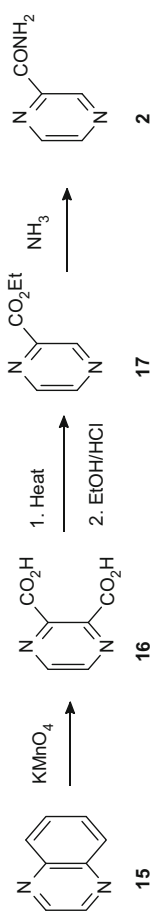
Scheme 13.3 Synthesis of pyrazinamide [25]

Scheme 13.4 Conversion of pyrazinamide to pyrazinoic acid
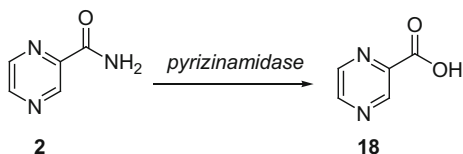
(a) Benzyloxycarbonylation to give **20**

In the first step DSM (**19**) trihydrochloride undergoes benzyloxycarbonylation by addition of benzyl chloroformate and sodium carbonate in aqueous acetone to give compound **20**.

(b) Protection of the hydroxyl groups in the furan ring to give **21**

The tertiary and primary alcohol group in the furan ring are protected by the addition of excess 2,2-dimethoxypropane in acetic acid to give compound **21**, the mono-isopropylidene derivative.

(c) Acetylation of compound **21**

Acetylation of compound **21** with acetic anhydride in the presence of catalytic amount of *p*-toluene sulfonic acid gave a hexaacetyl derivative **22**.

(d) Regioselective hydrolysis to compound **23**

Selective hydrolysis of compound **22** with aqueous acetic acid led to compound **23**, which has free primary and tertiary hydroxyl groups.

(e) Pfitzner-Moffatt oxidation to compound **3**

Compound **23** was converted into the aldehyde derivative **3** by Pfitzner-Moffatt oxidation with DMSO, dicyclohexylcarbodiimide, trifluoroacetic acid, and pyridine. The product was deacetylated with methanolic ammonia to give *N*-benzyloxycarbonylstreptomycin.

Mode of Action

Streptomycin **3** is a protein synthesis inhibitor. It binds to the S12 protein of the 30S subunit of the bacterial ribosome, interfering with the binding of formyl-methionyl-tRNA to the 30S subunit (Fig. 13.2).

This prevents the initiation of protein synthesis and leads to the death of microbial cells. Humans have structurally different ribosomes from bacteria, thereby allowing the selectivity of this antibiotic for bacteria [33].
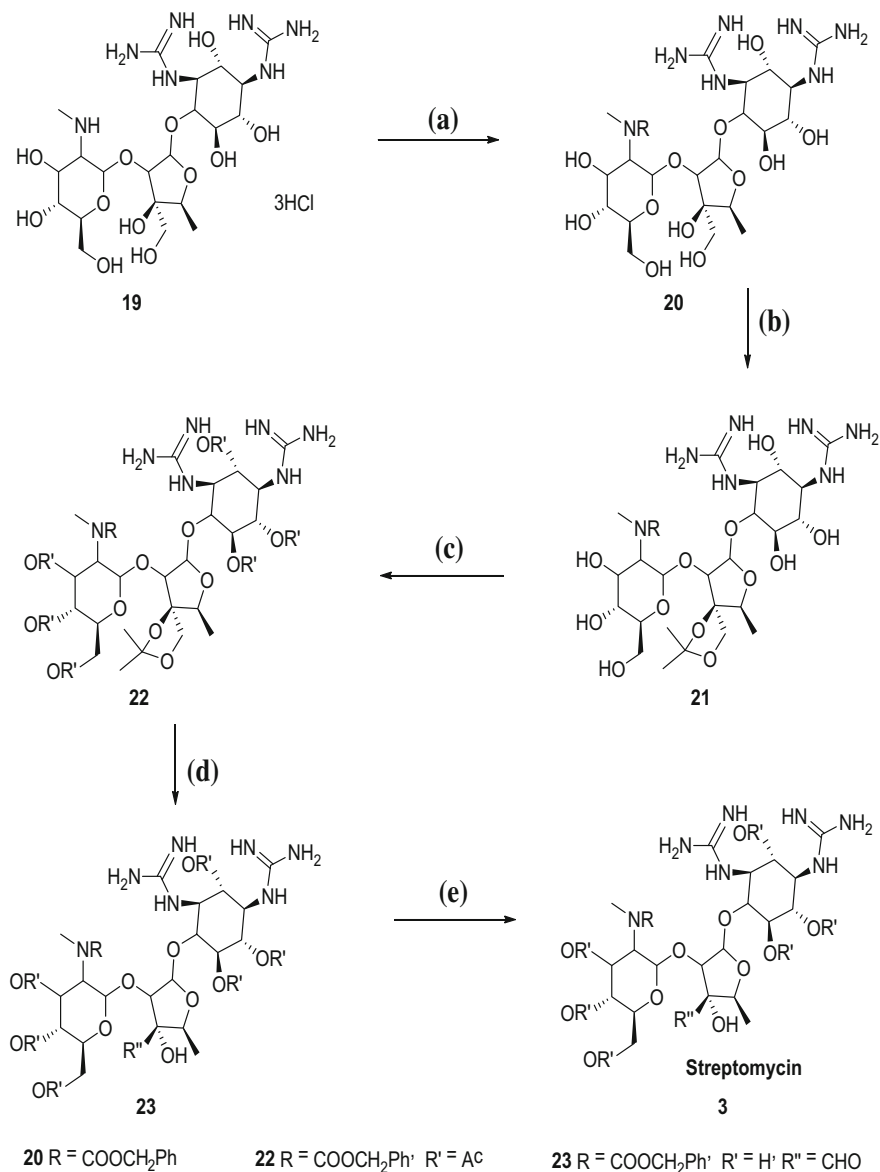
Scheme 13.5 Synthesis of streptomycin. Conditions: (a) CbCl, Na$_2$CO$_3$, CH$_3$COCH$_3$ (aq); (b) DMP, TsOH, CH$_3$CO$_2$H, MeOH; (c) (CH$_3$CO)$_2$O, *p*-TsOH; (d) CH$_3$COOH (aq); (e) DMSO, DCC, TFA, C$_5$H$_5$N, MeOH, NH$_3$
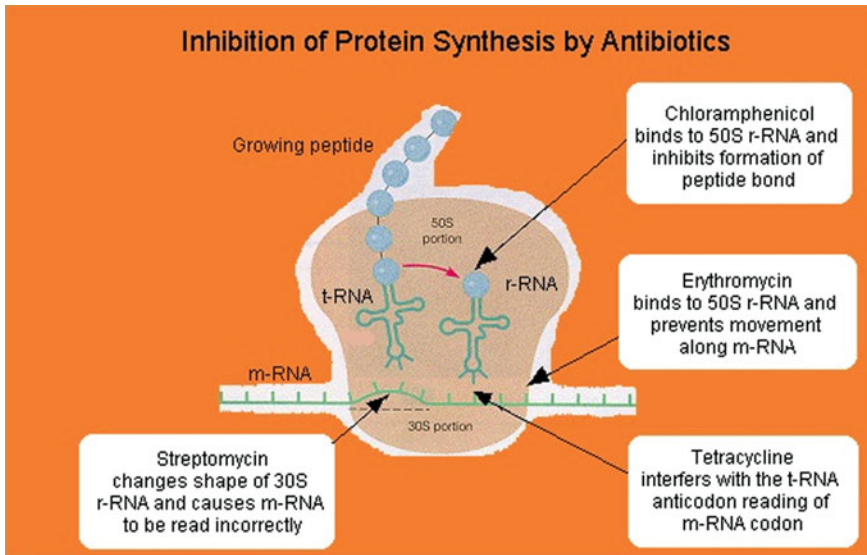
Fig. 13.2 Inhibition of protein synthesis by streptomycin **3** [41]

Mechanism of Resistance

Resistance to streptomycin and the other aminoglycosides in *M.tb.* usually develops by mutation of the ribosome target binding sites. Interestingly, although crossresistance is observed between amikacin and kanamycin [33], however, these drugs are not cross-resistant with streptomycin [33]. Mutations in the rpsL gene, which encodes the ribosomal protein S12, account for approximately half of all streptomycin-resistant clinical isolates, with the K43R mutation predominating [30].

In about 20% of streptomycin-resistant *M.tb.* clinical isolates, such resistance is associated with mutations in the rrs gene, which are usually clustered in the regions surrounding nucleotides 530 or 912 [30]. The vulnerability of rrs gene to mutation, leading to streptomycin resistance in *M. tuberculosis* and other slow-growing mycobacteria, can be explained by the fact that these mycobacterial species, unlike other bacteria, contain only a single copy of the rrs gene. Generally, mutations in the rpsL and rrs genes confer high-level (MIC > 1000 mg/L) or intermediate-level (MIC = 64–512 mg/L) resistance to streptomycin [34–41]. More recently, it has been shown that mutations in gidB, which encodes a conserved S-adenosylmethionine-dependent 16S rRNA methyltransferase, can confer low-level resistance to streptomycin [30].
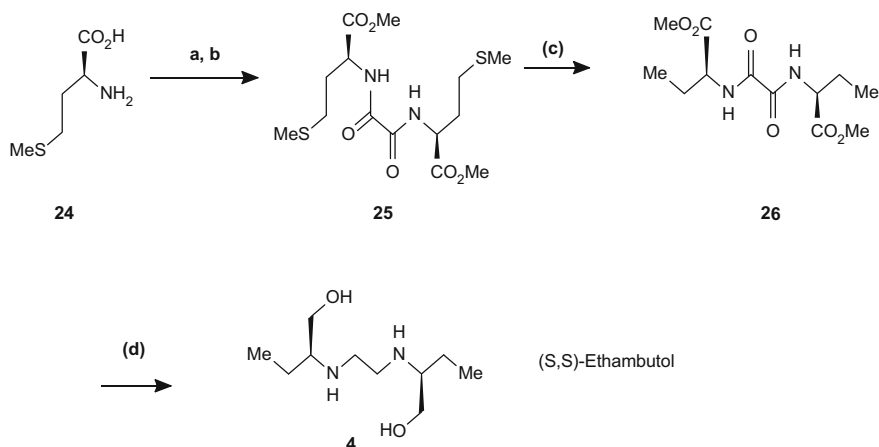
Scheme 13.6 Synthesis of ethambutol. Conditions: (a) MeOH, AcCl; (b) ClCOCOCl (0.5 equiv.), pyridine, CH_2Cl_2; (c) Raney (W-4), MeOH–H_2O (9:1), Δ; (d) LiAlH$_4$, THF, Δ [39]

13.3.2.4 Ethambutol

Ethambutol (EMB) was initially reported to have anti-tuberculosis activity in 1961. Like INH, EMB primarily kills actively multiplying bacilli and has very poor sterilizing activity.

Synthesis

Ethambutol **4** can be prepared efficiently by a four-step stereoselective synthesis (Scheme 13.6). The first step of the synthesis is esterification of **24** under standard conditions followed by treatment of the free amide with 0.5 equivalent of oxalyl chloride to form the desired oxalyl diamine derivative **25**. This key intermediate already incorporates the required carbon framework and the absolute configuration SS as in the target.

Raney nickel desulfurization of the terminal thiomethyl groups leads to **26**. LiAlH$_4$ is used as the reducing agent of the diamide and diester functional group to give the desired product **4** [42].

Mode of Action

Ethambutol is bacteriostatic against actively growing TB bacilli and works by obstructing the formation of the cell wall. It disrupts arabinogalactan synthesis by inhibiting the enzyme arabinosyl transferase [43]. Disruption of the arabinogalactan synthesis leads to increased permeability of the cell wall resulting in cell death [43].
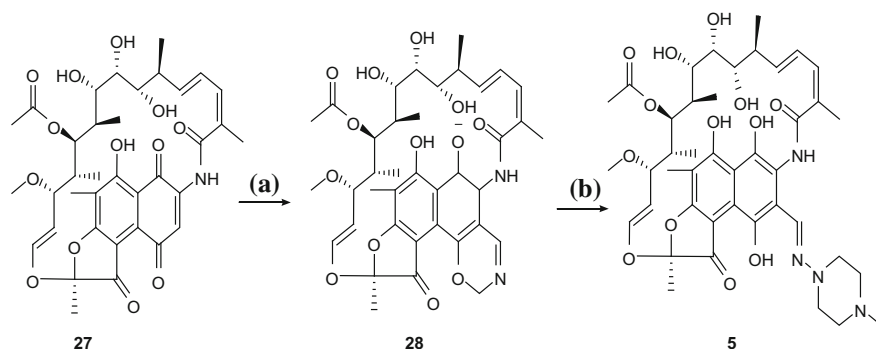
Scheme 13.7 Synthesis of rifampicin. Conditions: (a) $C_3H_9NO_2$; (b) $C_5H_{13}N_3$ (base)

Mechanism of Resistance

Resistance to EMB in *M.tb.* is usually associated with point mutations in the embCAB operon [44]. Genetic and biochemical studies have shown that the EmbA and EmbB proteins are involved in the formation of the proper terminal hexaarabinofuranoside motif during arabinogalactan synthesis [45]. As most EMB-resistant clinical isolates contain mutations in the EmbB gene [46], EmbB is the main target of EMB, although X-ray crystallographic data supporting this interaction are lacking.

Other potential mutations involved in EMB resistance include a Gln379Arg substitution in *M. tuberculosis* embR, as well as mutations in the rmlD, rmlA2, and Rv0340 genes. As many as one-quarter of all EMB-resistant *M.tb.* isolates do not harbor mutations in any of the genes described above, suggesting alternative mechanisms of EMB resistance [30].

13.3.2.5 Rifampicin and Other Rifamycins

Rifamycins were first isolated in 1957 from *Amycolatopsis* (formerly *Streptomyces*) *mediterranean* as part of an Italian antibiotic screening program [47]. Rifampicin was first used clinically in 1966.

Synthesis

According to U.S. Pat. No. 3,963,705, rifampicin, also known as rifampin, was obtained by reacting rifamycin S **27** with an *N*-bis-alkoxymethyl-amine or an *N*-bis-hydroxymethyl-amine to give a well-defined intermediate compound, namely a 1,3-oxazino[5,6-*c*]rifamycin **28** [48]. The latter reacts in a basic medium with the 1-amino-4-methylpiperazine to give rifampicin **5** (Scheme 13.7).

Mode of Action

Rifampicin is a bactericidal antibiotic drug of the rifamycin group. Rifampicin inhibits DNA-dependent RNA polymerase in the bacterial cells by binding its beta-subunit, thus preventing transcription to RNA and subsequent translation to proteins [33]. The high resistance, prolonged chemotherapy and side effects of the available first-line antituberculosis drugs highlight the need for new, safer and more effective antitubercular drugs.

Mechanism of Resistance

Although INH monoresistance is relatively common in *M. tuberculosis*, resistance to rifampicin alone is rare, and more than 90% of rifampicin-resistant isolates are also resistant to INH. Therefore, rifampicin resistance has been used as a surrogate marker for MDR-TB.

Resistance to rifampicin in *M. tuberculosis* arises at a frequency of 10^{-7} to 10^{-8} organisms, most commonly as single point mutations in the rpoB gene, which encodes the subunit of RNA polymerase [49]. In over 90% of rifampicin-resistant clinical isolates, point mutations cluster in an 81-base pair "hot-spot" region between codons 507 and 533 of the rpoB gene, with mutations in codons 531 [Ser] and 526 [His] predominating [50].

However, mechanisms of action and resistance (<5%) do not contain any mutations in the rpoB gene, suggesting alternative resistance mechanisms, potentially including altered rifampicin permeability or mutations in other RNA polymerase subunits [51]. Higher doses of the rifamycins, especially rifapentine, have the potential to further shorten the duration of TB treatment. Therefore, there is renewed interest in establishing the maximally tolerated dose of these drugs, and many clinical trials are planned or underway to examine the safety, pharmacokinetics, and efficacy of higher than standard doses of rifampicin or rifapentine in first-line TB treatment [52].

13.3.3 Second-Line TB Drugs

Although antibiotics developed in the 1950s are effective against a large percentage of TB cases, resistance to these first-line therapies has developed over the years, resulting in the growing emergence of multidrug-resistant (MDR), extensively drug-resistant (XDR) TB and even totally drug-resistant (TDR) TB. XDR-TB is caused by *M.tb.* resistant to INH **1** and RMP **5** plus any fluoroquinolone **29**, and at least one of the three following injectable drugs: capreomycin **30**, kanamycin **31** or amikacin **32** [12]. Figure 13.3 shows examples of second-line TB drugs that can be used for MDR-TB treatment.

Fluoroquinolone 29

Capreomycin 30

Kanamycin 31

Amikacin 32
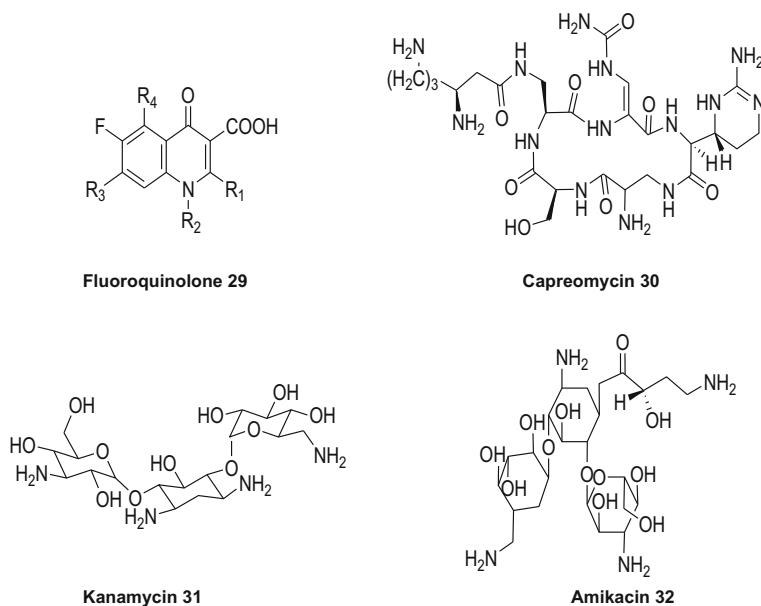
Fig. 13.3 Second-line TB drugs [12]

Totally-resistant TB is caused by *M.tb.* resistant to all first and second-line anti-TB drugs [12]. The second-line anti-TB drugs include para-aminosalicylic acid **33**, cycloserine **34**, ciprofloxacin **35**, ofloxacin **36**, ethionamide **37** and clofazimine **38** (Fig. 13.4).

The current prevailing scenarios of drug-resistant TB are particularly alarming and pose a significant threat to the control of the disease globally. It has been noted that TB cases will worsen with the growing human immunodeficiency virus (HIV) pandemic worldwide as the viral infection can weaken the host immune system. Therefore, there is an urgent need for new affordable drugs that can be used in a short period of time.

13.3.4 Challenges of Developing New Anti-TB Drugs

The discovery of new drugs has been hampered by several obstacles as discussed below. Table 13.1 summarizes the required properties of new anti-TB drugs [45].
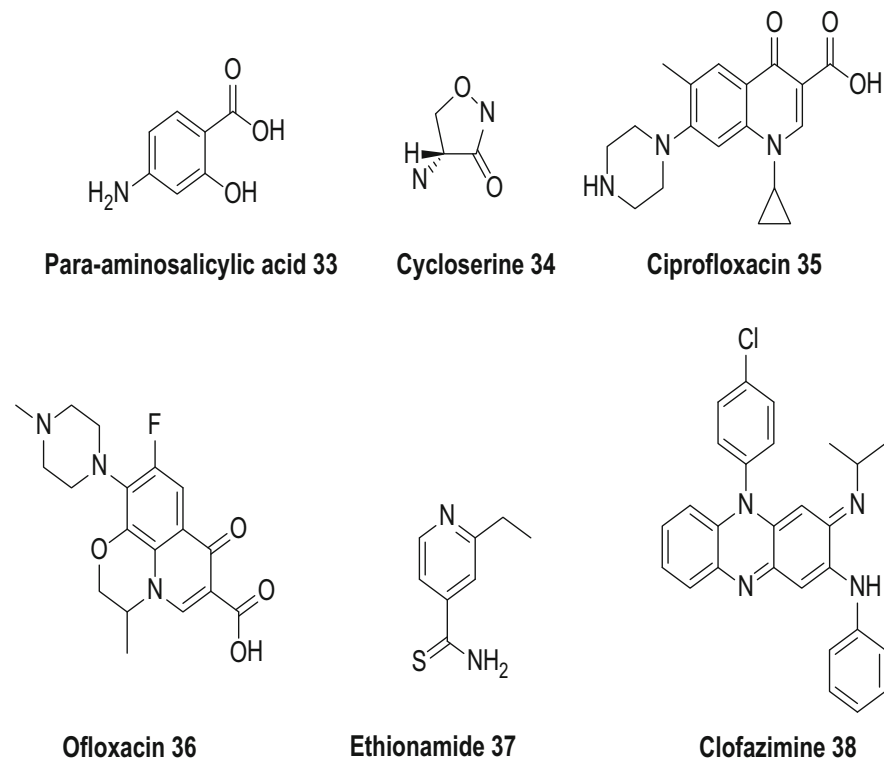
Fig. 13.4 Second-line anti-TB drugs

Table 13.1 Properties requirement for new anti-TB drugs synthesis

What a new drug should do	Characteristics required
Simplify treatment or reduce treatment duration	Strong bactericidal and sterilizing activity Low pill count, fixed-dose combinations Allow for intermittent therapy
Have an acceptable toxicity profile	A low incidence of treatment-limiting adverse events No overlapping toxicity profile with other TB drugs
Be active against MDR/XDR TB	No cross-resistance with first-line drugs
Be useful in HIV-infected patients with TB	Minimal interactions with antiretroviral drugs No overlapping toxicity profile with antiretroviral drugs
Be active against latent TB	Activity against dormant bacilli Favorable toxicity profile

13.3.5 Insufficient Profit Opportunity

The cost of developing a new drug is estimated to be between \$115-240 million [53]. To be profitable, market prices of new drugs should be relatively high, whereas the cost of a standard regimen is only about \$11 per patient [53]. As there is no investment return to instigate pharmaceutical companies, they tend to be reluctant to peruse research on the development of novel drugs.

13.3.6 Difficulty to Identify New Compounds with Activity Against M.tb.

Novel drugs should kill both the rapidly growing mycobacteria and the persisting mycobacterium in lesions (sterilizing activity) [53, 54]. However, because of the *M.tb.* drug resistance this is not observed and the molecular mechanism for this resistance is not yet fully understood.

13.3.7 Evaluation of New Compounds

There are currently no animal models available that can predict with accuracy the required treatment duration with newly identified compounds [55]. The guinea pig model is being explored as an alternative to a mouse model since it resembles TB pathology in humans more closely [56]. The phase of clinical testing of new anti-TB drugs is also time-consuming.

13.3.8 Scarcity of Trial Sites

There is also a scarcity of trial sites with sufficient research capacity to conduct clinical trials with large samples. It will be more advantageous if trials are performed in countries where the TB burden is highest but human and infrastructural capacity for performing large, high-quality phase III clinical trials is usually limited in these settings [57].

13.3.9 Quest for New Drug Candidates for TB Treatment

13.3.9.1 Fluoroquinolones

Fluoroquinolones (Fig. 13.5) are a promising class of drugs for the treatment of TB [58]. They are well distributed broadly throughout the body, which explains their efficacy against intracellular mycobacteria and they are registered as second-line anti-TB drugs [58–61].

Moxifloxacin **39** and Gatifloxacin **40** are candidates for shortening TB treatment. They have exhibited the lowest MICs [62–68] and exhibited greatest bactericidal activity as expressed in the rate of fall in Count Forming Unit (CFU). Their approved dose is 400 mg/day [65, 69–71].

Other fluoroquinolone and bifunctional fluoroquinolone–hydroxyquinoline derivatives have also been reported [72]. The fluoroquinolone derivatives were synthesized in two steps and the bifunctional fluoroquinolone–hydroxyquinoline derivatives in one step. They were evaluated for antimycobacterial activity.

The compounds that exhibited the best activity are the 1-(2-fluoro-4-nitrophenyl)quinolones, 7-piperidinyl derivative **41** and 7-(3,5-dimethylpiperazinyl) derivative **42**, which exhibited 97% and 98% inhibition, respectively.

Various diclofenac acid hydrazones and amides have also been synthesized and evaluated for in vitro and in vivo antimycobacterial activities against *M.tb.* [70].
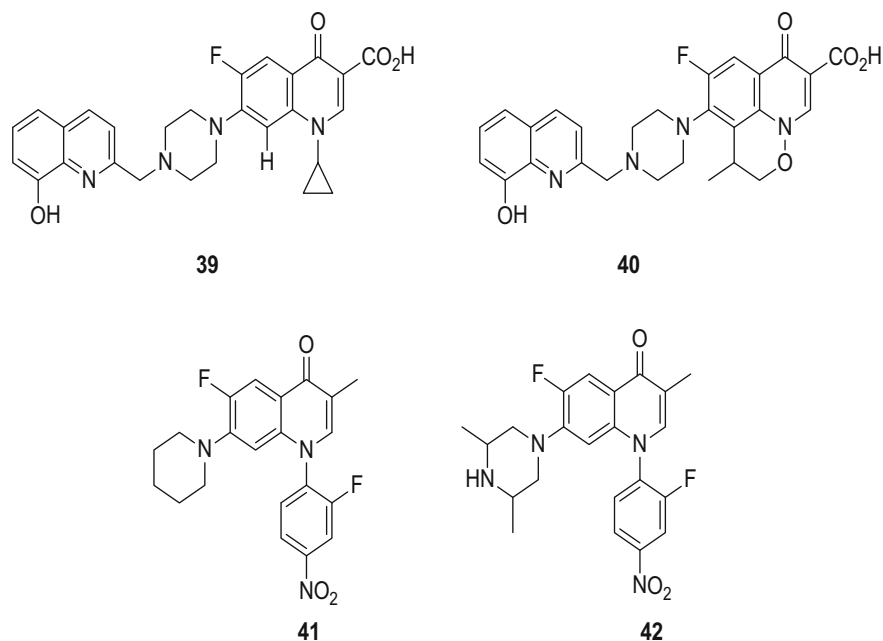
Fig. 13.5 Fluoroquinolone derivatives [62]

Fig. 13.6 Diclofenac acid derivative [73]
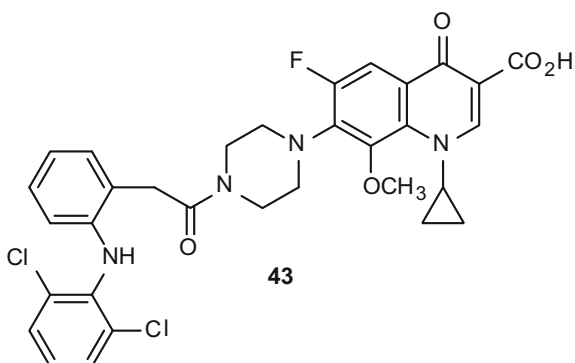
Preliminary results indicated that most of the compounds demonstrated higher in vitro antimycobacterial activity (MIC = 0.0383–7.53 μM) than diclofenac (MIC = 21.10 μM) and ciprofloxacin (MIC = 9.41 μM).

Among the synthesized compounds, **43** (Fig. 13.6) was found to be the most active compound in vitro with MIC of 0.0383 μM and was more potent than the first-line antitubercular drug isoniazid (MIC = 0.1822 μM) [73]. This compound was suited for further modification to obtain a more efficacious and potent antituberculosis drug.

Mechanism of Action

Moxifloxacin is a broad-spectrum 8-methoxy fluoroquinolone with activity against both Gram-positive and Gram-negative bacteria [73]. It inhibits bacterial DNA gyrase, an enzyme that is essential for the maintenance of DNA supercoils, which is necessary for chromosomal replications [73]. Gatifloxacin also blocks the bacterial DNA gyrase, thereby preventing chromosomal replication.

13.3.9.2 Rifamycin Derivatives

Rifampin (rifampicin) is the cornerstone in the current treatment of TB [74]. Rifamycin derivatives, such as rifapentine, rifabutin, and rifalazil (RLZ, also known as KRM1648 or benzoxazinorifamycin **45**), have been synthesized to improve antimycobacterial activity and prolong their half-life (Fig. 13.7).

Rifapentine was approved by the FDA in 1998 for the treatment of TB. Rifapentine appears to be safe and well-tolerated at once-weekly dosing and is currently being evaluated in Phase III efficacy trials for treatment of latent tuberculosis [65]. RLZ (rifalazil) **45** is a semisynthetic rifamycin derivative with a long half-life, which is highly active against a range of intracellular bacteria including *M. tuberculosis, Mycobacterium avium*, *Chlamydia trachomatis*, *Chlamydia pneumoniae,* and *Heli-*
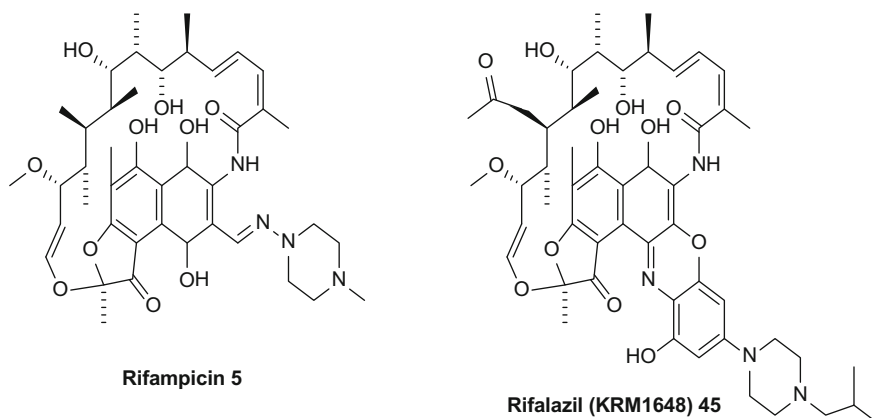
Fig. 13.7 Rifamycin derivatives

Fig. 13.8 Structure of
Linezolid
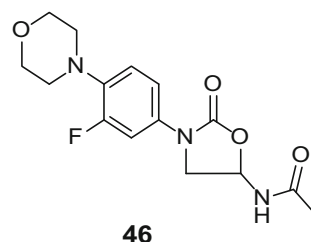
cobacter pylori. RLZ **45** is more active than RIF or rifabutin against *M. tuberculosis*
in mice both in vitro and in vivo [75].

13.3.9.3 Oxazolidinones

Oxazolidinones, discovered at DuPont in the 1970s and later sold to Pharmacia
Upjohn, are a class of compounds that are active against a variety of Gram-positive
bacteria, including *M.tb*.

Linezolid **46** is the first oxazolidinone to be developed and approved by the FDA
to treat single- or multiple-resistant Gram-positive bacterial infections (Fig. 13.8)
[76].

13.3.9.4 Nitroimidazopyran

A particularly promising candidate for TB treatment is nitroimidazopyran PA824 **47**,
derived from 5-nitroimidazoles (Fig. 13.9) [77].

Fig. 13.9 Structure of
nitroimidazopyran

47
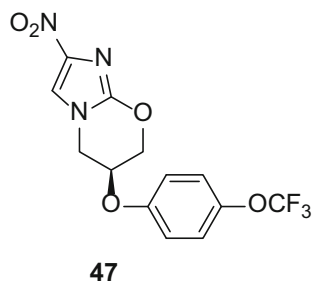
PA824 is highly active with MIC as low as 0.015–0.250 μg/ml against *M.tb.* and
MDR-TB. PA824 is a pro-drug that requires activation by a bacterial F420-dependent
glucose-6-phosphate dehydrogenase and nitroreductase to activate components that
then inhibit bacterial mycolic acid and protein synthesis [77].

13.3.10   Medicinal Plants

In most parts of Southern Africa, plants are used for medicinal purposes and have
been used to treat TB-infections. The structure of biologically active compounds
in plants varies, belonging to different classes of compounds such as alkaloids, ter-
penoids, coumarins/chromones, peptides and phenols [78]. This section focuses on
medicinal plant extracts/compounds that are currently being investigated as potential
antitubercular drugs.

Naphthoquinones exhibit a range of pharmacological properties such as antibacte-
rial [78–83], antiviral [84–86], trypanocidal [87–89], anticancer [90–92], antimalar-
ial [93–96], and antifungal activity [97–103]. A detailed study of a series of synthetic
and plant-derived naphthoquinone derivatives of the 7-methyljuglone **48** scaffold on
antibacterial activity against *M.tb.* was reported by Mahapatra et al. [7].

The purpose of the study was to examine the synthesis, antibacterial activ-
ity and cytotoxicity of a series of naphthoquinones [7]. The naphthoquinone, 7-
methyljuglone **48** (Fig. 13.10) has previously been isolated and identified as an

Fig. 13.10 Chemical
structure of 7-methyljuglone

48
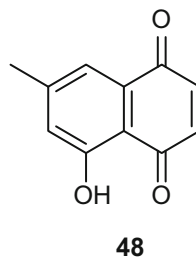
active component of *Euclea natalensis* root extracts, which displays antitubercular activity. Mahapatra et al. [7] showed that 7-methyljuglone exhibited the most potent and most selective antitubercular activity of all the compounds tested.

It is well known that HIV increases a person's susceptibility to TB infection due to the decline of CD4+ lymphocytes in number and function, resulting in a weakened immune system incapable of preventing the growth and local spread of *M.tb.* [104]. A challenge arises in the interaction of HIV and TB drugs in HIV and TB patients. For example, rifampicin has been recommended not to be used concurrently with almost all the anti-HIV NNRTIs and protease inhibitors due to their drug-drug interactions [105].

Therefore, there is an urgent need for new compounds that can target TB but do not interfere with drugs that are used to treat HIV. Xu et al. [105] embarked on the evaluation of anti-HIV active pyranocoumarins for their activity against *M.tb.* Focused libraries of compounds shown in Fig. 13.11 were synthesized and evaluated for their anti-TB activity in primary screening assays [105, 106].

VhaVenda traditional healers of the Limpopo Province, South Africa use *Lippia javanica* and *Carica papaya* to treat TB [107]. Other species such as *Chenopodium ambrosioides* L. (Amaranthaceae), *Nidorella anomala* Steetz, *Nidorella auriculata* DC., *Senecio serratuloides* DC. var. *serratuloides*, *Cassine papillosa* (Hochst) Kuntze, *Euclea natalensis* A.DC. and *Polygala myrtifolia* L. were found to be active against *M. tuberculosis* (MIC < 100 mg/ml) [108].

Compounds shown to be active were further assessed for MIC values. The amino derivatives (**58–60**) exhibited MIC values of 16 μg/mL each (Fig. 13.12) [105].

13.3.10.1   1-*N*-Iminosugars

Two 1-*N*-iminosugars, **61** and **62**, have been prepared as hexofuranose analogs in an efficient manner by a Ring Closing Metathesis-based route (Fig. 13.13) [109]. Both 3,4-disubstituted pyrrolidines displayed moderate inhibitory activity against *Mycobacterium smegmatis* galactan biosynthesis.

The two iminosugars **61** and **62** inhibit the biosynthesis of polysaccharides known as galactans. The main constituents of the galactans, galactofuranose residues, are not encountered in mammalian metabolism. Galactan biosynthesis, therefore, constitutes an attractive target for potential new TB drugs lacking deleterious side effects.

13.3.10.2   Phenoxyacetic Acid Derivatives

A series of phenoxyacetic acid derivatives have also been synthesized and the in vitro activity of the synthesized compounds against *M.tb.* H37Rv (MTB) and INH-resistant *M.tb.* (INHR-MTB) was studied [110].

Among the synthesized compounds, compound **63** (Fig. 13.14) was found to be the most active against *M.tb.* H37Rv (MTB) and INH-resistant *M.tb* (INHR-MTB) with minimum inhibitory concentration of 0.06 μg/ml.

(+)-Calanolide A
49

(-)-Calanolide A
50

(-)-Calanolide B
51

Soulattrolide
52

(-)-7,8-Dihydrocalanolide B
53

7,8-Dihydrosoulattrolide
54

(+)-12-Oxocalanolide A
55

(+/-)-7,8-Dihydro-12-oxocalanolide A
56

(+/-)-Calanolide D
57
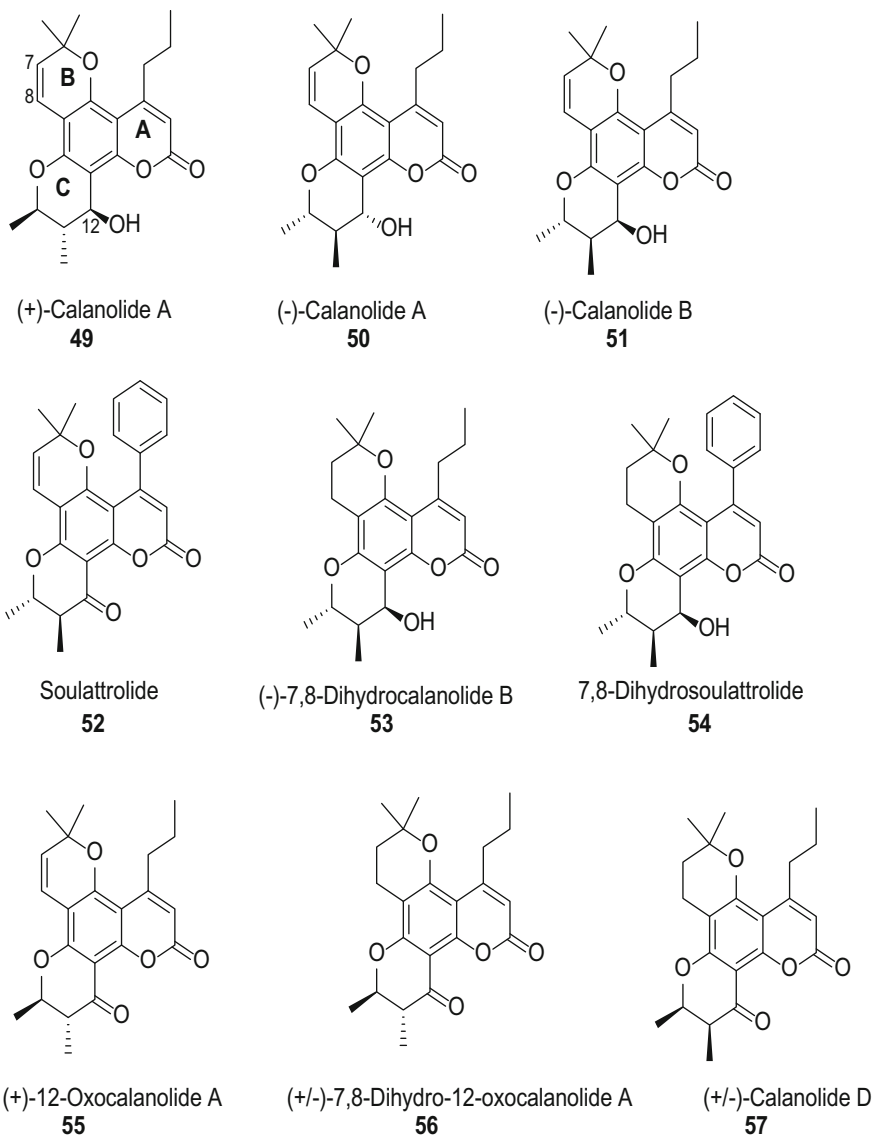
Fig. 13.11 Structures of pyranocoumarin compounds tested against *M. tuberculosis*
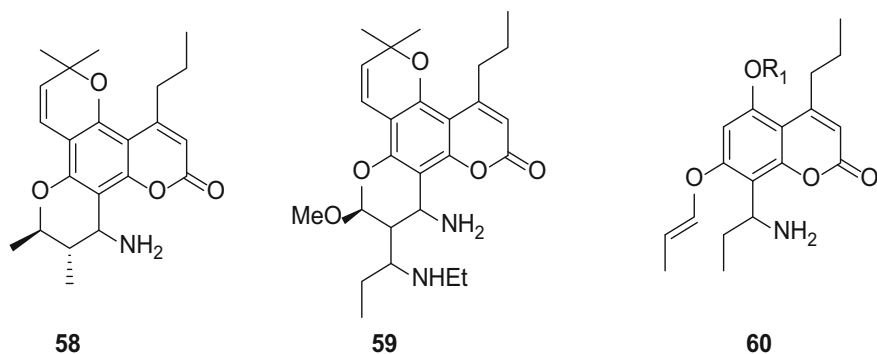
Fig. 13.12 Amino pyranocoumarin derivatives [105]

Fig. 13.13 Structure of iminosugars [109]
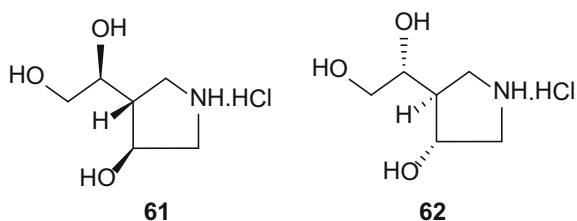
Fig. 13.14 Structure of phenoxyacetic acid derivative **63** [110]
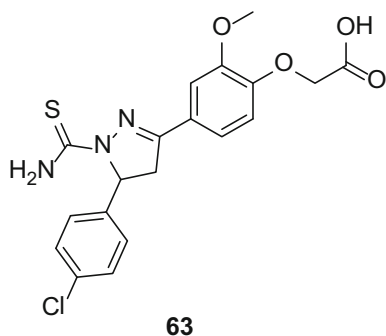
13.3.10.3 Diarylquinolines

Koul et al. [111] reported the antimycobacterial properties of diarylquinolines (DARQs). Chemical optimization of a lead compound led to a series of DARQs with potent in vitro activity against several mycobacteria, including *M.tb*. Molecules of the DARQ series have an MIC below 0.5 μg/ml against *M.tb*. H37Rv.

Antimycobacterial activity was confirmed in vivo for three of these compounds and the most active compound of the class, R207910 **64** ($MIC_{99} = 0.06$ μg/mL), is a pure enantiomer with two chiral centers. The lead compound, R207910 **64**, not only
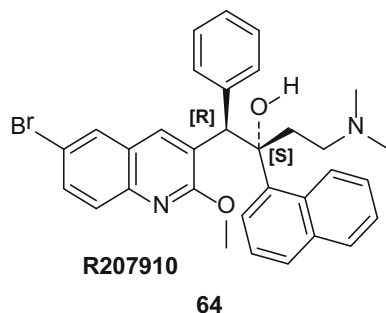
Fig. 13.15   Structure of diarylquinoline derivative **64** [111]

has several properties, both in vitro and in vivo, that may improve the treatment of TB, but also appears to act as a new target, providing an antimycobacterial spectrum different from those of current drugs (Fig. 13.15). Its clinical potential is currently being tested in patients.

13.4   Conclusion

After careful review with respect to first-line TB drugs and second-line TB drugs of their mode of action, it becomes significant that the compounds have offered a significant approach towards the treatment of *Mycobacterium tuberculosis (M.tb.)*. Therefore, understanding the mechanisms of mycobacterial action to the anti-tuberculosis drugs not only enables the development of more rapid molecular diagnostic tests and furnishes implications for designing new anti-tuberculosis drugs, but it also helps to implement measures to prevent the development resistance. Nevertheless, the development of drug resistance methods in patients and the factors supporting resistance development are poorly understood and necessitate further investigations. To this effect, the findings suggest further development of anti-TB agents that may contribute to the improvement of future chemotherapeutic agents from medicinal plants. The plants contain a diverse class of compounds which possess biologically active agents with activity against *Mycobacterium tuberculosis (M.tb.)*. Isolated active compounds from plant parts have exhibited excellent antitubercular activities, with IC_{50} values comparable to those of standard drugs.

References

1. Koch R (1982) The etiology of tuberculosis. Berl Klinische Wochenschr 19:221–230
2. WHO (1994) TB: a global emergency. WHO report on the TB epidemic (WHO/TB/94.177). Geneva, Switzerland. http://apps.who.int/iris/handle/10665/58749
3. World Health Organization (2018) Global tuberculosis report 2018. World Health Organization. http://www.who.int/iris/handle/10665/274453
4. WHO (2012) Tuberculosis, WHO report. http://www.who.int/mediacentre/factsheets/fs104/en/
5. WHO (2006) Global tuberculosis control: surveillance, planning, financing. WHO report. http://www.who.int/tb/publications/global_report/en/index.html
6. World Health Organization (2016) Global tuberculosis report. http://apps.who.int/medicinedocs/documents/s23098en/s23098en.pdf
7. Mahapatra A, Mativandlela SP, Binneman B, Fourie PB, Hamilton CJ, Meyer JJ, van der Kooy F, Houghton P, Lall N (2007) Activity of 7-methyljuglone derivatives against *Mycobacterium tuberculosis* and as subversive substrates for mycothiol disulfide reductase. Bioorg Med Chem 15:7638–7646
8. Sriram D, Yogeeswari P, Madhu K (2005) Synthesis and in vitro and in vivo antimycobacterial activity of isonicotinoyl hydrazones. Bioorg Med Chem Lett 15:4502–4505
9. McDermott W, Muschenheim C, Hadley SJ, Bunn PA, Gorman RV (1947) Streptomycin in the treatment of tuberculosis in humans: I. Meningitis and generalized hematogenous tuberculosis. Ann Intern Med 27:769–822
10. Mathema B, Kurepina NE, Bifani PJ, Kreiswirth BN (2006) Molecular epidemiology of tuberculosis: current insights. Clin Microbiol Rev 19:658–685
11. Youmans GP, Williston EH, Feldman WH, Hinshaw CH (1946) Increase in resistance of Tubercle bacilli to streptomycin: a preliminary report. Proc Mayo Clin 21:126–127
12. De Rosa M, Gising J, Odell LR, Larhed M (2014) Syntheses of new tuberculosis inhibitors promoted by microwave irradiation. Ups J Med Sci 119:181–191
13. David HL (1971) Resistance to D-cycloserine in the tubercle bacilli: mutation rate and transport of alanine in parental cells and drug-resistant mutants. Appl Microbiol 21:888–892
14. David HL, Newman CM (1971) Some observations on the genetics of isoniazid resistance in the tubercle bacilli. Am Rev Respir Dis 104:508–515
15. A Medical Research Council Investigation (1950) Treatment of pulmonary tuberculosis with streptomycin and para-amino-salicylic acid. Br Med J 2:1073–1085
16. Canetti G, Grossett J (1961) Percentage of isoniazid-resistant and streptomycin-resistant variants in wild strains of *Mycobacterium tuberculosis* on Loewenstein-Jensen medium. Ann Inst Pasteur (Paris) 101:28–46
17. Canetti G, Sutherland I, Svandova E (1972) Endogenous reactivation and exogenous reinfection: their relative importance with regard to the development of non-primary tuberculosis. Bull Int Union Tuberc 47:116–134
18. Kochi A, Vareldzis B, Styblo K (1993) Multidrug-resistant tuberculosis and its control. Res Microbiol 144:104–110
19. Centers for Disease Control and Prevention (CDC) (2003) Trends in aging–United States and worldwide. MMWR Morb Mortal Wkly Rep 52:101–104
20. Sycheva TP, Pavlova TN, Shchukina MN (1972) Synthesis of isoniazid from 4-cyanopyridine. Pharm Chem J 6:696–698
21. Zhang Y, Heym B, Allen B, Young D, Cole S (1992) The catalase-peroxidase gene and isoniazid resistance of *Mycobacterium tuberculosis*. Nature 358:591–593
22. Gangadharam PR, Harold FM, Schaefer WB (1963) Selective inhibition of nucleic acid synthesis in *Mycobacterium tuberculosis* by isoniazid. Nature 198:712–714
23. Brennan PJ, Rooney SA, Winder FG (1970) The lipids of *Mycobacterium tuberculosis* BCG: fractionation, composition, turnover and the effects of isoniazid. Ir J Med Sci 3:371–390
24. Zatman LJ, Kaplan NO, Colowick SP, Ciotti MM (1954) Effect of isonicotinic acid hydrazide on diphosphopyridine nucleotidases. J Biol Chem 209:453–466

25. Bekierkunst A (1966) Nicotinamide-adenine dinucleotide in tubercle bacilli exposed to iso-niazid. Science 152:525–526

26. Winder FG, Collins PB (1970) Inhibition by isoniazid of synthesis of mycolic acids in *Mycobacterium tuberculosis*. J Gen Microbiol 63:41–48

27. Takayama K, Wang L, David HL (1972) Effect of isoniazid on the *in vivo* mycolic acid synthesis, cell growth, and viability of *Mycobacterium tuberculosis*. Antimicrob Agents Chemother 2:29–35

28. Takayama K, Schnoes HK, Armstrong EL, Boyle RW (1975) Site of inhibitory action of isoniazid in the synthesis of mycolic acids in *Mycobacterium tuberculosis*. J Lipid Res 16:308–317

29. Banerjee A, Dubnau E, Quemard A, Balasubramanian V, Um KS, Wilson T, Collins D, de Lisle G, Jacobs WR Jr (1994) InhA, a gene encoding a target for isoniazid and ethionamide in *Mycobacterium tuberculosis*. Science 263:227–230

30. Karakousis PC (2009) Mechanisms of action and resistance of antimycobacterial agents. In: Mayers DL (ed) Antimicrobial drug resistance. Springer, pp 271–291

31. Martilla HJ, Soini H, Eerola E, Vyshnevskaya E, Vyshnevskly BI, Otten TF, Vasilyef AV, Viljanene MK (1998) A Ser315Thr substitution in KatG is predominant in genetically heterogeneous multidrug-resistant *Mycobacterium tuberculosis* isolates originating from the St. Petersburg area in Russia. Antimicrob Agents Chemother 42:2443–2445

32. Rouse DA, DeVito JA, Li Z, Byer H, Morris SL (1996) Site-directed mutagenesis of the katG gene of *Mycobacterium tuberculosis*: effects on catalase-peroxidase activities and isoniazid resistance. Mol Microbiol 22:583–592

33. Wade MM, Zhang Y (2004) Mechanisms of drug resistance in *Mycobacterium tuberculosis*. Front Biosci 9:975–994

34. Mitchison DA (1985) The action of antituberculosis drugs in short-course chemotherapy. Tubercle 66:219–225

35. Scorpio A, Zhang Y (1996) Mutations in pncA, a gene encoding pyrazinamidase/nicotinamidase, cause resistance to the antituberculous drug pyrazinamide in tubercle bacillus. Nat Med 2:662–667

36. Scorpio A, Lindholm-Levy P, Heifets L, Gilman R, Siddiqi S, Cynamon M, Zhang Y (1997) Characterization of pncA mutations in pyrazinamide-resistant *Mycobacterium tuberculosis*. Antimicrob Agents Chemother 41:540–543

37. Juréen P, Werngren J, Toro JC, Hoffner S (2008) Pyrazinamide resistance and pncA gene mutations in *Mycobacterium tuberculosis*. Antimicrob Agents Chemother 52:1852–1854

38. Raynaud C, Lanéelle MA, Senaratne RH, Draper P, Lanéelle G, Daffé M (1999) Mechanisms of pyrazinamide resistance in mycobacteria: importance of lack of uptake in addition to lack of pyrazinamidase activity. Microbiology 145:1359–1367

39. Peck RL, Hoffhine CE Jr, Folkers K (1946) Streptomyces antibiotics. IX: Dihydrostreptomycin. J Am Chem Soc 68:1390–1391

40. Tatsuoka S, Kusaka T, Miyake A, Inoue M, Hitomi H, Shiraishi Y, Iwasaki H, Imanishi M (1957) Studies on antibiotics. XVI. Isolation and identification of dihydrostreptomycin produced by a new streptomyces, *Streptomyces humidus* nov. sp. Pharm Bull 5:343–349

41. Ophardt CE (2003) Introduction to drug action: other antibiotics. http://chemistry.elmhurst.edu/vchembook/654antibiotic.html

42. Stauffer CS, Datta A (2002) Efficient synthesis of (S, S)-ethambutol from l-methionine. Tetrahedron 58:9765–9767

43. Mikusová K, Slayden RA, Besra GS, Brennan PJ (1995) Biogenesis of the mycobacterial cell wall and the site of action of ethambutol. Antimicrob Agents Chemother 39:2484–2489

44. Belanger AE, Besra GS, Ford ME, Mikusová K, Belisle JT, Brennan PJ, Inamine JM (1996) The embAB genes of Mycobacterium avium encode an arabinosyl transferase involved in cell wall arabinan biosynthesis that is the target for the antimycobacterial drug ethambutol. Proc Natl Acad Sci USA 93:11919–11924

45. Escuyer VE, Lety MA, Torrelles JB, Khoo KH, Tang JB, Rithner CD, Frehel C, McNeil MR, Brennan PJ, Chatterjee D (2001) The role of the embA and embB gene products in the biosynthesis of the terminal hexaarabinofuranosyl motif of *Mycobacterium smegmatis* arabinogalactan. J Biol Chem 276:48854–48862

46. Sreevatsan S, Stockbauer KE, Pan X, Kreiswirth BN, Moghazeh SL, Jacobs WR, Telenti A, Musser JM (1997) Ethambutol resistance in *Mycobacterium tuberculosis*: critical role of embB mutations. Antimicrob Agents Chemother 41:1677–1681

47. Sensi P (1983) History of the development of rifampin. Rev Infect Dis Suppl 3:S402–S406

48. Bruzzese T (1997) https://patents.google.com/patent/US4174320

49. Telenti A, Imboden P, Marchesi F, Lowrie D, Cole S, Colston MJ, Matter L, Schopfer K, Bodmer T (1993) Detection of rifampicin-resistance mutations in *Mycobacterium tuberculosis*. Lancet 341:647–650

50. Ramaswamy S, Musser JM (1998) Molecular genetic basis of antimicrobial agent resistance in *Mycobacterium tuberculosis*: 1998 update. Tuber Lung Dis 79:3–29

51. Musser JM (1995) Antimicrobial agent resistance in mycobacteria: molecular genetic insights. Clin Microbiol Rev 8:496–514

52. Ginsberg AM (2010) Drugs in development for tuberculosis. Drugs 70:2201–2214

53. Alqahtani JM, Asaad AM (2014) Anti-tuberculous drugs and susceptibility testing methods: current knowledge and future challenges. J Mycobac Dis 4:140

54. Nugent B, Parker MJ, McIntyre IA (2010) Nasogastric tube feeding and percutaneous endoscopic gastrostomy tube feeding in patients with head and neck cancer. J Hum Nutr Diet 23:277–284

55. Mitchison DA (2004) The search for new sterilizing anti-tuberculosis drugs. Front Biosci 9:1059–1072

56. Mitchison DA (2005) Shortening the treatment of tuberculosis. Nat Biotechnol 23:187–188

57. Ahmad Z, Fraig MM, Bisson GP, Nuermberger EL, Grosset JH, Karakousis PC (2011) Dose-dependent activity of pyrazinamide in animal models of intracellular and extracellular tuberculosis infections. Antimicrob Agents Chemother 55:1527–1532

58. Gillespie SH, Kennedy N (1998) Fluoroquinolones: a new treatment for tuberculosis? Int J Tuberc Lung Dis 2:265–271

59. Berning SE (2001) The role of fluoroquinolones in tuberculosis today. Drugs 61:9–18

60. Ginsburg AS, Grosset JH, Bishai WR (2003) Fluoroquinolones, tuberculosis, and resistance. Lancet Infect Dis 3:432–442

61. Paramasivan CN, Sulochana S, Kubendiran G, Venkatesan P, Mitchison DA (2005) Bactericidal action of gatifloxacin, rifampin, and isoniazid on logarithmic- and stationary-phase cultures of *Mycobacterium tuberculosis*. Antimicrob Agents Chemother 49:627–631

62. Stein GE (1996) Pharmacokinetics and pharmacodynamics of newer fluoroquinolones. Clin Infect Dis Suppl 1:S19–S24

63. Alvirez-Freites EJ, Carter JL, Cynamon MH (1996) *In vitro* and *in vivo* activities of gatifloxacin against *Mycobacterium tuberculosis*. Antimicrob Agents Chemother 46:1022–1025

64. Fung-Tomc J, Minassian B, Kolek B, Washo T, Huczko E, Bonner D (2000) *In vitro* antibacterial spectrum of a new broad-spectrum 8-methoxy fluoroquinolone, gatifloxacin. J Antimicrob Chemother 45:437–446

65. Gillespie SH, Billington O (1999) Activity of moxifloxacin against mycobacteria. J Antimicrob Chemother 44:393–395

66. Gillespie SH, Morrissey I, Everett D (2001) A comparison of the bactericidal activity of quinolone antibiotics in a *Mycobacterium fortuitum* model. J Med Microbiol 50:565–570

67. Nuermberger E, Grosset J (2004) Pharmacokinetic and pharmacodynamic issues in the treatment of mycobacterial infections. Eur J Clin Microbiol Infect Dis 23:243–255

68. Hu Y, Coates ARM, Mitchison DA (2003) Sterilizing activities of fluoroquinolones against rifampin-tolerant populations of *Mycobacterium tuberculosis*. Antimicrob Agents Chemother 47:653–657

69. Ji B, Lounis N, Maslo C, Truffot-Pernot C, Bonnafous P, Grosset J (1998) *In vitro* and *in vivo* activities of moxifloxacin and clinafloxacin against *Mycobacterium tuberculosis*. Antimicrob Agents Chemother 42:2066–2069

70. Shandil RK, Jayaram R, Kaur P, Gaonkar S, Suresh BL, Mahesh BN, Jayashree R, Nandi V, Bharath S, Balasubramanian V (2007) Moxifloxacin, ofloxacin, sparfloxacin, and ciprofloxacin against *Mycobacterium tuberculosis*: evaluation of *in vitro* and pharmacodynamic indices that best predict in vivo efficacy. Antimicrob Agents Chemother 51:576–582

71. Hazra B, Sur P, Roy DK, Sur B, Banerjee A (1984) Biological activity of diospyrin against Ehrlich ascites carcinoma in Swiss A mice. Planta Med 51:295–297

72. Zhao YL, Chen YL, Sheu JY, Chen IL, Wang TC, Tzeng CC (2005) Synthesis and antimycobacterial evaluation of certain fluoroquinolone derivatives. Bioorg Med Chem 13:3921–3926

73. Sriram D, Yogeeswari P, Devakaram RV (2006) Synthesis, *in vitro* and *in vivo* antimycobacterial activities of diclofenac acid hydrazones and amides. Bioorg Med Chem 14:3113–3118

74. Bock NN, Sterling TR, Hamilton CD, Pachucki C, Wang YC, Conwell DS, Mosher A, Samuels M, Vernon A, Tuberculosis Trials Consortium, Centers for Disease Control and Prevention, Atlanta, Georgia (2002) A prospective, randomized, double-blind study of the tolerability of rifapentine 600, 900, and 1,200 mg plus isoniazid in the continuation phase of tuberculosis treatment. Am J Respir Crit Care Med 165:1526–1530

75. Shoen CM, DeStefano MS, Cynamon MH (2000) Durable cure for tuberculosis: rifalazil in combination with isoniazid in a murine model of *Mycobacterium tuberculosis* infection. Clin Infect Dis Suppl 3:S288–S290

76. Barrett JF (2000) Linezolid pharmacia corp. Curr Opin Investig Drugs 1:181–187

77. Stover CK, Warrener P, Van Devanter DR, Sherman DR, Arain TM, Langhorne MH, Anderson SW, Towell JA, Yuan Y, McMurray DN, Kreiswirth BN, Barry CE, Baker WR (2000) A small-molecule nitroimidazopyran drug candidate for the treatment of tuberculosis. Nature 405:962–966

78. Mtunzi FM, Ejidike IP, Ledwaba I, Ahmed A, Pakade VE, Klink MJ, Modise SJ (2017) Solvent-solvent fractionations of *Combretum erythrophyllum* (Burch.) leave extract: studies of their antibacterial, antifungal, antioxidant and cytotoxicity potentials. Asian Pac J Trop Med 10:670–679

79. Osman SA, Abdalla AA, Alaib MO (1983) Synthesis of sulfanilamido-naphthoquinones as potential antituberculous agents. J Pharm Sci 72:68–71

80. Roushdi IM, Ibrahim ESA, Habib NS (1976) Synthesis of 1.4-naphthoquinones-4-aryl(aroyl)hydrazones of potential antimicrobial activity. Pharmazie 31:856–859

81. Devi Bala B, Muthusaravanan S, Choon TS, Ashraf Ali M, Perumal S (2014) Sequential synthesis of amino-1,4-naphthoquinone-appended triazoles and triazole-chromene hybrids and their antimycobacterial evaluation. Eur J Med Chem 85:737–746

82. Ravichandiran P, Premnath D, Vasanthkumar S (2014) Synthesis, molecular docking and antibacterial evaluation of new 1,4-naphthoquinone derivatives contains carbazole-6,11-dione moiety. J Chem Biol 7:93–101

83. Jordão AK, Novais J, Leal B, Escobar AC, dos Santos HM, Jr Castro HC, Ferreira VF (2013) Synthesis using microwave irradiation and antibacterial evaluation of new N, O-acetals and N, S-acetals derived from 2-amino-1,4-naphthoquinones. Eur J Med Chem 63:196–201

84. Brinkworth RI, Fairlie DP (1995) Hydroxyquinones are competitive non-peptide inhibitors of HIV-1 proteinase. Biochim Biophys Acta 1253:5–8

85. Crosby IT, Bourke DG, Jones ED, de Bruyn PJ, Rhodes D, Vandegraaff N, Cox S, Coates JAV, Robertson AD (2010) Antiviral agents 2. Synthesis of trimeric naphthoquinone analogues of conocurvone and their antiviral evaluation against HIV. Bioorg Med Chem 18:6442–6450

86. Mahapatra A, Tshikalange TE, Meyer JJM, Lall N (2012) Synthesis and HIV-1 reverse transcriptase inhibition activity of 1,4-naphthoquinone derivatives. Chem Nat Comp 47:883–887

87. Salmon-Chemin L, Buisine E, Yardley V, Kohler S, Debreu MA, Landry V, Sergheraert C, Croft SL, Krauth-Siegel RL, Davioud-Charvet E (2001) 2- and 3-substituted 1,4-naphthoquinone derivatives as subversive substrates of trypanothione reductase and lipoamide dehydrogenase from Trypanosoma cruzi: synthesis and correlation between redox cycling activities and in vitro cytotoxicity. J Med Chem 44:548–565

88. Pinto AV, de Castro SL (2009) The trypanocidal activity of naphthoquinones: a review. Molecules 14:4570–4590

89. López López LI, Nery Flores SD, Silva Belmares SY, Sáenz Galindo A (2014) Naphthoquinones: biological properties and synthesis of lawsone and derivatives—a structured review. Vitae 21:248–258

90. Kumar D, Sharma P, Singh H, Nepali K, Gupta GK, Jain SK, Ntie-Kang F (2017) The value of pyrans as anticancer scaffolds in medicinal chemistry. RSC Adv 7:36977–36999

91. Bhasin D, Chettiar SN, Etter JP, Mok M, Li PK (2013) Anticancer activity and SAR studies of substituted 1,4-naphthoquinones. Bioorg Med Chem 21:4662–4669

92. Qiu HY, Wang PF, Lin HY, Tang CY, Zhu HL, Yang YH (2018) Naphthoquinones: a continuing source for discovery of therapeutic antineoplastic agents. Chem Biol Drug Des 91:681–690

93. Yardley V, Snowdon D, Croft S, Hazra B (1996) *In vitro* activity of diospyrin and derivatives against *Leishmanial donovani*, *Trypanosoma cruzi* and *Trypanosoma brucei brucei*. Phytother Res 10:559

94. Schuck DC, Ferreira SB, Cruz LN, da Rocha DR, Moraes MS, Nakabashi M, Rosenthal PJ, Ferreira VF, Garcia CR (2013) Biological evaluation of hydroxynaphthoquinones as antimalarials. Malar J 12:234

95. Sharma A, Santos IO, Gaur P, Ferreira VF, Garcia CR, da Rocha DR (2013) Addition of thiols to o-quinone methide: new 2-hydroxy-3-phenylsulfanylmethyl[1,4]naphthoquinones and their activity against the human malaria parasite *Plasmodium falciparum* (3D7). Eur J Med Chem 59:48–53

96. Diogo EBT, Dias GG, Rodrigues BL, Guimarães TT, Valença WO, Camara CA, Oliveira RN, Silva MG, Ferreira VF, Paiva YG, Goulart MOF, Menna-Barreto RFS, Castro SL, Silva Junior EN (2013) Synthesis and anti-Trypanosoma cruzi activity of naphthoquinone-containing triazoles: electrochemical studies on the effects of the quinoidal moiety. Bioorgan Med Chem 21:6337–6348

97. Riffel A, Medina LF, Stefani V, Santos RC, Bizani D, Brandelli A (2002) *In vitro* antimicrobial activity of a new series of 1,4-naphthoquinones. Braz J Med Biol Res 35:811–818

98. Mbaveng AT, Kuete V (2014) Review of the chemistry and pharmacology of 7-methyljugulone. Afr Health Sci 14:201–205

99. Pawar O, Patekar A, Khan A, Kathawate L, Haram S, Markad G, Puranik V, Salunke-Gawalia S (2014) Molecular structures and biological evaluation of 2-chloro-3-(*n*-alkylamino)-1,4-naphthoquinone derivatives as potent antifungal agents. J Mol Struct 1059:68–74

100. Castro MA, Gamito AM, Tangarife-Castaño V, Zapata B, Miguel del Corral JM, Mesa-Arango AC, Betancur-Galvis L, San Feliciano A (2013) Synthesis and antifungal activity of terpenyl-1,4-naphthoquinone and 1,4-anthracenedione derivatives. Eur J Med Chem 67:19–27

101. Pemán J, Salavert M, Quindós G (2014) Invasive infection diseases by filamentous fungi. Rev Iberoam Micol 31:211–212

102. Gouda MA, Eldien HF, Girges MM, Berghot MA (2013) Synthesis and antioxidant activity of novel series of naphthoquinone derivatives attached to benzothiophene moiety. Med Chem 3:228–232

103. Babula P, Adam V, Havel L, Kizek R (2007) Naphthoquinones and their pharmacological properties. Ceska Slov Farm 56:114–120

104. Borin MT, Chambers JH, Carel BJ, Gagnon S, Freimuth WW (1997) Pharmacokinetic study of the interaction between rifampin and delavirdine mesylate. Clin Pharmacol Ther 61:544–553

105. Xu Z-Q, Pupek K, Suling WJ, Enache L, Flavin MT (2006) Pyranocoumarin, a novel anti-TB pharmacophore: synthesis and biological evaluation against *Mycobacterium tuberculosis*. Bioorg Med Chem 14:4610–4626

106. (a) Lele AC, Raju A, Khambete MP, Ray MK, Rajan MG, Arkile MA, Jadhav NJ, Sarkar D, Degani MS (2015) Design and synthesis of a focused library of diamino triazines as potential *mycobacterium tuberculosis* DHFR inhibitors. ACS Med Chem Lett 6:1140–1144 (b) Shaharyar M, Siddiqui AA, Ali MA, Sriram D, Yogeeswari P (2006) Synthesis and in vitro antimycobacterial activity of N1-nicotinoyl-3-(4'-hydroxy-3'-methyl phenyl)-5-[(sub)phenyl]-2-pyrazolines. Bioorg Med Chem Lett 16:3947–3949

107. Green E, Samie A, Obi CL Bessong PO, Ndip RN (2010) Inhibitory properties of selected South African medicinal plants against *Mycobacterium tuberculosis*. J Ethnopharmacol 130:151–157

108. Lall N, Meyer JJM (1999) In vitro inhibition of drug-resistant and drug sensitive strains of *Mycobacterium tuberculosis* by ethnobotanically selects South African plants. J Ethnopharmacol 66:347–354

109. Cren S, Wilson C, Thomas NR (2005) A rapid synthesis of hexofuranose-like iminosugars using ring-closing metathesis. Org Lett 7:3521–3523

110. (a) Ali MA, Shaharyar M (2007) Discovery of novel phenoxyacetic acid derivatives as antimycobacterial agents. Bioorg Med Chem 15:1896–1902 (b) Shaharyar M, Ali MA, Bakht MA, Murugan V (2008) Synthesis and antimycobacterial activity of 4-[5-(substituted phenyl)-4,5-dihydro-3-isoxazolyl]-2-methylphenols. J Enzyme Inhib Med Chem 23:432–436

111. (a) Koul A, Vranckx L, Dendouga N, Balemans W, Van den Wyngaert I, Vergauwen K, Göhlmann HW, Willebrords R, Poncelet A, Guillemont J, Bald D, Andries K (2008) Diarylquinolines are bactericidal for dormant mycobacteria as a result of disturbed ATP homeostasis. J Biol Chem 283:25273–25280 (b) Andries K, Verhasselt P, Guillemont J, Göhlmann HW, Neefs JM, Winkler H, Van Gestel J, Timmerman P, Zhu M, Lee E, Williams P, de Chaffoy D, Huitric E, Hoffner S, Cambau E, Truffot-Pernot C, Lounis N, Jarlier V (2005) A diarylquinoline drug active on the ATP synthase of *Mycobacterium tuberculosis*. Science 307:223–227

Chapter 14
Multivariate Analysis of Airborne Metallic Species in Sebele, Botswana

Sello Alfred Likuku and Khumoetsile Mmolawa

Abstract A total of 63 aerosol samples were collected at the Botswana University of Agriculture and Natural Resources (formerly, Botswana College of Agriculture) during the period of 02 April 2008–07 December 2008 and were analysed for concentrations of Al, Co, Cu, Fe, Pb, Mn, Ni and Zn using flame atomic absorption spectroscopy. Statistical receptor models were applied to investigate potential sources of the studied metals. Data exhibited enhanced enrichments of Zn (EFg = 76), Al (EFg = 14,391), Co (EFg = 19), Cu (EFg = 5), Pb (EFg = 3) and Ni (EFg = 2), which were attributed to contributions from non-crustal sources, whereas Mn and Fe (EFg < 2) were attributed to crustal origin, such as airborne dust. Data were subjected to principal component analysis (PCA) twice. From PCA-1, two principal components (PC) were revealed. PC-1 showed high positive loadings of Pb, Zn, Ni and Al, whereas PC-2 had loadings for Fe and Mn. On the other hand, PCA-2 had three principal components. PC-1 from PCA-2 showed strong loadings for Cu, Fe and Mn. PC-2 had strong loadings of Pb, Al and Zn, whereas loadings for PC-3 were comprised of Ni and Co. The difference between loadings of PCA-1 and PCA-2 suggested possibilities of mixed origins of the studied metals. Finally, air mass back-trajectory analysis showed that during the sampling period, there were only 5 cluster groups that represented significantly different transport pathways of aerosol samples, where only Zn and Ni mean concentrations revealed dependence on geographical origin of aerosol samples. Results of the analysed concentrations of Al, Co, Cu, Fe, Pb, Mn, Ni and Zn in aerosol samples showed that the presence of Fe and Mn in the atmosphere in the ambient air of Sebele is mainly due to contributions from lithogenic sources. Pb, Ni, Co, Al and Zn exist because of anthropogenic sources, whereas presence of Cu arises because of mixed origins. Trajectory analysis further

S. A. Likuku (✉)
Department of Physical Chemical Sciences, Botswana University of Agriculture and Natural Resources, Private Bag 0027, Gaborone, Botswana
e-mail: alikuku@buan.ac.bw; likuku_as@yahoo.com

K. Mmolawa
Department of Agricultural and Biosystems Engineering, Botswana University of Agriculture and Natural Resources, Private Bag 0027, Gaborone, Botswana
e-mail: kmmolawa@buan.ac.bw

shows that the anthropogenic Zn and Ni could also be present in the air sampled due to air mass transportation from distant sources.

Keywords Heavy metals · Geometric enrichment factors · Factor analysis · Back-trajectory analysis · Principal component analysis

14.1 Introduction

Airborne particulate matter is introduced in the atmosphere from a variety of natural (involving wind-blown dust) and anthropogenic (such as industrial processes and automobile emissions) sources and are small enough to be suspended in the air [1, 2]. These have negative effects on air quality and human health such as increased incidence of cardiovascular and respiratory diseases [3]. According to reports by the World Health Organisation, around 7 million people died in 2012 as a result of air pollution exposure [4]. These findings were based on data revealing strong links between both indoor and outdoor air pollution exposure and cardiovascular diseases, such as strokes and ischaemic heart disease, as well as between air pollution and cancer.

Research has revealed that the chemical composition of particulate matter, such as the presence of small amounts of toxic chemicals, is a more appropriate parameter for the assessment of particulate health effects as opposed to their mass concentrations [5, 6]. Thus, metallic species are a class of atmospheric pollutants that are key determinants of the health effects of particulate matter and appropriate identification and quantification of their sources and a comprehensive assessment of the risks they pose to human health are essential in prioritising mitigation requirements.

In light of the above, we characterised ambient concentrations of airborne metallic species with respect to eight elements: Al, Co, Cu, Fe, Pb, Mn, Ni and Zn in aerosol samples collected from Sebele, approximately 8 km from the capital city, Gaborone. Botswana is a moderately industrialised country with a relatively sparse population and pollution is probably not perceived to be a major problem at present. However, widespread vegetation fires and dust in the dry winter months result in high background levels of aerosols and ozone. Other sources of atmospheric pollution in Botswana are emissions of ultra-fine fly ash particles enriched with Co, Pb and Mn from the copper-nickel smelter emissions and the coal-powered Morupule power station in Palapye, which are approximately 400 and 300 km north east of the sampling station, respectively.

Recently, there has been an increasing influx of grey imports of passenger and other types of vehicles which are widely used within the city of Gaborone and many other major towns and villages in Botswana. These, together with an increased growth of light industry, could be a future source of air pollutants that may also lead to greater air pollution impacts.

This chapter brings together knowledge and skills attained through a research project entitled: "Factors influencing ambient air concentrations of pollutant species

in Gaborone". The chapter will elucidate heavy metal sources in particulate matter by applying multivariate statistical techniques and finally locate their geographical potential source regions via application of back-trajectories models.

14.2 Materials and Methods

14.2.1 Site Description

The climate controls of Botswana are influenced by the prevalent subtropical high-pressure belt that is dominant over southern Africa, which is, except in a few winter months (May–July), split by the continent to become the Atlantic Ocean High and the Indian Ocean High. The country has a semi-arid climate, with highly variable rainfall, both spatially and temporally. On annual averages, rainfall ranges from 250 mm in the extreme southwest to 650 mm in the extreme north [7]. The seasons are characterized by November–January (summer), February–April (autumn), May–July (winter) and August–October (spring). The summer months are generally wet and hot (20–40 °C), while the winter months are dry and cold (−5 to 20 °C).

The sampling site is approximately 8 km from the capital city of Botswana, Gaborone located within the Botswana University of Agriculture and Natural Resources on the roof top of a building which is 10 m above ground level (24.59° S, 25.94° E; 1004 m ASL). This site is close to commercial malls and the major highway with heavy traffic of the A1 road connecting the city and the northern part of the country (Fig. 14.1).
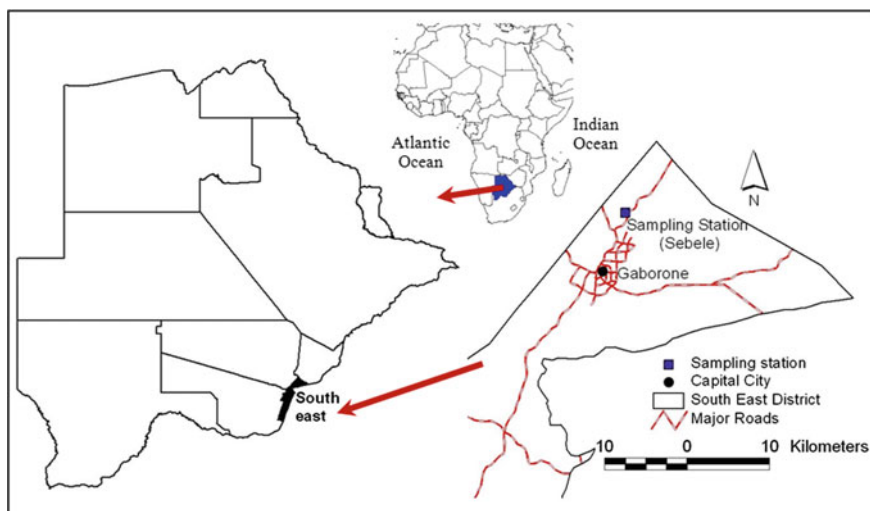
Fig. 14.1 Map of Botswana showing the sampling site in this study

14.2.2   Sampling Protocol

Collection of aerosol samples was done during the period of 02 April 2008–07 December 2008 and were analysed using a high volume sampler placed on the roof top and set to a flow rate of 1.7 m^3 min^{-1}. Sample duration was set to 72 h continuous sampling sucking in approximately 5000 m^3 through 20.3 by 24.5 cm glass fibre filter papers. The filter papers were preconditioned for 48 h in an oven at 25 °C and 40 ± 5% relative humidity and then weighed before and after the sampling using Sartorius ME 36S microbalance and concentrations were determined gravimetrically by subtracting the pre-sampling filter weight from post-sampling filter weight.

14.2.3   Chemical Processing and Analysis

Five hundred milligrams of the sample filters were digested in 20 ml freshly prepared aqua regia (1:3 HNO_3: HCl) on a hot plate for 3 h. After evaporation to dryness, samples were re-dissolved in 20 ml of 1% HNO_3, filtered through a 0.45 µm filter paper and then transferred into a 100 ml volumetric flask. The flask was filled to the mark with 1% HNO_3 v/v (diluted in deionised H_2O). Standard reference material was prepared using stock solution from SAARCHM and MERCK and was used to have a check on the accuracy of the results. The total concentrations of Al, Co, Cu, Fe, Pb, Mn, Ni and Zn in the filtrates were then determined using a flame atomic absorption spectrometer (Varian SpectrAA 220 FS) at wavelengths, λ (nm): Al = 309.3; Co = 240.7; Cu = 324.8; Fe = 372.0; Pb = 217.0; Mn = 279.5; Ni = 232.0 and Zn = 213.9, using air acetylene flame.

14.2.4   Analytical Quality Control

The National Institute of Standards and Technology (NIST) SRM 1649a (urban dust) was processed in the same way as the aerosol samples to validate experimental data obtained from extracted metal. Implementation of laboratory methods and laboratory quality assurance included the use of standard operating procedures, calibration with standards and analysis of reagent blanks outlined by Suvarapu and Baek [8]. The AAS was optimised and a calibration curve was produced using standards prepared from pipettes of 5 ml each of the 1000 mg/l stock solutions of Cu, Mn, Zn, Ni and 10 ml for Fe. Calibration curves for Cu, Mn, Zn, Ni and Fe were then prepared using the stock solutions. In the case of Co, 1.0 g of metal was dissolved with 1:1 nitric acid and the solution was diluted to 1 L to give 1000 µg/mL. For Al, 1.0 g was dissolved in 20 mL hydrochloric acid with the addition of a trace of a mercury salt to catalyze the reaction. Finally, the solution was diluted to give 1000 µg/mL Al. The calibration curves were linear in the concentration range with linear least-square fit regression

coefficients of $R^2 > 0.996$. The instrumental parameters were set depending on the type of analysis done and samples were analysed in triplicate to ensure precision. Data reported are the means computed from triplicate analysis. Relative standard deviation (RSDs) were less than 12%. The percent recovery of the analysed metals was between 85 and 115%.

14.3   Results and Discussion

14.3.1   Metal Concentrations

Time series of airborne metal concentration data, precipitation and wind speed during the sampling period are tabulated in the Appendix. Data revealed enhanced mean concentrations of Al (t = 10.57; df = 61; P = 0.0000) and Zn (t = 26.61; df = 61; P = 0.0000) for aerosols measurement collected during 02/04/08–19/05/08: 3900 ± 1400 ng/m³ for Al and 1400 ± 560 ng/m³ for Zn, compared to those obtained during the rest of sampling periods: 2300 ± 680 ng/m³ for Al and 60 ± 20 ng/m³ for Zn. Similarly, Pb was observed to exhibit a higher mean concentration (6 ± 2 ng/m³) during the same period but was almost undetectable in most samples during the rest of the sampling period. Nickel exhibits a high mean concentration (t = 4.67; df = 14; P = 0.0004) of 4 ± 1 ng/m³ during the 02/04/08–19/05/08 period as compared to the period 13/11/08–07/12/08 (mean concentration of 1.3 ± 0.3 ng/m³) and variable levels (ND-1.76 ng/m³) in between the two periods. Cobalt, however, showed relatively lower mean concentrations of 1.2 ± 0.3 ng/m³ (t = 8.92; df = 14; P = 0.0000) during the 02/04/08–19/05/08 period as compared to the period 13/11/08–07/12/08 (5 ± 1) ng/m³. There was no observable pattern in mean concentrations throughout the sampling period for the other studied metals (Cu, Fe and Mn).

Logarithmic transformation of data was performed to permit valid statistical inference for skewed metal concentration data and as a result, the geometric mean values were reported because they are a better measure of central tendency of this data type than the usual sample mean [9]. The aerosol data were log-normally distributed. The geometric mean and geometric standard deviations of the heavy metals with guidelines for specific metals are given in Table 14.1this. Observations showed a high variability (min–max) in the concentrations of each metal.

Correlation of the different elements in the air samples and meteorological parameters were calculated using the non-parametric Spearman Rank method. Table 14.2 shows the correlation between metals and some meteorological parameters (rainfall and wind speed). Significantly high negative correlation (P = 0.001) were observed between Cu, Fe, Mn, Ni and Pb with wind speed. Rainfall also revealed high (P = 0.001) negative correlations with Cu, Fe and Mn. No significant correlations were however observed between rainfall and Al, Co, Ni, Pb and Zn. Similarly, there were no significant correlations between wind speed and Al, Co and Zn. Inter-elemental correlations were also observed between some metals.

Table 14.1 Basic statistics for the measured aerosol concentrations with guidelines for specific metals

Metal	Measured metal concentrations (ng/m^3)			Emission guideline metal concentrations (ng/m^3)	
	Min–Max	GM	GSD	Annual averages	Reference source
Al	493.82–5354.18	1452.04	1.32	–	–
Co (2007)	0.13–262.69	2.03	1.36	5	United Kingdom Air Quality Standards [17]
Cu	0.94–35.43	2.74	1.24	–	–
Fe	37.22–1163.88	410.21	1.49	–	–
Mn	4.69–28.20	13.22	1.18	150	World Health Organization [18]
Ni (2007)	0.01–5.96	0.67	1.79	20	United Kingdom Air Quality Standards [17]
Pb	0.07–9.00	0.64	2.23	500	World Health Organization [18]
Zn	13.30–3224.44	92.70	5.17	–	–

14.3.2 Source Apportionment of Metallic Species

14.3.2.1 Enrichment Factor Analysis

Enrichment factors (EF) of metallic species in aerosol samples were determined based on the crustal abundance of elements given by Taylor [10] and that such elements, for example, Fe, Si, Al and Ti, have stable chemical composition, low spatial variability and are often less affected by human disturbances [11].

In this work Fe was used as first step in evaluating the degree of enrichment and the potential strength of metallic species emitting sources, following the method proposed by Zoller et al. [12] as described in Eq. (14.1).

$$EF = \frac{(Species/Fe)_{Air}}{(Species/Fe)_{Ref}} \tag{14.1}$$

where (Species/Fe)$_{Air}$ and (Species/Fe)$_{Ref}$ refer to concentration ratios of element to Fe in air and crust, respectively.

Evaluation of the geometric mean enrichment factor EF$_g$ for individual heavy metals was determined by Eq. (14.2) [13]:

Table 14.2 The Spearman rho correlation coefficients between heavy metals, rainfall and wind speed

	Al	Co	Cu	Fe	Mn	Ni	Pb	Zn	Rain	Wind
Al	1	0.34**	−0.05	−0.16	−0.07	0.31*	0.36**	0.66**	0.00	0.06
Co		1.00	−0.17	−0.39**	−0.37**	0.45**	0.50**	0.41**	0.17	0.15
Cu			1.00	0.56**	0.70**	0.13	0.22	−0.14	−0.42**	−0.40**
Fe				1.00	0.86**	0.05	−0.09	−0.27*	−0.48**	−0.34**
Mn					1.00	0.16	0.02	−0.20	−0.57**	−0.40**
Ni						1.00	0.59**	0.59**	−0.17	−0.43**
Pb							1.00	0.54**	−0.13	−0.43**
Zn								1.00	−0.01	−0.24
Rain									1.00	0.37**
Wind										1.00

**Correlation is significant at the 0.01 level (2-tailed); *Correlation is significant at the 0.05 level (2-tailed)

$$EF_g = \exp\left[\frac{1}{N}\sum_{i=1}^{N} EF_i\right] \tag{14.2}$$

where metallic species EF_g up to 2 are not considered to be enriched. Species with $2 < EF_g \leq 20$ are moderately enriched and those with $EF_g > 20$ are considered to be highly enriched and have different sources other than the crust.

Figure 14.2 presents results of geometrical enrichment factors of the metals.

The EF_g values of Zn ($EF_g = 76$) and Al ($EF_g = 14,391$) showed high enrichment of metals. Co ($EF_g = 19$), Cu ($EF_g = 5$), Pb ($EF_g = 3$) and Ni ($EF_g = 2$) are moderately enriched. Thus, these metals can be considered to possess contributions from non-crustal sources, whereas Mn and Fe ($EF_g < 2$) could be of crustal origin, such as the airborne dust.

Comparatively high mean concentrations of Al, Zn, Pb and Ni observed during sampling dates of 02/04/08–19/05/08 (bold dates in Appendix) compared to concentration means for the rest of sampling periods were ascribed to enhanced local dust emissions and anthropogenic activities. Aluminium generally comes from the crust due to its abundance in most soils whereas Zn, Pb and Ni may enter the atmosphere through industrial activities and burning of fossil fuel. During the period of 02/04/08–19/05/08 and before, there were a considerable number of soil excavation activities within the college campus, in preparation for construction of a number of buildings such as students' residential, lecture theaters and staff office blocks. This resulted in high Al concentrations due to local dust re-suspension by wind convection processes. Similarly, tear and wear and exhaust emission from machinery used during the excavation processes on the site also contributed to high concentration levels of Zn, Ni and Pb. Lead, Zn and Ni are often associated with fuel burning [14, 15]. Additionally, Zn is considered a good marker for tyre wear emissions [16].

The geometric mean concentrations of Co, Fe, Ni, Mn, Pb and Zn are within the lower range (Table 14.1) of the annual average guidelines [17, 18], suggesting very little to no effect of anthropogenic activities on air quality at the site. However, in

Fig. 14.2 Geometrical enrichment factors of the studied metals
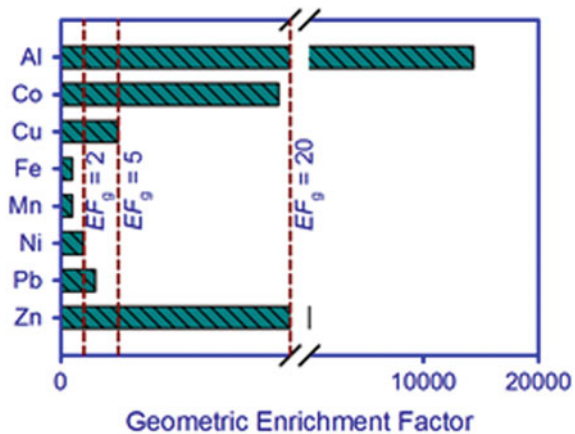
the assessment of potential effect of the measured metals to air quality at the site, baseline concentrations should be always considered to obtain a preliminary idea about possible sources of different elements, that is, crustal or anthropogenic. As can be seen from Fig. 14.2, geometric enrichment factors for Al and Zn ($EF_g = \gg 20$) are high suggesting that the metals may have resulted from anthropogenic sources. Park and Dam [19] reported enhanced levels of Zn concentrations at a sampling station in Korea, which were ascribed to dust coming from highly industrialized zones in China during long-range transport.

Al normally represents elements of earth origin. In this study however, highly enriched Al suggests contributions from construction activities, particularly during the sampling period of 02/04/08–19/05/08 (see Appendix). These results are supported by their correlation ($r = 0.66$; $P = 0.01$) as shown in Table 14.2, suggesting that the two (Al and Zn) may have originated from similar sources. Similarly, the highly enriched Co ($EF_g = 19$) having correlation coefficients, $r = 0.34$; $P = 0.01$ with Al and $r = 0.41$; $P = 0.01$ with Zn and moderate enrichments of Cu, Pb and Ni suggest contributions from anthropogenic sources. This analysis will however be clarified further by principal component analysis which will be explained later in this discussion.

As expected, significant negative correlations of rainfall ($P = 0.01$) with Cu, Fe and Mn are a result of washout of atmospheric particles by rainfall which also tends to reduced re-suspension of crustal dust. Similarly, significant negative correlations of wind speed ($P = 0.01$) with Cu, Fe, Mn, Ni and Pb suggest high dispersion conditions leading to lower aerosol concentrations. On the other hand, Al, Co, Ni, Pb and Zn show insignificant correlations with rainfall amount. Although this was unexpected, this may suggest that these elements occur in significantly different aerodynamic diameters, resulting in different settling times or washout ratios. Insignificant correlations between wind speed and Al, Co and Zn however suggest that these elements are probably originating from both local and distant sources.

14.3.2.2 Principal Component Analysis

Principal Component Analysis (PCA) is a dimension-reduction tool useful in reducing a large set of variables to a small set called principal components with the aim to clarify relationships between variables for easy analysis and interpretation. Principal Component Analysis was then performed to further establish possible factors that contribute towards the metal species concentrations and source apportionment. The number of significant Principal Components (PC) was selected on the basis of Varimax orthogonal rotation with Kaiser Normalisation with eigenvalues greater than 1.

Due to the observed mean concentrations differences of Al, Zn, Pb and Ni metal contents in aerosols for the dates 02/04/08–19/05/08 compared to means for the rest of sampling periods, data sets were subjected to principal component analysis twice: (1) with all data set combined together (PCA-1), and (2) data for 25/05/08–07/12/08 (PCA-2). Results obtained from the PCA-1 and PCA-2 are presented in Figs. 14.3 and 14.4, respectively.

Fig. 14.3 Results of the
Principal Component
Analysis (PCA-1)
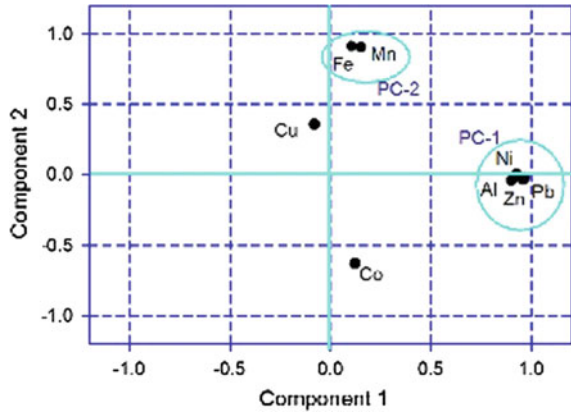
Fig. 14.4 Results of the
Principal Component
Analysis (PCA-2)
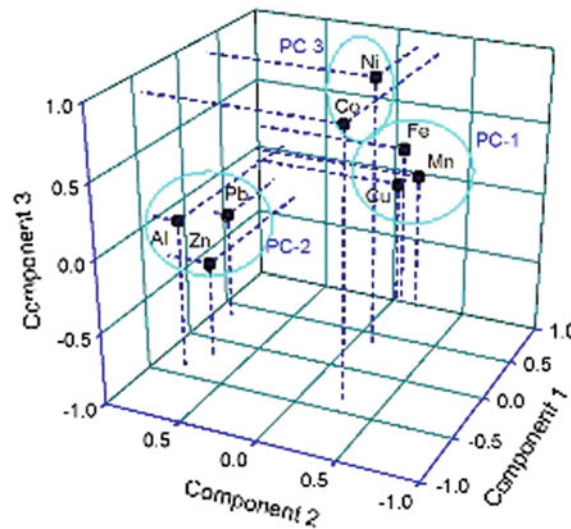
Principal Component Analysis (PCA-1): Two principal components comprising
72.01% cumulative total variance were retained after Varimax orthogonal rotation,
because subsequent eigenvalues were less than 1. The factor loadings are presented
in Table 14.3. The first principal component (PC-1) accounting for 44.8% variance
shows high positive loadings of Pb, Zn, Ni and Al, whereas the second component
PC-2 accounted for 27.3% of high positive loadings for Fe and Mn.

Cobalt and copper had very weak communalities (~0.4). This suggests that the
two are not in common with other metals studied, as depicted in Fig. 14.3.

Table 14.3 Factor loadings and communalities of metals (PCA-1)

Element	PC-1	PC-2	Communalities
Pb	0.968	−0.023	0.937
Zn	0.959	−0.036	0.920
Ni	0.926	0.004	0.858
Al	0.901	−0.043	0.813
Fe	0.106	0.912	0.842
Mn	0.154	0.907	0.847
Co	0.124	−0.629	0.411
Cu	−0.078	0.356	0.133
Eigen values	3.581	2.180	
% of Variance	44.761	27.251	
Cumulative %	44.761	72.013	

Table 14.4 Factor loadings and communalities of metals (PCA-2)

Element	PC-1	PC-2	PC-3	Communalities
Cu	0.987	−0.030	−0.097	0.984
Fe	0.983	−0.069	0.169	0.999
Mn	0.964	−0.178	−0.004	0.962
Pb	0.341	0.877	−0.234	0.940
Al	−0.395	0.805	0.043	0.806
Zn	−0.216	0.705	−0.316	0.643
Ni	0.345	−0.134	0.894	0.936
Co	−0.407	−0.275	0.868	0.994
Eigen values	3.473	2.045	1.747	
% of Variance	43.409	25.565	21.831	
Cumulative %	43.409	68.974	90.806	

Principal Component Analysis (PCA-2): Principal Component Analysis (PCA-2) revealed three component factors which comprised of 90.81% cumulative total variance (Table 14.4). PC-1 explains 43.41% of variance in the data set and has very strong loadings for Cu, Fe and Mn. The second principal component accounts for 25.57% of the variance and has strong loadings for Pb, Al and Zn. The last principal component (PC-3) accounted for 21.83% of the variance in the data set, with strong loadings for Ni and Co.

It is evident from the rotated component matrix depicted in Fig. 14.4 that all the eight metals analysed can be explained by three principal components. Furthermore, the communalities of the elements were very strong (> 0.8), which indicates that the retention of the three components was sufficient to explain all variances of the metals (Table 14.4).

From PCA-1, PC-1 was characterized by Pb, Zn, Ni and Al and PC-2 by Fe and Mn. PC-1 supports observed correlations depicted in Table 14.2. Thus, on the basis of these observations and the corresponding moderate to high EF_g values (Fig. 14.2), Pb, Zn, Ni and Al exist possibly because of anthropogenic contributions. Fossil fuel combustion, traffic emissions, wear of brake lining materials and several industrial processes are considered as major sources of Pb, Zn and Ni [20, 21].

Although elevated EF_g values of Al were unexpected, its presence in elevated forms and association with Pb, Zn and Ni could be attributed to industrial activities during construction. PC-2 (Fig. 14.3) was characterized by Fe and Mn. This supports the high correlation (r = 0.86; P = 0.01) between these metals (Table 14.2). The natural sources of Fe (~98%) vastly dominate its anthropogenic input [22], thus, Fe and Mn probably indicate soil mineral particles. The enrichment value of unity for Mn (taking into account that Fe was used for reference material) further suggests crustal origin of both metals, such as the airborne dust.

On the other hand, the second factor analysis (PCA-2) revealed three component factors which were comprised of 91% total cumulative variance. PC-1 was characterized by Cu, Fe and Mn (Table 14.4). Since Fe and Mn are tracers for natural sources and this PC has strong communalities of 0.999 and 0.962, respectively, it indicates the association of Cu, Fe and Mn with crustal sources. From the previous discussion, moderate EF values (Fig. 14.2) reported for Cu, Pb and Zn were suggested to be associated with contributions from anthropogenic sources. In this regard, the possibility of Cu resulting from both lithogenic and anthropogenic sources cannot be ruled out. However, according to results obtained from PCA-1 (Table 14.3), Cu had insignificant factor loadings in PC-1 but relatively weak loadings in PC-2 (elements which are characterized as either lithogenic or anthropogenic), whereas in PCA-2, Cu was strongly associated with the lithogenic Fe and Mn. These findings suggest that existence of copper in the measured aerosol samples in Gaborone is almost entirely due to lithogenic sources.

The second principal component (PC-2) was characterized by Pb, Al and Zn, which was ascribed to local anthropogenic sources. Since the sampling station was a few hundred metres away from the only highway connecting the city of Gaborone with the northern part of the country, high levels of Pb in air samples might be associated with fossil fuel consumption, whereas Zn levels could be a result of wear and tear of vulcanized rubber tyres, lubricating oils and corrosion of galvanized vehicular parts. As discussed before, the presence of Al in PC-2 is a result of emission from the local construction activity during the sampling period. Lastly, PC-3 was characterized by Co and Ni. Ni is commonly associated with emissions from industries such as electroplating, ferrous and non-ferrous foundries [13]. It was however difficult to associate the presence of Co and Ni with such industrial activities since the authors could not identify such industries within the sampling vicinity. In that case, interpretation of these results will be discussed in conjunction with findings from back-trajectory analysis.

14.3.2.3   Back Trajectory Analysis

Three-day back trajectories arriving at Sebele (24.59° S, 25.94° E) were computed using the PC Version 4.9 of the National Oceanic and Atmospheric Administration (NOAA)'s Air Resources Laboratory (ARL) Hybrid Single Particle Lagrangian Integrated Trajectory (HYSPLIT) [23] for the sampling period (April–December 2008). The model was run using Global Data Assimilation System (GDAS) archived meteorological data to determine air mass origins. As a control measure for self-consistency, trajectories were run three times daily with ending times of 06h00, 12h00 and 18h00 UTC (Coordinated Universal Time). Three different pressure levels corresponding to 500, 1000 and 1500 m above ground level (AGL), were run to determine the possibilities of shear within each six-hour time step. Trajectories found to have substantially different paths within the 500, 1000 and 1500 m AGL for a given model run were excluded from the calculations to avoid the possibility of shear in airflow. Then, only the 72 h back trajectories arriving at 12h00, 500 m AGL were considered in the calculations. The choice for 72 h back trajectories is supported by the fact that the mean aerosol lifetime is ~3 days whereas the 500 m elevation was considered to be within the mixing layer of the atmosphere. The arriving time of 12h00 UTC was chosen arbitrarily since there were no observed differences in trajectory paths between the 06h00, 12h00 and 18h00 ending times.

The measured metal concentration data for each element analysed were then associated with their corresponding 72 h back trajectory arriving at the sampling site to identify potential source regions. This was achieved by computing *t*-tests to determine whether the average metal concentrations associated with each cluster were significantly different. The air mass backward trajectories ending at the sampling station at an altitude of 500 m AGL for 25/05/08–07/12/08 sampling period using the HYSPLIT model are given in Fig. 14.5.

From the 63 back trajectories generated, 51 were consistent in air flow and are thus shown in Fig. 14.5a. After applying cluster analysis, the cluster plots indicating the percentage change in total spatial variance as clusters were combined and suggested 4 cluster groups and their percentage changes were as follows: 9 (57.19%), 5 (94.04%), 3 (46.32%) and 2 (252.45%). Cluster group 5 (94.04%) was then selected on the basis that it has enough clusters that represent different transport patterns and yet not so many to obscure the pattern (Fig. 14.5b).

The geometrical mean concentrations of heavy metals in aerosols for each cluster were then calculated. Table 14.5 shows the mean concentrations of heavy metals for data set sampled on 25/05/08–07/12/08. Mean concentrations for Co and Pb are not included since they were not detected in most of the samples during this study period (see Appendix).

Only Zn and Ni mean concentrations (Table 14.5) were found to exhibit geographical dependence as shown in Fig. 14.5. Trajectories in CL 2 carry aerosol particles which are relatively rich ($p < 0.5$) in Zn atoms compared to trajectory clusters 4 and 5. However, there is no significant differences in Zn mean concentrations between CL 1 and CL 3. Trajectory clusters 2 and 3 are slow-moving and continental. Air masses with high residence times over the continent and slow moving will tend to acquire
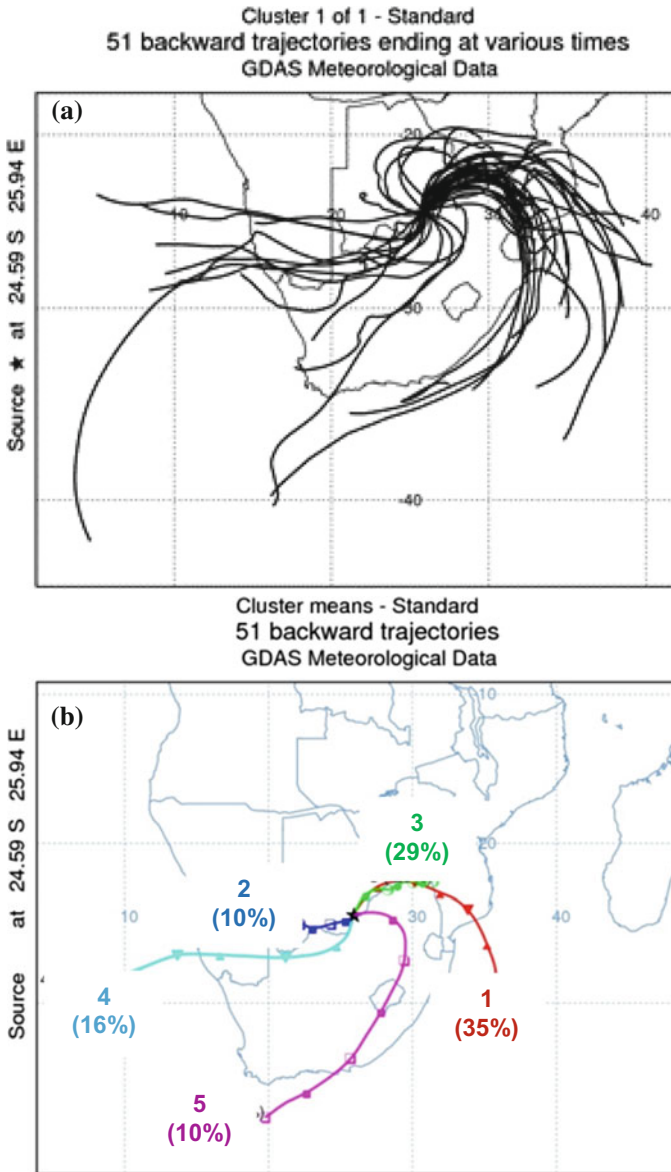
Fig. 14.5 **a** 72 h backward trajectories and **b** the corresponding cluster means

Table 14.5 Trajectory membership, geometric mean and geometric standard deviation per cluster (CL 1–5)

Cluster	Geometric mean ± Geometric standard deviation (ng/m^3)					
	Al	Cu	Fe	Mn	Ni	Zn
CL 1	1280 ± 460	2.6 ± 1.0	410 ± 230	12.4 ± 5.6	0.9 ± 0.5*	67 ± 21
CL 2	1210 ± 320	3.3 ± 1.0	510 ± 200	14.9 ± 4.1	1.1 ± 0.4*	80 ± 22*
CL 3	1380 ± 460	2.6 ± 0.8	530 ± 300	15.2 ± 6.6	1.0 ± 0.5*	63 ± 20
CL 4	1560 ± 730	6.7 ± 11.6	470 ± 240	12.7 ± 6.7	0.3 ± 0.4*	53 ± 18*
CL 5	1000 ± 280	3.1 ± 0.7	500 ± 140	13.4 ± 3.7	0.6 ± 0.8	51 ± 28*
Mean	1310 ± 490	3.4 ± 4.6	470 ± 240	14.1 ± 5.5	0.8 ± 0.5*	63 ± 22*

*Metal concentrations are significantly different ($P < 0.05$) between clusters as will be explained in text

characteristics distinctive to the land they are ambient to. Therefore, enhanced Zn concentrations associated with these air masses are results of industrial activities along the southern belt (CL 2) of Botswana and those that are along the eastern sides of Botswana (CL 3). Trajectory CL 1 is also along CL 3, but fast moving, with 1/3 of its entire time over the ocean before reaching the sampling station. It is expected that CL 1 be similar to CL 3, but slightly diluted by the oceanic clean air, as can be depicted from results in Table 14.5. A similar argument holds for observations made with Ni mean concentrations in clusters 1, 2 and 3, which are significantly ($p < 0.5$) high compared to Ni concentrations in cluster 4.

Further to the above, air mass trajectories provide information as to whether metal concentrations obtained from the study are local pollutants or transported from elsewhere, with the possibility of being trans-boundary. As discussed previously, the presence of Ni and possibly Co in the aerosol samples measured in the study could possibly be due to both local and trans-boundary contributions.

14.4 Conclusion

Correlations between Cu, Fe, Mn, Ni and Pb and rainfall and wind speed were observed. However, no significant correlations were observed between rainfall and Al, Co, Ni, Pb and Zn. Similarly, there were no significant correlations between wind speed and Al, Co and Zn. A large number of data set is needed to improve statistical significance for correlation analysis to be successful.

Factor analysis reveals that Pb, Ni, Co, Al and Zn exist because of anthropogenic contributions, whereas, Fe and Mn are from lithogenic sources. On the other hand, Cu exists from mixed sources.

Back-trajectories were used to locate geographical potential source regions of heavy metals. The presence of Zn and Ni in the aerosols measured at Sebele is due to air mass transportation processes.

Appendix

Dates (DDMMYY)		Mean metal concentrations (ng/m^3)								Rain	Wind
Deployed	Removed	Al	Co	Cu	Fe	Mn	Ni	Pb	Zn	mm	m/s
02/04/08	**05/04/08**	2483.00	0.91	2.07	282.67	8.70	2.58	3.90	1614.49	0.00	16.86
05/04/08	**08/04/08**	3774.59	0.88	2.89	401.12	13.24	2.14	7.01	1517.73	0.00	15.42
08/04/08	**11/04/08**	3145.57	1.50	1.91	310.43	10.16	3.05	4.03	1715.71	0.00	21.64
23/04/08	**26/04/08**	4033.46	1.32	3.53	545.93	19.90	3.19	5.95	2012.26	0.00	21.26
27/04/08	**30/04/08**	5047.02	1.48	3.48	1043.82	21.31	4.60	5.75	2606.00	0.00	17.38
10/05/08	**13/05/08**	2847.27	1.44	2.27	271.09	11.44	2.46	5.14	3224.44	0.00	19.25
13/05/08	**16/05/08**	4565.22	1.22	3.09	500.17	14.37	4.57	8.10	2742.62	0.00	18.44
16/05/08	**19/05/08**	5354.18	0.62	3.92	568.07	19.76	5.96	9.00	3077.38	0.00	29.53
25/05/08	28/05/08	1248.71	ND	0.94	134.24	7.04	0.92	ND	95.11	3.50	37.22
28/05/08	31/05/08	493.82	ND	3.75	426.12	13.98	1.01	0.44	31.68	0.00	18.47
01/06/08	04/06/08	1115.79	ND	2.33	402.27	12.48	1.42	ND	73.81	5.50	28.58
04/06/08	07/06/08	1371.42	ND	2.86	387.90	12.12	0.82	ND	91.35	0.00	14.32
07/06.08	10/06/08	1362.85	ND	2.68	368.77	12.57	0.72	ND	94.94	0.00	18.30
11/06/08	14/06/08	1115.56	ND	4.21	609.77	17.20	1.03	0.63	64.11	0.00	18.60
14/06/08	17/06/08	1339.96	ND	3.08	725.44	20.58	1.34	ND	80.86	0.00	23.35
17/06/08	20/06/08	1111.57	ND	1.66	508.57	13.49	1.09	ND	75.53	0.00	47.24
20/06/08	23/06/08	1298.05	ND	2.00	447.75	15.04	1.07	0.07	93.45	0.00	28.03
23/06/08	26/06/08	1490.81	ND	5.08	841.32	21.88	1.60	0.18	95.54	0.00	18.38
26/06/08	29/06/08	791.26	ND	3.40	663.12	17.85	1.22	ND	43.49	0.00	14.69
29/06/08	02/07/08	692.06	ND	3.72	572.03	15.53	0.88	ND	42.82	0.00	18.97
02/07/08	05/07/08	848.44	ND	1.79	603.88	18.39	1.15	ND	45.08	0.00	28.02
06/07/08	09/07/08	1123.44	ND	2.68	671.16	19.11	1.16	ND	55.53	0.00	27.51
09/07/08	12/07/08	1029.02	ND	2.54	465.80	15.22	0.88	ND	71.77	0.00	42.85
12/07/08	15/07/08	669.13	ND	2.14	142.74	6.97	0.48	ND	50.06	6.00	39.38
15/07/08	18/07/08	1004.36	1.23	3.99	356.86	14.28	0.77	0.28	76.48	0.00	39.06
18/07/08	21/07/08	1090.90	ND	3.42	510.78	15.16	0.96	ND	82.74	0.00	24.35
21/07/08	24/07/08	1180.97	ND	2.71	512.17	15.64	1.21	0.08	66.50	0.00	25.86
04/08/08	07/08/08	1312.00	ND	4.14	944.80	27.73	1.34	0.09	55.18	0.00	22.38
07/08/08	10/08/08	1114.19	ND	4.69	1163.88	28.20	1.53	ND	44.51	0.00	22.85
10/08/08	13/08/08	1070.68	0.18	2.39	684.19	19.60	1.12	ND	53.46	0.00	21.63
13/08/08	16/08/08	1044.46	ND	1.66	679.81	17.23	0.39	ND	43.38	0.00	37.92
16/08/08	19/08/08	1578.76	ND	1.04	422.14	10.08	ND	ND	77.18	0.00	74.06
19/08/08	22/08/08	1320.90	ND	2.23	454.27	11.64	ND	ND	65.72	0.00	36.47
22/08/08	25/08/08	1184.85	ND	2.70	590.64	13.75	ND	ND	59.56	6.00	32.50
26/08/08	29/08/08	599.25	ND	35.43	637.07	15.85	0.01	ND	21.71	0.00	30.42

(continued)

(continued)

Dates (DDMMYY)		Mean metal concentrations (ng/m^3)								Rain	Wind
Deployed	Removed	Al	Co	Cu	Fe	Mn	Ni	Pb	Zn	mm	m/s
29/08/08	01/09/08	1525.47	ND	3.78	814.79	20.30	ND	0.09	53.60	0.00	32.63
01/09/08	04/09/08	696.04	ND	3.04	663.60	18.71	0.14	ND	24.90	1.70	34.78
04/09/08	07/09/08	1837.20	ND	2.98	748.20	20.96	1.47	ND	76.08	0.00	43.19
08/09/08	11/09/08	1572.25	0.20	3.40	823.40	21.42	0.46	ND	68.22	0.00	36.76
11/09/08	14/09/08	1568.19	ND	1.84	357.20	10.26	0.14	ND	51.00	0.00	47.42
15/09/08	18/09/08	1363.02	0.20	3.13	593.86	14.24	0.24	ND	34.88	0.00	45.80
18/09/08	21/09/08	700.17	ND	2.83	486.33	14.48	0.15	ND	13.30	0.00	44.28
21/09/08	24/09/09	1305.41	ND	3.04	644.52	16.40	0.05	ND	23.55	6.00	33.77
24/09/08	27/09/08	2038.99	ND	4.21	37.22	22.58	0.25	ND	36.27	0.00	38.38
27/09/08	30/09/08	2996.07	0.13	2.31	386.33	12.22	0.22	ND	57.05	0.00	64.50
07/10/08	10/10/08	3107.55	ND	2.62	634.12	17.77	0.34	ND	55.18	0.00	47.31
10/10/08	13/10/08	757.10	ND	3.02	608.15	14.77	0.01	ND	27.81	0.00	37.82
13/10/08	16/10/08	2502.41	3.82	2.95	633.04	16.89	1.21	ND	94.66	0.00	49.59
23/10/08	26/10/08	1022.07	4.11	2.05	388.03	9.71	0.93	ND	37.94	6.00	75.73
26/10/08	29/10/08	637.86	0.31	2.19	289.53	7.01	0.03	ND	40.98	0.00	45.77
29/10/08	01/11/08	2154.42	ND	2.65	470.64	12.57	0.07	ND	82.10	0.00	51.29
01/11/08	04/11/08	2203.97	ND	2.59	351.34	10.63	0.59	ND	79.99	5.00	69.30
04/11/08	07/11/08	2131.34	ND	2.66	371.66	10.37	0.28	ND	73.81	4.00	77.26
07/11/08	10/11/08	1805.32	0.96	1.85	119.09	4.69	0.04	ND	68.02	29.50	67.01
10/11/08	13/11/08	2159.48	ND	2.38	141.11	4.82	1.00	ND	78.72	29.70	45.76
13/11/08	16/11/08	2126.56	2.87	2.26	159.28	7.27	0.78	0.51	93.78	18.50	34.39
16/11/08	19/11/08	1516.56	4.29	1.66	135.15	7.06	1.42	ND	85.21	22.50	55.97
19/11/08	22/11/08	1394.34	4.99	1.46	109.63	5.73	1.12	0.22	83.34	9.20	40.37
22/11/08	25/11/08	1057.21	4.11	2.15	165.67	6.62	1.12	0.14	89.16	2.20	25.43
25/11/08	28/11/08	1445.61	5.73	2.56	318.78	10.20	1.60	ND	74.94	0.00	41.70
28/11/08	01/12/08	1335.75	6.25	2.82	271.56	10.87	1.50	0.08	75.49	0.00	49.51
01/12/08	04/12/08	1185.38	4.36	3.99	462.28	13.87	1.76	0.40	78.90	0.00	53.23
04/12/08	07/12/08	1366.15	5.75	1.98	194.39	8.56	1.17	0.13	63.80	24.00	57.27

ND Not detected

Dates in DD/MM/YY format

References

1. Lim JM, Lee JH, Moon JH, Chung YS, Kim KH (2010) Source apportionment of PM10 at a small industrial area using positive matrix factorization. Atmos Res 95:88–100
2. Hu Z, Wang J, Chen Y, Chen Z, Cu S (2014) Concentrations and source apportionment of particulate matter in different functional areas of Shanghai, China. Atmos Pollut Res 5:138–144
3. Padoan E, Malandrino M, Giacomino A, Grosa MM, Lollobrigida F, Martini S, Abollino O (2016) Spatial distribution and potential sources of trace elements in PM10 monitored in urban and rural sites of Piedmont region. Chemosphere 145:495–507
4. WHO (2014) 7 million premature deaths annually linked to air pollution. WHO Department of Public Health, Environmental and Social Determinants of Health (PHE). Issue 63/March 2014. http://www.who.int/phe/health_topics/outdoorair/databases/cities/en/. Accessed 16 Aug 2018

5. Sielicki P, Janik H, Guzman A, Namieśnik J (2011) The progress in electron microscopy studies of particulate matters to be used as a standard monitoring method for air dust pollution. Crit Rev Anal Chem 41:314–334
6. Araújo IPS, Dayana B, Costa DB, Rita JB, de Moraes RJB (2014) Identification and characterization of particulate matter concentrations at construction jobsites. Sustainability 6:7666–7688
7. Batisani N, Yarnal B (2010) Rainfall variability and trends in semi-arid Botswana: implications for climate change adaptation policy. Appl Geogr 30:483–489
8. Suvarapu LN, Baek S-O (2017) Determination of heavy metals in the ambient atmosphere: a review. Toxicol Ind Health 33:79–96
9. Olivier J, Johnson WD, Marshall GD (2008) The logarithmic transformation and the geometric mean in reporting experimental IgE results: what are they and when and why to use them? Ann Allerg Asthma Immunol 100:333–337
10. Taylor SR (1964) Abundance of chemical elements in the coastal crust: a new table. Geochim Cosmochim Acta 28:1273–1285
11. Hong Y, Ma Y, Li C, Liu N, Gao S, Zhang Y (2011) Elemental size distribution characteristics of atmospheric particles on hazy days during winter in Shenyang. Res Environ Sci 24:637–644
12. Zoller WH, Gladney ES, Duce RA (1974) Atmospheric concentrations and sources of trace metals at the South Pole. Science 183:198–200
13. Kulshrestha UC, Kumar N, Saxena A, Kumari KM, Srivastava SS (1995) Identification of the nature and source of atmospheric aerosols near the Taj Mahal (India). Environ Monit Assess 34:1–11
14. Ozaki H, Watanabe I, Kuno K (2004) Investigation of the heavy metal sources in relation to automobiles. Water Air Soil Pollut 157:209–223
15. Adamiec E, Jarosz-Krzemińska E, Wieszała R (2016) Heavy metals from non-exhaust vehicle emissions in urban and motorway road dusts. Environ Monit Assess 188:369–380
16. Lawrence E, Ranjeet Sokhi R, Ravindra K, Mao H, Prain HD, Bull ID (2013) Source apportionment of traffic emissions of particulate matter using tunnel measurements. Atmos Environ 77:548–557
17. Air Quality Standards Regulations (2007) Environmental protection statutory instruments number 64. Printed and published in the UK by The Statutory Office Limited UK, pp48
18. WHO (2000) Air quality guidelines. World Health Organisation, Geneva, Switzerland
19. Park K, Dam DH (2010) Characterization of metal aerosols in PM10 from urban, industrial and Asian dust sources. Environ Monit Assess 160:289–300
20. Al-Momani I (2009) Assessment of trace metal distribution and contamination in surface soils of Amman, Jordan. Jordan J Chem 4:77–87
21. Al-Khashman O (2013) Assessment of heavy metals contamination in deposited street dusts in different urbanized areas in the city of Ma'an, Jordan. Environ Earth Sci 70:2603–2612
22. Al Obaidy A, Al Mashhadi A (2013) Heavy metal contaminations in urban soil within Baghdad City, Iraq. J Environ Prot 4:72–82
23. Draxler RR, Hess GD (2004) Description of the HYPSPLIT-4 modeling system. NOAA Technical Memorandum ERL ARL-224, Silver Spring, Maryland, USA

Chapter 15
Physicochemical Properties and Heavy Metals Accumulation in the Plant, Soil and Water from Municipal Landfill in Alice, South Africa

Nontobeko Gloria Maphuhla, Adebola O. Oyedeji, Francis Bayo Lewu, Opeoluwa O. Oyedeji and Muinat Nike Lewu

Abstract Many places around the world are faced with environmental challenges such as unacceptable waste disposal and pollution of water resources. Heavy metal pollution of soil, water, and plants, and their health effect on people is a persistent social issue. Numerous researches have highlighted the health risks of residents in close proximity to open dumpsites. Dumpsites are sources of heavy metal impurity and toxicity to the surrounding environment. This study aimed to investigate two sites (site A and control site B) for their physicochemical properties and concentrations of heavy metals in the soil, water and plants in and around these sites. Concentrations of four heavy metals, namely: Cu, Hg, Mn and Pb in the plant, water, and soil samples were measured using atomic absorption spectrophotometry (AAS) after sample digestion. Soil pH for both sites ranged from slightly acidic (6.67) to neutral (7.09), which falls within the normal range suggested by WHO. The physicochemical parameters of soil and water were found to be within the normal range, except electrical conductivity in water which was above the permissible limits recommended by WHO. Dumpsite soils (site A) had higher heavy metal concentrations compared

N. G. Maphuhla · O. O. Oyedeji
Department of Chemistry, Faculty of Science and Agriculture, University of Fort Hare, Private Bag X1314, Alice 5700, South Africa
e-mail: maphuhlang@webmail.co.za; 201214220@ufh.ac.za

O. O. Oyedeji
e-mail: ooyedeji@ufh.ac.za

A. O. Oyedeji (✉)
Department of Chemistry, School of Applied and Environmental Sciences, Walter Sisulu University, Mthatha 5099, South Africa
e-mail: aoyedeji@wsu.ac.za

F. B. Lewu
Department of Agriculture, Faculty of Applied Sciences, Cape Peninsula University of Technology, Wellington Campus, P.O. Box X8, Wellington 7655, Western Cape, South Africa
e-mail: LewuF@cput.ac.za

M. N. Lewu
ARC Infruitec-Nietvoorbij, Private Bag X5026, Stellenbosch 7599, South Africa
e-mail: LewuM@arc.agric.za

to site B. A noteworthy observation was the fact that Hg concentrations were the only one found to exceed the maximum permissible levels in soil (ranging from 1.08 to 8.45 mg/kg), *Acacia karroo* (1.71–13.27 mg/kg), and water (11.42–55.04 mg/L) while Mn only exceeded this limit in water samples (ranging between 0.023 and 1.106 mg/L). High Hg concentration in this study is a thing of concern.

Keywords *Acacia karroo* · Heavy metals accumulation · Landfill sites · Soil contamination · Water pollution

15.1 Introduction

One of the most valuable nation's assets is soil and it is the characteristic resource that determines the region's wealth. In soil heavy metals pollution changes the composition and the activity of microbial soil communities. The bioactivity, richness and microbial diversity decrease with the increase in the concentration of heavy metals [1]. The soil is the main sink for heavy metals released into the environment by five mentioned anthropogenic activities [2]. It is also the major source of metals in plants and vegetables since they absorb pollutants in their soluble form through roots and transfer them to other parts such as seeds and leaves [3].

Around the world, the heavy metals and metalloids cause a serious problem in the environment [4]. Heavy metals are natural components of the Earth's crust and are determined to have a density higher than 5 g/cm^3. The most common metals are Cu, Cd, Fe, Zn, and Ni. Metals like Fe are important for a living when present in a small required amount, while other elements like Hg are dangerous even at the small amount due to their certain physical and chemical properties [5]. They are non-biodegradable, persistent [6], and dangerous because they have a tendency to bio-accumulate and enter the food chain through plants and animals [7].

Metals are introduced into the soil from different sources such as the use of fertilizers containing phosphates, pesticides, vehicle emissions, industrial waste, lead-acid batteries, and from atmospheric deposition of metal and metalloids bearing particles [4]. The solubility and bioavailability of metal ions in the soil usually change due to the influence of factors such as soil pH, organic matter content and clay content [8].

Humans and animals are exposed directly and indirectly to these heavy metals through three primary routes, which are: ingestion, inhalation and skin absorption [9]. Uncontrolled and unmanaged dumpsites exist in many developing countries because they remain the cheapest method of waste disposal.

These open dumpsites can cause several years of human health risk [10]. Dumpsites produce health hazards due to the unpleasant smell generated by degrading activities of micro-organisms on organic waste. The unrestricted burning of municipal solid waste also results in serious environmental pollution, due to the release of thick, noxious smoke that pollutes the air [11].

Water pollution occurs as the result of human activities such as releases of effluents on water. A previous investigation revealed that many rural communities in

Eastern Cape and across South Africa especially among the poor rural population with limited investments in infrastructure suffer from lack of supply of healthy water and sanitation facilities [12].

Acacia karroo is an average large, single-stemmed and deciduous tree with a rounded crown, often broader than tall and it grows up to 12 meters high [13]. It belongs to the plant family of *Fabaceae,* and subfamily of *Mimosoideae*. This plant is known in many cultures, commonly known as Sweet thorn (English), Soetdoring (Afrikaans), Mookana (North Sotho), Mooka (Tswana), or umuNga (Zulu or Xhosa) [14]. The species consists of paired, greyish to white thorns, finely textured dark green leaves, and produces yellow pompoms flowers with sweet smelling [13]. Unlike other most pioneer plants, *Acacia karroo* fixes nitrogen through the symbiotic association with nitrogen-fixing microorganisms which increase the soil's fertility of the surrounding soil [15]. The aim of this study was to evaluate the influence of anthropogenic activities on the metal levels and physicochemical properties of soil, water and plants found in and around Alice landfill in order to document potential environmental hazards and possible risk to public health due to these activities.

15.2 Materials and Methods

15.2.1 Study Area and Site Description

Alice landfill site (site A) where the study samples were collected is located in Alice Township under Raymond Mhlaba Municipality in South Africa, and it is about ≈4 km from the Fort Hare University East campus in Alice, where the second site (site B) which is the control site is located. Site A covered about 2 ha of land and the entire dumpsite was full of natural vegetation which is indicative of either abundance or deficiency of certain minerals.

Site A was divided into three portions: portion A (east side) had lots of broken glasses; portion B (south side) was dominated by rusted tins and broken glasses with evidence of burnt waste, and portion C was outside the fence of the dumpsite and was only occupied by natural vegetation. However, site B is not a dumpsite but an undisturbed piece of land with its soil surface covered by natural vegetation and located near a mountain. The municipal water dam is located at about 200 m from the dumpsite and is close to a cattle kraal (Fig. 15.1).

15.2.2 Plant, Soil and Water Sample Collections

To determine the influence of dumped materials in the study site on the accumulation of heavy metals in plant tissues, leaf samples of *Acacia karroo* growing on the dumpsite (site A), were collected randomly with a stainless-steel knife. Plant samples
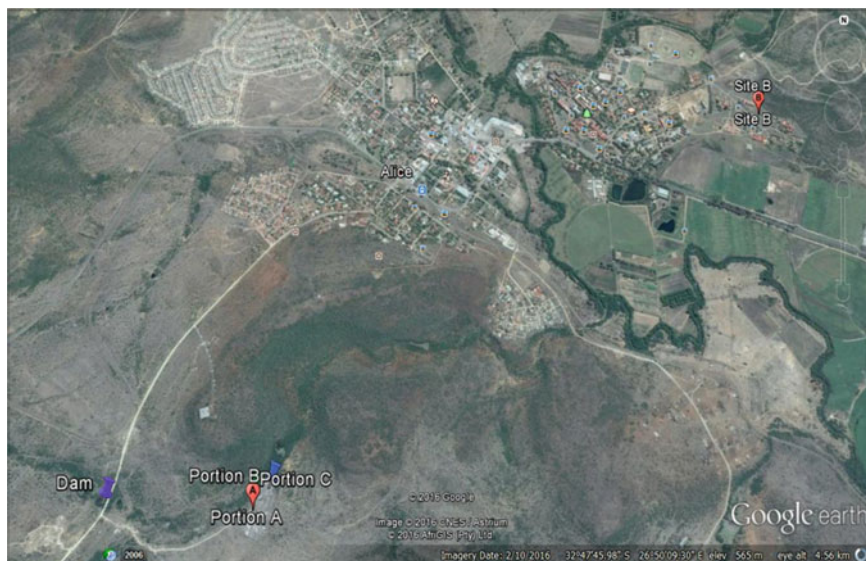
Fig. 15.1 Map of Alice indicating the municipal dam and sites where plants, soils, and water samples were collected. Image from Google Earth

were deposited in the herbarium of the Department of Botany, University of Fort Hare and identified by Professor A. Maroyi and voucher specimen with specimen number NG/01 [16]. Plant parts were separated, pre-cleaned with distilled water and dried to a constant mass at 80 °C in an oven. Dried samples were crushed into a fine powder using a laboratory grinder.

Milled samples were sieved through a 2 mm mesh to obtain a fine powder and were stored in a plastic bag [17].

The soil samples were collected two times a week for a period of six weeks. Samples were collected using a stainless-steel auger at the depth of 0–30 cm from each of the 3 portions (A, B and C) of site A to have a total of three samples for site A.

The fourth composite sample was collected from the control site B. The collected dry soil samples were placed in clean labelled polyethylene bags and then transported to the laboratory for further analysis.

Water samples were collected from the dam once a week for six weeks. Sterilized plastic bottles were rinsed with distilled water, dried and were used to collect water samples randomly below the water surface.

The samples were acidified using nitric acid to prevent further microbial activities and kept in an ice bag at 4 °C [18].

15.2.3 Determination of the Physicochemical Properties of Soil

Using a mortar and pestle, soil samples were crushed and sieved in a 2 mm mesh to remove coarse debris to obtain representative samples [19].

15.2.3.1 Moisture Content

Soil samples were added to a beaker of known mass and the combined mass of soil and beaker was measured. The samples were oven dried at 105 °C for 24 h until constant mass was obtained. Samples were cooled at room temperature and transferred into a clean plastic bag for further analysis [19].

Calculation

$$\% \, \text{Mass} \, = \, \left(\frac{\text{Air dried} - \text{Oven dried}}{\text{Oven dried}} \right) \, \times \, 100\%$$

15.2.3.2 pH

In a 100 ml beaker of known mass, 20 ml of calcium chloride solution was added to 20 g of sieved soil sample; the resulting mixture was stirred and allowed to stand for 30 min with occasional stirring. The determination of pH was done by immersing a hand-held glass electrode pH meter into the partially settled solution, making sure the electrode does not touch the walls of the beaker [20].

15.2.3.3 Organic Carbon (SOC)

A 1.0 g of soil sample was weighed into a 250 ml conical flask, 10 ml of $K_2Cr_2O_7$ was added and the flask was gently swirled to dissolve the soil. Then 20 ml of conc. H_2SO_4 was quickly added and mixed thoroughly and the flask was allowed to stand on a fume hood for 30 min to cool down. Thereafter, 200 ml of water was added and the formed suspension was filtered using a filter paper. About 3–5 drops of ferroin indicator were added and the solution was titrated with $FeSO_4$. The end point was approached when the solution changed from dark green to blue to reddish brown [21].

Calculation

$$\text{Organic carbon}\,(\%) = M \times \left(\frac{V1 - V2}{\text{Mass of soil}} \right) \times 0.39$$

$$\text{Organic matter}\,(\%) = \text{Organic carbon}\,(\%) \times 1.724$$

where M = concentration of $FeSO_4$, $V1$ = volume of blank, $V2$ = volume of $FeSO_4$, 0.39 = constant and 1.724 = constant.

15.2.3.4 Electrical Conductivity (Salinity)

A 10 ml of well-mixed water sample was added into a measuring cylinder. The previously prepared soil sample was added to the water until the contents of the container increased by 5 ml to bring the volume to 15 ml. More water was added to the mixture to bring the total volume to 30 ml. The content was shaken intermittently for 5 min and allowed to settle for 5 min. The EC probe was dipped into the solution to measure the electrical conductivity [22].

15.2.4 Determination of the Physicochemical Properties of Water

Analytical methods for water physicochemical properties which are temperature, pH, and electrical conductivity were measured at the collection site (dam that is ≈200 m from the dumpsite) using multi-parameter water quality instrument [18, 23].

15.2.4.1 Alkalinity

Two or three drops of phenolphthalein were added into 100 ml of collected water samples. The appearance of a pink color in water indicates alkalinity. The solution was titrated with 0.02 N H_2SO_4 until a clear solution was obtained [18].

15.2.4.2 Total Hardness

50 ml of water sample was mixed with 1–2 ml buffer of pH 10 and a few drops of Eriochrome black-T indicator. The mixture was then titrated with 0.01 M EDTA till the wine-red solution changed to blue [18].

Calculation

$$Hardness\ (mg/L)\ =\ \frac{C\ \times\ D\ \times\ 1000}{mL\ of\ sample}$$

where C = ml of EDTA for titration, D = mg of $CaCO_3$ equivalent to 1 ml of ethylenediamine-tetra-acetic acid (EDTA).

15.2.4.3 Total Dissolved Solids (TDS)

The evaporating dish and filter paper were washed, dried and weighed. Then 50 ml of the well-mixed water sample was pipetted and filtered using Whatman filter paper. The filtered sample was transferred into an evaporating dish and dried in an oven at 180 °C. The cooled dried sample in the evaporating dish was measured to obtain mass [23].

Calculation

$$Dissolved\ solids\ (mg/L)\ =\ \frac{(A-B)\ \times\ 1000}{mL\ of\ sample}$$

where A = mass of dried residue + dish (mg), B = is the mass of the dish.

15.2.5 Determination of Heavy Metals in the Plant, Soil and Water Samples

Acacia karroo samples: 2 g was weighed into a clean crucible, burnt to ashes at 450 °C and was then cooled in a desiccator. The ash was dissolved in 5 ml of 20% HCl, placed in a 100 ml volumetric flask and the solution was made up to the mark using deionized water [7].

Soil samples: 20 ml HNO_3 was measured and added to 10 g of the prepared soil sample in a 250 ml conical flask. The content in the flask was placed on a hot plate until the solution was reduced to 5 ml, after which 20 ml of distilled water was added until the suspension was reduced to 10 ml. When digestion was complete, the residue was allowed to cool to room temperature and was filtered using Whatman filter paper and the resulting solution was made up to 50 ml in a volumetric flask with distilled water [5].

Water samples: 100 ml of water sample was measured and placed in a conical flask containing 10 ml of conc. HNO_3. The mixture was heated gently and evaporated

on a hot plate to a volume of 20 ml. The heating was continued with the addition of necessary conc. HNO_3 until digestion was complete as shown by a light colored clear solution [18].

An atomic absorption spectrophotometer (AAS) was used to analyse copper (Cu), lead (Pb), mercury (Hg) and manganese (Mn) in the digested samples [3].

15.2.5.1 Statistical Analysis

The data were analyzed using the Microsoft office Excel and Statistical Package for the Social Sciences (SPSS). The data were subjected to analysis of variance (ANOVA) and significant difference between means was determined at $p \leq 0.05$.

15.3 Results and Discussion

15.3.1 Physicochemical Properties of Soil Samples

The results of the physicochemical properties of the soil samples in the dumpsite and the control site are presented in Table 15.1.

pH: The mean hydrogen ion concentration (pH) in the dumpsite (site A) ranged from 6.79 to 7.09, while in the control site (site B), the mean pH was 6.67 (see Table 15.1). All these pH values are classified as neutral pH range for soil, as pH range of 6.6–7.3 is indicative of a neutral pH. Soil pH measures soil acidity or basicity, and directly influences nutrient bioavailability.

For most plants, the optimum range of soil pH for healthy plant growth is 7.0. Some of the nutrients availability such as nitrogen, phosphorus, and potassium are generally lowered as soil pH decreases [24]. The results of this study indicated that all collected soil samples from both sites are within the standard pH range set by the WHO. They also show that soil pH slightly differs among the portions of dumpsite A.

The ANOVA results show that there was no statistical difference between two portions of site A (A and B), while portion C of site A and site B were significantly different compared to portions A and B of site A. The difference in pH may be attributed to the wet climate which has great potential to encourage soil acidity due to organic matter decomposition which produces hydrogen ions [25, 26]. The movement and the availability of macro and micronutrients in the soil are affected by pH and other soil components. The solubility of metallic contents of the soil increases as soil pH drops. These soluble ions become freely available in different fractions to increase the acidity of the soil environment. An acidic soil environment can ultimately alter the microbial population of the soil and therefore shift microbial growth in favour of the fungi species with a potential for enhanced micro and macronutrient solubility and mobility [25].

Table 15.1 Physicochemical properties of soils at both sites (Mean ± SD)

Collection site	Soil pH	Moisture content (%)	Organic carbon (%)	Organic matter (%)	Electrical conductivity (μS/cm)
Site A-portion A	7.06 ± 0.22[a]	12.30 ± 1.89[a]	1.10 ± 0.36[b]	1.87 ± 0.62[b]	536.67 ± 237.75[a]
Site A-portion B	7.09 ± 0.37[a]	13.48 ± 3.43[a]	1.33 ± 0.64[b]	2.30 ± 1.10[a]	421.98 ± 202.88[a]
Site A-portion C	6.79 ± 0.25[b]	11.07 ± 3.39[a]	1.19 ± 0.48[b]	2.05 ± 0.84[a]	470.58 ± 277.73[a]
Site B	6.67 ± 0.28[b]	10.16 ± 2.30[a]	2.01 ± 0.83[a]	3.46 ± 2.24[a]	127.69 ± 74.65[b]

Notes Letters a and b shows the significant difference between the variables

Data presented as the mean, n = 3; SD = Standard Deviation; Means with different letters within the same column shows a significant difference ($p < 0.05$)

Soil Moisture Content: The results in Table 15.1 showed that the average soil moisture contents in site A ranged from 11.07 to 13.48% while the average of site B was 10.16%. Soil moisture content is the amount of water present in the soil. The low levels of moisture in both sites may be due to the nature of the topography of these sites. Sites A and B were both located on hill slopes with site B hillier than site A. There was no significant difference noted between all portions of site A and site B. It is expected that this type of topography will encourage quick run-off of rainwater during rainy days before the soil could absorb enough water and hence, the resulting dry soils. The high temperature on sampling days is also a factor contributing to the high rate of evaporation of soil moisture and the resultant dry soil observed in this study. The combined effect of these two factors in addition to the natural vegetation occupying the soil surface with their water demand for growth and transpiration process is also seen as contributing factors [27] to the low moisture contents in the sites investigated.

Soil Organic Carbon (SOC) and Soil Organic Matter (SOM): SOC shows variation between sampling portions and ranged from 1.10 to 2.01% (see Table 15.1). Site A-portion A recorded the lowest SOC while site B located outside dumpsite A had the highest SOC. As expected, the SOM content of the soil samples followed the same trend as the SOC recorded above and is found to be low for site A while at optimum level at site B (Table 15.1). The ANOVA analysis shows a significant difference between site A and site B for SOC, while for SOM portion B and portion C of site A correlated significantly with the control site (site B).

SOC of about 2% (3.4% SOM) is widely suggested by several workers as the threshold level for sustaining soil quality, below which deterioration may occur [28, 29]. The most significant factors controlling SOC dynamics are temperature and precipitation [30]. Overall, the percentage of organic carbon in site B is optimum while that of site A is low. Low organic carbon and organic matter content in site A may be attributed to warm temperatures which decreased SOC due to increased microbial decomposition rate [31] of the organic materials in the dumpsite. Microbial activities also generate heat during decomposition process to further hasten the breakdown of organic materials in wastes. Decomposition is a biological process that includes the physical breakdown and biochemical transformation of complex organic molecules of dead material into simpler organic and inorganic molecules [32].

High decomposition rate aided by moisture and high temperature leads to an increase in the level of organic matter in the soil and subsequently, increasing the rate of metal ions absorption. Municipal wastes are known to have a high concentration of metals and this is because SOM has a large sorption capacity towards metals [33]. However, any form of human intervention influences the activity of soil organisms. When soil is disturbed through cultivation, tillage, burning of vegetation and so on, the soil generally contains lower levels of SOM than comparable lands under natural vegetation [34] which may be one of the reasons for the high SOM and SOC obtained in this study for the control site B compared to site A. Return of plant residues or organic wastes to the soil stimulates high microbial activity and increases SOM decomposition.

Electrical conductivity (EC): The EC of collected soil samples from site A were generally higher than that of site B (see Table 15.1). For instance, the EC of site A-portion A was more than four times higher than site B. Similarly, the EC in site A-portions B and C was also more than three times the EC in site B. In general, the values of EC in this investigation are well below the salinity threshold for soil. Soil EC is a major indicator of soil salinity. It is a measure of the number of salts in the soil but does not indicate the specific salt or ions that might be present. EC is a good indicator of the presence of salts like sodium, potassium, chloride or sulfate [35]. Saline soils are those with salt levels (EC) above 4 dS/m [36]. In the present study, the soil EC was found to be lower than the saline level. However, a good soil EC level for crop production will be somewhere between 200 and 1200 μS/cm (1.2 mS/cm). The difference between the means is statistically significant between site A and control site B. Soil EC that is lower than 200 μS/cm has insufficiently available nutrients for the plants and could be an indication of a sterile soil with little microbial activity.

On the other hand, EC above 1200 μS/cm may be an indication of too much dissolved salts (e.g. fertilizer) in the soil or a developing salinity problem from lack of drainage [37]. Although site B had the highest SOC and SOM, the soil EC value shows that the site has insufficiently available nutrients.

15.3.2 Physicochemical Properties of Water Samples

The physicochemical properties of the sampled water are presented in Table 15.2.

pH: Generally, the pH dynamics of the water samples was erratic and changes with every sample collection. For instance, while the pH of water changed from slightly acidic to slightly alkaline between week one and week two, it dropped significantly to acidic state in the third week followed by a slight increase during the fourth week. Thereafter, the pH of the sampled water progressively dropped to 5.41. The pH of drinking water recommended by WHO is 6.5–8.5 [35]. The pH of water is a good indicator of its quality and pollution extent. The pH values for all the collected water samples are within allowable limits for surface water [38], except for samples collected between week five and six which are both acidic with a mean value below the recommended standard range as shown in Table 15.2.

The pH of water samples collected in week six (5.41) was more strongly acidic than that of week five (6.39), and this might be caused by burning of waste and fossil fuels which releases carbon dioxide (CO_2) in air. When CO_2 dissolves in water, it creates weak acid such as carbonic acid. ANOVA results indicate that pH of samples was significantly different. Acidic water can pose a threat to aquatic life and human health [39].

At low pH, the acidic nature of the water may liberate toxic heavy metals like Ag, Al, Cd, Co, Cu, Hg, Mg, Ni, Pb and Zn [40].

Water Temperature: This also varied with every sampling, progressively reducing from 25.9 °C for week one to 14.05 °C in week six (Table 15.2). Variations in water temperature may be associated with wind force, inland water flow, the influx

Table 15.2 Physicochemical properties of sampled water (Mean ± SD)

Week	pH	Temperature (°C)	Electrical conductivity (mS/cm)	Total hardness (mg/L)	Total dissolved solids (mg/L)
One	6.91 ± 0.10^a	25.90 ± 0.28^a	35.15 ± 6.72^c	57.5 ± 2.12^a	600 ± 85^b
Two	7.02 ± 0.12^a	21.15 ± 1.34^b	30.30 ± 1.41^d	58.0 ± 1.41^a	720 ± 57^a
Three	6.67 ± 0.16^b	19.60 ± 3.25^c	21.65 ± 0.78^e	54.0 ± 2.83^b	615 ± 50^b
Four	6.86 ± 0.18^a	18.30 ± 4.10^d	44.45 ± 2.33^a	54.0 ± 1.41^b	545 ± 49^c
Five	6.39 ± 0.61^c	15.75 ± 7.28^e	40.70 ± 0.71^b	51.5 ± 6.36^c	420 ± 170^e
Six	5.41 ± 0.53^d	14.05 ± 2.47^e	53.85 ± 27.65^a	50.0 ± 1.41^d	485 ± 64^d

Notes Letters a to e in the means show that there is a statistical significant difference between the variables in the column
Data presented as the mean, n = 3; SD = Standard Deviation; Means with different letters within the same column show a significant difference ($p < 0.05$)

of the rainwater and atmospheric temperature [41]. Water temperature may vary with season and size of the water body, it may also vary on a daily basis. Water temperature is often lowest during the night and early morning and increased from mid to late afternoon [42], thus explaining the temperature variation observed in this study during the cause of water collection for a consecutive 6 week period.

Electrical conductivity (EC): As shown in Table 15.2, the EC values ranged from 21.65 to 53.85 mS/cm, which are well above healthy level and considered not suitable for irrigation, human and livestock consumption. The WHO normal range for electrical conductivity of water is 400–600 µS/cm [35]. In all the tested water samples, the values obtained for EC were higher than these permissible limits. There was a statistical significant difference noted between the collected samples. High EC level in the water may be indicative of the high amount of dissolved salts such as Ca, Cl and Mg present in soil water as ions. Also, salinity may be influenced by natural phenomena, like evapotranspiration and rainfall [43]. Evaporation of water from the dam surface due to high temperatures can concentrate the dissolved solids in the remaining water [44] while rainfall causes dilution.

Total Water Hardness: Water hardness ranges between 50.0 and 58.0 mg/L (Table 15.2). Water hardness is caused by a variety of dissolved multivalent metallic ions, predominantly calcium and magnesium cations. In this study, the water can be categorized as soft since hardness falls below 60 mg/L of dissolved ions [45, 46] and is, therefore, suitable for use as potable water. The analysis from ANOVA indicates significant difference between the samples. However, depending on pH and alkalinity, hardness above 200 mg/L can result in scale deposition, particularly on heating. On the other hand, soft waters with a hardness of less than 100 mg/L have a low buffering capacity and may be more corrosive to water pipes [47].

Total Dissolved Solids (TDS): The TDS of water ranged between 420 and 720 mg/L (Table 15.2). These values fall within the approved WHO standard for drinking water and that of South African guidelines for domestic water use which is in the range of 450–1000 mg/L [48]. The TDS results indicate the presence of solutes (inorganic salts and little organic materials) in water [47, 49], and may be attributed to the prevailing high rainfall, which causes significant dilution [50] of the dam. The ANOVA results show that there was statistical significant difference for TDS in water during the six weeks.

15.3.3   Concentration of Heavy Metals in Plant, Soil and Water Samples

Results of the concentrations of heavy metals in the soils, water, and *Acacia karroo* samples investigated in this study are presented in Table 15.3, Figs. 15.2 and 15.3 respectively.

Copper (Cu): Generally, values obtained for Cu in soil samples of site A were significantly higher than that of site B (Table 15.3). Site A-portion B recorded the

Table 15.3 Mean concentration of selected heavy metals in the soils of the study site (mean ± SD)

Collection site	Mean concentration of heavy metals			
	Cu	Hg	Mn	Pb
Site A-portion A	21.76 ± 19.33[ab]	8.45 ± 8.31[a]	30.12 ± 0.36[a]	1.57 ± 0.83[a]
Site A-portion B	25.19 ± 11.30[a]	6.68 ± 6.22[a]	29.36 ± 1.63[b]	2.30 ± 0.71[a]
Site A-portion C	11.82 ± 12.91[b]	4.58 ± 4.13[a]	29.01 ± 1.99[b]	0.81 ± 0.53[b]
Site B	2.67 ± 1.41[c]	1.08 ± 1.22[b]	16.80 ± 3.71[c]	0.44 ± 0.25[c]

Notes Letters a to c indicate the significant difference between the means, while the means with the same letter show that means do not differ significantly with each other in the column

Data presented as the mean, n = 3; SD = Standard Deviation; Means with different letters within the same column show a significant difference ($p < 0.05$)
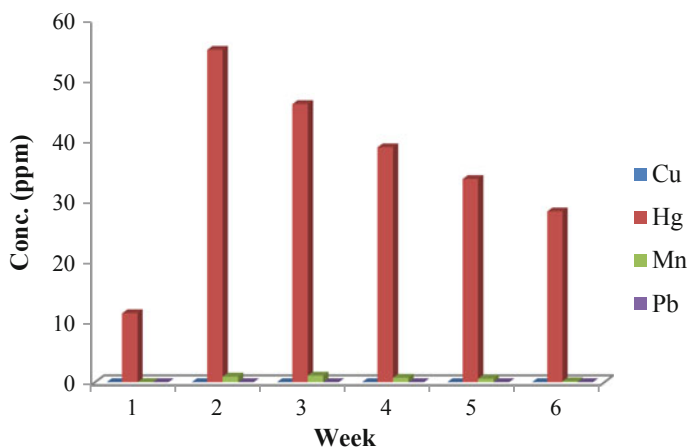
Fig. 15.2 Mean concentration of heavy metals in water from the dam
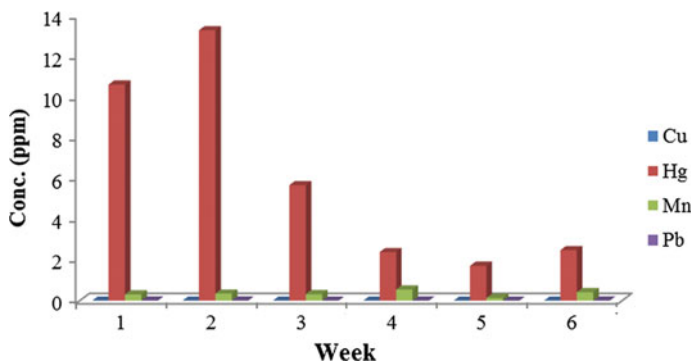
Fig. 15.3 Mean concentration of heavy metals in *Acacia karroo* from site A (dumpsite)

highest deposit of Cu with a significant ($p < 0.05$) increase in Cu deposit compared with site A-portion C and site B.

The highest deposit of Cu (25.19 ppm) at dumpsite A was more than nine times higher than the concentration in site B (2.67 ppm) while the lowest Cu deposit at site A was more than four times the concentration recorded in site B. Despite the high deposit of Cu in dumpsite A, there was no detectable trace of Cu in the water and *Acacia karroo* samples (Figs. 15.2 and 15.3).

WHO recommended 10 mg/kg and 2 mg/L as the maximum permissible limits of Cu for plants and drinking water respectively [51], while the permissible limit recommended by Dutch standard for soil is 36 mg/kg [52]. However, Cu concentration in soils of both study sites was much lower than the approved standard. In human beings, a high concentration of Cu causes metal fumes fever, hair and skin

decolorations, dermatitis, respiratory tract diseases, and some other fatal diseases [53].

Mercury (Hg): Mean concentration of mercury (Hg) was significantly higher ($p < 0.05$) in all the portions of site A compared to site B (Table 15.3). The deposit of this metal was higher in site A-portion A than portion B by about 21%, and with a significant ($p < 0.05$) 7.8 times more Hg deposit compared with site B. In addition, a significant high concentration of Hg was recorded in the water and *Acacia karroo* samples (Figs. 15.2 and 15.3). The mean concentrations of Hg for all collected soil, water, and *Acacia karroo* samples were found to be extremely above the approved limit of WHO. For instance, the permissible limit of Hg recommended by WHO for drinking water is 0.006 mg/L [45] which is much lower than the concentration of Hg found in the dam water (11.420–55.035 mg/L) evaluated in this study. WHO approved 1.0 and 0.03 mg/kg respectively as the maximum permissible limits of Hg for soil and plants [54], whereas in South Africa, the soil permissible limit for Hg is 0.93 mg/kg [55]. In our study, however, Hg concentrations ranged from 1.08 to 8.45 mg/kg in the dumpsites soils and 1.71–13.27 mg/kg in *Acacia karroo* samples. High concentration of Hg in the soil, water, and plant studied in the current investigation may be due to dumping and burning of industrial (municipal and medicinal) wastes which have been produced with mercury on the dumpsites. Exposure to disinfectants (like mercurochrome), antifungal agents, toiletries, creams and organometallics may increase Hg concentration, hence waste generated from these products may be a contributing factor to the high values obtained for these samples [56].

Also, the emissions from coal-using power plants nearby might have contributed significantly to the problem of high Hg levels in the soils of site A and the control site B. The *Acacia karroo* plants growing in site A must have absorbed a significant amount of Hg from the soil and transported this to other parts of the plants. Run-off of Hg-contaminated rainwater during rainfall from the dumpsite to the dam may have also elevated the concentration of Hg in the dam water. Mercury is a naturally occurring metallic element found in trace amount in water, soil, and air, and is a widespread environmental toxicant and pollutant which induces severe alterations in the body tissues and causes a wide range of adverse health effects [57, 58]. All forms of mercury are toxic and their effects include gastrointestinal toxicity, neurotoxicity, and nephrotoxicity [58].

Manganese (Mn): This metal occurs naturally in water, soil, and plants. It is an essential trace heavy metal required by plants and animals for normal growth. High concentration of Mn causes hazardous effects on the lungs and brains of humans [59]. Mn deposit in soil was significantly ($p < 0.05$) higher at site A, recording about twice the amount found in the site B (Table 15.3). Traces of Mn were also detected in the dam water and tissue of the *Acacia karroo* species (Figs. 15.2 and 15.3). Maximum permissible limit of Mn in plants recommended by WHO is 500 mg/kg and toxicity occurs in plants if this level is exceeded [60, 61]. WHO recommended 0.4 mg/L [47] in drinking water while 1 to 45 mg/kg was approved for soil [51].

Mean Mn concentrations for water samples in this study ranged from 0.023 ± 0.020 to 1.106 ± 0.780 mg/L and were all above the normal permissi-

ble limit, except for the samples collected in the first week (0.023 ± 0.020 mg/L). On the other hand, *Acacia karroo* samples recorded mean concentrations of Mn (0.14 ± 0.10 to 0.55 ± 0.39 mg/kg) which are below the normal standard. Likewise, the mean concentrations of Mn in all evaluated soil samples fall within the normal range set by the WHO. Land disposal of manganese-containing wastes is the principal source of manganese releases to the soil [61]. High values of Mn in the water samples may be as a result of a natural occurrence of this metal in surface water and groundwater, erosion of contaminated soils into the water as well as human activities which might have caused Mn contamination [62]. High concentration levels of Mn indicate that the potability of the dam water has been markedly impaired.

Lead (Pb): Deposition of Pb in the soil samples followed a similar trend observed for Cu where Pb concentration in site A-portion B was significantly ($p < 0.05$) higher than site A-portion C and site B, recording about 5.3 times more Pb deposit than site B (Table 15.3). Traces of Pb were also found in the dam water and plant tissue (Figs. 15.2 and 15.3). Dutch permissible limit for Pb in the soil is 85 mg/kg while WHO limits of this metal for plants and drinking water are 2.0 mg/kg [52] and 0.01 mg/L [47] respectively. High Pb concentration in the dumpsites soils compared to control site B may be due to large deposits of used batteries, used plastics (polyethylene) materials, lubrication oils and automobile exhaust fumes. Nevertheless, the lead concentrations in all the soil samples irrespective of the site were lower than the approved limit. Pb concentrations in both water and *Acacia karroo* were also found to be below the standard approved range. In water samples Pb concentration ranged from 0.0011 ± 0.0010 to 0.0044 ± 0.0030 mg/L while 0.003 ± 0.002 to 0.009 ± 0.010 mg/kg were the Pb concentration range obtained for *Acacia karroo* samples.

Lead has no biological importance [59] and is known for its harmful effects on humans as well as causing chronic neurological disorders, especially in foetus and children [63]. Lead poison causes a condition called plumbism or saturnism in a human body [64]. Although lead occurs naturally in the environment, anthropogenic activities such as fossil fuels burning, mining, and manufacturing contribute to its release in high concentrations to the environment [58].

Heavy metal concentration in plants can be caused by several factors which include soil metal concentrations, soil pH, cation exchange capacity, organic matter content, types and varieties of plants, and plant age. It is generally accepted that the metal concentration in soil is the dominant factor [60, 65]. Heavy metal availability can also be directly affected by the plant itself [66].

15.4   Conclusions

Generally, landfill site had a higher concentration of metals than control site probably due to wastes dump. The concentration of Hg and Mn in water samples were above the normal limits permitted by WHO and Hg was beyond the approved limits in both soil and plant samples. At the moment, heavy metal concentrations in the dumpsite

are not of a serious environmental problem according to WHO standard except Hg. Continuous accumulation of metals should be avoided to prevent threat to human health and the ecosystem in future. Specifically, the accumulation of Pb and Hg should be of concern because the US Government Agency for Toxic Substances and Disease Registry ranked these two metals among the three most toxic elements with arsenic ranked first [67].

They are capable of causing serious adverse effects to human health [67, 68], hence Pb and Hg should be well monitored. This study shows the need to sort wastes dumped at the dumpsite and to encourage recycling of the materials. Surrounding dams must be monitored to deliver less expensive quality municipal water. Modern waste disposal facilities for appropriate waste processing are important as well as community education to avoid indiscriminate disposal of wastes.

References

1. Xie Y, Fan J, Zhu W, Amombo E, Lou Y, Chen L, Fu J (2016) Effect of heavy metals pollution on soil microbial diversity and bermudagrass genetic variation. Front Plant Sci 7:755
2. Osunkiyesi AA, Taiwo AG, Olawunmi OA, Akindele OI, Sobo AA (2014) Environmental impact of heavy metal contaminants and micronutrients in soil samples of metal dumpsites in Abeokuta, Ogun State, Nigeria. IOSR J Appl Chem 7:52–55
3. Meng M, Li B, Shao JJ, Wang T, He B, Shi JB, Ye ZH, Jiang GB (2014) Accumulation of total mercury and methylmercury in rice plants collected from different mining areas in China. Environ Pollut 184:179–186
4. Kalantari MR, Shokrzadeh M, Ebadi AG, Mohammadizadeh C, Choudhary MI (2006) Soil pollution by heavy metals and remediation (Mazandaran-Iran). J Appl Sci 6:2110–2116
5. Ukpong EC, Antigha RE, Moses EO (2013) Assessment of heavy metals content in soils and plants around waste dumpsites in Uyo Metropolis, Akwa Ibom State. IJES 2:75–86
6. Nda-Umar UI, Nathaniel GS, Mann A, Yisa J (2012) Assessment of heavy metal species in some decomposed municipal solid wastes in Bida, Niger State, Nigeria. Adv Anal Chem 2:6–9
7. Ebong GA, Akpan MM, Mkpenie VN (2008) Heavy metal contents of municipal and rural dumpsite soils and rate of accumulation by *Carica papaya* and *Talinum triangulare* in Uyo, Nigeria. J Chem 5:281–290
8. Mitsios IK, Golia EE, Tsadilas CD (2005) Heavy metal concentrations in soils and irrigation waters in Thessaly region, Central Greece. Commun Soil Sci Plan 36:487–501
9. Azeez JO, Hassan OA, Egunjobi PO (2011) Soil contamination at dumpsites implication of soil heavy metals distribution in municipal solid waste disposal system: a case study of Abeokuta, Southwestern Nigeria. Soil Sediment Contam 20:370–386
10. Aucott M (2006) The fate of heavy metals in landfills: a review. New York Academy of Sciences, New York, USA
11. Njagi JM (2013) Assessment of heavy metal concentration in the environment and perceived health risks by the community around Kadhodeki dumpsite, Nairobi Country. Doctoral Dissertation, Kenyatta University, Kenya

12. Momba MNB, Tyafa Z, Makala N, Brouckaert BM, Obi CL (2006) Safe drinking water still a dream in rural areas of South Africa. Case study: the Eastern Cape Province. Water SA 32:715–720
13. Kotz JC, Treichel PM, Weaver GC (2005) Chemistry and chemical reactivity. Brooks & Cole, Belmont, USA
14. Taylor CL, Barker NP (2012) Species limits in *Vachellia (Acacia) karroo* (Mimosoideae: Leguminosae): evidence from automated ISSR DNA "fingerprinting". S Afr J Bot 83:36–43
15. Baroni L, Cenci L, Tettamanti M, Berati M (2007) Evaluating the environmental impact of various dietary patterns combined with different food production systems. Eur J Clin Nutr 61:279–286
16. Opaluwa OD, Aremu MO, Ogbo LO, Abiola KA, Odiba IE, Abubakar MM, Nweze NO (2012) Heavy metal concentrations in soils, plant leaves and crops grown around dump sites in Lafia Metropolis, Nasarawa State, Nigeria. Adv Appl Sci Res 3:780–784
17. Zhang H, Cui B, Xiao R, Zhao H (2010) Heavy metals in water, soils, and plants in riparian wetlands in the Pearl River Estuary, South China. Procedia Environ Sci 2:1344–1354
18. Tsade HK (2016) Atomic absorption spectroscopic determination of heavy metal concentrations in Kulufo River, Arbaminch, Gamo Gofa Ethiopia. J Environ Anal Chem 3:177
19. Parajuli PB, Duffy S (2013) Evaluation of soil organic carbon and soil moisture content from agricultural fields in Mississippi. Open J Soil Sci 3:81–90
20. Eckert D, Sims JT (2011) Recommended soil pH and lime requirement tests. In: Recommended soil testing procedures for the Northeastern United States. Northeast Regional Bulletin 493:19–26
21. Vlab.amrita.edu. (2013) Soil analysis—Determination of available organic carbon in the soil. Retrieved from http://vlab.amrita.edu/?sub%E2%80%89=%E2%80%892&brch%E2%80%89=%E2%80%89294&sim%E2%80%89=%E2%80%891552&cnt%E2%80%89=%E2%80%891. Accessed 25 May 2016
22. Motsara MR, Roy RN (2008) Guide to laboratory establishment for plant nutrient analysis, vol 19. Food and Agriculture Organization of the United Nations, Rome, Italy
23. Sam KK (2013) Determination of total dissolved solids (TDS) in water and wastewater. Inclusive Science and Engineering. Available at: http://www.inclusive-science-engineering.com/determination-total-dissolved-solids-tds-water-wastewater/. Accessed 26 Aug 2016
24. Nduwumuremyi A (2013) Soil acidification and lime quality: sources of soil acidity, effects on plant nutrients, the efficiency of lime and liming requirements. J Agr Allied Sci 2:26–34
25. Olaniran AO, Balgobind A, Pillay B (2013) Bioavailability of heavy metals in soil: impact on microbial biodegradation of organic compounds and possible improvement strategies. Int J Mol Sci 14:10197–10228
26. Oloyede-Kosoko SOA, Idowu AO, Ayoni OO (2015) Evaluation of water quality with World Health Organization and Nigeria Industrial Standards using geographic information system. World Sci News 24:18–42
27. Zhou W, Hui D, Shen W (2014) Effects of soil moisture on the temperature sensitivity of soil heterotrophic respiration: a laboratory incubation study. PLoSOne 9:e92531
28. Sato JH, Figueiredo CCD, Marchão RL, Madari BE, Benedito LEC, Busato JG, Souza DMD (2014) Methods of soil organic carbon determination in Brazilian savannah soils. Sci Agr 71:302–308
29. Musinguzi P, Tenywa JS, Ebanyat P, Tenywa MM, Mubiru DN, Basamba TA, Leip A (2013) Soil organic carbon thresholds and nitrogen management in tropical agroecosystems: concepts and prospects. J Sustain Dev 6:31–43
30. Deb S, Bhadoria PBS, Mandal B, Rakshit A, Singh HB (2015) Soil organic carbon: towards better soil health, productivity, and climate change mitigation. Clim Change Environ Sustainability 3:26–34
31. Hopkins FM, Filley TR, Gleixner G, Lange M, Top SM, Trumbore SE (2014) Increased below ground carbon inputs and warming promote loss of soil organic carbon through complementary microbial responses. Soil Biol Biochem 76:57–69

32. Ranjan R, Divya M, Bavitha M (2015) The importance of soil food web for a healthy environment and sustainable development. Int J Appl Res 1:15–20
33. Wild B, Schnecker J, Alves RJE, Barsukov P, Bárta J, Čapek P, Gentsch N, Gittel A, Guggenberger G, Lashchinskiy N, Mikutta R (2014) Input of easily available organic C and N stimulates microbial decomposition of soil organic matter in Arctic permafrost soil. Soil Biol Biochem 75:143–151
34. Xiao S, Zhang W, Ye Y, Zhao J, Wang K (2017) Soil aggregate mediates the impacts of land uses on organic carbon, total nitrogen, and microbial activity in a Karst ecosystem. Sci Rep 7:41402
35. Ullman JL (2013) Soil salinity in agricultural systems: the basics. Agricultural & Biological Engineering University of Florida. Available at: http://hos.ufl.edu/sites/default/files/faculty/gdliu/ullman.pdf. Accessed on 21 April 2018
36. Ray RW, Nyle CB (2016) The nature and properties of soils, 15th edn. Pearson, USA
37. Verma JK, Sharma A, Paramanick KK (2015) To evaluate the values of electrical conductivity and growth parameters of apple saplings in nursery fields. Int J Appl Sci Eng Res 4:321–332
38. Al-Badaii F, Shuhaimi-Othman M, Gasim MB (2013) Water quality assessment of the Semenyih River, Selangor, Malaysia. J Chem Article ID 871056
39. Postel S, Richter B (2012) Rivers for life: managing water for people and nature. Island Press, USA
40. Turhanen PA, Vepsäläinen JJ, Peräniemi S (2015) Advanced material and approach for metal ions removal from aqueous solutions. Sci Rep 5:8992
41. Sallam GA, Elsayed EA (2015) Estimating the impact of temperature and relative humidity change on the water quality of Lake Manzala Egypt. J Nat Resourc Dev 5:76–87
42. Middel A, Häb K, Brazel AJ, Martin CA, Guhathakurta S (2014) Impact of urban form and design on mid-afternoon microclimate in Phoenix local climate zones. Landscape Urban Plan 1:16–28
43. Mwangi FN (2014) Land use practices and their impact on the water quality of the Upper Kuils River (Western Cape Province, South Africa). Doctoral dissertation, University of Western Cape
44. Rehman HU, Akbar NU, Gul I, Gul N, Akhwan S, Sajed M, Khan P, Khan MA, Hamidullah SB, Wahab A (2015) Impacts of some physicochemical parameters of water and soil collected from Panjkora River, Pakistan. Global Veterinaria 15:57–61
45. Mgombezi D, Rao V, Vuai SH, Singh SK (2017) An investigation on effectiveness of cactus materials (*Opuntia Spp.*) as adsorbents for hard water treatment. Int J Sci Technol Res 6:239–244
46. USGS (2017) USGS water-quality information: water hardness and alkalinity. US Geological Survey Office of Water Quality. Available at: https://water.usgs.gov/owq/hardness-alkalinity.html. Accessed 28 Feb 2017
47. Kumar RRR, Series SC (2012) Water, soil, and sediment characterization: Sharavathi river basin, Western Ghats. Envis Technical Report, Environmental Information System (ENVIS) Centre for Ecological Sciences, Indian Institute of Science, Bangalore, India
48. Fisher-Jeffes LN, Armitage NP, Carden K (2017) The viability of domestic rainwater harvesting in the residential areas of the Liesbeek River Catchment, Cape Town. Water SA 43:81–90
49. Saana SBBM, Fosu SA, Sebiawu GE, Jackson N, Karikari T (2016) Assessment of the quality of groundwater for drinking purposes in the Upper West and Northern regions of Ghana. Springerplus 5:2001
50. Edokpayi JN, Odiyo JO, Msagati TA, Potgieter N (2015) Temporal variations in physicochemical and microbiological characteristics of Mvudi River, South Africa. Int J Environ Res Pub Health 12:4128–4140
51. Okeyode IC, Rufai AA (2011) Determination of elemental composition of soil samples from some selected dumpsites in Abeokuta, Ogun State, Nigeria, using atomic absorption spectrophotometer. Int J Basic Appl Sci 11:55–70
52. Ogundele DT, Adio AA, Oludele OE (2015) Heavy metal concentrations in plants and soil along heavy traffic roads in North Central Nigeria. J Environ Anal Toxicol 5:1

53. Shah A, Niaz A, Ullah N, Rehman A, Akhlaq M, Zakir M, Suleman Khan M (2013) Comparative study of heavy metals in soil and selected medicinal plants. J Chem Article ID 621265

54. Anyalogbu EAA, Anadi CC, Nweje-Anyalowu PC, Nnoli MC (2017) Use of waterleaf (*Talinum triangulare*) in the remediation of soil exposed to heavy metals: a green technology approach. World J Pharm Life Sci 3:48–53

55. Kamunda C, Mathuthu M, Madhuku M (2016) Health risk assessment of heavy metals in soils from the Witwatersrand gold mining basin, South Africa. Int J Environ Res Pub Health 13:663

56. Pagrut NS (2012) Heavy metal toxicity in canines with special reference to reproductive status. Doctoral dissertation, MAFSU, Nagpur, India

57. Asiamah G (2014) Heavy metal concentration in the Owere River at Konongo. Master dissertation, Kwame Nkrumah University of Science and Technology, Ghana

58. Tchounwou PB, Yedjou CG, Patlolla AK, Sutton DJ (2012) Heavy metal toxicity and the environment. In: Luch A (ed) Molecular, Clinical and Environmental Toxicology. Experientia Supplementum, vol 101. Springer, Basel, Switzerland

59. Jaishankar M, Tseten T, Anbalagan N, Mathew BB, Beeregowda KN (2014) Toxicity mechanism and health effects of some heavy metals. Interdisc Toxicol 7:60–72

60. Khan MU, Malik RN, Muhammad S (2013) Human health risk from heavy metal via food crops consumption with wastewater irrigation practices in Pakistan. Chemosphere 93:2230–2238

61. Trollip DL, Hughes JC, Titshall LW (2013) Sources of manganese in the residue from a water treatment plant. Water SA 39:265–270

62. World Health Organization (2011) Manganese in drinking-water: background document for development of WHO guidelines for drinking-water quality. Switzerland, Geneva

63. Neal AP, Guilarte TR (2013) Mechanisms of lead and manganese neurotoxicity. Toxicol Res 2:99–114

64. Garcés JBG, Artuz RIM (2012) Lead poisoning due to bullets lodged in the human body. Colomb Med 43:230–234

65. Naser HM, Sultana S, Mahmud NU, Gomes R, Noor S (2011) Heavy metal levels in vegetables with growth stage and plant species variations. Bangladesh J Agric Res 36:563–574

66. Hajar EWI, Sulaiman AZB, Sakinah AM (2014) Assessment of heavy metals tolerance in leaves, stems, and flowers of *Stevia rebaudiana* plant. Procedia Environ Sci 20:386–393

67. Rice KM, Walker EM Jr, Wu M, Gillette C, Blough ER (2014) Environmental mercury and its toxic effects. J Prev Med Pub Health 47:74–83

68. Flora G, Gupta D, Tiwari A (2012) Toxicity of lead: a review with recent updates. Interdisc Toxicol 5:47–58

Chapter 16
Chromate Ion Adsorption onto Nanostructured Mn–Fe Oxide: Kinetics and Equilibrium Study

Albert J. K. Kupeta, Eliazer B. Naidoo and Augustine E. Ofomaja

Abstract A nanostructured binary metal oxide adsorbent, from chloride salts of manganese and iron, was synthesized by co-precipitation method and applied in sequestration of chromate ions from simulated industrial wastewater. The prepared adsorbent was characterized using X-ray photoelectron spectroscopy (XPS), BET analysis and scanning electron microscopy (SEM) coupled with an energy dispersive X-ray spectrometer (EDS). Batch, kinetic and equilibrium experiments were performed to investigate the adsorption parameters. The pseudo second order kinetic ($R^2 \geq 0.9965$) and Langmuir equilibrium isotherm ($R^2 \geq 0.9994$) models showed good fits to the experimental adsorption data. Thermodynamic parameters (ΔG°, ΔH° and ΔS°) showed that the adsorption is spontaneous, exothermic and decreases randomness at the solid/liquid interface.

Keywords Adsorption · Chromate · Models · Nanostructured · Parameters

16.1 Introduction

Industrial effluents from mining, textile, pharmaceutical, automobile, metallurgy, etc. are laden with harmful organic and inorganic compounds which are deleterious to flora and fauna. The inorganic pollutants comprise of heavy metals such as chromium which are non-biodegradable and contaminate ecological food chains. Chromium is found in the hydrosphere as trivalent chromite [Cr(III)] and hexavalent chromate [Cr(VI)] ions [1, 2]. Chromite ions are less toxic while chromate ions ($CrO_4^{2-}/Cr_2O_7^{2-}$) are highly toxic even at ppb levels [3, 4]. Human exposure causes

A. J. K. Kupeta · E. B. Naidoo · A. E. Ofomaja (✉)
Biosorption and Wastewater Treatment Research Laboratory, Department of Chemistry, Faculty of Applied and Computer Sciences, Vaal University of Technology, P. Bag X021, Vanderbijlpark 1900, South Africa
e-mail: augustineo@vut.ac.za

A. J. K. Kupeta
e-mail: albertkupeta@yahoo.com

E. B. Naidoo
e-mail: bobby@vut.ac.za

mutations, cancers and hemorrhage amongst a myriad of other health problems [5]. Chromate ions inhibit plant development by interfering with important physiological processes such as chlorophyll synthesis [6]. The maximum contaminant level (MCL) for total chromium in potable water should not exceed 0.05 mg/dm^3 [7]. This makes it critical to develop efficient and cost-effective chromium remediation techniques from aqueous media.

Several technologies such as electrochemical reduction, membrane filtration, chemical precipitation, photocatalytic reduction, etc. have been applied in remediation of chromium-infested wastewaters [8–11]. A major drawback to utilization of these remediation technologies is cost, high energy demand, technical expertise coupled with production of noxious sludge [12]. Adsorption has become a cost-effective alternative amongst these heavy metal remediation techniques from the solvent phase [13].

Agricultural wastes, industrial wastes, metal oxides, activated carbon and microorganisms are some of the adsorbents that have been investigated and applied in clean-up of chromate-infested waters [1, 14–16]. Current research is focusing on the use of nanostructured adsorbents which have high surface areas, large adsorption capacities, fast kinetics and high selectivity towards the target pollutant [17, 18].

The objective of the present study was to synthesize a nanostructured Mn–Fe oxide adsorbent using simple co-precipitation method and investigate its technical applicability in the remediation of chromate ions from simulated industrial wastewater. Batch, kinetic and equilibrium experiments were conducted to determine the adsorption process variables. Kinetic and equilibrium data were modelled with a Quasi Newton regression algorithm of KyPlot software to determine the adsorption parameters.

16.2 Experimental

16.2.1 Chemical Reagents

All the chemicals used in the investigation were of analytical grade and purchased from Sigma-Aldrich (Germany). The chromate ion stock solution was prepared from $K_2Cr_2O_7 \cdot 7H_2O$ and ultrapure water from a MERCK Millipore (Germany) instrument.

16.2.2 Preparation of Nanostructured Mn–Fe Oxide Adsorbent

The binary nanometal oxide was synthesized by co-precipitation using a 2:1 mol ratio of $MnCl_2$ and $FeCl_3 \cdot 6H_2O$ at 299 K. To achieve the co-precipitation of the

binary system, a 3 mol/dm^3 NaOH solution was added dropwise to a mixture of the metal salts aqueous solution until pH 8. The suspension was magnetically stirred for 1 h at 400 rpm and then aged for 4 h. The solid material was separated from the liquid phase by centrifuging at 6000 rpm for 5 min, repeatedly washed with ultrapure water until neutral pH and then dried at 333 K in a thermostatic vacuum oven for 24 h. The resultant solid was pulverized and calcined in air at 773 K for 6 h, before being characterized and used for analysis.

16.2.3   Characterization of Mn–Fe Binary Oxide

The surface morphology of the adsorbent was investigated using a ZEISS Ultra/Plus FEG-SEM (Germany) scanning electron microscope coupled to an energy dispersive X-ray spectroscopy(EDS) analyzer at different magnifications. X-ray photoelectron spectroscopy (XPS) was used to identify the electronic states of the elements in the binary oxide on a PHI 5000 scanning ESCA microprobe (Japan). The adsorbent BET (Brunauer-Emmett-Teller) specific surface area, pore volume and pore sizes distribution were determined by computer-controlled N$_2$ adsorption at 77 K using a Tristar 3000 analyzer coupled to a VacPrep 061 degassing unit. The instruments were both supplied by Micromeritics Instrument Corporation (Australia).

16.2.4   Analytical Technique

Atomic absorption spectroscopy (AAS) on a SHIMADZU AA 7000 (Japan) spectrophotometer was used to determine total chromium remaining in solution after adsorption. Metal oxides can reduce hexavalent chromate ions to trivalent chromite ions. Use of spectroscopy to measure residual hexavalent chromate ion concentration might give a distorted adsorption capacity, as some of the chromate ions will not have been adsorbed, but merely reduced to chromite ions, and still be present in solution.

16.2.5   Adsorption Dynamics

To determine the influence of solution pH on adsorption of chromate ions onto Mn–Fe oxide, batch experiments were performed from pH 2–7 at 299 K in 250 cm^3 glass bottles containing 100 cm^3 of 100 mg/dm^3 chromate solution. The pH was adjusted using 0.1 mol/dm^3 NaOH or HCl. Since metals can leach in acidic media, the amounts of adsorbent metal components leaching into treated water at different pH values (2–6) were measured at 299 K, by agitating 0.05 g of adsorbent at 200 rpm in 100 cm^3 ultrapure water for 2 h. The suspension was centrifuged and analysed for Mn and Fe using AAS.

Both kinetic and equilibrium studies were performed with 0.05 g adsorbent in 250 cm^3 glass bottles with 100 cm^3 chromate ion solution at pH 3, using a stirring speed of 200 rpm. The kinetic experiments were conducted with different chromate ion concentrations (10–75 mg/dm^3). Aliquot samples (0.5 cm^3) were pipetted from the mother liquor at different time intervals (0.5, 1, 2, 3, 5, 30, 45, 60, 75, 90 and 120 min) and the residual chromium concentration determined by AAS. Equilibrium isotherm studies were performed at 299–319 K with various chromate ion concentrations (50–400 mg/dm^3). The adsorption process was stopped by centrifugation and the remaining chromium concentration was measured using AAS.

The adsorbed amount of chromate ions per unit mass of adsorbent q_e (mg/g) was given by Eq. (16.1):

$$q_e = \frac{(C_0 - C_e)V}{m} \tag{16.1}$$

where C_0 and C_e (mg/dm^3) are the initial and equilibrium chromate ion concentrations, m (g) is the adsorbent mass and V (dm^3) is the adsorbate volume.

16.3 Results and Discussion

16.3.1 Adsorbent Characterization

The SEM image for Mn–Fe binary nanostructured oxide is presented in Fig. 16.1. The surface of Mn–Fe oxide shows agglomeration of the nanoparticles and the image is consistent with previous research [19]. The micrograph shows that the particles are rough, non-uniform in size and shape. Pores are also visible on the micrograph and can be attributed to evolution of gases during drying [20]. The weight percentage composition by mass of Mn, Fe and O in the oxide determined from EDS data were 8.89, 50.58 and 40.42, respectively. This data is qualitative as it represents a miniscule portion of the nanomaterial.

The XPS detailed scans of Mn–Fe oxide are plotted in Fig. 16.2. The signal for Mn 2p core level in Fig. 16.2a shows a doublet due to spin coupling attributed to Mn 2p$_{3/2}$ (641.9 eV) and Mn 2p$_{1/2}$ (653.0 eV). The Mn 2p$_{3/2}$ peak is attributed to the presence of Mn^{2+} [21, 22]. The detailed XPS spectrum for Fe 2p in Fig. 16.2b is consistent with those found in the literature [23]. The Fe 2p$_{3/2}$ peak position (710.8 eV) and shape are characteristic of Fe^{3+} in iron oxy-hydroxides or iron oxides, most likely goethite, amorphous ferrihydrite or γ-Fe$_2$O$_3$ [22, 24, 25]. The shake-up signal at 715.7 eV further corroborates presence of Fe^{3+} and suggests high iron content in the sample [23]. Figure 16.2c shows a detailed XPS spectrum for O 1s. The main peak at 529.3 eV is ascribed to lattice oxygen in the form of O^{2-}, characteristic of the transition metal-oxygen bond. The peak at 531.1 eV ($\approx$1.8 eV above the main peak)
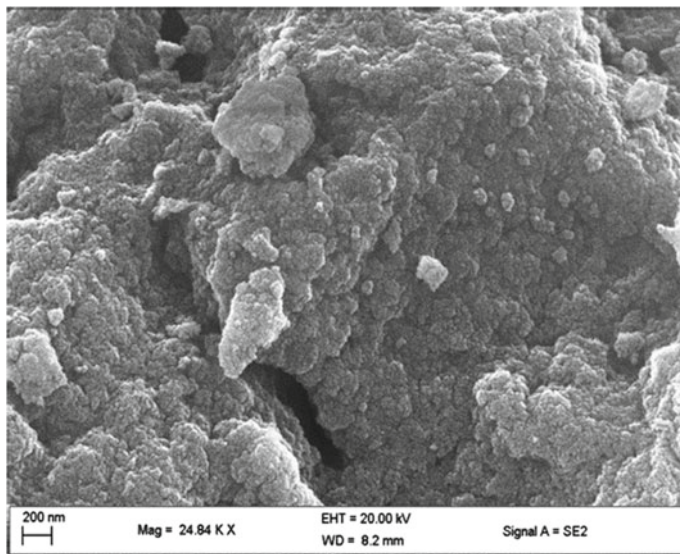
Fig. 16.1 Scanning electron micrograph of Mn–Fe binary oxide

is attributed to surface adsorbed oxygen, probably in the form of OH^- moieties or defective site in the oxide [21, 24–26].

The pore structure of the Mn–Fe nanometal oxide was determined by N_2 gas physisorption measurements (BET). The surface area, pore volume and pore size were found to be 217.5228 m^2/g, 0.2832 cm^3/g and 4.3657 nm, respectively.

16.3.2   Effect of pH on Adsorption

Solution pH determines adsorbent surface charge and adsorbate speciation. At pH at point of zero charge (pH_{pzc}) the adsorbent surface has zero charge. At pH < pH_{pzc}, the adsorbent surface is positively charged and is negatively charged at pH > pH_{pzc}. The pH_{pzc} of Mn–Fe oxide was found to be 5.28. The effect of pH on chromate adsorption is shown in Fig. 16.3.

The adsorption process is dependent on pH suggesting that electrostatic interactions and ion exchange might be part of the mechanism. At low pH, the chromate mainly exists as $HCrO_4^-$ [27] while the adsorbent surface is positively charged resulting in electrostatic attraction. The adsorption capacity is highest at pH 2 but leaching of adsorbent metal components into the treated water is also highest at that pH as shown in Table 16.1. Hence, a pH of 3 was taken as the optimum. An increase in solution pH greatly reduces the adsorption process due to repulsion between the negatively charged adsorbent surface and adsorbate.
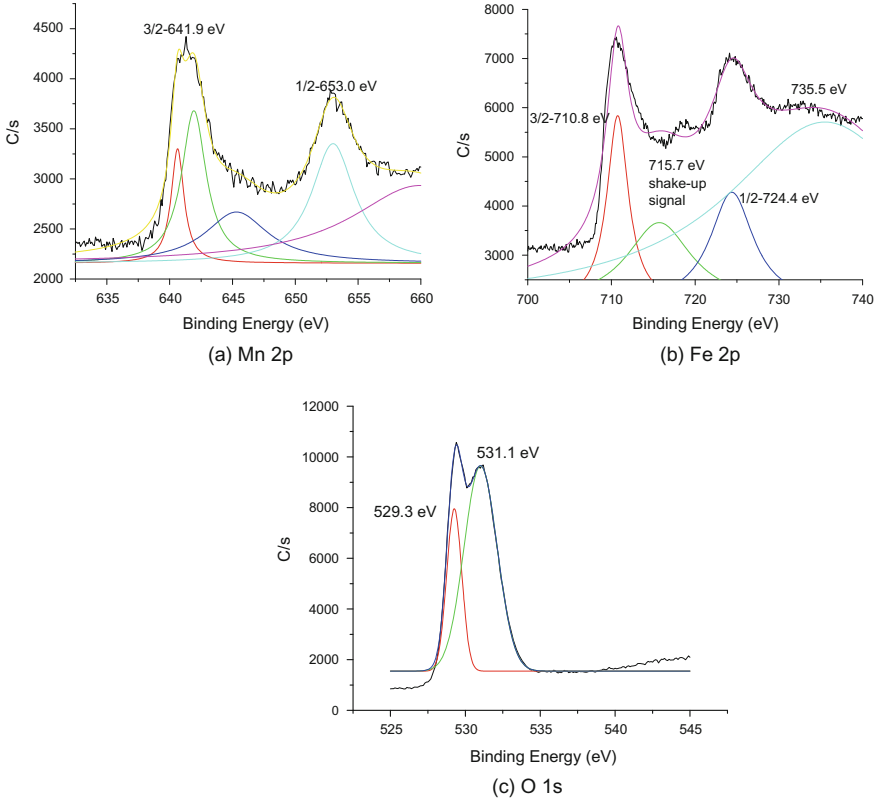
(a) Mn 2p

(b) Fe 2p

(c) O 1s

Fig. 16.2 X-ray photoelectron spectroscopy detailed scan for: **a** Mn 2p, **b** Fe 2p and **c** O 1s

Fig. 16.3 Influence of pH on adsorption of chromate ions onto Mn–Fe oxide
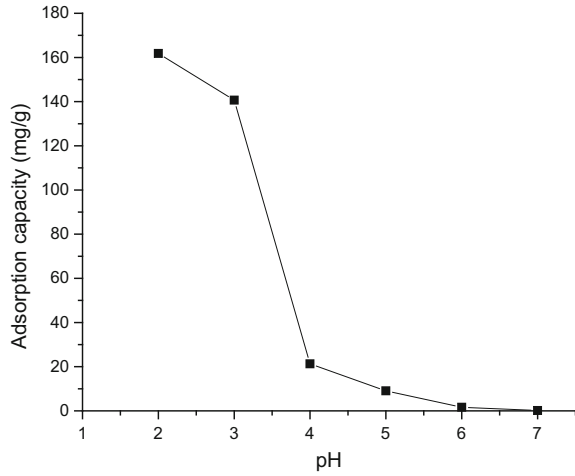
Table 16.1 Leaching of adsorbent components as a function of pH

pH	2	3	4	5	6
Mn (mg/dm^3)	0.0532	0.0346	0.0272	0.0232	0.0176
Fe (mg/dm^3)	0.0864	0.0429	0.0309	0.0113	0.0057

16.3.3 Kinetics of Chromate Adsorption

The adsorption kinetics of chromate ions onto the Mn–Fe oxide was modeled using non-linear forms of the pseudo first [28] and pseudo second order [29] kinetic equations. The pseudo first order kinetic equation describes adsorption which proceeds by diffusion through a boundary, and the pseudo second order kinetic equation predicts adsorption kinetics proceeding by monolayer chemisorption. The non-linear forms of the pseudo first and pseudo second order kinetic equations are presented as Eqs. (16.2) and (16.3), respectively as:

$$q_t = q_e\left(1 - e^{-k_1 t}\right) \tag{16.2}$$

and,

$$q_t = \frac{k_2 q_e^2 t}{1 + k_2 q_e t} \tag{16.3}$$

where q_t and q_e (mg/g) are the adsorbed amounts at time t and at equilibrium respectively, with k_1 (1/min) and k_2 (g/mg min) being the pseudo first and pseudo second order rate constants, respectively. A non-linear plot of q_t against t gave values for q_e and the rate constants k_1 and k_2. The initial adsorption rate, h (mg/g min) [30] in the pseudo second order equation is given by:

$$h = k_2 q_e^2 \tag{16.4}$$

Tables 16.2 and 16.3 show the pseudo first and pseudo second order kinetic equation parameters and the correlation coefficient error function, R^2. The results show

Table 16.2 Pseudo first order kinetic modeling of different chromate ion concentrations onto Mn–Fe binary nanometal oxide

	Concentration (mg/dm^3)				
	10	20	25	50	75
q_e (exp)	14.1440	27.9480	49.8440	83.6120	126.3920
q_e	13.7789	27.6127	48.1258	80.3509	121.2535
k_1	0.5222	0.4760	0.7684	1.1519	1.2962
R^2	0.9729	0.9809	0.9737	0.9613	0.9626

Table 16.3 Pseudo second order kinetic modeling of different chromate ion concentrations onto Mn–Fe binary nanometal oxide

	Concentration (mg/dm^3)				
	10	20	25	50	75
q_e (exp)	14.1440	27.9480	49.8440	83.6120	126.3920
q_e	14.2862	28.6278	50.0633	83.7557	126.1825
k_2	0.0591	0.0264	0.0253	0.0232	0.0171
h	12.0620	21.6361	63.4103	162.7484	281.8198
R^2	0.9979	0.9965	0.9982	0.9979	0.9972

that the experimental and calculated adsorption capacities increased with an increase in chromate ion concentration. This is attributed to a greater driving force, reducing mass transfer resistance resulting in an increase in collision frequency between adsorbate and adsorbent surface [31]. The results showed a better fit onto the pseudo second order kinetic equation, as observed from the higher values of the correlation coefficient ($R^2 \geq 0.9965$). The calculated adsorption capacities from the pseudo second order kinetic equation are closer to the experimental adsorption capacities than those predicted from the pseudo first order kinetic equation. The rate constant, k_1, does not show a trend with an increase in chromate ion concentration, but the rate constant, k_2, decreases with an increase in chromate ion concentration. A similar result was reported on adsorption of chromate ions onto dolomite [32]. The authors attributed the decrease in magnitude of k_2 to an increase in competition for active sites. The initial adsorption rate, h, increases with an increase in chromate ion concentration. This shows initial rapid uptake due to increase in chromate ions and indicates high affinity for adsorbate and fast adsorption kinetics characteristic of heavy metal adsorbates. Similar results were reported in literature by researchers who also observed high initial rates of adsorption of Zn^{2+} onto Lewatit S1468 [33] and Cd^{2+} onto biochar [34]. Kinetic equations are empirical, and their parameters cannot conclusively explain suitability of a model over another in justifying an adsorption process [31, 35, 36].

16.3.4 Isotherm Studies

The equilibrium adsorption data was modeled using non-linear forms of the Langmuir [37] and Freundlich [38] isotherm models. The Langmuir model is based on the following assumptions: (1) active sites are identical; (2) only reversible monolayer adsorption takes place; and (3) there is no interaction between adsorbed species. The non-linear form of the Langmuir isotherm equation is:

$$q_e = \frac{q_m k_b C_e}{1 + k_b C_e} \qquad (16.5)$$

where q_e (mg/g) is the equilibrium adsorption capacity, C_e (mg/dm^3) is the equilibrium adsorbate concentration, q_m (mg/g) and k_b (dm^3/mg) are the Langmuir constants representing maximum saturated monolayer coverage capacity and adsorption energy parameter respectively. The Langmuir constant, k_b, is a measure of affinity between adsorbate and adsorbent. A dimensionless separation factor R_L, determines shape of the isotherm [39] and is given by:

$$R_L = \frac{1}{1 + k_b C_0} \tag{16.6}$$

where C_0 (mg/dm^3) is the initial adsorbate concentration. If $R_L = 0$, irreversible (horizontal); $R_L < 1$, favorable (concave); $R_L > 1$, unfavorable (convex); and $R_L = 1$, linear [40].

The non-linear form of the Freundlich isotherm equation is:

$$q_e = K_F C_e^{\frac{1}{n}} \tag{16.7}$$

where K_F ((mg/g)/(mg/dm^3)^n) and n (dimensionless) are the Freundlich constants representing adsorption capacity and intensity of adsorption, respectively. The model assumes adsorption on a heterogeneous surface with interaction between adsorbed species. According to the model, the isotherm shape is unfavorable when $n > 1$, favorable when $n < 1$ and linear when $n = 1$ [41]. The Langmuir and Freundlich isotherm parameters are presented in Table 16.4. The results show that the Langmuir model ($R^2 \geq 0.9994$) showed a better fit to the adsorption data, in comparison to the Freundlich model ($R^2 \geq 0.9820$). The calculated R_L values were 0.45, 0.32, 0.20, 0.17 and 0.15, corresponding to 50, 100, 200, 300 and 400 mg/dm^3 initial adsorbate concentrations respectively. The R_L values decreased with an increase in initial adsorbate concentration. The magnitude of their values shows that the Langmuir isotherm shape is favorable. The Langmuir maximum adsorption capacity

Table 16.4 Langmuir and Freundlich isotherm modeling of chromate ion adsorption onto Mn–Fe oxide

	Temperature (K)				
	299	304	309	314	319
Langmuir					
q_m	186.2797	174.9995	151.9222	143.0998	138.6253
k_b	0.0246	0.0213	0.0198	0.0161	0.0136
R^2	0.9994	0.9998	0.9997	0.9998	0.9995
Freundlich					
K_F	28.3666	23.9522	20.4141	15.7352	12.6661
n	3.1793	3.0400	3.0417	2.7965	2.6057
R^2	0.9852	0.9833	0.9820	0.9867	0.9863

Table 16.5 Comparison of chromate ion adsorption capacities of various adsorbents

Adsorbent	Langmuir capacity (mg/g)	Best fit isotherm	References
Dolomite	10.01	Freundlich	[32]
Ceria nanoparticles	26.81	Langmuir	[42]
Iron fleshing	50.51	Langmuir	[43]
Mesoporous silica	193.85	Langmuir	[44]
Clarified sludge	26.31	Langmuir	[45]
Mn–Fe oxide	186.28	Langmuir	This study

(q_m) also decreases from 186.28 to 138.63 mg/g as the temperature increased from 299 to 319 K. This suggests that the adsorption process is exothermic.

The Langmuir maximum adsorption capacity of the nanostructured Mn–Fe oxide compares favorably with other adsorbents reported in the literature. The comparison results are presented in Table 16.5.

16.3.5 Adsorption Thermodynamics

The adsorption thermodynamics parameters for removal of chromate using Mn–Fe oxide are presented in Table 16.6 and were determined using:

$$\Delta G^\circ = -RT \ln k_b \qquad (16.8)$$

and the Van't Hoff equation, expressed as:

$$\ln k_b = \frac{-\Delta H^\circ}{RT} + \frac{\Delta S^\circ}{R} \qquad (16.9)$$

Table 16.6 Thermodynamic parameters for adsorption of chromate ions onto Mn–Fe oxide

Temperature (K)	ΔG° (kJ/mol)	ΔH° (kJ/mol)	ΔS° (J/mol K)
299	−17.784	−22.51	−15.67
304	−17.717		
309	−17.808		
314	−17.569		
319	−17.459		

where, ΔG° (kJ/mol) is the free Gibbs energy change, R (J/mol K) is the ideal gas constant, T (K) is the temperature, k_b (dm^3/mg) is the equilibrium constant and is derived from the Langmuir equation, ΔH° (kJ/mol) is the change in enthalpy and ΔS° (J/mol K) is the change in entropy of the reaction. A plot of ln k_b against $1/T$ from Eq. (16.9) gave ΔH° and ΔS° values ($R^2 = 0.9814$).

The negative enthalpy change (ΔH°) shows that the adsorption process is exothermic, while the negative free energy change (ΔG°) values imply that the process is feasible and spontaneous. The free energy change decreased in magnitude from -17.784 to -17.459 kJ/mol with an increase in temperature from 299 to 319 K. A negative entropy change (ΔS°) indicates decrease in randomness during the adsorption at the solid/liquid interface.

16.4   Conclusion

A porous, nanostructured binary metal oxide with a large surface area was prepared from chloride salts of manganese and iron by simple co-precipitation technique. The adsorption process was pH dependent, as low pH resulted in protonation of adsorbent surface enhancing removal of the chromate anions from the liquid phase. Kinetic studies showed that the experimental data best suited the pseudo second order kinetic model suggesting that chemisorption is the dominant adsorption mechanism. The Langmuir isotherm model showed the best fit to the experimental data suggesting that the adsorption occurs by monolayer coverage of the adsorbent surface. Calculation of thermodynamic parameters (ΔG°, ΔH° and ΔS°) showed that the adsorption is spontaneous, exothermic and exhibits reduced degree of randomness at the solid/liquid interface. Experimental data and thermodynamic parameters highlighted that the adsorption is exothermic. Increase in temperature reduced the adsorption capacity and the change in free energy. This investigation was undertaken to determine the technical applicability of adsorption of chromate ions onto the nanostructured Mn–Fe oxide prepared by simple co-precipitation. Further studies are in progress to elucidate the intrinsic mechanistic pathway of the adsorption process.

References

1. Dhal B, Thatoi HN, Das NN, Pandey BD (2013) Chemical and microbial remediation of hexavalent chromium from contaminated soil and mining/metallurgical solid waste: a review. J Hazard Mater 250–251:272–291

2. Headlam HA, Lay PA (2016) Spectroscopic characterization of genotoxic chromium(V) peptide complexes: oxidation of chromium(III) triglycine, tetraglycine and pentaglycine complexes. J Inorg Biochem 162:227–237

3. Kan C-C, Ibe AH, Rivera KKP, Arazo RO, de Luna MDG (2017) Hexavalent chromium removal from aqueous solution by adsorbents synthesized from groundwater treatment residuals. Sustain Environ Res 27:163–171

4. Pradhan D, Sukla LB, Sawyer M, Rahman KSM (2017) Recent bioreduction of hexavalent chromium in wastewater treatment: a review. J Ind Eng Chem 55:1–20

5. Yadav S, Srivastava V, Banerjee S, Weng CH, Sharma YC (2013) Adsorption characteristics of modified sand for the removal of hexavalent chromium ions from aqueous solutions: kinetic, thermodynamic and equilibrium studies. CATENA 100:120–127

6. Shahid M, Shamshad S, Rafiq M, Khalid S, Bibi I, Niazi NK, Dumat C, Rashid MI (2017) Chromium speciation, bioavailability, uptake, toxicity and detoxification in soil-plant system: a review. Chemosphere 178:513–533

7. US EPA (2011) Ground water and drinking water, Current drinking water standards. EPA 816-F-02

8. Zhang FS, Itoh H (2006) Photocatalytic oxidation and removal of arsenite from water using slag-iron oxide-TiO_2 adsorbent. Chemosphere 65:125–131

9. Alinnor IJ (2007) Adsorption of heavy metal ions from aqueous solution by fly ash. Fuel 86:853–857

10. Kabdaşli I, Arslan T, Ölmez-Hanci T, Arslan-Aloton I, Tünary O (2009) Complexing agent and heavy metal removals from metal plating effluent by electrocoagulation with stainless steel electrodes. J Hazard Mater 165:838–845

11. Fu F, Wang Q (2011) Removal of heavy metal ions from wastewaters: a review. J Environ Manag 92:407–418

12. Barakat MA (2011) New trends in removing heavy metals from industrial wastewater. Arab J Chem 4:361–377

13. Burakov AE, Galunin EV, Burakova IV, Kucherova AE, Agarwal S, Tkachov AG, Gupta VK (2018) Adsorption of heavy metal on conventional and nanostructured materials for wastewater treatment purposes: a review. Ecotoxicol Environ Saf 148:702–712

14. Lingamdinne LP, Koduru JR, Choi YL, Chang YY, Yang YK (2015) Studies on removal of Pb(II) and Cr(III) using graphene oxide base inverse spinel nickel ferrite nanocomposite as solvent. Hydrometallurgy 165:64–72

15. Vendruscolo F, Da Rocha-Ferreira GL, Filho NRA (2017) Biosorption of hexavalent chromium by microorganisms. Int Biodeterior Biodegradation 119:87–95

16. Sherlala AIA, Raman AAA, Bello MM, Asghar A (2018) A review of the applications of organo-functionalized magnetic graphene oxide nanocomposites for heavy metal adsorption. Chemosphere 193:1004–1017

17. Wang Y, Liu D, Lu J, Huang J (2015) Enhanced adsorption of hexavalent chromium from aqueous solutions on facilely synthesized mesoporous iron-zirconium bimetal oxide. Colloids Surf A Physicochem Eng Asp 481:133–142

18. Santhosh C, Velmurugan V, Jacob G, Jeong SK, Grace AN, Bhatnagar A (2016) Role of nanomaterials in water treatment applications: a review. Chem Eng J 306:1116–1137

19. Zhang G, Qu J, Liu H, Liu R, Wu R (2007) Preparation and evaluation of a novel Fe-Mn binary oxide adsorbent for effective arsenite removal. Water Res 41:1921–1928

20. Yufanyi DM, Ondoh AM, Foba-Tendo J, Mbadcam KJ (2015) Effect of decomposition temperature on the crystallinity of α-Fe_2O_3 (hematite) obtained from an iron(III) hexamethylenetetramine precursor. Am J Chem 5:1–9

21. Wang Y, Feng X, Villalobos M, Tan W, Liu F (2012) Sorption behaviour of heavy metals on birnessite: relationship with its Mn average oxidation state and implications for types of sorption sites. Chem Geol 292–293:25–34
22. Weilong W, Xiaobo F (2013) Efficient removal of Cr(VI) with Fe/Mn mixed metal oxide nanocomposites synthesized by a grinding method. J Nanomater 2013:1–8
23. Krishnan V, Heislbertz S, Natile MM, Glisenti A, Bertagnoli H (2005) Influence of preparation technique and iron doping on the structure and reactivity of mixed Fe–Ti–O nanocomposites. Mater Chem Phys 92:394–402
24. Glisenti A (2000) The reactivity of a Fe-Ti-O mixed oxide under different atmospheres: study of the interaction with simple alcohol molecules. J Mol Catal A Chem 153:169–190
25. Katsoyiannis IA, Zouboulis AI (2004) Biological treatment of Mn(II) and Fe(II) containing groundwater: kinetic considerations and product characterization. Water Res 38:1922–1932
26. Han R, Zou W, Zhang Z, Shi J, Yang J (2006) Removal of copper(II) and lead(II) from aqueous solution by manganese oxide coated sand: characterization and kinetic study. J Hazard Mater B137:384–395
27. Barrera-Díaz CE, Lugo-Lugo V, Bilyeu B (2012) A review of chemical, electrochemical and biological methods for aqueous Cr(VI) reduction. J Hazard Mater 223–224:1–12
28. Lagergren S (1898) Zurtheorie der sogenannten adsorption gelösterstoffe. Kungl Sven Vetensk Handl 24:1–39
29. Blanchard G, Maunaye M, Martin G (1984) Removal of heavy metals from water by means of natural zeolites. Water Res 18:1501–1507
30. Ho Y-S (1995) Adsorption of heavy metals from waste streams by peat. Ph.D. thesis, The University of Birmingham, Birmingham, UK
31. Hameed BH, El-Khaiary MI (2008) Malachite green adsorption by rattan sawdust: isotherm kinetic and mechanism modelling. J Hazard Mater 159:574–579
32. Albadarin AB, Mangwandi C, Al-Muhtaseb AH, Walker GM, Allen SJ, Ahmad NM (2012) Kinetic and thermodynamics of chromium ions adsorption onto low-cost dolomite adsorbent. Chem Eng J 179:193–202
33. Müller G, Janošková K, Bakalár T, Cakl J, Jiránková H (2012) Removal of Zn(II) from aqueous solutions using Lewatit S1468. Desalin Water Treat 37:146–151
34. Tran HN, You S-J, Chao H-P (2015) Effect of pyrolysis temperatures and times on the adsorption of cadmium onto orange peel derived biochar. Waste Manag Res 34:129–138
35. Khezami L, Capart R (2005) Removal of chromium(VI) from aqueous solution by activated carbon: kinetic and equilibrium studies. J Hazard Mater B123:223–231
36. Tran HN, You S-J, Hosseini-Bandegharaei A, Chao H-P (2017) Mistakes and inconsistencies regarding adsorption of contaminants from aqueous solutions: a critical review. Water Res 120:88–116
37. Langmuir I (1918) The adsorption of gases on plane surfaces of glass, mica and platinum. J Am Chem Soc 40:1361–1403
38. Freundlich H (1906) Uber die adsorption in losungen. Z Phys Chem 57A:385–470
39. Hall KR, Eagleton LC, Acrivos A, Vermeulen T (1966) Pore and solid diffusion kinetics in fixed-bed adsorption under constant-pattern conditions. Ind Eng Chem Fundam 5:212–223
40. Weber TW, Chakravorti RK (1974) Pore and solid diffusion models for fixed-bed adsorbers. AlChE J 20:228–238
41. Worch E (2012) Adsorption technology in water treatment: fundamentals, processes and modeling. Walter de Gruyter, Berlin
42. Zhang R, Wang B, Ma H (2010) Studies on chromium(VI) adsorption on sulfonated lignite. Desalination 255:61–66
43. Fathima NN, Aravindhan R, Rao JR, Nair BU (2005) Solid waste removes toxic liquid waste: adsorption of chromium (VI) by iron complexed protein waste. Environ Sci Technol 39:2804–2810

44. Tang L, Fang Y, Pang Y, Zeng G, Wang J, Zhou Y, Deng Y, Yang G, Cai Y, Chen J (2014) Synergistic adsorption and reduction of hexavalent chromium using highly uniform polyaniline–magnetic mesoporous silica composite. Chem Eng J 254:302–312
45. Bhattacharya AK, Naiya TK, Mandal SN, Das SK (2008) Adsorption, kinetics and equilibrium studies on removal of Cr(VI) from aqueous solutions using different low-cost adsorbents. Chem Eng J 137:529–541

Chapter 17
Spectroscopic, XRD, In Vitro Anti-oxidant, Antifungal and Antibacterial Studies of Heterocyclic Schiff Base Nickel(II) Complexes Bearing Anions

Ikechukwu P. Ejidike, Fanyana M. Mtunzi and Michael J. Klink

Abstract Ni(II) complexes, bearing Cl^-, Br^-, NO_3^-, and CH_3COO^-, have been synthesized with a tridentate Schiff base ligand, viz. 4-[(1E)-N-{2-[(Z)-benzylideneamino]ethyl}-ethanimidoyl]benzene-1,3-diol] (HL) and characterized by elemental analysis, FT-IR, ^{1}H NMR, UV-Vis, molar conductance, XRD and thermogravimetric analysis. The molar conductance values indicate that the complexes are non-electrolytes. IR spectra showed that the ligand (HL) behaves as a tridentate ligand with an oxygen-dinitrogen donor atom system. On the basis of electronic studies, a square-planar geometry has been assigned to the prepared Ni(II) complexes. The XRD study suggests a well-defined crystalline nanostructure for the as-synthesized complexes. Thermal analysis of the complexes indicates that the decomposition takes place in three to four steps. Scavenging potentials of the DPPH and ABTS radicals by the compounds were studied for their antioxidant capacities. The compounds were screened for antibacterial activity against *S. aureus*, *E. faecalis*, *K. pneumoniae* and *P. aeruginosa*, and antifungal activity against *C. albicans* and *C. neoformans* by rapid *p*-iodonitrotetrazolium chloride (INT) colorimetric assay in vitro and the results were compared with the antibiotics: neomycin as an anti-bacterial standard and amphotericin B as an anti-fungal standard.

I. P. Ejidike (✉) · F. M. Mtunzi
Department of Chemistry, Faculty of Applied and Computer Sciences, Vaal University of Technology, Vanderbijlpark 1911, South Africa
e-mail: ikechukwue@vut.ac.za

F. M. Mtunzi
e-mail: fanyana@vut.ac.za

I. P. Ejidike
Department of Chemical Sciences, Faculty of Science and Science Education, Anchor University, P.M.B. 001, Ipaja, Lagos, Nigeria

M. J. Klink
Department of Biotechnology, Faculty of Applied and Computer Sciences, Vaal University of Technology, Vanderbijlpark 1911, South Africa
e-mail: michaelk1@vut.ac.za

17.1 Introduction

Schiff base ligands and their biologically active complexes are significant groups of compounds providing potential positions as biochemically active compounds over the past few decades due to their antimicrobial, antifungal, and anticancer properties [1–3]. Schiff base ligands containing different donor atoms have shown a broad biological activity because of the variety of ways in which they are bonded to metal ions. This interaction provides an interesting series of ligands whose properties can be considerably modified by bringing together different organic substituents, thereby causing a variation in the final donor properties [4]. Unsymmetrical tridentate-ONO and tetradentate-ONNO type Schiff bases have been reported to act as potential chelating agents in their dianionic forms with various metallic moieties [5, 6]. The special class of compounds is also used as catalysts, corrosion inhibitor, pigments and dyes, polymer stabilizers, and intermediates in organic synthesis [7].

The reactions of metal ions with nitrogen, oxygen, and sulphur atoms from organic ligands are gaining attention in recent years and provided an enthusiastic series of compounds with diverse potentials [8, 9]. Schiff base-transition metal complexes synthesized using heterocyclic molecules have amplified the attention of many researchers towards the advances in bioinorganic chemistry discipline [10–12]. Biologically active metal complexes bearing Schiff bases derived from ethylenediamine, aniline, and aldehydes with different geometries have been reported to exhibit pronounced antimicrobial and antiradical activities due to chelation process dominantly affecting the general biological performance of the synthesized compounds [12–14].

The use of Schiff bases in biological or therapeutic applications as promising drug agents or biological probes and analytical tools has been reported by several researchers [15]. Biological and spectroscopic studies of Ni(II) complexes of N,N'-disalicylidene-3,4-diaminotoluene, N,N'-bis(3,5-di-tertbutylsalicylidene)-1,3-diaminopropane, tetrathiafulvalene-N,N'-phenylenebis(salicylideneimine), o-hydroxybenzaldehyde, o-hydroxyacetophenone ethylenediamine, and 1-phenylbutane-1,3-dione-mono-S-methylisothio-semicarbazone with 5-phenylazo-o-hydroxybenzaldehyde with tetrahedral, square planar, and octahedral geometries were reported to exhibit bioactivity against the growth of bacteria in vitro when examined for their antimicrobial potential [16]. Polydentate Schiff bases and their metal complexes incorporating N- , O-donors are essential to life processes due to their capability towards safeguarding living systems and cells from impairment caused by oxidative stress or free radicals, and they were also reported to exhibit moderate to strong scavenging activity on synthetic radicals [6, 12].

Thus, the present communication deals with the synthesis and characterization of bivalent transition metal Ni(II) complexes of a tridentate Schiff base with a N_2O donor atoms set and formulated as: [Ni(L)X] · nH$_2$O (where L = 4-[(1E)-N-

{2-[(Z)-benzylideneamino]ethyl}-ethanimidoyl]benzene-1,3-diol], X = Cl⁻, Br⁻, NO_3^-, CH_3COO^-) derived from the condensation of 2′,4′-dihydroxyacetophenone and benzaldehyde with ethylenediamine. The compounds have been characterized by elemental analyses, molar conductivity, ultraviolet-visible spectroscopy (UV-Vis), Fourier transform infrared spectroscopy (FT-IR), thermogravimetric analysis (TGA), proton nuclear magnetic resonance (^{1}H NMR), and X-ray diffractometry (XRD). The antibacterial, antifungal and antioxidant activities of the nickel(II) complexes were also investigated.

17.2 Experimental

17.2.1 Materials and Methods

Chemicals and solvents were of analytical grade and were used as obtained without auxiliary purification. Ascorbic acid, ethylenediamine, benzaldehyde, $NiCl_2 \cdot 6H_2O$, $Ni(NO_3)_2 \cdot 3H_2O$, DMF and DMSO were obtained from Merck (Johannesburg, South Africa). 2,2′-Azino-bis-3-ethylbenzothiazoline-6-sulfonic acid (ABTS), rutin hydrate, 2,2-diphenyl-1-picrylhydrazyl (DPPH), and butylated hydroxytoluene (BHT) were received from Sigma Chemical Co., USA, $NiBr_2 \cdot 3H_2O$ from Fluka (Buchs, Switzerland), while 2′,4′-dihydroxyacetophenone, $(CH_3COO)_2Ni \cdot 4H_2O$, and gallic acid were from Sigma–Aldrich (Johannesburg, South Africa).

17.2.2 Physical Measurements

Carbon, hydrogen, and nitrogen data were obtained on a Perkin Elmer elemental analyzer. Newly prepared 10^{-3} M DMF with EUTECH PC 7000 conductivity cell was used for the conductivity measurements. Perkin Elmer-FT-IR spectrometer (Spectrum 2000) in the range 4000–400 cm^{-1} was used for IR spectra data collection. Stuart melting point (SMP 10) apparatus was used for the melting points determination. ^{1}H NMR spectra were recorded with a Bruker Advance DPX-600 MHz spectrophotometer in d$_6$-DMSO and reported relative to TMS as an internal standard. Absorption data were documented with an UV–Vis spectrometer model: T80+, PG Instruments Ltd ranging from 200 to 800 nm in quartz cells of path length 1 cm. Powder X-ray diffraction (XRD) patterns were recorded on a Bruker AXS D8 Advance Powder X-ray diffractometer (X-ray source: Cu, $\lambda = 1.5406$ Å).

17.2.3 Synthesis of the Schiff Base Ligand: 4-[(1E)-N-{2-[(Z)-Benzylideneamino]Ethyl} Ethanimidoyl]Benzene-1,3-Diol (HL)

Previously reported method was followed for the Schiff base ligand preparation [6]. In a 250 mL round bottom flask, ethylenediamine (0.015 mol) in ethanol (20 mL) was carefully added to a solution of 2′,4′-dihydroxyacetophenone (0.015 mol), in ethanol (30 mL) and stirred for 60 min at room temperature, followed by dropwise addition over 10–15 min of benzaldehyde (0.015 mol) in ethanol (20 mL) at room temperature. The resulting mixture was refluxed with stirring for 3–4 h and left to stir further for 22–24 h at room temperature to give the desired product as a crystalline solid after suction filtration and washing with ethanol. The crude product was recrystallized from warm ethanol. The product was then allowed to dry in vacuum at 50 °C overnight.

HL: Dark-yellow solid; Yield: 3.03 g (71.50%); Decomp. Temp. (°C): 233–234; IR (ν_{max}/cm^{-1}): 1266 (C–O), 1538, 1436 (C=C), 1613 (C=N), 2981, 2894 (CH$_3$/CH$_2$), 3404 (OH); UV-Vis (DMF): λ_{max}/nm (cm^{-1}): 277 (36,101), 309 (32,362), 381 (26,247); Anal. Calcd. for C$_{17}$H$_{18}$N$_2$O$_2$ (%): C 72.32, H 6.43, N 9.92; Found (%): C 72.17, H 6.31, N 9.86.

17.2.4 General Procedure for the Synthesis of Nickel(II) Complexes

Preparation of the complexes were by the addition of 0.001 mol of nickel salts [NiCl$_2$ · 6H$_2$O (0.2377 g); NiBr$_2$ · 3H$_2$O (0.2726 g); Ni(NO$_3$)$_2$ · 6H$_2$O (0.2908 g); (CH$_3$COO)$_2$Ni · 4H$_2$O (0.2489 g)] dissolved in about 20 mL of ethanol, into a warmed ethanolic solution (20 mL) of HL (0.001 mol, 0.2823 g) in a 1:1 molar ratio. The colour of the solutions changed within a few minutes of interactions. The resulting solution was refluxed for 3 h. The precipitated solids of the metal complexes were filtered off from the reaction mixture, thoroughly rinsed with ethanol and dried over anhydrous calcium chloride (Scheme 17.1).

17.2.4.1 Synthesis of [OHC$_6$H$_3$O:C(CH$_3$):N(C$_2$H$_4$)N:CH:C$_6$H$_5$NiCl]

[Ni(L)Cl] · **3H$_2$O**: Red-brown solid; Yield: 155.9 mg (72.58%); Decomp. Temp. (°C): 203–204; Conductivity (µS cm^{-1}): 15.4; IR (ν_{max}/cm^{-1}): 3352 (O–H), 2907, 2805 (CH$_3$/CH$_2$), 1601 (C=N), 1539, 1441 (C=C), 1234 (C–O), 511 (Ni–N), 461 (Ni–O); UV-Vis (DMF): λ_{max}/nm (cm^{-1}): 278 (35,971), 316 (31,646), 388 (25,773), 439 (22,779), 545 (18,349); Anal. Calcd. for C$_{17}$H$_{23}$ClN$_2$NiO$_5$ (%): C 47.54, H 5.40, N 6.52; Found (%): C 48.04, H 5.18, N 6.87; F. Wt (g): 429.52.

Scheme 17.1 Proposed structures of the synthesized Schiff base (HL) and its Ni(II) complexes
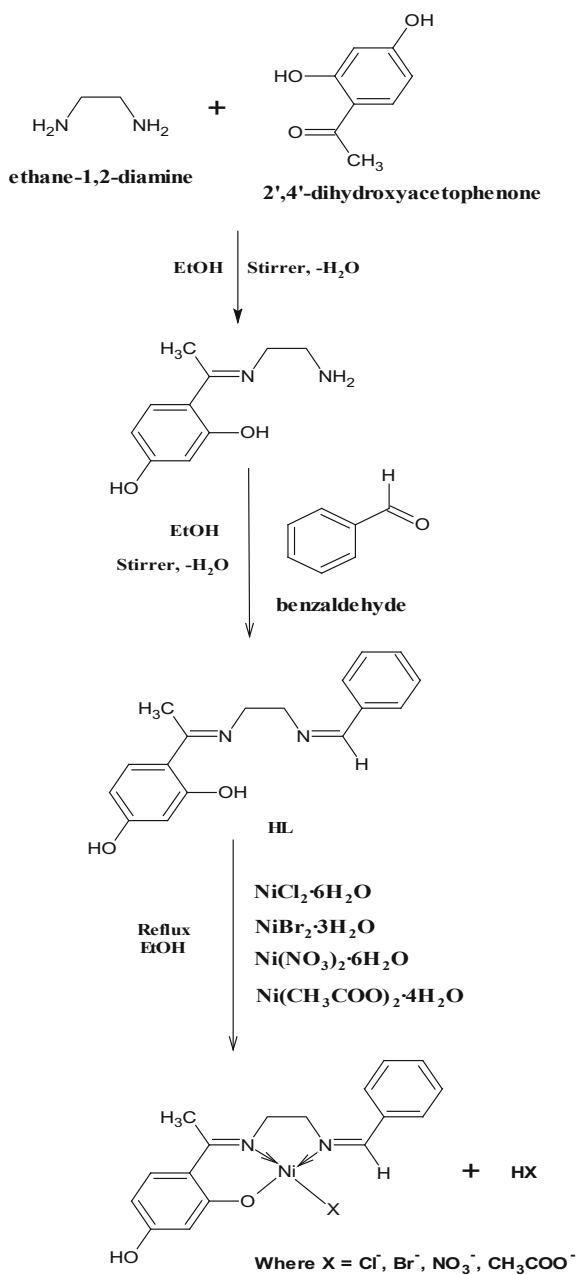
17.2.4.2   Synthesis of [OHC$_6$H$_3$O:C(CH$_3$):N(C$_2$H$_4$)N:CH:C$_6$H$_5$NiBr]

[Ni(L)Br] · **2H$_2$O**: Brownish-red solid; Yield: 148.3 mg (65.04%); Decomp. Temp. (°C): 198–200; Conductivity (μS cm^{-1}): 25.4; IR (ν_{max}/cm^{-1}): 3346 (O–H), 2989, 2917 (CH$_3$/CH$_2$), 1595 (C=N), 1537, 1442 (C=C), 1247 (C–O), 510 (Ni–N), 457 (Ni–O); UV-Vis (DMF): λ_{max}/nm (cm^{-1}): 279 (35,842), 318 (31,447), 397 (25,189), 432 (23,148), 554 (18,051); Anal. Calcd. for C$_{17}$H$_{21}$BrN$_2$NiO$_4$ (%): C 44.78, H 4.64, N 6.14; Found (%): C 45.12, H 4.29, N 6.51; F. Wt (g): 455.96.

17.2.4.3   Synthesis of [OHC$_6$H$_3$O:C(CH$_3$):N(C$_2$H$_4$)N:CH:C$_6$H$_5$NiNO$_3$]

[Ni(L)NO$_3$] · **3H$_2$O**: Brownish-red solid; Yield: 139.5 mg (61.18%); Decomp. Temp. (°C): 192–193; Conductivity (μS cm^{-1}): 23.2; IR (ν_{max}/cm^{-1}): 3339 (O–H), 2992, 2923 (CH$_3$/CH$_2$), 1607 (C=N), 1542, 1446 (C=C), 1435, 1303 (N–O: asym/sym), 1246 (C–O), 512 (Ni–N), 456 (Ni–O); UV-Vis (DMF): λ_{max}/nm (cm^{-1}): 279 (35,842), 316 (31,646), 395 (25,316), 436 (22,936), 560 (17,857); Anal. Calcd. for C$_{17}$H$_{23}$N$_3$NiO$_8$ (%): C 44.77, H 5.08, N 9.21; Found (%): C 44.92, H 5.52, N 9.33; F. Wt (g): 456.07.

17.2.4.4   Synthesis of [OHC$_6$H$_3$O:C(CH$_3$):N(C$_2$H$_4$)N:CH:C$_6$H$_5$NiCH$_3$COO]

[Ni(L)CH$_3$COO] · **2H$_2$O**: Reddish-brown solid; Yield: 145.6 mg (66.91%); Decomp. Temp. (°C): 190–191; Conductivity (μS cm^{-1}): 10.3; IR (ν_{max}/cm^{-1}): 3349 (O–H), 2977, 2937 (CH$_3$/CH$_2$), 1606 (C=N), 1533, 1439 (C=C), 1557, 1351 (OAc: asym/sym), 1241 (C–O), 501 (Ni–N), 459 (Ni–O); UV-Vis (DMF): λ_{max}/nm (cm^{-1}): 280 (35,971), 320 (31,250), 391 (25,575), 441 (22,676), 552 (18,116); Anal. Calcd. for C$_{19}$H$_{24}$N$_2$NiO$_6$ (%): C 52.45, H 5.56, N 6.44; Found (%): C 53.14, H 5.82, N 6.08; F. Wt (g): 435.10.

17.2.5   Biological Evaluations

17.2.5.1   Antioxidant Assay

2,2-Diphenyl-1-Picrylhydrazyl (DPPH) Free Radical Scavenging Activity (FRSA) Assay

DPPH radical scavenging activity evaluation is a standard assay in antioxidant activity studies. The scavenging activity of the prepared nickel(II) complexes was studied spectrophotometrically by DPPH method [6]. The method is a quick procedure for evaluating the scavenging capacities of potential compounds [6]. The radical scav-

enging properties of the as-synthesized complexes and ligand with DPPH radical were assessed within different concentrations (100, 200, 300, 400, and 500 µg/mL) of the test compounds in DMF solutions (1 mL), added to 1.0 mL of 0.4 mM DPPH in methanol and thoroughly vortexed. The mixtures were incubated at room temperature in the dark for 30 min, after which the scavenging power of the test samples was measured with respect to the decrease in the absorbance of DPPH at 517 nm. In this study, gallic acid, rutin and ascorbic acid were used as standard drugs. The colour change signifies that the DPPH is scavenged by the antioxidant, through the involvement of hydrogen to form stable DPPH molecule, leading to a decrease in the absorbance. All tests analyses were carried out in three replicates to obtain mean ± S.D.

ABTS: 2,2′-Azino-Bis(3-Ethylbenzothiazoline-6-Sulfonic Acid) Radical Scavenging Assay

Schiff base ligand (HL) and the Ni(II)-Schiff base complexes ABTS scavenging ability were evaluated following a previous method [12]. 7 mM ABTS solution and 2.4 mM potassium persulfate ($K_2S_2O_8$) solution in equal amounts were prepared as the working solution and left to react further in the dark for 12 h at room temperature. An absorbance of 0.706 ± 0.001 units at 734 nm required for the analysis was obtained by diluting 1 mL $ABTS^+$ solution. 1 mL of the test samples at concentrations 100, 200, 300, 400, and 500 µg/mL in DMF were mixed with 1 mL of the $ABTS^+$ solution, followed by the spectrophotometric reading at 734 nm after incubation in the dark for 15 min at room temperature. The samples for ABTS scavenging potentials alongside standard drugs [gallic acid, rutin and butylated hydroxyl toluene (BHT)] were assessed. Triplicate analysis was carried out. ABTS scavenging ability of the Ni(II)-Schiff base complexes were determined using previously described methods [6, 12].

The percentage inhibition of the radical scavenging activities was calculated using the Eq. 17.1:

$$\text{Percentage scavenging activity} = \frac{\text{Absorbance of control} - \text{Absorbance of sample}}{\text{Absorbance of control}} \times 100$$

(17.1)

where

$Abs_{control}$ is the absorbance of the radical + solvent;
Abs_{sample} is the absorbance of radical + sample [test samples/standard].

17.2.5.2 In Vitro Antimicrobial Studies

Micro-Dilution Bioassay

The strains for the present study were maintained in the Biotechnology Laboratory at Vanderbijlpark, Vaal University of Technology and consisted of two Gram-positive (*Staphylococcus aureus* ATCC-25923 and *Enterococcus faecalis* ATCC-29212), two Gram-negative (*Klebsiella pneumoniae* ATCC-13883 and *Pseudomonas aeruginosa* ATCC-15442) bacteria, and two fungi [*Candida albicans* (ATCC-14053) and *Cryptococcus neoformans* (ATCC-14116)]. The cultures of bacteria were maintained on Mueller Hinton Agar (MHA) plates at 4 °C, while the fungi were maintained on Yeast Malt (YM) broth plates at 4 °C throughout the study and used as stock cultures.

Antibacterial Activity: Determination of Minimum Inhibitory Concentration (MIC)

MIC of the as-synthesized Schiff base ligand and nickel(II) complexes against the bacterial strains was investigated by a rapid *p*-iodonitrotetrazolium chloride (INT) colorimetric assay [17]. Overnight cultures incubated at 37 °C in a water bath with an orbital shaker (Sallayicili: ST 30, Turkey) of Gram-positive: *Staphylococcus aureus* and *Enterococcus faecalis*, and Gram-negative: *Klebsiella pneumoniae* and *Pseudomonas aeruginosa* bacterial strains were diluted with sterile Mueller-Hinton (MH) broth to give a final inocula of approximately 10^6 CFU/mL (colony forming units). Stock solutions of the synthesized compounds were dissolved in DMSO to a concentration of 25 mg/mL. 100 μL of each test sample solution was serially diluted two-fold with sterile distilled water in a 96-well microtiter plate for each of the bacterial strains to a final concentration range of 6250.00–48.83 μg/mL. A 2-fold dilution of neomycin (Sigma-Aldrich, Germany) (1 mg/mL) was used as a positive control (antibiotic) against each bacterium to a final concentration range of 250.00–1.95 μg/mL, and dimethyl sulfoxide was used as the solvent control. 100 μL of each bacterial culture was added to each well. The plates were covered with a sterile plate sealer and then incubated at 37 °C for 24 h in 100% relative humidity.

Bacterial growth was indicated by the addition of 40 μL of 0.2 mg/mL *p*-iodonitrotetrazolium chloride (INT) (Sigma-Aldrich, Germany) and further incubation at 37 °C for 24 h. Since the colourless tetrazolium salt is biologically reduced to a red product due to the presence of active organisms, the MIC values were recorded visually as the lowest concentration that led to growth inhibition. A reddish-pink colour indicated bacterial growth in the wells.

Antifungal Activity: Determination of Minimum Inhibitory Concentration (MIC)

A modified microdilution method for fungi [17] was used to determine the antifungal activity of the synthesized compounds against *Candida albicans* and *Cryptococcus neoformans*. An overnight fungal culture was prepared in yeast malt (YM) broth. 400 µL of this culture was added to 4 mL sterile saline, and absorbance was read at 530 nm. The absorbance was then adjusted with sterile saline to give a 0.5 M McFarland standard solution. From this standardized fungal stock, a 1:1000 dilution with sterile YM broth was prepared to give a final inoculum of $\approx 10^6$ CFU/mL. Stock solutions of the synthesized compounds were dissolved in DMSO to a concentration of 25 mg/mL. 100 µL of each solution was serially diluted two-fold with sterile water in a 96-well microtitre plate. A similar two-fold dilution of amphotericin B (Sigma-Aldrich, Germany) (2.5 mg/mL) was used as the positive control to a final concentration range of 625.00–4.88 µg/mL, while DMSO was used as the solvent control. 100 µL of the diluted fungal culture was added to each well. The plates were covered with a sterile plate sealer and incubated at 37 °C for 24 h. As an indicator of growth, 40 µL (0.2 mg/mL) INT was added and the plates were incubated for a further 24 h at 37 °C. MIC value was recorded as the lowest concentration that inhibited fungal growth after 48 h.

17.3 Results and Discussion

17.3.1 Synthesis and Characterization of the Compounds

The Schiff base ligand, 4-[(1*E*)-*N*-{2-[(*Z*)-benzylideneamino]ethyl} ethanimidoyl]benzene-1,3-diol (HL) and its nickel(II) complexes were subjected to elemental analyses, IR, UV-vis and ^{1}H NMR spectral studies. Elemental analyses results (C, H, and N) are in good agreement with those required by the proposed formulae (Scheme 17.1). $NiX_2 \cdot nH_2O$ reacted with the tridentate Schiff base ligand (under reflux) giving rise to reddish-brown to brownish-red coloured complexes which are sparingly soluble in most organic solvents, but soluble in the polar aprotic solvents such as DMF and DMSO; the melting point analysis showed that the as-synthesized compounds were decomposing before melting. The analytical data collected for the compounds are in agreement with the structural formulae proposed [Ni(L)X] · n(H$_2$O) [where L = 4-[(1*E*)-*N*-{2-[(*Z*)-benzylideneamino]ethyl} ethanimidoyl]benzene-1,3-diol, X = Cl$^-$, Br$^-$, NO$_3^-$, CH$_3$COO$^-$] (see Scheme 17.1). The tridentate Schiff base ligand displayed significant chelating properties, as shown by the immediate precipitation of the complexes when HL encounters Ni^{2+} salt forming coloured complexes. The analytical data indicated that the metal to ligand ratio is 1:1 for all the complex systems. The preparation of the complexes may be represented by the Eq. (17.2) below:

$$NiX_2 \cdot nH_2O + HL \rightarrow [Ni(L)X] + HX + nH_2O \qquad (17.2)$$
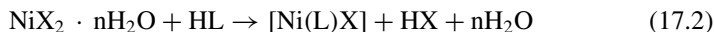
(where $X = Cl^-$, Br^-, NO_3^-, CH_3COO^-).

17.3.2 Infrared Absorption Spectra

The ligand to metal ion binding mode of the as-synthesized compounds was examined via the free ligand IR spectrum with potential ONN donor sites and compared with the spectra of the heterocyclic nickel(II) complexes. Broad band at 3404 cm^{-1} is attributed to ν(O–H) stretching vibrations in the free Schiff ligand. In the nickel complexes spectra, broad bands in the region 3339–3352 cm^{-1} are due to the ν(OH) stretching of the H$_2$O molecules associated with the complexes [10–12]. The disappearance of ligand broad stretching vibrations at 3404 cm^{-1} in the complexes can be attributed to the deprotonation of one phenolic OH and subsequent coordination to the metal center (Fig. 17.1). The involvement of a deprotonated phenolic moiety in

Fig. 17.1 FT-IR spectral bands of the Schiff base (HL) and Ni(II) complexes
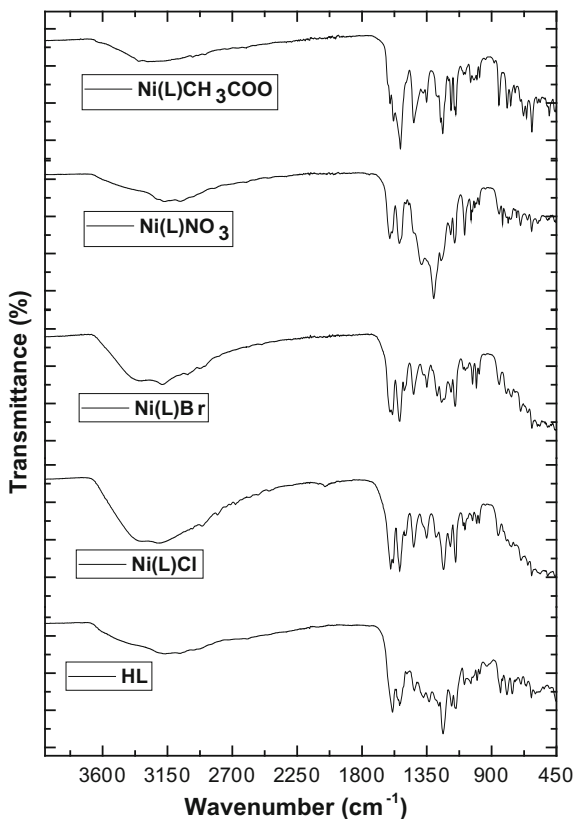
the complexes was affirmed by the ν(C–O) stretching band observed at 1266 cm^{-1} in the free ligand, undergoing a bathochromic shift to the extent of 19–32 cm^{-1} in the synthesized complexes [12, 15]. This shift to a lower frequency confirms the coordination of the phenolic oxygen leading to the formation of stronger C–O–M bond [12, 17].

The HL ligand showed a medium intensity ν(C=N) azomethine band at 1613 cm^{-1} [12, 18]. Upon complexation, this band was shifted towards lower frequency about 6–18 cm^{-1} in the heterocyclic Ni(II) compounds, indicative of nitrogen of the azomethine group bonding to the Ni ion [15, 18, 19]. This fact was further supported by the appearance of new bands assignable to ν(Ni–N) stretching vibrations in the region of 501–512 cm^{-1}. Another band appeared in the region 456–461 cm^{-1}, assignable to the interaction of the phenolic oxygen to the metal atom, ν(Ni–O) stretching vibrations (Fig. 17.1) [11, 12, 15, 18, 19].

In the [Ni(L)CH$_3$COO] spectrum, the asymmetric carboxyl ν_{asym}(COO$^-$) was shifted to a higher frequency 1557 cm^{-1} region, while the shift to a lower frequency region (1351 cm^{-1}) is assigned to symmetric carboxyl ν_{sym}(COO$^-$), signifying linkage of the carboxylate oxygen atoms to the Ni(II) ion. The difference between the ν_{asym}(COO$^-$) and ν_{sym}(COO$^-$) bands gave a separation value of 206 cm^{-1} suggesting that the binding of carboxylate group to Ni(II) ion is monodentate [11, 15, 17]. The infrared spectrum of the nitrato complex revealed three (N–O) stretching bands at 1435 cm^{-1} (ν_5), 1303 cm^{-1} (ν_1), and 1043 cm^{-1} (ν_2). The ν_5 and ν_1 stretching vibrations are separated (Δ) by 132 cm^{-1} suggesting the unicoordination pattern of nitrate ion within the complex sphere [15, 17]. The stretching vibrations in the region 790–860 cm^{-1} are assigned to water vibrational rocking modes confirming that the water molecules are not bonded directly to the Ni(II) ions [12, 18]. The ring skeletal vibrations, ν(C=C), were consistent in both the ligand (HL) and the Ni(II)-Schiff base complexes and were unaffected by complexation [12].

17.3.3 ^{1}H-NMR Spectral Studies

Proton NMR spectrum of the Schiff base ligand (HL) was documented in DMSO-d$_6$ using TMS as an internal standard at room temperature. The proton resonance of one of the O–H groups appeared at δ 9.76 ppm due to the presence of intramolecular hydrogen bonding [3, 11]. The single proton resonance in the spectrum of the ligand occurring at δ 8.39 ppm is assigned to the azomethine proton (–CH=N–) [11, 19]. Phenyl (benzaldehyde) protons (m, 5H, C$_6$H$_5$) were observed at δ 7.25–7.74 ppm. The protons of 2$'$,4$'$-dihydroxyacetophenone ring at 5 and 6 positions come up as a multiplet at δ 6.04–6.14 ppm (m, 2H, –C$_2$H$_2$), while at position 3, it occurred as a singlet at 6.36 ppm (s, H, –CH), and the enolic OH appeared at 5.39 ppm (s, 1H). The aliphatic protons (s, 4H, –C$_2$H$_4$) in the ethylenediamine chain showed a singlet peak at 3.83 ppm. The peak at 2.09 ppm (s, 3H, N=C–CH$_3$) is due to methyl protons of the azomethine group in the Schiff base ligand [11, 12, 15, 18, 19].

17.3.4   Molar Conductivity Measurements

The molar conductivity (Λ_m) in $\mu S\ cm^{-1}$ of the Ni(II) complexes is calculated using 10^{-3} M solutions in DMF, by the relation $\Lambda_m = k/c$. The molar conductance values were found in the range 10.3–25.4 $\mu S\ cm^{-1}$ indicating the non-electrolytic nature of the compounds [3, 12]. Furthermore, it designated the bonding of the anions to the nickel cation and the complexes may be formulated as [Ni(L)X] [where L = ONN Schiff base ligand, X = Cl^-, Br^-, NO_3^-, CH_3COO^-]. The order of conductivity of the Ni(II) complexes in terms of the anions is: $CH_3COO^- < Cl^- < NO_3^- < Br^-$ [2, 15, 17].

17.3.5   Electronic Absorption Spectra

The UV-Vis spectra of the Ni(II) complexes and its Schiff base ligand in DMF solutions were recorded at room temperature ranging from 200 to 800 nm. The free ligand showed absorption bands at 36,101, 32,362 and 26,247 cm^{-1} which may be attributable to intraligand π-π*, n-π* and charge transfer transitions (Fig. 17.2) [12, 18]. The longer wavelength band in the spectrum of the Schiff base is assigned to intramolecular charge transfer, while the other bands are due to π-π*, and n-π* transitions involving molecular orbitals of the (>C=N) azomethine groups which is influenced by charge transfer interaction [9, 15, 19].

The electronic spectra of the Ni(II) complexes exhibited a shoulder around 25,773–25,189 cm^{-1} attributable to M $\rightarrow$ L charge-transfer transitions (MLCT). The shifting of these bands in the complexes spectra followed the participation of the imine group nitrogen and phenolic group oxygen in bonding [9, 20]. Two absorption bands at around 23,148–22,676 and 18,349–17,857 cm^{-1} may be assigned to two spin-allowed transitions, $^1A_{1g}$ (D) $\rightarrow$ $^1A_{2g}$ (G), $^1A_{1g}$ (D) $\rightarrow$ $^1B_{2g}$ (G), respectively, characteristic of square-planar geometry around Ni(II) ion [12, 16, 21].

17.3.6   Powder X-ray Diffraction Spectroscopy

XRD pattern of the Ni(II) complexes bearing Cl^-, Br^-, NO_3^-, and CH_3COO^- were recorded in the range $2\theta = 0$–70° and are shown in Fig. 17.3. The pattern of the metal complexes was studied to obtain further evidence about the structure of the metal complexes at wavelength 1.5406 Å. The XRD pattern of the complexes shows well defined crystalline peaks indicating that the nickel(II)-Schiff base complexes were in crystalline phase [5]. The average crystallite size of the complexes d_{XRD} was calculated from XRD patterns using the Debye-Scherrer formula [17]:

$$d_{XRD} = 0.9\lambda/\beta(\cos\theta) \tag{17.3}$$

Fig. 17.2 Electronic absorption spectra of HL and Ni(II) complexes
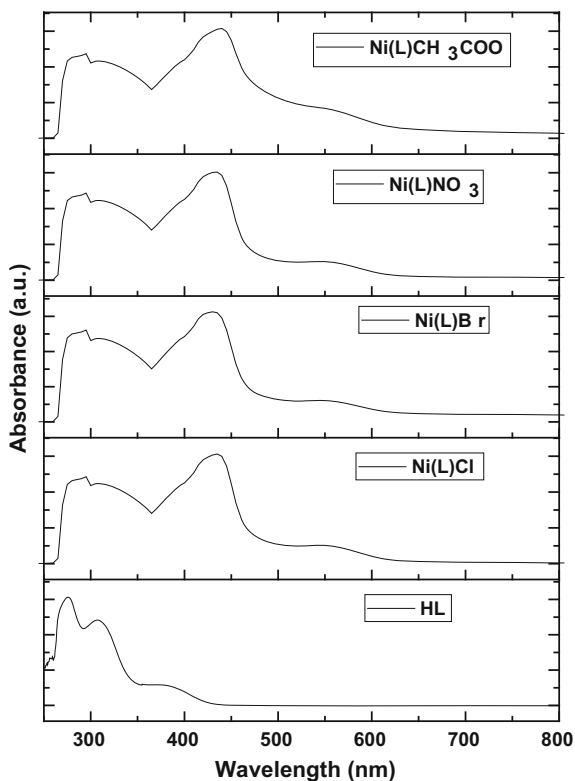
where 'λ' is the wavelength, 'β' is the full width at half maxima and 'θ' is the diffraction angle. Using the full width at half maximum intensity of the peaks, the pattern reveals the complexes to possess average crystallite sizes of 29, 27, 34, and 41 nm for [Ni(L)Cl], [Ni(L)Br], [Ni(L)NO$_3$] and [Ni(L)CH$_3$COO] respectively, suggesting a nanostructure for the as-synthesized complexes [18, 20].

17.3.7 Thermogravimetric Analysis (TGA) of the Complexes

The thermal studies of the synthesized Ni(II) complexes bearing different anions were investigated by thermogravimetric techniques. Thermogravimetric and derivative thermogravimetric analysis (TGA/DTA) of the synthesized nickel Schiff base compounds were carried out under a nitrogen atmosphere at a heating rate of 10 °C min^{-1} from 20 to 900 °C. TG/DTG results were plotted as percentage weight loss against temperature, providing insight into the nature, properties of various molecules and the residues obtained after thermal decomposition [2, 12, 13, 15, 20]. Decomposition of the complexes takes place in several steps. Water molecules were lost in between
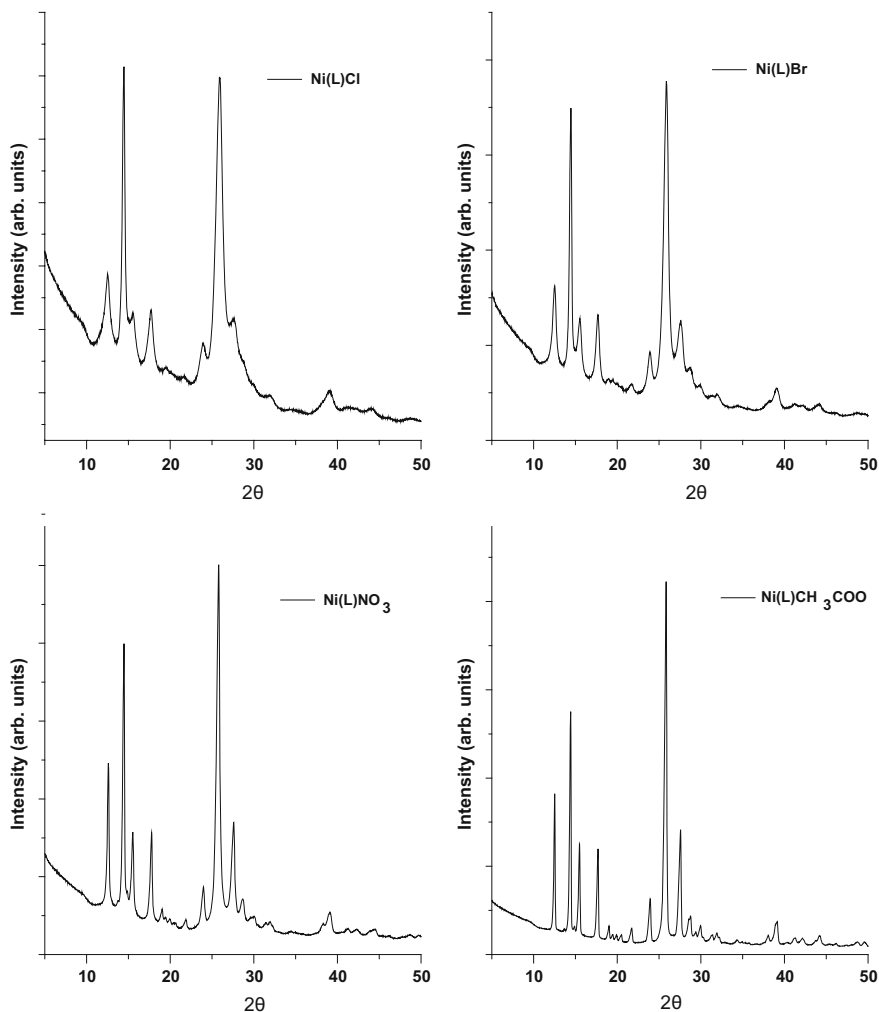
Fig. 17.3 Powder XRD patterns of the Ni(II) complexes

33 and 104 °C, and metal oxides were formed above 405 °C for the Ni(II) complexes (Fig. 17.4).

The complexes thermally decomposed in four successive decomposition steps with the exception of [Ni(L)Br] · 2H$_2$O exhibiting three decomposition steps. [Ni(L)Cl] · 3H$_2$O decomposition steps were in the temperature ranges 33–104, 254–304, 316–345, and 348–405 °C, and total mass loss was 62.43% (calc. 60.51%). [Ni(L)NO$_3$] · 3H$_2$O was stable up to 46 °C and its decomposition started at 48 °C and was complete at 536 °C, with TG temperatures of 48–90, 194–271, 280–311, and 411–536 °C giving rise to mass loss of about 60.43% (calc. 59.77%). The decomposition of [Ni(L)CH$_3$COO] · 2H$_2$O took place within the temperature range 44–434 °C.

Fig. 17.4 TG curves of the Ni(II)-Schiff base complexes
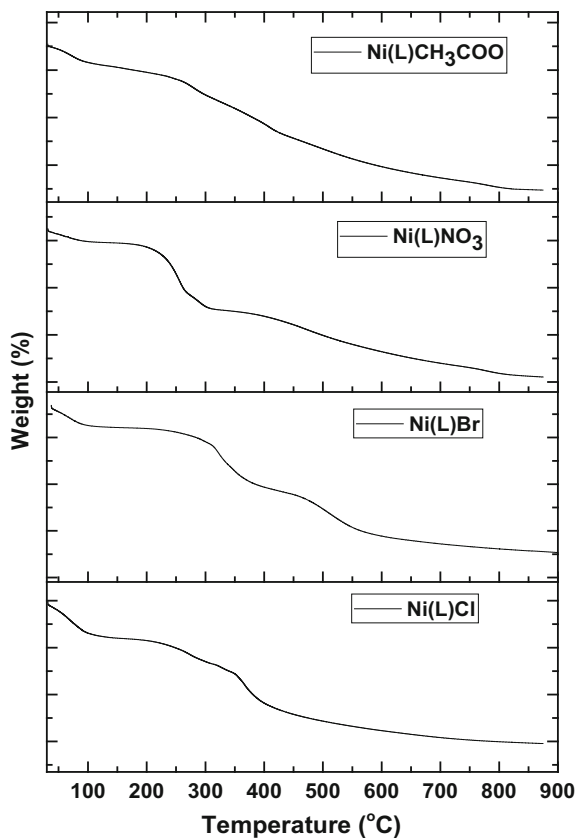
The decomposition steps were in the temperature range 44–99, 151–180, 256–304, and 392–434 °C, with mass loss of 54.37% (calc. 55.29%). The decomposition of the [Ni(L)Br] · 2H$_2$O occurred within the temperature range 40–584 °C. The decomposition temperature steps range from 40–101, 281–392, and 450–584 °C, with a mass loss of 64.67% (calc. 65.81%). The various steps in the decomposition of the metal complexes were as a result of dehydration step indicating the presence of water molecules in the complex, loss of anions (Cl$^-$, Br$^-$, NO$_3^-$, CH$_3$COO$^-$), the breakdown of the ligand and Schiff base ligand molecule, and the formation of NiO [11, 15, 17].

17.3.8 Antioxidant Assays

The production of free radicals brings about cell wall and DNA damage, leading to chronic diseases, such as cancers and cardiovascular diseases. The oxidative dam-

ages caused by reactive oxygen species on proteins, lipids, and nucleic acids may produce atherosclerosis, cancer, coronary heart disease, Parkinson's disease, and aging [4, 12]. Therefore, the ability of organic moieties like Schiff base ligands and their metal complexes to scavenge free radicals is a significant property. To prevent the free radical impairment in the body system, it is significant to administer chemotherapeutic drugs that may be rich in antioxidants.

Metal-based antioxidants have gained attention owing to their ability to safeguard cells and living organisms from damage caused by oxidative stress or scavenging free radicals [4, 22]. In this study, the antioxidant study was carried out using different concentrations of the Schiff base ligand (HL) and Ni(II) complexes in DMF as a solvent with 2,2-diphenyl-1-picrylhydrazyl (DPPH) and 2,2′-azino-bis(3-ethylbenzothiazoline-6-sulfonic acid) (ABTS) radicals. Ascorbic acid (vitamin C), rutin, gallic acid and butylated hydroxytoluene (BHT) were employed as standard agents.

17.3.8.1   DPPH (2,2-Diphenyl-1-Picrylhydrazyl) Radical Scavenging Assay

The quantitative antioxidant activity of the Schiff base (HL) and its Ni(II) complexes was evaluated spectrophotometrically by DPPH assay alongside the standards: rutin, gallic acid, and ascorbic acid. Reduction in the DPPH radical abilities was calculated based on the decrease in its absorbance at 517 nm prompted by antioxidants [12, 17]. The chelated Ni(II)-Schiff base complexes showed considerable DPPH radical scavenging ability in all the concentrations examined compared to the corresponding free ligand (HL). IC_{50} and its corresponding R^2 (correlation coefficient) values of the tested compounds are listed in Table 17.1.

[Ni(L)NO$_3$] showed significantly highest scavenging ability (IC_{50} = 2.54 ± 1.18 µM) compared to the other complexes: [Ni(L)Cl], [Ni(L)Br], [Ni(L)CH$_3$COO] with scavenging ability (IC_{50}): 3.03 ± 1.36, 2.97 ± 0.95, and 2.91 ± 0.71 µM respectively. Scavenging ability of the test samples on the DPPH radical can be ranked in the following order: [Gallic acid] > [Vit. C] > [Rutin] > [Ni(L)NO$_3$] > [Ni(L)CH$_3$COO] > [Ni(L)Br] > [Ni(L)Cl] > [HL] (Fig. 17.5). Consequently, the isolated Ni(II)-tridentate Schiff base complexes were observed to exhibit DPPH scavenging potentials at various concentrations, thereby making them potential compounds for developing anti-stress inducing agents [17].

17.3.8.2   ABTS: 2,2′-Azino-Bis(3-Ethylbenzothiazoline-6-Sulfonic Acid) Radical Scavenging Activity

The synthesized compounds were further measured for free radical scavenging activity by the ABTS method [12]. At 734 nm, the absorbance of the active ABTS$^+$ solution declined upon the addition of different concentrations of heterocyclic Ni(II) complexes and HL, and the same trend was observed for the standard drugs with respect

Table 17.1 In vitro antioxidant studies of the synthesized compounds and standard agents against DPPH[a] and ABTS[a] radicals

Compounds	DPPH activity		ABTS activity	
	IC$_{50}$ (µM)	R^2	IC$_{50}$ (µM)	R^2
HL	3.49 ± 1.57	0.913	2.77 ± 1.44	0.781
[Ni(L)Cl]	3.03 ± 1.36	0.921	2.91 ± 1.28	0.912
[Ni(L)Br]	2.97 ± 0.95	0.894	3.42 ± 0.86	0.892
[Ni(L)NO$_3$]	2.54 ± 1.18	0.940	3.94 ± 1.19	0.846
[Ni(L)CH$_3$COO]	2.91 ± 0.71	0.983	4.18 ± 1.48	0.798
Vit. C[a]	1.74 ± 1.19	0.976	–	–
Rutin[a]	2.49 ± 1.27	0.835	2.86 ± 0.92	0.931
Gallic acid[a]	1.44 ± 1.11	0.890	1.22 ± 1.08	0.949
BHT[a]	–	–	2.31 ± 1.30	0.971

(n = 3, X ± SEM), IC$_{50}$-Inhibitory concentration; shows the inhibition of the radicals by the examined compound at 50%, R^2 = correlation coefficient
[a]Standards
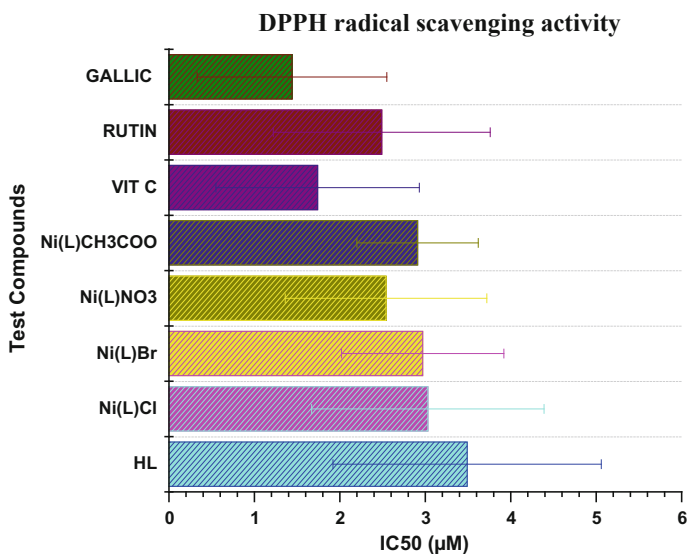
Fig. 17.5 DPPH scavenging potentials of HL, its Ni(II) complexes and standard drugs (n = 3)

ABTS radical scavenging activity
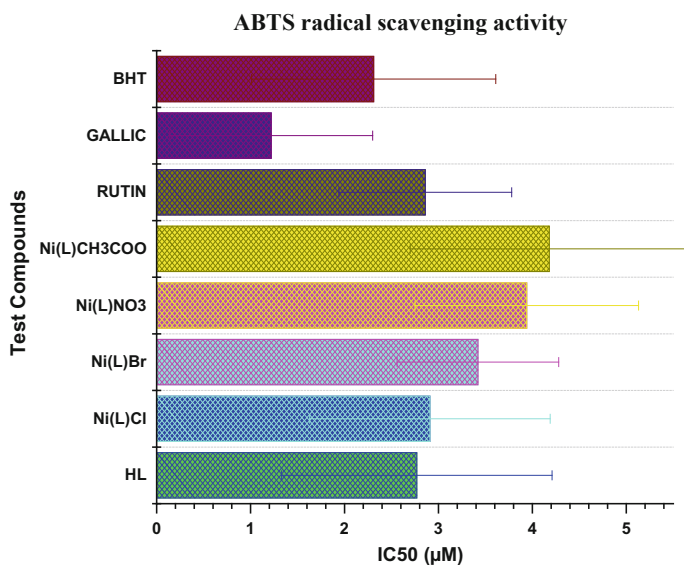
Fig. 17.6 ABTS activities of HL, its Ni(II) complexes and standard drugs (n = 3)

to the percentage ABTS inhibition [9]. The assay measures radical scavenging by electron donation. The coordination of metal ion to the Schiff base resulted in a lower spectrum of activity compared to that of the ligand (2.77 ± 1.44 μM) and standards drugs used [rutin (2.86 ± 0.92 μM), gallic acid (1.22 ± 1.08 μM) and BHT (2.31 ± 1.30 μM)]. The scavenging potentials of the ABTS$^+$ radical by the Schiff base (HL) and its Ni(II) complexes were found to exhibit moderate to high activities (Table 17.1) [12, 17].

[Ni(L)Cl] complex exhibited the highest ABTS scavenging activity amongst the studied complexes with an IC$_{50}$ value of 2.91 ± 1.28 μM and R^2 (correlation coefficient) of 0.912 while [Ni(L)CH$_3$COO] exhibited the least activity amongst the complexes with an IC$_{50}$ value of 4.18 ± 1.48 μM (Fig. 17.6). The ABTS scavenging activity pattern of the test compounds is found to be [Gallic acid] > [BHT] > [HL] > [Rutin] > [Ni(L)Cl] > [Ni(L)Br] > [Ni(L)NO$_3$] > [Ni(L)CH$_3$COO]. These results show that the compounds in this study possess the ability to scavenge different free radicals in different systems, signifying that they may be useful as therapeutic agents for averting cell oxidative damage and treating pathological damage related with radical generation and radical chains termination [4, 12, 22].

17.3.9 In Vitro Antimicrobial Activity

The Schiff base (HL) and the corresponding heterocyclic nickel(II) complexes were investigated against two gram-positive bacterial strains: *Staphylococcus aureus*

(ATCC-25923) and *Enterococcus faecalis* (ATCC-29212), two gram-negative bacterial strains: *Klebsiella pneumoniae* (ATCC-13883) and *Pseudomonas aeruginosa* (ATCC-15442), and two fungi: *Candida albicans* (ATCC-14053) and *Cryptococcus neoformans* (ATCC-14116). They were carried out using neomycin as a standard anti-bacterial control and amphotericin B as standard anti-fungal agent by *p*-iodonitrotetrazolium chloride (INT) colorimetric assay [17] in which the effectiveness of the test samples was observed at the lowest concentrations. The compounds were tested at the concentrations of 6250.00–48.83 µg/mL in DMSO as the solvent. The antimicrobial activity of the Schiff base ligand (HL) and the nickel(II) complexes against bacterial and fungal strains are presented in Table 17.2.

The Ni(II) complexes bearing different anions (Cl^-, Br^-, NO_3^-, CH_3COO^-) showed increased activities compared to the ligand (HL) but exhibited lower potentials as compared to the standard antibiotics: neomycin, and comparable antifungal activities to the amphotericin B as a standard anti-fungal drug under same study conditions (Figs. 17.7 and 17.8). The complexes showed moderate to good biological activity against the bacterial strains. [Ni(L)Br], [Ni(L)NO$_3$], [Ni(L)Cl] and [Ni(L)CH$_3$COO] were found to have good activity against *S. aureus* with MIC value of 390.6, 390.6, 781.3 and 781.3 µg/mL (Table 17.2 and Fig. 17.7). [Ni(L)Cl] and [Ni(L)NO$_3$] exhibited same minimum inhibitory concentration (781.3 µg/mL) towards *K. pneumoniae*. The susceptibility of the selected microorganisms towards [Ni(L)NO$_3$] in terms of MIC follows the order: *S. aureus* (390.6 µg/mL) > *K. pneumoniae* (781.3 µg/mL) > *E. faecalis* (1563 µg/mL) = *P. aeruginosa* (1563 µg/mL).

In vitro antifungal screening results of the Schiff base (HL) and its Ni(II) complexes tested against *C. albicans* and *C. neoformans* by microdilution method using yeast malt (YM) broth as the medium are shown in Table 17.2. [Ni(L)Cl], [Ni(L)Br], and [Ni(L)NO$_3$] complexes exhibited antifungal activity with MIC value of 48.83 µg/ml against *C. albicans*, while [Ni(L)Cl], [Ni(L)Br], and [Ni(L)CH$_3$COO] showed a MIC value of 48.83 µg/ml against *C. neoformans*, both comparable to amphotericin B (an antifungal drug).

Table 17.2 Minimum inhibitory concentration (MIC) (µg/mL) of the Schiff base ligand [HL] and its Ni(II) complexes

Compounds	Gram (+) bacteria		Gram (−) bacteria		Fungi	
	S. aureus	*E. faecalis*	*K. pneumoniae*	*P. aeruginosa*	*C. albicans*	*C. neoformans*
HL	1563	3125	1563	1563	781.3	195.3
[Ni(L)Cl]	781.3	1563	781.3	1563	48.83	48.83
[Ni(L)Br]	390.6	1563	1563	1563	48.83	48.83
[Ni(L)NO$_3$]	390.6	1563	781.3	1563	48.83	97.66
[Ni(L)CH$_3$COO]	781.3	1563	1563	1563	97.66	48.83
Neomycin[a]	1.953	3.906	1.953	3.906	–	–
Amphotericin B[a]	–	–	–	–	48.83	48.83
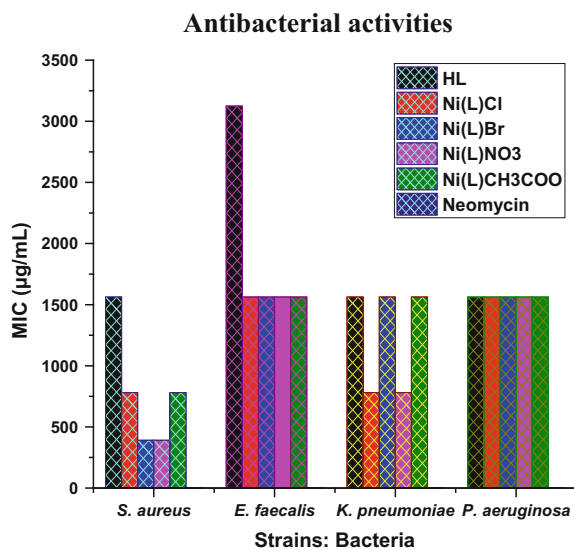
[a]Standards
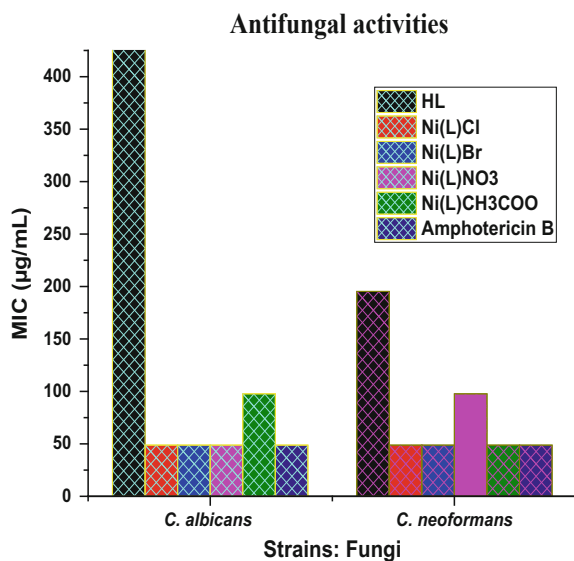
Cell wall synthesis disruption can be related to normal cell process blockage due to hydrogen-bond formation via cell constituent active centers with (>CH=N–) azomethine group (Fig. 17.9) present in the synthesized compounds [15, 19], this in turn brings about the cytoplasmic membrane damage and cell death [17, 19]. The higher biological activity of nickel complexes compared to that of the ligand (HL) can be explained by Overtone's Concept and Tweedy's Chelation Theory [5, 15, 18, 19]. Chelation reduces the polarity of the central metal ions due to the partial sharing of its positive charge with the donor groups and possible delocalization of π-electrons within the entire chelate ring, thus increasing the lipophilic nature of the nickel ions, which leads to liposolubility and permeability through the lipid layer of cell membranes [5, 12, 18].

The presence of different anionic groups coordinated to the Ni(II) ions resulted in bioactivity against strains at various concentrations and the effect on the normal cell membrane [1–3, 12]. The variation in the activity of nickel complexes against different organisms depends either on the impermeability of cells of the microbes or differences in the ribosomes of microbial cells [3, 6, 18]. The particle size of the compounds also partly affects their antimicrobial activity, because nanosized particles exhibit increased antimicrobial activity [6, 17].
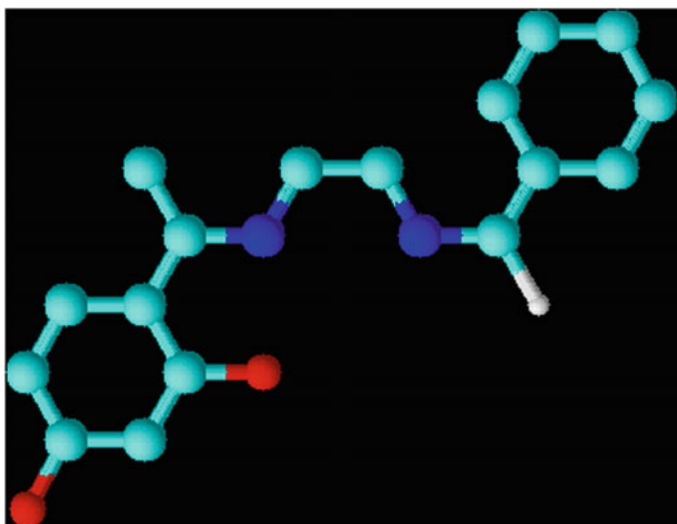
Fig. 17.9   3D structural optimization of the Schiff base (HL)

17.4 Conclusion

A tridentate Schiff base, 4-[(1*E*)-*N*-{2-[(*Z*)-benzylideneamino]ethyl}-ethanimidoyl]benzene-1,3-diol] derived from the condensation of 2′,4′-dihydroxyacetophenone and benzaldehyde with ethylenediamine, and its Ni(II) complexes bearing Cl^-, Br^-, NO_3^-, CH_3COO^- have been described and characterized by elemental analyses, molar conductivity, UV-Vis, FT-IR, thermal analysis, ^{1}H NMR, and XRD. Spectral data showed that the Schiff base HL acts as a tridentate chelating ligand, coordinating through the azomethine nitrogen atoms and the phenol oxygen atom. Conductivity measurements showed the complexes to be non-electrolytes in DMF. The microanalyses were in conformity with the proposed structures. Square-planar geometry was assigned to the synthesized complexes based on the elemental and spectral information. Free radical scavenging properties revealed that the Ni(II)-HL complexes possessed good antioxidant activities. The outcome from DPPH and ABTS inhibition studies revealed that the compounds are capable of donating electron or hydrogen atom, which in turn terminate the chain reactions in a dose-dependent pattern. The antibacterial and antifungal activities of the Schiff base (HL) and its heterocyclic nickel complexes were screened against bacterial and fungal strains: *S. aureus*, *E. faecalis*, *K. pneumoniae*, *P. aeruginosa*, *C. albicans*, and *C. neoformans*. [Ni(L)Br] and [Ni(L)NO$_3$] were found to have good activity against *S. aureus* with MIC value of 390.6 μg/mL. Furthermore, the MIC of some of the nickel complexes exhibited activity comparable to the standard drug for anti-fungal screening.

References

1. Alias M, Kassum H, Shakir C (2014) Synthesis, physical characterization and biological evaluation of Schiff base M(II) complexes. JAAUBAS 15:28–34
2. Shelke VA, Jadhav SM, Patharkar VR, Shankarwar SG, Munde AS, Chondhekar TK (2012) Synthesis, spectroscopic characterization and thermal studies of some rare earth metal complexes of unsymmetrical tetradentate Schiff base ligand. Arab J Chem 5:501–507
3. Sharaby CM, Amine MF, Hamed AA (2017) Synthesis, structure characterization and biological activity of selected metal complexes of sulfonamide Schiff base as a primary ligand and some mixed ligand complexes with glycine as a secondary ligand. J Mol Struct 1134:208–216
4. Ejidike IP, Ajibade PA (2015) Transition metal complexes of symmetrical and asymmetrical Schiff bases as antibacterial, antifungal, antioxidant, and anticancer agents: progress and prospects. Rev Inorg Chem 35:191–224
5. Joseyphus RS, Nair MS (2010) Synthesis, characterization and biological studies of some Co(II), Ni(II) and Cu(II) complexes derived from indole-3-carboxaldehyde and glycylglycine as Schiff base ligand. Arab J Chem 3:195–204

6. Ejidike IP, Ajibade PA (2016) Synthesis and *in vitro* anticancer, antibacterial, and antioxidant studies of unsymmetrical Schiff base derivatives of 4-[(1*E*)-*N*-(2-aminoethyl) ethanimidoyl]benzene-1,3-diol. Res Chem Intermed 42:6543–6555
7. Mostafa IR, Mohammed G, Abd-Elhamed AN, Kamal FS (2012) Synthesis, spectral, thermal and biological studies of Mn(II), Co(II), Ni(II) and Cu(II) complexes with 1-(((5-mercapto-1*H*-1,2,4-triazol-3-yl)imino)-methyl)naphthalene-2-ol. Chin J Chem 30:547–556
8. Kostova I, Sasa L (2013) Advances in research of Schiff-base metal complexes as potent antioxidants. Curr Med Chem 20:4609–4632
9. Ejidike IP, Ajibade PA (2016) Synthesis, characterization, anticancer, and antioxidant studies of Ru(III) complexes of monobasic tridentate Schiff bases. Bioinorg Chem Appl 9672451:1–9
10. Hingorani S, Agarwala BV (1990) Characteristic IR and electronic spectral studies on novel mixed ligand complexes of copper(II) with thiosemicarbazones and heterocyclic bases. Synth React Inorg Met-Org Chem 20:123–132
11. Alaghaz AMA, Zayed ME, Alharbi SA (2015) Synthesis, spectral characterization, molecular modeling and antimicrobial studies of tridentate azo-dye Schiff base metal complexes. J Mol Struct 1084:36–45
12. Ejidike IP, Ajibade PA (2017) Synthesis, spectroscopic, antibacterial and free radical scavenging studies of Cu(II), Ni(II), Zn(II) and Co(II) complexes of 4,4′-{ethane-1,2-diylbis[nitrilo(1*E*)eth-1-yl-1-ylidene]}dibenzene-1,3-diol Schiff base. J Pharm Sci Res 9:593–600
13. Mittal P, Joshi S, Panwar V, Uma V (2009) Biologically active Co(II), Ni(II), Cu(II) and Mn(II) complexes of Schiff bases derived from vinyl aniline and heterocyclic aldehydes. Int J Chem Tech Res 1:225–232
14. Gürbüz D, Çinarli A, Tavman A, Tan ASB (2015) Synthesis, characterization and antimicrobial activity of some transition metal complexes of N-(5-chloro-2-hydroxyphenyl)-3-methoxy-salicylaldimine. Bull Chem Soc Ethiop 29:63–74
15. Abd El-Wahab ZH, Mashaly MM, Salman AA, El-Shetary BA, Faheim AA (2004) Co(II), Ce(III) and UO$_2$(VI) bis-salicylatothiosemicarbazide complexes: binary and ternary complexes, thermal studies and antimicrobial activity. Spectrochim Acta A 60:2861–2873
16. Prakash A, Gangwar MP, Singh PC (2011) Synthesis, spectroscopy and biological studies of nickel(II) complexes with tetradentate Schiff bases having N$_2$O$_2$ donor group. J Dev Biol Tissue Eng 3:13–19
17. Ejidike IP (2018) Cu(II) complexes of 4-[(1*E*)-*N*-{2-[(*Z*)-benzylidene-amino]ethyl}ethanimidoyl] benzene-1,3-diol Schiff base: synthesis, spectroscopic, *in-vitro* antioxidant, antifungal and antibacterial studies. Molecules 23:1581
18. Emam SM (2017) Spectral characterization, thermal and biological activity studies of Schiff base complexes derived from 4,4′-methylenedianiline, ethanolamine and benzyl. J Mol Struct 1134:444–457
19. Al-Shaalan NH (2011) Synthesis, characterization and biological activities of Cu(II), Co(II), Mn(II), Fe(II), and UO$_2$(VI) complexes with a new Schiff base hydrazone: *O*-hydroxyacetophenone-7-chloro-4-quinoline hydrazone. Molecules 16:8629–8645
20. Neelakantan MA, Marriappan SS, Dharmaraja J, Jeyakumar T, Muthukumaran K (2008) Spectral, XRD, SEM and biological activities of transition metal complexes of polydentate ligands containing thiazole moiety. Spectrochim Acta A Mol Biomol Spectrosc 71:628–635
21. Chandra S, Qanungo K, Sharma SK (2012) New hexadentate macrocyclic ligand and their copper(II) and nickel(II) complexes: spectral, magnetic, electrochemical, thermal, molecular modeling and antimicrobial studies. Spectrochim Acta, Part A 94:312–317
22. Tetteh S, Dodoo DK, Appiah-Opong R, Tuffour I (2014) Spectroscopic characterization, *in vitro* cytotoxicity, and antioxidant activity of mixed ligand palladium(II) chloride complexes bearing nucleobases. J Inorg Chem 586131:1–7

Chapter 18
Synthesis of Heterocycle-Appended 4-Aminoquinazolines with Antiproliferative Properties and Potential to Inhibit Tyrosine Kinases

Malose Jack Mphahlele, Marole Maria Maluleka and Mmakwena Modlicious Mmonwa

Abstract The 4-anilinoquinazoline derivatives have established themselves as inhibitors of epidermal growth factor receptor (EGFR) tyrosine kinase phosphorylation. Molecular hybridization to replace the aniline moiety with a heterocyclic scaffold has been found to lead to heterocycle-appended quinazolines with enhanced biological properties and reduced side effects. We have also merged 7-amino-2-arylindole and 7-amino-2-arylbenzofuran moieties with the 2-aryl-4-chloroquinazolines to afford indole- and benzofuran-appended 4-aminoquinazoline analogues of gefitinib. The prepared molecular hybrids were evaluated for antigrowth effect against a panel of EGFR-positive cell lines, such as the human lung cancer (A549), epithelial colorectal adenocarcinoma (Caco-2), hepatocellular carcinoma (C3A), breast adenocarcinoma (MCF-7) and cervical cancer (HeLa) cell lines. These compounds were also evaluated for their ability to inhibit EGFR tyrosine kinase phosphorylation complemented with molecular docking into the adenosine triphosphate (ATP) binding site.

18.1 Introduction

Nitrogen-containing small heterocycles such as quinazolines and indoles continue to attract considerable attention in targeted therapies as antitumor drugs. The 4-anilinoquinazolines shown in Fig. 18.1, for example, have been found to produce anticancer activity through inhibition of the epidermal growth factor receptor tyrosine

M. J. Mphahlele (✉) · M. M. Maluleka · M. M. Mmonwa
College of Science, Engineering and Technology, University of South Africa, Florida Park, Roodepoort 1710, South Africa
e-mail: mphahmj@unisa.ac.za

M. M. Maluleka
e-mail: malulmm@unisa.ac.za

M. M. Mmonwa
e-mail: mmonwmm@unisa.ac.za
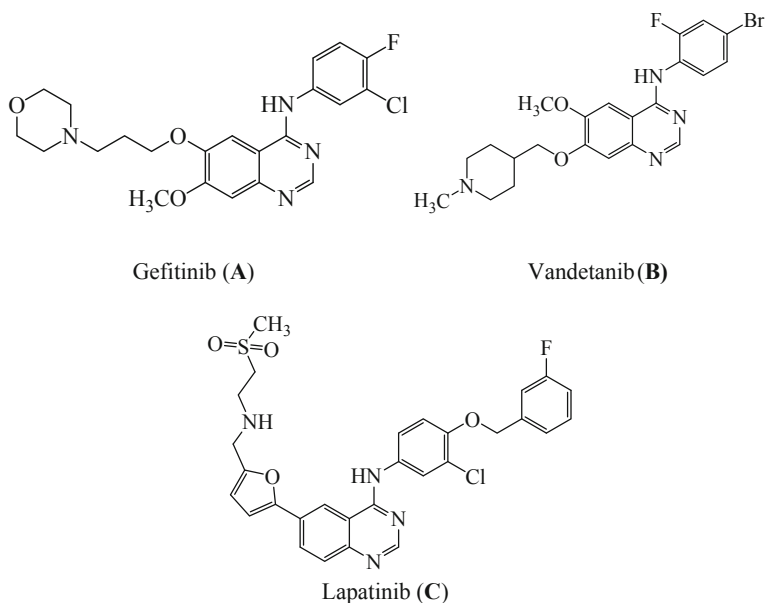
Fig. 18.1 Examples of the medicinally important 4-anilinoquinazolines with anticancer properties

kinase (EGFR-TK) phosphorylation, which results from competitive binding at the ATP site [1–3]. This receptor is overexpressed in various types of tumours including colon, non-small cell lung, prostate, breast and ovarian cancers [4, 5]. The EGFR continues to be an attractive target for the design and development of compounds that can specifically bind to it and inhibit its tyrosine kinase (TK) activity and its signal transduction pathway in cancer cells [6]. Gefitinib (**A**) shown in Fig. 18.1, is an example of a poly-substituted 4-anilinoquinazoline drug used for the treatment of non-small-cell lung cancer (NSCLC) with sensitive mutations of the EGFR [7]. Vandetanib (**B**), on the other hand, has been found to be a selective inhibitor that targets the vascular endothelial growth factor receptor (VEGFR) and the EGFR signal transduction pathways for the treatment of breast cancer [8]. Lapatinib (**C**) also shown in Fig. 18.1 is a 6-heteroaryl substituted 4-anilinoquinazoline derivative, which is an oral dual TK inhibitor that targets both EGFR and HER2 to inhibit the proliferation of breast cancer cells [9].

Most of the EGFR-TK inhibitors have a common 4-aminoquinazoline core and only differ in terms of the substituents and side chains. Structure–activity relationship studies investigating the ability of the 4-anilinoquinazolines to inhibit EGFR-TK activity revealed that both of the quinazoline nitrogen atoms are essential for anticancer activity [10]. Any nitrogen substitution in the ring system of a quinazoline resulted in decreased biological activity. Replacement of the quinazoline ring with a quinoline moiety, for example, resulted in 200-fold less affinity for EGFR [10]. The aniline moiety bearing lipophilic substituents such as chloro, bromo and tri-

fluoromethyl group was also important as it occupies the lipophilic pocket [11]. Drug resistance is the major problem in almost half of the small molecules that were developed for reversibly inhibiting EGFR tyrosine kinase [12]. This resulted when the amino acid threonine 790 was substituted by methionine (T790M) in the ATP binding pocket of EGFR causing resistance in inhibitors such as gefitinib and erlotinib [13].

In the design of new drugs, hybridization approach to merge two or more pharmacophores has been found to provide a more general method to obtain compounds with improved biological activities capable of overcoming multi-drug resistance. Cediranib/Recentin™ (**D**) shown in Fig. 18.2 is an example of an indole-ether quinazoline hybrid, which is a highly potent, orally bioavailable and selective vascular endothelial growth factor receptor (VEGFR) inhibitor for the treatment of cancer [14, 15]. 4-(1-Benzyl-1*H*-indol-3-yl)-6,7-dimethoxyquinazoline (**E**) represented in Fig. 18.2, on the other hand, is an example of an indole-quinazoline hybrid that was found to exhibit moderate ErbB-2 activity with little or no activity against EGFR [16]. The analogous 4-(indole-3-yl)quinazolines were found to be highly potent EGFR-TK inhibitors with excellent cytotoxic properties against several cancer cell lines [17]. The N^4-(1*H*-indol-5-yl)quinazoline-4,6-diamines (**F**), on the other hand, were found to exhibit significant anti-inflammatory properties and dose-dependent lipopolysaccharide-induced TNF-α and IL-6 release [18].

Cediranib (**D**)   (**E**)

(**F**)

Fig. 18.2 Examples of indole-appended quinazoline hybrids of biological importance

   Literature search revealed several methods for merging the quinazoline moiety
with other scaffolds to form molecular hybrids with enhanced biological properties.
These methods are discussed below.

18.2   Methods for Preparation of Indole-Quinazoline Hybrids

The 4-(indole-3-yl)quinazolines **5** shown in Scheme 18.1 were previously prepared
via the reaction of indolyl-magnesium derivatives **2** with 4-chloroquinazolines **3** in
diethyl ether under reflux followed by hydrolysis of the intermediates **4** [17]. The
indole-quinazoline hybrids **5b–f** were found to be potent inhibitors of EGFR-TK
activity with IC_{50} values ranging from 131 to 533 nM [16]. In addition, compounds
5c and **5f** were also found to inhibit human epidermal growth factor receptor 2-
tyrosine kinase (HER-2-TK) at 100 nM.

   Aluminium chloride-catalyzed cross-coupling of indoles **6** with 2,4-
dichloroquinazoline **7** in dry dichloroethane under nitrogen atmosphere at
75–80 °C previously afforded 2-chloro-4-(3-indolyl)quinazolines **8** (R = H, –CH$_3$)
(Scheme 18.2) [19]. Compounds **8** were further reacted with cyclic amines to form
2-amino-4-(3-indolyl)quinazolines, which were found to exhibit anti-leishmanial
and/or anti-proliferative activities against the prostate carcinoma (DU145), breast
adenocarcinoma (MCF-7), oral epidermal carcinoma (KB) and cervical carcinoma
(C33A) [19].

   Indium(III) chloride (InCl$_3$)-catalyzed hybridization of indole **9** with 4-
chloroquinazoline **10a** (R = H, R$'$ = N, R$''$ = Ph) or **10b** (R = Cl, R$'$ = CH, R$''$ = H)
in acetonitrile under microwave irradiation at 150 W and 120 °C afforded the 4-(1*H*-
indol-3-yl)-2-phenylquinazoline **11a** (R = H, R$'$ = N, R$''$ = Ph) in 78% yield or its
analogous 7-chloro-4-(1*H*-indol-3-yl)quinolone **11b** (R = Cl, R$'$ = CH, R$''$ = H) in
89% yield (Scheme 18.3) [20]. The use of phenol as a catalyst in the reaction of **9** with
10b afforded **11b** as a major product along with a 4-phenoxyquinoline. Furthermore,
11b was obtained in 82, 83, and 84% yields when boron trifluoride diethyl etherate
(BF$_3$·Et$_2$O), indium(III) trifluoromethanesulfonate or gallium trichloride were used
as catalysts, respectively. However, the use of ytterbium(III) trifluoromethanesul-
fonate or cerium ammonium nitrate as catalysts led to the recovery of the starting
material.

   N$'$-(2-Cyano-4-nitro-phenyl)-*N,N*-dimethylformamidine **13** was reacted with 5-
aminoindoles **14** in acetic acid under reflux to afford (6-nitro-quinazolin-4-yl)-(1*H*-
indol-5-yl)-amines **15** (R = –CH$_3$, propyl, allyl) (Scheme 18.4) [17]. Compound
13 used as precursor was, in turn, prepared via the condensation of 2-amino-5-
nitrobenzonitrile **12** with dimethylformamide dimethyl acetal in toluene under reflux
(Scheme 18.4). Compounds **15** were further reduced to their corresponding N^4-(1*H*-
indol-5-yl)-quinazoline-4,6-diamine derivatives which were also found to exhibit
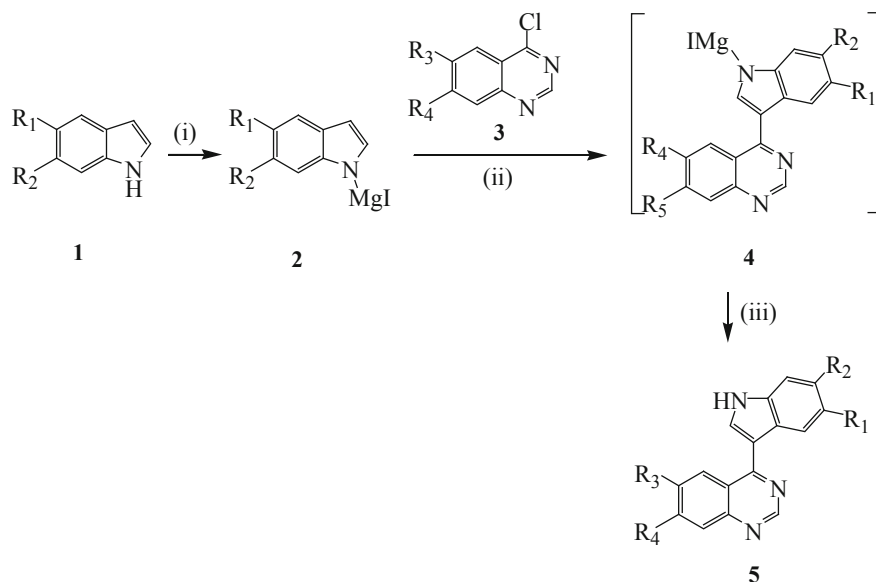
5	R_1	R_2	R_3	R_4	%Yield
a	H	H	H	H	45
b	Br	H	-OCH$_3$	-OCH$_3$	14
c	Cl	F	-OCH$_3$	-OCH$_3$	13
d	-CH$_3$	F	-OCH$_3$	-OCH$_3$	23
e	Cl	F	(see structure)	(see structure)	10
f	Cl	F	(see structure)	-OCH$_3$	21

Reagents and conditions: (i) Mg, I$_2$, CH$_3$I, Et$_2$O, 5 °C; (ii) Et$_2$O, reflux; (iii) H$_2$O

Scheme 18.1 Hybridization of **2** with **3** to afford **5**

anti-inflammatory properties against lipopolysaccharide-induced TNF-α and IL-6 expression [17].

   We considered our previous work on the antiproliferative properties of the 2-arylindoles [21] and the 4-anilinoquinazolines [22, 23] in combination with the literature analyses on bioactive compounds containing these moieties and decided to merge the 4-aminoquinazoline moiety with the indole and benzofuran rings, respectively.
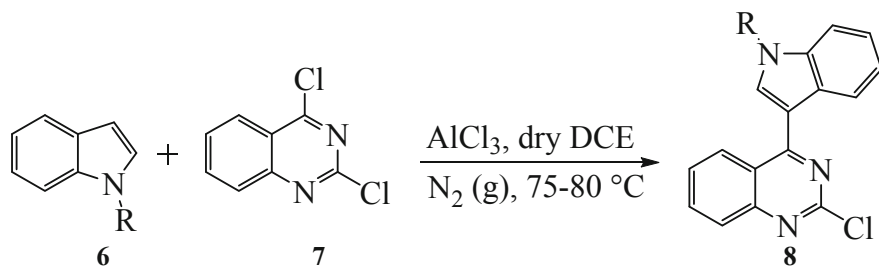
Scheme 18.2 Cross-coupling of **6** with **7** to afford **8**
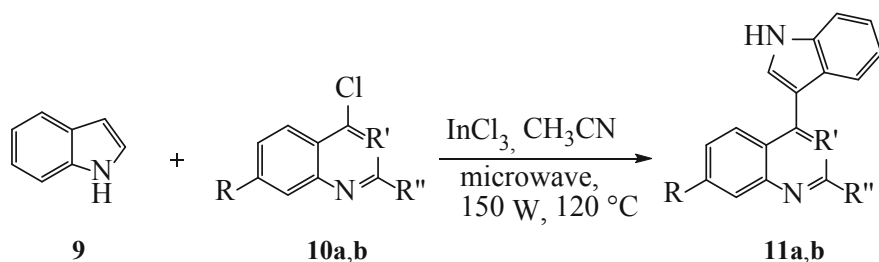
Scheme 18.3 Hybridization of **9** with **10** to afford **11**
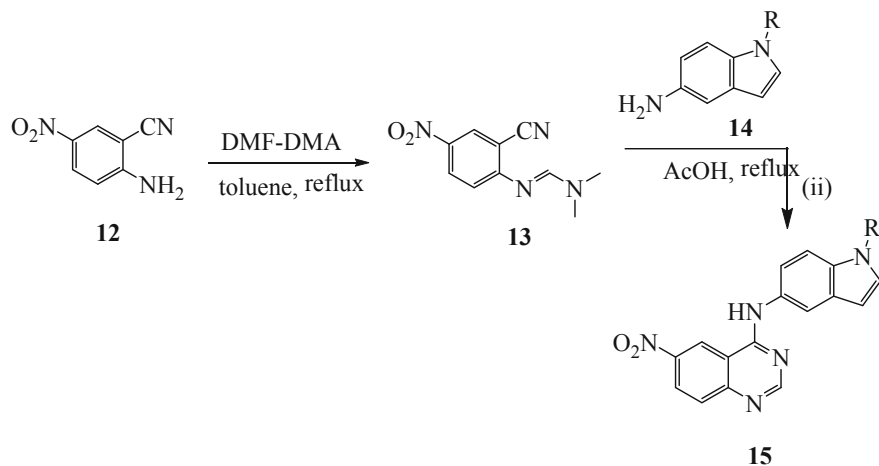
Scheme 18.4 Preparation of **15** from reaction of **13** with **14**

| 16a–d | 17a: X = H | | 18a–d |
| | 17b: X = 4-F | | 18e–h |

18	R	%Yield of 18
a	H	81
b	4-F	79
c	3-Cl	75
d	4-OMe	83
e	H	78
f	4-F	80
g	3-Cl	78
h	4-OMe	67
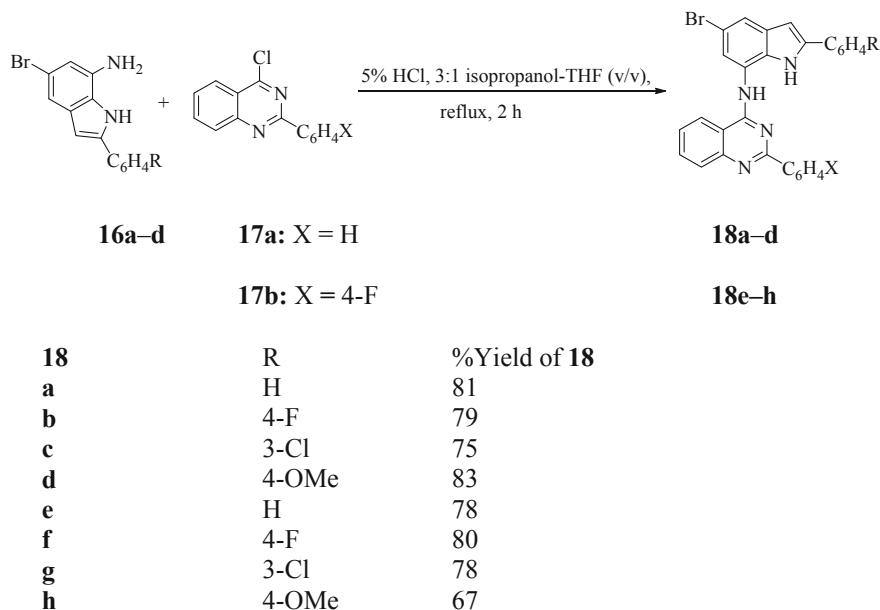
Scheme 18.5 Amination of **17** with **16** to afford indole-quinazoline hybrids **18**

18.3   Preparation of Indole-Appended Aminoquinazoline Hybrids

The indole-appended 4-aminoquinazolines **18a–h** were prepared via HCl catalyzed amination of the electrophilic 2-aryl-4-chloroquinazoline derivatives **17a** and **17b** with 7-aminoindoles **16a–d** in tetrahydrofuran-isopropanol (THF-iPrOH) mixture under reflux (Scheme 18.5) [24]. Compounds **18a–h** were evaluated for antigrowth effect in vitro against the human lung cancer (A549), epithelial colorectal adenocarcinoma (Caco-2), hepatocellular carcinoma (C3A), breast adenocarcinoma (MCF-7) and cervical cancer (HeLa) cell lines. Hybrids **18f** and **18g** were found to have cytotoxicity against most of the cancer cell lines and to inhibit the EGFR-TK activity against gefitinib (IC_{50} 38.9 nM) as a reference standard with the IC_{50} values 52.5 and 40.7 nM, respectively [24].

18.4   Preparation of Benzofuran-Appended Aminoquinazoline Hybrids

Despite what looks like a simple molecular framework, a thorough literature search revealed that no attempts have been made before towards the synthesis of benzofuran-

appended quinazoline hybrids in which the two pharmacophores are linked through a heteroatom bridge. We reacted the nucleophilic 7-aminobenzofurans **23a–e** with the electrophilic 6-bromo-4-chloro-2-(4-halogenophenyl)quinazoline **24a** (X = F) or **24b** (X = Cl) in the presence of 5% HCl in isopropanol (iPrOH) under reflux for 4 h (Scheme 18.6) [25]. We successfully isolated compounds characterized using a combination of spectroscopic (NMR, IR, MS) and single crystal X-ray diffraction technique as the corresponding benzofuran-aminoquinazoline hybrids **25a–e** or **25f–j**, respectively. Since the molecular construct of compounds **25a–j** resembles that of the EGFR-TK inhibitor, gefitinib, we evaluated them for antiproliferative effect against a panel of EGFR-positive cancer cell lines, namely, the A549, Caco-2, C3A (HepG2/C3A) and HeLa cell lines [25]. Among them compound **25d** showed significant cytotoxicity against the C3A cell line ($LC_{50} = 9.0 \, \mu M$) when compared to gefitinib ($LC_{50} = 5.01 \, \mu M$) and compound **25j** was also found to exhibit increased cytotoxicity against the Caco-2 cells ($LC_{50} = 18.4 \, \mu M$) more so than gefitinib ($LC_{50} = 27.9 \, \mu M$). Mechanistic studies demonstrated that the benzofuran-appended aminoquinazoline hybrids **25d** and **25j** induced apoptosis via activation of caspase-3 pathway. Moreover, compounds **25d** and **25j** exhibited significant and moderate inhibitory effects against EGFR ($IC_{50} = 29.3$ and 61.5 nM, respectively) when compared to gefitinib ($IC_{50} = 33.1$ nM).

Reagents & conditions:
(i) NBS, AcOH, reflux, 1.5 h; (ii) NIS, AcOH, reflux, 1 h
(iii) ArC≡CH, PdCl₂(PPh₃)₂, CuI, Cs₂CO₃, DMF(aq), reflux, 3 h;
(iv) NH₂OH.HCl, pyridine, reflux, 1 h; (v) TfOH, CH₃CN, reflux, 1 h
(vi) 5% HCl, iPrOH, reflux, 3 h

25a–e (X = F); **25f–j** (X = Cl)
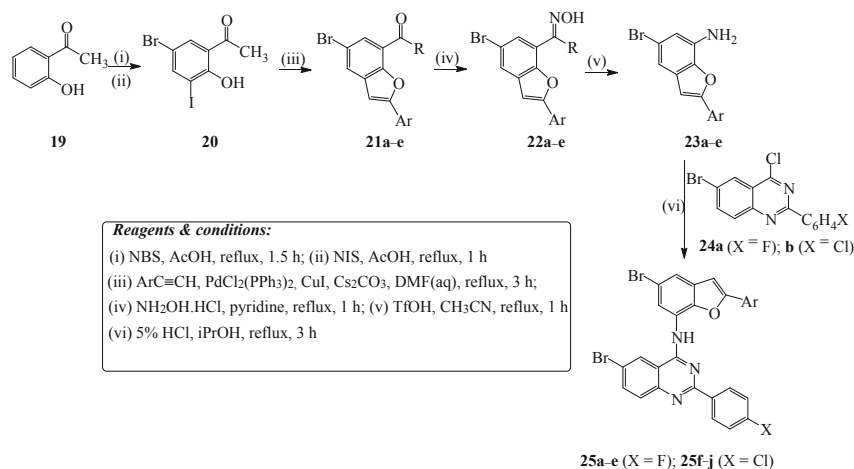
Ar	%Yield 21	%Yield 22	%Yield 23	%Yield 25a–e	%Yield 25f–j
C₆H₅-	73 (**21a**)	93 (**22a**)	62 (**23a**)	75 (**25a**)	83 (**25f**)
3-FC₆H₄-	76 (**21b**)	86 (**22b**)	78 (**23b**)	82 (**25b**)	81 (**25g**)
4-FC₆H₄-	76 (**21c**)	72 (**22c**)	71 (**23c**)	87 (**25c**)	78 (**25h**)
3-ClC₆H₄-	74 (**21d**)	81 (**22d**)	65 (**23d**)	78 (**25d**)	67 (**25i**)
4-CF₃OC₆H₄-	77 (**21e**)	78 (**22e**)	85 (**23e**)	82 (**25e**)	84 (**25j**)

Scheme 18.6 Amination of **24** with **23** to afford benzofuran-aminoquinazoline hybrids **25**

18.5 Conclusions and Perspective

We have demonstrated that the indole or benzofuran moieties can be linked with the quinazoline scaffold through an amino bridge to produce molecular hybrids with structural resemblance to the medicinally important 4-anilinoquinazoline derivatives. The prepared molecular hybrids have been evaluated for cytotoxicity in vitro against a panel of cancer cell lines and for inhibitory effect against the EGFR-TK phosphorylation. Since these compounds may also target proteins other than EGFR, future studies will also be extended to other types of protein kinases to explore the mechanism of action and selectivity of the title compounds. The observed results and structure activity relationship (SAR) form a basis for the design and synthesis of more potent heterocycle-appended aminoquinazoline hybrids in which the two pharmacophores are linked by a heteroatom bridge.

References

1. Fry DW, Kraker AJ, McMichael M, Ambroso LA, Nelson JM, Leopold WR, Connors RW, Bridges AJ (1994) A specific inhibitor of the epidermal growth factor receptor tyrosine kinase. Science 265:1093–1095
2. Bridges AJ (2001) Chemical inhibitors of protein kinases. Chem Rev 101:2541–2571
3. Zhao Z-Q, Yu Z-Y, Li J, Ouyang X-N (2016) Gefitinib induces lung cancer cell autophagy and apoptosis *via* blockade of the PI3 K/AKT/mTOR pathway. Oncol Lett 12:63–68
4. Woodburn JR (1999) The epidermal growth factor receptor and its inhibition in cancer therapy. Pharmacol Ther 82:241–250
5. Dobrusin EM, Fry DW (1992) Protein tyrosine kinases and cancer. Annu Rep Med Chem 27:169–178 (Chapter 18)
6. Zwick E, Bange J, Ullrich A (2001) Receptor tyrosine kinase signalling as a target for cancer intervention strategies. Endocr Relat Cancer 8:161–173
7. Hu S, Xie G, Zhang DX, Davis C, Long W, Hu Y, Wang F, Kang Z, Tan F, Ding L, Wang Y (2012) Synthesis and biological evaluation of crown ether fused quinazoline analogues as potent EGFR inhibitors. Bioorg Med Chem Lett 22:6301–6305
8. De Luca A, D'Alessio A, Maiello MR, Gallo M, Bevilacqua S, Frezzetti D, Morabito A, Perrone F, Normanno N (2014) Vandetanib as a potential treatment for breast cancer. Expert Opin Investig Drugs 23:1295–1303
9. Abouzid K, Shouman S (2008) Design, synthesis and *in vitro* antitumor activity of 4-aminoquinoline and 4-aminoquinazoline derivatives targeting EGFR tyrosine kinase. Bioorg Med Chem 16:7543–7551
10. Rewcastle GW, Denny WA, Bridges AJ, Zhou H, Cody DR, McMichael A, Fry DW (1995) Tyrosine kinase inhibitors. 5. Synthesis and structure-activity relationships for 4-[(phenylmethyl)amino]- and 4-(phenylamino)quinazolines as potent adenosine 5′-triphosphate binding site inhibitors of the tyrosine kinase domain of the epidermal growth factor receptor. J Med Chem 18:3482–3487
11. Ismail RSM, Ismail NSM, Abuserii A, El Ella DAA (2016) Recent advances in 4-aminoquinazoline based scaffold derivatives targeting EGFR kinases as anticancer agents. Future J Pharm Sci 2:9–19

12. Camp ER, Summy J, Bauer TW, Liu W, Gallick GE, Ellis LM (2005) Molecular mechanisms of resistance to therapies targeting the epidermal growth factor receptor. Clin Cancer Res 11:397–405
13. Yun CH, Mengwasser KE, Toms AV, Woo MS, Greulich H, Wong KK, Meyerson M, Eck MJ (2008) The T790M mutation in EGFR kinase causes drug resistance by increasing the affinity for ATP. Proc Natl Acad Sci USA 6:2070–2075
14. Wedge SR, Kendrew J, Hennequin LF, Valentine PJ, Barry ST, Brave SR, Smith NR, James NH, Dukes M, Curwen JO, Chester R, Jackson JA, Boffey SJ, Kilburn LL, Barnett S, Richmond GHP, Wadsworth PF, Walker M, Bigley AL, Taylor ST, Cooper L, Beck S, Jürgensmeier JM, Ogilvie DJ (2005) AZD2171: a highly potent, orally bioavailable, vascular endothelial growth factor receptor-2 tyrosine kinase inhibitor for the treatment of cancer. Cancer Res 65:4389–4400
15. Medinger M, Esser N, Zirrgiebel U, Ryan A, Jürgensmeier JM, Drevs J (2009) Antitumor and antiangiogenic activity of cediranib in a preclinical model of renal cell carcinoma. Anticancer Res 29:5065–5076
16. Lüth A, Löwe W (2008) Syntheses of 4-(indole-3-yl)quinazolines—a new class of epidermal growth factor receptor tyrosine kinase inhibitors. Eur J Med Chem 43:1478–1488
17. Lüth A, Lōwe W (2008) A novel synthesis of EGFR-tyrosine-kinase inhibitors with 4-(indol-3-yl)quinazoline structure. J Heterocyclic Chem 45:703–708
18. Hu J, Zhang Y, Dong L, Wang Z, Chen L, Liang D, Shi D, Shan X, Liang G (2015) Design, synthesis, and biological evaluation of novel quinazoline derivatives as anti-inflammatory agents against lipopolysaccharide-induced acute lung injury in rats. Chem Biol Drug Des 85:672–684
19. Kumar S, Shakya N, Gupta S, Sarkar J, Sahu DP (2009) Synthesis and biological evaluation of novel 4-(hetero) aryl-2-piperazino quinazolines as anti-leishmanial and anti-proliferative agents. Bioorg Med Chem Lett 19:2542–2545
20. Staderini M, Bolognesi ML, Menéndeza JC (2015) Lewis acid-catalyzed generation of C–C and C–N bonds on π-deficient heterocyclic substrates. Adv Synth Catal 357:185–195
21. Mphahlele MJ, Makhafola TJ, Mmonwa MM (2016) *In vitro* cytotoxicity of novel 2,5,7-tricarbo-substituted indoles derived from 2-amino-5-bromo-3-iodoacetophenone. Bioorg Med Chem 24:4576–4586
22. Paumo HK, Makhafola TJ, Mphahlele MJ (2016) Synthesis and *in vitro* cytotoxic properties of polycarbo-substituted 4-(arylamino)quinazolines. Molecules 21:1366–1383
23. Mphahlele MJ, Paumo HK, Choong YS (2017) Synthesis and *in vitro* cytotoxicity of the 4-(halogenoanilino)-6-bromoquinazolines and their 6-(4-fluorophenyl) substituted derivatives as potential inhibitors of epidermal growth factor receptor tyrosine kinase. Pharmaceuticals 10:87–104
24. Mphahlele MJ, Mmonwa MM, Aro A, McGaw LJ, Choong YS (2018) Synthesis, biological evaluation and molecular docking of novel indole-aminoquinazoline hybrids for anticancer properties. Int J Mol Sci 19:2232–2248
25. Mphahlele MJ, Maluleka MM, Aro A, McGaw LJ, Choong YS (2018) Benzofuran-appended 4-aminoquinazoline hybrids as epidermal growth factor receptor tyrosine kinase inhibitors: synthesis, biological evaluation and molecular docking studies. J Enzyme Inhib Med Chem 33:1516–1528

Chapter 19
Chemical Refinement of Chromium Metaphosphate Product Isolated from Geological Mineral Ore Samples

Trevor T. Chiweshe

Abstract Fusion of geological mineral ores (SARM 131, UG2 chromite and Merensky Reef) using ammonium phosphate salt as flux yielded chromium metaphosphate products ($Cr(PO_3)_3$) which contained Fe, Al, Si and Mg as impurities. Microscope, Raman and SEM-EDX spectroscopic analysis of the green $Cr(PO_3)_3$ products identified these impurities as dark inclusions which survived the fusion process which contained 4.5–6.1% (Fe), 3.1–4.6% (Si), 1.7–2.4% (Al) and 0.6–1.0% (Mg). A repeat of the fusion procedure using chromium salts (chlorides and nitrates) and oxide yielded $Cr(PO_3)_3$ products containing 0.7–4.8% (Si) and 0.6–2.8% (Al) as impurities. The source of impurities from these $Cr(PO_3)_3$ products was determined to be from the corrosion of the ceramic crucible. The removal of these impurities was achieved by heating the contaminated $Cr(PO_3)_3$ in *aqua regia* and isolating the insoluble dark particles as residues. SEM-EDX analysis of the final green product showed a pure chromium metaphosphate with no traces of impurities.

Keywords Chromium metaphosphate · Ammonium phosphate · Raman spectroscopy · SEM-EDX analysis

19.1 Introduction

In South Africa, the biggest source of chromite ($FeCr_2O_4$, 69–70%) is obtained from the Upper Group 2 deposits (UG2) in the Bushveld Igneous Complex (BIC), which is mainly beneficiated for its platinum group elements (PGE) content [1]. A low-grade chromite concentrate is produced as by-product from the PGE extraction process which accounts for approximately 30% of chrome produced in the country [2]. In 2013 world-wide chromium ore production reached 29 million tons with the balance of production made up by producers in India, Kazakhstan, Turkey and Russia. Statistics indicate that 95% of the chromium metal produced is consumed

T. T. Chiweshe (✉)
Institute for Groundwater Studies, University of the Free State, Nelson Mandela Drive, Bloemfontein 9300, South Africa
e-mail: chiweshetrevor@gmail.com

by the metallurgical industry for the production of specialized alloys and the rest in the refractory/foundry (3.2%) and chemical industries (1.6%) [3, 4].

The higher chromium content in the UG2 ores compared to the Merensky ores requires higher furnace temperatures to operate. This often results in sticky chrome compounds build-up in the furnaces which often requires constant monitoring to avoid frequent shutdown of the plant [5]. The gravity separation together with the flotation processes that were developed for the processing of the Merensky ore has its limitations in the beneficiation of the UG2 ore due to the smaller PGE mineral grain sizes and the high chromium levels.

In a number of previous studies, we investigated different PGE mineral ore samples from a PGE perspective [6]. The aims of these studies involved analytical method development and validation to ensure the accurate quantification of PGE in these ore samples. Complete sample dissolution was crucial for the complete and accurate chemical profiling of these ores. The use of sodium phosphate salts as flux (HNa_2PO_4/H_2NaPO_4) was extremely successful in the complete dissolution of the UG2 chromite, Merensky and SARM 131 samples, but the high Na^+ content in the form of easily ionized elements (EIE's), compromised the accurate quantification of the PGE in the final solutions using ICP technique. The replacement of the sodium salts with the ammonium analogues and the addition of an internal standard eliminated the analytical problem. Surprisingly, the chromium in these samples precipitated quantitatively after the dissolution of the melt in water. The isolated green precipitates were successfully identified as the chromium metaphosphate (C-type $Cr(PO_3)_3$) using XRD analysis [6].

Numerous $Cr(PO_3)_3$ synthetic methods have been reported [7, 8], some as early as 1846 [9]. Currently, six different chromium metaphosphates have been identified to date (i.e. A, B, C, D, E and F-types), but only two, namely B and C, were structurally characterized [10]. Other types of characterization of $Cr(PO_3)_3$ included magnetic properties, IR, UV/vis, ERS, and Mössbauer spectroscopy. The crystal structure of the C-type reported by Gruss and Glaum revealed a three dimensional structure with infinite PO_3^- chains and individual CrO_6 octahedral [11]. This super structure accounts for the high degree of chemical, mechanical and thermal stability which is evident in its insolubility in different mineral acids. Possible applications for this highly inert compound include anticorrosive inorganic pigments, catalysts and heat sensors [12, 13].

A discrepancy between the ICP and EDX analytical results prompted a revisit to the isolation of the green $Cr(PO_3)_3$ from the different mineral sources. The ICP analysis of the green precipitate revealed a product with high purity (and very little contamination), while the EDX showed the presence of approximately 5% Fe in the element analysis. The question thus arises if the isolation method produced products that may have Fe as a metaphosphate present, or do the presence of Fe may be attributed to contamination from the original sample (small amounts of unreacted mineral). It was also decided to include in this investigation the formation of $Cr(PO_3)_3$ using different pure chromium inorganic salts and oxide in order to determine the purity of the chromium products and the possible Fe source.

19.2 Experimental

19.2.1 Chemicals, Instrumentation and Experimental Procedures

19.2.1.1 Reagents and Labware

Chromium(III)chloride hexahydrate ($CrCl_3 \cdot 6H_2O$), chromium(III)nitrate nonahydrate ($Cr(NO_3)_3 \cdot 9H_2O$), chromium(VI) oxide (CrO_3) and ammonium dihydrogen phosphate (($NH_4)H_2PO_4$) (99%) were purchased from Merck whilst the ceramic crucibles (capacity, 150 mL) were purchased from Terra Nova Ceramics (South Africa). The certified reference material (SARM 131) was supplied by Xstrata Wonderkop Plant, South Africa whilst the UG2 chromite and the Merensky Reef mineral ore were obtained from the BIC near Rustenburg [14]. Hydrochloric acid (10 M), nitric acid (15 M), *aqua regia*, orthophosphoric acid (15 M) and sulphuric acid (18 M) were purchased from Sigma-Aldrich. Volumetric flasks used in this research study were of Blaubrand grade A type and the glass beakers were of the Schott Duran type. Ultra-pure deionized water (conductivity, 0.01 μS/cm) was used for all experimental analyses and all quantitative results were recorded as an average of 3 replicates.

19.2.1.2 Instrumentation

Sample fusion was achieved using a Barnstead Thermolyne furnace (max temperature 1300 °C) whilst a Shimadzu ICPS-7510 ICP-OES with a radial sequential plasma spectrometer was used for wet chemical analysis. Default settings/conditions for the ICP-OES measurements were used in order to achieve the best precision and accuracy of results (Table 19.1). The Eutech CyberScan (pH 1500) was used for the pH measurement. Characterization of the isolated chromium metaphosphates products were done using a Digilab (FTS 2000) infrared (IR) spectrometer, an Oxford X-Max^N energy dispersive X-ray spectrometer (EDX) equipped with a Tescan VEGA3

Table 19.1 Selected ICP-OES operating conditions for metal analysis

Parameter	Condition
RF power	1.2 kW
Coolant gas flow rate	14.0 L/min
Plasma gas flow rate	1.2 L/min
Carrier gas flow rate	0.7 L/min
Sample uptake method	Peristaltic pump
Type of spray chamber	Glass cyclonic
Type of nebulizer	Concentric
Injector tube diameter	3.0 mm

scanning electron microscope (SEM) (Center of Microscopy, University of the Free State) and a Renishaw InVia Raman spectrometer (Division of Chemistry and Environmental Sciences, Manchester Metropolitan University, UK).

19.2.2 Experimental Procedures

19.2.2.1 ICP-OES Multi-element Calibration Standards

Multi-element calibration standard solutions for the elemental analysis of impurities were prepared from the original standard solutions (1000 ppm) and were diluted to concentrations between 0.5 and 10.0 ppm in separate volumetric flasks (100.0 mL) using a 'Transferpette' micro-pipette. Hydrochloric acid (5.0 mL; 10 M) was added and the flasks were filled to the mark using ultra-pure deionized water.

19.2.2.2 Preparation and Characterization of Chromium Metaphosphate Products Isolated from SARM 131, UG2 Chromite, Merensky Reef, CrO_3, $CrCl_3 \cdot 6H_2O$ and $Cr(NO_3)_3 \cdot 9H_2O$

Powdered samples of SARM 131, UG2 chromite, Merensky Reef, CrO_3, $CrCl_3 \cdot 6H_2O$ and $Cr(NO_3)_3 \cdot 9H_2O$ were transferred into separate crucibles and mixed uniformly with $(NH_4)H_2PO_4$ salt in the ratio of 1:25. Each mixture was placed in a pre-heated furnace (800 °C) until a red-hot molten liquid (~25 min) was obtained. The solid green glassy melt obtained for each sample was dissolved in deionized water which resulted in an instant precipitation of the green solid products (previously identified as chromium metaphosphate—see discussion) with the percentage yield of 93, 87, 87, 83, 26 and 10% respectively. The chromium metaphosphate products were characterized using IR (Fig. 19.1).

19.2.2.3 Analysis of the Chromium Metaphosphate Products Using Raman Spectroscopy

The isolated chromium metaphosphate compounds from SARM 131, UG2 chromite, Merensky Reef, $Cr(NO_3)_3 \cdot 9H_2O$, $CrCl_3 \cdot 6H_2O$ and CrO_3 were further characterized using Raman spectroscopy. Samples analyzed using Raman spectroscopy were mounted on double-sided carbon tape fixed onto glass microscope slides. Analysis was done using either a Renishaw InVia Raman microscope or a DXR Raman scope fitted with a Peltier-cooled charge-coupled device detector. The source of excitement was a 514.5 nm Ar^+ laser in the case of the Renishaw and 532 or 780 nm in the case of the latter instrument. Data acquisition was carried out with the WireTM and Spectralcalc software packages from Renishaw (Fig. 19.2). Spectral identification
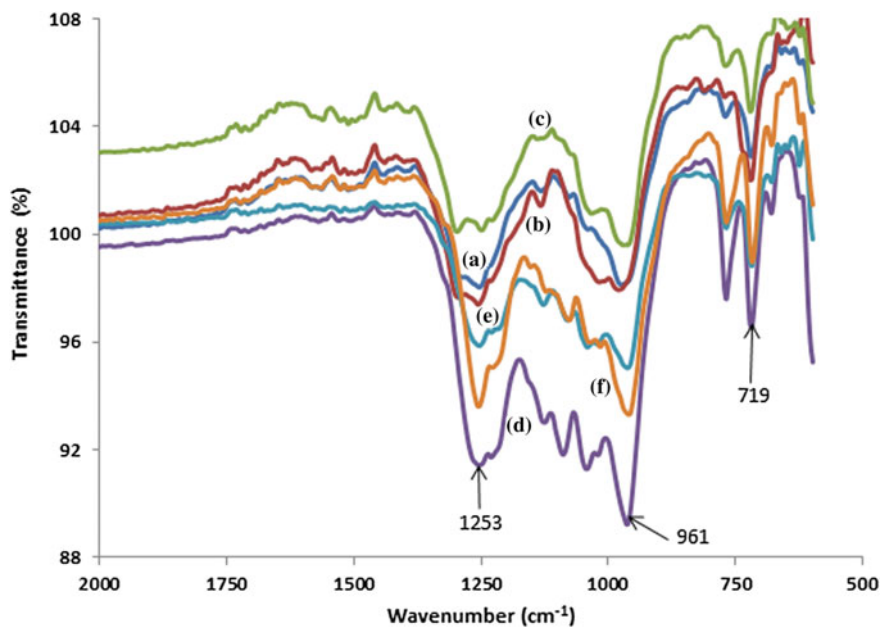
Fig. 19.1 Infrared spectra of the chromium metaphosphate products isolated from **a** SARM 131, **b** UG2 chromite, **c** Merensky Reef, **d** CrO_3, **e** $CrCl_3 \cdot 6H_2O$, and **f** $Cr(NO_3)_3 \cdot 9H_2O$

Fig. 19.2 Raman spectra of the chromium metaphosphate products isolated from **a** SARM 131, **b** UG2 chromite ore, **c** Merensky Reef ore, **d** $Cr(NO_3)_3 \cdot 9H_2O$, **e** CrO_3, and **f** $CrCl_3 \cdot 6H_2O$
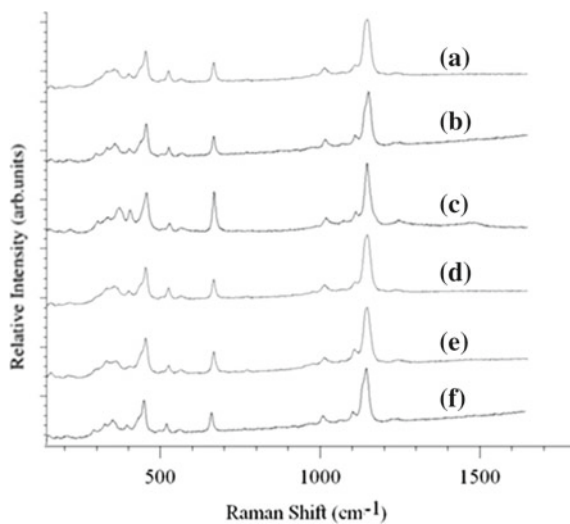
was done using an in-house spectral library, RRUFF database and a commercially available spectral library via Spectracalc software (GRAMS, Galactic Industries).

19.2.2.4   Analysis of the Chromium Metaphosphate Products Using SEM-EDX Spectroscopy

Samples of the chromium metaphosphates isolated from SARM 131, UG2 chromite ore, Merensky Reef ore, $Cr(NO_3)_3 \cdot 9H_2O$, CrO_3 and $CrCl_3 \cdot 6H_2O$ were mounted on aluminium pin stubs using double-sided carbon tape. Specimens were imaged using back scatter imaging and analyzed with a JSM-7800F Extreme-resolution Analytical Field Emission SEM (FE-SEM) equipped with an Oxford Instruments X-MaxN 80 EDX detector and Ztec EDX Software. Samples were analyzed at 10 kV and at WD of 10 mm. SEM-EDX images of the chromium metaphosphate product from the geological samples (SARM 131, UG2 chromite and Merensky Reef ore) were compared with the obtained images from the chromium salts and oxide (chromium nitrate, chromium chloride and chromium oxide) (Fig. 19.3).

19.2.2.5   Determination of Impurities in the Isolated Chromium Metaphosphates Products

A blank test analysis was performed to determine the source of impurities in the chromium metaphosphate products. Ammonium phosphate flux was heated in a ceramic crucible for *ca*. 25 min and the resultant melt was dissolved in deionised water and analysed using ICP-OES. Qualitative analysis results of the blank solution showed the presence of Si, Al and Mg in trace amounts (less than 5 ppm). Impurities in the chromium metaphosphate products were successfully isolated using *aqua regia* and semi-quantitative analysis of the isolated impurities using ICP-OES showed the presence of Ca, Fe, Si, Al and Mg (<5 ppm).

19.3   Results and Discussion

19.3.1   IR Spectroscopy

Chromium metaphosphate compounds were prepared by fusing SARM 131, UG2 and Merensky Reef (geological ores samples) with ammonium phosphate salt as flux using theratio of 1:25 respectively [15]. The isolated chromium products from the geological samples were visually compared with those from the $Cr(NO_3)_3 \cdot 9H_2O$, $CrCl_3 \cdot 6H_2O$ and CrO_3 (chromium salts and oxide samples) to determine any physical similarities or differences. Products obtained from the geological samples were more crystalline than those obtained from the salts and oxide. Characterization using IR
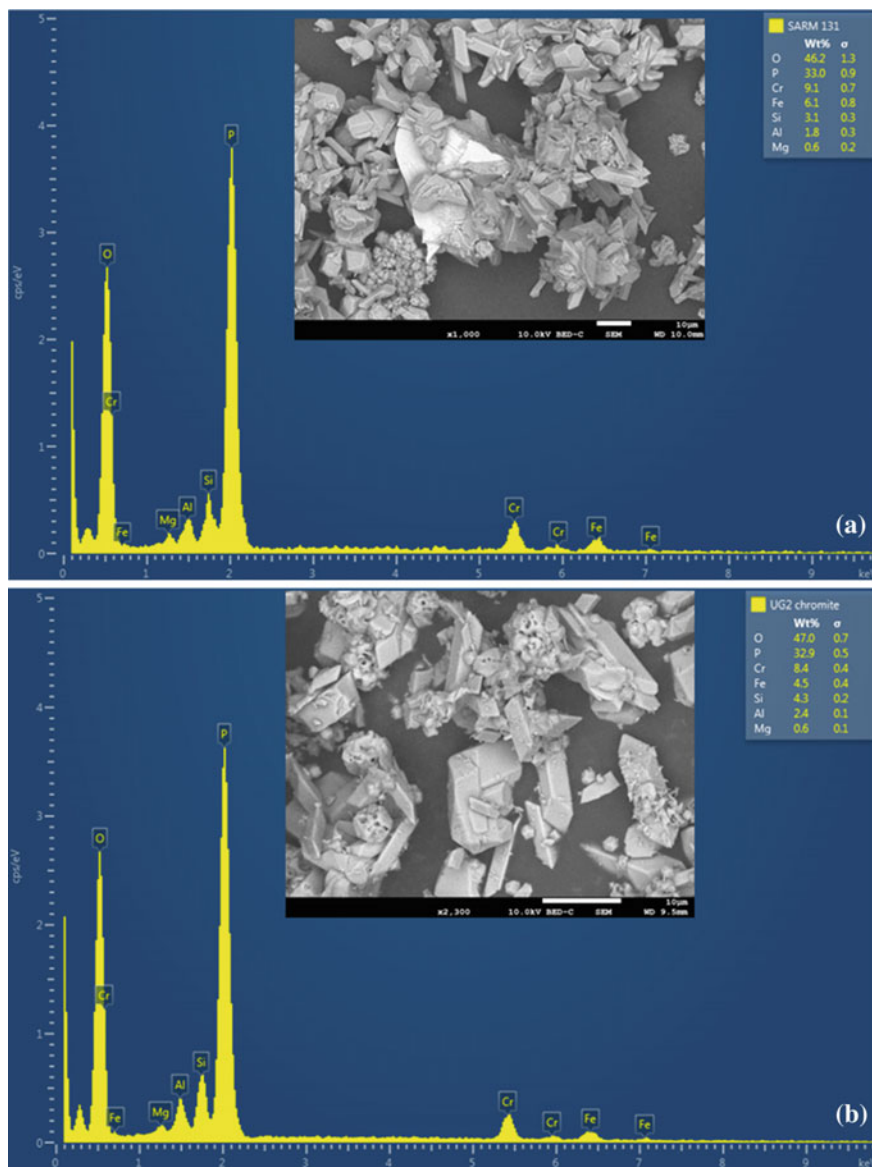
Fig. 19.3 SEM-EDX analysis of the Cr(PO$_3$)$_3$ products isolated from **a** SARM 131, **b** UG2 chromite ore, **c** Merensky Reef ore, **d** Cr(NO$_3$)$_3$·9H$_2$O, **e** CrCl$_3$·6H$_2$O, and **f** CrO$_3$
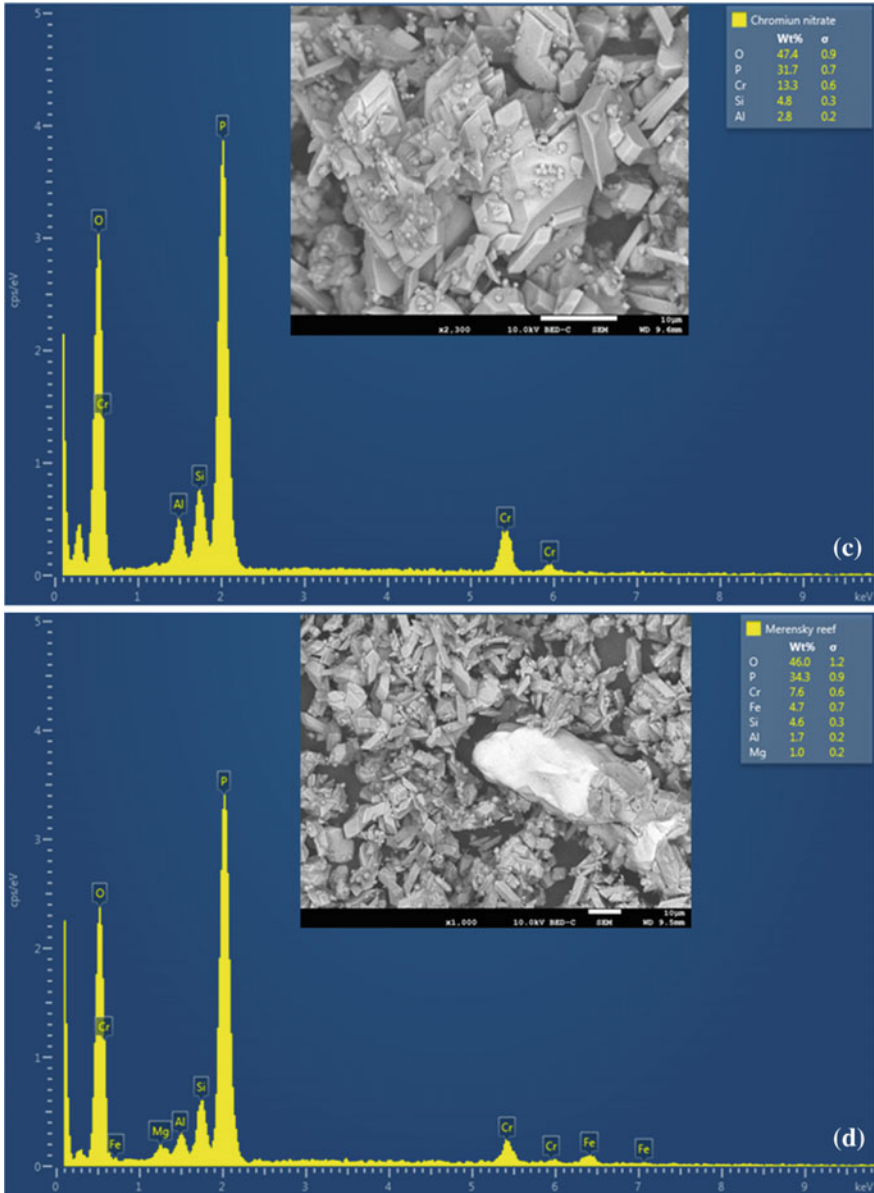
Fig. 19.3 (continued)
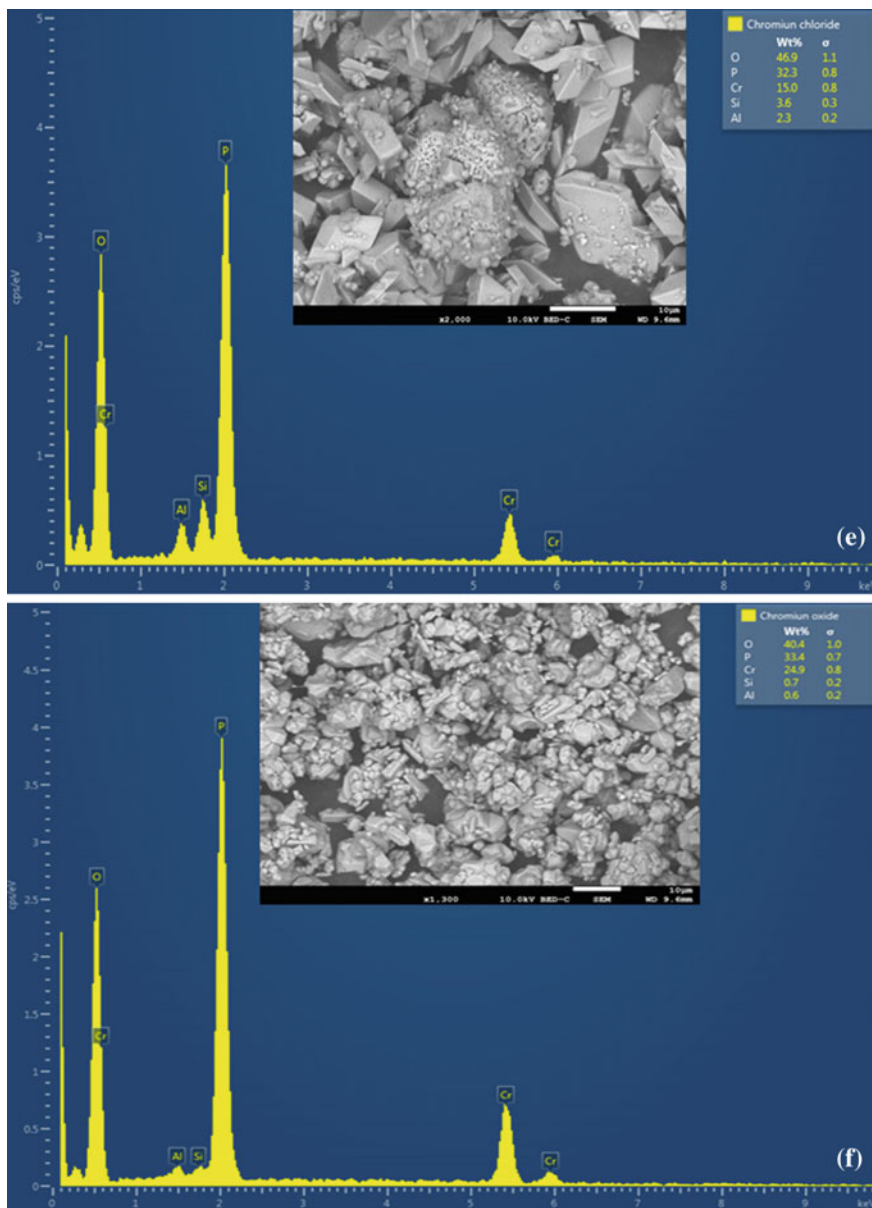
Fig. 19.3 (continued)

spectroscopy of all the products (see Fig. 19.1 and Table 19.2) showed common stretching frequencies in the region of 1250, 964, 767 and 713 cm^{-1} [16]. Stretching frequencies corresponding to the antisymmetric vibration of P–O groups were clearly visible in the region of 1250–1256 and 962–979 cm^{-1} whilst the symmetric stretching frequencies appeared in the region of 718–719 cm^{-1}. The broad band bearing two minor peaks appearing in the region of 1089–1137 and 1015–1043 cm^{-1} were due to the simultaneous existence of PO_2 and PO_3 groups [17]. The presence of these characteristic peaks confirmed the existence of chromium metaphosphate in all the isolated chromium products.

19.3.2 Raman Analysis

Characterization of the chromium metaphosphate products using Raman spectroscopy was designed to determine the presence of impurities and also to confirm the IR results. Raman images of the isolated chromium metaphosphate products isolated from the SARM 131, UG2 chromite, Merensky Reef, $Cr(NO_3)_3 \cdot 9H_2O$, $CrCl_3 \cdot 6H_2O$ and CrO_3 revealed granular particles that were less crystalline for the chloride, needle-like crystals for the nitrate and amorphous for the oxide. The white light images of SARM 131, UG2 chromite and Merensky Reef revealed angular crystalline particles that were cuboid in shape that varied in colour from white-grey to black with fewer dark inclusions. The $Cr(PO_3)_3$ particles from the chloride, nitrate and oxide were covered by an amorphous or crystalline appearing vivid green with no traces of dark inclusions. Some of the particles in all the samples were laser sensitive and fluoresced, but these were limited. All the $Cr(PO_3)_3$ samples displayed similar spectra, although quite a few of the spectra fluoresced. The obtained spectra for all the $Cr(PO_3)_3$ displayed prominent peaks in the region of 713 cm^{-1} followed by strong peaks at 1212, 1305, 216, 264 and 393 cm^{-1} and medium to medium-strong intensity bands at 1038, 1112, 602, 552, 527, 154 and 145 cm^{-1}. Some impurities displayed different spectra that resulted in the 1226 cm^{-1} band to be the weaker one and 677 cm^{-1} the strongest.

19.3.3 SEM-EDX Determination of Impurities in the Chromium Metaphosphate Products

Determination of impurities in the chromium metaphosphate products isolated from SARM 131, UG2 and Merensky Reef was further performed using SEM-EDX analysis to determine the morphological structure of the products. The results of the isolated chromium precipitates (see Fig. 19.3) isolated from the geological samples showed micro-crystalline, cubic crystal-like structure which suggested the possibility of a pure compound which were all similar to the products isolated from the chromium salts. Chromium metaphosphate product isolated from the oxide was visually dif-

Table 19.2 Infrared stretching frequencies of $Cr(PO_3)_3$ products isolated from $CrCl_3 \cdot 6H_2O$, $Cr(NO_3)_3 \cdot 9H_2O$, CrO_3, SARM 131, Merensky Reef ore and UG2 chromite ore

Assigned group	Stretching frequencies (V_{cm}^{-1})					
	Chloride	Nitrate	Oxide	SARM 131	Merensky Reef	UG2 chromite
$V_{as}(P–O)$	1254	1251	1254	1254	1250	1256
$V_s(P–O)PO_2$	1127	1133	1089	1134	1137	1134
$V(P–O)PO_3$	1040	1041	1043	1042	1034	1015
$V_{as}(P–O)$	962	962	963	973	971	979
$V_s(P–O)P–O–P$	768	767	768	775	769	768
$V_s(P–O)$	718	719	718	719	719	719

as—antisymmetric

s—symmetric

ferent with larger and more irregular, almost amorphous-like particles. The EDX spectra (Fig. 19.3) showed the presence of Cr, P and O as major elements with emission intensities increasing from Cr < O < P. The qualitative results reported revealed smaller amounts of Fe, Si, Al and Mg as impurities in the chromium products from the geological samples and Si and Al from the salts and oxide. The common difference between these two products was the presence of Fe and Mg in the geological samples (Table 19.3).

The presence of Fe and Mg elements in the final product was largely postulated to be the result of the undigested starting material (chromite, $(Fe, Mg, Al)Cr_2O_4$) or co-precipitation of these metals as phosphates. The elemental composition of P (32.2%) and O (45.8%) in the chromium metaphosphate were consistent in both products except for Cr which kept fluctuating between 7 and 25%. The fluctuations were due to the signal interference between the Cr $(K\alpha)$ and the O $(L\alpha)$ emissions (Fig. 19.4) which are some of the reasons that limit the accuracy of elemental analysis using EDX technique [18].

A blank analysis test was conducted using ammonium phosphate flux to determine the possible source of interference. Results obtained from this analysis showed the presence of Si (0.7–4.8%) and Al (0.6–2.8%) in the resultant melt. Visual analysis of the ceramic crucible under the microscope revealed parts of the crucible that were slightly corroded by the ammonium phosphate flux. The presence of Si and Al in all the isolated chromium metaphosphates compounds was clear evidence of the consistent attack of the ceramic crucible. The source of the remaining impurities (Fe and Mg) was determined by examining the dark particles which were previously identified using Raman spectroscopy.

Separation of the impurities using solubility differences was performed using concentrated mineral acids (HCl, HNO_3, H_2SO_4 and H_3PO_4) and organic solvents. The results yielded no positive results except for *aqua regia* which yielded a cloudy green suspension with dark particles (impurities) settling at the bottom. The heterogeneous mixture enabled the removal of the dark residue through decanting. The isolated dark

Table 19.3 EDX analysis results of the $Cr(PO_3)_3$ products isolated from the SARM 131, UG2 chromite, Merensky Reef, $Cr(NO_3)_3 \cdot 9H_2O$, $CrCl_3 \cdot 6H_2O$ and CrO_3 together with the EDX elemental composition of the dark impurities and the purified $Cr(PO_3)_3$

$Cr(PO_3)_3$ (%)	Cr	P	O	*Fe*	*Si*	*Al*	*Mg*
SARM 131	9.1	33.0	46.2	*6.1*	*3.1*	*1.8*	*0.6*
UG2 chromite	8.4	32.9	47.0	*4.5*	*4.3*	*2.4*	*0.6*
Merensky Reef	7.6	34.0	46.0	*4.7*	*4.6*	*1.7*	*1.0*
$Cr(NO_3)_3 \cdot 9H_2O$	13.3	31.7	47.4	–	*4.8*	*2.8*	–
$CrCl_3 \cdot 6H_2O$	15.0	32.3	46.9	–	*3.6*	*2.3*	–
CrO_3	24.9	33.4	40.4	–	*0.7*	*0.6*	–
Dark impurities	11.2	26.1	55.4	*3.8*	*1.2*	*2.0*	*0.5*
Purified $Cr(PO_3)_3$	27.3	34.3	37.4	–	–	–	–

Italics—Impurities

Fig. 19.4 Interference on the chromium signal with oxygen
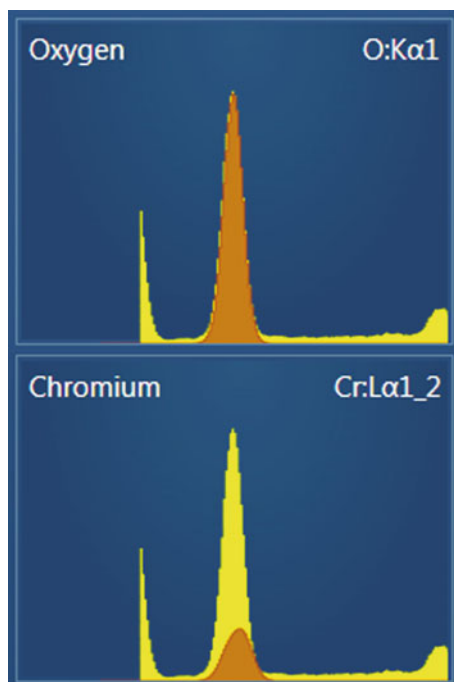
particles (impurities) were analysed using SEM-EDX analysis (see Table 19.3) and the results showed the presence of Fe (3.8 wt%), Si (1.2 wt%), Al (2.0 wt%) and Mg (0.5 wt%). Clear green chromium metaphosphate powder was obtained after the suspended green solution was left to stand overnight. SEM-EDX analysis results of the purified chromium metaphosphate product revealed the presence of Cr (27.3 wt%), P (34.3 wt%) and O (37.4 wt%) without traces of impurities.

19.4 Conclusion

Chromium metaphosphate products isolated from the geological samples (SARM 131, UG2 chromite and Merensky Reef) were found to contain particles of undigested starting material. Visual analysis using microscopy together with Raman analysis revealed the presence of dark inclusions in the chromium metaphosphates isolated from the geological samples. No traces of dark particles (undigested particles) were detected from the chromium metaphosphate isolated from the salts and oxide. The dark impurities were successfully separated from the chromium metaphosphate product using *aqua regia*. SEM-EDX analysis of the isolated dark particles (impurities) showed the presence of Fe, Si, Al and Mg. The purified $Cr(PO_3)_3$ contained Cr (27.3 wt%), P (34.3 wt%) and O (37.4 wt%) with no traces of impurities.

References

1. Schurmann LW, Grabe PJ, Steenkamp CJ (1998) Chromium, the mineral resources of South Africa. In: Council for Geoscience Handbook, 6th edn, vol 16, pp 90–105
2. Cramer LA, Basson J, Nelson LR (2004) The impact of platinum production from UG2 ore on ferrochrome production in South Africa. In: Proceedings of the tenth international ferroalloys congress, ISBN: 0-9584663-5-1
3. https://www.thebalance.com/metal-profile-chromium-2340130. Accessed 25 Jan 2018
4. Murthy YR, Tripathy SK, Kuma CR (2011) Chrome ore beneficiation challenges & opportunities—a review. Miner Eng 24:375–380
5. Barnes AR, Newall AF (2006) Spinel removal from PGM smelting furnaces. South Afr Pyrometallurgy:77–88
6. Chiweshe TT, Purcell W, Venter JA (2016) Evaluation of PGE liberation and chromium isolation in a solid UG2 chromitite concentrate at moderate temperatures using ICP-OES. JOM 68:1691–1700
7. Murashova EV, Chudinova NN, Ilyukhin AB (2007) Specific features of the crystal structure of erbium polyphosphate of the structural type C. Crystallogr Rep 52:230–234
8. IIiva D, Kovacheva D, Petkov C, Bogachev G (2001) Vibrational spectra of $R(PO_3)_3$ metaphosphates (R = Ga, In, Y, Sm, Gd, Dy). J Raman Spectrosc 32:893–899
9. Maddrell R (1846) On the metaphosphates. Mem Chem Soc 3:273
10. Bagieu-Beucher M, Guitel JC (1977) Structure cristalline de l'hexamétaphosphate de chrome: $Cr_2P_6O_{18}$. Acta Crystallogr Sect B 33:2529–2533
11. Gruss M, Glaum R (1996) Refinement of the superstructure of C-type chromium(III) tris(metaphosphate), $Cr(PO_3)_3$. Acta Cystallogr Sect C 52:2647–2650
12. Vesely D, Jaskova V (2009) Efficiency of anticorrosive pigments based on metal phosphates. Transfer inovácií 15:151–158
13. Lezama L, Rojo JM, Mesa JL, Rojo T, Olazcuaga R (1995) Synthesis and magnetic and electrical properties of the molybdenum and tungsten pyrophosphates MP_2O_7 (M = Mo, W). J Solid State Chem 115:146–151
14. Chiweshe TT (2014) Quantification of iridium and other platinum group metals in the presence of naturally occurring contaminants in geological ore. Doctoral thesis, University of the Free State, Bloemfontein, South Africa
15. Chiweshe TT, Purcell W (2017) Chromium isolation from different mineral ores. In: Conference Proceeding of EMC, pp 1–15
16. Stuart B (2004) Infrared spectroscopy: fundamentals and applications. Wiley, Hoboken, p 84
17. Rojo JM, Mesa JL, Lezama L, Rojo T (1997) Spectroscopic and magnetic properties of three $M(PO_3)_3$ (M = Cr and Mo) metaphosphates. J Mater Chem 7:2243–2248
18. Wassilkowska A, Czaplicka-Kotas A, Zielina M, Bielski A (2014) An analysis of the elemental composition of micro-samples using EDS technique. Tech Trans Chem 1:133–148

Chapter 20
Preparation and Characterization of Ag–TiO$_2$ Modified Polyethersulfone (PES) Membranes for Potential Applications in Water Treatment

Kate Kotlhao, Vusumzi E. Pakade, Fanyana M. Mtunzi, Richard M. Moutloali and Michael J. Klink

Abstract Silver–titanium dioxide/polyamide thin film composite (Ag–TiO$_2$/PA-TFC) membrane was fabricated by interfacial polymerization (IP) using polyethersulfone (PES) as a support material. The Ag–TiO$_2$ nanocomposites (NCs) were synthesized using precipitation and in situ chemical reduction method. Particles were characterized using ultraviolet visible spectroscopy (UV-Vis), Fourier transmission infrared (FTIR), X-ray diffractometer (XRD), energy dispersive X-ray (EDX) and scanning electron microscopy (SEM) and investigated for antimicrobial activity. The Ag–TiO$_2$/PA-TFC membrane was characterized with FTIR for the amide I functional group and contact angle for surface hydrophilicity. The Ag–TiO$_2$/PA-TFC membrane was further investigated for pure water flux and permeability, rejection, flux recovery and fouling resistance using 2,4-dichlorophenol (2,4-DCP) as the organic foulant. Modification of the polyamide thin film composite (PA-TFC) surface layer with Ag–TiO$_2$ NCs improved membrane hydrophilicity, permeation and fouling resistance properties. Pure water flux increased from a low of 6.60 Lm^{-2}h^{-1} for the neat membrane to a high of 9.77 Lm^{-2}h^{-1} for the composite membrane. A high flux recovery of 94.4% was achieved with the composite membrane. Total fouling was reduced by more than 27% from the neat PA-TFC to Ag–TiO$_2$/PA-TFC membrane.

K. Kotlhao · V. E. Pakade · F. M. Mtunzi · M. J. Klink (✉)
Faculty of Applied and Computer Sciences, Department of Chemistry/Biotechnology, Vaal University of Technology, Private Bag X021, Vanderbijlpark 1900, South Africa
e-mail: michaelk1@vut.ac.za

K. Kotlhao
e-mail: katekotlhao@gmail.com

V. E. Pakade
e-mail: vusumzip@vut.ac.za

F. M. Mtunzi
e-mail: Fanyana@vut.ac.za

R. M. Moutloali
Faculty of Science, Department of Applied Chemistry, University of Johannesburg, P.O. Box 17011, Doornfontein, Johannesburg 2028, South Africa
e-mail: rmoutloali@uj.ac.za

20.1   Introduction

Chlorophenols are among the pollutants that are increasingly reaching water sources such as rivers and dams [1]. They have been listed as priority pollutants because of the detrimental effects they pose to water quality, aquatic life, animals and humans [2]. Sources of chlorophenols in water include various wastes from paper and pulp industries, pesticides from agricultural lands, municipal water and mining industries [3].

Membrane technology leads the water treatment industry owing to the unique transport selectivity and separation principle [4]. However, membranes have a problem of fouling which limits their wider application. The resultant drawbacks in fouling are increased cost, breakdowns, frequent cleaning, membrane degradation and shorter life span [5]. One way of mitigating membrane fouling is by incorporation of nanomaterials (e.g. ZnO, TiO$_2$, Ag, etc.) onto the membrane surface [6]. Nanoparticles (NPs) possess several advantages such as antibacterial activity [7], photocatalytic [8] and hydrophilic properties. In a study by Safarpour et al. [9], the zeolite modified thin film composite (TFC) membranes showed enhanced membrane permeability (high flux) and high solute rejection. Zeolite membranes are however, limited in application because they are selective to charged molecules [10]. Carbon nanotubes are also nanomaterials usually used in membranes. They have high specific surface area, high mechanical strength, excellent water transport properties and chemical inertness [11]. However, the water purification mechanism of adsorption and desorption is generally not ideal for removal of low concentration foulants due to high losses [12].

Incorporation of Ag, ZnO and TiO$_2$ nanomaterials into the membrane surface layer results in better performance, in terms of permeability, antifouling properties, solute rejection and membrane lifetime [13]. Silver NPs are known to possess high antibacterial properties even at minimum concentrations of <0.001 mg/L [14].

Due to the mentioned detrimental effects of chlorophenols, there is need to come up with methods that specifically target pollutants of low molecular weight. Although conventional membranes such as nano-filtration (NF) and reverse osmosis (RO) are capable of rejecting 2,4-dichlorophenol (2,4-DCP), the prevalent drawback is fouling (organic and biofouling) which leads to reduced permeability and energy costs due to high pressure requirements. To overcome the challenges, the current study reports the synthesis of Ag–TiO$_2$ NCs using a combination of precipitation and an in situ chemical reduction method. The Ag–TiO$_2$ NCs were embedded into the PA-TFC membrane surface layer through interfacial polymerization using PES as a support material. The purpose of PES was to enhance flux because of its porous structure while the NCs particles were to enhance hydrophilicity and permeation, with the silver component reducing biofouling. The constricted pore size of the thin film layer

was for rejection of 2,4-DCP. The synthesized NCs particles were characterized using UV-Vis, FTIR, XRD, SEM and EDX. Disc diffusion and MIC tests were performed to investigate antimicrobial activity against *E. coli*. The fabricated membranes were characterized with ATR-FTIR and contact angle and their performance investigated using flux and permeability, percentage rejection of 2,4-DCP, flux recoveries and antifouling propensity. To the best of our knowledge, rejection of 2,4-DCP using the protocol described in this study has not been documented.

20.2   Experimental

20.2.1   Materials and Equipment

The chemicals used in the experiments were of analytical reagent grade and used without any further purification. Commercial polyethersulfone, 5 kDa was supplied by Microdyn Nadir. Sodium dodecyl sulphate (98.5%), piperazine (99%), trimesoylchloride (98%), anhydrous hexane (95%), polyvinylpyrrolidone (PVP Mw = 10,000 g/mol), titanium tetra-butoxide (97%), Ti(OC$_4$H$_9$)$_4$, acetic acid (CH$_3$COOH, 32%), silver nitrate (99%), sodium borohydride (NaBH$_4$, 99%) and sodium hydroxide (NaOH, 97%) were obtained from Sigma–Aldrich.

20.2.2   Synthesis of Silver–Titanium Oxide (Ag–TiO$_2$) NCs

The Ag–TiO$_2$ NCs particles were synthesized using precipitation and an in situ chemical reduction method [15]. A 50 ml ethanol solution with 7.7 ml titanium tetrabutoxide (TBT) was placed in a beaker and 10 ml acetic acid (AcOH) added slowly, under constant stirring at 4000 rpm. A 10 ml ethanol solution of silver nitrate (0.010 g), equivalent of 3.0 wt% to Ti(OC$_4$H$_9$)$_4$ was added into the reaction mixture and 10 min later 0.030 g of NaBH$_4$ (aq) in 10 ml ethanol was added to reduce silver ions to silver atoms. Immediately, 0.9 g of polyvinylpyrrolidone (PVP) dissolved in 10 ml of ethanol was added to prevent agglomeration. The mixture was stirred for a further 30 min after addition of PVP and it was allowed to maturate for 12 h. The precipitate was centrifuged at 2000 rpm for 10 min, washed with deionized water and ethanol, and then dried in an oven at 80 °C. The prepared powder was calcined at 500 °C for 2 h [16].

Table 20.1 Proportions of quantities of the organic phase, aqueous phase and the nanocomposites in the preparation of PA-TFC and Ag–TiO$_2$/PA-TFC membranes

PA-TFC/Ag–TiO$_2$ (wt%)	Organic phase		Aqueous phase		
	TMC (wt%)	Hexane (wt%)	Piperazine (wt%)	Water (wt%)	Nano-composites (wt%)
PA-TFC 0.0	0.4	99.6	2	98	0.0
PA-TFC 0.5	0.4	99.6	2	98	0.5
PA-TFC 1.0	0.4	99.6	2	98	1.0
PA-TFC 1.5	0.4	99.6	2	98	1.5
PA-TFC 2.0	0.4	99.6	2	98	2.0

20.2.3 Antimicrobial Activity

Disc diffusion and minimum inhibitory concentration (MIC) procedures were the same as in our previous paper [14].

20.2.4 Fabrication of PA-TFC Membranes

The procedure for the fabrication of PA-TFC membranes was adapted from Mbuli et al. [17]. For pre-treatment of the membranes, the ultra-filtration (UF) PES support membranes were soaked overnight in an aqueous solution of sodium dodecyl sulphate (0.5 wt%) before washing with deionized water for 1 h. Aqueous solutions of piperazine and varied amounts of NCs (Ag–TiO$_2$), and the organic phase of trimesoyl chloride (TMC) in hexane were prepared according to the quantities shown in Table 20.1. The mixtures were stirred in closed beakers for 1 h and the pH was adjusted to 8.0 using ammonium chloride.

The PES membrane support was adhered to the glass plate using a thin double sided tape. The aqueous solution was poured over the PES membrane and allowed to soak for 5 min. Excess solution was removed from the membrane using a rubber roller and immediately the organic phase was gently poured, covering the PES membrane for 60 s. After draining the excess organic phase, the PA-TFC was cured in the oven at 65 °C for 15 min to ensure complete polymerization. The fabricated membranes were washed three times with deionized water and stored wet and cold [18].

20.2.5 Characterization

The optical properties of the Ag–TiO$_2$ NCs suspensions were characterized using the Perkin Elmer UV-Vis, T80 double beam spectrophotometer. The absorption of

composites was carried out in the wavelength range from 200 to 900 nm. The FT-IR (Perkin Elmer, Spectrum 400) was used in the characterization of the Ag–TiO₂ NCs. Analysis was carried out from 40 to 4000 cm^{-1} wavenumbers. For analysis of the PA-TFC and Ag–TiO₂/PA-TFC membranes, attenuated total reflectance Fourier transform infrared (ATR–FTIR) spectroscopy (PerkinElmer Spectrum 100 spectrometer, USA) was used to study the changes on the chemical structure of the surface layers at wavenumbers ranging from 650 to 4000 cm^{-1}.

The XRD patterns for Ag–TiO₂ NCs particles were investigated using Shimadzu-XRD 700 X-Ray Diffractometer, Cu Kα radiation ($\lambda = 1.154056$ Å). Analysis was carried out in the 2θ range from 10° to 90°.

The morphology of the samples was determined using scanning electron microscopy (SEM), which also had an EDX functionality for elemental analysis and these were performed at Botswana Institute for Technology Research and Innovation laboratory (BITRI).

20.2.6 Hydrophilicity

Contact angle measures the hydrophobicity and hydrophilicity of the membrane. Contact angle measurements for pure PES, PA-TFC and Ag–TiO₂ (0.5–2.0 wt%)/PA-TFC were determined using DSA 10 Mk2 (Krüss, Germany) equipment. Details of the procedure are as stated in our previous paper [19].

20.2.7 Membrane Performance

Performance of the membrane was investigated using pure water flux and permeability (membrane hydraulic resistance), rejection of 2,4-DCP, and flux recovery using the stirred dead-end cell (Sterlitech, HP4750). Details of the stirred dead-end cell are as stated in Dipheko et al. [19]. Before the filtration experiments were conducted, the neat PES, PA-TFC and Ag–TiO₂/PA-TFC membranes, cut to the correct diameter, were compacted for 30 min at 1100 kPa to achieve stabilization. Pure water flux was calculated using Eq. (20.1).

$$J_{wo} = \frac{m}{A \cdot t} \tag{20.1}$$

where J_{wo} is the pure water flux (Lm^{-2}h^{-1}), m is the volume (L), A is the effective membrane area (m^2) and t is the permeation time (h). The average flux was obtained from three replicates.

For flux test, pure water was passed through the neat PA-TFC and prepared Ag–TiO₂/PA-TFC membranes. Pressure was increased from 200 to 800 kPa and the corresponding volume of permeate was recorded every 15 min, the average of

which was used to calculate flux using Eq. (20.1). The slope of the regression line plot of flux against transmembrane pressure is the measure of permeability [20].

Rejection for 2,4-DCP using neat PA-TFC and Ag–TiO$_2$/PA-TFC membranes was assessed. The concentration of the feed and permeate were analyzed using an ultraviolet visible spectrophotometer UV-2450 (Shimadzu). Percentage rejection of 2,4-DCP was calculated using Eq. (20.2) [21]:

$$R(\%) = \frac{C_f - C_p}{C_f} \times 100\%$$ (20.2)

where C_p is the concentration of 2,4-DCP in the permeate solution (mg/L) and C_f is the concentration of 2,4-DCP in the feed solution (mg/L). The calibration curve was prepared from 1 to 5 ppm. The standard solutions were prepared using 1:1 v/v of 2,4-DCP and 5.0 M sodium carbonate solution respectively [22].

20.2.8 Antifouling Properties

The antifouling tests for the neat PA-TFC and Ag–TiO$_2$/PA-TFC membranes were investigated using water flux recovery after fouling the membranes with 2,4-DCP solution. The membranes were subjected to pure water permeation for 60 min to obtain initial water flux (J_{wo}). The feed solution was then changed to 2,4-DCP and similarly filtered through the membranes to obtain (J_{wt}). The filtered membranes were cleaned with deionized water for 10 min to remove loosely adsorbed 2,4-DCP molecules. The membranes were re-assessed to obtain flux of cleaned membranes (J_{wc}) [21]. Water recovery ratios (FRR) were determined using Eq. (20.3):

$$FRR\ (\%) = \frac{J_{wc}}{J_{wo}}$$ (20.3)

where J_{wo}, J_{wt} and J_{wc} are the water fluxes of pure water, 2,4-DCP solution and cleaned membranes respectively.

Total fouling ratio (Rt), reversible fouling ratio (Rr) and irreversible fouling ratio (Rir) were calculated using Eqs. (20.4), (20.5) and (20.6) [23].

$$Rr(\%) = \left[\frac{J_{wc} - J_{wt}}{J_{wo}} \right] \times 100$$ (20.4)

$$Rir(\%) = \left[\frac{J_{wo} - J_{wc}}{J_{wo}} \right] \times 100$$ (20.5)

$$Rt = Rr + Rir$$ (20.6)

A lower Rt value means a better antifouling property, while a higher FRR value indicates a higher cleaning efficiency.

20.3   Results and Discussion

20.3.1   FT-IR

The FTIR spectra of Ag, TiO$_2$ and Ag–TiO$_2$ are shown in Fig. 20.1. In the Ag spectrum the peak at 3019 cm^{-1} was assigned to be the CH– stretch. The weak and broad peak appearing at 3186 cm^{-1} due to –OH stretching vibrations resulted from the adsorbed water on the surface of the nanoparticles. The more intense peak appearing at 1736 cm^{-1} was assigned to be the –C=O from PVP capping agent. Other peaks from PVP were the C–N stretching vibrations at 1220 cm^{-1}, the doublet peaks at 1449 cm^{-1} (weak) and 1365 cm^{-1} (strong) due to the attached CH$_2$ in the pyrrole ring and the ring C–C– appearing at 797 cm^{-1} [24]. The significant band at 444 cm^{-1} was assigned as the characteristic peak of the stretching mode of Ag [25]. From the FTIR spectrum of TiO$_2$ NPs, the results showed that the different peaks assigned due to PVP on Ag NPs spectrum were not observed. This was attributed to complete removal of PVP [24]. Similar results were obtained by Shajudheen et al. [26]. Their FTIR spectrum for PVP capped TiO$_2$ showed no peaks from PVP. The results indicate that Ag NPs bind more to PVP than TiO$_2$ because upon addition of silver to TiO$_2$, peaks characteristic to PVP were observed again in the Ag–TiO$_2$ spectrum.
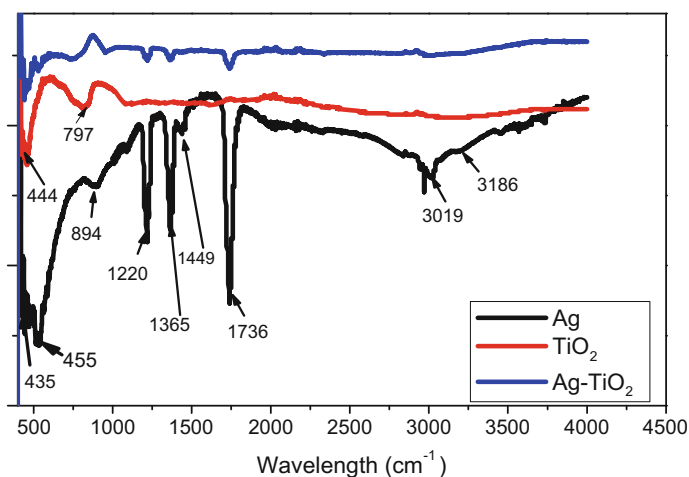
Fig. 20.1   FTIR spectra for Ag, TiO$_2$ NPs and Ag–TiO$_2$ NCs

20.3.2 UV-Vis

The UV-Vis optical absorption spectra for Ag, TiO_2 and Ag–TiO_2 are shown in Fig. 20.2. Tauc plots were used to establish the band gap energies (Eg). This is a plot of $(\alpha h\nu)^2$ versus photon energy in $h\nu$. The optical band gap energy Eg was determined by extrapolating the linear portion to $(\alpha h\nu)^2 = 0$ as in Eq. (20.7):

$$\alpha = K \frac{(h\nu - Eg)^2}{h\nu} \qquad (20.7)$$

where K is constant, $h\nu$ is the photon energy and Eg is the band gap energy for indirect transitions and α, the absorption coefficient. UV-Vis spectrum for TiO_2 NPs showed an absorption edge in the UV region at 350 nm with a calculated band gap of 3.54 eV. Upon addition of 3.0 wt% of Ag to TiO_2 as shown in the spectrum for Ag–TiO_2, there was an observable shift to 363 nm, which was due to introduction of Ag NPs. The red shift resulted in reduction of the band gap from 3.54 to 3.41 eV for TiO_2 and Ag–TiO_2 respectively [27]. In a successful interaction between Ag and TiO_2, an energy level of silver is introduced that lies above the conduction band and below the valence band of TiO_2, resulting in reduced band gap [28]. The broad surface plasmon resonance (SPR) peak observed in the Ag spectrum at 400 nm confirmed the formation of Ag NPs [7]. Previous studies have attributed the SPR peak to be due to spherically shaped Ag NPs [7].
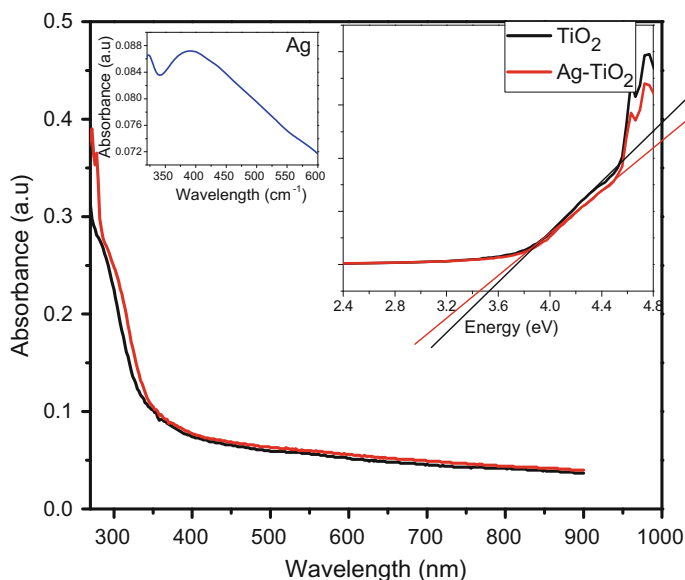
Fig. 20.2 UV-Vis spectra of TiO_2, Ag NPs and Ag–TiO_2 NCs

20.3.3 XRD

Figure 20.3a shows the XRD patterns for Ag, TiO$_2$ NPs and Ag–TiO$_2$ NCs. The diffraction peaks at (25.50°), (37.89°), (48.40°), (53.98°), (55.29°), (62.65°), (68.47°), (70.57°), and (75.34°) were indexed to (101), (004), (200), (105), (211), (204), (220), (220) and (215) crystalline planes respectively. This corresponded to the anatase phase of TiO$_2$ according to JCPDS Card No. (21-1272). The anatase phase was not affected by incorporation of Ag in the TiO$_2$ structure. All peaks for TiO$_2$ and Ag–TiO$_2$ were indexed and no peaks corresponding to silver oxide phase were observed indicating purity of the synthesized nanoparticles [29]. Figure 20.3b is an expansion of the (101) peak in the XRD pattern. A shift towards a smaller 2-theta value was observed in the Ag–TiO$_2$ nanocomposite. This suggests that some of the initial Ag$^+$ ions replaced the Ti^{4+} and subsequent atoms distributed on the surface of TiO$_2$ structure. It is further confirmed in the Ag–TiO$_2$ nanocomposite pattern because no peaks due to Ag were observed [30].
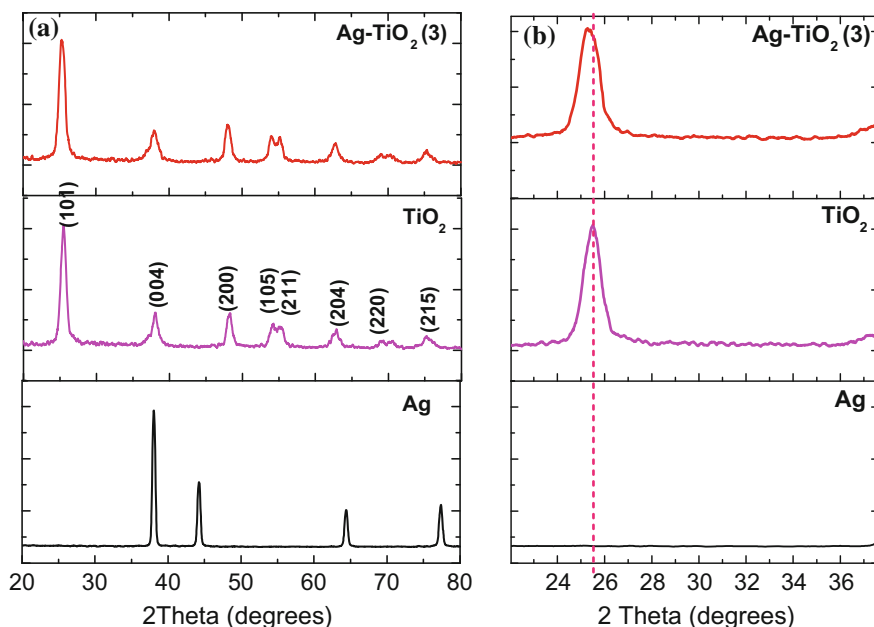
Fig. 20.3 **a** XRD patterns for Ag, TiO$_2$ NPs and Ag–TiO$_2$ (3 wt%) NCs and **b** an expansion of the XRD pattern at the (101) peak

20.3.4 SEM and EDX Analysis

The morphology of the nanoparticles and nanocomposites were investigated through SEM analysis. Figure 20.4a–f show SEM images and results of EDX analysis for Ag, TiO_2 NPs and Ag–TiO_2 (3 wt%) NCs respectively. The SEM image for Ag NPs showed mostly spherically-shaped particles (Fig. 20.4a). The TiO_2 micrograph (Fig. 20.4b) showed particles with non-uniform morphology with a few clusters of agglomerated particles. For Ag–TiO_2 (Fig. 20.4c), the SEM image revealed the presence of silver appearing as bright white irregular shaped tiny spots, most of the particles appearing spheroid or oblate spheroid [31].

Energy dispersive X-ray (EDX) analysis was performed to further establish the elemental presence and percentage weight of silver in the Ag–TiO_2 (3 wt%) NCs particles and formation of Ag, and TiO_2 nanoparticles. Figure 20.4d–f show the EDX spectra for Ag, TiO_2 and Ag–TiO_2 (3 wt%). In the EDX spectrum of Ag (Fig. 20.4d), the only element observed was Ag. For TiO_2, Ti and O elements were observed with no extra peaks of impurity (Fig. 20.4e). However, in Ag–TiO_2 (3 wt%) NCs particles, apart from Ag, Ti and O elements, there were some minor traces of vanadium observed (Fig. 20.4f). It was observed that V showed some overlap with Ti element and this could have had an effect on the percentage abundance of Ti. The presence of V was attributed to impurities from SEM instrument.

20.3.5 Antimicrobial Properties

Figure 20.5a shows the MIC results for TiO_2, Ag, and Ag–TiO_2 (1–5 wt%). The results indicate that TiO_2 alone could not inhibit the growth of *E. coli* bacteria. Upon incorporation of Ag to TiO_2, an increasing trend of inhibition against the bacteria was observed. At 3 and 5 wt% Ag to TiO_2 the minimum concentration for inhibition was 3.12 and 1.56 mg/L respectively. Growth inhibition of bacteria by nanoparticles is reported to be a result of a combination of factors such as size, morphology of nanoparticles and the characteristics of the organism being tested [32]. Figure 20.5b shows the results of disc diffusion with zones of inhibition at 0.0, 10.8 and 12.6 mm for TiO_2, Ag and Ag–TiO_2 respectively. The results are in agreement with MIC results.

20.3.6 Membrane Characterization

20.3.6.1 ATR-FTIR for Membranes

Figure 20.6 depicts the ATR-FTIR spectra of PES, PA-TFC and Ag–TiO_2/PA-TFC (0.5–2.0 wt%) membranes. The PES membrane consists of an aromatic ring and
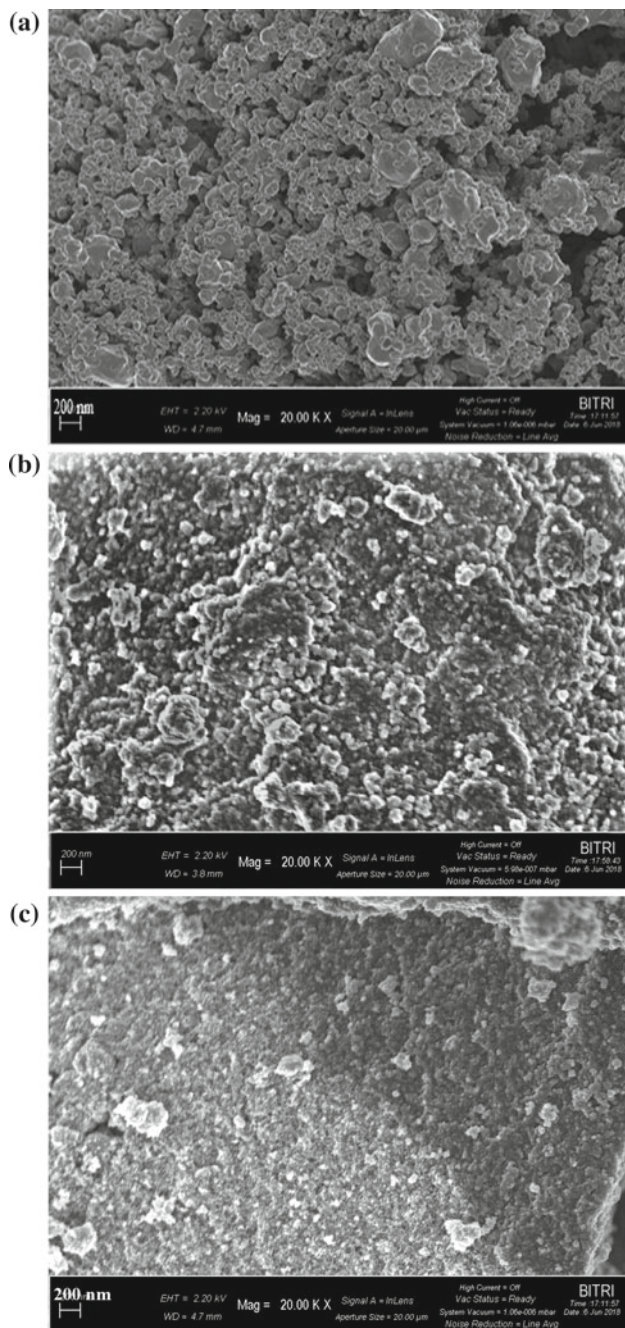
Fig. 20.4   SEM images and EDX spectra of Ag (**a**, **d**), TiO$_2$ (**b**, **e**) and Ag–TiO$_2$ (**c**, **f**) respectively
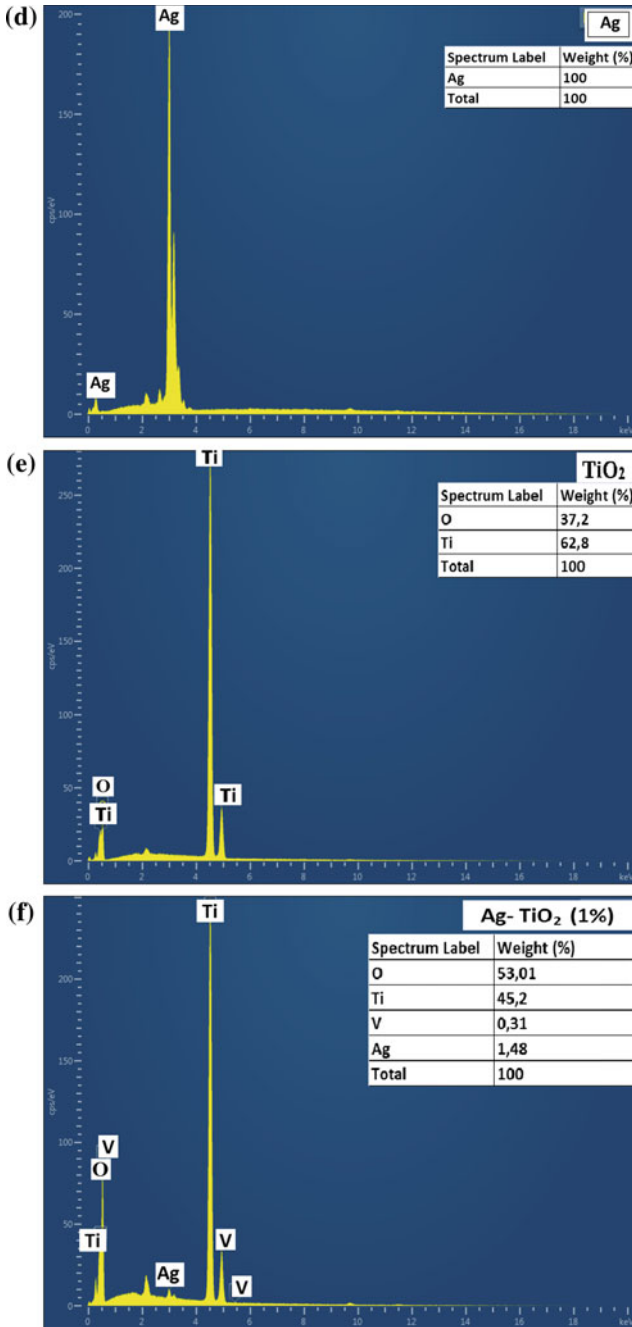
Fig. 20.4 (continued)
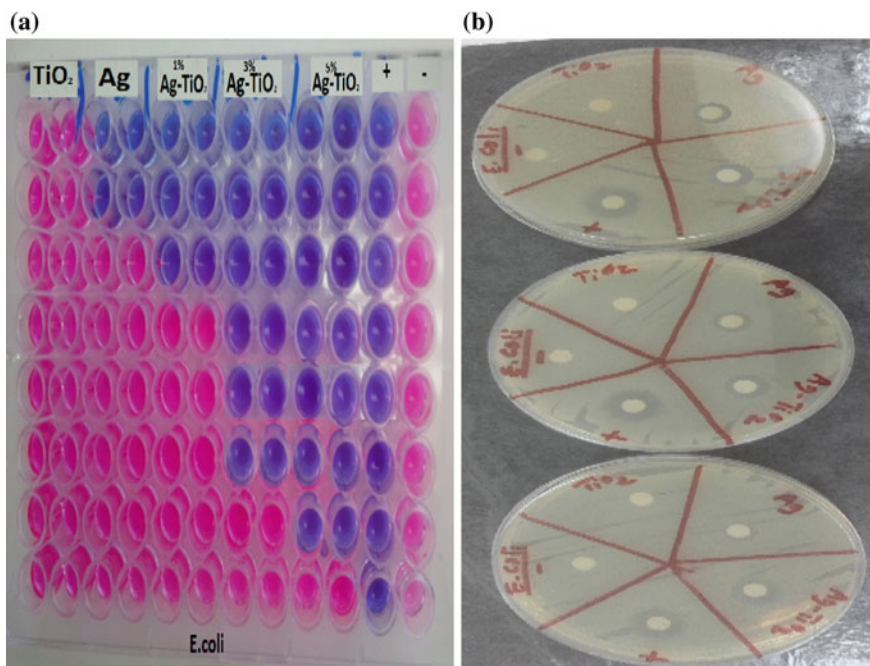
Fig. 20.5 **a** MIC results for Ag, TiO$_2$ and Ag–TiO$_2$ (1–5%) and **b** triplicate results of disc diffusion against *E. coli*
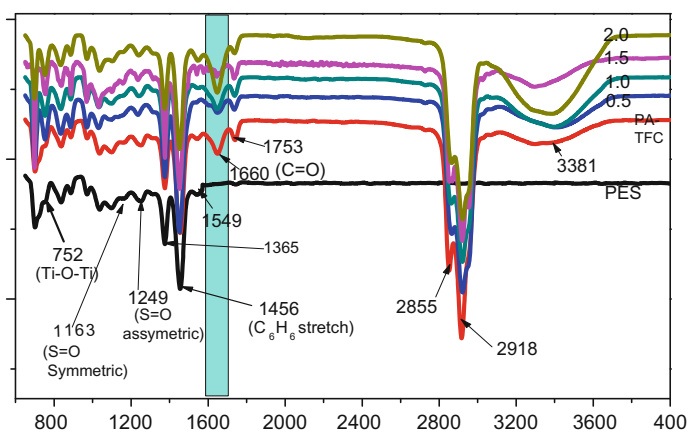
Fig. 20.6 The FTIR spectra of neat PES, PA-TFC and Ag–TiO$_2$/PA-TFC at different amounts of Ag–TiO$_2$: 0.0, 0.5, 1.0, 1.5 and 2.0 wt%

two sulfonyl groups. The asymmetric and symmetric S=O bands were observed at 1365 and 1163 cm^{-1} [33]. A band at 1660 cm^{-1} was due to the aromatic polyamide carbonyl carbon, C=O stretching (amide I). The band at 1753 cm^{-1} was assigned as the –C=O stretching from PVP as was observed in the FTIR spectra for NCs particles [34]. Strong bands that appeared at 2855 and 2918 cm^{-1} region on the PA-TFC and Ag–TiO$_2$/PA-TFC (0.5–2.0 wt%) membranes were due to the asymmetric and symmetric CH$_2$ stretching from piperazine aliphatic ring. The broad band at 3381 cm^{-1} was assigned as the –OH stretch [35]. The intensity of the –OH group on the membrane surface increased with increasing concentration of the Ag–TiO$_2$ NCs. Similar results were obtained by Li et al. [38] shown by the IR spectra of Ag–TiO$_2$/PDVF membrane. They also observed an increasing intensity of the –OH band with addition of Ag–TiO$_2$ on the PVDF membrane. They attributed it to increasing surface hydroxyl groups due to additional photocatalytic characteristic property of TiO$_2$ [36].

20.3.6.2 Membrane Hydrophilicity

The results in Fig. 20.7 show that as the amount of Ag–TiO$_2$ was increased on the PA-TFC membranes there was a decline in contact angle from 60.8° to 33.3° reaching an optimum at 1.5 wt% and an increase at 2.0 wt%. The decreasing trend in contact angle is due to increasing hydrophilicity of the membranes. Hydrophilic membranes have a contact angle between $0° < \theta < 90°$, while hydrophobic membranes have a contact angle of $90° < \theta < 180°$ [37]. Contact angles from a study by Li and coworkers, on incorporation of Ag–TiO$_2$ NCs into a PVDF membrane also revealed a remarkable increase in hydrophilicity with the angles reducing by 40°–60° [38].

Fig. 20.7 Water contact angles for PES, neat PA-TFC (0.0) and Ag–TiO$_2$/PA-TFC (0.5–2.0 wt%)
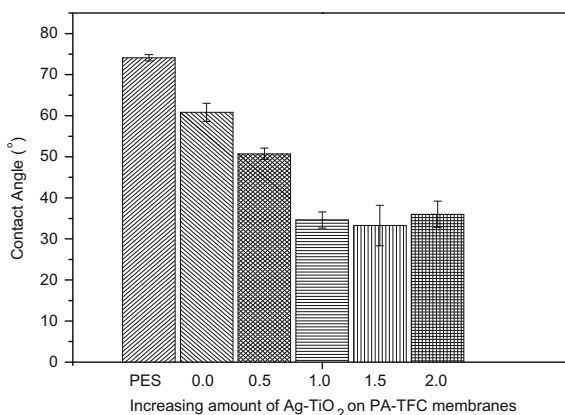
Table 20.2 Pure water hydraulic permeability for PES, PA-TFC and Ag–TiO₂/PA-TFC membranes

Membrane	Pure water hydraulic permeability $(Lm^{-2}h^{-1}/kPa)$
PES	0.100
PA-TFC	0.009
Ag–TiO₂/PA-TFC	0.021

20.3.7 Water Flux and Permeation

The results of membrane pure water permeation for PA-TFC and Ag–TiO₂/PA-TFC membranes are shown in Table 20.2. Pure water permeation increased from 0.009 to 0.021 $Lm^{-2}h^{-1}/kPa$ on PA-TFC and Ag–TiO₂/PA-TFC membranes respectively. This indicates enhanced water transportation across the modified membrane compared to the neat PA-TFC membrane.

20.3.8 Rejection of 2,4-DCP

Figure 20.8 shows the % rejection of 2,4-DCP using the PA-TFC and Ag–TiO₂/PA-TFC membranes and the insert is the calibration curve for 2,4-DCP. Rejection of 2,4-DCP from neat PA-TFC was 58%, which was comparable to the one obtained by Hidalgo et al. [39]. Upon modification with Ag–TiO₂, rejection of the 2,4-DCP increased to 84.8%. This was attributed to repulsive forces between the inherently negatively charged PA-TFC membrane and negatively charged molecule of 2,4-DCP
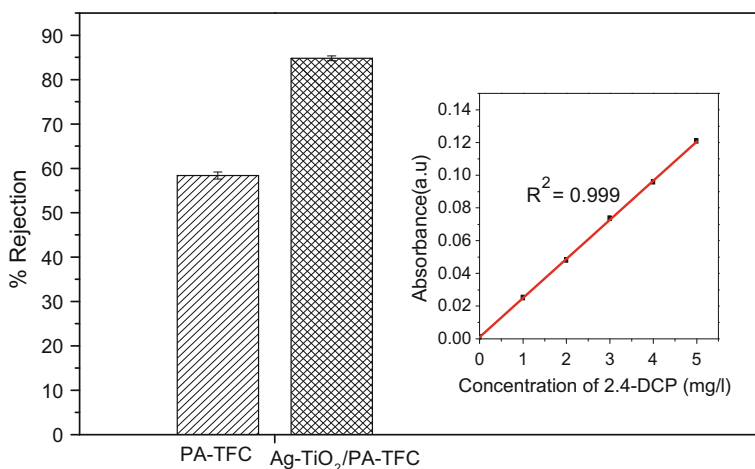
Fig. 20.8 % Rejection of 2,4-DCP using PA-TFC and Ag–TiO₂/PA-TFC membranes and the calibration curve of 2,4-DCP as obtained from UV-Vis spectroscopy

[40]. At pH above the pKa for 2,4-DCP (pKa 7.89), (which in this case was recorded as pH $= 8.44 \pm 0.035$), 2,4-DCP dissociates into the phenolate anion, hence the repulsive forces for rejection [41].

20.3.9 Evaluation of Antifouling Properties

Figure 20.9a presents the results of alternating flux cycles of pure water and 2,4-DCP against time. The results indicate that the Ag–TiO$_2$/PA-TFC membrane reached a relatively high pure water flux (J_{wo}) of 9.77 Lm^{-2}h^{-1} which was higher than that of the neat PA-TFC membrane at 6.60 Lm^{-2}h^{-1}. When pure water was replaced with 2,4-DCP, the flux (J_{wt}) was reduced for both membranes. Flux reduction in the PA-TFC membrane was more than in the Ag–TiO$_2$/PA-TFC membrane. Reduction in flux was attributed to adsorption of the molecules on the surface or within the membrane pore walls [42]. After the third filtration test of pure water obtained after cleaning the membranes to remove adsorbed 2,4-DCP molecules, the flux for Ag–TiO$_2$/PA-TFC membrane almost retained their initial flux (J_{wo}). The new pure water fluxes after cleaning (J_{wc}) was 9.43 Lm^{-2}h^{-1} for the Ag–TiO$_2$/PA-TFC membrane, which was higher than that of the neat PA-TFC membrane, 5.92 Lm^{-2}h^{-1}. This is an indication that the Ag–TiO$_2$/PA-TFC membrane showed improved antifouling properties owing to enhanced surface hydrophilicity [38].
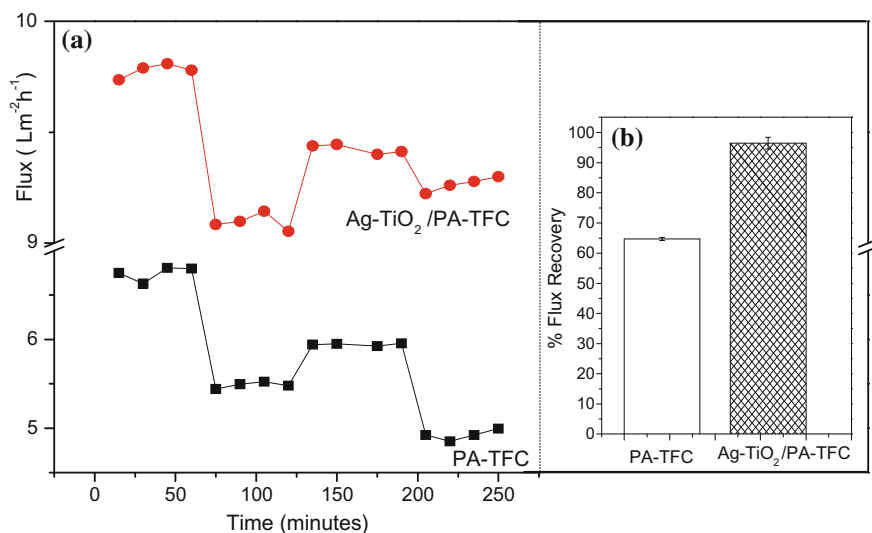
Fig. 20.9 **a** Alternating filtration experiments of pure water and 2,4-DCP solution during fouling tests using PA-TFC and Ag–TiO$_2$/PA-TFC membranes and **b** flux recovery obtained after cleaning the membranes

Flux recoveries (FRR) between 1st and 3rd cycles for the prepared membrane is presented in Fig. 20.9b. The results show that FRR (%) was improved from 64.7% (PA-TFC) to 94.4% (Ag–TiO$_2$/PA-TFC). This means that 2,4-DCP was loosely attached to the Ag–TiO$_2$/PA-TFC membrane due to improved hydrophilicity when compared to the neat PA-TFC membrane [43]. When surface hydrophilicity is high the membrane is capable of forming stable hydration layer through hydrogen bonding with water molecules to keep away the organic foulants from being adsorbed on the membrane surface [44].

It could further be deduced that modification of the PA-TFC with Ag–TiO$_2$ reduced total fouling of the membranes by 27% when compared with PA-TFC membrane. This indicated that the surfaces of the modified Ag–TiO$_2$/PA-TFC membrane were less prone to fouling [44]. The results further indicate that irreversible fouling was the major cause of fouling in the neat PA-TFC membrane due to adsorption of 2,4-DCP within the pores of the membrane and which was not easily removed by backwashing [21].

20.4   Conclusion

The PA-TFC membranes were prepared using interfacial polymerization. The polyamide C=O peak was observed at 1660 cm^{-1} from ATR-FTIR spectrum. The Ag–TiO$_2$ NCs were successfully blended into the PA membrane and resulted in enhanced hydrophilicity with contact angles reducing from 60.8° to 33.3°. As a result of the hydrophilic enhancement, the as-prepared membranes exhibited good rejection of 2,4-DCP. The Ag–TiO$_2$/PA-TFC membranes also exhibited enhanced flux recoveries which was an indication of good antifouling properties.

References

1. Al-Janabi KWS, Alazawi FN, Mohammed MI et al (2012) Direct acetylation and determination of chlorophenols in aqueous samples by gas chromatography coupled with an electron-capture detector. J Chromatogr Sci 50:564–568
2. Olujimi O, Fatoki O, Odendaal J et al (2010) Endocrine disrupting chemicals (phenol and phthalates) in the South African environment: a need for more monitoring. Water SA 36:671–682
3. Zendehdel R, Tayefeh-Rahimian R, Kabir A (2014) Chronic exposure to chlorophenol related compounds in the pesticide production workplace and lung cancer: a meta-analysis. Asian Pac J Cancer Prev 15:5149–5153
4. Ulbricht M (2006) Advanced functional polymer membranes. Polymer 47:2217–2262

5. Brami MV, Oren Y, Linder C et al (2017) Nanofiltration properties of asymmetric membranes prepared by phase inversion of sulfonated nitro-polyphenylsulfone. Polymer 111:137–147

6. Ouzzine M, Maciá-Agulló JA, Lillo-Ródenas MA et al (2014) Synthesis of high surface area TiO$_2$ nanoparticles by mild acid treatment with HCl or HI for photocatalytic propene oxidation. Appl Catal B Environ 154:285–293

7. Jyoti K, Baunthiyal M, Singh A (2016) Characterization of silver nanoparticles synthesized using *Urtica dioica* Linn leaves and their synergistic effects with antibiotics. J Radiat Res App Sci 9:217–227

8. Singh T, Srivastava N, Mishra PK et al (2016) Application of TiO$_2$ nanoparticle in photocatalytic degradation of organic pollutants. Mater Sci Forum 855:20–32

9. Safarpour M, Vatanpour V, Khataee A et al (2017) High flux and fouling resistant reverse osmosis membrane modified with plasma treated natural zeolite. Desalination 411:89–100

10. Giwa A, Akther N, Dufour V et al (2016) A critical review on recent polymeric and nano-enhanced membranes for reverse osmosis. RSC Adv 6:8134–8163

11. Sweetman MJ, May S, Mebberson N et al (2017) Activated carbon, carbon nanotubes and graphene: materials and composites for advanced water purification. C 3:18

12. Lee TH, Lee MY, Lee HD et al (2017) Highly porous carbon nanotube/polysulfone nanocomposite supports for high-flux polyamide reverse osmosis membranes. J Membr Sci 539:441–450

13. Zhang RX, Braeken L, Liu TY et al (2017) Remarkable anti-fouling performance of TiO$_2$-modified TFC membranes with mussel-inspired polydopamine binding. Appl Sci 7:81–95

14. Kotlhao K, Madiseng MD, Mtunzi FM et al (2017) The synthesis of silver, zinc oxide and titanium dioxide nanoparticles and their antimicrobial activity. Adv Mater Proceed 2:479–484

15. Sangchay W (2012) Effect of Ag doped on phase transformation, morphology and photocatalytic activity of TiO$_2$ powders. Int J Eng Res Appl 2:1593

16. Alabbad S, Adil SF, Assal ME et al (2014) Gold & silver nanoparticles supported on manganese oxide: synthesis, characterization and catalytic studies for selective oxidation of benzyl alcohol. Arabian J Chem 7:1192–1198

17. Mbuli BS, Mhlanga SD, Mamba BB et al (2017) Fouling resistance and physicochemical properties of polyamide thin film composite membranes modified with functionalized cyclodextrins. Adv Polym Technol 36:249–260

18. Dumée LF, Maina JW, Merenda A et al (2017) Hybrid thin film nano-composite membrane reactors for simultaneous separation and degradation of pesticides. J Membr Sci 528:217–224

19. Dipheko TD, Matabola KP, Kotlhao K et al (2017) Fabrication and assessment of ZnO modified polyethersulfone membranes for fouling reduction of bovine serum albumin. Int J Polym Sci 2017:Article ID 3587019

20. Kargari A, Khazaali F (2015) Effect of operating parameters on 2-chlorophenol removal from wastewaters by a low-pressure reverse osmosis system. Desal Water Treat 55:114–124

21. Makhetha T, Moutloali R (2018) Antifouling properties of Cu (tpa)@ GO/PES composite membranes and selective dye rejection. J Membr Sci 554:195–210

22. Bueno FG, Machareth MA, Panizzon GP et al (2012) Development of a uv/vis spectrophotometric method for analysis of total polyphenols from *Caesalpinia peltophoroides* Benth. Quim Nova 35:822–826

23. Rahimpour A, Jahanshahi M, Rajaeian B et al (2011) TiO$_2$ entrapped nano composite PVDF/SPES membranes: preparation, characterization, antifouling and antibacterial properties. Desalination 278:343–353

24. Gharibshahi L, Saion E, Gharibshahi E et al (2017) Influence of poly (vinylpyrrolidone) concentration on properties of silver nanoparticles manufactured by modified thermal treatment method. PLoS ONE 12:1–17

25. Shah A, Manikandan E, Ahmed MB et al (2013) Enhanced bioactivity of Ag/ZnO nanorods—a comparative antibacterial study. J Nanomed Nanotechol 4:2–6

26. Shajudheen VM, Vishwanathan K, Rani KA et al (2016) A simple chemical precipitation method of titanium dioxide nanoparticles using polyvinyl pyrrolidone as a capping agent and their characterization. Int Sci Index Chem Mol Eng 10:556–559

27. Alsharaeh E, Bora T, Soliman A et al (2017) Sol-gel-assisted microwave-derived synthesis of anatase Ag/TiO$_2$/GO nanohybrids toward efficient visible light phenol degradation. Catalysts 7:133–143

28. Gupta K, Singh RP, Pandey A et al (2013) Photocatalytic antibacterial performance of TiO$_2$ and Ag-doped TiO$_2$ against *S. aureus*, *P. aeruginosa* and *E. coli*. Beilstein J Nanotechnol 4:345–351

29. Talam S, Karumuri SR, Gunnam N (2012) Synthesis, characterization, and spectroscopic properties of ZnO nanoparticles. Nanotechnol 2012:Article ID 372505

30. Gafoor AKA, Musthafa MM, Pradyumnan PP (2012) AC conductivity and diffuse reflectance studies of Ag–TiO$_2$ nanoparticles. J Electr Mater 41:2387–2392

31. Khan S, Qazi IA, Hashmi I et al (2013) Synthesis of silver-doped titanium TiO$_2$ powder-coated surfaces and its ability to inactivate *Pseudomonas aeruginosa* and *Bacillus subtilis*. J Nanomater 2013:Article ID 531010

32. Jan T, Iqbal J, Ismail M et al (2013) Sn doping induced enhancement in the activity of ZnO nanostructures against antibiotic resistant *S. aureus* bacteria. Int J Nanomedicine 8:3679–3687

33. Smith BC (1998) Infrared spectral interpretation: a systematic approach. CRC Press, United States of America

34. Akbari A (2014) Preparation of novel thin-film composite nanofiltration membranes for separation of amoxicillin. J Nanostruct 4:199–210

35. Belfer S, Fainchtain R, Purinson Y, Kedem O (2000) Surface characterization by FTIR-ATR spectroscopy of polyethersulfone membranes-unmodified, modified and protein fouled. J Membr Sci 172:113–124

36. Kim S, Lee P, Bano S, Park Y, Nam S, Lee K (2016) Effective incorporation of TiO$_2$ nanoparticles into polyamide thin film composite membranes. J Appl Polym Sci 133:1–17

37. Isawi H, El-Sayed MH, Feng X, Shawky H, Abdel Mottaleb MS (2016) Surface nanostructuring of thin film composite membranes via grafting polymerization and incorporation of ZnO nanoparticles. Appl Surf Sci 385:268–281

38. Li J, Yan B, Shao X et al (2015) Influence of Ag/TiO$_2$ nanoparticle on the surface hydrophilicity and visible-light response activity of polyvinylidene fluoride membrane. Appl Surf Sci 324:82–89

39. Hidalgo A, León G, Gómez M et al (2013) Application of the Spiegler–Kedem–Kachalsky model to the removal of 4-chlorophenol by different nanofiltration membranes. Desalination 315:70–75

40. Shon H, Phuntsho S, Chaudhary D et al (2013) Nanofiltration for water and wastewater treatment-a mini review. Drink Water Eng Sci 6:59–77

41. Coday BD, Yaffe BG, Xu P et al (2014) Rejection of trace organic compounds by forward osmosis membranes: a literature review. Environ Sci Technol 48:3612–3624

42. Luján-Facundo MJ, Mendoza-Roca JA, Cuartas-Uribe B et al (2015) Evaluation of cleaning efficiency of ultrafiltration membranes fouled by BSA using FTIR–ATR as a tool. J Food Eng 163:1–8

43. Razmjou A, Mansouri J, Chen V (2011) The effects of mechanical and chemical modification of TiO$_2$ nanoparticles on the surface chemistry, structure and fouling performance of PES ultrafiltration membranes. J Membr Sci 378:73–84

44. Huang H, Yu J, Guo H et al (2018) Improved antifouling performance of ultrafiltration membrane via preparing novel zwitterionic polyimide. Appl Surf Sci 427:38–47

Chapter 21
Antibacterial, Antioxidant and Raw 264.7 Cell Line Proliferative Effect of 5-[(4-Nitro-Benzylidene)-Amino]-2H-Pyrazol-3-ol

Bamidele J. Okoli, Unisa Terblanche, Cornelius Cano Ssemakalu, Fanyana M. Mtunzi, Michael Pillay and Johannes Sekomeng Modise

Abstract Pyrazole derivatives are considered important scaffold that possesses cocktails of pharmacological activities. However, no study has assessed their effects on the proliferation of macrophages. In this study, 4-nitrophenyl derivative containing the $1H$-pyrazol-3-ol moiety HL_1 was synthesised, characterised and assessed for antibacterial as well as cell proliferative effects. HL_1 was characterised using an elemental analyser, TGA, XRD, and various spectrophotometric methods. The antibacterial effect of HL_1 on three Gram-positive bacterial strains: *Enterococcus faecalis*, *Staphylococcus aureus* and *Staphylococcus epidermidis* and three Gram-negative bacterial strains: *Klebsiella pneumoniae*, *Escherichia coli*, and *Pseudomonas aeruginosa* were determined using the minimal inhibition assays. The RAW 264.7 macrophage cell line was used to assess the effect of HL_1 on mitochondrial activity using the CellTiter® Blue Cell Viability Assay. The thermogram and diffractogram plots registered thermal stability slightly above the melting point of HL_1 and a crystal size of 13.01 nm, respectively. The characterisation studies indicated the

B. J. Okoli (✉) · C. C. Ssemakalu · J. S. Modise
Institute of Chemical and Biotechnology, Vaal University of Technology, Science Park, Private Bag X021, Vanderbijlpark, South Africa
e-mail: okolibj@binghamuni.edu.ng

C. C. Ssemakalu
e-mail: corneliuss@vut.ac.za

J. S. Modise
e-mail: joe@vut.ac.za

U. Terblanche · M. Pillay
Department of Biotechnology, Vaal University of Technology, Science Park, Private Bag X021, Vanderbijlpark, South Africa
e-mail: unisa@vut.ac.za

M. Pillay
e-mail: mpillay@vut.ac.za

F. M. Mtunzi
Department of Chemistry, Faculty of Applied and Computer Sciences, Vaal University of Technology, Science Park, Private Bag X021, Vanderbijlpark, South Africa
e-mail: fanyana@vut.ac.za

presence of azomethine moiety at 1701.65 cm^{-1}, δ_H 9.13 and δ_C 156.85 ppm in the FT-IR, ^{1}H, and ^{13}C NMR spectra, respectively. The synthesised pyrazole moiety exhibited significant antioxidant activity (IC$_{50} \leq 0.41 \pm 0.02\,\mu$M) compared to gallic and ascorbic acid (IC$_{50} \leq 0.58 \pm 0.01\,\mu$M) and preserved pharmacological integrity at high temperature but was found not to have any antibacterial effects. The effect of HL$_1$ on the Raw 264.7 cell line intimated a significant increase in the mitochondrial function of the macrophage cells (12.5 μg/ml [127 $\pm$ 3%; $P < 0.0007$] vs. control) indicating an increase in cell proliferation.

Keywords Azomethine · Pyrazol-3-ol · Antioxidant · Macrophage · Proliferation · Radical

21.1 Introduction

The azole, specifically the five-membered 2*H*-pyrazol-3-ol scaffold, has attracted attention due to the pharmacological potency acquired when coupled to an aromatic aldehyde unit [1]. The presence of the pyrazole nucleus can be traced in many pharmaceutically established drugs with diverse therapeutic activities [2, 3]. Over the past two decades, pyrazole-Schiff base derivatives have found diverse applications due to their potent antioxidant, antimicrobial, anti mycobacterial, anti-inflammatory, non-enzymatic protein glycation inhibition, gastric secretion stimulation, and antidepressant properties [4–6]. Many Schiff bases derived from pyrazole have been synthesized by condensation of 1*H*-pyrazol-3-amine derivatives and different aromatic aldehydes or ketones leading to polysubstituted pyrazoles as reported by Baluja and Chanda [7].

The continuous search for novel biologically active pyrazole derivatives coupled with the development of drug resistance of microbial strains has made it necessary to investigate the influence of these compounds on biological systems. Despite the research done to develop pharmaceutically potent pyrazole derivatives, no study has targeted the effect of pyrazole on the macrophages, an essential component of the mammalian immune system. Macrophages are widely distributed throughout the different tissues where they play a role in the phagocytosis of virally infected and cancerous cells as well as extrinsic threats such as pathogen invasion or breach in tissue [8].

In this study, we investigated the antimicrobial, antioxidant and RAW 264.7 macrophage proliferative effects of 4-nitrophenyl derivative containing the 2*H*-pyrazol-3-ol moiety.

21.2 Experimental Details

21.2.1 Chemicals

All chemicals and reagents used in this study were of analytical grade. 3-Amino-5-hydroxypyrazole, 4-nitrobenzaldehyde, 2,2-diphenyl-1-picrylhydrazyl (DPPH), quercetin, gallic acid, ascorbic acid, penicillin G, streptomycin, dimethyl sulfoxide (DMSO), hydrogen peroxide, 2,2′-azino-bis-3-ethylbenzthiazoline-6-sulphonic acid (ABTS) and potassium persulfate were obtained from Sigma Aldrich (St. Louis, MO). Potassium ferricyanide, trichloroacetic acid and ferric chloride were purchased from Merck (Darmstadt, Germany). Dulbecco's Modified Eagle Medium (DMEM), and Fetal Bovine Serum (FBS) were obtained from Thermo Fischer Scientific (Waltham, MA). Others like phosphate buffer, ethanol and glacial acetic acid were purchased from Promark and Rochelle Chemicals (Johannesburg, South Africa), respectively.

21.2.2 Instrumentation

The percentage elemental composition of the 5-[(4-nitro-benzylidene)-amino]-2H-pyrazol-3-ol was measured using a LECO analyser (CHNS628 analyser, Lakeview, MI). The maximum absorption and the melting point were measured using a UV-visible spectrophotometer (Agilent Technologies Cary 60, Santa Clara, CA) and Stuart digital apparatus (Vernon Hills, IL), respectively. ^{1}H- and ^{13}C-NMR chemical shifts (ppm) were recorded using a 400 MHz nuclear magnetic resonance spectrometer (Agilent Technologies). Thermal response was monitored on a thermogravimetric analyser (Perkin Elmer, Waltham, MA) operated at a temperature ranging between 30 and 900 °C at a heating rate of 10 °C/min under a nitrogen atmosphere. The X-ray diffractogram was recorded on a ZEISS Sigma 300 diffractometer (Zeiss, Oberkochen, Germany). The Spectrum 400 FT-IR (PerkinElmer) scanning between 4000 and 400 cm^{-1} was used to determine the different functional groups.

21.2.3 Synthesis of HL$_1$

An ethanolic solution of 3-amino-5-hydroxypyrazole (0.99 g; 9.98 mmol) was mixed with 4-nitrobenzaldehyde (3.02 g; 19.98 mmol) in 95% ethanol. To the mixture, 0.5 mL of glacial acetic acid was introduced and refluxed for 8 h. The product (HL$_1$) obtained was filtered, washed several times with 95% ethanol, recrystallized from cold ethanol solution and dried in an oven at 40 °C. The chemical formulation of the structure of HL$_1$ is shown in Fig. 21.1.
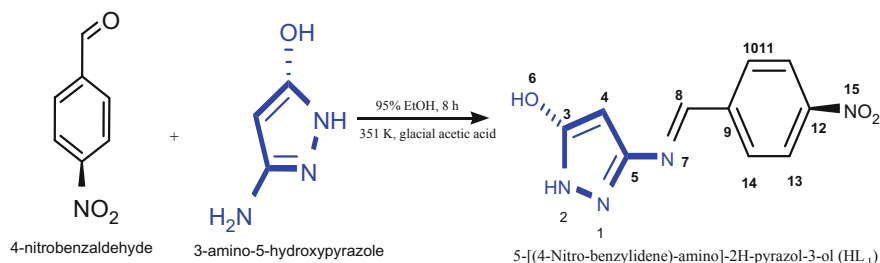
Fig. 21.1 Chemical synthesis of HL$_1$

21.2.4 Electronic Absorption Study

The wavelength maximum of HL$_1$ in DMSO was determined at room temperature and the molar absorptivity coefficient was calculated from the Lambert-Beer equation (21.1):

$$A = \varepsilon_{\lambda\max} bC \tag{21.1}$$

where A is the absorbance, b is the path length, C is the concentration of HL$_1$ (mol/L), and $\varepsilon_{\lambda\max}$ is the molar absorption coefficient (Lmol^{-1}cm^{-1}).

21.2.5 XRD Study

The X-ray diffractogram was investigated at 40 kV and 40 mA with Cu-Kα ($\lambda = 1.5406$ Å) radiation and the crystallite size (D) was calculated using Scherrer equation (21.2).

$$D = K\lambda/\beta \cos\theta \tag{21.2}$$

where K is the equipment constant (0.94), λ is the wavelength (1.5406 Å), and β is the integral height to width of the diffraction peak.

21.2.6 Antioxidant Assays

The antioxidant activity of HL$_1$ was evaluated and compared with three positive controls: quercetin, gallic acid and ascorbic acid.

21.2.7   DPPH Radical Scavenging Activity

The DPPH (300 µL, 0.05 mM) radical ethanolic solution was mixed with various concentrations (4.31, 2.15, 1.08, 0.54, and 0.27 µM) of HL_1 and incubated for 30 min in the dark. Changes in the absorbance of the mixtures were measured at 517 nm on a UV-Vis spectrophotometer [9]. The percentage radical scavenging activities (%RSA) was calculated from Eq. (21.3) and the half maximal inhibitory concentration (IC_{50} µM) of the test compounds was determined by linear regression analysis. All analyses were carried out in triplicate.

$$\%RSA = 100 \frac{(\text{Abs. of DPPH control} - \text{Abs. of HL1})}{(\text{Abs. of DPPH control})} \tag{21.3}$$

21.2.8   ABTS Radical Cation Decolourisation Assay

The blue-green 2,2′-azino-bis-3-ethylbenzothiazoline-6-sulphonic acid radical cation ($ABTS^{·+}$) solution was prepared by dissolving 960.2 mg of ABTS in a 250 mL solution of 0.0024 mM potassium persulfate and stored away for 24 h. Thereafter, the absorbance was adjusted to 0.9547 at 734 nm with distilled water. Exactly 40 µL of various concentrations (4.31, 2.15, 1.08, 0.54, and 0.27 µM) of HL_1 or control was added to 3 mL of the $ABTS^{·+}$ solution and incubated for 30 min at 25 °C in the dark and the changes in the concentration of $ABTS^{·+}$ were measured at 734 nm. The decolourisation of the blue-green solution was used as a template to evaluate the percentage proton-donating potential (%PDP) of the test compounds [10] and was estimated from Eq. (21.4). The IC_{50} (µM) of the compounds was determined by linear regression analysis. All analyses were carried out in triplicate.

$$\%PDP = 100 \frac{(\text{Abs. of ABTS control} - \text{Abs. of HL1})}{(\text{Abs. of ABTS control})} \tag{21.4}$$

21.2.9 H_2O_2—Scavenging Activity

The H_2O_2-scavenging activity of the test compound was evaluated according to the method of Ruch et al. [11] with slight modifications. To 100 µL aliquot of the test compounds, 0.4 mL of 50 mM phosphate buffer was added followed by 0.6 mL of 2 mM H_2O_2 solution prepared in 50 mM phosphate buffer (pH 6.8). The absorbance of the mixture was measured at 230 nm and the %H_2O_2-scavenging activity was computed from Eq. (21.5). The IC_{50} (µM) of HL_1 or controls was determined by linear regression analysis. All analyses were carried out in triplicate.

$$\% \ H_2O_2 \ \text{scavenging activity} = 100 \frac{(\text{Abs. of} \ H_2O_2 - \text{Abs. of} \ HL1)}{(\text{Abs. of} \ H_2O_2)} \qquad (21.5)$$

21.2.10 Ferric Reducing Power

The ferric reducing activity was determined according to the method of Oyaizu [12]. In brief, a 0.5 mL aliquot of HL_1 was mixed with 2 mL phosphate buffer (0.2 M, pH 6.8) and 2 mL potassium ferricyanide (0.03 μM). The mixture was incubated for 30 min at 45 °C, followed by the addition of 2 mL of 0.61 mM trichloroacetic acid. A 2 mL portion of the above mixtures was transferred into 2 mL of distilled water and 0.4 mL ferric chloride (0.1% w/v) in a test tube. Then, the absorbance was measured at 700 nm after 10 min and the reducing power was estimated as a function of the absorbance. The same protocol was applied to the controls and all the determinations were carried out in triplicate.

21.2.11 Cell Culture

A murine macrophage cell line RAW 264.7 (Cellonex, Johannesburg, South Africa) was cultured and maintained in complete cell culture medium consisting of DMEM supplemented with 10% Fetal Bovine Serum (FBS) and antibiotics (10,000 U/mL penicillin G and 10 mg/mL streptomycin) at 37 °C in a 5% CO_2 incubator (ESCO, Horsham, PA). The culture medium was replaced with fresh medium every three days until the cells were 80% confluent. The cells were washed, trypsinised and prepared for the cell proliferation assay.

21.2.12 Cell Proliferation Assay

The effect of HL_1 on the viability of the RAW 264.7 cell line was evaluated using the CellTiter® Blue Cell Viability Assay (Promega, Cat. No. G8081, Madison, WI) according to the manufacturer's instructions with a few modifications. The RAW 264.7 cells were seeded in a 96-well microtiter plate (100 μL per well) at a concentration of 5×10^4 cells/mL in a complete cell culture medium and incubated at 37 °C in a 5% humidified CO_2 incubator. After 24 h of incubation, the cell culture medium was replaced with fresh complete cell culture medium containing different concentrations of the HL_1 (6.25, 12.5, 25, 50 and 100 μg/mL). Four control groups were set up consisting of (i) cell culture medium only (negative control to determine background absorbance), (ii) untreated cells (vehicle control), (iii) medium with 0.1% DMSO (used as solvent for compound), and (iv) cells treated with hydrogen perox-

ide (H_2O_2) used as the negative control. After treatment, the cells were incubated for different time intervals (24, 96 and 168 h) at 37 °C in a humidified 5% CO_2 incubator. At the end of each incubation period, 20 µL of CellTiter® Blue Reagent was added to each well containing the remaining culture medium. The plate was then agitated for 10 s and incubated at 37 °C for 4 h in a humidified 5% CO_2 incubator. Thereafter, 100 µL medium containing CellTiter® Blue reagent was transferred into a 96-well microtiter plate, and the absorbance of the dissolved resorufin dye was determined at 570 and 600 nm, respectively, using an EPOCH 2 (BioTek, Winooski, VT) plate reader.

21.2.13 Antibacterial Property

The microorganisms used in the present investigation included reference strains from the American Type Culture Collection (ATCC) and National Collection of Type Cultures (NCTC). These included three Gram-positive bacterial strains: *Enterococcus faecalis* [ATCC 49533], *Staphylococcus aureus* [obtained from a local hospital in Vanderbijlpark, South Africa] and *Staphylococcus epidermidis* [ATCC 12228], and three Gram-negative bacterial strains: *Klebsiella pneumoniae* [ATCC BAA-1706], *Escherichia coli* [NCTC 11954] and *Pseudomonas aeruginosa* [ATCC 25619]. All the bacterial strains were individually inoculated in Mueller-Hinton Broth and incubated for 24 h before use in the broth microdilution method.

The antibacterial activity of the synthesized compound (HL_1) was evaluated against the selected bacterial strains using the broth microdilution method as described by De Rapper et al. [13] and Akhalwaya et al. [14] with slight modifications. A 1000 mg/mL stock solution of HL_1, dissolved in dimethyl sulfoxide (DMSO), was diluted to a working concentration of 300 mg/mL Microtiter 96-well plates (Nunc Roskilde, Denmark) were prepared by adding 100 µL sterilized deionized water aseptically to each well. Thereafter, 100 µL of the test compound (HL_1) was added to the first row of each microtiter plate. Two-fold serial dilutions were carried out down each column to obtain concentrations from 150 to 1.17 mg/mL at a total volume of 100 µL per well. Standardized bacterial cultures (100 µL) at a concentration of 1×10^6 colony forming units (CFU)/mL were then added to each well of their respective microtiter plates. To detect bacterial growth, 30 µL resazurin indicator dye (0.015%) was added to each well before incubation. Resazurin is an oxidation-reduction indicator that undergoes colorimetric changes (from blue to pink or colorless) in response to reduction by mitochondrial reductases and other diaphorases such as dihydrolipoamine dehydrogenase, NAD(P)H, quinone oxidoreductase and flavin reductase [15]. The inoculated microtiter plates were sealed using a sterile adhesive film and incubated at 37 °C for 24 h. Amoxycillin (2.5 mg/mL) (Melford, Chelsworth, United Kingdom) and neomycin (2.5 mg/mL) were included as positive controls. Dimethyl sulfoxide was included as a negative control to confirm that the solvent did not exert any antibacterial effect and a culture control ensured that the broth could support bacterial growth. According to the Clinical Laboratory

Standards Institute guidelines [16] for broth microdilution, the minimum inhibitory concentration (MIC) is defined as the lowest concentration that completely inhibits the microorganism from multiplying and producing visible growth in the test solution. After inspection of the microtiter plates, 10 µl of the MIC well content was plated on nutrient agar plates and incubated for another hour at 37 °C to confirm the antibacterial property of the synthesized compound. All experiments were done in triplicate.

21.2.14   Statistical Analysis

Statistical analysis was carried out with Origin Pro software (Origin Lab Corporation, Northampton, MA 01060 USA), and results are expressed as means $\pm$ standard deviation.

21.3   Results

21.3.1   Synthesis and Characterization of HL_1

The product (HL_1) was collected as a regatta powder. Yield 61.8%; m.p. 283–285 °C; λ_{max} 316 and 393 nm, and ε 1.3419 $\times$ 10^5 $Lmol^{-1}cm^{-1}$; IR (cm^{-1}) 3352 (w), 3108 (w), 2859 (w), 1702 (m), 1624 (m), 1515, 1344 (s), 1199, 1107, 1014 (m), 856, 814 (m) and 697 (m).^{1}H NMR (400 MHz, DMSO-d_6) δ 9.11 (s, 1H), 8.34–8.31 (m, 2H), 8.19–8.16 (m, 2H), 6.35 (s, 1H), 4.01 (s, 1H), 2.53 (s, 1H) (Fig. 21.2).

^{13}C NMR (100 MHz, DMSO-d_6) δ 160.47, 157.64, 152.56, 148.99, 138.89, 129.57, 129.43, 124.50, 124.40, 87.21 (Fig. 21.3). Anal calculated for $C_{10}H_8N_4O_3$: %C, 51.73; %H, 3.47; %N, 24.13. Found: %C 51.17, %H 3.97, %N 24.76.

21.3.2   Thermal Profile of HL_1

The thermogravimetric plot of HL_1 is presented in Fig. 21.4. Four major exothermic peaks corresponding to various thermal responses were observed at 80, 200, 287 and 430 °C with a weight loss of 3, 9, 20 and 48%, respectively.

21.3.3   X-Ray Diffractogram of HL_1

The X-ray diffractogram of HL_1 presented in Fig. 21.5 produced a unique diffraction pattern confirming the crystalline nature of HL_1. The diffractogram registered seven
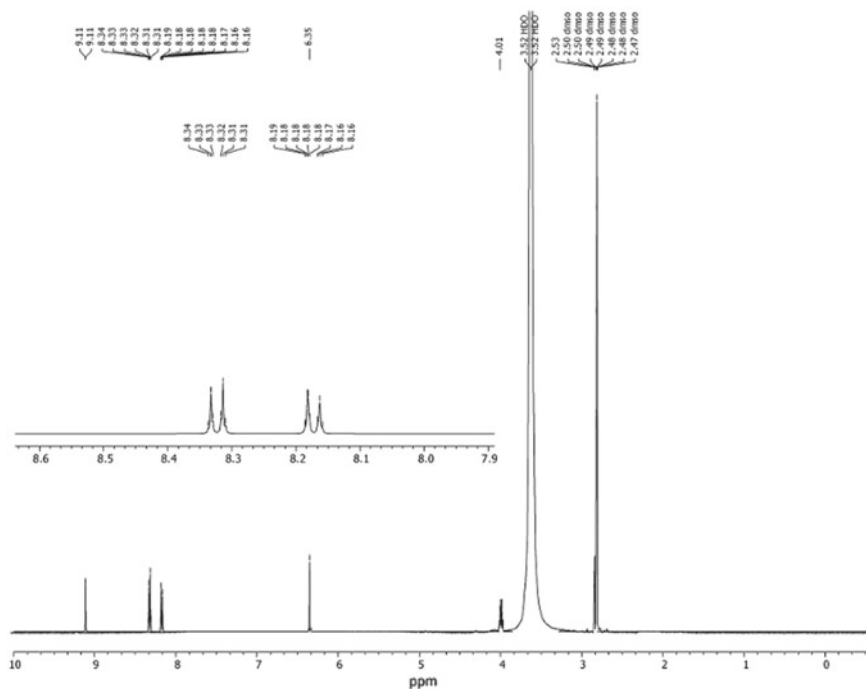
Fig. 21.2 ^{1}H NMR spectrum of HL$_1$

(7) reflection peaks in the range of 0°–70° with a maximum at 34.24° and the crystal size determined using Scherrer formula was 13.01 nm.

21.3.4   Antioxidant Activity of HL$_1$

The antioxidant activities of HL$_1$ and controls were evaluated by DPPH, ABTS, H_2O_2 scavenging and ferric reducing power in vitro assays. The IC$_{50}$ values for the different assays were obtained from the plots of the % radical inhibition against concentration with $R^2 \geq 0.9635$ (Table 21.1).

The IC$_{50}$ values of HL$_1$ were significant ($p < 0.05$) compared to the controls. HL$_1$ showed very potent radical scavenging potential with IC$_{50}$ of $0.29 \pm 0.09 - 0.41 \pm 0.02$ μM (Table 21.1) and ferric reducing power of 0.0045 ± 0.007 (Fig. 21.6) compared to gallic acid and ascorbic acid, with quercetin being slightly more potent.
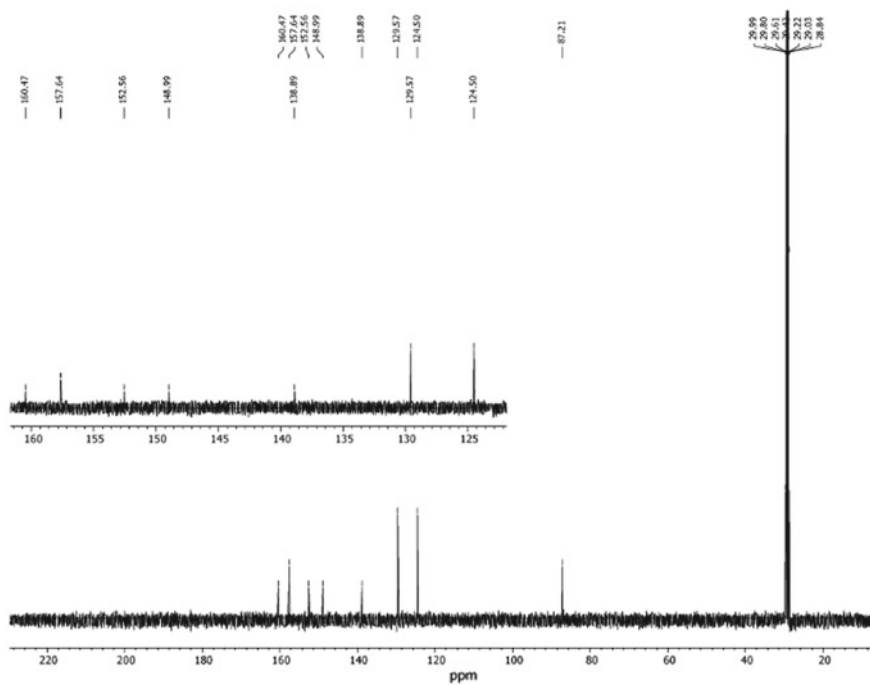
Fig. 21.3 ^{13}C NMR spectrum of HL$_1$
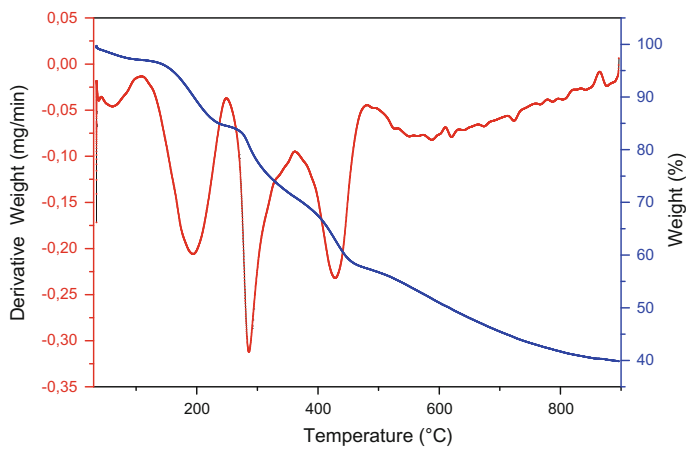
Fig. 21.4 Thermogram of HL$_1$
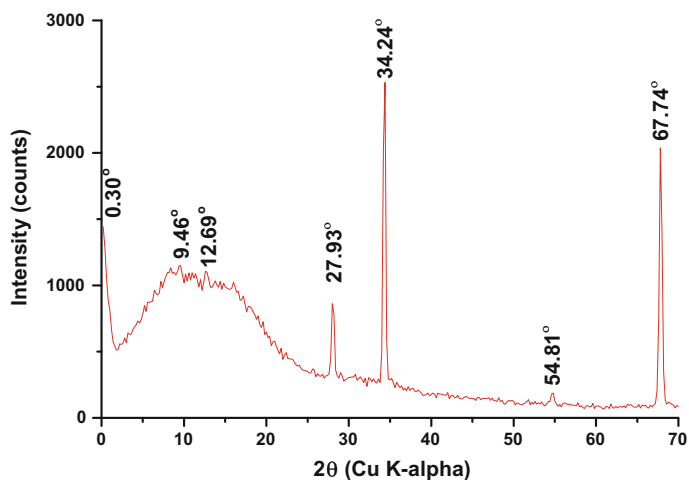
Fig. 21.5 Diffractogram of HL_1

Table 21.1 Scavenging activity of HL_1

Compounds	DPPH assay		ABTS assay		H_2O_2-scavenging activity	
	IC_{50} (µM)	R^2	IC_{50} (µM)	R^2	IC_{50} (µM)	R^2
HL_1	0.29 ± 0.09*	0.9943	0.41 ± 0.02*	0.9953	0.35 ± 0.26*	0.9635
Quercetin	0.24 ± 0.03	0.9891	0.27 ± 0.01	0.9849	0.27 ± 0.11	0.9857
Gallic acid	0.42 ± 0.09	0.9917	0.58 ± 0.01	0.9959	0.46 ± 0.22	0.9728
Ascorbic acid	0.35 ± 0.07	0.9965	0.53 ± 0.02	0.9947	0.44 ± 0.03	0.9740

The values are expressed as means ± SD (n = 3). *Significant parameters; p value < 0.05
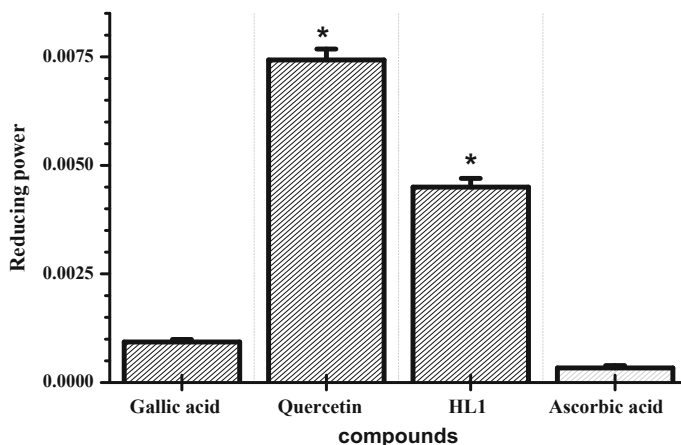
Fig. 21.6 Total reducing power of HL_1 and controls (0.2 mg/mL) measured at 700 nm. The values are expressed as means ± SD (n = 3). *Significant parameters; p value < 0.05

21.3.5   Effect of HL$_1$ on Cell Viability

When the Raw 264.7 cells were stimulated for a day with HL$_1$ at concentrations of 6.5, 12.5, 25 and 50 µg/mL, an increase in cell viability was observed (Fig. 21.7). HL$_1$ at a concentration of 12.5 µg/mL resulted in a highly significant ($p < 0.0007$) increase in cell viability ($127 \pm 3\%$) compared to the untreated cells ($100 \pm 3\%$). When HL$_1$ was used at 100 µg/mL, a significant ($p < 0.009$) reduction in cell viability ($83 \pm 1\%$) in comparison to the untreated cells was observed after day 1. When the RAW 264.7 cells were stimulated with HL$_1$ at 6.5, 12.5, 25 and 50 µg/mL for 4 days, a slight but non-significant increase in cell viability was observed. However, 4 days of stimulation of the RAW 264.7 cells with HL$_1$ at a concentration of 100 µg/mL resulted in a further significant ($p < 0.001$) decrease in cell viability ($47.0 \pm 4.7\%$) compared to the untreated cells ($100.0 \pm 1.8\%$). After 7 days of stimulation with HL$_1$ at concentrations of 12.5, 25 and 50 µg/mL, percentage cell viability remained slightly higher than that observed in the untreated cells. However, the percentage viability ($107.0 \pm 0.96\%$) in cells stimulated with HL$_1$ at a concentration of 12.5 µg/mL was highly significant ($p < 0.00008$) compared to that observed in the untreated cells ($100.0 \pm 3.04\%$). On the contrary, 7 days of stimulation with HL$_1$ at a concentration of 6.5 µg/mL resulted in a highly significant ($p < 0.0009$) decrease in cell viability ($76.0 \pm 1.96\%$) compared to that observed in the untreated cells ($100.0 \pm 3.04\%$). A highly significant ($p < 0.0004$) decrease in the percentage cell viability ($40.0 \pm 4.56\%$) was observed when HL$_1$ was used at a concentration of 100 µg/mL in comparison to the untreated cells.
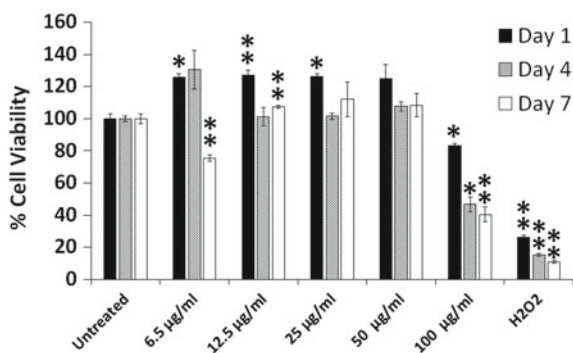
Fig. 21.7 Percentage viability following the stimulation of RAW 264.7 cells with HL$_1$ at 6.5, 12.5, 25, 50 and 100 µg/mL for 1, 4 and 7 days. The untreated cells were used as a negative control whereas the H$_2$O$_2$ was used as a positive control. The error bars indicate the standard error of the mean of quadruplicate experiments. *Indicates that the mean had a $p < 0.05$ in comparison to the untreated cells. **Indicates that the mean had a $p < 0.0001$ in comparison to the untreated control

Table 21.2 The in vitro antibacterial activity of HL_1 using the broth microdilution method

Bacterial strains	Minimum inhibitory concentration in mg/mL			
	HL_1	DMSO	Antibacterial agents	
			Amoxicillin	Neomycin
Gram-positive				
E. faecalis	9.38	–	0.31	1.25
S. aureus	4.69	–	<0.005	<0.005
S. epidermidis	4.69	–	<0.005	<0.005
Gram-negative				
K. pneumoniae	9.38	–	0.31	<0.005
E. coli	9.38	–	<0.005	<0.005
P. aeruginosa	9.38	–	<0.005	<0.005

21.3.6   Antibacterial Activity

The results of the antibacterial activity of 5-[(4-nitro-benzylidene)-amino]-2H-pyrazol-3-ol (HL_1) against six bacterial strains using the broth microdilution method are summarized in Table 21.2. Amoxicillin and neomycin (2.5 mg/mL) were used as reference antibiotics for comparison purposes. The results showed predominantly similar antibacterial activity against the selected bacterial strains (Table 21.2) but were considerably less compared to the standards used.

21.4   Discussion

Two bands were observed in the electronic absorption spectrum of 5-[(4-nitro-benzylidene)-amino]-2H-pyrazol-3-ol (0.02 µM) in DMSO. The two bands with wavelengths of 316 and 393 nm are typical of Π–Π* transitions and the n–Π* transitions of the aromatic rings and azomethine group, respectively [17]. The ^{1}H and ^{13}C NMR spectra of HL_1 confirm the presence of azomethine group with proton and carbon signals at δ 9.11 (H-8) and δ 157.64 (C-8) ppm [18] respectively, and further confirmation was observed at 1702 cm^{-1} in the FT-IR spectrum. The deshielded carbon signal at δ 160.47 (C-3) ppm confirms the presence of an oxymethine unit of the pyrazol-5-ol moiety. Signals from the aromatic protons were observed at 8.34–8.16 ppm while the corresponding aromatic carbons peaked at δ 152.56 (C-5), 148.99 (C-12), 138.89 (C-9), 129.57 (C-14), 129.43 (C-10), 124.50 (C-11), 124.40 (C-13), 87.21 (C-4) ppm (Fig. 21.3). The sharp absorption bands in the fingerprint region at 1575–1507 cm^{-1} are in concordance with the aromatic signals on the ^{1}H and ^{13}C NMR spectra [19]. Other notable characteristic bands at 1624 and 1515 cm^{-1} are attributed to the bending and stretching vibrations of –N–H and –O–N, with the corresponding proton signals at 2.53 (H-2) and 4.01 (H-6) ppm, respectively.

The thermal profile of HL$_1$ at the operating temperature of 30–900 °C and the mechanism of thermal decomposition are presented in Figs. 21.4 and 21.8, respectively. The TGA and DTA plots revealed four thermal events at 80, 100, 287 and 430 °C with a corresponding weight loss of 3, 9, 20 and 48%, respectively. The mass loss of 3% at 80 °C and 9% at 100 °C is attributed to the removal of crystallising solvent (ethanol) and adsorbed moisture, respectively. The presence of adsorbed moisture is an indication of the hygroscopic nature of HL$_1$ [20]. After dehydration, above the melting point (283 °C) the first thermal decomposition step took place at 287 °C, corresponding to the loss of nitrogen (IV) oxide which accounts for 20% of the weight of HL$_1$ to produce 3-((phenylmethylidene)amino)-1H-pyrazol-5-ol (**III**). At a temperature >430 °C, the compound (**III**) carbonises corresponding to 48% weight loss; this is equivalent to the percentage of carbon relative to the mass of HL$_1$ introduced into the thermal analyser. The evaluation of the thermal profile proved that 5-[(4-nitro-benzylidene)-amino]-2H-pyrazol-3-ol is slightly stable above the melting point. Thereafter, the integrity of the compound becomes compromised leading to the production of 3-((phenylmethylidene)amino)-1H-pyrazol-5-ol (**III**).

The X-ray powder diffraction study was conducted to study the specific chemistry, atomic arrangement and crystallinity of HL$_1$. The diffractogram of HL$_1$ (Fig. 21.5) recorded seven crystalline peaks confirming the crystallinity of HL$_1$. The nanocrystalline size of 13.01 nm calculated from Scherrer equation (21.2) is an important residual factor associated with the ordered arrangement of atoms in a crystalline compound, which directly influences the compound properties [21]. According to the study of Carballo and Wolf [22], the rate of biological interaction of a compound is significantly influenced by the crystallite size. Hence, the large crystallite size is expected to have some degree of influence on the biological activity.

Derivatives of pyrazole have been known to exhibit significant in vitro antioxidant activity and in vivo COX-II inhibition [23]. Our investigation into the antioxidant potential of HL$_1$ showed similar scavenging potentials against 2,2-diphenyl-1-picrylhydrazyl, 2,2′-azino-bis-3-ethylbenzothiazoline-6-sulphonic acid and peroxide radicals (Table 21.1) compared to gallic acid, quercetin and ascorbic acid as observed in previous studies [24–26]. The total antioxidant potential of
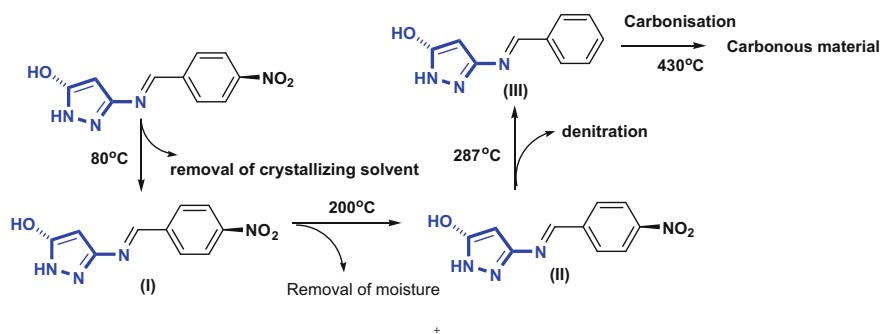
Fig. 21.8 Mechanism of thermal decomposition of HL$_1$

HL_1 was effectively estimated by the reduction of Fe^{3+} to Fe^{2+} as a function of HL_1 to donate either an electron to the vacant *d*-orbital or proton which invariably is measured as the reduction capacity of the evaluated compound [27]. Consequently, in this study the reducing power is in the order of quercetin > HL_1 > gallic acid > ascorbic acid (Fig. 21.6). There is a significant difference ($p < 0.05$) in the ferric reducing power, with HL_1 showing comparative activity to quercetin. The scavenging potentials and total reducing power can be justified by the structural features of the ring structures such as the hydroxyl, carboxylic acid or lactone groups [28]. The number of –OH groups and the ability to delocalize electrons within the complex structure to stabilise the phenoxy and carboxylate ions [29, 30], influenced the antioxidant activity of quercetin relative to HL_1.

Infectious diseases, resulting in approximately 50,000 deaths per day, remain one of the leading health-related problems worldwide. The efficacy of many of the currently available antibacterial agents that kill or prevent the reproduction of microorganisms, is rapidly declining due to the emergence of multidrug-resistant organisms (MDRO). In addition, infections caused by multidrug-resistant bacteria are associated with prolonged treatment regimens resulting in an increased financial burden on the healthcare sector [31]. The urgent need for the development of new classes of antibacterial agents is evident. However, the synthesis of new antibacterial agents is restricted by the search for new substances that are effective against microorganisms but non-toxic to mammalian cells. The antibacterial properties of pyrazole and many pyrazole derivatives have been investigated with variable degrees of antibacterial potential. In the current study, the newly synthesized lactam-type Schiff base pyrazole derivative was tested for its antibacterial activity against *E. faecalis*, *S. aureus*, *S. epidermidis*, *K. pneumoniae*, *E. coli* and *P. aeruginosa* with amoxicillin and neomycin as reference antibacterial agents. The investigation revealed that HL_1 was active against all the tested bacterial strains and that the solvent, DMSO, had no inhibitory effect on any of the tested bacterial strains (Table 21.2). Based on the results, a similar MIC value (9.38 mg/mL) was recorded for *K. pneumoniae*, *E. coli*, *P. aeruginosa* and *E. faecalis,* with a slightly lower MIC value (4.69 mg/mL) for *S. epidermidis* and *S. aureus.* Studies have indicated that Gram-negative bacteria are more resistant to antimicrobial agents as compared to Gram-positive bacteria due to the presence of a largely impermeable cell wall [32]. Upon comparing the antibacterial potential of the newly synthesized Schiff base with that of the reference compounds (amoxicillin and neomycin), it was concluded that HL_1 displayed poor antibacterial activity against all tested bacterial strains.

The cell viability results showed that HL_1 at low concentrations, particularly at 12.5 µg/mL, significantly increased the number of viable macrophage cells (Fig. 21.7). The increase in cell viability is perhaps due to an increase in mitochondrial activity which could have resulted from the proliferation or self-renewal of the macrophages. The link between an increase in mitochondrial activity and cell proliferation has been established in various studies [33, 34]. Clearly, the results showed that HL_1 could act as a macrophage growth factor although the exact mode of action remains unknown. It is possible the HL_1 could have promoted the proliferation of macrophages through the upregulation of the colony stimulating factor

receptors. The proliferation or self-renewal of macrophages in vivo has been documented and is shown to result from the presence of growth factors and cytokines such as macrophage colony stimulating factor (M-CSF), granulocyte macrophage stimulating factor GM-CSF [34], IL-4 [8, 35] or IL-34 [36]. Similar reasons could be postulated for the proliferation of macrophages in this study. Furthermore, the proliferation of macrophages has been linked to the increased expression of the colony stimulating factor 1 receptor (CSF-1R) [34]. Although a time-based decrease in the proliferative capability of HL_1 was observed, proliferation still remained above that observed in the untreated macrophages. The ability for HL_1 to induce a sustained increase in macrophage proliferation could either result in a positive or negative outcome. The proliferation of resident macrophages is desirable for pathogen control or wound repair especially in a situation where an inflammatory response could have resulted in the depletion of the resident macrophages [35]. On the contrary, macrophage proliferation has also been associated with inflammatory pathology such as in obesity-associated tissue inflammation [37] and type II diabetes [38]. However, the negative or positive outcome largely would depend on whether the resident macrophages are either classically (M1) or alternatively (M2) activated. The M1 macrophages are associated with the production of pro-inflammatory cytokine, phagocytosis and play a key role in the initiation of an immune response whereas the M2 macrophages induce proliferation and are associated with wound healing and tissue repair [39]. The potential applications that might involve HL_1 should take into cognizance the ability of this compound to induce and maintain macrophage proliferation.

21.5 Conclusion

Our study underlines the fact that the pyrazole derivative (HL_1) is stable beyond the melting point with potent antioxidant potentials but poor antibacterial activity. Future work will focus on profiling the cytokines and chemokines produced by the macrophages in response to HL_1. Furthermore, gene and protein expression studies will be done to establish the influence that HL_1 may have on the expression of CSF-1R. This will provide some information on the mechanism through which HL_1 was able to induce and sustain macrophage proliferation. This approach could provide a basis for the practical applications of HL_1.

References

1. Karrouchi K, Radi S, Ramli Y et al (2018) Synthesis and pharmacological activities of pyrazole derivatives: a review. Molecules 23:134
2. Ajay Kumar K, Jayaroopa P (2013) Pyrazoles: synthetic strategies and their pharmaceutical applications—an overview. Int J PharmTech Res 5:1473–1486
3. Khan MF, Alam MM, Verma G et al (2016) The therapeutic voyage of pyrazole and its analogs: a review. Eur J Med Chem 120:170–201
4. Hampp C, Hartzema A, Kauf TL (2008) Cost-utility analysis of rimonabant in the treatment of obesity. Value Heal 11:389–399
5. Luttinger D, Hlasta DJ (1987) Antidepressant agents. Annu Rep Med Chem 22:21–30
6. Tsutomu K, Toshitaka N (1978) Effects of 1,3-diphenyl-5-(2-dimethylaminopropionamide)-pyrazole [difenamizole] on a conditioned avoidance response. Neuropharmacology 17:249–256
7. Baluja S, Chanda S (2016) Synthesis, characterization and antibacterial screening of some Schiff bases derived from pyrazole and 4-amino antipyrine. Rev Colomb Ciencias Químico-Farmacéuticas 45:201
8. Italiani P, Boraschi D (2014) From monocytes to M1/M2 macrophages: phenotypical vs. functional differentiation. Front Immunol 5:514
9. Blois MS (1958) Antioxidant determinations by the use of a stable free radical. Nature 181:1199–1200
10. Wolfenden BS, Willson RL (1982) Radical-cations as reference chromogens in kinetic studies of ono-electron transfer reactions: pulse radiolysis studies of 2,2′-azinobis-(3-ethylbenzthiazoline-6-sulphonate). J Chem Soc Perkin Trans 2(2):805–812
11. Ruch RJ, Cheng SJ, Klaunig JE (1989) Prevention of cytotoxicity and inhibition of intercellular communication by antioxidant catechins isolated from Chinese green tea. Carcinogenesis 10:1003–1008
12. Oyaizu M (1988) Antioxidative activities of browning products of glucosamine fractionated by organic solvent and thin layer chromatography. Nippon Shokuhin Kogyo Gakkaishi 35:771–775
13. De Rapper S, Kamatou G, Viljoen A, Van Vuuren S (2013) The in vitro antimicrobial activity of *Lavandula angustifolia* essential oil in combination with other aroma-therapeutic oils. Evid-Based Compl Alt Med 2013:1–10
14. Akhalwaya S, van Vuuren S, Patel M (2018) An in vitro investigation of indigenous South African medicinal plants used to treat oral infections. J Ethnopharmacol 210:359–371
15. Rampersad SN (2012) Multiple applications of Alamar Blue as an indicator of metabolic function and cellular health in cell viability bioassays. Sensors 12:12347–12360
16. Subramaniam P, Nandan N (2011) Effect of xylitol, sodium fluoride and triclosan containing mouth rinse on *Streptococcus mutans*. Contemp Clin Dent 2:287
17. Petrus ML, Bouwer RKM, Lafont U et al (2014) Small-molecule azomethines: organic photovoltaics via Schiff base condensation chemistry. J Mater Chem A 2:9474–9477
18. Wawer V, Koleva T, Dudev I (1997) ^{1}H and ^{13}C NMR study and AM1 calculations of some azobenzenes and N-benzylideneanilines: effect of substituents on the molecular planarity. J Mol Struct 412:153–159
19. Malladi S, Isloor AM, Isloor S et al (2013) Synthesis, characterization and antibacterial activity of some new pyrazole based Schiff bases. Arab J Chem 6:335–340
20. Soliman EA, El-Kousy SM, Abd-Elbary HM, Abou-zeid AR (2013) Low molecular weight chitosan-based Schiff bases: synthesis, characterization and antibacterial activity. Am J Food Technol 8:17–30
21. Ohira T, Yamamoto O (2012) Correlation between antibacterial activity and crystallite size on ceramics. Chem Eng Sci 68:355–361
22. Carballo LM, Wolf E (1978) Crystallite size effects during the catalytic oxidation of propylene on Ptγ-Al$_2$O$_3$. J Catal 53:366–373

23. Naim MJ, Alam O, Nawaz F et al (2016) Current status of pyrazole and its biological activities. J Pharm Bioallied Sci 8:2–17
24. Sahoo J, Kumar Mekap S, Sudhir Kumar P (2015) Synthesis, spectral characterization of some new 3-heteroaryl azo 4-hydroxy coumarin derivatives and their antimicrobial evaluation. J Taibah Univ Sci 9:187–195
25. Karrouchi K, Chemlal L, Taoufik J et al (2016) Synthèse, activités anti-oxydantes et analgésiques de bases de Schiff dérivées du 4-amino-1,2,4-triazole porteur d'un noyau pyrazole. Ann Pharm Fr 74:431–438
26. Pasupala P (2017) Synthesis and antioxidant studies of Schiff bases of 2-pyrazole substituted quinoline derivatives. Res J Pharm Biol Chem Sci 8:1415–1420
27. Siddhuraju P, Mohan PS, Becker K (2002) Studies on the antioxidant activity of Indian Laburnum (*Cassia fistula* L.): a preliminary assessment of crude extracts from stem bark, leaves, flowers and fruit pulp. Food Chem 79:61–67
28. Shukla S, Mehta A, Bajpai VK, Shukla S (2009) In vitro antioxidant activity and total phenolic content of ethanolic leaf extract of *Stevia rebaudiana* Bert. Food Chem Toxicol 47:2338–2343
29. Joyeux M, Lobstein A, Anton R, Mortier F (1995) Comparative antilipoperoxidant, antinecrotic and scavenging properties of terpenes and biflavones from Ginkgo and some flavonoids. Planta Med 61:126–129
30. Silva FAM, Borges F, Ferreira MA (2001) Effects of phenolic propyl esters on the oxidative stability of refined sunflower oil. J Agric Food Chem 49:3936–3941
31. Cole ST (2014) Who will develop new antibacterial agents? Philos Trans R Soc B Biol Sci 369:20130430
32. Malanovic N (2016) Gram-positive bacterial cell envelopes: The impact on the activity of antimicrobial peptides. Biochim Biophys Acta—Biomembr 1858:936–946
33. Antico Arciuch VG, Elguero ME, Poderoso JJ, Carreras MC (2012) Mitochondrial regulation of cell cycle and proliferation. Antioxid Redox Signal 16:1150–1180
34. Van Den Bogert C, Spelbrink JN, Dekker HL (1992) Relationship between culture conditions and the dependency on mitochondrial function of mammalian cell proliferation. J Cell Physiol 152:632–638
35. Jenkins SJ, Ruckerl D, Cook PC et al (2011) Local macrophage proliferation, rather than recruitment from the blood, is a signature of TH2 inflammation. Science 332:1284–1288
36. Jenkins SJ, Ruckerl D, Thomas GD et al (2013) IL-4 directly signals tissue-resident macrophages to proliferate beyond homeostatic levels controlled by CSF-1. J Exp Med 210:2477–2491
37. Amano SU, Cohen JL, Vangala P et al (2014) Local proliferation of macrophages contributes to obesity-associated adipose tissue inflammation. Cell Metab 19:162–171
38. Braune J, Weyer U, Hobusch C et al (2017) IL-6 regulates M2 polarization and local proliferation of adipose tissue macrophages in obesity. J Immunol 198:2927–2934
39. Martinez FO, Gordon S (2014) The M1 and M2 paradigm of macrophage activation: time for reassessment. F1000Prime Rep 6:13

Chapter 22
Thermal Modelling of Pulsed Laser Ablation of Silicon Nitride Ceramics

Ntombikazi Jojo, Cebolenkosi Philani Ntuli, Lerato Cresilda Tshabalala and Sisa Pityana

Abstract Pulsed laser systems have become a growing field in the past few years, especially in the treatment of the hard to machine engineering materials through conventional contact methods. As the challenge of the selection of efficient machining parameters is apparent, the modeled time dependent surface temperature and stress field evolution profiles will aid in improving the experimental design process. Due to the temperature gradient between the irradiated surface and the interior regions, excessive thermal residual stresses are induced in and around the heat affected zone. Depending on the laser intensity, the thermal stresses induced may lead to formation of micro-cracks and their propagation which can reduce the component fatigue life during its application. The current study aimed at understanding the evolution and distribution of thermal stresses on the material and to also evaluate the effect of laser energy intensity on the temperature and the induced thermal stresses. As a result of high temperatures involved, and a short interaction time associated with practical experiments, a computational approach in COMSOL Multiphysics was used. In the present research, the thermal modeling of High Frequency Nd:YAG in the machining of sintered silicon nitride ceramics was conducted. From the results, the model indicated that heating the target materials surface raises the temperature gradient which induced compressive thermal stresses. Two cycles were observed, the heating cycle where the laser was ON (0–250 ns) and cooling cycle during laser OFF time (after 250 ns).

N. Jojo (✉) · C. P. Ntuli

Department of Chemical, Metallurgical and Materials Engineering, Tshwane University of Technology, Pretoria West Campus, Room 2-152, Pretoria 0001, South Africa
e-mail: ntombitut@gmail.com

C. P. Ntuli
e-mail: cebontuli@gmail.com

L. C. Tshabalala · S. Pityana
Council for Scientific and Industrial Research (CSIR), National Laser Center, 46A Building, PO Box 395, Pretoria 0001, South Africa
e-mail: Ltshabalala1@csir.co.za

S. Pityana
e-mail: spityana@csir.co.za

22.1   Introduction

Outstanding mechanical and physical properties like high hardness, chemical stability and high thermal resistance have encouraged the use of silicon nitride (Si_3N_4) in several engineering applications such as crucibles, machine tools, optical and electronic devices [1, 2]. However, the low precision obtained during machining of Si_3N_4 has been an industrial challenge due to the hard and brittle nature of the material. Traditionally, grinding and polishing are employed for mechanical machining, yet they have been found to be accompanied by undesired surface damages like low reproducibility of surface roughness and micro-cracks [3]. The propagation of these surface cracks affects the material by lowering properties such as the toughness—which reduces the operational efficiency of the component.

To overcome these drawbacks, pulsed laser ablation (PLA) also known as pulsed laser machining (PLM) has been identified as a potential technique, as it has been an area of interest for several researchers in the past years [4–6]. It has been proven as a non-contact process with a capacity to machine even hard materials such as silicon nitride, alumina (Al_2O_3) and silicon carbide (SiC) ceramics with high accuracy and fast processing rates [7]. Pulsed laser ablation is a rapid heating and cooling process which is accomplished when the surface absorbs laser (photon) energy which is then converted into thermal energy. The magnitude of the laser energy absorbed depends on the initial absorptivity of the material and the temperature at the surface of the ceramic changes as the result of this absorbed energy [8]. PLA involves material removal by allowing the material to undergo heat conduction, melting and evaporation, melt expulsion and cooling as illustrated in Fig. 22.1, depending on the laser intensity which as the result determines the surface temperature of the ceramic [9]. The intense and localised heating of laser beam provides an extremely efficient method to increase the surface temperature of the work piece without affecting the bulk material, making the machining process convenient [10]. The quality of the ablation process depends on the processing parameters (pulse energy, laser frequency,
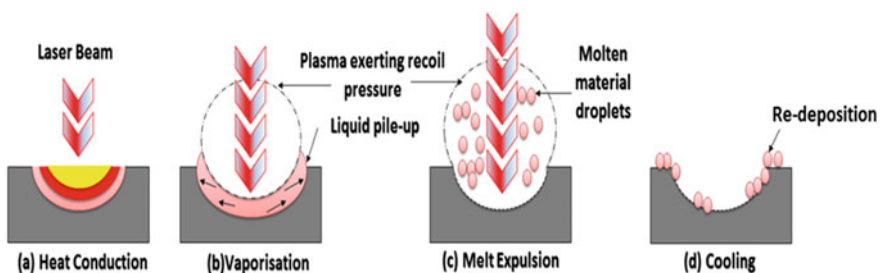
Fig. 22.1 Different phenomena in the surface of the material during PLA

pulse duration and peak power of the laser) and on the thermo-physical properties of the material such as density, latent heat of vaporization, and boiling point [7, 10].

However, due to the temperature gradient caused by the simultaneous heat conduction (by energy from the laser pulse), self-quenching (by the bulk material) and convection (by the environment) on the surface of the ceramic, excessive thermal stresses are induced in and around the heat affected zone. When the induced thermal stresses are above the silicon nitride's fractural strength (830 MPa), these stresses may promote micro-cracks formation and their propagation which reduces the component fatigue life during service [11]. Alongside other parameters such as pulse duration and laser beam diameter, laser pulse energy has a significant influence on the amount of heat transferred to raise the temperature of the material [6], which in return affects the induced thermal stresses.

There have been considerable efforts made by scholars on quantifying the thermal stresses induced on ceramics. The investigated approaches have been both experimental and computational work. In the early years, Ortiz and Molinari [12], conducted a review of microstructural thermal stresses in ceramic to study evolution of stresses in ceramics (PbTiO₃) which produced micro cracks in the grain boundaries of the ceramics. It was discovered that spontaneous micro cracking had significant influence on the mechanical, optical and thermal properties of the material. Most researchers such as Ortiz and Molinari [12] and Anderoglue [13], have used X-ray diffraction to measure the residual stress. It was discovered that when the residual stresses exist within the material, the inter-planar spacing becomes different than that of an unstressed state. This difference is proportional to the magnitude of the residual stress.

There are other alternative methods such as macroscopic residual stresses measurement which was investigated by Pfeiffer and Rombach [14], Prevey [15] including recent methods such as micro-Raman spectroscopy. Baratish et al. [16] also conducted a study on the evolution of thermal residual stresses in laser drilled alumina ceramics using Raman spectroscopy method. It was discovered that laser drilling of alumina induced thermal residual stresses which were initially tensile at the edge of the hole and transformed to compressive as the distance from the hole enlarged. Baratish et al. [16] also developed a two-dimensional surface flux model using COM-SOL Multiphysics to quantify the induced thermal stresses in order to compare with those measured by Raman spectroscopy.

Hence, the current study aimed at understanding the evolution and distribution of thermal stresses on the material and also to evaluate the effect of laser pulse energy on the resulting surface temperature and the thermal stresses. Additionally, the changes in the material surface morphology and chemistry associated with laser interaction phenomena will be evaluated. In this work, an Nd:YAG pulsed laser is used to study the physical interactions between pulsed laser beam and silicon nitride ceramic material. Due to high temperatures involved, and a short interaction time associated with practical experiments, a computational approach in COMSOL Multiphysics version 4.3 was employed. A two-dimensional time dependent laser ablation of silicon nitride will be demonstrated.

22.2 Methodology

22.2.1 Sample Preparation and Laser Ablation

A sintered silicon nitride ceramic (14% α-Si_3N_4, 76% β-Si_3N_4, 3% Al_2O_3, 2% Y_2O_3 and 5% SiC) was supplied by CeramTech, Germany. Pulsed laser ablation was performed using a 1064 nm, nanosecond (250 ns) neodymium-doped yttrium aluminium garnet (Nd:YAG) laser system (Quanta ray, spectral, 10 kHz frequency, manufactured by Laser tech, USA). The specimen was cross sectioned and the simulation was based on section AA, studying the effect of a single pulse illustrated in Fig. 22.2a, b. A two dimensional, time dependent model which represents a silicon nitride rectangular geometry of dimensions $1200 \times 200\ \mu m^2$ was created, as shown in Fig. 22.2c. The
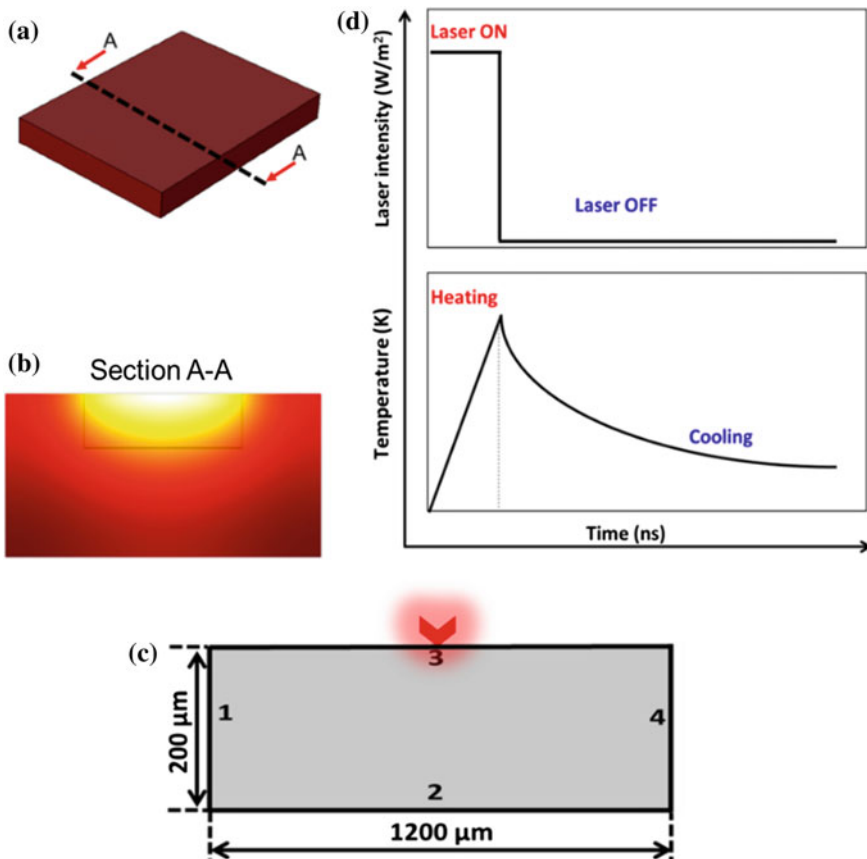
Fig. 22.2 Silicon nitride ceramic **a** in three dimensions **b** cross sectioned surface **c** single pulsed laser micro-machining two dimensional model geometry, and **d** waveform demonstrating the ON time of the laser

Table 22.1 Materials and process parameters for laser ablation of silicon nitride

Name	Expression	Units	Description	Ref
E_p	0.1, 0.15, 0.2	mJ	Pulse energy	[–]
Pw	250	Ns	Pulse time	[–]
D_b	40	μm	Laser beam diameter	[–]
λ	1064	μm	Wavelength	[–]
f0	10	kHz	Pulse frequency	[–]
Rc	0.14	[–]	Reflectivity	[17]
Kio	0.416	[–]	Extinction coefficient	[–]
Ac	1.47	1/m	Absorptivity	[–]
Em	0.7	[–]	Emissivity	[17]
ρ	3.440	g/cm^3	Density	[18]
K	28	W/m K	Thermal conductivity	[18]
C_p	800	J/(kg K)	Specific heat	[19]
A	4.4E−6	1/K	Thermal expansion coefficient	[19]
E	3.10E + 11	Pa	Elastic modulus	[19]
V	0.24	[–]	Poisson's ratio	[19]

Table 22.2 Summary of boundary conditions in the target material during PLA model

Physics	Physical condition	Boundary no.	Boundary condition	Variable
Heat transfer	Laser beam pulse	3	Heat flux	Q (W/m^2)
	Natural convective cooling	1, 3, 4	Convective cooling	h W/m^{2}K
	Radiation	3	Surface-to-ambient radiation	[–]
	Thermal insulation	2	Insulation	[–]
Thermal stresses	Prescribed displacement	1, 2, 3, 4	Linear elastic material	[–]

model involved Gaussian beam laser profile with laser ablation parameters defined as displayed in Tables 22.1 and 22.2 summarising the boundary conditions.

22.2.2 Thermal Stress Modelling

Thermal stresses were modelled in COMSOL Multiphysics version 4.3 (a), employing heat transfer and thermal stress physics. The model was based on the following assumptions:

- Initial roughness of the target surface has not been considered when modelling the surface ablation.
- The intensity of the beam used is of a Gaussian spatial distribution.
- Heat is supplied only by a single pulse.
- Pulse incidents on the centre of the target material in boundary 3 as illustrated in Fig. 22.2c.
- Boundary 2 is assumed to be insulated.
- The heat transfer in PLA can be solved using a 2D heat conduction.
- Heat flux acts as a thermal load for the induced thermal stress.
- Heat transfer modes are conduction, radiation and convection.
- Solid mechanics mode is linear elastic material for all boundaries.
- Thermal stresses are solved using Hooke's law.

The heat transfer governing equations and the heat flux are represented in Table 22.3, where the pulse ON time was represented by inserting a waveform $Pulse\left(t + \left(\frac{1}{f}\right)\right)$ represented in Fig. 22.2d.

The geometry was then meshed to extra fine element size. The flowchart of the model is indicated in Fig. 22.3. The laser treated surfaces were also taken for SEM analysis with compositions detected by EDX (Table 22.4).

Table 22.3 Model equations

Boundary condition	Equation	Equation number
Heat transfer	$\rho C_p \frac{\partial T}{\partial t} + \rho C_p u \nabla T = \nabla \cdot (k \nabla T) + Q$ $T = T_{amb} = 298$ K	22.1
Heat flux (Q)	$Q(x, t) =$ $I_o \times Ac \times Gaussian\ space \times Pulse\left(t + \left(\frac{1}{f}\right)\right)$	22.2
	$Gaussian\ space = \exp\left[\left(-0.5\left(\frac{x-x0}{r}\right)^2\right)\right]$	22.3
	$Pulse\left(t + \left(\frac{1}{f}\right)\right) = 1, 0 < t < Pw; Pw < t <$ $Pw + \left(\frac{1}{f}\right)$ $\left(\frac{1}{f}\right)$ represents the time step	22.4
Radiation	$-n \cdot (-k \nabla T) = \varepsilon \sigma (T^4 amb - T^2)$ $\varepsilon = 0.7$ $\sigma = $ Stefan-Boltzmann constant $(5.67 \times 10^{-8}$ W/m^{2}K^4)	22.5
Convection	$-n \cdot (-k \nabla T) = h \cdot (T_{amb} - T)$ $h = 10 W/(m^2 \cdot K)$	22.6
Thermal stresses	$\sigma_{ther} = s$	22.7
	$s - s_o = C(\in -\varepsilon_o - \varepsilon_{inel})$	22.8
	$\in_{nel} = \alpha(T - T_{amb})$	22.9
	$\sigma_{ther} = \frac{E\alpha}{1-\nu} \Delta T$	22.10
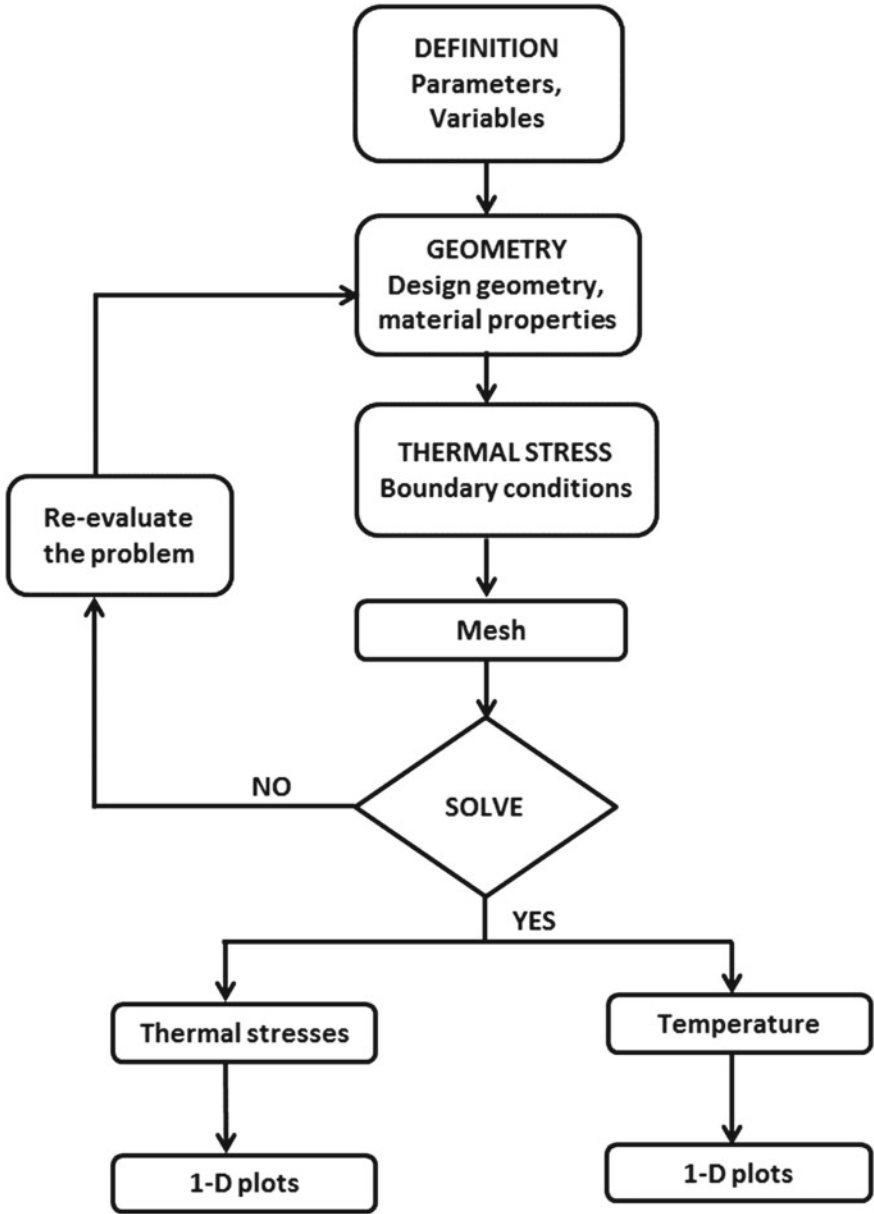
Fig. 22.3 Flowchart of the computational model

Table 22.4 List of chemical equations during laser ablation of silicon nitride

Physical process	Chemical equation	Equation number	Refs.
Dissociation	$Si_3N_{4(S)} + 910 \text{ kJ/mol} \rightarrow 3Si_{(l)} + 2N_{2(g)}$	22.11	[20]
Dissociation	$SiC_{(s)} + 115.52 \text{ kJ/mol} \rightarrow Si_{(l)} + C_{(s)}$	22.12	[21]
Solidification	$Si_{(l)} \leftrightarrow Si_{(s)} + 50.22 \text{ kJ/mol}$	22.13	[4]
Dissociation	$Al_2O_{3(s)} + 163.00 \text{ kJ/mol} \rightarrow 2Al_{(l)} + \frac{3}{2}O_{2(g)}$	22.14	[22]
Oxidation	$2Si_3N_{4(s)} + 3O_{2(g)} + 4076.88 \text{ kJ/mol} \rightarrow 6SiO_{(g)} + 4N_{2(g)}$	22.15	[22]
Oxidation	$SiO_{(g)} + \frac{1}{2}O_{(g)} \rightarrow SiO_{2(g)} + 1336.08 \text{ kJ/mol}$	22.16	[20]
Oxidation	$2C_{(s)} + O_{2(g)} \rightarrow 2CO_{(g)} + 221.05 \text{ kJ/mol}$	22.17	[20]
Oxidation	$2CO_{(g)} + O_{2(g)} + 565.97 \text{ kJ/mol} \rightarrow 2CO_{2(g)}$	22.18	[4]

22.3   Results and Discussion

One dimensional ablation of silicon nitride ceramics was simulated using COM-SOL Multiphysics. Silicon nitride ceramic was heated with a single laser pulse of a Gaussian spatial distribution. The laser energy was varied from 0.1, 0.15 to 0.2 mJ.

22.3.1   Thermal Stress Modelling

The surfaces of the target material are illustrated in Fig. 22.4, with (a) representing heated surface and (c) representing thermally stressed surface at respective laser energy and pulse width (250 ns). The temperature (Fig. 22.4b) and thermal stress profiles (Fig. 22.4d) as a function of specimen width (x) were then predicted. The temperature distribution was predicted on the top surface (boundary 3). Due to Gaussian distribution of the laser beam, the beam center had higher laser energies which gradually decreased towards the edges of the ceramic. This led to higher surface temperature in the central region compared to the edges as observed in Fig. 22.4b. As a result, the material experienced higher temperature gradient, in so doing inducing higher compressive thermal stresses in the center than at the edges of the material (Fig. 22.4d). At the laser energy of 0.1 mJ, maximum temperature reached was 2800 K in the beam center. This resulted into maximum of 5.5 GPa of thermal stresses in the center, decreasing towards the beam edges according to thermal gradient difference. At increased laser energy of 0.15 and 0.2 mJ, the surface temperature also increased as observed in Fig. 22.4b to maximum of 4000 and 5300 K respectively in the beam center. This also influenced the resulting thermal stresses to 8.7 and 11.9 GPa respectively (Fig. 22.4d).

Figure 22.5a, b illustrate the temperature and thermal stress distribution with respect to time on the material. Initially, the material was at room temperature (273 K). As soon as the 0.1 mJ pulse was incident on the surface of the material, the energy
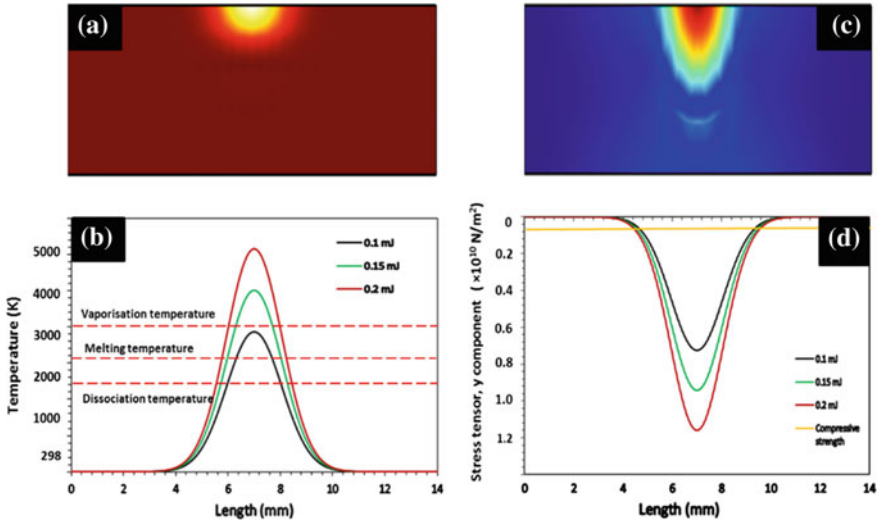
Fig. 22.4 **a** Heated surface output **b** surface peak temperatures along the width **c** thermal stressed surface output, and **d** maximum induced thermal stresses along the width
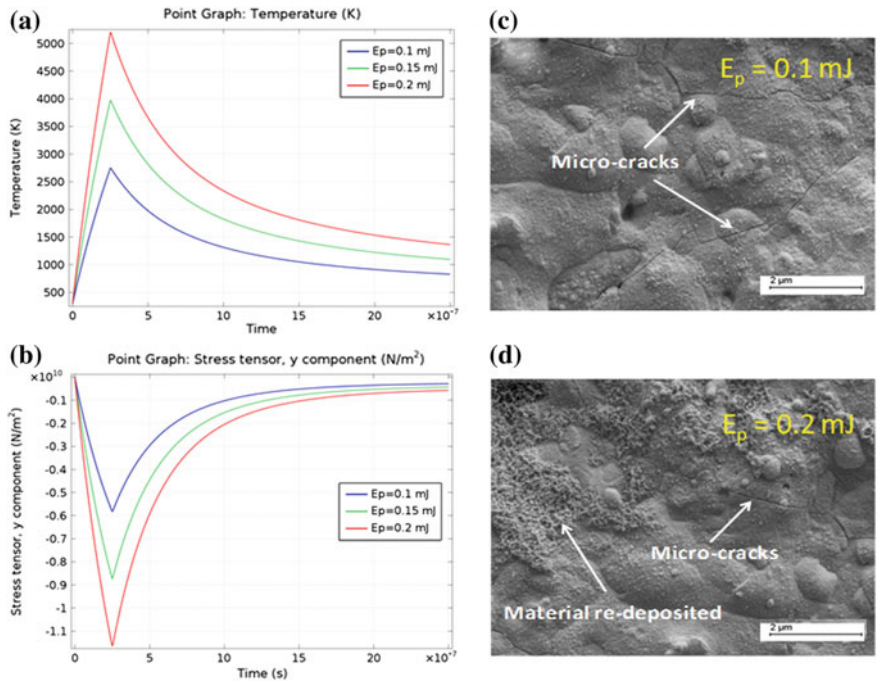
Fig. 22.5 **a** Computational plot of time and peak temperatures **b** time and induced thermal stresses, **c** and **d** SEM image at pulse energy 0.1 and 0.2 mJ

was transferred to the material and converted into heat which was absorbed by the material, raising the surface temperature of the material to maximum of 2800 K. This took place between 0–250 ns when the laser was ON in the heating cycle (Fig. 22.5a). When the laser is incident, the surface temperature increased with increasing irradiation time, reaching maximum temperature at laser ON-time and then decreased. As soon as the laser was turned OFF, the cooling cycle began wherein the surface temperature gradually dropped down approaching the room temperature. This was the case for all the different energy pulses simulated as observed in Fig. 22.5a. As previously observed, the thermal stresses also followed the temperature distribution where in this case between 0 and 250 ns the stresses were increasing, then slowly decreased with time when the laser was OFF (Fig. 22.5b).

It can be observed in Fig. 22.4b, d that the induced thermal stresses were higher than 830 MPa which is the fractural strength of silicon nitride for all the laser energies. This allowed the possibility of extensive surface damages such as micro-cracks in the region illustrated in Fig. 22.5c, d.

22.3.2   Surface Chemistry and Topography

Figure 22.5c, d illustrate scanning electron microscopy (SEM) images of the machined surfaces captured demonstrating the nucleated micro-cracks in respective laser energy intensities. Figure 22.5c illustrates the cracks that developed when the surface was ablated with the pulse energy of 0.1 mJ. The melt pool is evident on the residual surface. At increased pulse energy of 0.2 mJ, the material that vaporized and redeposited during crystallization can also be seen on the residual surface in Fig. 22.5d, corresponding to the temperature above vapor point obtained while ablating at this energy pulse.

The as received and ablated surfaces were further taken for analysis by EDX. Fig 22.6a illustrates the SEM surface of as received with Fig. 22.6b representing the EDX results, while Fig. 22.6c, d illustrate the SEM and EDX of laser ablated surface respectively. It is observed that the EDX result for as received indicates high nitrogen content of 54.10% which is followed by silicon at 19.74% and oxygen at 12.97%. However, after machining the surface with a pulsing laser the EDX results indicate a high drop of nitrogen to 11.00% with an increase in silicon to 52.02%. The change in composition was as the result of the reactions that took place during ablation where the material underwent melting, vaporisation and re-solidification. The occurrence of these laser treatment phenomena is observed in the SEM of the laser treated surface which indicates the redeposited material on the residual surface as discussed earlier.

The dissociation of silicon nitride and silicon carbide that took place are described by Eqs. 22.11 and 22.12. For this work, the enthalpy for all the dissociation reactions was provided by the laser pulse. The silicon provided by Eqs. 22.11 and 22.12 solidified according to Eq. 22.13 and led to an increase in silicon (19.74–52.02%) detected by EDX in the residual surface in Fig. 22.6d. The dissociation of silicon nitride also

(a) As-recieved   20 µm

(b) Spektrum 11

Element	Mass (%)	Atom (%)
C	10.41	13.66
N	54.10	60.87
O	12.97	12.77
Al	2.79	1.63
Si	19.74	11.07

Skalenbereich 317 cts Cursor: 0.129 (18 cts)   keV

(c) $E_p = 0.15$ mJ   Microcracks   2 µm

(c) Spektrum 7

Element	Mass (%)	Atom (%)
C	8.25	13.62
N	11.00	15.57
O	25.71	31.87
Al	3.02	2.22
Si	52.02	36.72

Skalenbereich 871 cts Cursor: 0.092 (42 cts)   keV
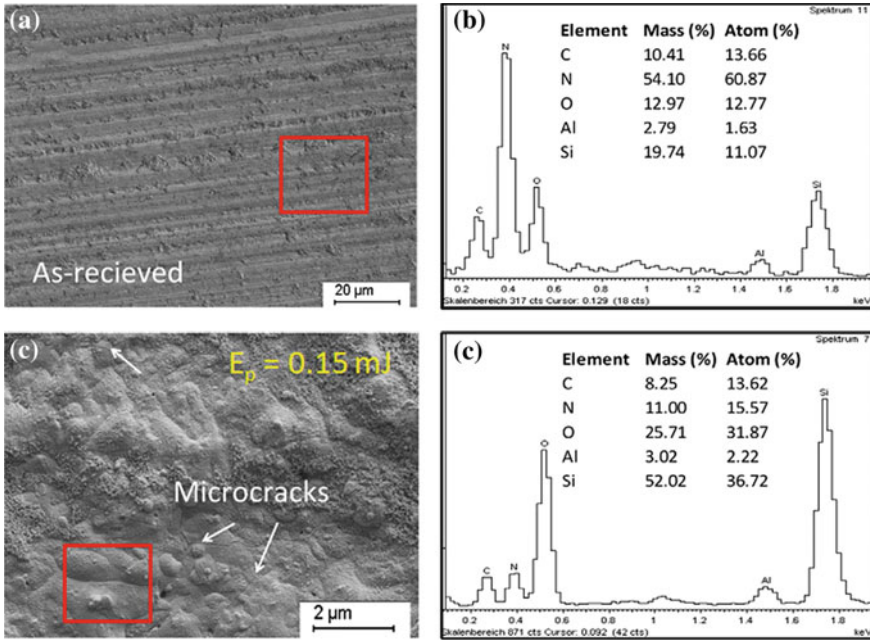
Fig. 22.6 **a** SEM of the as received surface, **b** EDX of the as received surface, **c** SEM of machined at 0.15 mJ pulse energy, and **d** EDX of the machined surface at 0.15 mJ

led to the loss detected in nitrogen (54.10–11.00%) where the released nitrogen gas escaped to the atmosphere contributing to plasma (plume gases) formation previously illustrated in Fig. 22.1b, c. Aluminium oxide also underwent dissociation as per Eq. 22.14 resulting in aluminium increase from 2.79 to 3.02%. There were also several oxidation reactions that took place.

The increase in oxygen from 12.97 to 25.71% was the result of silicon nitride oxidation at enthalpies 4076.88 kJ/mol as per Eq. 22.15 forming vapours of SiO. The formed SiO vapour was further oxidised to form solid SiO_2 (Eq. 22.16) which redeposited onto the surface. The carbon from SiC dissociation (Eq. 22.12) reacted with the oxygen in the atmosphere forming carbon dioxide according to Eqs. 22.17 and 22.18 with about 2.16% of carbon lost to the atmosphere, contribution to the plume gases. The formation of these oxides (silicon dioxide and carbon dioxide) led to an increase in detected oxygen content in the residual surface.

22.4 Conclusions

A two dimensional COMSOL Multiphysics model of laser ablation of silicon nitride ceramics has been developed. The evolution and distribution of thermal stresses

were studied together with changes in surface temperature on the material. The pulse energy was varied from 0.1, 0.15 to 0.2 mJ to evaluate the effect of laser pulse energy on the resulting surface temperature and the thermal stresses. The changes in the material surface morphology and chemistry associated with laser interaction phenomena's were also evaluated. The following were found:

- Energy was transferred from the laser source to the surface of the material, raising the temperature to as high as 2800 K at 0.1 mJ, also taking into consideration the heat loss through convection and radiation.
- The model indicated that heating the target materials surface raises the temperature gradient which induced compressive thermal stresses.
- Two cycles were observed, the heating cycle where the laser was ON (0–250 ns) and cooling cycle during laser OFF time (after 250 ns).
- A steep heating curve was observed in the first 250 ns, followed by a gradual decrease in the slope after 250 ns when the material was cooling.
- Gaussian distribution of heat also influenced the surface temperature and compressive stress distribution was higher in the beam center, decreasing towards the edges of the target material.
- Increasing the pulse energy led to an increase in surface temperature, which later increased the induced stresses.
- Under all the energy conditions, the resulting thermal stresses were above the target materials flexural strength, increasing the possibility of evolution and expansion of surface micro-cracks which were observed under SEM microscopy.
- Surface morphology of the material was dominated by dissociation and oxidation reactions on the residual surface, with most dominant reactions being endothermic.
- The heat for endothermic reaction was provided by the laser pulse.
- Ablating the material with a pulsing laser increased the surface content of silicon, aluminium and oxygen while there was a decrease in nitrogen and carbon content.

References

1. De Faoite D, Browne DJ, Chang-Diaz FR, Stanton KT (2011) A review of the processing, composition, and temperature-dependent mechanical and thermal properties of dielectric technical ceramics. Mater Sci 47:4211–4235
2. Klotizibach U, Lasagni FA, Panzner M, Franke V (2011) Laser ablation. Adv Struct Mater 10:29–45
3. Zhang GM, Amand DK, Ghosh S, Ko MK (1993) Study of the formation of macro and micro cracks during machining of the ceramics. NIST Spec Publ 847:465–478
4. Samant AN, Dahotre NB (2009) Differences in physical phenomena governing laser machining of structural ceramics. Ceram Int 35:2093–2097

5. Vora HD, Dahotre NB (2015) Multiphysics theoretical evaluation of thermal stresses in laser machined structural alumina. Lasers Manuf Mater Process 2:1–23
6. Vasantgadka AN, Bhandarkar UV, Josho SS (2010) A finite element model to predict the ablation depth in pulsed laser ablation. Thin Film Solids 519:1421–1430
7. Majumda JD, Manna I (2013) Introduction to laser-assisted fabrication of metals. Mater Sci 161:1–69
8. Dubey AK, Yadava V (2008) Laser beam machining—a review. Int J Mech Tools Manuf 48:609–628
9. Samant AN, Dahotre NB (2008) Computational prediction in single-dimensional laser machining of alumina. Int J Mach Tools Manuf 48:1345–1353
10. Meijer J (2004) Laser beam machining (LBM), state of the art and new opportunities. J Mater Process Technol 149:2–17
11. Zhang W, Yao YL (2001) Feasibility study of inducing desirable residual stress distribution in laser micro-machining. Transactions of the North American Manufacturing Research Institution of SME (NAMRC XXIX), pp 413–420
12. Ortizs M, Molinari A (1988) Microstructural thermal stresses in ceramic materials. Mech Phys Solids 36:385–400
13. Anderoglue O (2004) Residual stress measurement using X-ray diffraction. Master of Science Thesis, Texas A&M University, USA
14. Pfeiffer W, Rombach M (1999) Macroscopic and microscopic residual stresses in ceramics due to contact loading. Adv X-Ray Anal 41:493–500
15. Prevey PS (1986) X-ray diffraction residual stress techniques. Am Soc Metals 380–392
16. Baratish A, Narasimhamurthy HN, Aditya G, Anand B, Satyanarayana BS, Krishna M (2015) Evaluation of thermal residual stresses in laser drilled alumina ceramics using micro-Raman spectroscopy and COMSOL Multiphysics. Optics Laser Technol 70:76–84
17. Rihakova L, Chmelickova H (2015) Review article: laser ablation of glass, silicon, and ceramics. Adv Mater Sci Eng 2:1–6
18. Riley FL (2000) Silicon nitride and related materials. J Am Ceram 83:245–265
19. Smith FW (2006) Foundation of material science and engineering, 4th edn. Mc Graw Hill, New York, USA
20. Shulka PP, Lawrence J (2010) Surface characterization and compositional evaluation of a fibre laser processed silicon nitride engineering ceramic. Laser Eng 20:359–380
21. Samant AN, Dahotre NB (2009) Laser machining of structural ceramics. J Eur Ceram Soc 29:969–993
22. Vora HD, Santhanakrishnan S, Harimkar SP, Boetcher SKS, Dahotre NB (2013) One-dimensional multi-pulse laser machining of structural alumina: evolution of surface topography. Inter J Adv Manuf Technol 68:69–83

Chapter 23
Comparative HPLC Study of Isomers of *N*,*N*′-2,3-Butylenebis(Trifluoroacetylacetoniminato) Copper(II) and Palladium(II) Chelates Using Silica-Based and Zirconia-Based Stationary Phase

David Tanyala Takuwa

Abstract   The development of newer columns in chromatography is geared towards improving their selectivity towards given analytes or improvement in the column chemical stability. In recent years, the development of zirconia stationary phase brought hope of working at extended pH and high temperatures when compared to silica-based stationary phase. In this study, isomers of both copper and palladium were studied by varying pH and temperature on silica based columns (SymmetryShield™ C18 (150 mm × 3.9 mm), J'sphere ODS H-80, C18 (150 mm × 4.6 mm)) and zirconia based column (DiamondBond-C18 (150 mm × 4.6 mm)). The results obtained revealed that increase in pH on zirconia-based columns led to the formation of multi-charged retention sites that resulted in the baseline resolution of the four isomers, in contrary to silica-based columns that could not resolve the four isomers under the same condition, but within pH range of 2–8. Temperature variations did not yield any improvement on the results obtained with silica-based columns. Silica columns were limited to maximum temperatures of 60 °C. The effect of high temperature on the DiamondBond C-18 was found to reduce the retention times and increase selectivity, resolution and column efficiency of the compounds, which are factors desirable for successful chromatography. In addition, there was improvement in the peak height on DiamondBond C-18 column, which could be beneficial for quantitative analyses through enhanced signal to noise ratio for lower detection limits. This study revealed the benefits of zirconia substrate due to its extended pH ranges and high temperatures, making this newer column to be of interest for application of a variety of chromatographic analyses.

Keywords HPLC · Chelates · Isomers · Silica and zirconia stationary phases · pH and temperature

D. T. Takuwa (✉)
Department of Chemistry, University of Botswana, P/Bag UB 00704, Gaborone, Botswana
e-mail: takuwadt@mopipi.ub.bw

23.1 Introduction

The development of organic compounds incorporating metals, such as those finding utility as drugs [1] and in applications such as selective sensor electrodes [2] and catalysis [3] continue to necessitate analytical application of high performance liquid chromatography (HPLC). Recently, a challenge has been in preparing compounds with high purity of an active isomer. Isomers are compounds that have identical type and number of atoms, but differ in their spatial conformation. Sometimes these isomers may display closely similar chemical and physical properties, making it difficult to resolve them using conventional analytical separation methods. In biological and clinical systems, it has been observed that a non-active isomer may contribute to side effects, toxicity, and/or even be antagonist to the activity of the active isomer [4]. The synthesis and catalytic application of particular metal complex isomers for specialized reactions is also receiving considerable attention [5, 6].

In the last few decades, many reversed-phase HPLC stationary phases have been developed with aims of improving their efficiency, selectivity and chemical stability with hopes of increasing the separation power of this technique [7–9]. Unfortunately, such developments have received little attention with respect to the separation of isomers of metal complexes. A common scenario where reversed-phase HPLC columns are utilized for isomer separation, is when they are employed with a chiral selector [2, 3]. Such application of HPLC columns which reduces emphasis on resolution is likely to result in minimizing the benefits that these newer stationary phases could offer as separation systems, and also results in unnecessary extra costs for specific detection.

The zirconia substrate is of particular interest because of its thermal and chemical stability with the possibility for use over a wider pH range than the silica based columns [10]. The zirconia substrate also has the ability to display different surface charges depending on the pH and type of buffer, allowing electrostatic interactions of this surface with the analyte [10, 11]. Jackson et al. [12] used a carbon coated zirconia column to separate isomers of pharmaceutical compounds. However, the isomers were derivatized with Mosher's reagent to make diastereomeric pairs before their determination. When comparing selectivities of zirconia-based columns, DiamondBond-C18 and ZirChrom-Carb displayed an improved selectivity over the other zirconia-based columns in the separation of bases, non-electrolytes, isomers, and diastereomers [13]. These two columns were capable of giving a baseline resolution of the ethylbenzene and p-xylene, a separation which is usually difficult with conventional reversed-phase HPLC columns. A decade ago, baseline separation of toluidine, aminophenol, nitroaniline, nitrophenol and dihydroxybenzene isomers was achieved by a zirconia stationary phase modified with dodecylamine-*N*,*N*-dimethylenephosphoric acid [14].

The goal of this study is to take advantage of the improved selectivity and electrostatic interactions of a zirconia phase with the analyte when pH and temperature are varied, thereby to determine if this stationary phase separates metal complex positional isomers. The isomers of copper(II) and palladium(II) complexes were

chosen because of ongoing effort in drug development and catalysis using organic complexes of these metals around the world [1, 14–16]. Temperature and pH variations are known to contribute to the best peak shape and resolution of these isomers within the shortest possible time [17, 18]. Reversed-phase silica-based columns were compared with reversed-phase DiamondBond-C18, a zirconia column, in separating the isomers of Cu(II) and Pd(II) N,N'-2,3-butylenebis(trifluoroacetylacetoniminato) complexes in this study.

23.2 Experimental

23.2.1 Instrumentation

The chromatographic measurements were performed using model 2695 HPLC instrumentation equipped with a Waters 2487 dual wavelength absorbance detector (Waters, Milford, MA, USA). The data were acquired and processed with a Compaq Pentium III computer equipped with millennium 32 software (Waters, Milford, MA, USA). Temperature of the columns was regulated using a model 7956 heater chiller (Jones Chromatography, UK). pH was measured by a Corning 125 pH meter on aqueous samples before mixing with the organic modifier. The pH meter was calibrated with pH 4.0 and 7.0 standard solutions each time a buffer solution was prepared. Columns used were SymmetryShield™ C18 (150 mm × 3.9 mm), J'sphere ODS H-80, C18 (150 mm × 4.6 mm) with silica stationary phase, both from Waters Inc., Milford, USA and DiamondBond-C18 (150 mm × 4.6 mm) manufactured by ZirChrom Separations, Anoka, MN, USA. A frit (0.5 µm stainless steel) from UpChurch Scientific and C-18 water reversed-phase sentry guard columns were connected between the injection port and the column to protect the column from damage from materials in the sample.

23.2.2 Chemicals

An HPLC grade acetonitrile (Fisher Scientific) was used as solvent or organic modifier. Monobasic potassium phosphate and phosphoric acid (HPLC grade) (Fisher Scientific) were used to prepare buffer solutions at pH 2.15, 7.20 and 12.15. These values correspond to the three-pKas of phosphoric acid, each optimizing buffering capacity for phosphate buffer. A mobile phase of 50% acetonitrile and 50% 30 mM phosphate buffer at the respective pHs was used throughout the study. The analytes were all detected at 275 nm. This wavelength was determined from ultraviolet/visible absorption spectra of the compounds analyzed.

The metal complex isomers used were *cis* and *trans* copper(II) and palladium(II) chelates of N,N'-2,3-butylenebis(trifluoroacetylacetonimine), Cu(bnTFA$_2$)

Fig. 23.1 Representative
structure of N,N'-2,3
butylenebis(trifluoroacetylacetoniminato)
metal chelates (M = Cu(II)
or Pd(II))
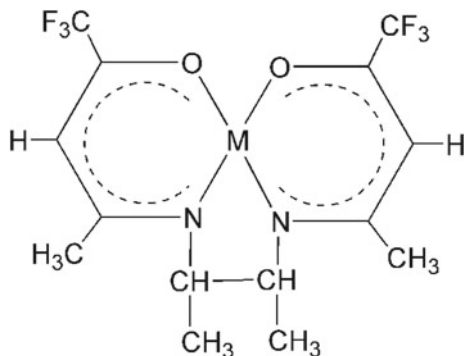
and Pd(bnTFA$_2$) (Fig. 23.1). These metal complex isomers were prepared in an
earlier study and donated by Professor Uden [19, 20].

23.3 Results and Discussion

23.3.1 Optimization of Working Conditions

The separation of Cu(II) and Pd(II) chelates of N,N'-2,3-
butylenebis(trifluoroacetylacetoniminato) was initially investigated with 50%
acetonitrile and 50% of 30 mM phosphate buffer mobile phase (pH 2.15) with
J'sphere ODS H-80 and SymmetryShield, C18 columns at 5 °C. Lower temperature
is known to increase the retention of isomers with subsequent improvement in
resolution [17, 21]. The statistics of the results in this study were reported with 95%
confidence level. For the silica based columns, SymmetryShield and J'sphere under
the above conditions, the Cu(II) isomers were separated with baseline resolution,
with the *cis* isomer being less retained (Fig. 23.2a, b, peaks 1 and 2). A symmetrical
peak (USP tailing factors ca. 1.0) was observed for the Pd(II) isomers indicating
no resolution at all (Fig. 23.2a, b, peaks 3 and 4). Variation of organic modifier and
buffer concentrations did not produce any improvement in the resolution of the Pd(II)
isomers. Also, no improvement was observed in the resolution of Pd(II) isomers
when the temperature was reduced to 0 °C. There was no significant difference in
the retention times, USP tailing factors and USP resolution of all the analytes at
both 5 and 0 °C for the silica-based columns. When the temperature was increased
to 40 °C, there was no improvement in the resolution of the complexes, except the
reduction of retention times. The areas of the peaks did not differ significantly as a
function of temperature, which was an additional indication that the analyte was not
lost or degraded as temperature was increased.

When no resolution on the Pd(II) isomers was obtained using the silica-based
columns, the DiamondBond-C18, with a zirconia substrate, was evaluated. Similar
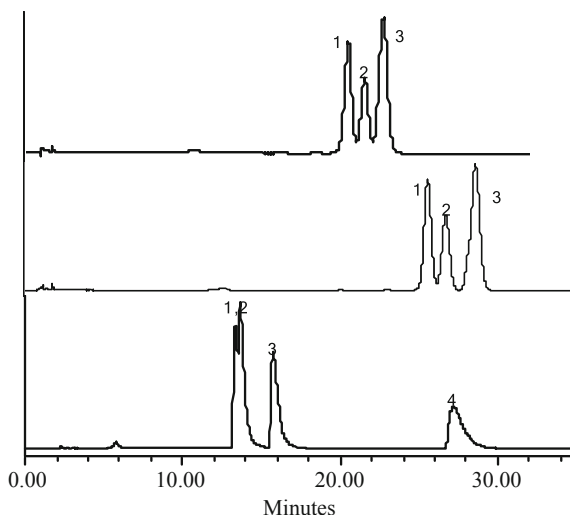
Fig. 23.2 Chromatograms of Cu(II) and Pd(II) *N,N′*-2,3-butylenebis(trifluoroacetylacetoniminato) isomers using: **a** SymmetryShield™ C18, **b** J'sphere ODS H-80, **c** DiamondBond-C18 columns in (50:50 v/v) acetonitrile:30 mM phosphate buffer (pH 2.15) at column temperature 5 °C and detection wavelength 275 nm. Peaks (1 = *cis*-Cu(II) and 2 = *trans*-Cu(II) isomer; 3 = *trans*-Pd(II) and 4 = *cis*-Pd(II) isomers)

conditions as for the silica-based columns were used with this column: (50:50 v/v) acetonitrile:30 mM phosphate buffer (pH 2.15), with a temperature of 5 °C. In contrast to the results obtained with silica-based columns, the Pd(II) isomers were completely resolved (Fig. 23.2c, peaks 3 and 4) but there was very little resolution of the Cu(II) isomers, a doublet peak being formed (Fig. 23.2c, peaks 1 and 2). The *trans* isomer was less retained than the *cis* in the case of Pd(II) isomers, which is reversed from the elution order for the Cu(II) isomers on the silica-based columns.

Reduction in temperature to 0 °C and variations in the concentrations of organic modifier and buffer solution did not resolve the Cu(II) isomers on the DiamondBond-C18. When the temperature was increased to 40 °C, the doublet peak observed for Cu(II) isomers was lost, and a single symmetrical peak with a USP tailing factor of 1.06 was produced. Lower temperatures typically give better resolution of isomers because of a reduced rate of isomerization, which ensures each isomer can pass through the column unchanged [17]. Hence, the loss of resolution for the Cu(II) isomers at an elevated temperature might be due to an increased rate of inter-conversion between the *trans* and *cis* isomers. However, it could also be that the *cis* isomer for Cu(II) was relatively more desorbed than the *trans* isomer at high temperature leading to less retention time for the former, resulting in co-elution of the two isomers. When comparing the results obtained on the silica-based columns to those from DiamondBond-C18, it was clear that the separation of Cu(II) and Pd(II) isomers was controlled by different mechanisms. To understand the behavior of these isomers, 50% acetonitrile and 50% of 30 mM phosphate buffer mobile phase at 5 °C were selected for further studies.

23.3.2   Effect of Changing pH of the Phosphate Buffer Solution

23.3.2.1   Effect of Phosphate Buffer at pH 7.20

The results obtained from above study indicated that variations in the organic content of the mobile phase and column temperature would be very difficult to manipulate to get resolution of the Cu(II) and Pd(II) isomers in a single chromatogram using either silica or DiamondBond-C18 based columns. However, the other option was to vary the pH of the mobile phase with hopes of creating a substrate with different electrostatic interaction, especially for the zirconia-based column. For silica-based columns the results obtained by increasing pH from 2.15 to 7.20 were not significantly different from each other, which was from being very acidic to being neutral. Resolution was only observed for the Cu(II) isomers and not Pd(II) isomers, as was the case at pH 2.15. The retention factors, USP tailing factors, USP resolution and USP plate count for the analytes were also not significantly different between pH 2.15 and 7.20 for these columns (Table 23.1).

The above results suggested one mechanism that predominantly controlled the separation of these isomers at both the pHs when using silica-based columns. In an effort to explain the separation mechanism that was occurring on the silica columns, it is noted that the surface of the silica substrate has zero charge at pH below 3, thereafter it becomes slightly negative up to about pH 7, and then gets strongly negative as pH is increased after 7 [22, 23]. Based on the zero charged surface of the silica substrate at pH 2.15, separation of the isomers would be controlled mainly by hydrophobic interactions, which strongly suggests that the copper(II) complexes are likely to be more hydrophobic than the Pd(II) isomers. The size of Cu^{2+} ion is relatively smaller than that of Pd^{2+} enabling bnTFA, the chelate to enclose it completely thus making the metal complex behave like an organic molecule with very weak electrostatic interactions, allowing this molecule to interact with the C-18 substrate on the silica column predominantly through "reverse phase mode" interaction.

Increasing the pH from 2.15 to 7.20 on the silica-based columns created a weakly negatively charge surface on the silica substrate. However, the effect of this negatively charged surface seems to have had very little effect on the resolution of the Pd(II) isomers. Silica-based columns are generally believed to undergo a two-mode retention separation mechanism involving reversed-phase (hydrophobic) interactions and ionic exchange (usually for basic compounds) interactions [24]. Hydrophobic interactions predominate at lower pH, whereas ion exchange interaction is strong at high pH. Unfortunately, the benefits of ion exchange surface on silica-based columns are not fully utilized because the silanol groups on the silica substrate start dissolving with increase in pH above 7.5, producing irreproducible data with poor column efficiency [25].

On the other hand, when pH was increased from 2.15 to 7.20 using the DiamondBond-C18 column, resolution of both the Cu(II) and Pd(II) N,N'-2,3-butylenebis(trifluoroacetylacetoniminato) isomers was observed (Fig. 23.3).

Table 23.1 Comparison of chromatographic behavior of Cu(II) and Pd(II) N,N'-2,3-butylenebis(trifluoroacetylacetoniminato) isomers on J'sphere ODS H-8 C18 and SymmetryShield™ C18 columns using (50:50 v/v) acetonitrile:30 mM phosphate buffer at pH 2.15 and 7.20 at column temperature of 5 °C and wavelength 275 nm

Column	Metal complex isomers	Retention factor (k') (× 10)		USP resolution		USP tailing factors		USP plate count (× 10^4)	
		pH 2.15	pH 7.20	pH 2.15	pH 7.20	pH 2.15	pH 7.20	pH 2.15	pH 7.20
J'sphere ODS H-8 C18	Cis-Cu(bnTFA₂)	2.06	2.07	–	–	1.01	1.03	1.57	1.57
	Trans-Cu(bnTFA₂)	2.15	2.17	1.36	1.40	1.01	0.98	1.70	1.70
	Trans/Cis-Pd(bnTFA₂)	2.29	2.31	1.86	1.92	1.04	1.02	1.35	1.40
Symmetry Shield C18	Cis-Cu(bnTFA₂)	1.15	1.17	–	–	0.94	0.86	1.05	0.95
	Trans-Cu(bnTFA₂)	1.21	1.24	1.22	1.20	0.98	0.87	1.05	0.98
	Trans/Cis-Pd(bnTFA₂)	1.28	1.27	1.18	1.24	0.95	0.88	0.96	0.86

Fig. 23.3 Chromatogram for Cu(II) and Pd(II) *N*,*N*′-2,3-butylenebis(trifluoroacetylacetoniminato) isomers using DiamondBond C-18 column using 50:50 (v/v) acetonitrile:30 mM phosphate buffer (pH 7.20) at column temperature 5 °C and detector wavelength 275 nm

According to Henry [22] the net charge on a zirconia surface is strongly positive at low pH of below 3. Above pH 3, the charge on the surface becomes weakly positive until about pH 6.5, where it becomes close to zero until about pH 7.5. Thereafter, it steadily becomes strongly negative with increase in pH. The reduction in the positive electrostatic interaction of the zirconia substrate from low pH to mid pH increases the hydrophobicity of the column as pH is increased. At low pH, hard Lewis bases such as phosphate, nitrate, hydroxide, carboxylate and fluoride ions adsorb strongly to the zirconia (hard Lewis acid sites) substrate altering the charge that would be otherwise observed on this surface [26]. In this study using the phosphate buffer in the eluent, the PO_4^{3-} ions adsorbed to the zirconia substrate creating a negative charge surface even at lower pH, where bare zirconia usually displays a positive charge [11, 26]. In the presence of an ion exchange surface (e.g. due to PO_4^{3-} ions) on a hydrophobically coated zirconia column [23] (e.g. zirconia coated with polybutadiene), a three-site retention model for interaction of a zirconia substrate and analyte has been proposed [24, 26]. The proposed three-site retention model for zirconia-based columns includes "pure" reversed-phase, "pure" ion exchange and hydrophobically assisted ion-exchange sites.

The existence of multipoint interaction between the stationary phase and analyte has been used to improve selectivity and separation of complex compounds such as chiral isomers [27]. It is believed that the Pd(II) ion in the bnTFA complex could possibly have Lewis acidic sites which interacted with the hard Lewis base, PO_4^{3-} ions, adsorbed on the zirconia substrate at low pH, producing a multipoint interaction between the Pd(II) isomers and the stationary phase. At lower pH ca. 2.15 with the phosphate buffer, the ionic exchange retention mode is likely to have predominated over the interaction of the zirconia substrate and the analytes. It was expected that since "pure" hydrophobic (reversed phase) interaction is limited at this pH, the more hydrophobic Cu(II) isomers would not be separated, but their resolution should improve with increase in pH, since the hydrophobicity of the zirconia is improved with increase of pH to about 7 [22, 23]. At pH 7.20 both the Cu(II) and Pd(II) *N*,*N*′-2,3-butylenebis(trifluoroacetylacetoniminato) isomers were resolved with baseline

resolution on the DiamondBond-C18 column as was predicted (Fig. 23.3, peaks 1–4). At mid-range pH, zirconia substrate displays a mixture of ionic interaction and hydrophobic interaction which under controlled chromatographic conditions could separate both hydrophobic and non-hydrophobic species [23, 26].

An interesting observation at both pH 2.15 and 7.20 was that the *cis* Pd(II) *N*,*N*′-2,3-butylenebis(trifluoroacetylacetoniminato) isomer was retained more than the *trans* isomer when using the DiamondBond C-18, which was opposite behavior to that on the silica-based columns for Cu(II) isomers. The behavior of the Pd(II) isomers was attributed to the shape selectivity of DiamondBond-C18 column. DiamondBond C-18 is made up of spherical and porous carbon clad particles covalently bonded with octadecyl groups, making this column combine partitioning mechanism with shape selectivity, leading to possible resolution of the two isomers [23, 28]. In addition, the pore size of the DiamondBond C-18 (300 Å) could also have contributed to the selectivity in the retention of the Pd(II) isomers as explained in previous studies [9, 29, 30]. The pore size of J'sphere ODS H-8 C-18 and Symmetry Shield™ C-18 is 80 and 100 Å, respectively. From literature [29, 30], it is argued that narrow pore of columns leads to the crowding of the ligands (polymeric or alkyl) on the chromatographic substrate hindering accessibility to the stationary phase. This could explain why Pd(II) isomers could not be resolved by the two silica-based columns. The *cis* Pd(II) isomer is planar, with both methyl groups equatorial and can relatively easily access the zirconia substrate due to its linear shape, and interact with charged zirconia substrate, as compared to the *trans* isomer, which has one of the methyl groups shifted to the axial position. The *cis* isomer would then interact with the PO_4^{3-} ions adsorbed on the zirconia acidic sites, thereby being more retained due to enhanced electrostatic interactions. On the other hand, the *trans* isomer, which had a twisted shape, would have a respectively limited interaction with the PO_4^{3-} ions on the zirconia acidic sites resulting in reduced electrostatic interactions and leading to less retention of this isomer, thereby producing resolution between these isomers [19]. To test the theory that Pd(II) isomers could incorporate hard Lewis acidic sites, which interacted with the hard Lewis base ions (PO_4^{3-}) on the zirconia substrate to effect resolution, an experiment was conducted in which the DiamondBond-C18 column was used without any hard Lewis base at low pH. In that experiment, chromatographic conditions were kept constant with the exception of phosphate buffer, which was replaced with hydrochloric acid to lower the pH to 2.15. The use of hydrochloric acid to lower the pH produced a zirconia substrate that has no negatively charged surface as was the case with phosphate buffer, since the chloride ion is not a strong Lewis base [23, 24, 26]. Under these conditions, there was no resolution observed for either the Cu(II) or Pd(II) isomers. Two peaks were observed at 14 and 16 min representing the unresolved Cu(II) and Pd(II) isomers respectively. For the Cu(II) isomers, the results were expected since it has been established that the column has limited hydrophobic sites at low pH, which could affect resolution of these isomers. In the case of Pd(II) isomers, lack of hard Lewis base ions resulted in limited electrostatic interaction with the stationary phase and the Lewis acidic sites of the Pd(II) because of the weak electrostatic interactions which could oth-

erwise affect resolution of these isomers. Also, earlier research on ZirChrom-PBD has established that it is very difficult to cover all the available Zr(IV) acidic sites on the zirconia substrate when coating the stationary phase with polybutadiene [8, 31]. Using the same argument, it could be reasoned that Zr(IV) acidic sites could also be available on the carbon clad bonded DiamondBond-C18 column which would have had a repulsive electrostatic interaction with the Pd(II) Lewis acidic sites affecting the retention of these isomers, with subsequent negative effects on their resolution. The retention time of the *cis*-Pd(II) isomer when using phosphate buffer at pH 2.15 was about 27 min but 16 min with hydrochloric acid at the same pH. This is a strong indication that the significant reduction in retention times of this isomer could be due to electrostatic repulsion interaction between the Zr(IV) Lewis acidic sites and Pd(II) Lewis acidic sites.

23.3.2.2   Effect of Phosphate Buffer at pH 12.15

The optimized conditions of 50% acetonitrile and 50% of 30 mM phosphate buffer mobile phase at a column temperature of 5 °C were used with pH of the buffer increased to 12.15. The silica-based columns in this study were not used at pH 12.15 because the silanol groups could dissolve. At this high pH, silica-based columns have strong negatively charged surface, which perhaps could have produced electrostatic interaction with the Pd(II) N,N'-2,3-butylenebis(trifluoroacetylacetoniminato) isomers with subsequent resolution.

The results obtained at pH 12.15 were compared to those at pH 7.20 when using the DiamondBond C-18 column. At pH 12.15 all the isomers had baseline resolution (Fig. 23.4, peaks 1–4).

From the above results, it was observed that there was an improvement of about 39% in the resolution between the Cu(II) isomers and a 11% reduction between the resolution of Pd(II) isomers. The resolution between the Cu(II) isomer and Pd(II) isomer, peaks 2 and 3 on Fig. 23.4, increased by 4%. In general, it was observed that the retention times of all the isomers increased from low pH (2.15) and reaching a
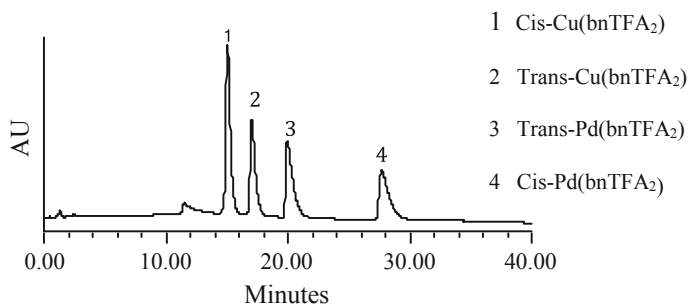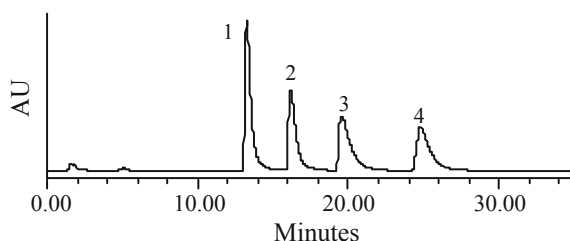

Fig. 23.4   Chromatograms for Cu(II) and Pd(II) N,N'-2,3-butylenebis(trifluoroacetylacetoniminato) isomers using DiamondBond C-18 column using 50:50 (v/v) acetonitrile:30 mM phosphate buffer (pH 12.15) at column temperature of 5 °C and wavelength 275 nm, Peaks (1 = *cis*-Cu(bnTFA$_2$), 2 = *trans*-Cu(bnTFA$_2$), 3 = *trans*-Pd(bnTFA$_2$) and 4 = *cis*-Pd(bnTFA$_2$))

maximum at mid pH (7.20) and then reducing as pH was increased, and being lowest at pH 12.15. Hu et al. [26] found a similar trend when determining the effects of varying pH of mobile phase using phosphate buffer when studying drug compounds on ZirChrom-PBD column. The explanation to that behavior was attributed to the nature of the zirconia substrate and polybutadiene coating as pH was increased. At about pH 7, the hydrophobic and electrostatic interaction for zirconia-based columns is equally strong, enhancing hydrophobic, hydrophobically assisted ion-exchange and electrostatic interactions between the analyte and the stationary phase, which could lead relatively to strong retention of both hydrophobic and slightly polar species [24, 26]. In the same study, Yang et al. [24] reported that hydrophobic interaction between some drugs with ZirChrom-PBD increased with increase in pH. The hydrophobic interaction was believed to be due to the polybutadiene coating and the analytes. The conclusion derived from that study was that hydrophobic interactions for the ZirChrom-PBD column are dominant at high pH, even though the zirconia substrate is negatively charged [22, 26]. The same behavior is believed to exist for the DiamondBond C-18 column. That was evident based on the increased resolution obtained between the Cu(II) isomers, which according to our finding would separate well on a more hydrophobic substrate, as was the case on silica-based columns at low and mid pH. Therefore, if hydrophobic interaction on the DiamondBond C-18 is dominant at high pH, the resolution between the Cu(II) isomers would be expected to be highest at that pH. In our study, the highest resolution of the Cu(II) isomers was observed at pH 12.15 supporting the above argument. On the other hand, Pd(II) isomers which is believed to have Lewis acidic sites produced the highest resolution at low pH where ionic interactions were dominant and lowest at high pH where hydrophobic interaction was dominant as was evident by reduction in the resolution between the Pd(II) isomers at pH 12.15 when compared to lower pH.

To determine the stability of the compounds studied as pH was varied, the peak area of each of the four isomers was compared at pH 2.15, 7.20 and 12.15 with 95% confidence level. There was no significant difference in the peak areas of all the isomers as pH was varied, suggesting that the isomers were not lost either through decomposition or strong adsorption to the column. In general, efficiency, resolution and USP tailing factors were improved at pH 12.15, producing good quality chromatographic data. It is very clear from our studies that the resolution of the Pd(II) isomers required strong electrostatic interaction, which could only be satisfied by the DiamondBond C-18. The stationary phase of silica-based columns have strong negative charge at high pH; unfortunately most of these columns could not be used because of dissolution of silica at high pH.

To determine whether the separation of the Cu(II) and Pd(II) isomers at pH 12.15 is dependent on only phosphate buffer, a second experiment was conducted by keeping all the chromatographic conditions constant with the exception of the buffer, where sodium hydroxide was used to keep the pH at 12.15. A baseline resolution was observed for both the Cu(II) and Pd(II) isomers. The retention factors, USP tailing factors, resolution and USP plate counts of these isomers were not significantly different when phosphate buffer was replaced with sodium hydroxide. These results indicated that the separation of the two metal complexes at high pH did not depend on

the type of buffer. It was evident that for the Pd(II) isomers to have baseline resolution, a substrate with substantially electrostatic interaction was required, and the zirconia-based column satisfied that requirement. Earlier research to obtain baseline resolution for Cu(II) and Pd(II) N,N'-2,3-butylenebis(trifluoroacetylacetoniminato) isomers on a single chromatogram was not successful using silica-based columns using both normal or reversed-phase HPLC [20, 32] or gas chromatography [19].

23.3.3   Effect of Temperature on the DiamondBond C-18 Column

Zirconia-based columns are also known to improve the quality of chromatographic data with increase in temperature [9, 33]. Therefore, using chromatographic conditions at pH 12.15 with the phosphate buffer, the temperature of DiamondBond C-18 was varied from 0 to 80 °C. Lower temperatures have been used to improve peak shape, peak height and resolution of thermal labile metal complexes using both normal [17] and reversed-phase HPLC [21]. Earlier studies on the effect of temperature on the HPLC of metal complexes has reported decomposition of the metal complexes as a function of temperature [21]. Therefore in our study, as the temperature was increased, the area, tailing and shape of the peaks of the isomers were closely monitored to determine any signs of decomposition or unexpected interaction of the analytes with the column. It was observed that no decomposition or unexpected interaction occurred between the analytes and the column up to 80 °C. The column pressure was lowered substantially with increase in the column temperature, which could have allowed use of high flow rates if there was need to do so. There was an improvement in the peak shapes, increase in peak height and reduction in retention of the isomers as temperature was varied from 0 to 80 °C, (Fig. 23.5, peaks 1–4). The increase in peak height leads to improvement on the signal to noise ratio with subsequent benefits in the detection limits of the analytes.

When comparing the results obtained at 60 and 80 °C, no significant difference was observed in the chromatographic behavior of all the isomers. Even though working with high temperature could be beneficial, caution is required that the analytes are not decomposed at elevated temperatures, and also the life span of the column is compromised with increase in temperature, therefore the lower temperature, 60 °C was selected as the optimum in our study. In general, there was improvement in USP tailing factors for all the isomers as temperature was increased. The USP tailing factors of Pd(II) isomers had an improvement of over 50% (Table 23.2) which produced more symmetrical peak shapes of these isomers (Fig. 23.5, peaks 3 and 4). A symmetrical peak leads to improvement in the resolution of the peaks and improves the quantification of the peak area, which could benefit both qualitative and quantitative analyses. These results are in contrary to those obtained by Henderson et al. [21] where the peak shapes of metal diketonate complexes improved with reduction in temperature using silica-based columns with reversed-phase HPLC. On the other
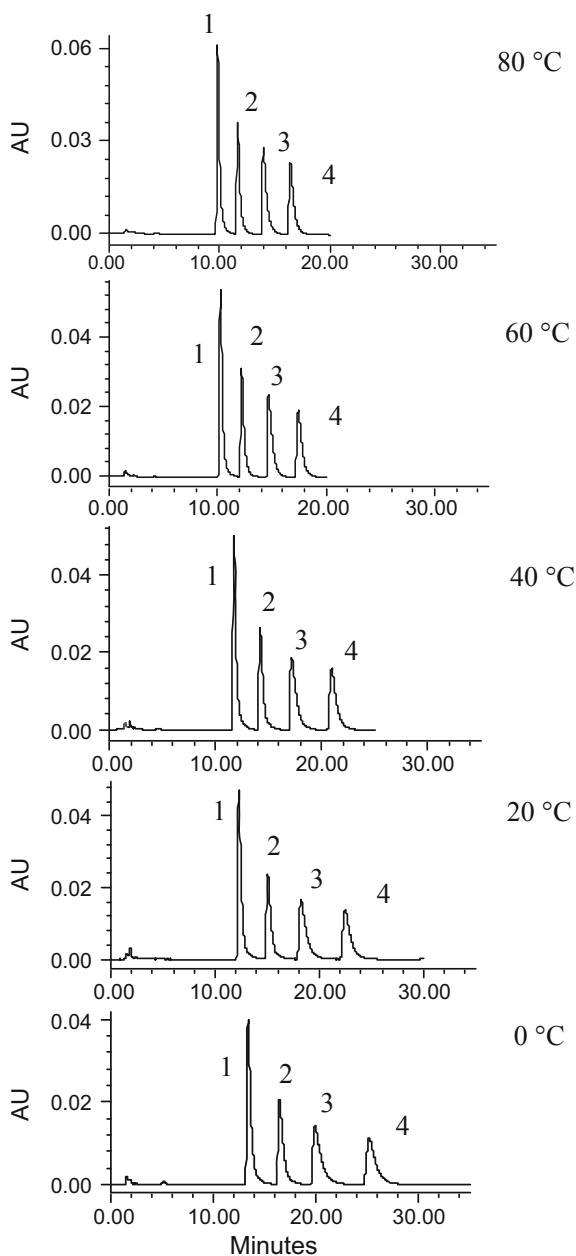
Fig. 23.5 Chromatograms for Cu(II) and Pd(II) N,N'-2,3-butylenebis(trifluoroacetylacetoniminato) isomers on a DiamondBond C-18 column at different column temperatures using 50:50 (v/v) acetonitrile:30 mM phosphate buffer at pH 12.15 and wavelength 275 nm, Peaks (1 = cis-Cu(bnTFA$_2$), 2 = $trans$-Cu(bnTFA$_2$), 3 = $trans$-Pd(bnTFA$_2$) and 4 = cis-Pd(bnTFA$_2$))

Table 23.2 Comparison of chromatographic behavior for Cu(II) and Pd(II) N,N'-2,3-butylenebis(trifluoroacetylacetoniminato) isomers on a DiamondBond C-18 column using 50:50 (v/v) acetonitrile:30 mM phosphate buffer at pH 12.15 and column temperatures of 0 and 60 °C at wavelength 275 nm

Metal complex isomer	Retention time (min)		USP resolution		USP tailing factors		USP Plate count ($\times 10^3$)	
	0 °C	60 °C	0 °C	60 °C	0 °C	60 °C	0 °C	60 °C
Cis-Cu(bnTFA$_2$)	13.15	10.53	–	–	1.40	1.38	7.31	8.78
Trans-Cu(bnTFA$_2$)	16.26	12.51	4.88	4.02	1.13	1.01	9.90	9.52
Trans-Pd(bnTFA$_2$)	19.89	15.14	3.63	4.53	2.73	1.22	3.83	8.98
Cis-Pd(bnTFA$_2$)	24.57	18.06	3.29	4.60	2.43	1.08	4.76	13.2

hand, in a different study using a zirconia-based column, ZirChrom-PBD, it was observed that narrower peaks were produced at 100 °C compared to 40 °C when analyzing alkylbenzenes using reversed-phase HPLC [34].

As temperature was increased from 0 to 60 °C in our study there was a slight reduction of about 18% between the resolution of Cu(II) isomers. Therefore, in this case lower temperature improved resolution of the Cu(II) isomers. A similar behavior by fac and mer isomers of aluminum beta-diketonates has been reported using silica-based columns on normal-phase HPLC, where the two isomers improved in resolution with decrease in temperature. On the other hand, the Pd(II) isomers had an improvement in resolution of about 40%, which was in agreement with results obtained by Li and Carr [34, 35] when analyzing alkylbenzenes and polyaromatic hydrocarbons using a coated polybutadiene-zirconia column on reversed-phase HPLC. However, it was also found that some compounds reduced in resolution, even though their resolution was still acceptable. Their study concluded that elevating the temperature on polybutadiene-coated zirconia leads to different selectivities of the compounds which could lead to different resolution behavior as was observed in our case. High selectivity would lead to improved resolution, and vice versa. It is believed that the DiamondBond C-18 displayed similar behavior, with the Pd(II) isomers expected to improve in resolution based on the observed selectivity of this column towards these isomers. In contrary, the Cu(II) isomers did not improve in resolution since the DiamondBond C-18 has a limited selectivity towards these isomers at high temperature.

23.3.4 Effect of Temperature on Retention of the Isomers and on Efficiency of DiamondBond Column

When the temperature was elevated from 0 to 60 °C, the retention time of all the isomers in our study was found to reduce by at least 20% with no adverse effects on resolution, Table 23.2 and Fig. 23.5. Lower retention times are very desirable

due to reduction in overall analyses time and savings of the organic modifier. Literature review revealed that lower retention times of compounds have been reported at elevated temperatures for both silica and zirconia-based columns using normal and reversed-phase HPLC [17, 21, 34–36]. The decrease in retention times of the analytes at elevated temperatures can be attributed to the increased mass transfer resistances between the mobile phase and stationary phase. The column efficiency was reported as USP plate counts. In general, there was an improvement in the column efficiency especially for the Pd(II) isomers. For the Pd(II) isomers, the column efficiency improved by over 50%, Table 23.2. The column efficiency of a polybutadiene coated-zirconia column was also found to increase with elevation in temperature [34].

23.4 Conclusion

In this study, we have demonstrated the separation power of zirconia-based stationary phase on metal complex isomers. The chemical stability of zirconia column plays an important role in this regard when compared to the silica-based columns, which usually cannot be used in the more important ionic region above pH 8. It is evident that the Pd(II) isomers required a stationary phase with substantial electrostatic sites; otherwise it would have been very difficult to manipulate the conventional silica columns to effect any resolution of these isomers. The increase in the hydrophobicity of the zirconia-based columns at high pH opens new avenues for chromatographers to explore, especially where they might have been limited by the stability of the stationary phase to conduct experiments requiring a hydrophobic stationary phase at high pH. The use of high pH was found to improve resolution of the isomers, and also reduction in retention times, which could be beneficial in routine analysis in time and organic modifier savings. The ability of the zirconia-based columns to display multi-charged retention sites with different buffers at different pHs make these columns worth considering when dealing with complex matrix. These zirconia-based columns offer a possibility to optimize the charge on the stationary phase through the use of different buffers at different pHs to obtain a substrate which could simultaneously display equally strong hydrophobic, ionic and cationic sites to separate compounds with zwitter ions and various isomers through multipoint interactions. The Diamond-Bond C-18 column has the capabilities of combining partitioning mechanism with shape selectivity making this column ideal for separation of isomers. The effect of temperature on the DiamondBond C-18 column was found to reduce the retention times and increase selectivity, resolution and column efficiency of some compounds, which are factors desirable for successful chromatography. The improvement in the peak height can also be beneficial for quantitative analyses through enhanced signal to noise ratio for lower detection limits. Sadly though, this column has not received enough attention as that afforded to the ZirChrom-PBD. The other zirconia-based columns such as the ZirChrom-Carb, ZirChrom-PE and ZirChrom-PS have also received very little attention from the chromatographers. It is with hope that this

study will direct chromatographers to explore the benefits of the other zirconia-based columns, especially the DiamondBond C-18.

References

1. Dillon CT, Hambley TW, Kennedy BJ, Lay PA, Zhou QD, Davies NM, Biffin JR, Regtop HL (2003) Gastrointestinal toxicity, antiinflammatory activity and superoxide dismutase activity of copper and zinc complexes of the antiinflammatory drug indomethacin. Toxic Res Toxicol 16:28–37
2. Ganjali MR, Emami M, Salavati-Niasari M (2002) Novel copper (II)-selective sensor based on a new hexadentates Schiff's base. Bull Korean Chem Soc 23:1394–1398
3. Enders D, Bettray W (1996) Recent advances in the development of highly enantioselective synthetic methods. Pure Appl Chem 68:569–580
4. Misl'anova C, Hutta M (2003) Role of biological matrices during the analysis of chiral drugs by liquid chromatography. J Chromatogr B 797:91–109
5. Rochon FD, Kong PC, Melanson R, Skov KA, Farrell N (1991) Characterization and properties of monammine nitroimidazole complexes of platinum [PtCl$_2$(NH$_3$)(NO$_2$IM)]—crystal and molecular-structure of *cis*-aminedichloro(1-((((2-hydroxyethyl) amino)carbonyl)methyl)-2-nitroimidazole)platinum(II). Inorg Chem 30:4531–4535
6. Paek SH, Co TT, Lee DH, Park YC, Kim TJ (2002) 1,2-ferrocenediylazaphosphine 3: a new class of planar ligands for Cu-catalyzed cyclopropanation. Bull Korean Chem Soc 23:1702–1708
7. Minakuchi H, Nakanshi K, Soga N, Ishizuka N, Tanaka N (1996) Octadecylsilylated porous silica rods as separation media for reversed-phase liquid chromatography. Anal Chem 68:3498–3501
8. Li J, Carr PW (1997) A study of the efficiency of polybutadiene-coated zirconia as reversed-phase chromatographic support. Anal Chem 69:2193–2201
9. ZirChrom Separations Inc, HPLC column product guide 2002–2003
10. Rigney MP, Weber TP, Carr PW (1998) Preparation and evaluation of a polymer-coated zirconia reversed-phase chromatographic support. J Chromatogr A 484:273–291
11. Rigney M, Funkenbusch P, Carr PW (1990) Physical and chemical characterization of microporous zirconia. J Chromatogr A 499:291–304
12. Jackson PT, Kim T-Y, Carr PW (1997) Diasteriomeric selectivity of carbon-coated zirconia reversed-phase liquid chromatographic media. Anal Chem 69:5011–5017
13. Zirchrom Technical Bulletin #232 and #240, Product Application Notes, ZirChrom Separations, Inc, Anoka, MN, USA
14. Yao LF, He HB, Feng YQ, Da SL (2004) HPLC separation of positional isomers on a dodecylamine-*N*,*N*-dimethylenephosphoric acid modified zirconia stationary phase. Talanta 64:244–251
15. Gais HJ, Jagusch T, Spalthoff N, Gerhards F, Frank M, Raabe G (2003) Highly selective palladium catalyzed kinetic resolution and enantioselective substitution of *trans* allylic carbonates with sulfur nucleophiles: asymmetric synthesis of allylic sulfides, allylic sulfones, and allylic alcohols. Chem Eur J 9:4202–4221
16. Szczepanik W, Ciesiolka J, Wrzesinski J, Skala J, Jezowaska-Bojczuk M (2003) Interaction of aminoglycosides and their copper(II) complexes with nucleic acids: implication to the toxicity of these drugs. Dalton Trans 8:1488–1494
17. Henderson DE, Saltzman ST, Uden PC, Cheng Z (1988) Physicochemical studies of fac-mer isomerism of aluminium beta-diketonates by high performance liquid chromatography at low temperature. Polyhedron 7:369–377
18. Henderson DE, Novak FP (1982) Low temperature, normal phase for separation of thermally labile species. J Chromatogr Sci 20:256–259

19. Uden PC, Blessel K (1973) Resolution of volatile *N*,*N′*-2,3-butylenebis(trifluoroacetylacetoniminato)copper(II), nickel(II), and palladium(II) by gas-liquid chromatography. Inorg Chem 12:352–356
20. Clark PJ, Trebble IE, Uden PC (1982) Adsorption HPLC of tetradentate β-ketoimine copper, nickel and palladium chelates. Polyhedron 1:785–790
21. Henderson DE, O'Conner DJ, Kirby JF, Sears CP III (1985) Low temperature, normal-phase HPLC for separation of thermally labile species. J Chromatogr Sci 23:477–483
22. Henry R (2002) Highly selective zirconia-based phases for HPLC applications. Am Lab 69:18–25
23. Dai J, Yang X, Carr P (2003) Comparison of the chromatography of octadecyl silane bonded silica and polybutadiene-coated zirconia phases based on a diverse set of cationic drugs. J Chromatogr A 1005:63–82
24. Yang X, Dai J, Carr PW (2003) Analysis and critical comparison of the reversed-phase and ion-exchange contributions to retention on polybutadiene coated zirconia and octadecyl silane bonded silica phases. J Chromatogr A 996:13–31
25. Cox GB (1993) The influence of silica structure on reversed-phase retention. J Chromatogr A 656:353–367
26. Hu Y, Yang X, Carr PW (2002) Mixed-mode reversed-phase and ion-exchange separations of cationic analytes on polybutadiene-coated zirconia. J Chromatogr A 968:17–29
27. Allenmark SG (1988) Chromatographic Enantioseparation: methods and Applications. Wiley, New York
28. SUPELCO, Discovery Zr: High pH and High Temperature HPLC, Bulletin 931, Pennsylavania, USA
29. Dolan DW, Snyder LR, Wilson N, Nelson M (2000) Characterization of HPLC column selectivity. An oral presentation at HPLC 2000, Seattle, WA, USA, 25–30 June
30. Wilson NS, Dolan JW, Snyder LR, Carr PW, Sander LC (2002) Column selectivity in reversed-phased liquid chromatography III. The physico-chemical basis of selectivity. J Chromatogr A 961:217–236
31. Li J, Carr PW (1996) Retention characteristics of polybutadiene-coated zirconia and comparison to conventional bonded phases. Anal Chem 68:2857–2868
32. Walters FH, Uden PC (1986) The use of encoded structural data to predict the liquid chromatographic retention behavior of tetradentate metal complexes. Anal Lett 19:375–384
33. Dolan J (2002) LC–GC North America 20:524–530
34. Li J, Carr PW (1997) Effect of temperature on the thermodynamic properties, kinetic performance, and stability of polybutadiene-coated zirconia. Anal Chem 69:837–843
35. Li J, Carr PW (1997) Evaluation of temperature effects on selectivity in RPLC separations using polybutadiene-coated zirconia. Anal Chem 69:2202–2206
36. Li J, Carr PW (1997) Fast separation at elevated temperature on polybutadiene-coated zirconia reversed-phase material. Anal Chem 69:3884–3888

Chapter 24
Copper-Based Nanoparticles, Their Chemistry and Antibacterial Properties: A Review

Zehra Edis, Samir Haj Bloukh, Akram Ashames and May Ibrahim

Abstract Copper nanoparticles (CuNPs) have different structural properties and effective biological activities. One of the major proven applications of CuNPs is antimicrobial activity. The advantage of CuNPs is the control over particle size and compositions to provide additional applications. The synthesis of CuNPs through green synthesis, chemical, physical and biological methods is possible. The toxicity and stability of CuNPs are important for its use as antimicrobial agent. This work reviews the behavior of CuNPs and copper-based NPs as antimicrobial agents in different media under various conditions.

keywords Copper · Nanoparticles · Antimicrobial agents

24.1 Introduction

Bacterial infection became a worldwide threat because many bacteria have developed a resistance against antibiotics. Therefore, the search for new antimicrobial agents is vital for the survival of the human species. Historically, metals played an important role in fighting bacterial infections. Recently, metal-based nanoparticles (NPs) moved into the spotlight as new antimicrobial agents [1]. NPs possess unique properties such as small size and high surface-to-volume ratios. The large surface area of the NPs enhances their interaction with the microbes to carry out broad-spectrum antimicrobial action [2]. Many metal-based NPs such as gold, zinc, titanium, cop-

Z. Edis (✉) · S. Haj Bloukh · A. Ashames · M. Ibrahim
Department of Pharmaceutical Sciences, Ajman University (AU), College of Pharmacy and Health Sciences, P.O. Box 346, Ajman, UAE
e-mail: z.edis@ajman.ac.ae

S. Haj Bloukh
e-mail: s.bloukh@ajman.ac.ae

A. Ashames
e-mail: a.ashames@ajman.ac.ae

M. Ibrahim
e-mail: may.ibrahim@ajman.ac.ae

per, and magnesium, have antibacterial activities [1]. Additionally, metal NPs can be associated with other nanostructures and used as carriers for antimicrobial drugs, increasing potential applications. Since ancient times, mankind utilizes copper to disinfect water and wounds. In the 1880s, mixtures of copper sulfate, lime and water, or copper sulfate and sodium carbonate were used in the US and France as fungicides. However, copper ions and copper compounds can be toxic to microorganisms, humans and the environment if present in large amounts [3].

CuNPs are part in many antimicrobial formulations and in products like synthetic and natural textiles, biomedical and surgical devices, food processing and packaging, as well as in water purification. This review focuses on bioactivities of CuNPs and copper-based NPs with a spot on their toxicity. Moreover, the possible mechanism of their mode of action on microbes has been reviewed [2]. Many factors can affect the antimicrobial activity of the NPs including formulation process, environment, bacterial defense mechanism and physical characteristics of NPs [4]. NPs can greatly increase the production of Reactive Oxygen Species (ROS), which consequently can damage and inactivate essential biomolecules, including DNA, proteins, and lipids [5]. They are probably able to participate in subcellular reactions, as their size is close to biological molecules, i.e., large protein complexes. Therefore, NPs have shown an ability to inhibit the growth of bacteria [6, 7].

Copper is cheap and easily available, therefore the synthesis of CuNP is cost effective. An added advantage of CuNPs is their ability to oxidize and form copper oxide NPs, together in mixtures of polymers or macromolecules [8, 9]. On the other hand, there is an upsurge in resistance to other metals NPs due to genetic alterations in bacteria. Combined with the mammalian cell toxicity results, Cu-based nanoparticle coatings for antimicrobial wound care could offer a distinct advantage over the more widespread use of metal-based coatings, which do not appear to be as effective in eliminating pathogenic microorganisms and show a high degree of mammalian cell cytotoxicity [10]. However, CuNPs have major limitations. Smaller CuNPs offer higher activity, but may aggregate in clusters causing a decrease in essential properties [11]. In addition, rapid oxidation of CuNPs takes place on exposure to air. Copper is oxidized to CuO and Cu_2O, and converts into Cu^{2+} during preparation and storage, making it is difficult to synthesize CuNPs in an ambient environment. Therefore, alternative pathways are available to synthesize metal nanoparticles in the presence of polymers. Polymers such as polyvinylpyrrolidone, polyethylene glycol, chitosan need surfactants like cetyltrimethylammonium bromide as stabilizers and to form coatings on the surface of nanoparticles [9, 12]. Copper is an essential metal for the human body, but in large doses it could cause toxicity [3]. Toxicity of Cu compounds was generally ranked as: Cu^{2+} > nano Cu(0) > nano $Cu(OH)_2$ > nano CuO > micron-scale Cu compounds. In addition to ROS generation, CuNPs can damage DNA plasmids [13]. CuO NPs are most potent regarding cytotoxicity and DNA damage in human lung epithelial cells [14]. Besides being an antimicrobial agent, CuNPs can act as biosensors and catalysts with well known optical, colorimetric and catalytic properties [15–17].

24.2   Methods of Synthesis

Physical, chemical, green and biological methods produce CuNPs and copper-based nanoparticles. Chemical reduction is the most widespread method, which involves using different reducing agents such as hydrazine, ascorbic acid, hypophosphite or sodium borohydride [12]. The shape, activity and size of formed CuNPs depend on both the type of copper salt and reducing agent [18]. The chemical approach also includes the microemulsion technique, but involves the use of large concentration of surfactant [11]. Other techniques to prepare CuNPs include thermal reduction, a capping agent method, sonochemical reduction and metal vapor synthesis [9]. Other physical methods are pulse laser ablation/deposition and pulsed wire discharge. These physical methods require expensive instruments and excessive energy consumption, which makes them less popular [12].

The living organisms such as bacteria and fungi have a great potential for the synthesis of metal NPs. Unlike chemical methods, there are no toxic effects on the environment and the by-products generated are harmless [19]. One study has reported the synthesis of copper nanoparticles, which involves the non-pathogenic bacterial strain *Bacillus cereus* [20] and *Pseudomonas stutzeri* [21]. Both microorganisms give spherical NPs. Synthesis of bimodal sized CuNPs from inexpensive oxidized copper salts by an extracellular metal-reduction process using anaerobic *Thermoanaerobacter* bacteria is possible. The outcome were well-suspended, bimodal colloidal CuNPs (70–150 and 5–10 nm) [22].

Plant extracts are also useful to synthesize CuNPs by using *Garcinia mangostana* and *Plantago asiatica* leaf extract as reducing agent [23, 24]. The preparation of Copper oxide nanoparticles (CuONPs) with spherical shape by a green route using black bean is possible [25]. The aqueous extract of *Thymus vulgaris L.* leaves can function as reducing and capping agent for CuONPs [26].

The synthesis of CuNPs in the presence of polymers as stabilizers is well studied. Chitosan, starch and cellulose stabilize the CuNPs and prevent their coagulation and oxidation [11]. Native cyclodextrins can function as stabilizer for CuNPs as well. The size of the CuNPs depends on the type of native cyclodextrin [27].

24.3   Mechanisms of Antibacterial Action

In the literature, many explanations of CuNPs against microorganisms are available. The antimicrobial effect of CuNPs is due to the release of copper ions [28]. Cu^{2+} ions are also small enough to disrupt bacteria cell membranes and gain entry in order to disrupt enzyme function. Additionally it has indirect effects through changes in the surrounding charge environment of microorganisms. However, copper ions and copper compounds can be toxic to microorganisms, humans and the environment. Combining polymers with CuNPs decrease their toxicity because polymers form a reservoir for the Cu ions [29, 30].

NPs cause more damage on the bacterial cells, because Cu ions may form ROS on the surface in the presence of various amine functional groups originating from biological molecules [28, 31]. After entering into the cell, NPs may bind with DNA molecules and damage the helical structure by cross-linking within and between the nucleic acid strands. Copper ions inside bacterial cells also disrupt biochemical processes [32]. Moreover, copper ions have the facility to form chelates with biomolecules, which may cause functional protein inactivation [33].

Some studies assumed that NPs can diffuse across the membrane directly when the size is small enough [33]. Meanwhile, ion channels and transporter proteins pass NPs to cross the plasma membrane. Some NPs enter cells via "endocytosis": the membrane surrounds them, and vesicles transport NPs into cells [33]. Intracellular ROS influence induced by CuNPs takes place. NPs can directly interact with oxidative organelles such as mitochondria, redox active proteins stimulate ROS production in cells, and ions produced by NPs can induce ROS by various chemical reactions. ROS can induce DNA strand breakage, and affect gene expression.

The action of CuNPs mainly originates from the direct interaction of Cu^{2+} species with the cell components. Cu^{2+} is reduced to Cu^+ by the cell components and is mainly responsible for the inactivation of bacteria [34]. In other studies, copper nanoparticles were described acting as effective antibacterial agent against the wide range of bacterial species due to interactions with phosphorous and –SH groups leading to DNA and protein denaturation [35, 36]. Overall, smaller particle size leads to better antimicrobial action [30, 37].

24.4   Cu and Cu Salts Nanoparticles as Antimicrobial Agent

24.4.1   Cu Nanoparticles

CuNPs have promising applications in wound healing due to their high biological activity [38]. They exert antimicrobial effects on a wide range of microorganisms including pathogenic bacteria. The bactericidal effect of CuNPs were compared based on diameter of the zone of inhibition (ZOI) in disk diffusion tests and minimum inhibitory concentration (MIC) and minimum bactericidal concentration (MBC) of nanoparticles dispersed in batch cultures. CuNPs have a broad-spectrum antibacterial effect on both Gram-positive and Gram-negative bacteria. The antimicrobial properties of copper nanoparticles against *Escherichia coli*, *Bacillus subtilis* and *Staphylococcus aureus* were screened [35]. An oxide layer formed on the CuNPs, which increased antimicrobial activity towards *B. subtilis* [35]. The antibacterial activity of CuNPs produced by inert gas condensation method [39] against *E. coli* resulted in the formation of cavities in the bacterial cell wall [39].

CuNPs synthesized by using Tween 80 for the reduction of copper acetate hydrate and refluxing between 190 and 200 °C [40] showed more inhibitory activity against

bacteria than in case of fungi. The ZOI for *E. coli* (26 mm) was larger than for *C. albicans* (23 mm) [40].

CuNPs synthesis using microwave in the absence of any stabilizing agent has been reported [41]. The reaction in basic ethanol solution needs ascorbic acid as reducing reagent. The disk diffusion tests showed an interesting antibacterial activity against both Gram-positive and Gram-negative bacteria. The authors suggested that the CuNPs can be used for the treatment of leather [41]. The effect of precursors and reducing agents on the shape and size of CuNPs are important factors [18]. The CuNPs with different shape, size and with strong antimicrobial activity have high potential application in the field of biomedical and food packaging industries [18].

The anti-biofilm activity of CuNPs against *P. aeruginosa* allows its use as coating agents on surgical devices and medical implants to manage biofilm associated infections. A maximum of 94% biofilm inhibition against a *P. aeruginosa* biofilm was reported [42].

In addition to chemical means of CuNPs production, researchers also utilized physical methods. The wire electric explosion method resulted in CuNPs with sizes between 50 and 100 nm. The influence of physicochemical properties such as particle size and storage of CuNPs upon their toxicity to bacteria were investigated [43]. It was determined that small NPs displayed more antimicrobial activity. Additionally, the suspensions storage time was an important factor altering antimicrobial properties of small nanoparticle suspensions. For CuNPs of 50 nm, toxicity decreased after 24-h storage, while suspensions of larger CuNPs above 100 nm displayed no such dependence [43].

The influence of the synthesis conditions on size, aggregation status and charge of nanoparticles in aqueous solutions, as well as the resulting antibacterial properties of water suspensions of CuNPs towards the different strains of bacteria are interdependent. Water dispersions of CuNPs inhibited the growth of test cells for bacteria. The use of deeply purified water and alcohol-containing stabilizers in the synthesis of nanoparticles via metals electric erosion prevents the CuNPs coagulation and significantly influences their physicochemical characteristics and, consequently, antibacterial properties. The increase of toxic effect is inversely correlated to particle size and aggregation degree of the synthesized dispersions. The particles with less size have better migration activity and increase the impact on the cell by easier penetration [44].

The use of plant extracts for the synthesis of nanoparticles is one form of green technology. The synthesis of CuNPs by using *Magnolia kobus* leaf extract as reducing agent is successful. These biologically synthesized CuNPs exerted high antibacterial activity against *E. coli*. The inhibition is inversely proportional to the average nanoparticle sizes [45].

The preparation of CuNPs by using citrus juice demonstrated a significant inhibitory action against *E. coli* followed by *K. pneumoniae, P. aeruginosa, Propionibacterium acnes* and *S. typhi*. The plant pathogenic fungi in the same study lead to high inhibition [46]. CuNPs synthesized by *Garcinia mangostana* leaf extract as reducing agent with copper nitrate as starting material are highly active against *E. coli* and *S. aureus* [23].

The methods of synthesis of the above CuNPs together with their antibacterial activity are summarized in Table 24.1.

24.4.2   CuO Nanoparticles

Various CuONPs are potential antimicrobial agents. The synthesis by thermal plasma technology resulted in CuONPs, which showed activity against a range of bacterial pathogens, including methicillin-resistant *S. aureus* (MRSA) and *E. coli*. Incorporation of nanoparticles into polymers is required for ideal inhibition [28].

Electrochemical reduction is another method for the preparation of CuONPs [47] and depends on using tetrabutyl-ammonium bromide as structure directing agent. The reduction process takes place under an inert atmosphere of nitrogen. Such nanoparticles are prepared using a simple electrolysis cell in which the sacrificial anode is a commercially available copper metal sheet, while the platinum sheet is the cathode. The influence of the parameters such as current density, solvent polarity, distance between electrodes, and concentration of stabilizers on the particles size are relevant. The nanoparticles proved against the human pathogens like *E. coli* and *Staphylococcus* strains excellent antibacterial activity [47].

The preparation of CuONPs by a gel combustion method [48] is possible with a mixture of cupric nitrate trihydrate and citric acid and heating until a gel forms. The gel leads at 200 °C to an amorphous powder, which was further annealed at different temperatures to obtain different sizes of CuO nanoparticles. CuONPs exhibited inhibitory effects against both Gram-positive and Gram-negative pathogens. The temperature affected the particles size and consequently its antibacterial activity [48]. CuO is effective as antibacterial agent against multidrug resistant biofilm forming bacteria (anti-biofilm and time-kill-assay). The CuO displayed maximum antibacterial activity against methicillin resistant *S. aureus* (MRSA) followed by *E. coli*. CuONPs have high potential of absorption, adsorption, penetration and availability, which make them an essential antibiofilm agent [49]. The nanoparticles formed were highly pure and showed excellent antimicrobial activity against various bacterial strains [50].

Polymers such as polyethylene glycol (PEG) are useful for the production of differently shaped copper oxide nanomaterials with simple, reproducible chemical and hydrothermal methods [51]. There is an influence of PEG on the morphological control. The prepared nanomaterials exhibited new types of surface morphologies such as rice grain-like, needle-like and plate-like. The shape effect on anti-bacterial property of the prepared CuO formed was evaluated against two Gram-positive bacteria as well as against the Gram-negative. Among three CuO nanostructures, the plate-like CuO displayed more powerful antibacterial activity than grain or needle shaped CuO [51].

Another approach for the synthesis of CuONPs includes copper nitrate as starting material and *L-tryptophan* as a capping agent [34]. The generation of free radicals by CuO lead to toxicity towards *E. coli.* [34]. CuONPs are also important for

Table 24.1 Synthesis of CuNPs and their antimicrobial activity

Precursor	Method of synthesis	Size and shape	Antimicrobial activity	Ref.
Nitrate salt of copper	Chemical reduction involving NaBH$_4$ as reducing agent	Spherical (6–16 nm)	Most active against *B. subtilis*. MIC (μg/mL) for *E. coli*: 140; *B. subtilis*: 20; *S. aureus*: 140	[35]
Pure copper metal	Inert gas condensation method	Agglomerated in clusters (12 nm)	Antibacterial activity against *E. coli* at concentration of 60 μg Cu^0/mL and above with 100% inhibition	[39]
Copper acetate hydrate	Reduction using Tween 80	Not mentioned	Highest activity against *E. coli* and *C. albicans*. ZOI for *E. coli* (26 mm); *C. albicans* (23 mm)	[40]
Copper acetate hydrate and copper nitrate hydrate	Microwave irradiation using ascorbic acid and NaOH in ethanol	7 nm	ZOI for *S. aureus* (5.55 mm), *E. coli* (2.6 mm), *B. subtilis* (2.8 mm)	[41]
Copper acetate, copper chloride and copper sulfate	Reduction using NaOH and ascorbic acid	Various sizes and shapes	*E. coli:* ZOI for CuNPs/NaOH: 12.0–12.5 mm and for CuNPs/ascorbic acid: 10.5–11.8 mm. *L. monocytogenes*: ZOI for CuNPs/NaOH: 14.8–18.5 mm and for CuNPs/ascorbic acid: 11.7–13.6 mm	[18]
Copper sulfate	Thermal decomposition	Average size: 55 nm and spherical	Inhibition of clinical isolates of *P. aeruginosa* biofilm at 100 ng/ml concentration. Maximum biofilm inhibitions between 64 and 91%	[42]

Table 24.1 (continued)

Precursor	Method of synthesis	Size and shape	Antimicrobial activity	Ref.
Not mentioned	Wire electric explosion in argon medium with addition of H_2	50 nm and 100 nm	MIC for *E. coli* for physiological solution: 4 mg/L for the freshly prepared suspension and 5 mg/L for the 24-h suspension. MIC for *E. coli* for fresh water solution: 0.25 mg/L, and 2 mg/L for 24-h suspension	[43]
Copper cathode	Electric erosion of copper cathodes	Spherical with average sizes of 38, 29 and 20 nm	ZOI for *E. coli* (4.2 mm), *P. aeruginosa* (3.0 mm), *S. aureus* (3.1 mm) and for *B. cereus* (only under the disc)	[44]
Copper sulfate	*Magnolia kobus* leaf extract	37–110 nm	*E. coli*: antibacterial activity highest at the leaf broth concentration of 15% achieving antibacterial activities of 40, 95 and 99% inhibition	[45]
Copper sulfate	Fruit juice of *C. medica* Linn.	10–60 nm	Active against *E. coli* (ZOI:26 mm), *K. pneumonia* (ZOI:23 mm), *P. aeruginosa* (ZOI:22 mm), *P. acnes* (ZOI:21 mm), *S. typhi* (ZOI:20 mm and the plant pathogenic fungi *F. culmorum* (ZOI:33 mm)	[46]

(continued)

Table 24.1 (continued)

Precursor	Method of synthesis	Size and shape	Antimicrobial activity	Ref.
Copper nitrate	*Garcinia mangostana* leaf extract as reducing agent	Spherical and agglomerated (20–25 nm)	Active against *E. coli* and *S. aureus* at concentrations of 0.2, 0.4, 0.6, 0.8 and 1.0 µg/mL. Most active against *S. aureus*. ZOI for *E. coli* (0.8 µ/mL): 1.3 mm; (0.8 µ/mL) *S. aureus*: 1.7 mm	[23]

wound healing [52]. They were prepared and subsequently deposited onto the surface of the cotton fibers by ultrasonic irradiation. These nanoparticles are physically adsorbed onto the cotton fiber surface. The CuO cotton fiber nanocomposites show high antimicrobial activity [52].

The thermal decomposition method results in CuONPs as well [53]. CuONPs have high antioxidant and antibacterial activity. Their bactericidal effect against *E. coli* and *P. aeruginosa* is well documented [53]. Another method for CuO NPs called "colloid-thermal green synthesis" is eco-friendly due to using extract of *gum karaya* as reducing agent. The synthesized CuONPs have antibacterial activity against *E. coli and S. aureu*s. The increase in precursor concentration affects the particle size and the morphology of synthesized CuO nanoparticles [54].

Another green synthesis of CuONPs is possible by using tea leaf and coffee powder extracts under microwave irradiation [55]. These nanoparticles possess notable antibacterial activity against human pathogens [55]. The *Tabernaemontana divaricate* leaves resulted in highly stable, spherical CuONPs. Antimicrobial activity of NPs showed maximum ZOI against the urinary tract pathogen *E. coli* [56].

The preparation of CuO nanocrystals by the wet chemical method [57] is successful with copper acetate and hexamethylenetetramine as precursors. The antibacterial study was carried out against *E. coli*. TEM analysis reveals that CuO nanocrystals caused disturbance to the cell wall, which led to the irreversible damage to the cell envelope finally leading to cell death [57].

Antibacterial activity depends on the shape of NPs shape. Antibacterial test showed that the spherical shaped CuONPs inhibited Gram-positive bacteria and the sheet shaped were more active on Gram-negative bacteria [58].

Table 24.2 lists briefly the methods of synthesis of the above CuONPs together with their antibacterial activity.

Table 24.2 Synthesis of CuONPs and their antimicrobial activity

Precursor	Method of synthesis	Size and shape	Antimicrobial activity	Ref.
Not mentioned	Thermal plasma technology	22.4–94.8 nm	*MRSA* and *E. coli*: MIC ranging from 100 µg/mL to 5000 µg/mL	[28]
Copper sheet	Electrochemical reduction	5–10 nm and spherical	ZOI for *E. coli*: 5 and 9 mm for 50 and 100 µL, and for *Staphylococcus* strains: 12 and 16 mm for 50 and 100 µL	[47]
Copper nitrate trihydrate	Gel combustion	20 nm	MIC varies according to the temperature the CuO NPs were annealed. *E. coli*: 20–65 µg/mL; *P. aeruginosa*: 28–55 µg/mL; *B. subtilis*: 30–70 µg/mL; *S. aureus*: 25–75 µg/mL	[48]
Copper acetate	Chemical reduction (NaOH as reducing agent)	23 nm	Highest effect against *E. coli* (MIC 31.25 µg/mL) and *E. faecalis* (MIC 31.25 µg/mL)	[50]
Copper nitrate trihydrate	Reduction with polyethylene glycol and NaOH	Rice grain-like, needle-like and plate-like	*E. coli* (MIC 6.25 µg/mL) and *S. iniae* (MIC 3.125 µg/mL)	[51]
Copper nitrate	Reduction with NaOH and using *L-tryptophan* as capping agent	Well separated and uniformly distributed	MIC value of *E. coli* for CuO and Cu_2O were found as 0.1 mM and 0.05 mM respectively	[34]

(continued)

Table 24.2 (continued)

Precursor	Method of synthesis	Size and shape	Antimicrobial activity	Ref.
Copper sulfate	Deposition of CuO nanoparticles onto the cotton fibers via the ultrasound irradiation of metal hydroxide	10–15 nm	The cotton fibers were clear and show no bacterial growth for CuO-coated cotton with 100% inhibition of *E. coli* and *S. aureus*	[52]
Copper sulfate	Direct thermal decomposition	15–30 nm and nearly spherical	Various concentrations of nano CuO (1, 2.5 and 4 mg/mL) were effective against *E. coli* (Optical density at 600 nm OD 0.9 for 1 mg/mL; inhibition starts after 9 h), *P. aeruginosa* (OD 0.5 for 4 mg/mL; inhibition starts after 9 h), *S. aureus* (OD 1.2 for 2.5 mg/mL; inhibition starts after 4 h) and *B. circulens* (OD 0.5 for 4 mg/mL; inhibition starts after 9 h)	[53]
Copper chloride	Colloid-thermal synthesis process using *gum karaya*	4.8 ± 1.6 nm and 7.8 ± 2.3 nm	MIC: 103.5 ± 4.71 µg/mL for *E. coli* and 120.4 ± 8.16 µg/mL for *S. aureus*	[54]
Copper nitrate	Microwave assisted reduction using tea leaf as reducing agent	50–100 nm and spherical	ZOI: *Shigella dysenteriae* (6–12 mm); *Vibrio cholerae* (6–12 mm); *S. pneumoniae* (6–10.5 mm); *S. aureus* (7–12 mm)	[55]

(continued)

Table 24.2 (continued)

Precursor	Method of synthesis	Size and shape	Antimicrobial activity	Ref.
Copper sulphate	Reduction using *Tabernaemontana* leaf extract	48 ± 4 nm and spherical	ZOI observed in *E. coli* at a concentration of 25 μg/mL: 17 ± 1 mm	[56]
Copper acetate	Chemical reduction using hexam-ethylenetetramine	6.0 ± 0.5 nm	*E. coli*: MIC 2.5 μg/mL	[57]
Copper acetate Copper nitrate	Co-precipitation with NaOH acting as stabilizing compound	Spherical (35 ± 5.6 nm) and sheet shaped (257.12 ± 13.6 nm)	Nanosphericals: *B. subtilis* (MIC 0.22 ± 0.0028 mg/mL) and *M. luteus* (MIC 0.20 ± 0.010 mg/mL) Nanosheets: *E. coli* (MIC 0.20 ± 0.05 mg/mL) and *P. vulgaris* (MIC 0.16 ± 0 mg/mL)	[58]

24.4.3   Halide and Sulfide Salts of Copper Nanoparticles

Copper iodide nanoparticles (CuINPs) were synthesized by co-precipitation method to produce NPs with an average size of 8 nm [31]. They are able to kill both Gram-positive and Gram-negative bacteria. Among the bacteria tested, *E. coli* DH5α is more sensitive and *B. subtilis* is more resistant to CuINPs. They have the ability to produce reactive oxygen species (ROS) which causes damage on DNA in both Gram-positive and Gram-negative bacteria. Consequently, the suppression of transcription takes place as revealed by reporter gene assay. Furthermore, they induce membrane damage as determined by atomic force microscopy (AFM). Thus, production of ROS and membrane damage are major mechanisms of the bactericidal activity of the CuINPs [31].

Another study aimed to investigate the incorporation of polyacrylic acid (PAA) coated CuINPs as dental adhesives [59]. Significantly greater antibacterial properties were demonstrated for PAA-CuI containing adhesives. A reduction in *Streptococcus mutans* viable cell count resulted. The authors assumed that PAA-CuI NPs are an effective additive to adhesive blends as it renders them antibacterial [58]. Moreover, PAA-coated CuINPs were incorporated into the glass ionomer matrix [60]. The use of copper-doped glass ionomer based materials under composite restorations contribute to an increased longevity of adhesive restorations because of their enhanced antibacterial properties [60].

Copper sulfide nanoparticles (CuSNPs) have been emerging as a promising platform for photothermal cancer therapy, bio-molecular sensing and molecular imaging.

The antibacterial activity of the nanoparticles in infected zebrafish was evaluated [61]. CuSNPs exhibit very good antibacterial activity against Gram-positive and Gram-negative bacteria. A bacterial colony count test proved that the CuSNPs depleted the infectious bacteria from the fish body within 24 h. Moreover, the NPs exhibited good hemo-compatibility with human red blood cells [61].

The green synthesis of CuSNPs is possible by using the culture supernatant of *Serratia nematodiphila* for reduction of copper sulfate into CuSNPs [62]. The CuSNPs were 9 to 20 nm in size. Antibacterial activity of CuSNPs against urinary tract infection (UTI) pathogens such as *E. coli*, *S. aureus*, *P. vulgaris* and *K. pneumoniae*. CuSNPs showed good bactericidal properties against the UTI after completing successful clinical trials [62].

24.4.4 Cu-Based Nanoparticles with Antimicrobial Activity

24.4.4.1 CuNPs with Polymers

Antimicrobial metals added into a polymer can lead to composite materials. This method depends on both the final application and the polymer matrix used. Metals can be either incorporated on the surface of a polymer or embedded into the matrix [63].

The use of polymers for developing nanocomposites with antimicrobial activity does not only involve a supporting role for nanoparticles, but can also enhance the antibacterial performance of nanocomposites. This behavior is related mainly to three explanations. First, the synergy between the polymer and copper nanoparticles that increases the antibacterial capacity of the material (nanocomposite). Second, the polymers ability for long-term ion release, thus prolonging the antibacterial activity of nanocomposite. Third, the influence of increasing the surface area, associated with the fine dispersion of copper nanoparticles in the polymer, on the level of antibacterial activity [29].

Two general approaches can be distinguished for the preparation of polymer/metal nanocomposites depending on where the nanoparticles are prepared. The first one is in situ by using the polymer matrix as the reaction medium. The second one is ex situ, by synthesizing the particle and then incorporating it into the polymer with just the dispersion medium as matrix [63].

Cellulose is a natural polymer and works well together with CuNPs. Regenerated cellulose (RC) films were used to coat CuNPs via the chemical reduction method [64]. CuNPs were firmly embedded on the surface of the RC films. The RC films coated with Cu nanoparticles showed efficient antibacterial activity against *S. aureus* and *E. coli* [64]. Natural cellulose from cotton needs first conversion into carboxymethyl derivatives before loading CuNPs onto the cotton fibers. They have antibacterial activity against the multi-drug resistant pathogen *Acinetobacter baumannii* [10].

Another group regenerated cellulose from *Acetobacter xylinum* bacteria [65]. CuNPs were successfully loaded into this cellulose matrix and the cellulose-Cu mem-

branes exhibited homogeneous structure. These membranes exhibited a significant antibacterial activity influenced by the CuNPs content. The authors recommended that these membranes might have a great potential for use in the wound dressing and other biomedical areas [65].

Another study reported the comparison between cellulose from *Acetobacter xylinum* and cellulose from plant origin. Two cellulose matrices (vegetable and bacterial) formed nanocomposites with copper nanoparticles and nanowires [66]. The inhibitory effect of these nanocomposites against *S. aureus* and *K. pneumoniae* indicate that the chemical nature and morphology of the nanocomposites have great influence on the antibacterial action. The increase in antibacterial activity is directly related to the increase of copper content in the composites. The cellulosic matrices also show an effect on the antibacterial efficiency of the nanocomposites, with vegetal cellulose fibers acting as the most effective substrate. These nanocomposites have a potential application in packaging or paper coatings [66].

In order to develop the cellulose antimicrobial properties, a hybrid cellulose material was synthesized using 2,2,6,6-tetramethylpiperidine-1-oxyl (TEMPO). In particular, wood celluloses can convert to individual nanofibers 3–4 nm wide with several microns length by TEMPO-mediated oxidation and successive mild disintegration in water [66]. The synthesis of CuNPs involves chemical reduction by sodium borohydride on the TEMPO nanofibrillated cellulose (TNFC) template. The resulting nano-material is embedded into a polyvinyl alcohol (PVA) matrix. The incorporation of hybrid TNFC-copper nanoparticles within PAV matrix gives films with antimicrobial properties. The morphology of TNFC-copper nanoparticles confirmed spherical CuNPs with an average size of 9.2 nm. The exposure to nonpathogenic *E. coli* DH5α on the nanocomposite films causes microbial reduction [67].

An in situ rapid one-pot synthesis of spherical CuNPs incorporated into cellulose network in a water-based solvent system is another method [68]. The polycrystalline CuNPs of 200–500 nm were well distributed in the regenerated cellulose matrix. The antimicrobial testing resulted in a successful growth inhibition of *E. coli* and *S. aureus* strains by 80% and 95%, respectively [68].

The green synthesis of CuNPs and cellulose matrix by *Terminalia catappa* [69] and *Ocimum sanctum* leaf extracts [70] as reducing agent delivers good results. These nanocomposites are suitable for food packaging due to their antimicrobial activities.

The production of antimicrobial textile nanocomposite by in situ synthesis of Cu-based nanoparticles on cotton fabrics modified with different polycarboxylic acids is available. Treated cotton fabric had excellent antibacterial activity by inhibiting 99.9% of *E. coli* and *S. aureus* [71].

Chitosan is a naturally occurring polymer and has a widespread use in many fields of medical applications. Incorporation of chitosan with CuNPs to form nanocomposites is well known. These nanocomposites have high antibacterial activity against MRSA and multidrug resistant *E. coli* clinical isolates. CuNPs can be synthesized via chemical reduction method using ginger (*Zingiber officinale*) extract and L-ascorbic acid. The NPs with chitosan were more active against MRSA strains and have lower antibacterial activity against *E. coli* in comparison with pure CuNPs [72].

Microwave heating technique leads to the formation of chitosan/copper nanocomposite [73]. The antimicrobial effects of the nanocomposite against *S. aureus* and *Salmonella enterica* were tested. The composite film was effective in the alteration of the cell wall and reduction of microbial concentration in the liquid culture for both bacteria tested [73]. This nanocomposite can be prepared by an approach based on femto second laser ablation in aqueous solution giving stable nanocomposite [74].

Molecular iodine stabilizes the copper/chitosan nanoparticles [75]. The NPs were unstable in atmospheric conditions leading to the formation of oxides of Cu. Addition of molecular iodine to the medium following the synthesis step results in stable NPs. Antibacterial activity screenings on *E. coli* and *B. cereus* resulted in low MIC values for CuNPs. The iodinated chitosan-CuNPs composite attaches to the bacterial cell wall causing destruction to the membrane and eventually leading to cell death [75].

Some studies used synthetic polymers such as polyethylene to support the NPs. Polyethylene modified with copper nanoparticles (PE-CuNPs) have been investigated against *Listeria monocytogenes (L. monocytogenes)* in order to clarify the antibacterial mechanism and to determine the extent of release of Cu^{2+} [76]. CuNPs released from the nanocomposites can penetrate into the cell wall and the plasma membrane of bacteria. The antibacterial abilities of the nanocomposite against *L. monocytogenes* are associated with both bactericidal and bacteriolytic effects [76]. In a further study, PE-CuNPs are effective against *E. coli*. PE-CuNPs completely suppressed the number of live bacteria after 12 h incubation [77].

Starch was used with CuNPs to produce an antimicrobial nanocomposite as well [30]. Water soluble monodisperse CuNPs of about 10 nm diameter were prepared by microwave irradiation using starch as green capping agent. The resulting Cu–starch conjugate solution exhibited excellent bactericidal action against *S. aureus, E. coli and S. typhi*. In addition, these nanocomposites exhibit also lower toxicity than copper ions [30].

Alginate is a naturally occurring polymer and stabilizes CuNPs. The CuNPs-alginate composite was prepared via microwave irradiation and is an effective antimicrobial agent [78]. Calcium alginate impregnated on cotton fabric loaded with CuNPs was effective against *E. coli* [79].

Polyvinylalcohol (PVA) is a water soluble synthetic polymer. PVA cryogel–copper nanocomposites were prepared. The gelation of PVA is possible through the freeze–thaw method. An aqueous solution of PVA is frozen at −20 °C and then thawn back to room temperature repeating this processes several times. The physical crosslinking of PVA chains by successive freezing–thawing cycles are able to form crystallites by strong interchain hydrogen bonding. This offers large, free spaces between the cross-linked networks in the swollen polymer that can act as nanoreactors for the nucleation and growth of the CuNPs [80]. The PVA cryogel–copper nanocomposites demonstrated significant antibacterial effects against *E. coli*, *S. aureus*, *P. aeruginosa*, *V. cholerae* and *B. subtilis*. The biocompatibility test revealed that the biocompatibility of the nanocomposite increases on increasing the concentration of PVA. This nanocomposite is suitable for antimicrobial purposes such as packaging, wound dressing and as antibacterial materials [80].

Polyaniline, a synthetic polymer well known for its high conductivity, is a good as dispersion medium of CuNPs leading to enhanced antimicrobial properties. The synthesis of the nanocomposite by simple in situ polymerization method is successful [78]. The CuNPs are uniformly dispersed in the polymer and inhibit effectively *E. coli*, *S. aureus* and *C. albicans*. The nanocomposite exhibits higher antimicrobial activity than any component acting alone [81].

Hyaluronic acid (HA) is an essential component of the extracellular matrix of the skin. HA doped with CuNPs was reported as an antibacterial active nanocomposite [82]. Films of HA doped with NPs enhanced skin recovery and controlled bacterial infections of wounds. The antibacterial results proved the activity against *E. coli*, *S. aureus*, *S. epidermidis* and *P. aeruginosa*. Toxicological tests in rats showed no alterations in hepatic parameters. These films may be useful promoters of skin recovery for grades I and II cutaneous burns and as scaffolds [82].

Polyurethanes are biocompatible polymers with valuable properties. New biologically active polyurethanes with copper nanoparticles were prepared [83]. The polymer/NPs matrix synthesis by electron beam evaporation technology and vacuum deposition method confirms the uniform distribution of NPs in the polymer matrix. Polyurethanes containing Cu nanoparticles possess bactericidal/bacteriostatic effects against bacteria, fungi and yeast-like fungi. The resulting biologically active metal-containing polyurethane materials are valuable for medical purposes [83].

Another group prepared was copper metal and copper oxide nanoparticles in a polypropylene matrix [84]. These composites possess strong antimicrobial behavior against *E. coli* that depends on the contact time between the sample and the bacteria. After just 4 h of contact, these samples were able to kill more than 95% of the bacteria [84].

Sphere-shaped and monodispersed CuNP coated with poly(styrene-co-sulfonic acid) was successfully synthesized by a green and facile synthesis method [85]. This monodispersing system showed excellent antibacterial properties against *E. coli* and *S. aureus* [85]. CuNPs embedded in polylactic acid, merge the antibacterial properties of copper nanoparticles with the biodegradability of the polymer matrix. This nanocomposite showed activity against *Pseudomonas* species [86].

The methods of synthesis of the above polymer CuNPs together with their antibacterial activity are listed in Table 24.3.

24.4.4.2   CuNPs with Other Metals as Antimicrobial Agents

Besides the NPs of pure metals, bimetallic NPs have gained attention because they exhibit better or different properties compared to pure, single-metal NPs [87]. Moreover, the change in compositional percentage of metals offers way for changing the properties of bimetallic NPs according to the desired applications. Recent studies reveal that Cu–Ag NPs possess better antibacterial activity than individual Cu or Ag NPs against both Gram-negative and Gram-positive pathogens [87].

The synthesis of nanoparticles containing Ag/Cu in the form of bimetallic nanoparticles (alloy and core-shell) as well as ionic species was reported [88].

Table 24.3 Synthesis of polymer-CuNPsCuO NPs and their antimicrobial activity

Polymer used	Method of synthesis	Size and shape	Antimicrobial activity	Refs.
Regenerated cellulose from cotton	Chemical reduction using $NaBH_4$ as reducing agent and $CuSO_4$ as precursor	Nanorod particles about 60 nm length and 25 nm diameter	Active against *S. aureus* and *E. coli*. After 30 min. of exposure the bacterial concentrations showed 4-log reduction in *S. aureus* and 3-log reduction in *E. coli* when using the Cu/cellulose nanocomposite film	[64]
Regenerated cellulose from bacteria	Chemical reduction using $CuCl_2$ as precursor	Cu element distributed uniformly in the membrane	ZOI: *S. aureus* (20–29 mm); *B. subtilis* (10.8–21.5 mm); *C. albicans* (19–29 mm); *E. coli* (14.3–20 mm); *P. aeruginosa* (10–16.2 mm)	[65]
TEMPO nanofibrillated cellulose (TNFC)	Chemical reduction using $NaBH_4$ and $CuSO_4$ as precursor	Spherical, around 9 nm	Reduction of *E. coli* increased on 1-week exposure to films containing 0.4, 0.5, and 0.6% of CuNPs. PVA film containing copper content of 0.6 wt% resulted in 5-log microbial reduction in *E. coli* DH5α	[67]
Cellulose dissolving pulp	Chemical reduction using formaldehyde and sodium hydroxide as reducing agent and $CuSO_4 \cdot 5\ H_2O$ as precursor	15–30 nm in size and well distributed in cellulose	After 72 h, the optical density (OD) remained the same in *E. coli* (0.32 OD), but continued to decline in *S. aureus* (0.08 OD)	[68]

(continued)

Table 24.3 (continued)

Polymer used	Method of synthesis	Size and shape	Antimicrobial activity	Refs.
Cellulose	Green reduction using *Terminalia catappa* leaf extract	10–60 nm	ZOI: *E. coli* (12 mm)	[69]
Cellulose	Green reduction using *Ocimum sanctum* leaf extract	Spherical (60–70 nm)	ZOI: *E. coli* (8 mm, 14 mm and 18 mm for different concentrations)	[70]
Cotton fibers	In situ synthesis and sodium borohydride as a reducing agent	Not mentioned	Bacterial reduction R: 99.9% for *E. coli* ATCC 25922 and *S. aureus* ATCC 25923 with number of bacterial colonies CFU < 10	[71]
Chitosan	Chemical reduction using ginger extract and ascorbic acid and copper acetate as precursor	15–20 nm in size and roundish structures 770 ± 90 nm in size	100% inhibition against MRSA and *E. coli* strains in concentration of 0.7 µg/ml	[72]
Chitosan	Microwave oven and Cu metal as starting material	10.6 ± 1 nm	Reduction of microbial concentration in liquid culture exposed to film: *S. aureus* (3.3×10^6 cell/ml initial to 3.0×10^5 cells/ml final concentration) and *S. typhi* (3.3×10^6 cell/ml initial to 1.8×10^5 cells/ml final concentration)	[73]
Chitosan	Femto second laser ablation	Not mentioned	Growth inhibition after 4 h contact at 10^4–10^5 cfu/mL range against *E. coli*	[74]

(continued)

Table 24.3 (continued)

Polymer used	Method of synthesis	Size and shape	Antimicrobial activity	Refs.
Chitosan	Chemical reduction using hydrazine as reducing agent and $CuSO_4$ as precursor	Spherical and average diameters 8 ± 4 nm	MIC: *E. coli* (130.8 µg/mL); *B. cereus* (165.13 µg/mL)	[75]
Polyethylene	Chemical reduction of $CuCl_2$ with sodium borohydride in the presence of sodium citrate	2–4 nm	PE-CuNPs 5 wt% result with the highest viability of 60% after 10 h of incubation time by *L. monocytogenes* [76] and 110% by *E. coli* [77]	[76, 77]
Starch	Microwave irradiation and copper nitrate as starting agent	10 nm	MIC: *E. coli* (1.6 $\pm$ 0.22 µg/mL); *S. aureus* (3.2 $\pm$ 0.41 µg/mL); *S. typhi* (3.6 $\pm$ 0.43 µg/mL)	[30]
Alginate	Microwave heating, copper nitrate and ascorbic acid	3–10 nm	ZOI: *S. aureus* (12 mm); *E. coli* (10 mm) and *S. enterica serovar typhimurium* (12 mm)	[78]
PVA	Chemical reduction using hydrazine	Average particle size of around 20 nm	ZOI: *E. coli* (~3 mm); *S. aureus* (~12.5 mm); *P. aeruginosa* (~23 mm); *V. cholerae* (~25 mm); *B. subtilis* (~26 mm)	[80]
Polyaniline	Oxidative polymerization with $CuCl_2 \cdot 2H_2O$ as starting material	Uniformly dispersed in the polymer and narrow size distribution (6 nm)	100% cell reduction of *E. coli*, *S. aureus*, and *C. albicans* for concentrations of nanocomposite (1, 2, 5, 10, and 20 ppm) by Cu/PANI	[81]

(continued)

Table 24.3 (continued)

Polymer used	Method of synthesis	Size and shape	Antimicrobial activity	Refs.
Hyaluronic acid	Chemical liquid deposition-solvated metal atom dispersion	13.33 nm	MIC of 0.048 mg/mL for *E. coli*, *S. aureus*, *S. epidermis* and *P. aeruginosa*	[82]
Polyurethane	Deposition of the vapor flow from the vapor phase	Average particle size: 52 nm	Bacteria, fungi and yeast-like fungi show growth inhibition zones of 0–2 mm as highest sensitivity against Cu/Ag (200/69 ppm) combination	[83]
Polypropylene	Use of a Brabender plastic order under a nitrogen atmosphere	Average size: 10 nm	*E. coli:* after 4 h of contact reduction of the bacterial concentration by PP/CuP 90% and PP/CuOP 99%	[84]
Poly(styrene-co-sulfonic acid)	Glucose or NaBH$_4$ and Cu(NO$_3$)$_2$3H$_2$Oas starting material	Average diameter: 120 nm	MIC: *E. coli* (2 g/L); *S. aureus* (4 g/L)	[85]
Polylactic acid	Pulsed laser ablation in liquid	Spherical and mean diameter of 36 ± 9 nm	*Pseudomonas* species cell load decreased to 6.0 Log CFU/mL in CuNPs-C-PLA compared to blank sample PLA (7.4 Log CFU/mL)	[86]

These NPs impregnated in cotton-polyester textiles exhibited antimicrobial properties against *E. coli*, *S. aureus*, and *C. albicans* [88]. Microwave was used for the preparation of bimetallic NPs of copper and silver using starch as stabilizing agent and ascorbic acid as the reducing agent [89]. Another group has prepared these nano-alloys through chemical co-reduction method. The metal salts dissolved in aqueous solution with hydrazine hydrate as reducing agent in the presence of sodium citrate as complexing agent and cysteine as stabilizer, prevented the oxidation of copper [90]. Their antibacterial behavior against *E. coli* strains, revealed far better activity compared to AgNPs nanoparticles [90].

Silver salts NPs with copper are valuable antimicrobial agents. The preparation of silver sulfide (Ag$_2$S) NPs doped with copper by simple chemical co-precipitation method is possible [91]. The morphological study showed products of spherical

shape with a diameter size of 30 nm. The antibacterial test revealed that the Cu doped Ag_2S nanoparticles have increased antibacterial performance compared with un-doped Ag_2S nanoparticles [91].

Zinc was reported as an antimicrobial agent in the literature as well as in combination with Cu in the form of copper doped with zinc sulfide (Cu:ZnS). The NPs are potential antibacterial agents. These NPs were prepared through a solvo-thermal approach using mercapto-succinic acid and sodium citrate as differential capping agents [92]. For the assessment of the antibacterial properties of Cu:ZnS nano systems, the disk diffusion assay was performed against both Gram-positive and Gram-negative bacteria. There is promising antibacterial activity for the prepared Cu:ZnS, with a noticeable activity of nanosystem synthesized with mercaptopropionic acid making them a novel class of potential antibacterial agents [92].

24.4.4.3 CuNPs with Nanomaterials as Antimicrobial Agents

Many research groups have tested the antibacterial activity of metal nanoparticles with other nanostructure materials. Carbon nanotube (CNT) together with CuNPs are antimicrobial agents [93]. Chemical reduction method followed by high energy ball milling method was used for the preparation. The antimicrobial activity of Cu/CNTs nanocomposite against *Providencia species*, *Bacillus species* and *E. coli* is high. The findings indicate that this nanocomposite can stop bacterial growth [93]. Multi wall carbon nanotubes (MWCNT) and copper nanocomposite were prepared by using a reduction method. MWCNT/Cu nanocomposite killed 75% of *E. coli*. This nanocomposite has uses in biomedical devices and antibacterial controlling systems [94].

Antimicrobial applications of graphene with silver and copper NPs were investigated. Copper monometallic and Ag/Cu bimetallic NPs were grown in-situ on the surface of graphene, synthesized by chemical vapor deposition [95]. The bimetallic Ag/CuNP-graphene hybrids exhibit superior performance, achieving complete bacterial inhibition. This prominent performance is due to the synergistic action of the combination of the two different metals that coexist on the surface as well as the improving role of the graphene support [95]. Graphene was also incorporated with copper salts. An antibacterial agent made from copper oxide nanoparticles loaded onto the surfaces of graphene oxide sheets was reported [96]. The authors suggested that this have great potential for managing crop diseases.

The Cu/Ag bimetal nanoparticles were carbonized with steam to produce porous carbon beads doped with metal NPs [97]. The prepared bimetal (Cu and Ag) NPs-doped beads exhibited significantly larger anti-bacterial activities than single-(Cu or Ag) metal-doped beads for both Gram-positive *S. aureus* and Gram-negative *E. coli*. The prepared bimetal beads remained effective for 120 h, completely inhibiting the bacterial growth, and therefore, they are potential antibacterial agents for water purification [97].

24.4.4.4   CuNPs with Silica

Mixtures of silicone and copper NPs have powerful antimicrobial activities than monometallic NPs. Silicon dioxide (SiO_2) NPs were prepared as the core and CuNPs as the shell [98]. The inhibition of *E. coli* is stronger than that of *S. aureus* and *C. albicans* after 24 h incubation [98]. The antibacterial efficacy was evaluated against *B. subtilis*. The authors suggested the enhancement of Cu bioavailability (i.e., more soluble Cu) due to its core-shell design [99]. In order to obtain an antimicrobial gel, a starch based hydrogel reinforced with silica coated CuNPs was developed and tested against *E. coli* and *S. aureus* strains. The hydrogels maintained the antimicrobial activity for at least four cycles of use. A dermal acute toxicity test showed that the material could be considered as slightly irritant, showing its biocompatibility. This silica-CuNP loaded hydrogel may show high possibility for applications in various clinical fields, such as wound dressings and fillers [100].

24.4.4.5   CuNPs with Proteins and Amino Acids

Bovine serum albumin (BSA) is a widely studied protein. A method for the synthesis of BSA and copper nanocomposite showed the formation of a well-dispersed hexagonal Cu-BSA composite [101]. The synthesized copper nanocomposites containing BSA material exhibited good antibacterial potential against both Gram-positive and Gram-negative bacterial strains. Transmission electron microscopy and cytoplasmic leakage analysis revealed that the Cu-BSA composite attached to the bacteria causes irreversible membrane injury leading to leak of intracellular metabolites and finally death of the organism [101]. Another study reported a comparison of the antibacterial properties of copper-amino acids chelates and CuNPs against *E. coli*, *S. aureus* and *E. faecalis*. The preparation of copper-amino acids chelates by using a soybean aqueous extract is a valuable green method. Copper chelates have enhanced antimicrobial activity against *E. faecalis* [102].

24.5   Conclusion

In the last few decades, the number of infectious diseases caused by different pathogenic bacteria increased while resistance towards various types of antibiotics accelerated. Therefore, finding new and more effective antibacterial agents became a serious need for the survival of the human race.

Interest in inorganic and metallic nanoparticles as antimicrobial agents is now over a decade old. Nanoparticles are even effective in very small amounts. A large number of particles can be produced with high surface area to volume ratio. Currently, a broad variety of metals and their compounds are used in microbiological research for their potential antimicrobial activity.

Owing to their electrical, optical, and catalytic properties, copper nanoparticles are widely used and have various medical, antifungal, and antibacterial applications. Several mechanisms, including disruption of plasma membrane integrity caused by lipid peroxidation and oxidative damage to DNA and protein, are directly related to the antimicrobial activity of copper. In many cases, the production of ROS is associated with the cell damage.

At low concentrations copper is a cofactor for metalloproteins and enzymes, therefore, it has the advantage of low toxicity for animal cells when compared to other metals. In addition, copper is inexpensive in relation to other metals with antibacterial properties such as silver.

Different polymers are useful as matrices to support copper nanoparticles and generate composite materials with antimicrobial properties. The use of polymers for developing nanocomposites with antimicrobial activity does not only provide a supporting function for nanoparticles, but can also enhance the antibacterial performance of nanocomposites. The preparation of hybrid composites based on copper nanoparticles-cellulose has generated a large number of materials with antibacterial activity.

References

1. Pelgrift RY, Friedman AJ (2013) Nanotechnology as a therapeutic tool to combat microbial resistance. Adv Drug Deliv Rev 65:1803–1815
2. Dizaj SM, Lotfipour F, Barzegar-Jalali M, Zarrintan MH, Adibkia K (2014) Antimicrobial activity of the metals and metal oxide nanoparticles. Mater Sci Eng, C 44:278–284
3. Ingle AP, Duran N, Rai M (2014) Bioactivity, mechanism of action, and cytotoxicity of copper-based nanoparticles: a review. Appl Microbiol Biotechnol 98:1001–1009
4. Slavin YN, Asnis J, Häfeli UO, Bach H (2017) Metal nanoparticles: understanding the mechanisms behind antibacterial activity. J Nanobiotechnol 15:1–20
5. Hoseinzadeh E, Makhdoumi P, Taha P, Hossini H, Stelling J, Kamal MA et al (2017) A review on nano-antimicrobials: metal nanoparticles, methods and mechanisms. Curr Drug Metab 18:120–128
6. Hemeg HA (2017) Nanomaterials for alternative antibacterial therapy. Int J Nanomed 12:8211–8225
7. Panariti A, Miserocchi G, Rivolta I (2012) The effect of nanoparticle uptake on cellular behavior: disrupting or enabling functions? Nanotechnol Sci Appl 5:87–100
8. Cioffi N, Torsi L, Ditaranto N, Tantillo G, Ghibelli L, Sabbatini L et al (2005) Copper nanoparticle/polymer composites with antifungal and bacteriostatic properties. Chem Mater 17:5255–5262
9. Usman MS, El Zowalaty ME, Shameli K, Zainuddin N, Salama M, Ibrahim NA (2013) Synthesis, characterization, and antimicrobial properties of copper nanoparticles. Int J Nanomed 8:4467–4479
10. Cady NC, Behnke JL, Strickland AD (2011) Copper-based nanostructured coatings on natural cellulose: nanocomposites exhibiting rapid and efficient inhibition of a multi-drug resistant

wound pathogen, *A. baumannii*, and mammalian cell biocompatibility *in vitro*. Adv Funct Mater 21:2506–2514

11. Din MI, Rehan R (2017) Synthesis, characterization, and applications of copper nanoparticles. Anal Lett 50:50–62

12. Khodashenas B, Ghorbani HR (2014) Synthesis of copper nanoparticles: an overview of the various methods. Korean J Chem Eng 31:1105–1109

13. Keller AA, Adeleye AS, Conway JR, Garner KL, Zhao L, Cherr GN et al (2017) Comparative environmental fate and toxicity of copper nanomaterials. Nano Impact 7:28–40

14. Karlsson HL, Cronholm P, Gustafsson J, Möller L (2008) Copper oxide nanoparticles are highly toxic: a comparison between metal oxide nanoparticles and carbon nanotubes. Chem Res Toxicol 21:1726–1732

15. Hatamie A, Zargar B, Jalali A (2014) Copper nanoparticles: a new colorimetric probe for quick, naked-eye detection of sulfide ions in water samples. Talanta 121:234–238

16. Kim DK, Yoo SM, Park TJ, Yoshikawa H, Tamiya E, Park JY et al (2011) Plasmonic properties of the multispot copper-capped nanoparticle array chip and its application to optical biosensors for pathogen detection of multiplex DNAs. Anal Chem 83:6215–6222

17. Ojha NK, Zyryanov GV, Majee A, Charushin VN, Chupakhin ON, Santra S (2017) Copper nanoparticles as inexpensive and efficient catalyst: a valuable contribution in organic synthesis. Coord Chem Rev 353:1–57

18. Shankar S, Rhim JW (2014) Effect of copper salts and reducing agents on characteristics and antimicrobial activity of copper nanoparticles. Mater Lett 132:307–311

19. Rubilar O, Rai M, Tortella G, Diez MC, Seabra AB, Durán N (2013) Biogenic nanoparticles: copper, copper oxides, copper sulphides, complex copper nanostructures and their applications. Biotechnol Lett 35:1365–1375

20. Tiwari M, Jain P, Chandrashekhar Hariharapura R, Narayanan K, Bhat KU, Udupa N et al (2016) Biosynthesis of copper nanoparticles using copper-resistant *Bacillus cereus*, a soil isolate. Process Biochem 51:1348–1356

21. Varshney R, Bhadauria S, Gaur MS, Pasricha R (2010) Characterization of copper nanoparticles synthesized by a novel microbiological method. JOM 62:102–104

22. Jang GG, Jacobs CB, Gresback RG, Ivanov IN, Meyer HM, Kidder M et al (2015) Size tunable elemental copper nanoparticles: extracellular synthesis by thermoanaerobic bacteria and capping molecules. J Mater Chem C 3:644–650

23. Prabhu YT, Venkateswara Rao K, Sesha Sai V, Pavani T (2017) A facile biosynthesis of copper nanoparticles: a micro-structural and antibacterial activity investigation. J Saudi Chem Soc 21:180–185

24. Nasrollahzadeh M, Momeni SS, Sajadi SM (2017) Green synthesis of copper nanoparticles using *Plantago asiatica* leaf extract and their application for the cyanation of aldehydes using $K_4Fe(CN)_6$. J Colloid Interface Sci 506:471–477

25. Nagajyothi PC, Muthuraman P, Sreekanth TVM, Kim DH, Shim J (2017) Green synthesis: *in-vitro* anticancer activity of copper oxide nanoparticles against human cervical carcinoma cells. Arab J Chem 10:215–225

26. Nasrollahzadeh M, Sajadi SM, Rostami-Vartooni A, Hussin SM (2016) Green synthesis of CuO nanoparticles using aqueous extract of *Thymus vulgaris* L. leaves and their catalytic performance for N-arylation of indoles and amines. J Colloid Interface Sci 466:113–119

27. Suárez-Cerda J, Espinoza-Gómez H, Alonso-Núñez G, Rivero IA, Gochi-Ponce Y, Flores-López LZ (2017) A green synthesis of copper nanoparticles using native cyclodextrins as stabilizing agents. J Saudi Chem Soc 21:341–348

28. Ren G, Hu D, Cheng EWC, Vargas-Reus MA, Reip P, Allaker RP (2009) Characterization of copper oxide nanoparticles for antimicrobial applications. Int J Antimicrob Agents 33:587–590

29. Tamayo L, Azócar M, Kogan M, Riveros A, Páez M (2016) Copper-polymer nanocomposites: an excellent and cost-effective biocide for use on antibacterial surfaces. Mater Sci Eng, C 69:1391–1409

30. Valodkar M, Rathore PS, Jadeja RN, Thounaojam M, Devkar RV, Thakore S (2012) Cytotoxicity evaluation and antimicrobial studies of starch capped water soluble copper nanoparticles. J Hazard Mater 201–202:244–249

31. Pramanik A, Laha D, Bhattacharya D, Pramanik P, Karmakar P (2012) A novel study of antibacterial activity of copper iodide nanoparticle mediated by DNA and membrane damage. Colloid Surf B 96:50–55

32. Kim YH, Lee DK, Cha HG, Kim CW, Kang YC, Kang YS (2006) Preparation and characterization of the antibacterial Cu nanoparticle formed on the surface of SiO_2 nanoparticles. J Phys Chem B 110:24923–24928

33. Chang Y-N, Zhang M, Xia L, Zhang J, Xing G (2012) The toxic effects and mechanisms of CuO and ZnO nanoparticles. Materials (Basel) 5:2850–2871

34. Meghana S, Kabra P, Chakraborty S, Padmavathy N (2015) Understanding the pathway of antibacterial activity of copper oxide nanoparticles. RSC Adv 5:12293–12299

35. Ruparelia JP, Chatterjee AK, Duttagupta SP, Mukherji S (2008) Strain specificity in antimicrobial activity of silver and copper nanoparticles. Acta Biomater 4:707–716

36. Schrand AM, Rahman MF, Hussain SM, Schlager JJ, Smith DA, Syed AF (2010) Metal-based nanoparticles and their toxicity assessment. Interdisc Rev Nanomed Nanobiotechnol 2:544–568

37. Zain NM, Stapley AGF, Shama G (2014) Green synthesis of silver and copper nanoparticles using ascorbic acid and chitosan for antimicrobial applications. Carbohydr Polym 112:195–202

38. Rakhmetova AA, Alekseeva TP, Bogoslovskaya OA, Leipunskii IO, Olkhovskaya IP, Zhigach AN et al (2010) Wound-healing properties of copper nanoparticles as a function of physicochemical parameters. Nanotechnol Russ 5:271–276

39. Raffi M, Mehrwan S, Bhatti TM, Akhter JI, Hameed A, Yawar W et al (2010) Investigations into the antibacterial behavior of copper nanoparticles against *Escherichia coli*. Ann Microbiol 60:75–80

40. Ramyadevi J, Jeyasubramanian K, Marikani A, Rajakumar G, Rahuman AA (2012) Synthesis and antimicrobial activity of copper nanoparticles. Mater Lett 71:114–116

41. Galletti AMR, Antonetti C, Marracci M, Piccinelli F, Tellini B (2013) Novel microwave-synthesis of Cu nanoparticles in the absence of any stabilizing agent and their antibacterial and antistatic applications. Appl Surf Sci 280:610–618

42. Lewis Oscar F, MubarakAli D, Nithya C, Priyanka R, Gopinath V, Alharbi NS et al (2015) One pot synthesis and anti-biofilm potential of copper nanoparticles (CuNPs) against clinical strains of *Pseudomonas aeruginosa*. Biofouling 31:379–391

43. Zakharova OV, Godymchuk AY, Gusev AA, Gulchenko SI, Vasyukova IA, Kuznetsov DV (2015) Considerable variation of antibacterial activity of Cu nanoparticles suspensions depending on the storage time, dispersive medium, and particle sizes. Biomed Res 2015:412530

44. Godymchuk A, Frolov G, Gusev A, Zakharova O, Yunda E, Kuznetsov D et al (2015) Antibacterial properties of copper nanoparticle dispersions: influence of synthesis conditions and physicochemical characteristics. IOP Conf Ser Mater Sci Eng 98:012033

45. Lee HJ, Song JY, Kim BS (2013) Biological synthesis of copper nanoparticles using *Magnolia kobus* leaf extract and their antibacterial activity. J Chem Technol Biotechnol 88:1971–1977

46. Shende S, Ingle AP, Gade A, Rai M (2015) Green synthesis of copper nanoparticles by *Citrus medica* Linn. (Idilimbu) juice and its antimicrobial activity. World J Microbiol Biotechnol 31:865–873

47. Jadhav S, Gaikwad S, Nimse M, Rajbhoj A (2011) Copper oxide nanoparticles: synthesis, characterization and their antibacterial activity. J Clust Sci 22:121–129

48. Azam A, Ahmed AS, Oves M, Khan MS, Memic A (2012) Size-dependent antimicrobial properties of CuO nanoparticles against gram-positive and -negative bacterial strains. Int J Nanomed 7:3527–3535

49. Agarwala M, Choudhury B, Yadav RNS (2014) Comparative study of antibiofilm activity of copper oxide and iron oxide nanoparticles against multidrug resistant biofilm forming uropathogens. Indian J Microbiol 54:365–368

50. Ahamed M, Alhadlaq HA, Khan MAM, Karuppiah P, Al-Dhabi NA (2014) Synthesis, characterization, and antimicrobial activity of copper oxide nanoparticles. J Nanomater (Article ID 637858)

51. Ananth A, Dharaneedharan S, Heo MS, Mok YS (2015) Copper oxide nanomaterials: synthesis, characterization and structure-specific antibacterial performance. Chem Eng J 262:179–188

52. El-Nahhal IM, Zourab SM, Kodeh FS, Selmane M, Genois I, Babonneau F (2012) Nanostructured copper oxide-cotton fibers: synthesis, characterization, and applications. Int Nano Lett 2:1–5

53. Das D, Nath BC, Phukon P, Dolui SK (2013) Synthesis and evaluation of antioxidant and antibacterial behavior of CuO nanoparticles. Colloid Surf B 101:430–433

54. Padil VVT, Černík M (2013) Green synthesis of copper oxide nanoparticles using *gum karaya* as a biotemplate and their antibacterial application. Int J Nanomed 8:889–898

55. Sutradhar P, Saha M, Maiti D (2014) Microwave synthesis of copper oxide nanoparticles using tea leaf and coffee powder extracts and its antibacterial activity. J Nanostructure Chem 4:86

56. Sivaraj R, Rahman PKSM, Rajiv P, Salam HA, Venckatesh R (2014) Biogenic copper oxide nanoparticles synthesis using *Tabernaemontana divaricate* leaf extract and its antibacterial activity against urinary tract pathogen. Spectrochim Acta A Mol Biomol Spectrosc 133:178–181

57. Hassan MS, Amna T, Yang OB, El-Newehy MH, Al-Deyab SS, Khil MS (2012) Smart copper oxide nanocrystals: synthesis, characterization, electrochemical and potent antibacterial activity. Colloid Surface B 97:201–206

58. Laha D, Pramanik A, Laskar A, Jana M, Pramanik P, Karmakar P (2014) Shape-dependent bactericidal activity of copper oxide nanoparticle mediated by DNA and membrane damage. Mater Res Bull 59:185–191

59. Sabatini C, Mennito AS, Wolf BJ, Pashley DH, Renn WG (2015) Incorporation of bactericidal poly-acrylic acid modified copper iodide particles into adhesive resins. J Dent 43:546–555

60. Renné WG, Lindner A, Mennito AS, Agee KA, Pashley DH, Willett D et al (2017) Antibacterial properties of copper iodide-doped glass ionomer-based materials and effect of copper iodide nanoparticles on collagen degradation. Clin Oral Investig 21:369–379

61. Ayaz Ahmed KB, Anbazhagan V (2017) Synthesis of copper sulfide nanoparticles and evaluation of *in vitro* antibacterial activity and *in vivo* therapeutic effect in bacteria-infected zebrafish. RSC Adv 7:36644–36652

62. Malarkodi C, Rajeshkumar S (2017) *In vitro* bactericidal activity of biosynthesized CuS nanoparticles against UTI-causing pathogens. Inorg Nano-Metal Chem 47:1290–1297

63. Palza H (2015) Antimicrobial polymers with metal nanoparticles. Int J Mol Sci 16:2099–2116

64. Jia B, Mei Y, Cheng L, Zhou J, Zhang L (2012) Preparation of copper nanoparticles coated cellulose films with antibacterial properties through one-step reduction. ACS Appl Mater Interfaces 4:2897–2902

65. Shao W, Wang S, Wu J, Huang M, Liu H, Min H (2016) Synthesis and antimicrobial activity of copper nanoparticle loaded regenerated bacterial cellulose membranes. RSC Adv 6:65879–65884

66. Pinto RJB, Daina S, Sadocco P, Neto CP, Trindade T (2013) Antibacterial activity of nanocomposites of copper and cellulose. Bio Med Res Int 2013:280512

67. Zhong T, Oporto GS, Jaczynski J, Jiang C (2015) Nanofibrillated cellulose and copper nanoparticles embedded in polyvinyl alcohol films for antimicrobial applications. Biomed Res Int 2015:456834

68. Eivazihollagh A, Bäckström J, Dahlström C, Carlsson F, Ibrahem I, Lindman B, Edlund H, Norgren M (2017) One-pot synthesis of cellulose-templated copper nanoparticles with antibacterial properties. Mater Lett 187:170–172

69. Muthulakshmi L, Rajini N, Nellaiah H, Kathiresan T, Jawaid M, Rajulu AV (2017) Preparation and properties of cellulose nanocomposite films with *in situ* generated copper nanoparticles using *Terminalia catappa* leaf extract. Int J Biol Macromol 95:1064–1071

70. Sadanand V, Rajini N, Varada Rajulu A, Satyanarayana B (2016) Preparation of cellulose composites with *in situ* generated copper nanoparticles using leaf extract and their properties. Carbohydr Polym 150:32–39

71. Marković D, Deeks C, Nunney T, Radovanović Ž, Radoičić M, Šaponjić Z, Radetić M (2018) Antibacterial activity of Cu-based nanoparticles synthesized on the cotton fabrics modified with polycarboxylic acids. Carbohydr Polym 200:173–182

72. Holubnycha V, Pogorielov M, Korniienko V, Kalinkevych O, Ivashchenko O, Peplinska B, Jarek M(2017) Antibacterial activity of the new copper nanoparticles and Cu NPs/ chitosan solution. In: IEEE 7th international conference on Nanomaterials: Applications and Properties (NAP) 201:2–5

73. Cárdenas G, Díaz VJ, Meléndrez MF, Cruzat CC, García Cancino A (2009) Colloidal Cu nanoparticles/chitosan composite film obtained by microwave heating for food package applications. Polym Bull 62:511–524

74. Ancona A, Sportelli MC, Trapani A, Picca RA, Palazzo C, Bonerba E et al (2014) Synthesis and characterization of hybrid copper-chitosan nano-antimicrobials by femtosecond laser-ablation in liquids. Mater Lett 136:397–400

75. Mallick S, Sharma S, Banerjee M, Ghosh SS, Chattopadhyay A, Paul A (2012) Iodine-stabilized Cu nanoparticle chitosan composite for antibacterial applications. ACS Appl Mater Interfaces 4:1313–1323

76. Tamayo LA, Zapata PA, Vejar ND, Azócar MI, Gulppi MA, Zhou X et al (2014) Release of silver and copper nanoparticles from polyethylene nanocomposites and their penetration into *Listeria monocytogenes*. Mater Sci Eng, C 40:24–31

77. Tamayo LA, Zapata PA, Rabagliati FM et al (2015) Antibacterial and non-cytotoxic effect of nanocomposites based in polyethylene and copper nanoparticles. J Mater Sci Mater Med 26:129

78. Díaz-Visurraga J, Daza C, Pozo C, Becerra A, von Plessing C, García A (2012) Study on antibacterial alginate-stabilized copper nanoparticles by FT-IR and 2D-IR correlation spectroscopy. Int J Nanomed 7:3597–3612

79. Bajpai SK, Bajpai M, Sharma L (2012) Copper nanoparticles loaded alginate-impregnated cotton fabric with antibacterial properties. J App Pol Sci 126:E319–E326

80. Chaturvedi A, Bajpai AK, Bajpai J, Sharma A (2015) Antimicrobial poly(vinyl alcohol) cryogel-copper nanocomposites for possible applications in biomedical fields. Des Monomers Polym 18:385–400

81. Bogdanović U, Vodnik V, Mitrić M, Dimitrijević S, Škapin SD, Žunič V et al (2015) Nanomaterial with high antimicrobial efficacy copper/polyaniline nanocomposite. ACS Appl Mater Interfaces 7:1955–1966

82. Cárdenas-Triviño G, Ruiz-Parra M, Vergara-González L, Ojeda-Oyarzún J, Solorzano G (2017) Synthesis and bactericidal properties of hyaluronic acid doped with metal nanoparticles. J Nanomater 2017 (Article ID 9573869)

83. Savelyev Y, Gonchar A, Movchan B, Gornostay A, Vozianov S, Rudenko A et al (2017) Antibacterial polyurethane materials with silver and copper nanoparticles. Mater Today Proc 4:87–94

84. Delgado K, Quijada R, Palma R, Palza H (2011) Polypropylene with embedded copper metal or copper oxide nanoparticles as a novel plastic antimicrobial agent. Lett Appl Microbiol 53:50–54

85. Zhang N, Yu X, Hu J (2014) Synthesis of copper nanoparticle-coated poly(styrene-co-sulfonic acid) hybrid materials and its antibacterial properties. Mater Lett 125:120–123

86. Longano D, Ditaranto N, Cioffi N, NisoF Di, Sibillano T, Ancona A et al (2012) Analytical characterization of laser-generated copper nanoparticles for antibacterial composite food packaging. Anal Bioanal Chem 403:1179–1186

87. Banik M, Patra M, Dutta D, Mukherjee R, Basu T (2018) A simple robust method of synthesis of copper-silver core shell nano-particle: evaluation of its structural and chemical properties with anticancer potency. Nanotechnol 29:325102

88. Paszkiewicz M, Go A, Rajski A, KowalE, Sajdak A, Zaleska-Medynska A (2016) The antibacterial and antifungal textile properties functionalized by bimetallic nanoparticles of Ag/Cu with different structures. J Nanomat 2016 (Article ID6056980)

89. Valodkar M, Modi S, Pal A, Thakore S (2011) Synthesis and anti-bacterial activity of Cu, Ag and Cu-Ag alloy nanoparticles: a green approach. Mater Res Bull 46:384–389

90. Taner M, Sayar N, Yulug IG, Suzer S (2011) Synthesis, characterization and antibacterial investigation of silver-copper nanoalloys. J Mater Chem 21:13150–13154

91. Fakhri A, Pourmand M, Khakpour R, Behrouz S (2015) Structural, optical, photoluminescence and antibacterial properties of copper-doped silver sulfide nanoparticles. J Photochem Photobiol B 149:78–83

92. Chaliha C, Nath BK, Verma PK, Kalita E (2016) Synthesis of functionalized Cu:ZnS nanosystems and its antibacterial potential. Arab J Chem (article in press)

93. Singhal SK, Lal M, Lata Kabi SR, Mathur RB (2012) Synthesis of Cu/CNTs nanocomposites for antimicrobial activity. Adv Nat Sci Nano Sci Nanotechnol 3:045011

94. Mohan R, Shanmugharaj AM, Sung Hun R (2011) An efficient growth of silver and copper nanoparticles on multiwalled carbon nanotube with enhanced antimicrobial activity. J Biomed Mater Res B 96:119–126

95. Perdikaki A, Galeou A, Pilatos G, Karatasios I, Kanellopoulos NK, Prombona A et al (2016) Ag and Cu monometallic and Ag/Cu bimetallic nanoparticle-graphene composites with enhanced antibacterial performance. ACS Appl Mater Interfaces 8:27498–27510

96. Li Y, Yang D, Cui J (2017) Graphene oxide loaded with copper oxide nanoparticles as an antibacterial agent against: *Pseudomonas syringae* pv. tomato. RSC Adv 7:38853–38860

97. Khare P, Sharma A, Verma N (2014) Synthesis of phenolic precursor-based porous carbon beads *in situ* dispersed with copper-silver bimetal nanoparticles for antibacterial applications. J Colloid Interface Sci 418:216–224

98. Zhang N, Gao Y, Zhang H, Feng X, Cai H, Liu Y (2010) Preparation and characterization of core-shell structure of SiO_2@Cu antibacterial agent. Colloid Surface B 81:537–543

99. Maniprasad P, Santra S (2012) Novel copper (Cu) loaded core-shell silica nanoparticles with improved Cu bioavailability: synthesis, characterization and study of antibacterial properties. J Biomed Nanotechnol 8:558–566

100. Villanueva ME, Diez AMDR, González JA, Pérez CJ, Orrego M, Piehl L et al (2016) Antimicrobial activity of starch hydrogel incorporated with copper nanoparticles. ACS Appl Mater Interfaces 8:16280–16288

101. Rastogi L, Arunachalam J (2013) Synthesis and characterization of bovine serum albumincopper nanocomposites for antibacterial applications. Colloid Surf B 108:134–141

102. Dealba-Montero I, Guajardo-Pacheco J, Morales-Sánchez E, Araujo-Martínez R, Loredo-Becerra GM, Martínez-Castañón GA et al (2017) Antimicrobial properties of copper nanoparticles and amino acid chelated copper nanoparticles produced by using a soya extract. Bioinorg Chem Appl (Article ID 1064918)

Chapter 25
Modification of QuEChERS Method for Acidic Pesticide (Imidacloprid) in Citrus Fruit and Some Processed Citrus Juices Using Ultra Performance Liquid Chromatography Coupled with a Triple Quad Detector (UPLC-TQD)

Michael J. Klink, Thembi Mphiwa, Ikechukwu P. Ejidike, Vusumzi E. Pakade, Neelan Laloo and Fanyana M. Mtunzi

Abstract The drive to expand food production to feed the ever increasing population in the face of plant diseases, insects damaging crops and/or causing diseases and harsh weather conditions, makes it difficult for farmers to maintain the levels of demand for satisfying markets the world over. Use of agrochemicals becomes the favored choice for farmers to mitigate these agricultural challenges. Food testing laboratories have to keep up with techniques to measure low levels of various agrochemical residues in a variety of crops. This study aims to adjust or modify the QuEChERS (quick, easy, cheap, effective, rugged and safe) method to improve recovery of analytes including Imidacloprid pesticide. The study also aims to evaluate the effect of Primary Secondary Amine (PSA) in the sample extraction steps of QuEChERS method towards the extraction of Imidacloprid. Different citrus samples (oranges, grapefruit, lemons, clementines, satsuma, 50% orange juice, 100% orange

M. J. Klink (✉) · I. P. Ejidike · V. E. Pakade · N. Laloo · F. M. Mtunzi
Faculty of Applied and Computer Sciences, Department of Chemistry/Biotechnology, Vaal University of Technology, Private Bag X021, Vanderbijlpark 1900, South Africa
e-mail: michaelk1@vut.ac.za

I. P. Ejidike
e-mail: destinedchild12@gmail.com

V. E. Pakade
e-mail: vusumzip@vut.ac.za

N. Laloo
e-mail: laloon@vut.ac.za

F. M. Mtunzi
e-mail: Fanyana@vut.ac.za

T. Mphiwa
Department of Agriculture, Forestry and Fisheries, Private Bag X250, Pretoria 0001, South Africa
e-mail: ThembiM@daff.gov.za

juice and 100% grapefruit juice) were extracted using the QuEChERS method protocol and the QuEChERS method without PSA. The results were satisfactory for both the methods used. Imidacloprid was found to favor the basic environment created by the use of PSA during the cleanup step.

25.1 Introduction

The citrus industry is the third largest after deciduous trees and vegetables in South Africa and contributes about 19% of the total gross value of the country. The citrus fruit industry comprises of four broad categories, namely oranges, easy peelers (soft citrus), grapefruit, lemons and limes [1]. The South African citrus industry is orientated towards the production of fresh fruits which need to have a high level of "eye appeal". Production districts are widely spread across the country with climate profiles ranging from Mediterranean in the Western Cape and subtropical in KwaZulu Natal, North and East Gauteng [2]. The evaluation of quality and food safety aspects of citrus is of great importance to the citrus growers and consumers of citrus and it is also imperative for international trade in this commodity. Citrus fruit has long been valued as part of a nutritious and tasty diet. It is the most common source of vitamin C but it also contains essential nutrients including potassium, calcium, copper and vitamin B6 [3].

South Africa is one of the few countries in which native red scale insects have attacked the citrus orchards. It is thought to originate from South China and it is a severe pest for citrus in South Africa. They are found on all parts of the plant but are most noticeable on the fruit. The effect of red scale on an orange may cause discoloration, shoot distortion and leaf drop. The fruit may become pitted, unattractive and unmarketable. When red scale is dense on the tree it kills all parts or branches within the tree [3]. Historical records indicate that the spraying program for citrus in South Africa was implemented between 1945 and 1946. Organophosphate insecticides (Parathion and Chlorpyrifos) were used for control of red scale. This led to the development of resistance to organophosphates by red scale. The citrus growers were then forced to adopt an integrated spray program as quickly as possible. Mixtures of insect growth regulators (pesticides) plus oil have emerged as treatments for red scale control [4].

In order to prevent and control the effect of the red scale insects on citrus fruit, spray programs containing Imidacloprid, an acidic pesticide, and other growth regulators are used. Imidacloprid is a systemic chloronicotinyl insecticide which belongs to a class of chemicals called neonicotinoid. The high insecticidal activity of Imidacloprid works by binding to the nicotinergic acetylcholine receptor in the insect nervous system, which interferes with chemical signal transmission in the stimuli.

The blockage leads to the accumulation of a neurotransmitter, acetylcholine, resulting in excitation, paralysis and eventually death [5, 6].

Food testing laboratories have to keep up with techniques to measure low levels of various agrochemical residues in a variety of crops. Chemists working at the US Department of Agriculture in 2003 introduced a technique of QuEChERS that was simple and built on extraction techniques of the past, and yet effectively isolated trace pesticides from a variety of fruits and vegetables. The technique of QuEChERS (quick, easy, cheap, effective, rugged and safe, and pronounced 'catchers') was developed by Lehotay et al. [6]. The method uses $MgSO_4$ and NaCl for salting out extraction/partitioning and dispersive solid-phase extraction (d-SPE) for clean-up. With this approach, unlike the previous methods developed for traditional chromatographic detection systems (e.g. UV/Vis absorbance, fluorescence, element selective detectors), the QuEChERS approach takes advantage of the wide analytical scope and high degree of selectivity and sensitivity provided by gas and liquid chromatography (GC and LC) coupled to mass spectrometry (MS) for detection. Only a few pesticides were problematic with the approach [7, 8].

In 2010 the QuEChERS method was amended by Lehotay et al. [6], such that for fruits and vegetables, the samples are homogenized and the comminuted sample is extracted with $MgSO_4$, NaCl, trisodium citrate dehydrate and disodium hydrogen citrate sesquihydrate using acetonitrile as the extraction solvent and dispersive solid-phase extraction (d-SPE) for clean-up [7, 9]. According to Akoijam et al. [10], the samples were extracted with acetonitrile, cleaned up by treatment with primary secondary amine sorbent and graphitized carbon. Lehotay and Anastassiades emphasised that QuEChERS uses aliquots with internal standard for analysis instead of the multiple liquid–liquid partitioning steps and isolation of the entire extract performed in traditional methods [9–11].

In older methods developed previously, to extend the analytical polarity range to cover organochlorines, organophosphates and organonitrogen in a single procedure, acetone rather than acetonitrile was used for the initial extraction [7]. Even though acetone is readily miscible with water, the separation of water from this solvent is impossible without the use of non-polar solvents. On the other hand, ethyl acetate is only partially miscible with water, which necessitates excessive addition of non-polar solvents to separate it from water. However, the highly polar pesticides do not separate in it. Unlike traditional methods, the QuEChERS method does not entail a solvent evaporation step to further concentrate the analytes in the final extract prior to analysis. Instead, the extracts are readily injected for analysis in UPLC (ultra-performance liquid chromatographic) instrument [12–14].

Advantages of using acetonitrile as a solvent are that the sample extract contains fewer interfering substances than the corresponding ethyl acetate and acetone extracts, and acetonitrile can be separated easily from water. Therefore, this makes acetonitrile the preferred extraction solvent for QuEChERS method. In multiclass, multi-residue pesticide analyses, the sample preparation method inherently necessitates broad analytical scope which makes it impossible to obtain a high degree of clean-up without reducing recoveries for some pesticides. The greatest difficulty that

all multiclass, residue methods possess is that certain pesticides do not give high and consistent recoveries with the method [9].

Acidic conditions help to reduce losses of these pesticides. QuEChERS method faces criticism for not being perfect, according to Lehotay et al. [6]. Although different QuEChERS versions recommend that the clean-up method using Primary Secondary Amine (PSA) be included in the process, the PSA neutralizes the acidity of the acidic pesticides resulting in loss of recoveries. QuEChERS method is widely used by international and local, regulatory and private laboratories as a preferred method of detection for multi-residues of agrochemicals in food. The version of QuEChERS method implemented in Analytical Services North laboratory gives unsatisfactory recoveries for Imidacloprid in citrus samples. As a regulatory laboratory testing samples for export markets, methods employed should at least give recovery values ranging from 70 to 120% as recommended by EU Quality Control measures for pesticides residue analysis [15].

Therefore, considering the importance of citrus for the South African economy, this study aims to adjust or modify the QuEChERS method to improve recoveries of analytes including Imidacloprid pesticide. It also aims to evaluate the effect of Primary Secondary Amine (PSA) in the sample extraction steps of QuEChERS method towards the extraction of Imidacloprid.

25.2 Experimental

25.2.1 *Materials and Equipment*

Neat Imidacloprid pesticide standard (99.9%), $MgSO_4$ (99.9%) anhydrous powder, trisodium citrate dihydrate and disodium hydrogen citrate sesquihydrate (99.9%) were obtained from Sigma Aldrich. Primary Secondary Amine, analytical reagent grade, was from Agilent technologies. Romil was the supplier for acetonitrile and ultra-pure water (both UPS ultra-pure). Formic acid (99%) was purchased at Fluka. Sodium chloride, in powdered form, was obtained from Rochelle Chemicals. Nitrogen gas—LC makeup gas-(99.999%) and argon gas—LC collision gas-(99.99%) were obtained from Afrox. Acetone, Burdick and Jackson high purity solvents were obtained from Merck. All the reagents were purchased in Johannesburg, South Africa.

The Ultra Performance Liquid Chromatograph coupled with Triple Quad Detector (UPLC-TQD) was used. The LC system comprises a column, Acquity UPLC BEH C18 2.1 mm × 100 mm × 1.7 μm and an Acquity UPLC BEH C18 1.7 μm vanguard pre-column 2.1 mm × 5 mm. The column temperature and the sample temperature for the instrument were 40 and 10 °C respectively. A flow rate of 0.450 ml/min was used. Mobile phase A was 100% water with 0.1% formic acid. Mobile phase B was 100% acetonitrile with 0.1% formic acid. Weak needle wash was at the ratio of 90% water and 10% acetonitrile and strong needle wash was at the ratio of 90% acetonitrile

and 10% water. The total run of the instrument was 10 min and the injection volume was 5 μl, partial loop injection.

An ionization mode electrospray ionization (ESI) in the positive mode coupled to a Waters AQUITY-LC was used for soft ionization resulting in analyte fragmentation and increasing the sensitivity and selectivity of the LC/MS method. Nitrogen was used as a desolvation gas at 600 L/h and as a cone gas at 10 L/h. Capillary voltage of 3.50 kV and source temperature of 120 °C were used. The acquisition was multiple reaction monitoring (MRM). The collision gas used was argon at 2×10^{-3} mBar.

Sigma 3-16 centrifuge PK was used with the 50 ml polypropylene centrifuge tubes. For weighing standards, PSA and $MgSO_4$, the Mettler AT 261 delta range balance with an accuracy of 4 decimal places was used. However, samples were weighed using the Top-loading Precisa 6200D SCS balance of 2 decimal place accuracy. Samples and standards were mixed with the ultra—turrax mixer (PRO 250 Model) and the vortex mixer (Labex) respectively. The standards and samples were stored in the fridge and freezer using amber vials. To avoid cross contamination, all apparatus used were either new or used after thorough cleaning.

25.2.2   Sample Collection

A total of 24 samples of eight citrus fruits and citrus fruit juice commodities comprising of three samples of each were collected from different markets and grocery shops in Gauteng Province. The selected samples were oranges, grapefruit, lemon, satsuma, clementine, 50% orange juice, 100% orange juice and 100% grapefruit juice. These fruits and juices are regular buys in South Africa. A representative sample was made by combining three different samples from different sources of supply into one sample. The samples were homogenized and frozen at −20 °C until analysis was resumed (within six months).

25.2.3   Optimization of Imidacloprid Insecticide

The Imidacloprid standard was prepared and optimized for detection on the Ultra Performance Liquid Chromatograph coupled with Triple Quad Detector (UPLC-TQD) instrument ensuring identification, better separation and quantification of the analyte of interest. Imidacloprid has a molecular weight of 256 g/mol, which was confirmed by infusion in quad one of the UPLC-TQD instrument using nitrogen generator as a makeup gas. When Imidacloprid was transferred from quad one to the collision cell, argon gas was used for fragmentation of base ion 256 and fragments 209 and 175 were the best ions for quantification and confirmation and were detected in quad three.

25.2.4 Sample Extraction and Clean-up

The homogenized eight different citrus samples (oranges, grapefruit, lemon, satsuma, clementine, 50% orange juice, 100% orange juice and 100% grapefruit juice) were tested for Imidacloprid residue using QuEChERS, (quick, easy, cheap, effective, rugged and safe) method with and without slight modification. About 10 g of each commodity was mixed with 10 ml acetonitrile and sample preparation tubes containing a mixture of four salts (4.0 g magnesium sulfate and 1.0 g sodium chloride for facilitating the extraction of pesticides to be more selective and for water removal, 1.0 g trisodium citrate dihydrate and 0.5 g disodium hydrogen citrate sesquihydrate to buffer the organic phase to protect pH labile pesticides) in a centrifuge tube. Thorough shaking for two minutes was performed; the aqueous phase was separated from organic phase by centrifugation for five minutes at 5000 rpm [13, 16].

The organic phase containing the partitioned pesticides residue was subjected to clean-up using 0.25 g PSA and 0.75 g $MgSO_4$ in 50 ml centrifuge tubes. After shaking for two minutes, the samples were centrifuged for five minutes at 5000 rpm. The supernatant was collected and capped into 2 ml vials for analysis on the UPLC-TQD instrument. The pH readings for each sample were taken between every step during preparation. The comparison between the recovery results was performed. Further study on recoveries was performed using the QuEChERS protocol (with PSA) method and the modified (without PSA) method by spiking three aliquots of orange samples at a concentration level of 0.25 ppm. The orange samples were prepared varying the acidity of the orange. For the first sample the pH was not adjusted, the pH was adjusted to 2.00 on the second sample and to 10.93 on the third sample [16].

The effects of the QuEChERS salts and PSA were evaluated by preparation of three aliquots of a reagent blank (water) varying the acidity of the blank samples where the pH was not adjusted on the first sample, the pH was adjusted to 2.18 on the second sample and to 10.85 on the third sample. Further trials were done by preparation of an orange sample and the reagent blank pH of both samples was adjusted to below 1.0 (0.94 and 0.97). The extraction and the clean-up were performed for both the samples. Recovery results were calculated [14, 17, 18].

25.2.5 Recovery Studies and Quality Control

Imidacloprid was identified by matching the retention time of the sample with its standard. Recoveries of Imidacloprid were measured by analyzing eight samples of each commodity fortified at 0.250 mg/kg. A five level calibration curve (0.05; 0.10; 0.25; 0.50 and 1.0 mg/kg) was plotted for Imidacloprid certified reference standard using the orange as a matrix match of representatives for different citrus commodities (orange will be used as a matrix for all citrus commodities in preparation of standards)

for quantification of samples. The 0.05 mg/kg was the lowest standard determined for use in quantification of Imidacloprid.

25.3 Method Validation

In this study, validation data sets were carried out according to the European SANCO/12571/2013 guidelines [19]. The results comparison for all the trials, validation for both the methods (without the use of PSA and with the use of PSA) and the following parameters were addressed: accuracy/trueness (recoveries), linearity, precision (repeatability and reproducibility), limit of detection, limit of quantification and measurement of uncertainties [19].

25.3.1 Linearity

Linearity was tested in the range of 0.05–0.50 mg/kg using both the mobile phase A solution and orange matrices (with PSA and without PSA), all sets of standards were injected in triplicate. Orange was used as a matrix matched standard to ensure accurate quantification and to account for any enhancement/suppression due to matrix effects on calibration standards. The percentage matrix effect of the calibration curve was determined by testing the linearity of the detector response of Imidacloprid in solvent (mobile phase A) and in the orange matrices over the range of 0.05–0.50 mg/kg. The correlation coefficient, percentage matrix effect and percentage residual for Imidacloprid calibration curve were calculated (Fig. 25.1).
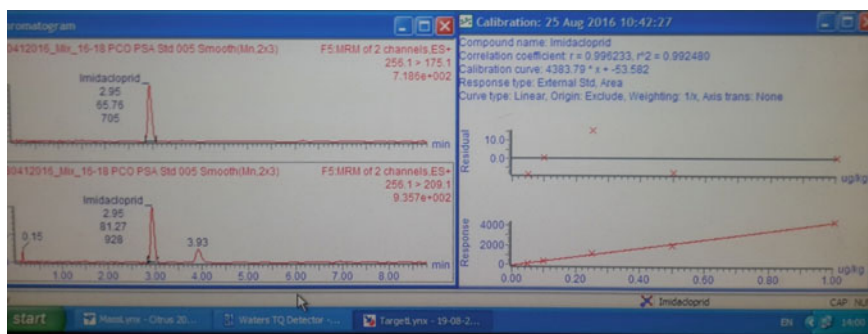
Fig. 25.1 Calibration curve, residuals and chromatogram for Imidacloprid pesticide

25.3.2 Accuracy

The accuracy of the method was determined by fortifying five orange samples five times at five different concentration levels (0.10, 0.15, 0.25, 0.50 and 1.0 ppm) using Imidacloprid standard. Acceptable recoveries will be in the range of 70–120%.

25.3.3 Precision

25.3.3.1 Repeatability

The repeatability was tested five times for five fortification levels of Imidacloprid at five different concentration levels (0.10, 0.15, 0.25, 0.50 and 1.0 mg/kg). The %Relative Standard Deviation (%RSD) was calculated.

25.3.3.2 Reproducibility

The reproducibility was determined five times for one fortification level (0.50 mg/kg) using three analysts on three different days. The %RSD for each analyst and for three analysts was calculated.

25.3.4 Limit of Detection and Limit of Quantification

The errors of the intercept and the slope were used for calculation of limit of detection (LOD) and limit of quantification (LOQ). The theoretical LOD and LOQ were calculated for Imidacloprid to detect the lowest level of analyte that can be accurately detected and measured.

25.4 Results

A total of eight different representative citrus samples covering the fresh fruit and processed fruit product categories were tested for the presence of Imidacloprid residues. The representative citrus samples were a fresh orange, grapefruit, lemon, clementine, satsuma, 50% orange juice, 100% orange juice and 100% grapefruit juice (Table 25.1).

QuEChERS extraction method with and without the use of primary secondary amine (PSA), was used to extract the Imidacloprid residues from the eight different citrus samples. The pH values for extracts from these different matrices ranged

Table 25.1 Imidacloprid recovery determinations for fresh citrus fruit and processed products (fruit juices)

Citrus samples	pH of neat matrix sample	pH of extracts without PSA	Results of sample blank (mg/kg)	Results of spiked samples (mg/kg)	Recovery (%)	pH of extract after adding PSA	Results of neat sample in PSA (mg/kg)	Results of spiked sample in PSA (mg/kg)	Recovery (%)
Orange	4.25	4.00	0.0463	0.3011	101.72	8.65	0.0237	0.2668	97.05
Grapefruit	3.92	3.64	0.0000	0.3042	121.44	8.01	0.0000	0.2346	93.65
Lemon	3.14	3.38	0.0000	0.2890	115.37	7.57	0.0000	0.2335	93.21
Clementine	4.23	3.59	0.0000	0.2176	88.87	8.29	0.0000	0.2055	82.04
Satsuma	4.65	3.86	0.0527	0.2947	96.61	8.82	0.0207	0.3077	114.57
Orange juice (50%)	3.22	3.62	0.0000	0.2506	100.04	7.83	0.0000	0.2061	82.28
Orange juice (100%)	3.80	3.78	0.0000	0.2925	116.77	8.50	0.0000	0.2072	82.71
Grapefruit juice (100%)	3.55	3.76	0.0000	0.2571	102.63	8.51	0.0000	0.2465	98.40

between 3.14 and 4.65. Imidacloprid recovery determinations for fresh citrus fruits and processed products (fruit juices) were performed. Imidacloprid was successfully optimized and fragmentation ions (m/z 209 and 175) were used for quantification and confirmation.

Although the results for both the methods were within the accepted recovery range of 70–120%, samples tested using the method without the use of PSA produced higher recoveries than for the method using PSA. Over and above the use of the cleaning effect of PSA, there are also properties of pH adjustment. For analytes (i.e. Imidacloprid) that are pH sensitive, it helps to adjust the analyte environment to be favourable. If the analyte is recovered at the acceptable range of 70–120%, then the environment is favourable [20]. From the experiments performed, recoveries of samples with very low and very high acid proved to be outside the accepted range of recoveries which proved that the pH of the sample plays a vital role in achieving good results (Tables 25.2, 25.3, 25.4 and 25.5).

Prior to validation of both the methods (with the use of PSA and without the use of PSA), linearity was tested in the range of 0.05–0.50 mg/kg using neat solvents and orange extract as a matrix solvent/match for calibration standards (Table 25.6). The correlation coefficient for Imidacloprid in neat standards was 0.9996, for the matrix matched standards without the use of PSA was 0.9956, and for the matrix standards with the use of PSA was 0.9941.

The percentage matrix effect for the method without the use of PSA was 77% and with the use of PSA it was 95%. The range of the residuals was 2.23–7.37% for the neat standards, 0.20–3.03% for the standards without the use of PSA and 0.18–11.30% for the standards in PSA.

The accuracy of the method was evaluated on the basis of the recoveries and statistical accuracy as an additional measure (Fig. 25.2). The recoveries for the method with the use of PSA ranged from 97 to 111% and for the method without PSA the range was from 89 to 103%. The accepted range of recoveries is 70–120% according to

Table 25.2 Recovery results for orange sample fortified at 0.05 mg/kg with adjusted pH levels

Type of matrix	pH of the neat matrix (sample puree) before adjustment	pH of sample puree after pH adjustment	pH of extract after adding PSA	pH of final extract (2 ml extract + 8 ml MPA)	Imidacloprid concentration recovered from spiked samples with PSA added (mg/kg)	% Recovery
Orange A	4.25	Not adjusted	7.21	3.40	0.0383	76.45
Orange B	4.25	2.00	2.36	2.67	0.0352	70.26
Orange C	4.25	10.93	8.27	3.32	0.0672	134.13

MPA Mobile phase A (99.9% water +0.1% formic acid)
PSA Primary secondary amine

Table 25.3 Recovery results for reagent blank (water) fortified at 0.25 mg/kg with adjusted pH levels

Type of matrix	pH of water (reagent blank) before extraction	pH of water (reagent blank) extract without pH adjust-ment	pH of water (reagent blank) extract with pH adjust-ment	pH of water (reagent blank) extract after adding PSA	Imidacloprid concentration recovered from spiked water (reagent blank) samples with PSA added (mg/kg)	% Recovery
Water E	7.63	5.27	Not adjusted	8.98	0.2302	91.90
Water F	7.51	5.13	2.09	2.83	0.1921	76.69
Water G	7.44	5.05	10.91	9.18	0.2122	84.71

N.B. Water resembled the sample matrix and the 10 ml acetonitrile was used to extract the analyte as per the QuEChERS method

Table 25.4 Recovery results for reagent blank (water) fortified at 0.05 mg/kg with adjusted pH levels

Type of matrix	pH of water (reagent blank) before extraction	pH of water (reagent blank) extract without pH adjust-ment	pH of water (reagent blank) extract with pH adjust-ment	pH of water (reagent blank) extract after adding PSA and acidifica-tion with MPA	Imidacloprid concentration recovered from spiked water (reagent blank) samples with PSA added and acidification with MPA (mg/kg)	% Recovery
Water E	7.63	5.27	Not adjusted	3.69	0.0546	108.98
Water F	7.51	5.13	2.09	2.69	0.0467	93.21
Water G	7.44	5.05	10.91	4.49	0.0601	119.96

N.B. Water resembled the sample matrix and the 10 ml acetonitrile was used to extract the analyte as per the QuEChERS method
MPA mobile phase A (99.9% water +0.1% formic acid)
PSA primary secondary amine

Table 25.5 Imidacloprid recovery results (experiment showing the effect of pH)

Type of matrix	pH of sample puree	Acidified pH	pH of sample puree with CH₃CN	pH of sample extract before adding PSA	pH of sample extract after adding PSA	pH of 2 ml extract and 8 ml MPA	Final extract with adjusted pH < 1	Results of orange sample in PSA (mg/kg)	Results of spiked orange sample in PSA (mg/kg)	% Recovery
Spiked orange sample	3.86	0.94	1.23	3.23	6.67	2.68	0.87	0.0000	0.0063	31.44
Spiked water sample	5.63	0.97	1.11	3.22	4.96	2.70	0.97	0.0000	0.0000	0.00

MPA Mobile phase A (99.9% water +0.1% formic acid)

Table 25.6 Linearity (correlation coefficient (r), % residual, matrix factor and % matrix)

Matrix matched standards (mg/kg)	QuEChERS method with PSA	QuEChERS method without PSA	Neat standards
	r = 0.9941% matrix effect = 94.99%	r = 0.9956% matrix effect = 77.35%	r = 0.9996
	% Residual	% Residual	% Residual
0.05	0.18	2.78	7.26
0.10	6.59	0.20	7.37
0.25	0.20	3.03	3.15
0.50	11.30	2.50	5.29
1.00	5.04	1.55	2.23
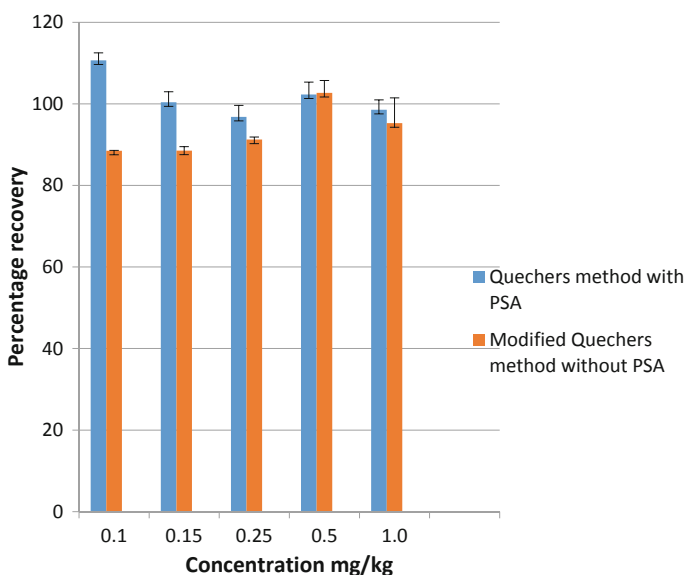
Fig. 25.2 Percentage recoveries for QuEChERS method with PSA and without PSA

Ortelli et al. [21]. For the statistical accuracy evaluation, the calculated t-distribution (t_{calc}) results for the method without the use of PSA ranged from a t_{calc} of 0.38–5.48 and for the method with PSA the following t_{calc} values of 0.48–10.37 were achieved.

For the orange matrix the repeatability was tested five times for five fortification levels of Imidacloprid (0.10; 0.15; 0.25; 0.50 and 1.0 mg/kg). The repeatability results obtained using the method without PSA had a %RSD with a minimum of 4.36 to a maximum of 18.79 for each aliquot and %RSD with a minimum of 4.32 to a maximum of 21.98 for within aliquots. The method with PSA had a %RSD with a minimum of 2.68 to a maximum of 29.10 for each aliquot and a minimum of 3.65 to a maximum of 19.37 for within aliquots (Fig. 25.3).
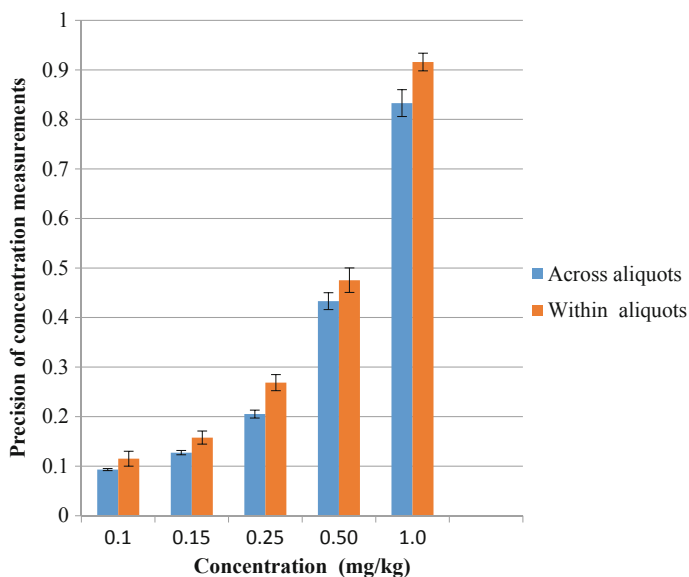
Fig. 25.3 Repeatability results (with PSA)—precision measurements

The reproducibility was determined five times for one fortification level (0.50 mg/kg) using three analysts on three different days (Fig. 25.4). Reproducibility with %RSD for the method without PSA was at a minimum of 4.34 to a maximum of 5.20 for each aliquot and %RSD with a minimum of 0.98 to a maximum of 7.62 for within aliquots injections. The method with PSA had a %RSD with a minimum of 3.88 to a maximum of 7.39 for across aliquots and a minimum of 7.67 to a maximum of 16.30 for within aliquots injections.

The limit of detection and the limit of quantification for the method without PSA were determined as 0.0170 and 0.0565 mg/kg respectively, and for the method with PSA they were 0.0348 and 0.1161 mg/kg.

25.5 Discussion

The acceptable criteria set for correlation coefficient is 0.990 which means that there is a 99% accurate relation between the concentrations and the peak areas used for plotting the calibration curve. The results below the 0.990 level are due to outliers on the calibration curve and they will be rejected to minimize random errors associated with these outliers. The correlation coefficient for the neat standards was 0.9996, whereas for the matrix matched standards without the use of PSA and with the use of PSA it was 0.9956 and 0.9941 respectively. All the calibration curves satisfied the
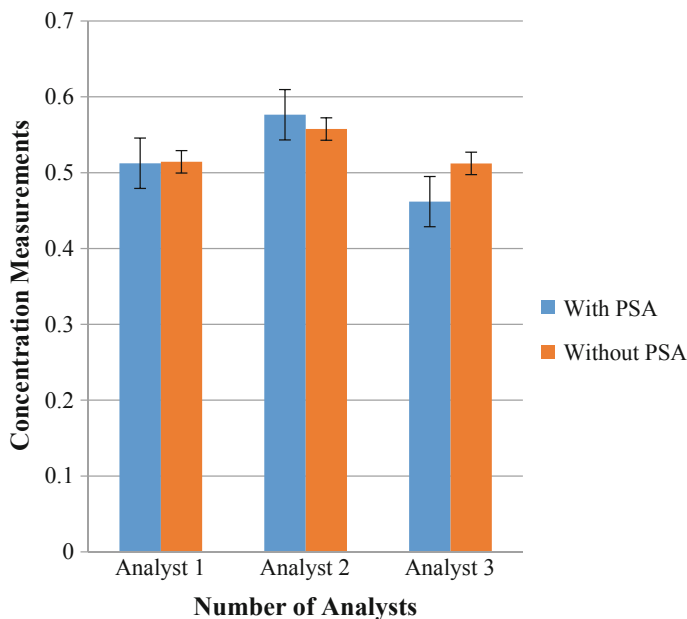
Fig. 25.4 Reproducibility results—different analyst measurements

set criteria of 0.990 level, but the neat standards curve has a better correlation than the other two calibration curves in matrix.

The matrix effect (ME) is a measure used to estimate if the matrix substantially influences the sensitivity of the analyte. The matrix factor, determined as the ratio of slopes of calibration curves of a matrix matched curve divided by the neat curve, is used to calculate percentage matrix effect (%ME) [20, 21]. Criteria set for the matrix effect is 20% variation between the neat and the matrix matched standards calibration curve, allowing the use of either one of them. When the matrix effects are higher than 20% it provides for the use of matrix matched standards only. The matrix effects for the methods without the use of PSA were 77% and with the use of PSA were 95%. Both methods favor the use of matrix matched standards although the method with PSA provides more accurate results than the method without PSA.

Residuals are calculated to avoid reliance on correlation coefficients solely, to ensure that the fit is satisfactory in the region relevant to the residues detected. The acceptable variation for the residuals is 20% which implies that a maximum of 20% level of errors will be acceptable for the calibration curve. The range of the residuals was 2.23–7.37% for the neat standards, 0.20–3.03% for the standards without the use of PSA and 0.18–11.30 for the standards in PSA.

Accuracy determinations for a range of recoveries are acceptable between 70 and 120% when working within the concentration levels of 0.1–1.0 mg/kg. The results outside the 70–120% recovery range will be rejected. The recoveries for the method without the use of PSA were in the range of 89–103% and for the method with PSA

were in the range of 97–111%. The method with PSA proved to have better stability. For the statistical evaluation of accuracy, variation was acceptable up to the critical value of 2.78 using the confidence level of 95%. The results for the method without use of PSA were in the range of 0.38–5.48 and for the method with PSA were in the range of 0.48–10.37. From the data obtained, all the results that did not comply were due to the instrument injection repeatability and the analyst fortification [22].

The 20% RSD variation was acceptable for the evaluation of the precision (repeatability and reproducibility). For repeatability the results obtained using the method without PSA had a %RSD with a minimum of 4.36% to a maximum of 18.79% for each aliquot and %RSD with a minimum of 4.32% to a maximum of 21.98% within aliquots. The method with PSA had a %RSD with a minimum of 2.68% to a maximum of 29.10% for each aliquot and a minimum of 3.65% to a maximum of 19.37% within aliquots. For both methods the results that were outside the 20% deviation were caused by the instrument injection repeatability. The %RSD for reproducibility of the method without PSA was at a minimum of 4.34% to a maximum of 5.20% for each aliquot and %RSD with a minimum of 0.98% to a maximum of 7.62% within injections. The method with PSA had a %RSD with minimum of 3.88% to a maximum of 7.39% for each aliquot and a minimum of 7.67% to a maximum of 16.30% within injections. The method without the use of PSA performed better than the PSA method.

The errors of the intercept and the slope were used for calculation of limit of detection (LOD) and limit of quantification (LOQ). The results for the limit of detection and the limit of quantification for the method without PSA were 0.0170 and 0.0565 mg/kg respectively, whereas for the method with PSA they were 0.0348 and 0.1161 mg/kg respectively.

25.6   Conclusion

Different citrus samples (oranges, grapefruit, lemons, clementine, satsuma, 50% orange juice, 100% orange juice and 100% grapefruit juice) were extracted using the QuEChERS method protocol and the QuEChERS method without PSA.

Upon validating the two methods they were found to compare as follows: linearity evaluated by using the matrix effect parameter was found to support the use of matrix matched standards for both methods. The method with PSA gave better sensitivity to the analyte as exhibited by the matrix effect values ($\%ME_{\text{(method with PSA)}} = 94.99$ and $\%ME_{\text{(method without PSA)}} = 77.35$) compared to the method without PSA.

Accuracy evaluation for both the methods gave similar variations in terms of recovery range values, 14 for the method without PSA calculated from minimum of 89% to a maximum of 103% recoveries. Similarly the method with PSA gave a range of 14 calculated from minimum of 97 to a maximum of 111% recoveries. The precision was determined to be better for the method with PSA [range of 3.20 achieved through the difference of minimum %RSD of 4.20 from the maximum

%RSD of 7.40], than for the method without PSA [range of 9.32 achieved through the difference of minimum %RSD of 1.44 from the maximum %RSD of 10.12].

Therefore, the modified QuEChERS method (method without PSA) is a less preferred method compared to the method with PSA. Better stability/robustness is exhibited by the method with PSA.

From the experiments conducted, it is evident that PSA as a weak base also performs the function of buffering the extract in the method. When PSA is added to a mildly acid extract with pH of 5.27 (Table 25.3) it adjusted the pH to 8.98. In a strong acidic medium with pH of 2.09, the PSA fails to neutralize the pH of the extract thus giving the final value of pH of 2.83. These experiments showed that there is buffering effect by PSA over and above the clean-up purpose as cited by the literature.

The results were satisfactory for both the methods used. Imidacloprid is an acidic fungicide which is not best recovered from samples with a very low pH of less than 1. The acidity of each citrus sample will have to be checked and adjusted before the analysis resumes for better recovery results.

References

1. DAFF (2012) Department of Agriculture, Forestry and Fisheries annual report 2011/12. Pretoria, South Africa, pp 196. Available at http://www.daff.gov.za/doaDev/topMenu/AnnualReports/2011-12/AR2012.pdf
2. Goren R, Mendel K (1989) Proceedings of the Sixth International Citrus Congress vol 2, Tel Aviv, Israel, March 6–11, 1988. Balaban, Israel
3. Food Agricultural Organization (1999) Nutritional and health benefits of citrus fruits. Food Agricultural Organization, Rome, Italy
4. Bedford ECG, Grobler JH (1981) Proceedings of the International Citrus Congress. International Society of Citriculture, Tokyo, Japan
5. Cox C (2001) Herbicide fact sheet, atrazine: environmental contamination and ecological effects. J Pestic Reform 21:15–21
6. Lehotay SJ, Son KA, Kwon H, Koesukwiwat U, Fu W, Mastovska K, Hoh E, Leepipatpiboon N (2010) Comparison of QuEChERS sample preparation methods for the analysis of pesticide residues in fruits and vegetables. J Chromatogr A 1217:2548–2560
7. Lehotay SJ, Anastassiades M, Majors R (2010) The QuEChERS revolution. LC GC Europe 23:1–12
8. Anastassiades M, Lehotay SJ, Stajnbaher D, Schenck FJ (2003) Fast and easy multiresidue method employing acetonitrile extraction/partitioning and "dispersive solid-phase extraction" for the determination of pesticide residues in produce. JAOAC Int 86:412–431
9. Lehotay SJ, Mastovská K, Lightfield AR (2005) Use of buffering and other means to improve results of problematic pesticides in a fast and easy method for residue analysis of fruits and vegetables. JAOAC Int 88:615–629
10. Akoijam R, Singh B, Mandal K (2015) Development and validation of a quick, easy, cheap, effective, rugged and safe method for the determination of Imidacloprid and its metabolites in soil. J Chromatogr Sci 53:542–547

11. Wilkowska A, Biziuk M (2011) Determination of pesticide residues in food matrices using the QuEChERS methodology. J Food Chem 125:803–812

12. Lehmann E, Oltramare C, de Alencastro LF (2018) Development of a modified QuEChERS method for multi-class pesticide analysis in human hair by GC-MS and UPLC-MS/MS. Anal Chim Acta 999:87–98

13. Frenich AG, Vidal JLM, Pastor-Montoro E, Romero-Gonzalez R (2008) High-throughput determination of pesticide residues in food commodities by use of ultra-performance liquid chromatography-tandem mass spectrometry. Anal Bioanal Chem 390:947–959

14. Prestes OD, Friggi CA, Adaime MB, Zanella R (2009) QuEChERS—a modern sample preparation method for pesticide multiresidue determination in food by chromatographic methods coupled to mass spectrometry. Quim Nova 32:1620–1634

15. Gonzalez-Curbelo MA, Socas-Rodriguez B, Herrera-Herrera AV, Gonzalez-Salamo J, Hernandez-Borges J, Rodriguez-Delgado MA (2015) Evolution and application of the QuEChERS method. Trends Anal Chem 71:169–185

16. Plössl F, Giera M, Bracher F (2006) Multiresidue analytical method using dispersive solid-phase extraction and gas chromatography/ion trap mass spectrometry to determine pharmaceuticals in whole blood. J Chromatogr A 1135:19–26

17. da Silva Sousa J, de Castro RC, de Albuquerque AG, Lima CG, Lima LK, Milhome MA, do Nascimento RF (2013) Evaluation of an analytical methodology using QuEChERS and GC-SQ/MS for the investigation of the level of pesticide residues in Brazilian melons. Food Chem 141:2675–2681

18. Wu C-C (2017) Multiresidue method for the determination of pesticides in Oolong tea using QuEChERS by gas chromatography-triple quadrupole tandem mass spectrometry. Food Chem 229:580–587

19. European Commission (2013) Guidance document on analytical quality control and validation procedures for pesticide residues analysis in food and feed. SANCO/12571/2013, pp 41. Available at http://www.crl-pesticides.eu/library/docs/fv/SANCO12495-2011.pdf

20. Kittlaus S, Schimanke J, Kempe G, Speer K (2013) Development and validation of an efficient automated method for the analysis of 300 pesticides in foods using two-dimensional liquid chromatography-tandem mass spectrometry. J Chromatogr A 1283:98–109

21. Ortelli D, Edder P, Corvi C (2005) Pesticide residues survey in citrus fruits. Food Addit Contam 22:423–428

22. European Commission (2002) Commission Decision (EC) of 12 August 2002 implementing Council Directive 96/23/EC concerning the performance of analytical methods and interpretation of results. Off J Eur Commun L221:8–36

Chapter 26
Rheological Characterization, In Vitro and Ex Vivo Drug Release, Therapeutic Effectiveness and Safety Studies of Diclofenac Sodium, Loaded with Micronized Fumed Silicon Dioxide Gel

Mohammad W. Islam, Abd Elazim A. Ali, Abdullah K. Alkindi and Aliasgar Shahiwala

Abstract The present research has been undertaken with the aim to develop a topical gel formulation of diclofenac sodium using a micronized fumed silicon dioxide (Aerosil) gelled with a liquid paraffin (non-polar vehicle). The two gels, 8% (formulation A) and 10% (formulation B) were prepared from hydrophilic colloidal silicon dioxide (Aerosil 200) and their physicochemical characterization and efficacy as oleaginous ointment bases were investigated. They were evaluated for physicochemical properties such as homogeneity, grittiness, viscosity, pH, spreadability, drug content, skin irritancy, in vitro drug and ex vivo drug release. Compatibility studies were carried out using FT-IR spectroscopy. Developed gels were found to be comparable to marketed products in all physicochemical aspects tested. No significant changes in the peak pattern of IR spectra of pure diclofenac sodium implies that no chemical incompatibility between drug and excipients used in the formulations. Drug permeation through the rat abdominal skin membrane was slow as compared to the synthetic membrane for all the formulations tested. Permeation data for all the tested formulations were found to follow zero-order kinetics with Fickian diffusion mechanism, indicating that drug permeations were independent of the drug concentrations in the gels. The prepared gels showed significant analgesic activity in rats as compared to the control value. Also, the application of gels showed no skin irritation

M. W. Islam (✉) · A. E. A. Ali
Department of Pharmaceutical Sciences, College of Pharmacy, Ajman University, Ajman, UAE
e-mail: m.islam@ajman.ac.ae

A. E. A. Ali
e-mail: ajac.azim@ajman.ac.ae

A. K. Alkindi
Ministry of Health, Dubai, UAE
e-mail: abdullah@alkindimoh.gov.ae

A. Shahiwala
Department of Pharmaceutics, Dubai Pharmacy College for Girls, Dubai, UAE
e-mail: alishahiwala@gmail.com

447

throughout the entire observation period. Based on the results of this investigation, formulation A with 8% aerosil gel base in liquid paraffin was found to be a promising formulation for further clinical investigations.

26.1 Introduction

Diclofenac sodium is a potent member of the non-steroidal anti-inflammatory drugs (NSAIDs), widely used because of its strong analgesic, antipyretic and anti-inflammatory effects [1, 2]. An oral dose of diclofenac sodium causes an increased risk of serious gastrointestinal adverse events including bleeding, ulceration, and perforation of the stomach or the intestines that could be fatal. The presence of these oral adverse effects necessitates investigating other routes of drug delivery of diclofenac sodium. Topical application has many advantages over the conventional dosage forms. In general, they are deemed more effective and less toxic than conventional formulations due to the bilayer composition and structure [3]. Transdermal delivery of the drug can improve its bioactivity with reduction of the side effects and enhance the therapeutic efficacy [4, 5].

The delivery of drugs onto the skin is recognized as an effective means of therapy for local dermatologic diseases. It can penetrate deeper into the skin and hence give better absorption [6]. Percutaneous absorption of drugs from topical formulations involves the release of the drug from the formulation and permeation through skin to reach the target tissue. The release of the drug from topical preparations depends on the physicochemical properties of the vehicle and the drug employed [7–9]. The difficult aspect of the transdermal delivery system is to overcome the barrier of stratum corneum against foreign substances [10].

Ali et al. [11], Sheriff and Enever [12], Guy et al. [13], and Arellano et al. [14] earlier reported on micronized fumed silicon dioxide (Aerosil) based oleaginous type base. Recently, Lu and Fassihi reported the use of colloidal silicon dioxide to enhance gel viscosity [15]. The use of colloidal silicon dioxide-type for any given formulation needs to be determined experimentally as a rule of thumb [16].

Considering the importance of colloidal silicon dioxide, our present study was carried out to develop topical gel formulations of diclofenac sodium using aerosil with liquid paraffin combination and to investigate the possibility of dermal application of the developed gel formulations and their physicochemical characterization and efficacy in comparison to marketed diclofenac gels.

26.2 Materials and Methods

Aerosil 200 was purchased from Sigma-Aldrich, Taufkirchen, Germany. Diclofenac sodium was a gift sample from Global Pharma, Dubai, United Arab Emirates. An analytical grade of liquid paraffin was used.

26.2.1 Preparation of Buffer

The phosphate buffer was prepared according to USP standards. Its temperature was maintained at 37 °C and it was degassed using Grant ultra-sonic bath. The pH of the buffer was 6.8.

26.2.2 Preparation of Gel

Preparation of gel formulation using aerosil was a two-step process. Aerosil 200 was compounded in liquid paraffin at two different concentrations, i.e. 8 and 10%, and then 1% diclofenac sodium was incorporated into the base. Prepared gels were allowed to equilibrate for at least 24 h at room temperature [17–19]. Further characterizations and evaluation were performed with the two prepared gels, i.e. 8% aerosil gel as formulation A and 10% aerosil gel as formulation B and compared with marketed product 1 as formulation C and marketed product 2 as formulation D. All the gels contained 1% diclofenac sodium.

26.2.3 Characterization of Formulations

The gels were characterized for pH, viscosity, spreadability, consistency, extrudability, and viscosity through standard methods.

26.2.4 Drug Content

Drug contents of the gels were determined by dissolving an accurately weighed quantity (1 g) of gels in 100 ml of phosphate buffer (pH 6.8) [20]. These solutions were transferred quantitatively to volumetric flasks and appropriate dilutions were made with the same buffer solution. The resulting solutions were then filtered with 0.45 mm membrane filters before subjecting the solution to spectrophotometric analysis for diclofenac sodium at 276.0 nm using phosphate buffer (pH 6.8) as blank. Drug

content was determined from the standard curve of diclofenac sodium. Aliquots of different concentrations were prepared by suitable dilutions after filtering the stock solution and their absorbances were measured. Drug content was calculated using the equation, which was obtained by linear regression analysis of the calibration curve [20]. To ensure content uniformity of the gels, they were sampled from different locations in the mixer and assayed for the drug content.

26.2.5 Measurement of pH

The pH values of the prepared gels were measured by a digital type pH meter, by dipping the glass electrode into the sample. The reaction was performed at room temperature (25 ± 2 °C). The measurements were performed in triplicate [21].

26.2.6 Spreadability

The spreadability of gels was evaluated through an extensometer set up, which consists of two glasses. The gel sample (0.25 g) was placed on the lower immovable glass plate. The upper glass plate (movable) was placed on the top of the sample. Force was generated by adding known weight (50 g) on the upper glass plate. By this method, spreadability was measured on the basis of 'slip' and 'drag' characteristics of gels [22]. The experiment was repeated thrice at a constant temperature. The spreadability was then calculated by using the formula [23]:

$$S = (M \times L)/T$$

where

M   weight tied to upper slide;
L   length of glass slides;
T   time taken to separate the slides.

26.2.7 Homogeneity

All developed gels were tested for homogeneity by visual inspection after the gels set in the container. They were tested for their appearance and the presence of any aggregates [23].

26.2.8 Grittiness

All the formulations were evaluated microscopically for the presence of particles, if any. No appreciable particulate matter was seen under a light microscope [23].

26.2.9 Extrudability

The formulations were filled in the collapsible tubes after the gels were set in the container. The extrudability of the formulation was determined in terms of weight in grams required to extrude a 0.5 cm ribbon of gel in 10 s. The measurement of extrudability of each formulation was carried out in triplicate and the average values are presented. The extrudability was then calculated by using the following formula [24]:

Extrudability = Applied weight to extrude gel from tube (in g)/Area (in cm^2).

26.2.10 Viscosity Measurement

The viscosity of the formulations was determined using a Brookfield digital viscometer equipped with T-bar Spindle D. The gel sample (5 g) was placed in the sample holder of the viscometer and allowed to settle for 5 min and the viscosity was measured at a rotating speed of 50 rpm at room temperature (25–27 °C). The viscosity measurements were made in triplicate using fresh samples.

26.2.11 Fourier Transform-Infrared Spectroscopy (FTIR) Study

FTIR (Manufacturer: Shimadzu; Model: IR Affinity-l) was used to check compatibility and interaction between the drug and excipients. The spectra of pure diclofenac sodium and the different combinations, embedded in KBr discs were recorded in the range of 4000–400 cm^{-1} using IR spectroscopy. The study was performed on the following:

(1) Liquid paraffin; (2) Diclofenac sodium; (3) Aerosil 200;
(1 + 2) Liquid paraffin + Diclofenac sodium;
(1 + 3) Liquid paraffin + Aerosil 200;
(1 + 2 + 3) Liquid paraffin + Diclofenac sodium + Aerosil 200;
(2 + 3) Diclofenac sodium + Aerosil 200.

26.2.12 Preparation of Skin for Ex Vivo Drug Permeation Studies

For the preparation of rat skin, male white Sprague Dawley rats, weighing 150–200 g were used and anesthetized with brief ether inhalation and killed by cervical dislocation. Hairs were removed with an electric clipper and the abdominal skin was carefully excised. The adhering fat and debris were carefully removed from the skin samples and kept in -20 °C deep freeze until used in the diffusion studies. The skin samples were soaked in isotonic saline solution for 30 min before starting permeation studies.

26.2.13 In Vitro and Ex Vivo Skin Permeation Studies

In vitro and ex vivo permeation studies were carried out using vertical Franz cells (Copley Scientific, England). The basic configuration of the experimental apparatus is composed of (a) a donor compartment, wherein the formulation is applied to a semipermeable membrane where the drug released will permeate; and (b) a receiver chamber, wherein samples can be withdrawn for drug analysis. The receptor compartment was filled with phosphate buffer of pH 6.8 and continuously stirred with a small magnetic bar at a speed of 50 rpm during the experiments to ensure homogeneity and maintained at 37.2 ± 0.5 °C [25]. A known amount of the test formulation (256 mg) was applied on the membrane/skin over an area of 1.131 cm^2 and placed across the donor compartment. Cellulose membrane (0.45 μm) and rat skin were used as diffusion barriers. Aliquots of 1 ml were withdrawn periodically at intervals of 30 min for the first 3 h, and then at intervals of 60 min for the next 3 h (i.e. readings recorded at 0.5, 1, 1.5, 2, 2.5, 3, 4, 5, and 6 h and each sample was replaced with equal volume of fresh dissolution medium. This dilution of the receiver content was taken into account when evaluating the penetration data. The samples were analyzed spectrophotometrically at 276 nm (Shimadzu UV-Visible-1800). In vitro drug permeation results were presented as cumulative % drug permeated [26, 27].

26.2.14 Drug Release Kinetic Studies

To analyze the mechanism of drug release from the topical gel, the release data were fitted to the following equations:

(a) Zero-order equation:

$$Q = k_0 t$$

where Q is the amount of drug released at time t, and k_0 is the zero-order release rate.

(b) First-order equation:

$$\ln(100-Q) = \ln 100 - k_1 t$$

where Q is the percentage of drug release at time t, and k_1 is the first-order release rate constant.

(c) Korsmeyer–Peppas model for the mechanism of drug release (first 60% drug release)

$$F = (M_t/M) = K_m t^n$$

where F is the fraction of drug released at time 't', M_t is the amount of drug released at time 't', M is the total amount of drug in dosage form, K_m is the kinetic constant, and n is the diffusion or release exponent.

26.2.15   In Vivo Analgesic Activity

The tail flick method was utilized to study the antinociceptive activity in rats. The automatic tail flick analgesiometer (Tail flick apparatus, UGO BASILE®, Germany) was used. Mice were held in the restrainer. Reaction time was recorded as the interval between exposing the tail to the light beam and the withdrawal of the tail. A cut-off time of 20 s was imposed as a protection against tissue damage [28]. Tail flick latency in seconds was recorded at 0 (as pre-drug value), 0.5, 1, 2, and 4 h after drug administration. Each animal served as its own control. The change in latency time was calculated as $T - T_0$ (where T_0 is the latency at zero time).

26.2.16   Skin Irritation Test

Three adult New Zealand white albino rabbits of either sex weighing 1.5–2.0 kg were housed individually, and maintained under standard conditions. The aerosil 200 gel base, formulation A and formulation B were tested for their skin irritation tests. Approximately 24 h before initiation of the experiment, the backs of the animals were clipped free of fur at four sites using an animal clipper without any abrasion with an area of 6 cm². In each group, the skin of one rabbit was left intact and the skin of the other rabbit was abraded with a clipper head so as to penetrate the horny layer of the epidermis without causing bleeding. A 0.5 g quantity of sample of the gel base/gel was weighed and then evenly applied to each site [29].

Table 26.1 Skin irritation visual scoring scale

Erythema formation and eschar formation	Score	Edema formation	Score
No erythema	0	No edema	0
Very slight erythema, barely perceptible	1	Very slight edema, barely perceptible	1
Well defined erythema	2	Slight edema (edges of area well defined by definite raising)	2
Moderate to severe erythema	3	Moderate edema (raised approximately 1 mm)	3
Severe erythema (beet redness) to slight eschar formation (injury in-depth)	4	Severe edema (raised more than 1 mm and extending beyond the area of exposure)	4

All the four sites were covered with a non-occlusive absorbent gauze patch and held in place with non-irritating tape. The patch was wrapped with a semi-occlusive bandage for the duration of 4 h. Rabbits were kept in the restrainer for 4 h. Following the 4 h exposure period, the collars and wrappings were removed and any remaining test materials were removed with a wet disposable paper towel without altering the integrity of the epidermis [29].

All the animals were observed for dermal reactions at 4, 24, 48 and 72 h. Following the removal of the gauze patch, the test sites were examined for erythema and edema in accordance with Draize scoring criteria (Table 26.1) [30].

26.3 Data Analysis and Statistics

Determination of flux and permeability:

In in vitro and ex vivo experiments, the cumulative amount of diclofenac permeated per unit area was plotted against time and the slope of the linear portion of the plot was used as steady-state flux (J_{SS}). The permeability coefficient (K_p) was calculated with the following equation:

$$K_p = J_{SS}/CV$$

in which CV is the total donor concentration of the formulation. The lag time was determined by extrapolating the linear portion of the cumulative amount permeated per unit surface area–time plot to the abscissa. Results were expressed as mean $\pm$ SD (Standard deviation) and the data were analyzed by SPSS 20.0 statistical software. A paired sample t-test was used to examine the statistical difference in the release profile between formulations. The value of $p < 0.05$ was considered as statistically significant.

26.4   Results and Discussion

The increasing use of oleogels for topical/transdermal drug delivery is attributed to their long-term stability and ease of preparation [31]. Two simple oleogels were prepared in this investigation using aerosil and liquid paraffin and were characterized for different physicochemical properties.

26.4.1   *Appearance/Clarity, Homogeneity and Grittiness*

The prepared gels were tested for homogeneity by visual inspection after the gels have been set in the container. They were tested for their appearance and presence of any aggregates. The formulation A and formulation B did not show any aggregates and lumps ($\times 100$). No particulate matter were found in either gel. Both formulated transdermal gels showed good homogeneity and were slightly opaque in nature (Table 26.2). The prepared gels were also visually inspected for their consistency and the presence of clogs. Both the prepared formulations appeared to be smooth with uniform texture, and were semi-transparent in clarity with no clogs, as shown in Table 26.2.

26.4.2   *pH*

The pH of formulation A and formulation B was found to be 6.45 and 6.55 at 22 °C, respectively, which are considered acceptable to avoid the risk of irritation after skin application [32]. For a gel, the range of pH between 5 and 7 is considered good, as below 5 the solubility of active ingredient decreases [33]. Hence, it was concluded that the formulations A and B would not produce any local irritation to the skin. The results are shown in Table 26.2.

Table 26.2 Shape, appearance, grittiness and homogeneity parameters for formulation A and B

Formulation	Type of solids	pH	Appearance/clarity	Grittiness	Homogeneity
A	Semi-solid, amorphous	6.45	Semi-transparent	No particulate matter	Homogeneous
B	Semi-solid, amorphous	6.55	Semi-transparent	No particulate matter	Homogeneous

26.4.3 Drug Content

Diclofenac sodium content was estimated by a UV-visible spectrophotometer and absorbance was measured at 276 nm. The method was validated for linearity, accuracy, and precision. The method obeys Beer's Law in the concentration range of 1–10 µg/ml.

The gel samples were taken from different locations and analyzed for drug contents. The percentage drug content of prepared gel formulations i.e. formulation A and formulation B were found to be 98.47 ± 2.10 and $96.61 \pm 3.30\%$ respectively (Table 26.3). The percentage drug content of formulations was found to be within the I.P. (Indian Pharmacopoeia) limits.

26.4.4 Spreadability

Spreadability is a term expressed to denote the extent of the area to which the gel readily spreads on application to the skin or the affected area. The spreadability of the formulation A was found to be 13.79 ± 2.45 g cm/s while that of formulation B was 13.55 ± 1.32 g cm/s (Table 26.3).

Uniform spreadability of the gels ensures the uniform delivery of a standard dose of the drug to the required area. The value of spreadability also indicates the therapeutic efficiency of the formulation [33]. The gels taking longer to separate the slides possess good adherence properties; transdermal application of such gels at pathological sites offers a great advantage resulting in a faster release of drug directly to the site of action as compared to those with higher spreadability properties [34].

26.4.5 Extrudability

The extrusion of the gel from the tube is important during its application and in patient acceptance. Gels with high consistency may not extrude from tube whereas low viscous gels may flow quickly. Hence suitable consistency is required in order to extrude the gel from the tube. The extrudability of formulation A and formulation B was determined to be 223 ± 22.1 and 235 ± 36.0 g/cm^2, respectively (Table 26.3).

Table 26.3 Characterization of diclofenac sodium gel formulations loaded with aerosil gel

Formulation	Spreadability (g cm/s)	Extrudability (g/cm^2)	Drug content (%)	Viscosity (cps) at 20 °C	Viscosity (cps) at 25 °C
A	13.79 ± 2.45	223 ± 22.1	98.47 ± 2.10	$141{,}500 \pm 135$	$140{,}000 \pm 145$
B	13.55 ± 1.32	235 ± 36.0	96.61 ± 3.30	$152{,}000 \pm 155$	$150{,}000 \pm 167$

Values are the mean of 3 observations (n = 3)

26.4.6 Viscosity Measurement

The viscosity determined for the formulation A was $141,500 \pm 135$ and $140,000 \pm 145$ cps at 25 °C and formulation B was $152,000 \pm 155$ and $150,000 \pm 167$ cps at 25 °C (Table 26.3). From the results, it was found that the formulation A showed less viscosity than formulation B. The data of the viscosity showed an increase in the viscosity as the amount of colloidal silicon dioxide with liquid paraffin was increased from 8 to 10%. In aerosil gel, all the effects are related to the ability to disperse aerosil fumed silica particles to form a network of aggregates.

Viscosity is an important physical property of topical formulations which affects the rate of drug release [35]. Increased consistency was ascribed to the polymer entanglement [36]. In earlier studies, the oliogels were found to be thixotropic in nature with pseudoplastic flow behavior. They have also been reported to maintain their consistency over a wide temperature range (25–60 °C) [11]. Based on higher viscosity, the application in pharmaceutical products is suitable where stickiness is required such as an oral gel.

26.4.7 FT-IR Study

The IR spectra of pure diclofenac sodium and the different combination gels are represented in Figs. 26.1, 26.2, 26.3, 26.4 and 26.5. FT-IR was used to check the compatibility and interaction between the drugs and the drug excipients. The spectra of pure diclofenac sodium and the different combinations, embedded in KBr discs,
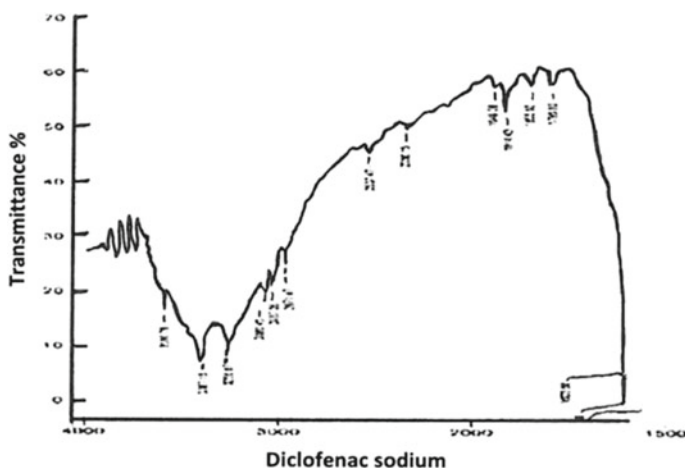
Fig. 26.1 FT-IR spectrum of diclofenac sodium

Fig. 26.2 FT-IR spectra of (1 + 2) versus diclofenac sodium

Fig. 26.3 FT-IR spectra of (1 + 3) versus diclofenac sodium

were recorded in the range of 4000 and 1500 cm^{-1} at the points 4000, 3500, 3000, 2500, 2000, 1750 and 1500 cm^{-1}.

There were no significant changes observed in the peak pattern of the IR spectra of pure diclofenac sodium and of the combinations (drug + excipients), indicating that there is no chemical incompatibility between the drug and the excipients in the formulations used in Table 26.4.

Fig. 26.4 FT-IR spectra of $(1 + 2 + 3)$ versus diclofenac sodium

Fig. 26.5 FT-IR spectra of $(2 + 3)$ versus diclofenac sodium

26.4.8 Transdermal Drug Delivery System Using Franz Diffusion Cell

In vitro drug release studies of gel formulations were carried out through cellophane membrane and rat skin and are plotted along with two marketed drugs i.e. formulation C and formulation D. These formulations were subjected to a diffusion study and their release kinetics were observed (Figs. 26.6 and 26.7; Tables 26.5 and 26.6).

The cumulative percentage of drug released in 6 h through rat skin from formulations A, B, C and D were found to be 80.16 ± 8.90, 61.17 ± 9.81, 85.52 ± 9.97, and 83.10 ± 8.20, respectively (Table 26.5). The permeation of drug from prepared

Table 26.4 Compatibility between diclofenac sodium and the excipients

Sample	Combinations	Result
Liquid paraffin	Liquid paraffin alone (1)	
Diclofenac sodium	Diclofenac sodium alone (2)	
Aerosil 200	Aerosil 200 alone (3)	
Sample A	1 + 2 (prepared IR disc using liquid paraffin + diclofenac sodium)	Concordant
Sample B	1 + 3 (prepared IR disc using liquid paraffin + aerosol 200)	Concordant
Sample C	1 + 2 + 3 (prepared IR disc using liquid paraffin + diclofenac sodium + aerosil 200)	Concordant
Sample D	2 + 3 (prepared IR disc using diclofenac sodium + aerosil 200)	Concordant
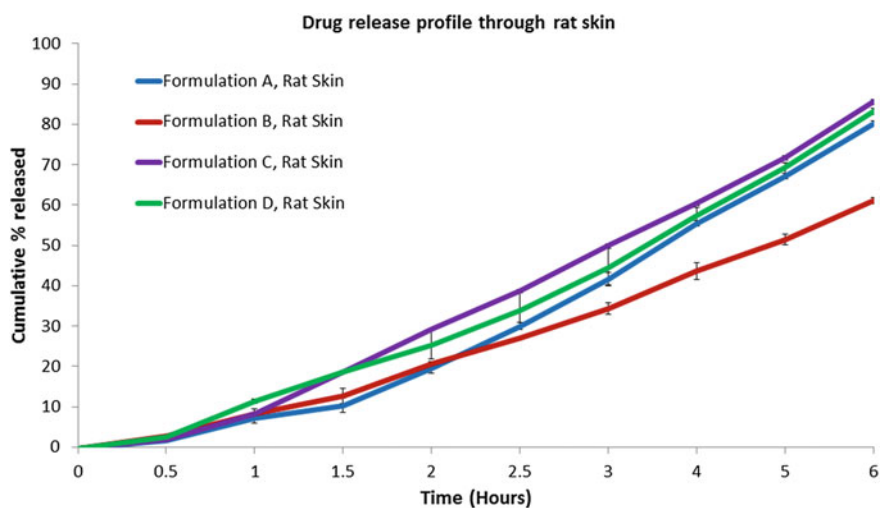
Fig. 26.6 Comparison of drug release profiles of formulations A–D through rat skin in a Franz diffusion cell

formulations (A and B) was compared to that of the marketed drugs (C and D) as shown in Table 26.5 and Figs. 26.6 and 26.7.

Formulation A showed a higher percentage of drug release as compared to formulation B but was slightly lower than the marketed products which had a marginally higher percentage of drug released. The higher viscosity decreases the release of active substance from the formulation. The increased amount of aerosil results in greater complexity of cross-links between neighboring particles and a larger number of networks per unit area [37].

The cumulative percentage of drug released in 6 h through the synthetic membrane from formulations A, B, C and D was found to be 86.69 ± 8.42, 70.86 ± 7.72,
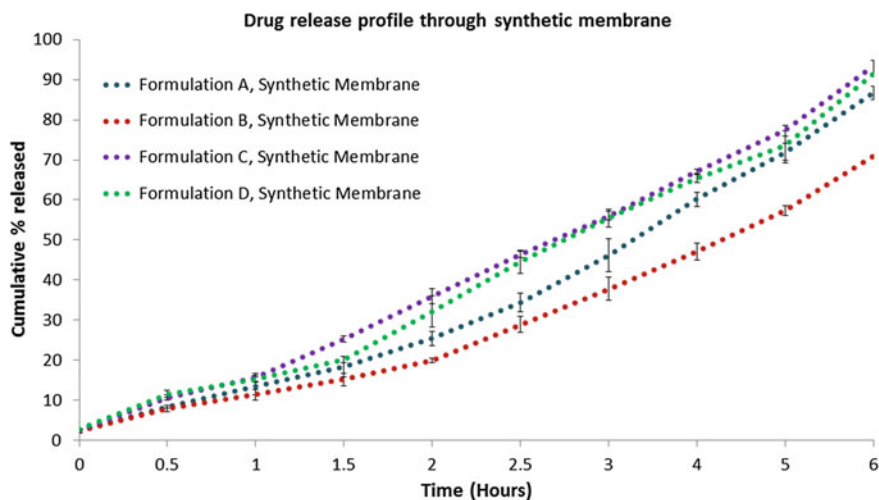
Fig. 26.7 Comparison of drug release profiles of formulations A–D through a synthetic membrane in a Franz diffusion cell

Table 26.5 Cumulative percentage of drug released in 6 h through rat skin and synthetic membrane

Formulation	Permeation medium	Total % conversion
A	Rat skin	80.16 ± 8.90
B	Rat skin	61.17 ± 9.81
C	Rat skin	85.52 ± 9.97
D	Rat skin	83.10 ± 8.20
A	Synthetic membrane	86.69 ± 8.42
B	Synthetic membrane	70.86 ± 7.72
C	Synthetic membrane	93.33 ± 7.49
D	Synthetic membrane	91.30 ± 7.14

Table 26.6 Flux and permeability coefficient for the different formulations

Formulation	Permeation medium	Drug flux J (μg/h/cm^2)	Permeability coefficient K_P (cm/h)
A	Rat skin	121.02 ± 8.47	0.0945 ± 0.0017
B	Rat skin	91.80 ± 4.59	0.0717 ± 0.0008
C	Rat skin	129.38 ± 20.70	0.1011 ± 0.0061
D	Rat skin	118.98 ± 15.65	0.0930 ± 0.0061
A	Synthetic membrane	129.15 ± 10.33	0.1009 ± 0.0040
B	Synthetic membrane	118.81 ± 7.13	0.0928 ± 0.0028
C	Synthetic membrane	146.70 ± 27.87	0.1146 ± 0.0092
D	Synthetic membrane	145.42 ± 17.44	0.1136 ± 0.0064

93.33 ± 7.49, and 91.30 ± 7.14, respectively. The permeation of drug from formulation A was comparable to that of the formulations C and D while the permeation of drug from formulation B was the lowest of all formulations, as shown in Table 26.5 and Figs. 26.6 and 26.7. Marketed products have a little higher drug release that may be related to the concentration of the gelling agent. The high viscosity of gels competes with the release of active substance from the formulation.

It was observed that formulation A produced better drug release as compared to formulation B, both in in vitro drug diffusion study using synthetic membrane as well as in ex vivo penetration study using rat abdominal skin and may be due to its low viscosity. Compared to the rat skin, drug release from the synthetic membrane was more, probably due to its simple structure.

The comparison of skin permeation data with that of the synthetic membrane is not a simple task [38]. However, in vitro evaluations are essential tools for the development and screening of formulations, and could predict in vivo cutaneous absorption [39, 40].

The percentage or fraction drug permeation provides information on the % or fraction of applied dose absorbed across the skin in a specified time. In order to derive a more meaningful parameter, the duration of exposure must be indicated along with the amount applied per unit area, which is known as flux. Permeability coefficient (K_p) which is a flux value normalized for concentration, represents the rate at which the chemical penetrates the skin (cm/hour). Flux is usually calculated from the slope of the linear portion of the plot of the cumulative amount of drug permeated per unit area versus time and K_p is then calculated by dividing the flux with initial concentration applied on the skin. When Fick's first law prevails under steady-state conditions (Fickian diffusion), the flux can be easily obtained from the slope of drug permeated per unit area versus time plot.

On the basis of the drug permeation results from both synthetic membrane and rat abdominal skin, the mean flux and permeability coefficient (K_p) values were calculated. The present results reveal that the flux and K_p values were higher in case of synthetic membrane compared to rat abdominal skin when compared for same formulations (Table 26.6). This is obvious as rat skin provides a more complex barrier for drug permeation as compared to the synthetic membrane. The flux and K_p values were highest for marketed product formulation C, followed by prepared product formulation A in case of both synthetic membrane and rat abdominal skin, while flux and K_p values were lowest for the prepared formulation B amongst the formulations tested.

26.4.9   Drug Release Kinetics

The in vitro drug release data were subjected to the goodness of fit test by linear regression analysis according to zero order, first order kinetic equation and Korsmeyer–Peppas model in order to determine the mechanism of the drug release. The results of linear regression analysis data including the regression coefficient are summarized in Table 26.7.

Table 26.7 Drug release data fitted to various kinetic models

Formulation	Permeation medium	Zero order		First order		Korsmeyer-Peppas		
		K_0	R^2	K_1	R^2	n	K_{KP}	R^2
A	Rat skin	13.13	0.99	0.27	0.98	0.12	7.14	0.95
B	Rat skin	9.48	0.99	0.15	0.97	0.12	4.34	0.96
C	Rat skin	13.59	0.99	0.30	0.95	0.13	6.32	0.95
D	Rat skin	12.89	0.98	0.28	0.99	0.12	8.05	0.90
A	Synthetic membrane	14.40	0.99	0.31	0.92	0.15	4.22	0.98
B	Synthetic membrane	11.71	0.99	0.19	0.95	0.15	2.81	0.99
C	Synthetic membrane	15.07	0.98	0.40	0.91	0.15	5.38	0.88
D	Synthetic membrane	15.28	0.98	0.38	0.92	0.16	4.07	0.89

Based on the results, highest correlation coefficient (>0.99) were found when release data were fitted to a zero order model. Hence, results confirm that all the formulations followed zero-order kinetics. Zero-order release is preferable as it provides constant plasma drug concentrations throughout the period of drug diffusion from the applied formulation. To know the mechanism of drug release, the release data were fitted to the Korsmeyer–Peppas model. For all the formulations, release exponent (n) values were less than 1 (n < 0.45) which corresponds to Fickian diffusion mechanism. The Fickian diffusion-based drug release for all the tested formulations further confirms that the rate of release is independent of the drug concentrations in the gels.

26.4.10   Analgesic Activity

Both formulations A and B with 1% diclofenac sodium as a topical formulation were tested for their analgesic activity using the tail flick method in rats. The gels were applied topically by rubbing the gels on the tail for a fixed time of 1 min and both were found to induce a significant analgesic activity in rats as compared to the control value (Table 26.8). The diclofenac sodium acts on the cyclooxygenase pathway of prostaglandins synthesis [41].

26.4.11   Skin Irritation Test

Formulation A loaded with 1% diclofenac sodium was assessed for irritancy test on male White New Zealand rabbits, using the dorsal area on the restrained animal following the application of an aliquot of aerosil gel. The rabbits were observed for visually apparent cutaneous changes (erythema and edema) and scored on normal

Table 26.8 Analgesic activity of the prepared formulations

Treatment	Mean reaction time (s) ± SEM				
	Pre-drug	30 min	1 h	2 h	4 h
Control	2.30 ± 0.64	85.76 ± 13.31	119.02 ± 17.31	111.30 ± 13.28	96.20 ± 10.32
A	2.01 ± 0.24	92.77 ± 13.55	133.63 ± 18.53**	134.12 ± 13.56**	139.43 ± 16.88***
B	3.31 ± 0.35	99.23 ± 10.45	132.33 ± 25.33*	144.12 ± 18.24**	149.43 ± 18.90***

Significantly different from the treated control (*$P < 0.05$, **$P < 0.01$, ***$P < 0.001$)
Values represented Mean ± SEM (n = 6)

Table 26.9 Irritancy test on male white New Zealand rabbits

Reaction time (h)	Aerosil gel base				Formulation A				Formulation B			
	Erythema		Edema		Erythema		Edema		Erythema		Edema	
	Intact skin	Abraded skin	Intact skin	Abraded skin	Intact skin	Abraded skin	Intact skin	Abraded skin	Intact skin	Abraded skin	Intact skin	Abraded skin
4	0	0	0	0	0	2	0	0	0	2	0	2
24	0	0	0	0	0	0	0	0	0	0	0	0
48	0	0	0	0	0	0	0	0	0	0	0	0
72	0	0	0	0	0	0	0	0	0	0	0	0

and abraded skin. The irritation test results indicated that the application of gel base, formulation A and B was associated with no skin irritation throughout the entire observation period. However, mild erythema at the earlier observation times were recorded in abraded skin in formulation A and B, which disappeared the following second day (Table 26.9).

26.5   Conclusion

The present study showed the comparative evaluation of two oleogels developed under this investigation with marketed gels containing diclofenac sodium. The formulated oleogels with 8 and 10% aerosil showed smooth and homogeneous appearance with suitable pH, spreadability, extrudability, homogeneity, and viscosity. In vitro and ex vivo drug permeation studies suggested similar drug permeation from the developed formulations as that of marketed diclofenac gels through both the synthetic membrane and rat skin. Developed formulation A (8% aerosil) showed faster drug release compared to formulation B (10% aerosil) due to its lower viscosity. Prepared gels showed significant analgesic effect without any sign of skin irritation in rats. Based on the results of this investigation, formulation A with 8% aerosil gel base in liquid paraffin was found to be a promising formulation for further clinical investigations due to its thixotropic nature with good physicochemical integrity and comparability with marketed products.

References

1. Sanna V, Peana TA, Moretti DLM (2009) Effect of vehicle on diclofenac sodium permeation from new topical formulations: *in vitro* and *in vivo* studies. Curr Drug Deliv 6:93–100
2. Skoutakis VA, Carter CA, Mickle TR et al (1988) Review of diclofenac and evaluation of its place in therapy as a non-steroidal anti-inflammatory agent. Drug Intell Clin Pharm 22:850–859
3. Jani R, Mallikarjuna KJSC (2010) Preparation and evaluation of topical gel Valdecoxib. Int J Pharm Sci Res 2:51–54
4. Kumar V, Sathali AH, Kumar A (2010) Formulation and evaluation of diclofenac potassium ethosomes. J Pharm Pharm Sci 2:82–86
5. FitzGerald GA, Patrono C (2001) The coxibs, selective inhibitors of cyclooxygenase-2. N Engl J Med 345:433–442
6. Mikari BV, Korde SK, Mahadik KR, Kokare CR (2010) Formulation and evaluation of topical liposomal gel for fluconzole. Indian J Pharm Sci 44:324–325
7. Green PG, Flanagan M, Shroot B, Guy RH (1993) Ionotophoretic drug delivery. In: Walters KA, Handgraft J (eds) Pharmaceutical skin penetration enhancement. Marcel Dekker, New York, USA, pp p311–p333
8. Patel J, Patel B, Banwait H et al (2011) Formulation and evaluation of topical aceclofenac gel using different gelling agent. Int J Drug Dev & Res 3:156–164

9. Dey S, Mazumdar B, Patel JR (2009) Enhance percutaneous permeability of acyclovir by DMSO from topical gel formulation. IJPSPP 1:13–18

10. Tas C, Ozkan Y, Okyar A, Savaser A (2007) *In vitro* and *ex vivo* permeation studies of etodolac from hydrophilic gels and effect of terpenes as enhancers. Drug Deliv 14:453–459

11. Ali AA, Geneidi AS, Salama RB (1978) A new oil-based aerosil gel "OLAG". Indian J Pharm Sci 40:139

12. Sherriff M, Enever RP (1979) Rheological and drug release properties of oil gels containing colloidal silicon dioxide. J Pharm Sci 68:842–845

13. Guy RH, Hadgraft J, Bucks DA (1987) Transdermal drug delivery and cutaneous metabolism. Xenobiotica 7:325–343

14. Arellano A, Santoyo S, Martin C, Ygartua P (1998) Influence of propylene glycol and isopropyl myristate on the *in vitro* percutaneous penetration of diclofenac sodium from Carbopol gels. Eur J Pharm Sci 7:129–135

15. Lu Z, Fassihi R (2015) Influence of colloidal silicon dioxide on gel strength, robustness, and adhesive properties of diclofenac gel formulations for topical application. AAPS Pharm SciTech 16:636–644

16. Töricht E, Erös I (1977) Investigation of salves containing highly disperse silicon dioxide (in German). Pharmazie 32:109–113

17. Devi US, Ganesan M, Mohanta GP, Manavalan R (2002) Design and evaluation of tetracycline hydrochloride gels. Indian Drugs 39:552–554

18. Attia MA, Gibaly EI, Shaltout SE, Fetih GN (2004) Transbuccal permeation, anti-inflammatory activity and clinical efficacy of piroxicam formulated in different gels. Int J Pharm 276:11–28

19. Mohamed MI (2004) Optimization of chlorphenesin emulgel formulation. AAPS Journal 6:1–7

20. Sera UV, Ramana MV (2006) *In vitro* skin absorption and drug release—a comparison of four commercial hydrophilic gel preparations for topical use. Ind Pharmacist 73:356–360

21. Shivhare UD, Jain KB, Mathur VB et al (2009) Formulation development and evaluation of diclofenac sodium gel using water-soluble polyacrylamide polymer. Dig J Nanomater Bios 4:285–290

22. Gupta GD, Gaud RS (2005) Release rate of Tenoxicam from acrypol gels. Ind Pharmacist 5:69–76

23. Kaur LP, Garg R, Gupta GD (2010) Development and evaluation of topical gel of minoxidil from different polymer bases in the application of alopecia. Int J Pharmacy Pharm Sci 2:43–47

24. Rathore RPS, Nema RK (2008) Formulation and evaluation of topical gels of Ketoprofen. Asian J Pharm Clinical Res 1:12–16

25. Franz TJ (1975) Percutaneous absorption. On the relevance of *in vitro* data. J Invest Dermatol 64:190–195

26. Tas C, Ozkan Y, Savaser S, Baykara T (2003) *In vitro* release studies of chlorpheniramine maleate from gels prepared by different cellulose derivatives. IL Farmaco 58:605–611

27. Chowdary KPR, Kumar PA (1996) Formulation and evaluation of topical drug delivery systems of ciprofloxacin. Ind J Pharm Sci 58:47–50

28. Eddy NB, Leimbach D (1953) Synthetic analgesics. II. Dithienylbutenyl- and dithienylbutylamines. JPET 107:385–393

29. Griffiths CEM (1995) Nicotinamide 4% gel for the treatment of inflammatory *acne vulgaris*. J Dermatol Treat 6:S8–S10

30. Morgan RL, Castles TR, Zwicker GM, Taylor A (1985) Toxicologic pathology, skin irritation testing in rabbits complicated by dermal mucormycosis. Toxicol Pathol 13:185–191

31. Murdan S (2005) Organogels in drug delivery. Expert Opin Drug Deliv 2:489–505

32. USP (2002) The Official Compendia of Standards. First Annual Asian edition, p 554

33. Moin A, Deb TK, Osmani RAM, Bhosale RR, Hani U (2016) Fabrication, characterization, and evaluation of microsponge delivery system for facilitated fungal therapy. J Basic Clin Pharm 7:39–48

34. Chien YW (1992) Novel drug delivery systems, 2nd edn. Marcel Dekker Inc, New York, p 499

35. Lucero MJ, Vigo J, Leon MJ (1994) A study of shear and compression deformations on hydrophilic gels of tretinoin. Int J Pharm 106:125–133

36. Pose-Vilarnovo B, Rodriguez-Tenreiro C, Dos Santos JFR et al (2004) Modulating the drug release with cyclodextrins in hydroxypropyl methylcellulose gels and tablets. J Control Release 94:351–363
37. Zhang L, Parsons DL, Navarre C, Kompella UB (2002) Development and *in-vitro* evaluation of sustained release poloxamer 407 (P407) gel formulations of ceftiofur. J Control Release 85:73–81
38. Ruela AL, Perissinato AG, Lino ME, Mudrik PS, Pereira GR (2016) Evaluation of skin absorption of drugs from topical and transdermal formulations. Braz J Pharm Sc 52:527–544
39. Thakker K, Chern W (2003) Development and validation of *in vitro* release tests for semisolid dosage forms—Case study. Online database: https://docplayer.net/36516602-Development-and-validation-of-in-vitro-release-tests-for-semisolid-dosage-forms-case-study.html
40. Frum Y, Khan GM, Sefcik J, Rouse J, Eccleston GM, Meidan VM (2007) Towards a correlation between drug properties and *in vitro* transdermal flux variability. Int J Pharm 336:140–147
41. Rosenfeld GC, Loose DS (2006) Pharmacology. Lippincott Williams & Wilkins, Philadelphia, USA, pp 165–170

Chapter 27
Kinetics and Mechanism of Cr(VI) Adsorption onto NaOH Treated Pine and Magnetite-Pine Composite

Agnes Pholosi, Eliazer B. Naidoo and Augustine E. Ofomaja

Abstract Magnetite nanoparticles were coated on pine cone biomass (NTP-NC) by co-precipitation method and the effect of the magnetite coating on Cr(VI) uptake, mechanism, kinetic performance and diffusion of sodium hydroxide treated pine cone (NTP) was studied. Evidence of adsorption-coupled reduction mechanism was observed using change in solution hydrogen ion concentration (ΔH^+), oxidation reduction potential (ORP) and amounts of total Cr, Cr(III) and Cr(VI) left in solution for both coated and uncoated adsorbents. FTIR spectra showed that Cr was removed as Cr(III) by both oxygenated functional groups of pine cone and Fe–O and maghemite peaks were formed due to reduction reaction. The pseudo-second-order and pseudo-nth-order best described Cr(VI) removal for both adsorbents giving similar values of equilibrium capacity. The equilibrium capacities of Cr(VI) for NTP and NTP-NC were 7.01 and 9.40 mg/g respectively. The kinetic performance using the Wu's expression showed that Cr(VI) adsorption onto NTP-NC drastically approached equilibrium and had lower half-life as compared with NTP. External mass transfer and surface adsorption contributed largely to the rate controlling step and their contributions were higher for NTP-NC than for NTP due to the larger surface area and reactivity of the magnetite coating.

Keywords Adsorption-coupled reduction mechanism · Kinetic performance · Magnetite coated pine cone · Cr(VI) removal · Pine cone power

A. Pholosi (✉) · E. B. Naidoo · A. E. Ofomaja
Biosorption and Wastewater Treatment Research Laboratory, Department of Chemistry, Faculty of Applied and Computer Sciences, Vaal University of Technology, P. Bag X021, Vanderbijlpark 1900, South Africa
e-mail: agnesp@vut.ac.za; agnes.pholosi07@gmail.com

E. B. Naidoo
e-mail: bobby@vut.ac.za

A. E. Ofomaja
e-mail: augustineo@vut.ac.za

27.1 Introduction

The interaction between pollutant molecules or ions and active sites on adsorbent surfaces is an important phenomenon in many industrial processes such as catalysis, adsorption and other separation techniques. Porous materials applied as adsorbent for water treatment contain active sites on their external and internal surfaces allowing for surface adsorption, external and intraparticle diffusion to contribute to the removal mechanism of pollutants. The adsorption properties of lignocellulosic materials for chromium(VI) (Cr(VI)) have been attributed to acidic functional groups on the adsorbent surface which can take part in ion-exchange, complexation, chelation and hydrogen bonding with pollutant species in solution [1, 2]. Two mechanisms for lignocellulosic material adsorption of Cr(VI) have been proposed: (i) an electrostatic mechanism in which at low pH, the protonated acidic functional groups on the biomaterial carrying a positive charge attract the negatively charged Cr(VI) species [3–5]; and (ii) the adsorption-coupled reduction mechanism in which Cr(VI) is reduced to Cr(III) either in solution (Direct reduction) or after being adsorbed (Indirect reduction) by electron-donor groups of the biomaterial that have lower reduction potential values than that of Cr(VI) [6, 7]. The Cr(III) ions formed in solution may then form complexes with Cr(III)-binding groups on the biomaterial surface or released into bulk solution by repulsion between Cr(III) and other positively charged groups on the biomaterial [8]. Adsorption of pollutants using biomaterials has been associated with limitations such as the kinetic restriction [9], low adsorption rates of pollutants [10] and problems associated with separation of solids from solution [11]. It is therefore desirable to incorporate small sized functional material with high surface area to improve diffusion, surface adsorption and ease of separation from solution.

In recent times, iron magnetic nanoparticles have been incorporated into biomaterials to eliminate the numerous drawbacks associated with their use as adsorbent for Cr(VI) removal. Examples of these applications are in the use of magnetite coated chitosan [9], magnetotactic bacteria [12], magnetic cellulose [13] and magnetic lignin composite [14] for the removal of Cr(VI) from aqueous solution. Although a few number of literature exist on the kinetics and mechanism studies of Cr(VI) removal by magnetite-biomaterial composites, scanty literature show complete evidence of the adsorption-coupled reduction mechanism or compare the differences between the mechanism of the biomaterial and the magnetite-biomaterial composite. This study therefore seeks to (i) examine the operating mechanism of Cr(VI) adsorption onto NTP and NTP-NC, (ii) compare the kinetics and kinetic performance of Cr(VI) uptake on both samples, and (iii) examine the effect of magnetite coating on NTP on the diffusion of Cr(VI) onto the adsorbents. The kinetic data of Cr(VI) uptake onto NTP and NTP-NC were modelled with three kinetic models and three diffusion models using regression program of the KyPlot 2.0 software which uses Quasi-Newton algorithm for finding the parameter values which minimize the sum of the squares of the errors (ERRSQ).

27.2 Materials and Methods

27.2.1 Materials

Pine tree cones were collected from a plantation in Vanderbijlpark, South Africa. The scales on the cones were then removed and blended in a food processing blender. The resultant powder was sieved and particles below 90 μm were collected and used for analysis. Stock solution of Cr(VI) was prepared by dissolving an accurately weighed amount of $K_2Cr_2O_7$ in deionized water.

27.2.2 Methods

27.2.2.1 Preparation of NaOH Treated Pine-Magnetite Nanocomposite (NTP-NC)

This procedure involved dissolving 2.1 g of $FeSO_4 \cdot 7H_2O$ and 3.1 g of $FeCl_3 \cdot 6H_2O$ under inert atmosphere in 0.08 dm^3 of double distilled water with vigorous stirring. The solution was heated to 80 °C and 0.03 dm^3 of 25% ammonium hydroxide and 1.5 g of sodium hydroxide treated pine (NTP) were added. The reaction was left to run for 30 min at 80 °C under constant stirring. The resulting NTP-NC was washed several times with deionized water and ethanol.

27.2.2.2 Characterization

The FTIR spectra of NTP and NTP-NC before and after Cr(VI) adsorption were recorded on a Perkin-Elmer (USA) ATR-FTIR Spectra 400 spectrometer in the range 500–4000 cm^{-1} to elucidate the functional groups present. The nanocrystal size and morphology of the NTP-NC were observed by transmission electron microscopy (TEM) on a JEOL 2010 FET TEM (Japan). A Tristar 3000 instrument coupled to a VacPrep 061 degassing unit was used to determine the sample surface area, pore volume and pore size under a N_2 gas atmosphere.

27.2.2.3 Effect of Solution pH

The effect of solution pH was performed in a batch system in which 0.5 g of the adsorbent was contacted in six 0.25 dm^3 beakers containing 0.075 dm^3 of 75 mg/dm^3 Cr(VI) solutions set at pH 1 to 10 at 26 °C and agitated at 200 rpm for 2 h. After 2 h of agitation, the solution was filtered to remove the solid adsorbent and the clear solution was analysed for Cr(VI) left using Ultra Violet-Visible spectrophotometer (UV/Vis)

at 460 nm, total Cr was analysed using atomic absorption spectrometer (AAS) while Cr(III) in solution was determined by calculating the difference between total Cr and Cr(VI).

27.2.2.4 Kinetic Studies

Batch contact kinetic experiments were performed by contacting 0.5 g of the adsorbent materials with 0.075 dm^3 of Cr(VI) solution of concentrations 25, 75, 100, 125 and 150 mg/dm^3 in five conical flasks agitated 200 rpm for 2 h at 26 °C set to pH 2. Aliquot (0.0001 dm^3) of sample was withdrawn at given interval, filtered and diluted appropriately and analysed for Cr(VI) left using UV-Vis spectrophotometer at 460 nm.

27.3 Results and Discussion

27.3.1 Brunauer-Emmett-Teller (BET) Surface Area Analysis

The BET surface areas for the NTP and NTP-NC were observed to be 2.25 and 54.8 m^2/g as shown in Table 27.1. The magnetization of the NTP caused a drastic increase in surface area and pore volume of the NTP. Such increase in BET surface area for magnetized lignocellulosic waste has been reported for orange peel powder (47.03 m^2/g) and magnetite-orange peel powder (65.19 m^2/g) [15], sodium hydroxide treated wheat straw (22.3 m^2/g) and Fe_3O_4-sodium hydroxide treated wheat straw

Table 27.1 Characteristics of NTP and NTP-NC

	NTP	NTP-NC
Surface properties		
BET surface area (m^2/g)	2.25	54.8
Pore volume (cm^3/g)	0.0177	0.1522
Pore size (nm)	23.10	10.17
FTIR peaks		
–OH	3334 cm^{-1}	3256 cm^{-1}
–CH_2, –CH_3	2897 cm^{-1}	2913 cm^{-1}
C–O	1627, 1602 cm^{-1}	1627 cm^{-1}
C=C	1509 cm^{-1}	1507 cm^{-1}
O–CH_3	1421 cm^{-1}	1416 cm^{-1}
C–O–C	1028 cm^{-1}	1024 cm^{-1}
Fe–O		564 cm^{-1}

(a) **(b)**
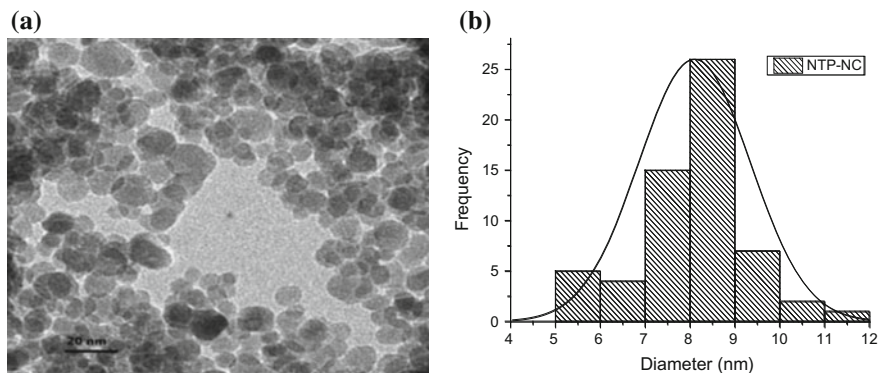
Fig. 27.1 TEM image and size distribution of NTP-NC nanocomposite

(57.5 m^2/g) [16], tea waste (22.3 m^2/g) and Fe_3O_4-tea waste (27.5 m^2/g) [17]. The possible reason for the increase in BET surface area and pore volume can be attributed to the small size of Fe_3O_4 particles formed on the surface of the lignocellulosic material. It was also observed that pores of smaller sizes were obtained when Fe_3O_4 was applied in the modification of lignocellulosic materials. It is believed that the nucleation of Fe_3O_4 particles within the matrix of NTP may be responsible for the increased pore volume.

27.3.2 Transmission Electron Microscopy (TEM)

TEM image and size distribution of NTP-NC are shown in Fig. 27.1a, b, while the calculated size of the particles is shown in the histogram. The TEM image of NTP-NC revealed that the particles were spherical in nature with mean diameter of about 7.94 nm.

27.3.3 FTIR Analysis

Table 27.1 shows the peaks of major functional groups present on the NTP and NTP-NC surface. The peaks at 3334, 2897 and 1602 cm^{-1} correspond to hydrogen bond stretching of α-cellulose, CH and CH_2 of cellulose and C–O of lignin [18] in NTP. The peaks at 1509, 1421 and 1028 cm^{-1} represent C=C stretching of aromatic rings, methoxy (O–CH_3) from lignin and symmetric C–O–C stretching of lignin [19]. The composite on the other hand contains functional groups related to both NTP and Fe_3O_4 nanoparticles. The hydrogen bond stretching shifted to 3256 cm^{-1}, and a reduction in the intensity and position of CH and CH_2 cellulose peaks to 2913 cm^{-1} was observed. The C–O peak was also found to reduce in intensity and shifted to

$1627\,\mathrm{cm}^{-1}$ while the C–O–C stretching shifted to $1024\,\mathrm{cm}^{-1}$ indicating an interaction between the Fe_3O_4 particles and oxygenated groups of lignin. The presence of Fe–O and Fe–OH were indicated by a peak at $564\,\mathrm{cm}^{-1}$ [20, 21].

27.3.4 Effect of pH on the Adsorption of Cr(VI) from Solution

The results indicate that the percentage of Cr(VI) removal for both adsorbents were lower at higher solution pHs and higher at lower solution pHs and NTP-NC had higher Cr(VI) removal than NTP (Fig. 27.2a, b). At lower solution pHs the dominant Cr(VI) species are $HCrO_4^-$ and $Cr_2O_7{}^{2-}$ while the surface of the adsorbents is positively charged due to accumulation of H^+ ions. Therefore, two mechanistic pathways can be proposed:

(i) Electrostatic interaction

$$X - COOH(s) + HCrO_4^-(aq) + H^+(aq) \rightarrow X - COOH_2^+ - HCrO_4^-(s) \quad (27.1)$$

$$X - 2COOH(s) + 2H^+(aq) + Cr_2O_7^{2-}(aq) \rightarrow X - 2COOH_2^+ - Cr_2O_7^{2-}(s) \quad (27.2)$$

(ii) Adsorption coupled reduction mechanism

$$Cr_2O_7^{2-}(aq) + 14H^+(aq) + 6e^- \rightarrow 2Cr^{3+}(aq) + 7H_2O(aq) \quad (27.3)$$

$$HCrO_4^-(aq) + 7H^+(aq) + 3e^- \rightarrow Cr^{3+}(aq) + 4H_2O(aq) \quad (27.4)$$
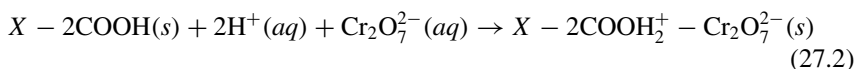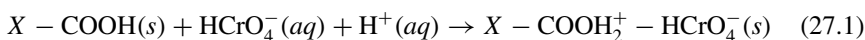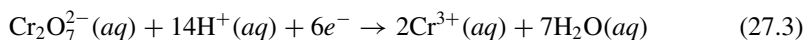
Fig. 27.2 Plot of the amount of Cr concentration left in solution and the changes in H^+ concentration at different solution pH for **a** NTP and **b** NTP-NC

The electrons required for the reduction process to occur (Eqs. (27.3) and (27.4)) are supplied by the electronegative atom in the functional group. Magnetite contains both Fe^{2+} and Fe^{3+} species in its structure [Fe(II)Fe(III)$_2$O$_4$] and the Fe^{2+} present in the structure acts as the potential reducing agent [22, 23] as shown below:

$$6Fe_3O_4(s) + 10H^+(aq) + 2CrO_4^{2-} \rightarrow 9\gamma - Fe_2O_3(s) + 2Cr^{3+}(aq) + 5H_2O(aq)$$

$$(27.5)$$
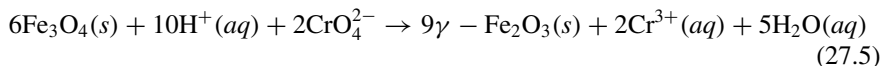
In this process the magnetite, Fe_3O_4 is converted to Fe_2O_3 which coats the magnetite surface and Cr(III) hydroxide produced is precipitated on the magnetite further reducing its activity [24]. To prove which mechanism is predominant for Cr(VI) removal using NTP and NTP-NC, the amount of Cr concentration left in solution (total chromium, Cr(VI) and Cr(III)) and changes in H^+ concentration were plotted against different solution pH and the results are shown in Fig. 27.2a, b. It is known that the reduction of Cr(VI) to Cr(III) consumes H^+ and releases OH^- which raises the solution pH. The results for ΔH^+ at the end of the adsorptio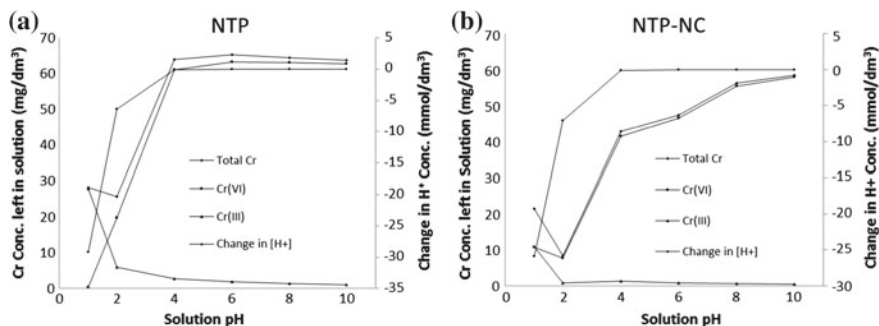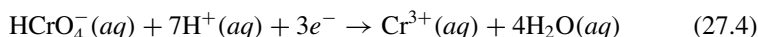n revealed that the values for ΔH^+ were larger at lower initial solution pH's (higher Cr removal) and became small and almost constant above initial pH 4. These results indicate that Cr(VI) removal was associated with the consumption of H^+ (Eqs. (27.1)–(27.4)) and the higher removal of Cr(VI) for NTP-NC also corresponded with higher ΔH^+. Cr(VI) ion in acidic solution has a positive redox potential value and in the presence of an electron donor becomes unstable and can be reduced to Cr(III) [25]. Before adsorption, the initial concentrations of total Cr and Cr(VI) measured using atomic absorption spectrometer and UV-Vis, respectively, were found to be very similar (≈ 75 mg/dm^3). After adsorption, the concentration of total Cr in the pH 1 solution was observed to have reduced to 28.36 mg/dm^3 for NTP and 21.56 mg/dm^3 for NTP-NC respectively, while the Cr(VI) concentrations were 0.40 mg/dm^3 for NTP and 10.66 mg/dm^3 for NTP-NC. The difference can therefore be attributed to the presence of Cr(III) produced by the reduction of Cr(VI). With solution pH 2, the concentration of Cr(III) left in solution was lower than that of solution pH 1 for both samples. The reason is that at pH 1 there is an abundance of H^+ ions in solution which accumulate on the functional groups on the adsorbent making the surfaces of the adsorbent positively charged and repelling away the positively charged Cr(III) ions from the adsorbent surfaces [26]. At solution pH 2, it is believed that there is less accumulation of H^+ ions at the adsorbent surfaces which led to reduced electrostatic repulsion and increased adsorption of Cr(III) from solution. This increase in Cr(III) adsorption is also confirmed by the reduction in total Cr in solution between solution pH 1 and 2. However, the lower total Cr, Cr(VI) and Cr(III) left in the solution for NTP-NC as compared with NTP suggest higher conversion of Cr(VI) to Cr(III) and removal of Cr(III) from solution.

27.3.5   FTIR Evidence for the Adsorption of Cr(III)

When Cr(III) is formed during adsorption-coupled reduction of Cr(VI), it undergoes hydrolysis and/or complexation depending on the solution pH and the total Cr(III) and may lead to the formation of various Cr(III) species [27]. As solution pH increases, the solubility of Cr(III) reduces and the chances of Cr(III) precipitation increase. At solution pH 1–4, Cr^{3+} and $Cr(OH)^{2+}$ are the major species and at solution pH ranging from 4–10, Cr(III) species (hydroxo complexes), such as $Cr(OH)^{2+}$, $Cr(OH)_2^+$ and $Cr(OH)_3$ are the dominant forms which at higher pH is readily transformed into the soluble complex, $Cr(OH)_4^-$. After adsorption of Cr(VI) onto NTP for 2 h, the final solution pH was 2.44. FTIR spectra of the unloaded NTP and Cr(VI) loaded NTP show similar peaks with shifting, splitting and increase and decrease in intensities of some peaks (Fig. 27.3). The differences between the Cr(III) loaded and unloaded NTP are: (i) the –OH stretching at 3334.04 cm^{-1} which is reduced and shifted to 3326.98 cm^{-1}; (ii) the C–H stretching at 2897.86 cm^{-1} which splits into three at 2876.33, 2885.89 and 2991.43 cm^{-1}; (iii) the carboxylate and carbonyl stretching at 1627.34 and 1602.99 cm^{-1} shifted to 1657.93 and 1602.83 cm^{-1} and (iv) the appearance of a new peak at 1731.11 cm^{-1}.

According to the proposal by the adsorption-coupled reduction mechanism, the Cr(III) formed may be complexed by ligands such as carboxylates of the biomaterial. The reduction and shift observed in the –OH band are attributed to the C–O bonds in cellulose and hemicellulose interacting with Cr(III) in solution. Vinodhini and Nilanjana [28] made similar observation in the adsorption of Cr(VI) onto neem sawdust. Reduction and splitting of the C–H peaks after Cr(III) adsorption have been reported by Barbu et al. [29] and were attributed to Cr(III) after adsorption.
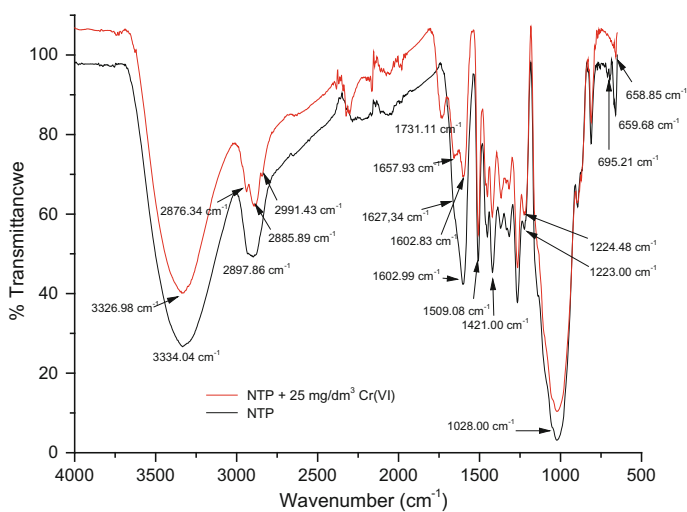
Fig. 27.3 FTIR spectra of NTP before and after adsorption
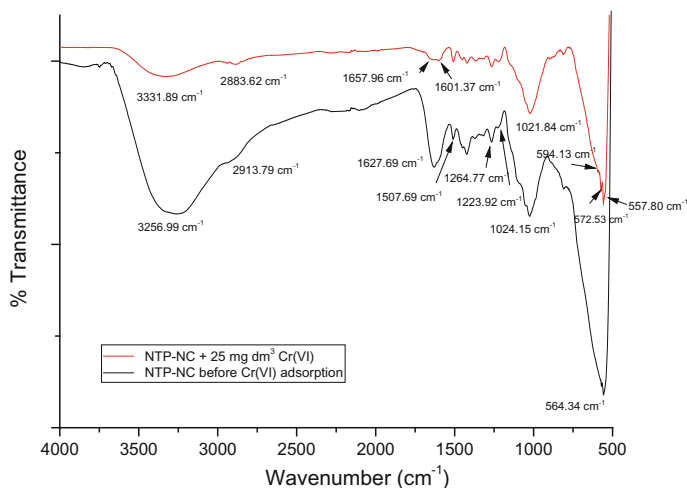
Fig. 27.4 FTIR spectra of NTP-NC before and after adsorption

Shift in the carboxylate and carbonyl peaks in the adsorption of Cr(III) has been attributed to the carboxylate group coordinated bidentate and monodentate to the Cr(III) cations in the NTP [29]. The complexation of Cr(III) by carboxylate groups on marine macro-algae *Laminaria digitata* showing FTIR peaks in similar range have been reported [27].

After adsorption of Cr(VI) onto NTP-NC for 2 h, the final solution pH was observed to be 2.53, and the peak at 564.34 cm^{-1} was observed to have split into several new peaks (Fig. 27.4). These emerging peaks are characteristic of Fe–O bonds of maghemite (γ-Fe$_3$O$_4$), for example the characteristics peaks of maghemite were observed at 595.21, 685.65 cm^{-1} [30, 31] and 582.70, 634.91 cm^{-1} [32] suggesting a change in the iron oxide phase (Fe$_3$O$_4$ to γ-Fe$_2$O$_3$) due to the conversion of Cr(VI) to Cr(III) by magnetite nanoparticles. According to Peterson et al. [24], Cr(III)(hydr)oxide produced is precipitated on the magnetite surface. In this study, Fe–O peak was observed to split into three peaks at 557.80, 572.53 and 594.13 cm^{-1} which was due to the presence of α-Cr$_2$O$_3$ in the NTP-NC surface indicating that Cr(III) was formed during the adsorption process [33]. Finally, it was also observed that the carboxylate group at 1627.69 cm^{-1} was broadened and was split into two peaks at 1657.93 and 1609.37 cm^{-1} suggesting that complexation between Cr(III) and carboxylate ions also occurred [29].

27.3.6 Adsorption Kinetics

The pseudo-first order kinetic model can be used to follow adsorption kinetics which proceeds by diffusion through a boundary [34] and the non-linear form of the pseudo-

first order model is given as:

$$q_t = q_e\left(1 - e^{-k_1 t}\right) \tag{27.6}$$

where q_t and q_e are the amount adsorbed at time t and at equilibrium and k_1 is the rate constant of the pseudo-first-order kinetic model. On the other hand, adsorption processes that proceed by surface chemisorption are described by the pseudo-second-order model [35] with the non-linear form:

$$q_t = \frac{k_2 q_e^2 t}{1 + k_2 q_e t} \tag{27.7}$$

The pseudo-nth order kinetic model was developed to determine accurately the order of kinetic processes based on adsorption capacity instead of pre-setting the order of the kinetics reaction. The pseudo-nth order kinetics has the advantage of giving the accurate kinetic order. The expression for the pseudo-nth order is given below [36]:

$$q_t = q_e - \left(q_e^{(1-n)} + (n-1)k_n t\right)^{\frac{1}{(1-n)}} \tag{27.8}$$

The results of the batch kinetic experiments revealed that Cr(VI) removal by NTP was lower than that for NTP-NC for all the concentrations of Cr(VI) applied in this study (Tables 27.2 and 27.3). The higher capacities of the NTP-NC over NTP can be attributed to its stronger ability to reduce Cr(VI) to Cr(III) and to complex Cr(III) from aqueous solution as observed from the lower concentrations of Cr(VI) and Cr(III) left in solution for NTP-NC than for NTP after adsorption at pH 2. The pseudo-first order rate constant, k_1, was observed to increase with increasing initial concentration of Cr(VI) in solution indicating that concentration gradient between the bulk solution and the adsorbent surface is a major driving force for the adsorption process. The pseudo-second-order rate constant, k_2, was also found to increase with increasing Cr(VI) concentration in solution and its values for NTP were lower than for NTP-NC, signifying that Cr(VI) removal was based not only on the concentration gradient, but on the surface area and the availability of active sites on the adsorbent surface (Tables 27.2 and 27.3). When the values of pseudo-second-order rate constant, k_2, were compared with those of pseudo-nth-order rate constant, k_n, it was observed that for both samples, the values of k_2 and k_n were quite similar. It was also observed that the values for the order of the kinetics, n, were all close to 2.0 for both samples. Finally, initial sorption rate, h, of the pseudo-second-order model was observed to increase with increasing Cr(VI) concentration in solution and its values were higher for NTP-NC than for NTP.

These results again confirm the effect of surface area and variety of surface functionality on the removal of Cr(VI) by NTP and NTP-NC respectively.

Table 27.2   Kinetic data for the adsorption of Cr(VI) onto NTP

Kinetic model	25 mg/dm^3	75 mg/dm^3	100 mg/dm^3	125 mg/dm^3	150 mg/dm^3
Pseudo-first order					
Exp. q (mg/g)	0.87	2.20	3.39	5.22	7.01
Model q (mg/g)	0.80	2.07	3.19	4.88	6.58
k_1 (min^{-1})	0.1620	0.3386	0.5144	0.8160	1.0934
r^2	0.9931	0.9931	0.9889	0.9931	0.9885
Variable error	0.0017	0.0096	0.0333	0.0096	0.1358
Pseudo-second order					
Exp. q (mg/g)	0.87	2.20	3.39	5.22	7.01
Model q (mg/g)	0.87	2.25	3.40	5.23	7.01
k_2 (g mg/min)	0.1788	0.1975	0.2220	0.2336	0.2435
h (mg/g min)	0.1353	0.9998	2.5663	6.3896	11.9656
r^2	0.9975	0.9986	0.9966	0.9990	0.9990
Variable error	0.00061	0.0019	0.0103	0.0067	0.0114
Pseudo-nth order					
Exp. q (mg/g)	0.87	2.20	3.39	5.22	7.01
Model q (mg/g)	0.97	2.27	3.42	5.21	6.98
n	2.20	2.05	2.05	1.96	1.94
k_n (min^{-1})	0.1713	0.1892	0.2097	0.2483	0.2680
r^2	0.9976	0.9986	0.9966	0.9990	0.9991
Variable error	0.00069	0.0022	0.0119	0.0077	0.0130

27.3.6.1   Relationship Between Pseudo-Second Order Parameters and Adsorption Performance

Wu et al. [37] described a parameter called the approaching equilibrium factor, R_W, which gives a relationship between the pseudo-second-order model constants and the characteristic kinetic curve. The approaching equilibrium factor, R_W, is defined as:

$$R_w = \frac{1}{1 + k_2 q_e t_{ref}} \qquad (27.9)$$

The characteristic adsorption curve is called approaching equilibrium in the range $1 > R_w > 0.1$ (zone I); well approaching pseudo equilibrium in the range $0.1 > R_w > 0.01$ (zone II); and drastically approaching equilibrium when $R_w < 0.01$ (zone III). For the adsorption of Cr(VI) by NTP and NTP-NC from Cr(VI) solutions of concentrations 25–150 mg/dm^3, the values of R_w were in the range of 0.1–0.01 for NTP and in the range 0.06–0.007 for NTP-NC. These results indicate that the NTP/Cr(VI) system falls under zone II meaning that the adsorption system well

Table 27.3 Kinetic data for the adsorption of Cr(VI) onto NTP-NC

Kinetic model	25 mg/dm³	75 mg/dm³	100 mg/dm³	125 mg/dm³	150 mg/dm³
Pseudo-first order					
Exp. q (mg/g)	1.41	3.67	5.50	7.48	9.38
Model q (mg/g)	1.23	3.48	5.20	7.07	8.90
k_1 (min⁻¹)	0.2361	0.5216	0.8118	1.1514	1.4459
r^2	0.9928	0.9861	0.9875	0.9873	0.9910
Variable error	0.0043	0.0495	0.0940	0.1701	0.1879
Pseudo-second order					
Exp. q (mg/g)	1.41	3.67	5.50	7.48	9.38
Model q (mg/g)	1.48	3.71	5.53	7.50	9.40
k_2 (g mg/min)	0.1875	0.2081	0.2281	0.2497	0.2561
h (mg/g min)	0.4107	2.8643	6.9755	14.0456	22.6290
r^2	0.9960	0.9933	0.9990	0.9982	0.9997
Variable error	0.0024	0.0242	0.0080	0.0249	0.0069
Pseudo-nth order					
Exp. q (mg/g)	1.41	3.67	5.50	7.48	9.38
Model q (mg/g)	1.49	3.71	5.54	7.50	9.35
n	2.04	2.00	2.02	2.01	1.96
k_n (min⁻¹)	0.1843	0.2078	0.2219	0.2461	0.3045
r^2	0.9960	0.9933	0.9990	0.9982	0.9997
Variable error	0.0028	0.0282	0.0092	0.0290	0.0068

approaches equilibrium while the NTP-NC system falls within zone II and into zone III meaning drastically approaching equilibrium. Therefore, the NTP-NC adsorbent will approach equilibrium adsorption of Cr(VI) more strongly than the NTP adsorbent in the removal of Cr(VI) from aqueous solution. Kinetic performance of the adsorbent can also be defined by the pseudo-second-order constant, $k_2 q_e$ (min⁻¹). At the half-life of the adsorption process (i.e. $t = t_{0.5}$), we have $q_t = 0.5 q_e$ and

$$t_{0.5} = \frac{1}{k_2 q_e} \tag{27.10}$$

It is evident that $k_2 q_e$ is the only parameter of Eq. (27.10). The $k_2 q_e$ value is equal to the inverse of the half-life of adsorption process, describing the actual meaning of pseudo-second order adsorption parameter better. The calculated values of the pseudo-second order rate parameter, $k_2 q_e$, ranged from 0.16 to 1.71 min⁻¹ for NTP and 0.28 to 2.41 min⁻¹ for NTP-NC as the initial concentration of Cr(VI) increased from 25 to 150 mg/dm³. The higher rate parameter, $k_2 q_e$, for NTP-NC suggests that the removal of Cr(VI) from solution by NTP-NC is more rapid than those of NTP. The rate parameter, $k_2 q_e$, increases with the initial concentration of Cr(VI), initial

sorption rate, h, and second-order rate constant k_2, for NTP and NTP-NC. The half-life of the pseudo-second-order model was found to be lower for NTP-NC than for NTP at all Cr(VI) concentrations applied. These results indicate that when a given mass of the adsorbent is contacted with a fixed concentration of Cr(VI), the ability to reduce the initial Cr(VI) concentration to half its original value is greater for NTP-NC than for NTP. The half-life was also observed to decrease with increasing concentration for NTP (from 6.43 to 0.59 min) and NTP-NC (from 3.60 to 0.42 min). In engineering practice, there is a need to draw a relationship between the operating time and the amount of adsorption. The relationship can be expressed through the relationship below:

$$t_x = \frac{W}{k_2 q_e} \tag{27.11}$$

$$\text{where } W = \frac{q_t}{(q_e - q_t)} \tag{27.12}$$

Since the fraction of pollutant adsorbed can be defined as $X = q_t / q_e$ and $W = X / (1 - X)$, at equilibrium, $q_t / q_e = 1$, $W = \text{infinity}$ and $t_x = \text{infinity}$. As X gradually approaches 1, W and t_x increase rapidly. The relationship between the operating time, t_x, and the metal ion adsorbed at each Cr(VI) initial concentration for NTP and NTP-NC was determined. This information can be used to make decisions on scale up and design purposes. The results revealed that the time taken to increase the fraction of pollutant adsorbed from X = 0.60 to 0.97 were all much shorter for NTP-NC than for NTP at all Cr(VI) initial concentrations. It was also observed that the operating time decreased with increasing concentration for both adsorbents. This means that shorter operating times are required to achieve a desired fractional removal of pollutant as initial Cr(VI) concentration increases due to the greater increase in pseudo-second order rate constant, k_2, with increase in initial concentration.

27.3.7 Diffusion Modelling

Diffusion of pollutant from aqueous solution onto porous materials plays a vital role in the adsorption process since pollutants may need to reach active sites or surfaces via diffusion processes.

27.3.7.1 External Mass Transfer Model

The external mass transfer rate constant was evaluated using the plot of C_t/C_0 against time for the adsorption of different concentrations of Cr(VI) onto NTP and NTP-NC at the beginning of the adsorption period (0–3 min). The results revealed that the value of k_s increased with increasing Cr(VI) concentration for both samples,

and the values of k_s were higher for NTP-NC (Tables 27.4 and 27.5). This increase can be attributed to the contribution of concentration driving force to the adsorption process, meaning that, as initial concentration increases, the concentration driving force is able to overcome the boundary resistance and causing an increase in the external mass transfer. The higher values of k_s for NTP-NC can be attributed to the higher specific surface area which leads to the high external mass transfer rates [38]. To determine the controlling process in the initial stages for both samples, the initial sorption rates for the pseudo-first order ($h_1 = k_1 q_e$) and pseudo-second-order ($h_2 = k_2 q_e^2$) were determined and the values of h_1, h_2 and k_s were plotted against Cr(VI) concentrations for both samples. The plots in Figs. 27.5a–c show that only the data points for k_s against C_0 gave linear relationships. This result signifies that external mass transfer was the controlling factor over film diffusion at the initial stage and the higher r^2 values for Cr(VI) adsorption onto NTP-NC indicate the higher participation of external mass transfer in the NTP-NC-Cr(VI) system.

Table 27.4 Kinetic data for the diffusion of Cr(VI) onto NTP

Diffusion model	25 mg/dm^3	75 mg/dm^3	100 mg/dm^3	125 mg/dm^3	150 mg/dm^3
Mass transfer					
k_s (min^{-1})	0.0420	0.0584	0.0718	0.1000	0.1118
r^2	0.9970	0.9672	0.8831	0.8155	0.7421
Intraparticle diffusion model					
k_p (mg g^{-1} min$^{-0.5}$)	0.0809	0.1218	0.1106	0.1422	0.1143
C	0.2896	1.3430	2.814	4.2113	6.1681
r^2	0.9151	0.8723	0.9411	0.8770	0.9648
Double-exponential model					
K_{D1} (mmol/dm^3)	0.2364	0.2297	0.2198	0.2084	0.2055
D_1 (min^{-1})	0.00708	0.0132	0.0161	0.1867	0.0200
r^2	0.9982	0.9921	0.9853	0.9828	0.970
K_{D2} (mmol/dm^3)	0.0701	0.0872	0.0903	0.0911	0.0925
D_2 (min^{-1})	0.00708	0.0132	0.0161	0.1867	0.0200
r^2	0.9808	0.9475	0.9038	0.899	0.049
k_e (m/min)	0.0418	0.0214	0.0186	0.0168	0.0158
k_i (m/min)	0.0530	0.0556	0.0665	0.0827	0.0940
Effective diffusion					
Di (cm^2/s)	2.40×10^{-5}	2.98×10^{-5}	3.09×10^{-5}	3.11×10^{-5}	3.16×10^{-5}
r^2	0.9808	0.9475	0.9058	0.8828	0.8547

Table 27.5 Kinetic data for the diffusion of Cr(VI) onto NTP-NC

Diffusion model	25 mg/dm^3	75 mg/dm^3	100 mg/dm^3	125 mg/dm^3	150 mg/dm^3
Mass transfer					
k_s (min^{-1})	0.0802	0.1095	0.1318	0.1505	0.1558
r^2	0.9355	0.9041	0.8286	0.7731	0.7055
Intraparticle diffusion model					
k_p (mg g^{-1} min$^{-0.5}$)	0.0896	0.1241	0.1236	0.1322	0.1117
C	0.7689	2.7892	4.6211	6.5412	8.5654
r^2	0.9072	0.9062	0.8923	0.9024	0.9483
Double-exponential model					
K_{D1} (mmol/dm^3)	0.2545	0.2340	0.2211	0.2183	0.2175
D_1 (min^{-1})	0.0098	0.0170	0.0190	0.0200	0.0205
r^2	0.9947	0.9858	0.9744	0.9687	0.9621
K_{D2} (mmol/dm^3)	0.080	0.0957	0.0972	0.0985	0.0991
D_2 (min^{-1})	0.0098	0.0170	0.0190	0.0200	0.0205
r^2	0.9560	0.9207	0.8803	0.8631	0.8405
k_e (m/min)	0.00250	0.00127	0.00092	0.00081	0.00078
k_i (m/min)	0.0052	0.0054	0.0062	0.0068	0.0071
Effective diffusion					
Di (cm^2/s)	3.28×10^{-9}	3.92×10^{-9}	3.99×10^{-9}	4.04×10^{-9}	4.06×10^{-9}
r^2	0.9500	0.9267	0.8803	0.8631	0.8406
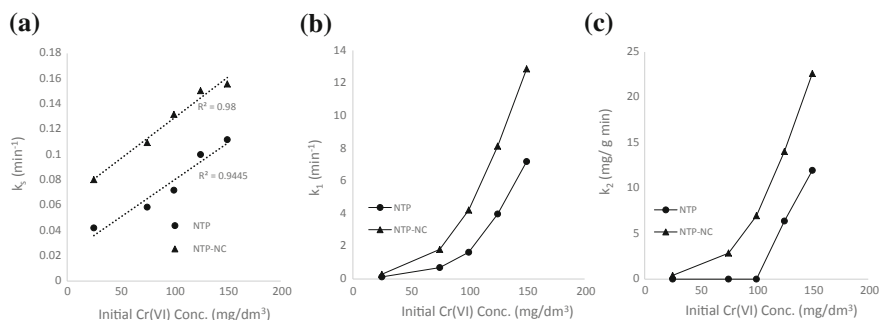
Fig. 27.5 Relationship between **a** mass transfer constant **b** pseudo first-order rate constant and **c** pseudo second-order rate constant with initial Cr(VI) concentration

27.3.7.2   Intraparticle Diffusion

According to Weber and Morris [39], if the rate limiting step is intraparticle diffusion, a plot of Cr(VI) adsorbed against the square root of the contact time should yield a straight line passing the origin. The most widely applied intraparticle diffusion equation for adsorption system is given by Weber and Morris [39]:

$$q_t = k_p t^{0.5} + C \tag{27.13}$$

where k_p is intraparticle diffusion rate constant (mg g^{-1} min^{-1}) and the intercept of the plot, C, reflects the boundary layer effect or surface adsorption. The larger the intercept, the greater the contribution of the surface adsorption in the rate-limiting step. The results show that the values of k_p were found to increase with increasing Cr(VI) concentration but reduce at 150 mg/dm^3 for both samples (Tables 27.4 and 27.5). The increase in k_p with initial concentration can be attributed to increased external mass transfer of Cr(VI) ions from aqueous solution to the adsorbent surface. The value of the intercept, C, increased with increasing Cr(VI) concentration for both adsorbents but NTP-NC had higher intercept values.

This means that contribution of surface adsorption to the rate limiting steps increased for both adsorbents, but surface adsorption contributed more to NTP-NC than onto NTP.

27.3.7.3   Double Exponential Diffusion (DED) Model

Double exponential diffusion (DED) model represents a two-step adsorption as proposed by Wilczak and Keinath [40]:

$$q_t = q_e - \frac{D_1}{m_{ads}} \exp\left(-K_{D_1} t\right) - \frac{D_2}{m_{ads}} \exp\left(-K_{D_2} t\right) \tag{27.14}$$

where D_1 and D_2 are adsorption rate parameters (min^{-1}) of the rapid and slow steps respectively, and K_{D_1} and K_{D_2} are the mass transfer parameters (mg/dm^3) controlling the overall kinetics. The DED model assumes that the rapid mass transfer coefficient, K_{D_1}, covers diffusion into both internal and external surfaces, while the slow step mass transfer coefficient, K_{D_2}, covers intraparticle diffusion alone. Both the external (k_e, m/min) and the internal (k_i, m/min) mass transfer can be calculated from the expressions below:

$$K_{D_1} = (k_e + k_i) S_e \frac{m_{ads}}{V} \frac{C_0}{C_0 - C_{eq}} \tag{27.15}$$

$$K_{D_2} = k_i S_i \frac{m_{ads}}{V} \frac{C_0}{C_0 - C_{eq}} \qquad (27.16)$$

where S_e and S_i are the external and internal surface area (m^2/g) while C_0 and C_{eq} are the initial and equilibrium concentrations of Cr(VI) (mg/dm^3) and V is the volume (dm^3). This diffusion model describes a two-step adsorption mechanism controlled by diffusion or a surface adsorption in which two different adsorption sites are present. The results of this study show that the values of D_1 and D_2 indicating the rate parameters of the rapid and slow steps were equal for both adsorbents at all concentrations suggesting that the adsorption takes place on one type of adsorption site [40].

The adsorption rate parameters, D_1 and D_2 for both adsorbents were observed to increase with increasing concentration and the values were higher for NTP-NC confirming the higher surface adsorption for NTP-NC (Tables 27.4 and 27.5). On the other hand, the values of K_{D_1} in the rapid stage for both samples were found to reduce with increasing concentration, with higher values for NTP-NC. This means that the effect of mass transfer on the overall kinetics is reduced as concentration increases for both samples and this can be related to the increase in surface adsorption with concentration. The higher values of K_{D_1} for NTP-NC can be attributed to the higher effect of external mass transfer. The values of K_{D_2} in the slow stage for both samples were found to increase with increasing concentration and the values for NTP-NC were higher. This result indicates that mass transfer parameter controlling the overall kinetics increased with concentration in the slow stage. As concentration increased the control of mass transfer on the overall kinetics in the slow step increased.

It is generally considered that about 30% of the total internal surface area is near the outer region of the sorbent particle and this region is also classified as part of the external surface [41] in which external and intraparticle diffusion are involved in the mass transfer. The internal surface accounts for the remaining 70% of the total surface area where mass transfer is controlled solely by intraparticle diffusion. For this reason, the external mass transfer, k_e, is controlled by both external and intraparticle diffusion, while the internal diffusion, k_i, is controlled solely by intraparticle diffusion. The results obtained in this study showed that the values, k_e, decrease with increasing concentrations for both samples and the k_e values were larger for NTP (Tables 27.4 and 27.5). A decrease in the value of k_e with increasing concentration suggests that both external and intraparticle diffusion reduce the mass transfer rate as concentration increases. The lower k_e values for NTP-NC suggest a stronger influence of external and intraparticle diffusion on mass transfer rate. On the other hand, an increase in the value of k_i with increasing concentration suggests that intraparticle diffusion increases the mass transfer rate as concentration increases. The lower k_i values for NTP-NC suggest a stronger influence of intraparticle diffusion on mass transfer rate for NTP-NC.

27.4 Conclusion

Magnetite coating of pine cone powder has been shown to modify the kinetics, kinetic performance and the mechanism of Cr(VI) adsorption onto its surface. The change in solution hydrogen ion concentration (ΔH^+) and amounts of total Cr, Cr(III) and Cr(VI) left in solution pointed to the fact that the mechanism of Cr(VI) removal was adsorption-coupled reduction which was slightly modified by the presence of magnetite coating. The good fit of the kinetic data to the pseudo-second-order model, pseudo-nth-order model and the external mass transfer suggests that both external mass transfer and surface diffusion played an important role in the adsorption process and their impact was stronger for NTP-NC than for NTP.

References

1. Vithanage M, Rajapaksha AU, Ahmad M, Uchimiya M, Dou X, Alessi DS, Ok YS (2015) Mechanisms of antimony adsorption onto soybean stover-derived biochar in aqueous solutions. J Environ Manage 151:443–449
2. Hu H, Zhang J, Lu K, Tian Y (2015) Characterization of *Acidosasa edulis* shoot shell and its biosorption of copper ions from aqueous solution. J Environ Chem Eng 3:357–364
3. Demirbas A (2005) Adsorption of Cr(III) and Cr(VI) ions from aqueous solution on to modified lignin. Energy Sour 27:1449–1455
4. Rawajfih Z, Nsour N (2008) Thermodynamic analysis of sorption isotherms of chromium(VI) anionic species on reed biomass. J Chem Thermodyn 40:846–851
5. Park D, Ahn CK, Kim YM, Yun Y-S, Park JM (2008) Enhanced abiotic reduction of Cr(VI) in a soil slurry system by natural biomaterial addition. J Hazard Mater 160:422–427
6. Gao H, Liu Y, Zeng G, Xu W, Li T, Xia W (2008) Characterization of Cr(VI) removal from aqueous solutions by a surplus agricultural waste-rice straw. J Hazard Mater 150:446–452
7. Sumathi KMS, Mahimairaja S, Naidu R (2005) Use of low-cost biological wastes and vermiculite for removal of chromium from tannery effluent. Bioresour Technol 96:309–316
8. Miretzky P, Cerelli AF (2010) Cr(VI) and Cr(III) removal from aqueous solution by raw and modified lignocellulosic materials: a review. J Hazard Mater 180:1–9
9. Thinh NN, Hanh PTB, Ha LTT, Anh LN, Hoang TV, Hoang VD, Dang LH, Khoi NV, Lam TD (2013) Magnetic chitosan nanoparticles for removal of Cr(VI) from aqueous solution. Mater Sci Eng 33:1214–1218
10. Safarik I, Horska K, Svobodova B, Safarikava M (2012) Magnetically modified coffee grounds for dyes removal. Eur Food Res Technol 234:345–350
11. Yan H, Yang L, Yang Z, Yang H, Li A, Cheng R (2012) Preparation of chitosan/poly(acrylic acid) magnetic composite microspheres and applications in the removal of copper(II) ions from aqueous solutions. J Hazard Mater 229:371–380
12. Qu Y, Zhang X, Xu J, Zhang W, Guo Y (2014) Removal of hexavalent chromium from wastewater using magnetotactic bacteria. Separ Puri Technol 136:10–17
13. Sun X, Yang L, Li Q, Zhao J, Li X, Wang X, Liu H (2014) Amino-functionalized magnetic cellulose nanocomposite as adsorbent for removal of Cr(VI): synthesis and adsorption studies. Chem Eng J 241:175–183

14. Song Z, Li W, Liu W, Yang Y, Wang N, Wang N, Gao H (2015) Novel magnetic lignin composite sorbent for chromium(VI) adsorption. RSC Adv 5:13028–13935

15. Gupta VK, Nayak A (2012) Cadmium removal and recovery from aqueous solutions by novel adsorbents prepared from orange peel and Fe_3O_4 nanocomposites. Chem Eng J 180:81–90

16. Pirbazari AE, Saberikhah E, Kozani SSH (2014) Fe_3O_4–wheat straw: preparation, characterization and its application for methylene blue adsorption. Wat Res Indust 7:23–27

17. Panneerselvam P, Morad N, Tan KA (2011) Magnetic nanoparticle (Fe_3O_4) impregnated onto tea waste for the removal of nickel(II) from aqueous solution. J Hazard Mater 186:160–168

18. Santra D, Sarkar M (2016) Optimization of process variables and mechanism of arsenic(V) adsorption onto cellulose nanocomposite. J Mol Liq 224:290–302

19. Ghali AE, Marzoug IB, Baouab HMV, Roudesli MS (2012) Separation and characterization of new cellulose fibres from the *Juncus acutus* plant. BioResour 7:2002–2018

20. Can MM, Ozcan S, Ceylan A, Firat T (2010) Effect of milling time on the synthesis of magnetite nanoparticles by wet milling. Mater Sci Eng, B 172:72–75

21. Dorniani D, Kura AU, Hussein MZB, Fakurazi S, Shaari AH, Ahmad Z (2014) Controlled-release formulation of perindopril erbumine loaded PEG-coated magnetite nanoparticles for biomedical applications. J Mater Sci 49:8487–8497

22. Kendelewicz T, Liu P, Doyle CS, Brown GE Jr (2000) Spectroscopic study of the reaction of aqueous Cr(VI) with Fe_3O_4 (111) surfaces. Surf Sci 469:144–163

23. Villacís-García M, Villalobos M, Gutiérrez-Ruiz M (2015) Optimizing the use of natural and synthetic magnetite with very small amounts of coarse Fe(0) particles for reduction of aqueous Cr(VI). J Hazard Mater 281:77–86

24. Peterson ML, White AF, Brown GE, Parks GA (1997) Surface passivation of magnetite by reaction with aqueous Cr(VI): XAFS and TEM results. Environ Sci Technol 31:1573–1576

25. Yu RF, Chi FH, Cheng WP, Chang JC (2014) Application of pH, ORP, and DO monitoring to evaluate chromium(VI) removal from wastewater by the nanoscale zero-valent iron (nZVI) process. Chem Eng J 255:568–576

26. Suksabye P, Nakajima A, Thiravetyan P, Baba Y, Nakbanpote W (2009) Mechanism of Cr(VI) adsorption by coir pith studied by ESR and adsorption kinetic. J Hazard Mater 161:1103–1108

27. Dittert IM, Vilar VJP, da Silva EAB, de Souza SAM, de Souza AAU, Botelho CMS, Boaventura BAR (2012) Adding value to marine macro-algae *Laminaria digitata* through its use in the separation and recovery of trivalent chromium ions from aqueous solution. Chem Eng J 193:348–357

28. Vinodhini V, Nilanjana D (2009) Mechanism of Cr(VI) biosorption by neem sawdust. J Sci Res 4:324–329

29. Barbu M, Stoia M, Stefanescu O, Stefanescu M (2010) Thermal and FT-IR studies on the interaction between $Cr(NO_3)_3 \cdot 9H_2O$ and some diols. Chem Bull "Polltehnica" Uni (Timisoara) 55:180–185

30. Seraj S, Mirzayi B, Nematollahzadeh A (2014) Superparamagnetic maghemite/polyrhodanine core/shell nanoparticles: synthesis and characterization. Adv Powder Technol 25:1520–1526

31. Nematollahzadeh A, Seraj S, Mirzayi B (2015) Catecholamine coated maghemite nanoparticles for the environmental remediation: hexavalent chromium ions removal. Chem Eng J 277:21–29

32. Nazari M, Ghasemi N, Maddah H, Motlagh MM (2014) Synthesis and characterization of maghemite nanopowders by chemical precipitation method. J Nanostruct Chem 4:1–5

33. Muñoz BEL, Robles RR, García JLI, Gutiérrez MTO (2011) Adsorption of basic chromium sulfate used in the tannery industries by calcined hydrotalcite. J Mex Chem Soc 55:137–141

34. Lagergren S (1898) Zurtheorie der sogenannten adsorption gelosterstoffe. Kungliga Svenska Vetenskapsakademiens. Handl Band, 1–39

35. Ho YS (1995) Adsorption of heavy metals from waste streams by peat. Ph.D. Thesis, The University of Birmingham, Birmingham, UK

36. Özer A (2007) Removal of Pb(II) ions from aqueous solutions by sulphuric acid-treated wheat bran. J Hazard Mater 141:753–760

37. Wu FC, Tseng RL, Huang SC, Juang RS (2009) Characteristics of pseudo-second-order kinetic model for liquid-phase adsorption: a mini-review. Chem Eng J 151:1–9

38. Ofomaja AE, Naidoo EB (2011) Biosorption of copper from aqueous solution by chemically activated pine cone: a kinetic study. Chem Eng J 175:260–270
39. Weber WJ Jr, Morris JC (1963) Kinetics of adsorption on carbon from solution. J Sanit Eng ASCE 89:31–59
40. Wilczak A, Keinath TM (1993) Kinetics of sorption and desorption of copper(II) and lead(II) on activated carbon. Wat Environ Res 65:238–244
41. Lo KSL, Leckie JO (1993) Kinetic studies adsorption-desorption of Cd and Zn onto Al_2O_3/solution interface. Wat Sci Technol 28:39–45

Chapter 28
Photocatalytic Degradation of Tetracycline Using C/TiO$_2$ Composites Synthesized *via* Different Hydrothermal Methods

Ekemena O. Oseghe, Titus A. M. Msagati and Augustine E. Ofomaja

Abstract Composite materials consisting of pine cone-derived-carbon and TiO$_2$ were prepared by three different hydrothermal methods [microwave (CT-MW), autoclave (CT-AC), and reflux (CT-R)] and by physical mixing (CT-PM). The purpose of preparing these materials was to evaluate their photocatalytic performance in tetracycline hydrochloride degradation under visible-LED light. The photocatalytic performance of the materials based on their apparent rate constant (K$_{app}$) was in a decreasing order of CT-MW > CT-AC > CT-R > CT-PM. The K$_{app}$ of the materials was observed to be inversely proportional to their electron-hole recombination rate. The composite material prepared by microwave method (CT-MW) apart from its photocatalytic performance, is also more economical, based on the time and simplicity of its preparation.

Keywords C/TiO$_2$ composite · Hydrothermal synthesis · Photocatalytic degradation · Tetracycline hydrochloride · Visible-LED light

28.1 Introduction

Pharmaceuticals meant to be elixirs of life have become harbingers of death. This is because they disrupt the endocrine system, cause drug resistance and are toxic to aquatic lives [1, 2]. Pharmaceuticals are generally used for different purposes by animals and humans [3]. They are most times incompletely metabolized, resulting in either its parent compound or intermediate been excreted into the environment such as

E. O. Oseghe (✉) · A. E. Ofomaja
Chemistry Department, Faculty of Applied and Computer Science, Vaal University of Technology, Vanderbijlpark Campus, Andries Potgieter Boulevard, Vanderbijlpark 1900, South Africa
e-mail: eoseghe@gmail.com

A. E. Ofomaja
e-mail: aus_ofomaja@yahoo.com

E. O. Oseghe · T. A. M. Msagati
Nanotechnology and Water Sustainability Research Unit, College of Science, Engineering and Technology, University of South Africa-Science Campus, Florida 1710, South Africa
e-mail: msagatam@unisa.ac.za

water. This makes them ubiquitous in surface water, some drinking water and ground water [4]. Pharmaceuticals are persistent and bioaccumulate in the environment and hence pose as threats to aquatic lives [5]. Based on their potential to negatively impact humans and the environment, pharmaceuticals are classified as emerging contaminants [6].

Tetracycline as a pharmaceutical has been globally and extensively used, hence its traces and metabolites have been detected in the environment [7, 8]. It accumulates in the environment and can cause adverse effects such as endocrine disruption and antibiotic resistance. Therefore, it is classified as an emerging micropollutant [9].

Titania (TiO$_2$) amongst semiconductor photocatalysts has been considerably applied in the degradation of organic pollutants [10]. However, limitations of wide band gap energy and fast electron-hole recombination rate have encouraged studies on improving its photocatalytic efficiency [11]. One approach adopted over the years to reduce the band gap energy and electron-hole recombination rate of TiO$_2$ has been to dope/load with either metals [12] or non-metals [13]. Carbon has been increasingly investigated in the modification of TiO$_2$. This is because carbon can cause a red shift in the absorbance and as well improve charge separation efficiency of carbon-modified-TiO$_2$ when compared to unmodified TiO$_2$ [14]. Several hydrothermal methods for preparing C/TiO$_2$ composite have been reported. Rangel-Mendez et al. [15] reported a reduced band gap energy and red shift in the absorbance of C/TiO$_2$ synthesized by microwave. Saud et al. [16] also synthesized C/TiO$_2$ *via* the autoclave method and reported an enhanced light absorption, improved charge separation and photocatalytic efficiency. Mu et al. [17] reported an improved photocatalytic activity of TiO$_2$ modified with C$_{60}$ derivative prepared by reflux. While some of the hydrothermal processes are easy, time-saving, and economical, the reverse is the case for others.

To the best of our knowledge the optical properties and photocatalytic efficiency of C/TiO$_2$ synthesized via different hydrothermal methods have not been compared. Therefore, in this study, we prepared composite materials consisting of pine cone-derived-carbon and TiO$_2$ *via* different hydrothermal methods. The synthesized materials were characterized and applied in the degradation of tetracycline hydrochloride (TH) as model pharmaceutical under visible-LED light.

28.2 Experimental

28.2.1 Preparation of Carbon from Pine Cone

Pine cones obtained from Vaal University of Technology, Vanderbijlpark Campus, South Africa were washed, dried at 90 °C for 48 h and pulverized. Approximately 10 g of the ground sample was pyrolyzed intermittently at a microwave power of 1000 W for 1 h in an inert environment. The pyrolyzed sample after cooling was washed with ultra-pure water (3 × 50 mL) and ethanol before drying at 60 °C overnight.

28.2.2 Synthesis of C-TiO$_2$ Composite by Different Methods

Weighed masses (20 mg) of the obtained carbon (C) and 200 mg of commercial TiO$_2$ (≥99%, Sigma Aldrich) were dispersed by sonication in a 15 mL solvent consisting of distilled H$_2$O and ethanol (≥95%, ACE) at 3:2 ratio. The resulting mixture was stirred for 1 h at room temperature and was subjected to refluxing at 120 °C for 24 h. The composite material after cooling was recovered by centrifuging, washed with 2 × 20 mL distilled H$_2$O and 20 mL ethanol and was dried in the oven overnight at 60 °C. The material obtained by this method (reflux) was marked CT-R. The same procedure was followed in preparing other composite materials except that the mixtures after 1 h stirring were microwave treated at 800 W for 5 min (CT-MW), or Teflon-sealed autoclave treated at 140 °C for 4 h (CT-AC). The last composite material marked as CT-PM was prepared by physically mixing 20 mg of C and 200 mg of TiO$_2$.

28.2.3 Characterisations

Shimadzu XRD-7000 X-ray diffractometer with a Cu Kα radiation ($\lambda = 0.15406$ nm) was used to analyze the materials for phase and crystallinity. The morphology of the materials was examined on a JEOL JEM-2010 and ZEISS Ultra/Plus FEG-SEM instrument. Photogenerated electron-hole recombination rate of the materials was analyzed using a Perkin Elmer LS 55 fluorescence spectrophotometer with an excitation wavelength of 310 nm. The surface functional groups and binding energies of the samples were investigated by Fourier transmission infrared (FTIR) spectrometer (PerkinElmer spectrum 100 series attached to a universal ATR accessory) and X-ray photoelectron spectroscopy (Thermo ESCALAB 250Xi) using monochromatic Al Kα (1486.7 eV) source.

28.2.4 Photocatalytic Tests

Catalyst (20 mg) was dispersed in a 200 mL TH solution (5 mg/L) by sonicating for 5 min. The mixture was stirred in the dark for 45 min to attain sorption equilibrium before irradiating (25 W visible-LED light strip) for 2 h. Aliquot of the mixture was sampled after every 20 min, filtered using a 0.45 μm filter, and immediately measured using a T80 + UV-vis spectrophotometer at 360 nm.

28.3   Results and Discussion

The morphology of CT-MW is presented in Fig. 28.1. The TEM (Fig. 28.1a) and SEM (Fig. 28.1b) micrographs show that CT-MW possess particles of different shapes that are aggregated and agglomerated with characteristic interparticle voids. The average particle size as obtained from the SEM micrograph was 47 nm. Figure 28.1c is the energy dispersive X-ray (EDX) spectrum of CT-MW which clearly reveals that it consists of titanium, carbon and oxygen only. SEM, TEM micrographs, and EDX spectra of other materials are presented in Fig. 28.2. All materials showed similar characteristic morphology and elemental composition.

Powder X-ray diffractograms which provide information on crystallite sizes, phases, and percentage composition of the phases of the materials are presented in Fig. 28.3. The materials possess peaks typical for polycrystalline anatase and rutile phase of TiO_2. No peak for carbon was identified in the diffractograms. This might be due to the relatively lower scattering intensity of carbon compared to TiO_2 which is more in terms of percentage composition. Seemingly similar system shows the same trend in the result [18]. However, compared to the pristine TiO_2 (25.74°), the composite materials exhibited a shift in the peaks which is attributed to the presence of carbon. The peaks of the materials shifted in the order of CT-AC > CT-PM > CT-MW > CT-R with corresponding values of 25.45°, 25.32°, 25.27°, 25.21° respectively. Anatase TiO_2 peaks appeared at approximately 25.45°, 37.62°, 38.58°,
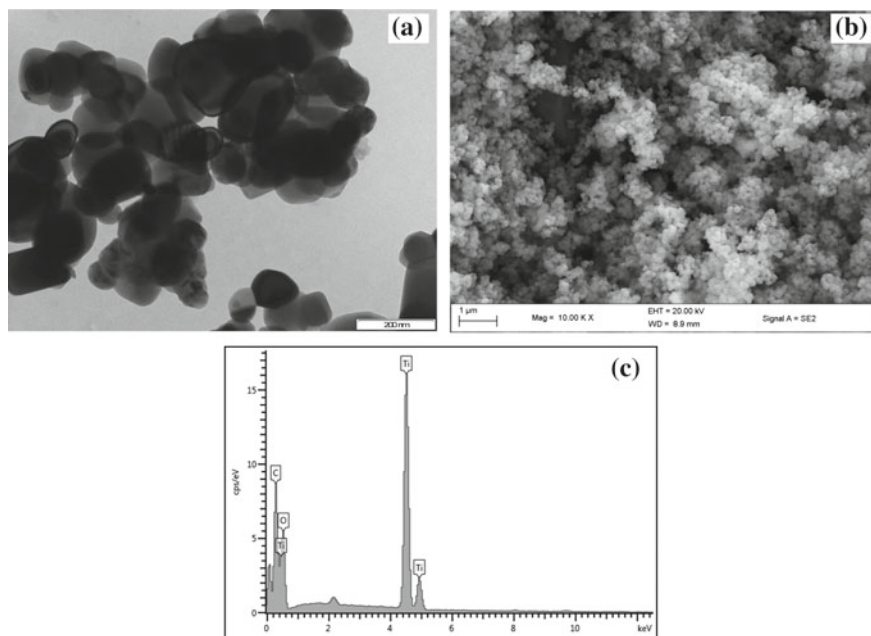

Fig. 28.1 **a** TEM micrograph, **b** SEM micrograph, and **c** EDX spectrum of CT-MW
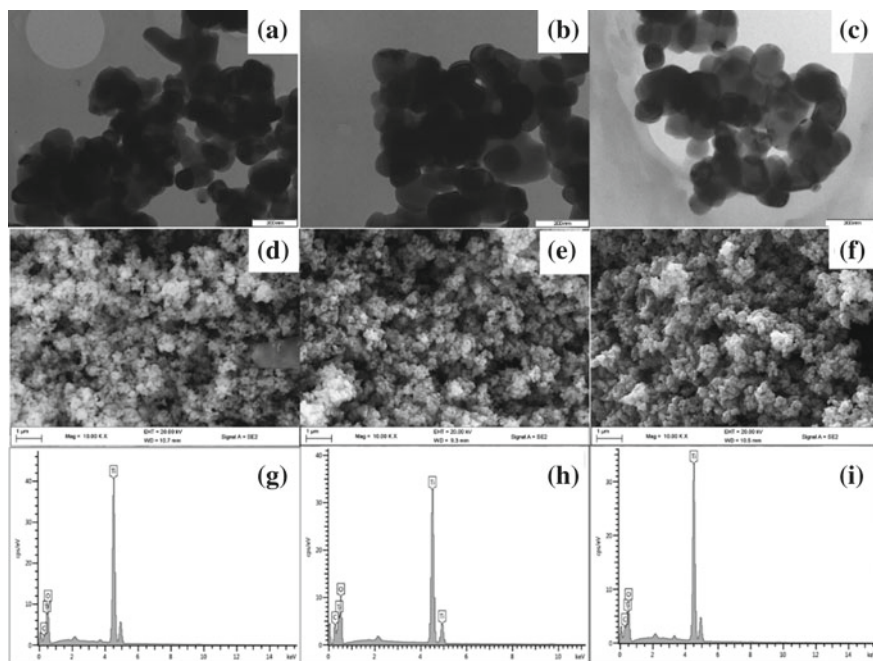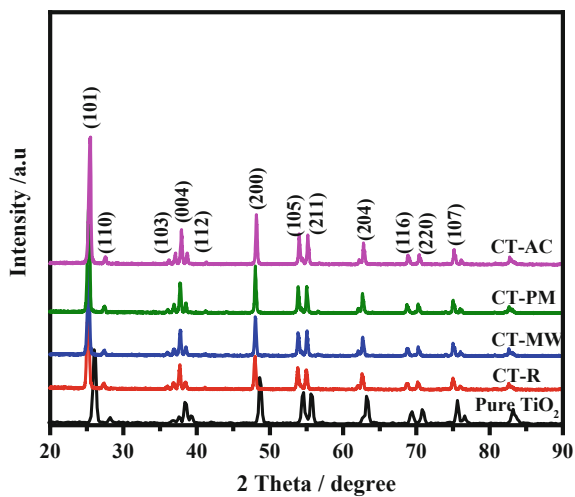
Fig. 28.2 TEM micrograph of **a** CT-AC; **b** CT-R; **c** CT-PM; SEM micrograph of **d** CT-AC; **e** CT-R; **f** CT-PM; EDX spectrum for **g** CT-AC; **h** CT-R; **i** CT-PM

Fig. 28.3 X-ray
diffractograms of the
materials

39.46°, 48.89°, 54.73°, 55.73°, 55.96°, 63.55°, 69.52°, and 75.01° which according to JCPDS 21-1272, corresponds to (101), (103), (004), (112), (200), (105), (211), (204), (116), (220), and (107) reflections respectively. Peak for rutile phase appeared at 27.80° which corresponds to (110) reflection (JCPDS 21-1276). Scherrer's equation (Eq. 28.1) was used to estimate the crystallite sizes, D, for anatase TiO_2 phase.

$$D = \frac{K\lambda}{\beta \cos\theta} \tag{28.1}$$

where $K \approx 0.9$ (Scherrer's constant), $\lambda = 0.15406$ nm (wavelength of the X-ray), β is the full width at half maximum height (FWHM) of the diffraction peaks, and θ is the diffraction angle of the peaks. Values of β and θ were obtained from the anatase (101) reflection. The estimated crystallite sizes for the composite materials synthesized via different routes were 23.31, 22.23, 21.21, and 19.76 nm corresponding to CT-AC, CT-MW, CT-PM, and CT-R respectively. The crystallite size (17.56 nm) of the pristine TiO_2 was found to be lower than the composite materials and therefore corroborates the idea that carbon favours the growth of crystallite size. In order to estimate the percentage of anatase and rutile in the materials Spurr and Myers equation [19] adapted by Fagan et al. [20], was used (Eqs. 28.2 and 28.3).

$$\%rutile = \frac{1}{1 + 0.8[I_A/I_R]} \tag{28.2}$$

$$\%anatase = 100 - \%rutile \tag{28.3}$$

where I_A and I_R represent peak intensities of the anatase (101) and rutile (110) reflections respectively. The differences in the estimated percentage content of anatase and rutile amongst the composite materials were insignificant (Table 28.1). However, CT-MW showed the highest percentage of anatase (94.55%) and the least percentage of rutile phase (5.45%).

The functional groups on the surface of the composite materials were identified by Fourier transform-infrared (FTIR) analysis. Figure 28.4 shows the FTIR spectra of the materials synthesized via different routes. Four distinct bonding peaks appearing around 3304, 1600, 1038 and 953 cm^{-1} were observed. These peaks are ascribed to surface adsorbed OH–, H_2O, C–O, Ti–O bonds respectively. The peak appearing at

Table 28.1 Percentage TiO_2 phase composition of the composite material*s*

Samples	Crystallite phase (%)	
	Anatase	Rutile
CT-MW	94.55	5.45
CT-AC	94.33	5.67
CT-PM	94.24	5.76
CT-R	94.02	5.98

Fig. 28.4 FTIR spectra of
the materials
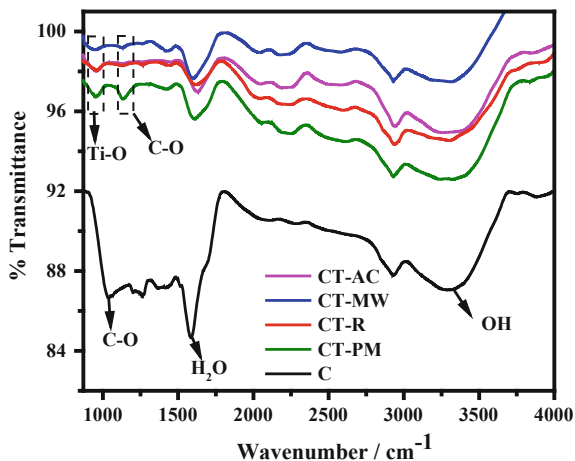
1038 cm^{-1} for the carbonaceous material is ascribed to C–O bonding [21]. This C–O
bonding peak of all the composite materials aside from CT-PM relatively disappeared
suggesting the formation of the Ti–O–C bond. It is therefore logical to infer that no
Ti–O–C bond was formed in the CT-PM because it is a physically mixed composite
material.

Information on the surface chemical composition and binding energies of the
surface elements in all the composite materials was obtained by XPS analysis.
Figure 28.5a shows the survey spectrum of all the materials. Three photoelectron
peaks at approximately 284, 458 and 529 eV corresponding to carbon (C 1s), tita-
nium (Ti 2p) and oxygen (O 1s) respectively were observed. Two obvious peaks
identified at around 458 and 464 eV on the Ti 2p spectrum of Fig. 28.5b are typical
for Ti 2p$_{3/2}$ and Ti 2p$_{1/2}$ of TiO$_2$ respectively. All the composite materials had similar
binding energies.

The splitting between these two peaks for all the composite materials are 5.7 eV
and therefore refers to the normal state of Ti^{4+} in the materials [22]. Figure 28.5c
shows the spectrum of C 1s for all the composite materials after deconvolution. Three
peaks appeared around 284, 286, and 288 eV and correspond to C–C bond with sp^2
orbital, C–O and C=O bonds respectively. These three peaks were observed in all the
composite materials except CT-MW (only two peaks). Figure 28.5d shows the peaks
for the O 1s spectrum at around 529.7 and 531.0 eV for all the materials attributed
to Ti–O and C=O respectively [21, 23]. An extra peak at 530.3 eV may be attributed
to the surface hydroxyl groups (–OH) from the loaded carbon as observed in the O
1s spectrum of CT-MW.

The photocatalytic performance of the materials was evaluated by carrying out
photodegradation experiments of TH solution (5 mg/L) under visible LED light strip.
Figure 28.6a–c show the results of the photodegradation experiments. The result in
Fig. 28.6a shows that after 2 h of the experiment, TH degraded differently in the
presence of each material. The order of performance was CT-PM < CT-R < CT-
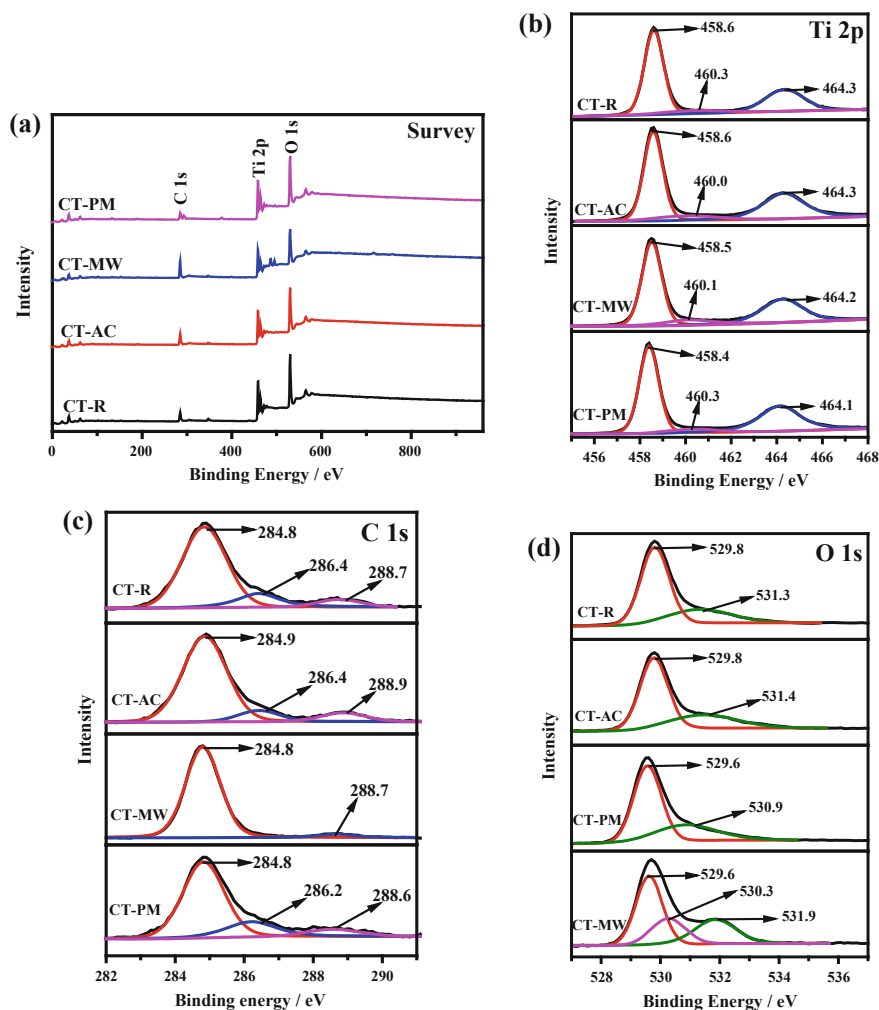
Fig. 28.5 a XPS survey, b Ti 2p, c C 1s, and d O 1s spectra of the materials

MW < CT-AC with a corresponding percentage removal of 44, 50, 52, and 56% respectively. Kinetics study on the photocatalytic performance of the materials was carried by employing the linear pseudo-first order model (Eq. 28.4)

$$Ln\frac{C}{C_O} = K_{app}t \qquad (28.4)$$

where C is the concentration of TH, C_o is the initial TH concentration, K_{app} is the rate constant (min^{-1}), and t is the duration of the photocatalytic experiment [24–26]. Figure 28.6b, c show that results obtained from the photodegradation experiment
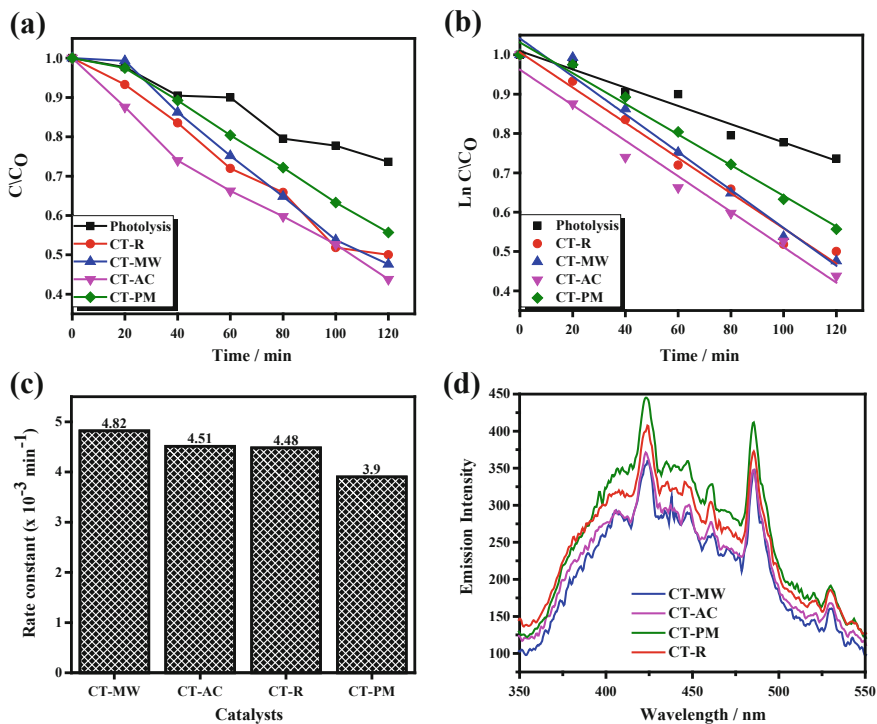
Fig. 28.6 a Photocatalytic degradation, **b** pseudo first order kinetics, **c** apparent rate constant of TH degradation, and **d** photoluminescence spectra of the composite materials

fitted well with the pseudo-first order kinetics. It is interesting to observe that CT-MW exhibited the highest apparent rate constant ($K_{app} = 4.82 \times 10^{-3}$ min^{-1}) compared to CT-AC which had K_{app} of 4.51×10^{-3} min^{-1}.

An inverse proportionality between the K_{app} (Fig. 28.6c) and electron-hole recombination rate (Fig. 28.6d) of the materials was observed. Photoluminescence spectra (PL) are obtained when there is photogenerated electron-hole recombination. The higher the intensity of the PL spectra, the higher the electron-hole recombination rate. The reverse occurs when the intensity of the PL spectra is lower [27]. Carbon in a composite sample of a photocatalyst such as C/TiO$_2$, C/BiOBr is reported to reduce photogenerated electron-hole recombination rate since it acts as electron sink directly or indirectly by promoting the formation of defects (oxygen vacancies) that act as electron sinks [28–30]. TiO$_2$ emission peaks appear at 424–485 nm for self-trapped excitons and 530 nm typical for oxygen vacancy [25, 31]. From Fig. 28.6d, CT-MW has the lowest self-trapped exciton and oxygen vacancy peaks and implies having the least electron-hole recombination rate which was reflected in its photocatalytic performance. This implies that the method of preparing C/TiO$_2$ composite influences its electron-hole recombination and invariably reflected in the photocatalytic performance of the materials.

28.4 Conclusion

In summary, C/TiO_2 was successfully synthesized by different hydrothermal methods. Sample CT-AC had the highest crystallite size of 23.31 nm, while CT-R had the least crystallite size (19.76 nm). Not much difference was observed when the percentage TiO_2 phase of the materials was compared. However, CT-MW exhibited the highest percentage of anatase TiO_2.

All the synthesized composite materials showed variations in electron-hole recombination rate. The differences in their electron-hole recombination rate were reflected in their photodegradation performance (K_{app}). Based on the photocatalytic performance, simplicity, and time of material preparation, C/TiO_2 prepared via microwave in this study is favoured.

References

1. Hassani A, Khataee A, Karaca S (2015) Photocatalytic degradation of ciprofloxacin by synthesized TiO_2 nanoparticles on montmorillonite: effect of operation parameters and artificial neural network modeling. J Mol Catal A Chem 409:149–161
2. Santos LHMLM, Araújo AN, Fachini A, Pena A, Delerue-Matos C, Montenegro MCBSM (2010) Ecotoxicological aspects related to the presence of pharmaceuticals in the aquatic environment. J Hazard Mater 175:45–95
3. Ekpeghere KI, Lee JW, Kim HY, Shin SK, Oh JE (2017) Determination and characterization of pharmaceuticals in sludge from municipal and livestock wastewater treatment plants. Chemosphere 168:1211–1221
4. Ye Z, Weinberg HS, Meyer MT (2007) Trace analysis of trimethoprim and sulfonamide, macrolide, quinolone, and tetracycline antibiotics in chlorinated drinking water using liquid chromatography electrospray tandem mass spectrometry. Anal Chem 79:1135–1144
5. Fathinia M, Khataee K, Naseri A, Aber S (2015) Monitoring simultaneous photocatalytic-ozonation of mixture of pharmaceuticals in the presence of immobilized TiO_2 nanoparticles using MCR-ALS: identification of intermediates and multi-response optimization approach. Spectrochim Acta A Mol Biomol Spectrosc 136:1275–1290
6. Liang R, Luo S, Jing F, Shen L, Qin N, Wu L (2015) A simple strategy for fabrication of Pd@MIL-100(Fe) nanocomposite as a visible-light-driven photocatalyst for the treatment of pharmaceuticals and personal care products (PPCPs). Appl Catal B176–177:240–248
7. Martín J, Santos JL, Aparicio I, Alonso E (2015) Pharmaceutically active compounds in sludge stabilization treatments: anaerobic and aerobic digestion, wastewater stabilization ponds and composting. Sci Total Environ 503–504:97–104
8. Xu Y, Guo C, Luo Y, Lv J, Zhang Y, Lin H, Wang L, Xu J (2016) Occurrence and distribution of antibiotics, antibiotic resistance genes in the urban rivers in Beijing, China. Environ Pollut 213:833–840
9. Zhou Y, Yang Q, Zhang D, Gan N, Li Q, Cuan J (2018) Detection and removal of antibiotic tetracycline in water with a highly stable luminescent MOF. Sens Actuators B Chem 262:137–143

10. Fujishima A, Zhang X, Tryk DA (2008) TiO$_2$ photocatalysis and related surface phenomena. Surf Sci Rep 63:515–582
11. Daghrir R, Drogui P, Robert D (2013) Modified TiO$_2$ for environmental photocatalytic applications: a review. Ind Eng Chem Res 52:3581–3599
12. Oseghe EO, Ndungu PG, Jonnalagadda SB (2015) Synthesis of mesoporous Mn/TiO$_2$ nanocomposites and investigating the photocatalytic properties in aqueous systems. Environ Sci Pollut Res 22:211–222
13. Huang WC, Ting JM (2017) Novel nitrogen-doped anatase TiO$_2$ mesoporous bead photocatalysts for enhanced visible light response. Ceram Int 43:9992–9997
14. Bello A, Manyala N, Barzegar F, Khaleed AA, Momodu DY, Dangbegnon JK (2016) Renewable pine cone biomass derived carbon materials for supercapacitor application. RSC Adv 6:1800–1809
15. Rangel-Mendez JR, Matos J, Cházaro-Ruiz LF, González-Castillo AC, Barrios-Yáñez G (2018) Microwave-assisted synthesis of C-doped TiO$_2$ and ZnO hybrid nanostructured materials as quantum-dots sensitized solar cells. Appl Surf Sci 434:744–755
16. Saud PS, Pant B, Alam AM, Ghouri ZK, Park M, Kim HY (2015) Carbon quantum dots anchored TiO$_2$ nanofibers: Effective photocatalyst for waste water treatment. Ceram Int 41:11953–11959
17. Mu S, Long Y, Kang SZ, Mu J (2010) Surface modification of TiO$_2$ nanoparticles with a C60 derivative and enhanced photocatalytic activity for the reduction of aqueous Cr(VI) ions. Catal Commun 11:741–744
18. Cheng G, Xu F, Xiong J, Tian F, Ding J, Stadler FJ, Chen R (2016) Enhanced adsorption and photocatalysis capability of generally synthesized TiO$_2$-carbon materials hybrids. Adv Powder Technol 27:1949–1962
19. Spurr RA, Myers H (1957) Quantitative analysis of anatase-rutile mixtures with an X-ray diffractometer. Anal Chem 29:760–762
20. Fagan R, McCormack DE, Hinder S, Pillai SC (2016) Improved high temperature stability of anatase TiO$_2$ photocatalysts by N, F, P co-doping. Mater Des 96:44–53
21. Zhang J, Zhang X, Dong S, Zhou X, Dong S (2016) N-doped carbon quantum dots/TiO$_2$ hybrid composites with enhanced visible light driven photocatalytic activity toward dye wastewater degradation and mechanism insight. J Photochem Photobiol A 325:104–110
22. Akhavan O, Ghaderi E (2009) Photocatalytic reduction of graphene oxide nanosheets on TiO$_2$ thin film for photoinactivation of bacteria in solar light irradiation. J Phys Chem C 113:20214–20220
23. Cong Y, Li X, Qin Y, Dong Z, Yuan G, Cui Z, Lai X (2011) Carbon-doped TiO$_2$ coating on multiwalled carbon nanotubes with higher visible light photocatalytic activity. Appl Catal B 107:128–134
24. Li S, Cai J, Wu X, Zheng F, Lin X, Liang W, Chen J, Zheng J, Lai Z, Chen T et al (2014) Fabrication of positively and negatively charged, double-shelled, nanostructured hollow spheres for photodegradation of cationic and anionic aromatic pollutants under sunlight irradiation. Appl Catal B160:279–285
25. Teng F, Zhang G, Wang Y, Gao C, Chen L, Zhang P, Zhang Z, Xie E (2014) The role of carbon in the photocatalytic reaction of carbon/TiO$_2$ photocatalysts. Appl Surf Sci 320:703–709
26. Haroune L, Salaun M, Ménard A, Legault CY, Bellenger JP (2014) Photocatalytic degradation of carbamazepine and three derivatives using TiO$_2$ and ZnO: effect of pH, ionic strength, and natural organic matter. Sci Total Environ 475:16–22
27. Parayil SK, Kibombo HS, Wu CM, Peng R, Baltrusaitis J, Koodali RT (2012) Enhanced photocatalytic water splitting activity of carbon-modified TiO$_2$ composite materials synthesized by a green synthetic approach. Int J Hydrogen Energy 37:8257–8267
28. Parayil SK, Kibombo HS, Koodali RT (2013) Naphthalene derivatized TiO$_2$–carbon hybrid materials for efficient photocatalytic splitting of water. Catal Today 199:8–14
29. Shao P, Tian J, Zhao Z, Shi W, Gao S, Cui F (2015) Amorphous TiO$_2$ doped with carbon for visible light photodegradation of rhodamine B and 4-chlorophenol. Appl Surf Sci 324:35–43

30. Zhao C, Li W, Liang Y, Tian Y, Zhang Q (2016) Synthesis of BiOBr/carbon quantum dots microspheres with enhanced photoactivity and photostability under visible light irradiation. Appl Catal A 527:127–136
31. Tripathi AK, Singh MK, Mathpal MC, Mishra SK, Agarwal A (2013) Study of structural transformation in TiO_2 nanoparticles and its optical properties. J Alloys Compd 549:114–120

Chapter 29
Antiulcer and Cluster of Differentiation-31 Properties of *Cucumis melo* L. on Indomethacin-Induced Gastric Ulceration in Male Wistar Rats

G. I. Adebayo-Gege, Bamidele J. Okoli, P. O. Oluwayinka, A. F. Ajayi and Mtunzi Fanyana

Abstract Non-steroidal anti-inflammatory drugs (NSAIDs) usage has contributed to the increase in morbidity and mortality rate in the population with peptic ulcer disease and has led to the search of other means of treatment especially using dietary substances as preventive measures. Our study, therefore, investigated the effect of *Cucumis melo* aqueous extract on the indomethacin-induced gastric ulcer and the role of the cluster of differentiation 31 (CD31) in angiogenic response in male Wistar rats. Thirty male Wistar rats (130 ± 20 g) were divided into six groups (n = 5), viz Group I (control), II (ulcer untreated), and III-VI (ulcer and treated with 25, 50,

G. I. Adebayo-Gege
Department of Physiology, Faculty of Basic Medical Sciences, Bingham University, New Karu, Nasarawa State, Nigeria
e-mail: funbimbola@gmail.com

Gastrointestinal Tract Secretion and Inflammation Units, Department of Physiology, Faculty of Basic Medical Sciences, College of Medicine, University of Ibadan, Ibadan, Nigeria

B. J. Okoli (✉)
Institute of Chemical and Biotechnology and Department of Chemistry, Vaal University of Technology, Southern Gauteng Science and Technology Park, Private Bag X021, Vanderbijlpark, Sebokeng, South Africa
e-mail: okolibj@binghamuni.edu.ng

P. O. Oluwayinka
Department of Anatomy, Faculty of Basic Medical Sciences, Bingham University, New Karu, Nasarawa State, Nigeria
e-mail: oluwadele@yahoo.com

A. F. Ajayi
Department of Physiology, Faculty of Basic Medical Sciences, Ladoke Akintola University of Technology, Ogbomoso, Nigeria
e-mail: aajayi22@lautech.edu.ng

M. Fanyana
Institute of Traditional Knowledge and Traditional Medicine, Dihlare Remedy, Vaal University of Technology, Southern Gauteng Science and Technology Park , Sebokeng, South Africa
e-mail: fanyana@vut.ac.za

501

75 and 100% *C. melo* aqueous extract for two weeks). Animals were examined for gastric acid secretion by titrimetric method, and the ulcer was measured. Histological analysis and immunohistochemistry staining for expression of CD31 were carried out. Total gastric acidity was significantly decreased in the groups IV-VI (2.10 ± 0.18–1.03 ± 0.08 mEq/L compared to groups II (3.65 ± 0.15 mEq/L) and III (2.95 ± 0.27 mEq/L), $p < 0.05$. However, no significant difference in total gastric acidity in groups IV-VI compared to group I (1.04 ± 1.03 mEq/L) was observed. The ulcer score was significantly decreased in the groups IV-VI compared to groups II and III, and the incidence of ulcer was inhibited by 8.62, 47.59, 54.01, and 73.06% in groups III, IV, V and VI, respectively. Histological assessment revealed a moderate to mild ulceration in the gastric mucosa with few numbers of inflammatory cells in all groups pre-treated with *C. melo* extract. Immunohistochemical localisation of CD31 nuclei in the gastric mucosa cells was significantly decreased in the group II with an expression of 6.0% compared to group I (17.0%) and all the pre-treated groups with the extract (14.0–29.7%). In conclusion, antisecretory properties of *C. melo* extract at different concentrations were responsible for its anti-ulcer activity and accelerated healing of gastric ulcer via angiogenic activities.

Keywords *Cucumis melo* · *ad labtium* · Gastric acidity · Histological assay · Inflammatory · Immunohistochemistry · Ulcer score

29.1 Introduction

The prevalence of NSAID-mediated gastrointestinal disorder has become a great concern to scientists and the public at large. There are several mechanisms involved in the mediation of non-steroidal anti-inflammatory drugs (NSAIDs), which include gastric mucosal integrity, cellular spawning and migration at the ulcer edge, and development of granulation tissue at the ulcer base, eventually leading to ulcer healing [1, 2]. Hence, the use of NSAIDs has become valuable therapeutic agents in the treatment of arthritic conditions with increasing prevalence or formation of gastro-duodenal ulcer [1, 3].

The process of angiogenesis plays unique roles in the formation of new blood vessels, an essential component of granulation tissue maturation and wound healing. It has been noted that to determine drugs that are potent in treatment against NSAIDs assaults on the GIT, it must also exhibit or mediate angiogenic response [1]. There are several synthetic anti-ulcer drugs for the treatment of NSAIDs induced ulcer; however, they are costly and have serious side effects. Hence, the need for formulation of dietary sources is imperative in the treatment of ulceration with less or no side effect and less expensive.

Studies have shown over many decades that natural products from either animal or plant sources are used for the treatment of gastrointestinal disorders [4]. Numbers of plants-derived drugs are being used for prevention or treatment of GIT disorders ranging from acute to chronic diseases. So many plants classified as fruits possess

high vitamins, minerals, fibre, phytochemicals and antioxidants in their pulps, seeds and rinds, yet were not given much attention in the diets of individuals especially in Nigeria [5]. Their nutritive values and therapeutic potential were ignored, hence are discarded or seen as unimportant [6].

Several plants belonging to the family of *Cucurbitaceae* have been found to possess an excellent deal of anti-inflammatory, antioxidant, wound healing properties, for instance, luffa and cucumbers in different organic extracts have shown marked anti-ulcer properties [7]. *Cucumis melo* L. belongs to the *Cucurbitaceae* family. The ripe oval-shaped creamy yellowish fruit is delicious with a distinct aroma and a good source of pro-vitamin A, riboflavin, thiamine, folic acid and vitamin C [8–10]. Phytochemical screening of the seeds of *C. melo* reveals the presence of biologically active metabolites such as chromone derivatives, glycosides, triterpenoids, and other flavonoids [11–13]. The active principles in these extracts are principally antioxidant prophylactic agents for both health and disease management [14], while the seeds have lithotripsy, laxative, demulcent and cooling properties. In folk medicine, kernel from the seed was used in the treatment of chronic eczema, renal disorders, painful and burning micturition, ulcers in the urinary tract, jaundice, helminthic, cardiovascular diseases, and tussive emesis [15–18]. Furthermore, the plant has been reported with strong antiulcer activities, due to its antioxidant potential [19], and anti-hyperlipidemic activity in triton induced hyperlipidemia was reported in rats as equipotent [20]. Earlier studies on the *Cucurbitaceae* family showed that *C. melo* pulp extract possesses anti-diabetic properties on streptozotocin induced diabetic rats [21]. Adekunle and Oluwo reported the anti-fungal potency of *C. melo* on *Aspergillus* species, *Mucor* species, *Phycomyces* species and *Rhizopus* species [22]. Our study is focused on investigating the anti-ulcer potential of *C. melo* with particular emphasis on angiogenesis modulation by the expression cluster of differentiation 31 (CD31) during the healing of indomethacin-induced gastric ulcer in male Wistar rats.

29.2 Materials and Methods

29.2.1 Chemicals and Reagents

Indomethacin (Medrel pharmaceuticals, India), buffered 10% formal saline solution, 0.9% saline solution, Na_2CO_3, phenolphthalein reagent, 0.1 N NaOH, and CD31 endothelial marker NCL-END (Novacastro laboratories, UK).

29.2.2 Preparation of C. melo Aqueous Extract

C. melo fruits were washed to remove dirt, then the thin yellow outermost pericarp and the almost white fleshy mesocarp were cut into smaller pieces, and the seeds

were removed. The pericarp and mesocarp were blended and filtered with a clean sifter to separate the juice from the solid particles. The concentrated juice was diluted with distilled H_2O to give 75, 50, and 25% v/v solutions. Fresh preparations were made daily.

29.2.3 Indomethacin-Induced Ulcer

The animals were pre-treated with different aqueous extract concentrations of *C. melo* for two weeks. Prior to ulceration by oral gavage with 40 mg/kg body weight of indomethacin, the animals were fasted for 24 h.

29.2.4 Experimental Animals and Design

Thirty male albino rats of Wistar strain (weighing 130 ± 20 g) were obtained from the National Veterinary Research Institute, Vom, Jos, Nigeria. They were housed in the Central animal facility of the Faculty of Basic Medical Sciences, Bingham University to acclimatise for two weeks, fed with standard feed and water *ad labtium*. They were maintained under standard laboratory conditions and were fed with commercially formulated rat pellets and distilled water. After the acclimatisation period, the thirty male Wistar strain rats were divided into six experimental groups (n = 5), viz. Group I-control, II-ulcer untreated (indomethacin-induced gastric ulcer, INDo), III-VI were treated with 25, 50, 75, and 100% *C. melo* aqueous extract for two weeks prior to gastric ulcer induction, respectively. Figure 29.1 is a graphical summary of the experimental design.

29.2.5 Acute Toxicity Test

On the day of treatment, the animals were fasted overnight. Group I (control) received sterile water, given orally. Experimental groups (III-VI) were orally treated with *C. melo* aqueous extract at single doses of 25, 50, 75 and 100%, respectively. Animals were observed individually for general behavioural and body weight changes, toxic symptoms, and mortality during the first 30 min, periodically during the first 24 h, and at daily intervals thereafter for a total of 14 days. At the end of 14 days study period, all surviving rats were anesthetized and acute toxicity values (LD_{50}) were estimated [23, 24].
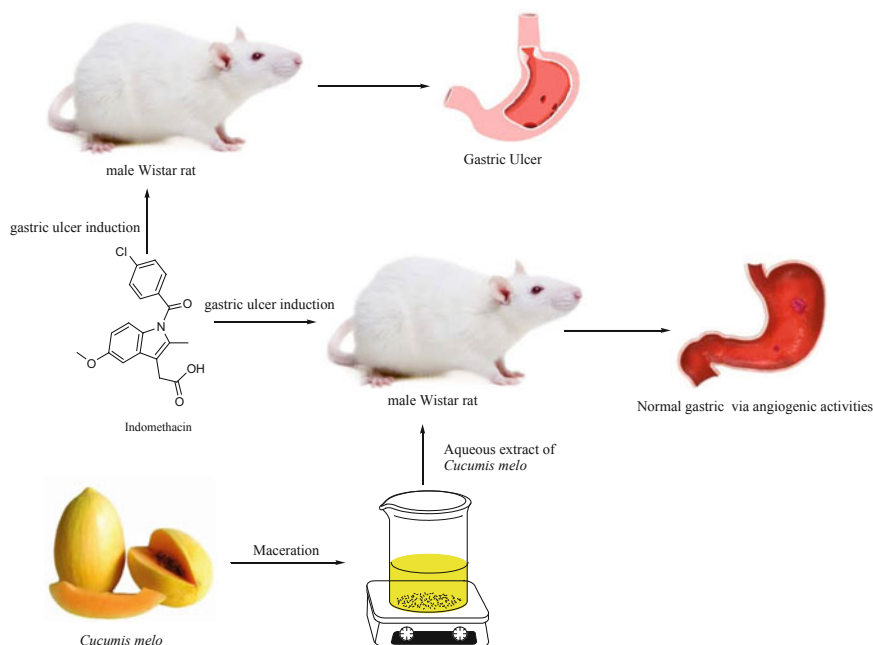
Fig. 29.1 Graphical summary of experimental design

29.2.6 Relative Organ Weight

On day 14 of treatment, all surviving rats were anesthetized and carefully dissected out and the absolute weight of the stomach was recorded. The relative stomach weight of each surviving Wistar rat was then calculated as in Eq. (29.1) [25]:

$$\text{Relative stomach weight} = \left(\frac{\text{Absolute stomach weight (g)}}{\text{Body weight of rat on sacrifice day (g)}}\right)100 \quad (29.1)$$

29.2.7 Estimation of Total Acidity

In a 25 ml conical flask containing 0.5 ml gastric juice, 2 drops of phenolphthalein solution were added and titrated with 0.01 N NaOH until the appearance of purple colour. The volume of NaOH consumed was also recorded and the total acidity was calculated by using Eq. (29.2) below:

$$\text{Acidity} = \left(\frac{\text{Volume of NaOH} \times \text{Normality of NaOH}}{0.1}\right)\text{mEq/L/100 g} \quad (29.2)$$

Table 29.1 Gastric lesions rating criteria

Gastric lesions	Criteria
Normal stomach	0.0
Punctuate hemorrhage or pinpoint ulcer	0.5
Two to more small hemorrhagic ulcers	1.0
Ulcers greater than 3 mm in diameter	3.0

29.2.8 Estimation of the Gastric Ulcer Scoring, Ulcer Index, and Percentage Inhibition

After 4 h of gastric ulcer induction, the animals were sacrificed under anesthesia while the stomachs were dissected along the greater curvature and washed with normal saline. Gastric ulcer scoring was carried out by estimating the gastric lesions formed based on the criteria of Alphin and Ward [26] (Table 29.1).

The ulcer index and percentage inhibition were calculated according to Eqs. (29.3) and (29.4), respectively.

$$UI = UN + US + UP \times 10^{-1} \tag{29.3}$$

where, UI, UN, US and UP are the ulcer index, mean number of ulcers per rat, mean severity score, and percentage of rat with ulcer, respectively.

$$Percentage\ inhibition = \left(\frac{\text{Ul control} - \text{U1 Pretreated}}{\text{U1 control}} \right) 100 \tag{29.4}$$

29.2.9 Histological Assay

The excised stomachs were washed in cold saline, fixed in 10% formalin overnight and processed for routine paraffin embedding. Thereafter, stomach was 5 μm sectioned, mounted on the slide, deparaffinised, rehydrated and stained with hematoxylin and eosin (H and E). The stomach sections were viewed under a light microscope (Olympus XSZ-107BN) at $100\times$ magnification.

29.2.10 Immunohistochemistry

Selective imaging antigen study was done through the use of Avidin-biotin-peroxidase complex (ABC) technique proposed by Hsu et al. [27]. Antigen was masked during fixing and embedding procedures were unmasked by heat and treat-

ment with 3,3′-diaminobenzidine solutions, followed by complexation of the primary antibodies to a specific binding protein. Visualization of CD31 was done using a second step biotinylated antibody, followed by amplification with streptavidin-horseradish peroxidase which converts the substrate diaminobenzidine into a brown coloured precipitate at the site of reaction which was observed as the positive reaction.

29.2.11 Evaluation of Immunohistochemistry Results

The expression of CD31 proteins, the intensity of staining and quantity of the stained cells were evaluated in proportion to the ulcerated areas. Brown staining of the cytoplasm and nucleus of cells were viewed under $40\times$ magnification. Area of expressions was quantified with immunohistochemistry image analysis toolbox (Image J) [28].

29.2.12 Statistical Analysis

The results were expressed as mean $\pm$ SEM, ANOVA was employed to compare differences among variables. *P*-value was set at 0.05 to determine the level of significance.

29.3 Results and Discussion

The world's leading gastrointestinal disorder is both gastric and duodenal ulcers, with about 10% of the world's population affected [29]. The physiopathology of ulcer disease is attributed to factors such as helicobacter infection, and generally the mucosa defences [30]. Endogenous gastroprotective factors like nitric oxide (NO) and prostaglandins (PGs), have been considered important regulators of blood flow and mucus secretion [31, 32]. Damage caused by NSAIDs such as indomethacin is said to be mediated via suppression of synthesis of gastric prostaglandins, and increase in gastric acid secretion in animals and humans [33].

29.3.1 Effect of Aqueous Extract of C. melo on Relative Organ Weight

In Fig. 29.2, the results on the effect of *C. melo* aqueous extract on the relative stomach weight of the rats induced with ulcer were presented. There was a significant increase
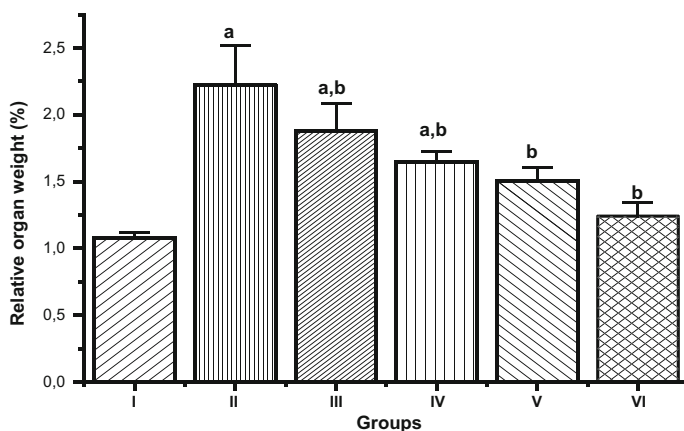
Fig. 29.2 Effect of *C. melo* aqueous extract on the relative stomach weight of the ulcer induced rats, $p < 0.05$. All values are expressed as mean $\pm$ SEM

in the relative stomach weight of the ulcer induced rats compared to the control, $p < 0.05$.

However, a significant decrease in relative stomach weight of all the rats treated with the *C. melo* extract was observed compared with the indomethacin-induced group. Consequently, an increase in extract dose results in a decrease in the relative organ weight. It has been suggested from previous experiments in our laboratory that alteration of the cyto-architecture of gastric mucosa increased intensive mucosal edema, inflammation and ulceration via increase in the relative stomach weight and treatment with *C. melo* decreased the relative weight.

29.3.2 Acute Toxicity Studies

The administration of *C. melo* aqueous extract at different doses to the animals revealed no significant behavioural changes such as weakness and sluggishness in the animals, nor mortality at the doses administered. Therefore, oral LD_{50} was not determined because mortality was not observed.

29.3.3 Effect of **C. melo** Aqueous Extract on Total Gastric Acidity

The activity of the extract on total gastric acidity of the animals induced with ulcer is shown in Fig. 29.3. There was a significant increase in the total gastric acidity of group II, on extract administration there was a significant decrease in the total

Fig. 29.3 Effect of the *C. melo* aqueous extract on the total gastric acidity of the animals induced with ulcer, $p < 0.05$. All values are expressed as mean ± SEM
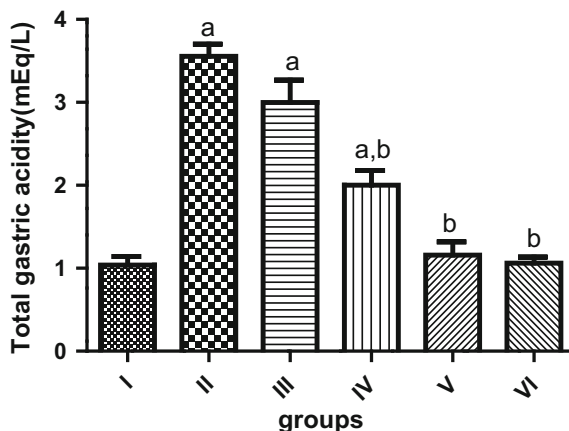
gastric acidity for groups IV, V and VI compared with group II, $p < 0.05$. However, no significant difference was observed between groups II and III, as well as between groups V, VI and I; but there was a significant increase in groups II-IV compared with group I.

Studies have shown that analysis of the gastric acidity and mucosal integrity is used to confirm the status of the stomach following exposure to pharmacological agents [34]. The increase in total gastric acidity has been linked to increased hydrogen ion concentration in gastric juice, and this is a primary cause of ulcer or gastric damage [35]. Gastric injury is however attributed to erosion of mucin content which is evident by reduction in defensive factors such as reduced mucus secretion, reduced blood flow and ulceration facilitated by increased external aggressive agents (drugs, chemicals) which enhance the aggressive internal factors on mucosal epithelial cells [34, 36].

Increase in total gastric acidity with an increase in the relative weight of the stomach following treatment with indomethacin indicates a significant alteration in the balance of both aggressive and defensive factors all resulting in tissue damage (Fig. 29.2), since endogenous prostaglandins have long been implicated in the inhibitory regulation of gastric acid secretion [33].

This however indicated altered hydrophobicity and reduced protective ability of mucosal membrane against indomethacin-induced ulceration.

29.3.4 Effect of the **C. melo** *Aqueous Extract on the Ulcer Score, Index and Percentage Inhibition*

The ulcer score in the animals with induced indomethacin ulceration (group II) was significantly high compared with the control (group I). Administration of different concentrations of the extract significantly decreases the ulcer score towards control,

Table 29.2 Effect of *C. melo* aqueous extract on ulcer score, index and percentage inhibition of animals

Groups	Ulcer score	Ulcer index	Percentage inhibition
I (control, distilled water)	0.00 ± 0.00	–	–
II (40 mg/kg INDo, b.w.)	5.80 ± 0.12	1.45 ± 0.03	–
III (25% *C. melo* + INDo)	5.30 ± 0.29	1.33 ± 0.07	8.62
IV (50% *C. melo* + INDo)	3.04 ± 0.14	0.80 ± 0.04	47.59
V (75% *C. melo* + INDo)	2.68 ± 0.07	0.67 ± 0.02	54.01
VI (100% *C. melo* + INDo)	1.68 ± 0.09	0.39 ± 0.04	73.06

compared with group II, $p < 0.05$. In group III, no significant difference in the ulcer score compared with group II was observed as shown in Table 29.2.

From Table 29.2, the ulcer index decreases significantly in groups IV, V, VI compared with groups II and III, $p < 0.05$. The percentage inhibition was significantly increased in group VI. The incidence of ulcer was prevented on a dose-dependent pattern.

The gastric ulcer score and ulcer index also revealed the inability of gastric mucosal to withstand the hemorrhagic erosion of the indomethacin (Table 29.2). This is in line with the reports of Beck et al., Chattopadhyay et al., and Muhammed et al., where indomethacin was reported to have caused alterations in gastric secretions of rats [36–38]. Treatment with different concentrations of extract decreased the total gastric acidity and relative weight of the stomach, gastric ulcer score and index. From the results, it showed a dose-dependent treatment as 100% of *C. melo* caused more decrease in relative weight of stomach, gastric acidity and ulcer score compared with both groups I and II, suggestive of their possible gastroprotective attributes. Extracts of *C. melo* increased the percentage inhibition, which is consistent with its ability to protect the gastric ulceration by indomethacin. There was an increasing percentage of inhibition at the highest dose.

29.3.5 Histological Studies

The photomicrographs of rat stomachs after ulceration and treatment with *C. melo* aqueous extract viewed at $100\times$ magnification are presented in Plate 29.1. A significant decrease in the ulceration of the gastric mucosa of the stomachs of the animals treated with different doses of the extract was observed. Administration of 100% *C. melo* extract significantly decreased the ulcer formation compared with all groups. The H and E stains show a mild and moderate erosion of mucosa of the stomach, with
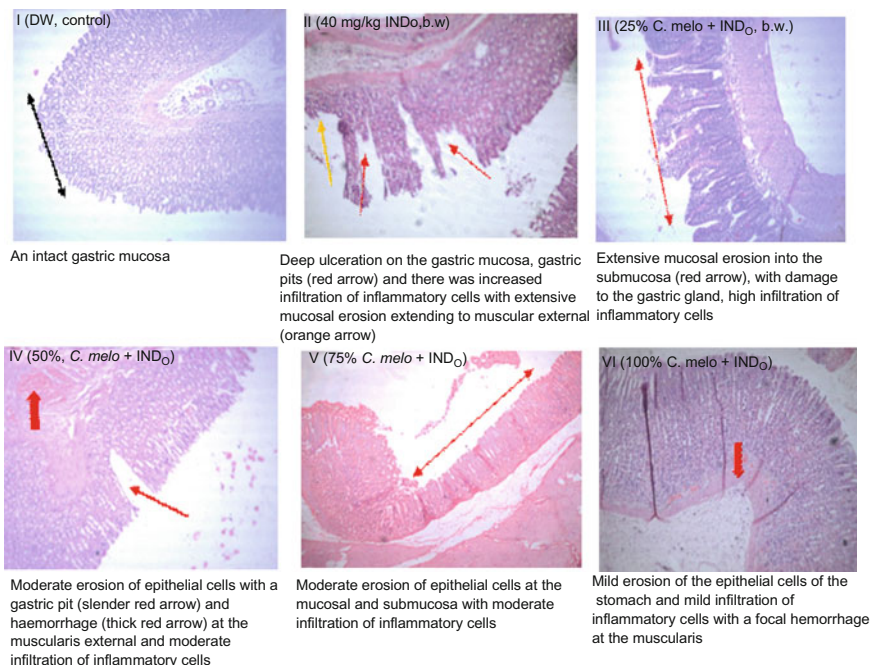
Plate 29.1 Photomicrographs of rat stomachs after indomethacin-induced gastric ulceration and treatments with *C. melo* aqueous extract $100\times$ magnification

moderate or few infiltrations of inflammatory cells in all the treated groups compared with I (control) and II (indomethacin-induced gastric ulcer group).

Evidence from the histological studies in the indomethacin-treated group showed a deep ulceration extending to muscular mucosa with severe infiltration of inflammatory cells, hence confirming severe erosion on the stomach tissue (Plate 29.1) in group II. Pre-treatment with the extract showed a moderate to mild erosion at the epithelial layer, with moderate to mild infiltration of inflammatory cells at a dose-dependent concentration. It is observed that increase in concentration of *C. melo* extract from 25 to 100% reduced ulcer formation from moderate to mild.

29.3.6   Immunohistochemical Localisation of CD31 Nuclei

Plate 29.2 shows the effect of the aqueous extract on indomethacin-induced ulceration on the immunohistochemical localisation of CD31. From this study, immunohistochemical localisation of CD31 in group I indicates a mild percentage expression of 17.0% and the percentage significantly decreased to 6.0% in group II, $p < 0.05$. However, in groups III-VI, there was a significant increase in percentage expression (19.9, 19.7, 29.7%) compared with groups I, II and III, $p < 0.05$.

(a)

(b)

(c)

(d)

(e)

(f)
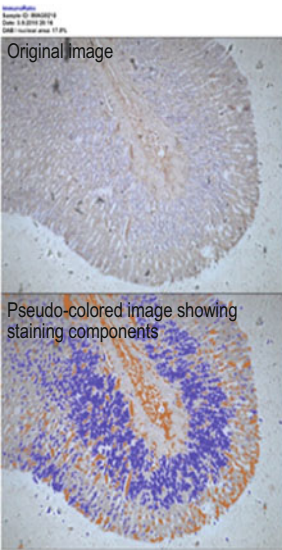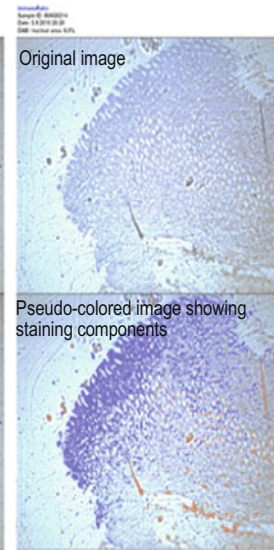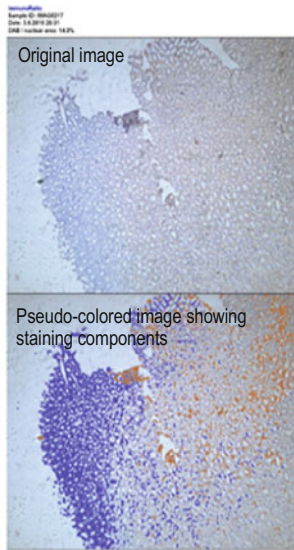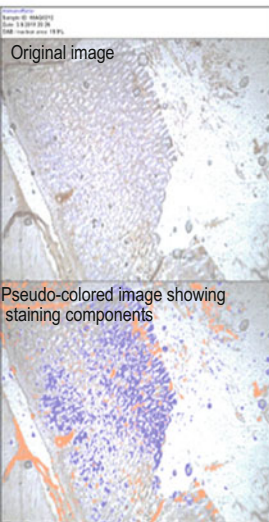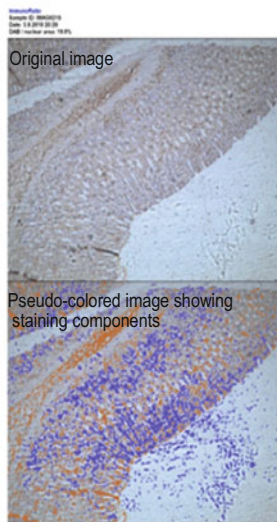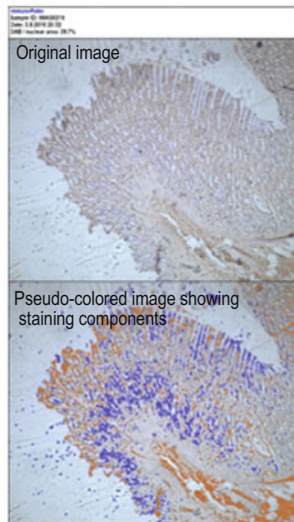
Effect of *C. melo* aqueous extract on indomethacin-induced ulceration. Original image: *Photomicrograph of immunostained tissue with the expression of CD31*, pseudo-coloured image: *percentage of positively stained nuclear area (labeling index) using colour deconvolution algorithms separating stains; brown colour indicates localisation of CD31 expression while blue stains indicate the area of no expression.* **a** Group I (control), immunohistochemical localisation of CD31 in normal control with mild staining. Percentage expression is about 17.0%. **b** Group II (IND$_O$), mild positively stained CD31 significantly decreased compared with control both in number and intensity of expression (about 6.0%). **c** Group III (25% *C. melo* + INDo) shows a significant increase compared with groups I and II, moderate expression of about 14.0%. **d** Group IV (50% *C. melo* + INDo) and **e** Group V (75% *C. melo* + INDo) showed significant expression of CD31 of about 19.9 and 19.7%, respectively compared with I, II and III. **f** Group VI (100% *C. melo* + INDo) expression is about 29.7%, a significant increase compared with all groups, $p < 0.05$

Combination of events which are genetically cell repair process including release of preformed mucus, reduced gastric acidity, wound retraction re-epithelialization, angiogenesis, and tissue remodeling has been implicated in ulcer-healing process after toxicological injury [39]. Apart from the neutralization of luminal acid, the protective factors also offer protection against both endogenous aggressors and exogenous gastro-toxic agents such as indomethacin, thereby enhancing the rate of local healing process [40].

The process of angiogenesis is a re-growth of blood vessels into the ulcerated area, i.e. essential for healing to take place as the increased flow of nutrients and oxygen to the ulcerated or breached tissue accelerates the healing [41]. This initial step is of utmost importance for healing to occur. The CD31 is a protein molecule which is essential for leucocyte migration, angiogenesis and integrin activation [42]. Clinics and laboratories data have shown that NSAIDS induce gastric ulcer as well as inhibit the process of gastroduodenal ulcers altering essential growth factors, decreasing endothelium ontogenesis and angiogenesis in the ulcer bed [43]. Angiogenesis involves a mutual reciprocation of cellular systems and is crucial in external and internal wound healing process [44]. New blood vessels formation is modulated by fibroblast growth factor and CD31 (proangiogenic factors), as well as endostatin (antiangiogenic factor). Disequilibrium production of the antiangiogenic versus proangiogenic factors could impair angiogenesis and wound healing process [45].

Reports have shown that CD31 is recently recognized for its angiogenic role as well as mediating endothelial cell migration in vitro [46]. Treatment with *C. melo* extract gave the highest expression of CD31 on gastric mucosa of the stomach at a dose of 100%. This indicates that the molecular process of ulcer healing by the extractis via angiogenesis and this could be responsible for faster healing activity observed in all the groups treated. However, it should be noted that angiogenesis is critical for the improvement of gastric mucosa and prevention of ulcer relapse.

29.4 Conclusion

In conclusion from our findings, we presume that the antisecretory properties of *C. melo* in different concentrations were responsible for the anti-ulcer activity. The observed suggestive mechanism by *C. melo* which accelerates gastric ulcer healing could be via angiogenic activities. However, further studies should be carried out to determine its dependent pathway or pattern.

References

1. Banerjee N, Banerjee M, Ganguly S, Bandyopadhyay S, Das JK, Bandyopadhay A, Chatterjee M, Giri AK (2008) Arsenic-induced mitochondrial instability leading to programmed cell death in the exposed individuals. Toxicology 246:101–111
2. Hirose H, Takeuchi K, Okabe S (1991) Effect of indomethacin on gastric mucosal blood flow around acetic acid-induced gastric ulcers in rats. Gastroenterology 100:1259–1265
3. Hawkins C, Hanks GW (2000) The gastroduodenal toxicity of nonsteroidal anti-inflammatory drugs: a review of the literature. J Pain Symptom Manag 20:140–151
4. Dallas C, Michael R (1990) The diet and health benefits of HCA. Keats Publishing, New York
5. Rabiu S, Muhammad SA (2015) Antiulcerogenic effect of aqueous seed and rind extracts of *Citrullus lanatus* (water melon) in ethanol-induced gastric ulcer albino rats. Niger J Basic Appl Sci 23:111–115
6. Tindall HD (2004) Rambutan cultivation. FAO Plant Products and Protection Paper, Rome, Italy
7. Dhasan PB, Jegadeesan M, Kavimani S (2010) Antiulcer activity of aqueous extract of fruits of *Momordica cymbalaria* Hook f. in Wistar rats. Pharmacogn Res 2:58–61
8. Eitenmiller RR, Johnson CD, Bryan WD, Warren DB, Gebhardt SE (1985) Nutrient composition of cantaloupe and honeydew melons. J Food Sci 50:136–138
9. Kolayli S, Kara M, Tezcan F, Erim FB, Sahin H, Ulusoy E, Aliyazicioglu R (2010) Comparative study of chemical and biochemical properties of different melon cultivars: standard, hybrid, and grafted melons. J Agric Food Chem 58:9764–9769
10. Laur LM, Tian L (2011) Pro vitamin A and vitamin C contents in selected California-grown cantaloupe and honeydew melons and imported melons. J Food Compos Anal 24:194–201
11. Chen C, Qiang S, Lou L, Zhao W (2009) Cucurbitane-type triterpenoids from the stems of *Cucumis melo*. J Nat Prod 72:824–829
12. Akihisa T, Kimura Y, Kasahara Y, Kumaki K, Thakur S, Tamura T (1997) 7-oxodihydrokarounidiol-3-benzoate and other triterpenes from the seeds of Cucurbitaceae. Phytochemistry 46:1261–1266

13. Aruoma OI (2003) Methodological considerations for characterizing potential antioxidant actions of bioactive components in plant foods. Mutat Res Mol Mech Mutagen 523–524:9–20
14. Peng J, Jones GL, Watson K (2000) Stress proteins as biomarkers of oxidative stress: effects of antioxidant supplements. Free Radic Biol Med 28:1598–1606
15. Nadkarni KM, Nadkarni AK (2007) Indian materia medica, vol 1. Popular Prakashan, Bombay
16. Kirtikar KR, Basu BD (1935) Indian medicinal plants. Lalit Mohan Publication, Allahabad, pp 1655–1656
17. Zinchenko TV, Mindlin MZ, Prokopovich NN (1955) Anthelmintic properties of *Cucumis melo* seeds. Farmakol Toksikol 18:41–43
18. Milind P, Kulwant S (2011) Musk melon is eat-must melon. Int Res J Pharm 2:52–57
19. Yuan Y, Padol IT, Hunt RH (2006) Peptic ulcer disease today. Nat Clin Pract Gastroenterol Hepatol 3:80–89
20. Bidkar JS, Ghanwat DD, Bhujbal MD, Dama GY (2012) Anti-hyperlipidemic activity of *Cucumis melo* fruit peel extracts in high cholesterol diet induced hyperlipidemia in rats. J Complement Integr Med. https://doi.org/10.1515/1553-3840.1580
21. Sathishsekar D, Subramanian S (2005) Antioxidant properties of *Momordica charantia* (bitter gourd) seeds on Streptozotocin induced diabetic rats. Asia Pac J Clin Nutr 14:153–158
22. Adekunle AA, Oluwo OA (2008) The nutritive value of *Cucumis melo* var. agrestis Scrad (Cucurbitaceae) seeds and oil in Nigeria. Am J Food Technol 3:141–146
23. Shafaei A, Esmailli K, Farsi E, Aisha AFA, Abul Majid AMS, Ismail Z (2015) Genotoxicity, acute and subchronic toxicity studies of nano liposomes of *Orthosiphon stamineus* ethanolic extract in Sprague Dawley rats. BMC Complement Altern Med 15:360
24. Valente MJ, Araújo AM, Silva R, de Lourdes Bastos M, Carvalho F, de Pinho PG, Carvalho M (2016) 3,4-Methylenedioxypyrovalerone (MDPV): *in vitro* mechanisms of hepatotoxicity under normothermic and hyperthermic conditions. Arch Toxicol 90:1959–1973
25. Aniagu S, Nwinyi F, Akumka D (2005) Toxicity studies in rats fed nature cure bitters. Afr J Biotechnol 4:72–78
26. Alphin R, Ward J (1976) Action of hexapyrronium bromide on gastric secretion in dogs and ulceration in rats. Arch Inter Pharmacol Ther 168:82–100
27. Hsu S, Raine L, Fanger H (1981) Use of avidin-biotin peroxidase complex (ABC) in immunoperoxidase techniques. J Histochem Cytochem 29:577–580
28. Tuominen VJ, Ruotoistenmäki S, Viitanen A, Jumppanen M, Isola J (2010) ImmunoRatio: a publicly available web application for quantitative image analysis of estrogen receptor (ER), progesterone receptor (PR), and Ki-67. Breast Cancer Res 12:R56
29. Zapata-Colindres JC, Zepeda-Gómez S, Montaño-Loza A, Vázquez-Ballesteros E, de Jesús Villalobos J, Valdovinos-Andraca F (2006) The association of *Helicobacter pylori* infection and nonsteroidal anti-inflammatory drugs in peptic ulcer disease. Can J Gastroenterol 20:277–280
30. Jain KS, Shah AK, Bariwal J, Shelke SM, Kale AP, Jagtap JR, Bhosale AV (2007) Recent advances in proton pump inhibitors and management of acid-peptic disorders. Bioorg Med Chem 15:1181–1205
31. Morsy MA, Heeba GH, Abdelwahab SA, Rofaeil RR (2012) Protective effects of nebivolol against cold restraint stress-induced gastric ulcer in rats: role of NO, HO-1, and COX-1,2. Nitric Oxide—Biol Chem 27:117–122
32. Suleyman H, Albayrak A, Bilici M, Cadirci E, Halici Z (2010) Different mechanisms in formation and prevention of indomethacin-induced gastric ulcers. Inflammation 33:224–234
33. Arai I, Hirose H, Usuki C, Muramatsu M, Aihara H (1987) Effects of indomethacin and cold-stress on gastric acid secretion and ulceration. The effects of anti-acid secretory agents in rats. Res Commun Chem Pathol Pharmacol 57:313–327
34. Befrits R, Samuelsson K, Johansson C (1984) Gastric acid inhibition by antral acidification mediated by endogenous prostaglandins. Scand J Gastroenterol 19:899–904
35. Abdallah IZA, Khattaba HAH, Heebab GH (2011) Gastroprotective effect of *Cordia myxa* L. fruit extract against indomethacin-induced gastric ulceration in rats. Life Sci J 8:433–445
36. Adhikary B, Yadav SK, Roy K, Bandyopadhyay SK, Chattopadhyay S (2011) Black tea and theaflavins assist healing of indomethacin-induced gastric ulceration in mice by antioxidative action. Evid-Based Complement Altern Med 2011:11–22

37. Muhammed Ashraf VK, Thamotharan G, Sengottuvelu HS, Haja Sherief S, Sivakumar T (2012) Evaluation of anti ulcer activity of *Ficus pumila* L. leaf extract in albino rats. Gjrmi 1:340–351
38. Beck PL, Xavier R, Lu N, Nanda NN, Dinauer M, Podolsky DK, Seed B (2000) Mechanisms of NSAID-induced gastrointestinal injury defined using mutant mice. Gastroenterology 119:699–705
39. Wallace JL, Devchand PR (2005) Emerging roles for cyclooxygenase-2 in gastrointestinal mucosal defense. Br J Pharmacol 145:275–282
40. Alanko J, Riutta A, Holm P, Mucha I, Vapatalo H, Metsa-Ketela T (1999) Modulation of arachidonic acid metabolism by phenols: relation to their structure and antioxidant/prooxidant properties. Free Radic Biol Med 26:93–201
41. Stefan F, Karen A, Olivier F, Ralph A (2005) Innate immunity and angiogenesis. Circ Res 96:15–26
42. Gumina R, Kirschbaum N, Rao P, Van Tuinen P, Newman P (1996) The human PECAM1 gene maps to 17q23. Genomics 34:229–232
43. Schmassmann A (1998) Mechanisms of ulcer healing and effects of nonsteroidal anti-inflammatory drugs. Am J Med 104:43S–51S
44. Jones M, Wang H, Peskar B, Levin E, Itani B, Sarfeh I, Tarnawski A (1999) Inhibition of angiogenesis by nonsteroidal anti-inflammatory drugs: insight into mechanisms and implications for cancer growth and ulcer healing. Nat Med 5:1418–1423
45. Wallace JL, Granger DN (1996) The cellular and molecular basis of gastric mucosal defense. FASEB J Off Publ Fed Am Soc Exp Biol 10:731–740
46. DeLisser HM, Christofidou-Solomidou M, Strieter RM et al (1997) Involvement of endothelial PECAM-1/CD31 in angiogenesis. Am J Pathol 151:671–677

Chapter 30
Presence of Polycyclic Aromatic Hydrocarbons (PAHs) in Water and Sediment from Owo River and Ologe Lagoon: A Focus on Distribution, Source Apportionment, Human and Ecological Risk Assessment

Kafeelah Yusuf, Blessing Okolie and Akeem Aderibigbe

Abstract Polycyclic aromatic hydrocarbons (PAHs) are pollutants of concern due to their toxic, persistent and long-term adverse effects to the aquatic life. This study was undertaken to assess the human health and ecological risk of 16 PAHs in water and sediments. 16 PAHs were analyzed in a total of 6 water and sediment samples. The results obtained indicate the prevalence of high molecular weight PAHs in all the samples. PAHs concentrations in water and sediment samples from all the sampling sites were in the range of 182.53–218.02 ng/L and 9626.00–9885.67 ng/kg, respectively. The toxic equivalent quantity (TEQ) value of all PAHs in sediments in the range of 3.05–3.54 µg/kg was lower than the safe level (600 µg/kg). The mean effects range median quotient (M-ERM-Q) for Owo river and Ologe lagoon sediments were 1.19×10^{-2} and 1.40×10^{-2} indicating low probability (<10% incidence) of acute toxicity caused by PAHs in the sediment. Health risk assessment was conducted using incremental life time cancer risk (ILCR) models coupled with benzo[a]pyrene toxic equivalent method. The exposure pathways considered in this study were direct water ingestion and dermal contact under residential scenario. The cancer risk was predominantly contributed (greater than 98%) by dermal exposure rather than the oral in both adults and children. The total ILCR is found to be greater than the low safety risk of 1-in-10,000. The results of the study will be useful for the regulatory policy makers in understanding the actual impact of the contamination on the end users.

K. Yusuf (✉) · B. Okolie · A. Aderibigbe
Department of Chemistry, Lagos State University, P.M.B. 10001, LASU Post Office, Badagry Express Way, Ojo, Lagos, Nigeria
e-mail: kafyusuf@yahoo.co.uk

B. Okolie
e-mail: blessed234@yahoo.com

A. Aderibigbe
e-mail: shinaaderibigbesamuel@gmail.com

30.1   Introduction

The scarcity of water resources in Nigeria, combined with pollution by different industries and lack of proper waste management, call for improved measures to manage the release of PAHs into the aquatic environment. Lagos state lies to the south-western part of Nigeria [1]. It shares boundaries with Ogun state both in the north and the east and is bounded on the west by the Republic of Benin. In the south, it stretches for 180 km along the coast of the Atlantic Ocean. Lagos state lies between longitudes $20° 42'$ and $30° 42'E$ and latitudes $60° 22'$ to $60° 42'N$. It is the smallest state in Nigeria and occupies an area of about 3577 km^2, out of which 787 km^2 consists of lagoons and creeks. These water bodies act as sinks for the disposal of industrial and domestic wastes from industries and homes located in the Lagos metropolis. Lagoons play an important role in the drinking water supply and irrigation of farmlands, thus the water quality is closely related to the public health. However, available information about the risk assessment of lagoon water quality on public health is very limited [2]. Ologe lagoon is a natural semi-enclosed fresh water body situated about 30 km south west of Lagos on the Lagos-Badagry express way. It is located in Oto-Awori in Ojo local Government Area, Lagos state, and the indigenous inhabitants are the Aworis. Ologe lagoon is bounded in the north by Igbesa and Agbara in Ogun state and Ijanikin town in Lagos state and in the south by Gbanko and Badagry creek. It lies between longitudes $6° 27'$ and $6° 30'N$ and latitudes $3° 2'$ and $3° 7'E$ with a surface area of 9.4 km^2 and a mean depth of 2.5 m [1]. Towo-Owo is a nearby town that has a river called Owo river, the major freshwater inlet into the lagoon, with a catchment area of approximately 1122 km^2 above Agbara and the river is tapped for drinking water supply by the Lagos State Water Corporation at Ishasi. The outlet of the lagoon is on a section of the coastline which discharges into the Atlantic Ocean (25 km away). The lagoon plays an important role in the drinking water supply and provides a source of living to some inhabitants through transportation, agricultural food, fishing activities and irrigation of farmlands for local residents, thus the water quality in this lagoon can greatly influence the health of local residents. The lagoon is subjected to threats from human activities, among which are open defecation, sand dredging, domestic waste dumping by inhabitants at the banks and discharge of effluents by Agbara Industrial Estate which is increasingly fierce with the rapid development of industry, agriculture and urban construction over the last 25 years.

Sewage of industrial plants, agricultural and urban runoffs, aquaculture industry and other human activities are possible sources of PAHs [3, 4]. PAHs can adversely affect not only human health through drinking water but also sensitive species of organisms [4]. A great amount of PAHs may enter the water bodies, and accumulate, bio-accumulate or bio-magnify in food chains [4, 5]. The negative impacts on

human health and the ecosystem due to their teratogenic, carcinogenic and mutagenic characteristics may be caused by the accumulation of high levels of PAHs in environmental compartments [6]. Meanwhile, the negative impacts may even be greater in the aquatic environment [7]. Although the water quality of Owo river and Ologe lagoon is closely related to the health of local residents, limited data concerning the risk assessment of PAHs in the waters of Owo river and Ologe lagoon are available. Owo river and Ologe lagoon play a key role in the drinking water supply and source water for agricultural and industrial activities in the area. In recent years, Agbara town in Lagos has developed into a major area for industrial transfer; various kinds of industry, such as heavy chemicals, textile, electrical, foods and beverages and pharmaceutical, have settled there. Consequently, the immense pressures on the ecological integrity and freshwater resources which occurred via the process of industrial transfer have received increasing concern.

The quantitative identification of possible sources and contributions of PAH contaminants among the water and sediments are essential for better understanding of the cycling and fate of PAHs and are of great significance regarding the control of PAHs in aquatic environments. Therefore, the objectives of this work were to study the distribution characteristics of PAHs, carry out a human health and ecological risk assessment, identify possible sources of the 16 PAHs in the water and sediments and estimate the implications of PAH loadings to ecosystem and human health.

30.2 Materials and Methods

30.2.1 Materials and Chemicals

Merck silica gel was used for column chromatography. Dichloromethane, *n*-hexane and acetone 99.5% were obtained from Aldrich; solvents were double distilled to remove impurities. Sodium chloride, anhydrous sodium sulphate, sodium carbonate, analytical grade pyrene (Pyr), acenaphthene (Ace), benzo[a]anthracene (BaA), benzo[a]pyrene (BaP), benzo[b]fluoranthene (BbF), benzo[ghi]perylene (BghiP), dibenz[a,h]anthracene (DahA), fluoranthene(Flu), fluorene (Fl), indeno[1,2,3-cd]pyrene (InP), naphthalene (Nap) and phenanthrene (Phe) were supplied by Aldrich.

30.2.2 Sampling Area, Sampling and Sample Preparation

Sediment and water samples were collected from six sampling points of the Owo river and Ologe lagoon in October and November 2017. The study area comprises predominantly sedimentary and basement rocks complex. The sampling positions

Table 30.1 Location and primary characteristics of sampling sites

Sampling site	Longitude	Latitude	Full description
1	6°25 and 6°31 N	3°1 and 3°5 E	The wastewaters contain suspended solids, inorganic acids, bases; metals, degradable and non-biodegradable organics, oils and greases
2	6°27 and 6°30 N	3°2 and 3°7 E	The effluent discharged altered the physical, chemical and biological nature of Owo river
3	6°27 and 6°31 N	3°4 and 3°9 E	The ecological balance of the river was disturbed along the watercourse
4	6°29 and 6°31 N	3°6 and 3°9 E	Increased in industrial activities led to further deterioration of the water quality entering the Ologe lagoon
5	6°25 and 6°30 N	3°6 and 3°9 E	The lagoon was under pollution stress due to the prevailing harsh conditions, especially high temperature, restricted benthic diversity and development fauna of an intertidal ecosystem. No industry sited upstream
6	6°25 and 6°31 N	3°1 and 3°3 E	Human activities are reduced to bathing and fishing. The site served as reference point due to absence of discharge into the river

were located using a global positioning system, specific latitude/longitude of the samples along with basic characteristics and information as listed in Table 30.1.

Wastewater effluent samples were collected from Agbara wastewater treatment plant (WWTP). The samples were transported in ice chests and kept in the laboratory. The water samples were kept at 4 °C as recommended for PAH samples before analysis. Sediment samples were placed into polyethylene plastic bags and transported in a similar fashion as the water samples. In the laboratory, sediment samples were air-dried, homogenized, ground with an agate pestle and mortar, and sieved with 0.5 mm analytical sieves.

30.2.3 Extraction and Analysis of PAHs

Liquid-liquid extraction was used for the extraction of PAHs in water samples, as described in APHA [8]. A 500 ml sample was saturated with 75 g NaCl and transferred to a separatory funnel. PAHs in the sample were extracted three times using *n*-hexane. After vigorous shaking, the extract was dehydrated using anhydrous sodium sulfate, and concentrated to 2.0 ml with a rotary evaporator at 35–40 °C. Soxhlet extraction was used for the extraction of sediment samples [9]. Ten grams of sediment sample

were weighed into an extraction thimble, which had been pre-extracted with a mixture of n-hexane and dichloromethane, placed in a Soxhlet extractor and extracted with 250 ml of *n*-hexane and chloromethane mixture (1:1 v/v) for 16 h. The extract was concentrated to about 5.0 ml using a rotary vacuum evaporator.

The clean-up of water and sediment samples was performed using the method outlined by Kafilzadeh [10] where silica/alumina column chromatography was used for clean-up and separation of water and sediments. Saturated aliphatic and aromatic hydrocarbons were washed with 20 ml of *n*-hexane and 30 ml of a mixture of hexane and dichloromethane (90:10) (v/v) respectively. The volume of the eluted fraction was reduced to 1 ml and then the aromatic hydrocarbon fraction was injected into a gas liquid chromatograph equipped with a mass spectrometer detector (GC-MS) [11]. Analyses of PAHs were performed using a 7890A series, Agilent gas chromatograph coupled to 5975C Mass Selective Detector. Column oven temperature was programmed from 40 to 310 °C with initial temperature maintained for 5 min, then 15 °C/min to 100 °C, then 10 °C/min to 210 °C and to a final temperature of 310 °C at 5 °C/min. The GC was fitted with a HP-5 MS low bleed capillary column (30 m × 0.320 mm i.d., 0.25 μm film thickness). The carrier gas was helium. Volume injected = 1 μl. The entire 16 PAHs were analyzed and their concentrations were reported as μg/kg dry weight for the sediment and ng/L for water samples. The chromatograms showing the PAHs in water and sediment samples are presented in Fig. 30.1a, b.

30.2.4 Quality Assurance/Quality Control (QA/QC)

The quality assurance/quality control was performed using the method outlined by Yavar-Ashayeri et al. [12] where the analytical method validation was performed using the analysis of samples spiked with a known amount of analytes measured in duplicate. The average recovery for the spikes in sediments and water samples ranged between 85–96, and 92–97%, respectively. Therefore, analytical accuracy is within the order of 10%. No amount of the target PAHs was found in the procedural blank samples. For each PAH, the limit of detection (LOD) was considered as the sample concentration corresponding to three times the standard deviation of the areas obtained in six injections of the solution with the lowest concentration used for the calibration curve. The estimated limit of quantification (LOQ) was considered to be three times the LOD.

30.2.5 Toxic Equivalency Factor (TEF)

By TEF method, the toxicity of each PAH congener compound was expressed relative to the reference compound BaP or in other words, the concentrations of all PAH compounds were transformed to a BaP equivalent concentration. This methodology
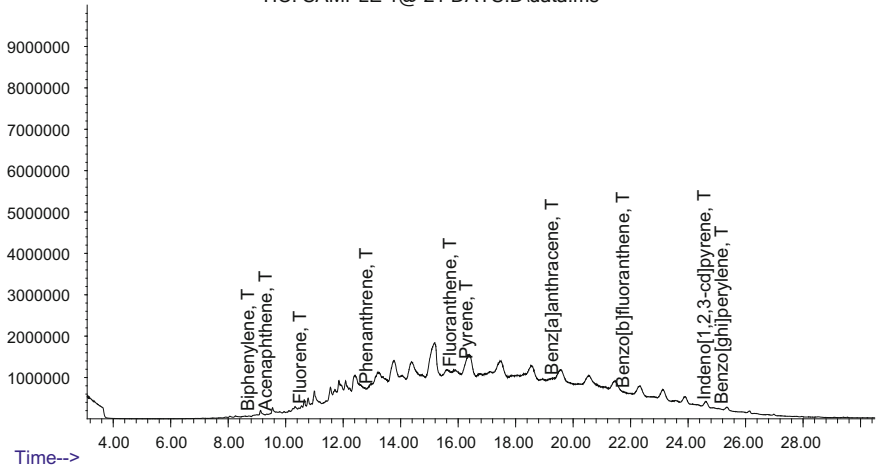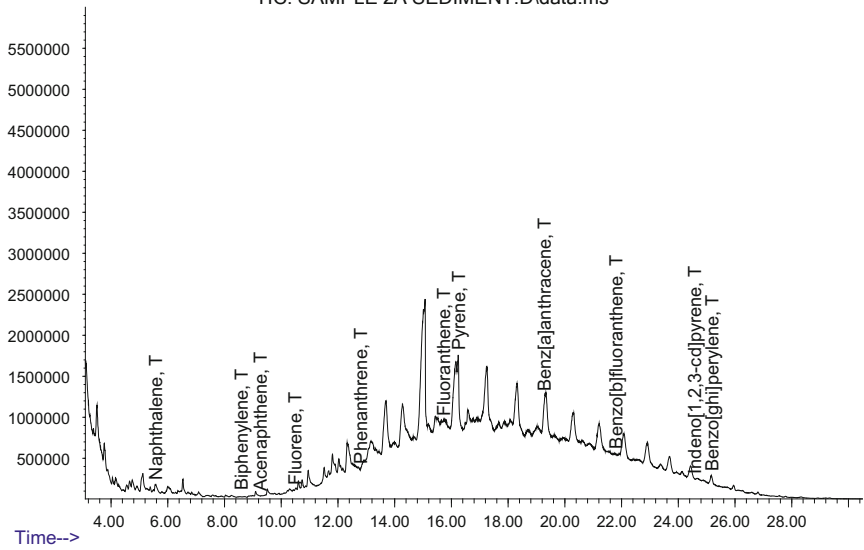
Fig. 30.1 Typical sample chromatogram of the PAHs in water (**a**) and sediment (**b**)

Table 30.2 Toxic equivalence factors (TEFs) for individual PAHs relative to BaP [13]

Compound	TEF	Compound	TEF
Naphthalene (Nap)	0.001	Benz[a]anthracene (BaA)	0.1
Acenaphthene (Ace)	0.001	Benzo[b]fluoranthene (BbF)	0.1
Fluorene (Fl)	0.001	Benzo[a]pyrene (BaP)	1
Phenanthrene (Phe)	0.001	Indeno[1,2,3-cd]pyrene (InP)	0.1
Fluoranthene (Flu)	0.001	Dibenz[a,h]anthracene (DahA)	1
Pyrene (Pyr)	0.001	Benzo[g,h,i]perylene (BghiP)	0.001

has been adopted for risk for PAHs [5]. Toxic equivalents of BaP were calculated by:

$$TEQ_{BaPeq} = \sum TEF_i \times C_i \tag{30.1}$$

where

TEF$_i$ Toxic equivalency factor for a PAH compound;
TEQ$_{BaPeq}$ Toxic equivalents of a benzo[a]pyrene reference compound or BaPequivalent concentration for all PAH compounds;
C$_i$ Concentration of individual PAH compound.

Toxic equivalency factor for each PAH and calculated TEQ values are shown in Table 30.2. TEFs by Nisbet and LaGoy [13] were adopted.

30.2.5.1 Exposure Assessment

The exposure routes for PAH contaminated water and sediment considered for exposure assessment in this study were: direct water ingestion and dermal contact. Exposure assessment was performed for two age groups: adults of age 21–70 years and children of age 0–5 years. This is to enable clear distinction in risk output results. Exposure dose for dermal contact was calculated using Eq. 30.2 [14]:

$$DAD = (DA_{event} \times EV \times EF \times ED \times SA)/(BW \times AT) \tag{30.2}$$

$$DA_{event\text{-}Water\ contact} = 2 \times FA \times Kp \times Cw \times \sqrt{(6 \times \tau_{event})} \times t_{event}/\pi$$
$$DA_{event} = Cs \times CF \times AF \times ABS_d$$

Exposure due to direct ingestion of contaminated water was quantified by Eq. 30.3 [15]:

$$CDI = (Cw \times IR \times ED \times EF)/(BW \times AT) \tag{30.3}$$

where

DAD	dermally absorbed dose (mg/kg-day),
DA_{event}	absorbed dose per event (mg/cm^2-event),
EV	event frequency (events/day),
EF	exposure frequency (days/year),
ED	exposure duration (years),
SA	skin surface area available for contact (cm^2),
BW	body weight (kg),
AT	averaging time or time over which exposure is averaged (days),
FA	fraction absorbed water $(-)$,
Kp	dermal permeable coefficient (cm/h),
τ_{event}	lag time per event (h/event),
t_{event}	event duration (h),
CF	conversion factor (cm^3/L),
CDI	chronic daily intake (mg/kg-day) and
IR	ingestion rate (L/day).

For the point estimates of human risk, the mean values were considered. For example, input parameters for adults were taken as: BW: 49.29 kg, ED: 25 years, CF = 1000 cm^3/L, EF: 350 days/year, Kp: 0.69 cm/h, t_{event}: 0.484 h, τ_{event}: 2.69 h/event, SA: 19,771 cm^2, IR: 1.38 L/day, AT: 25550 days, EV: 1 event/day, FA: 1.0. Similarly for children the values were: BW: 10.22 kg, ED: 2.5 years, CF = 1000 cm^3/L, EF: 350 days/year, Kp: 0.69 cm/h, t_{event}: 0.77 h, τ_{event}: 2.69 h/event, SA: 5838 cm^2, IR: 0.65 L/day, AT: 25550 days, EV: 1 event/day, FA: 1.0.

30.2.5.2 Toxicity Assessment

Toxicity of each PAH congener was represented with the toxicity of BaP compound. The average oral cancer slope factor (CSF_O) of BaP was taken as 7.27 for risk calculations [16].

The dermal cancer slope factor was calculated using Eq. 30.4 [14]:

$$CSF_{ABS} = CSF_o/ABS_{GI} \tag{30.4}$$

where

CSF_O	oral cancer slope factor (mg/kg-day),
CSF_{ABS}	dermal cancer slope factor (mg/kg-day), and
ABS_{GI}	gastro intestinal absorption factor (Dimensionless)

The ABS_{GI} value for BaP is taken as 0.31 [16].

30.2.5.3 Risk Characterization

Incremental life time cancer risk for oral ingestion was calculated from Eq. 30.5 [15]:

$$ILCR_O = CDI \times CSF_O \qquad (30.5)$$

whereas incremental life time cancer risk for dermal contact was calculated from Eq. 30.6 [14]:

$$ILCR_D = DAD \times CSF_{ABS} \qquad (30.6)$$

where

$ILCR_O$ oral incremental life time cancer risk, and
$ILCR_D$ dermal incremental life time cancer risk.

30.2.5.4 Toxicity Assessment in Sediment

The concentrations of the effects range low (ERL) and effects range median (ERM) were applied to evaluate the impact of individual PAHs on the aquatic sediment ecosystem [17, 18]. Principally, the concentrations were compared with the ERL and ERM [19]. In addition, the mean ERM quotients (mERMQ) were also implemented in the present study to further investigate the combined ecological risk of PAHs (Eq. 30.8).

$$ERMQ_i = C_i/CERM_i \qquad (30.7)$$

$$mERMQ = \Sigma(ERMQ_i)/n \qquad (30.8)$$

where $CERM_i$ is the corresponding quality value of the ERM for individual PAHs. According to Long and MacDonald [20], the mERMQ can be divided into four categories (<0.1, 0.11–0.50, 0.51–1.50, and >1.50), which were identified as low, medium-low, medium-high, and high-priority risk, respectively, and coincided with ≤10, 25–30, 46–53, and ≥75% incidences of ecological risk, respectively.

Table 30.3 Concentration of the 12 individual PAHs and Σ 12 PAHs in the water and wastewater samples (ng/L)

PAH	No of rings	Owo river		Ologe lagoon		Industrial wastewater	
		Mean	SD	Mean	SD	Mean	SD
Nap	2	BDL		BDL		BDL	
Ace	2	10.14	4.43	3.34	1.37	4.01	0.08
Fl	3	17.67	3.30	12.72	7.28	14.84	5.17
Phe	3	7.63	4.09	8.47	3.78	11.41	8.59
Flu	4	6.86	4.83	9.77	1.65	6.45	0.57
Pyr	4	5.88	5.78	4.54	1.86	5.15	0.07
BaA	4	7.14	5.17	8.16	2.72	12.11	7.90
BbF	5	19.27	9.07	11.08	3.04	20.00	0.00
BaP	5	11.30	6.15	34.46	19.72	14.07	5.94
InP	6	26.67	9.43	35.00	5.00	20.00	0.00
DahA	5	33.33	4.71	25.00	5.00	70.00	50.00
BghiP	6	43.33	20.55	30.00	10.00	40.00	20.00
Mean PAHs		17.20	7.05	16.59	5.58	19.82	8.94
$\sum$ Total PAH		189.22		182.53		218.02	
$\sum$ Total PAH$_{Carc}$		133.91		135.54		164.07	
Total LPAH		35.44		24.52		30.25	
Total HPAH		153.78		158.01		187.77	
LPAH/HPAH		0.23		0.16		0.16	
Flu/Flu + Pyr		0.54		0.68		0.56	
InP/InP + BghiP		0.38		0.54		0.33	
BaA/228		0.03		0.04		0.05	

30.2.6 Statistical Analysis and Risk Assessment

The software of SPSS statistics (version 16) was applied for data statistical analysis as shown Tables 30.3 and 30.4.

30.3 Results and Discussion

30.3.1 Concentrations and Distribution of PAHs

PAHs do not usually exist as separate entities in environmental media; they are often regarded as a mixture and the total concentration of their mixture is often

Table 30.4 Concentration of the 12 individual PAHs and Σ 12 PAHs in the sediment (ng/kg)

PAH	No of rings	Owo river		Ologe lagoon	
		Mean	SD	Mean	SD
Nap	2	351	459.42	BDL	
Ace	2	529.83	172.96	665.00	248.81
Fl	3	684.00	242.37	660.00	317.75
Phe	3	288.17	14.04	453.00	131.13
Flu	4	494.83	209.27	399.00	231.63
Pyr	4	230.50	40.38	458.25	107.45
BaA	4	344.00	195.30	256.00	157.46
BbF	5	1000.00	0.00	835.00	466.76
BaP	5	1000.00	0.00	1075.00	466.70
InP	6	1718.33	614.01	1000.00	805.36
DahA	5	1745.00	892.59	2250.00	794.36
BghiP	6	1500.00	707.11	1574.75	693.01
Mean PAHs		823.81	295.62	875.09	401.86
$\sum$ Total PAH		9885.67		9626.00	
$\sum$ Total PAH$_{Carc}$		6963.33		6734.75	
Total LPAH		1853.00		1778.00	
Total HPAH		8032.67		7848.00	
LPAH/HPAH		0.23		0.23	
Flu/Flu + Pyr		0.68		0.47	
InP/InP + BghiP		0.53		0.39	
BaA/228		1.51		1.12	

used to describe their distribution. 16 PAHs recommended by the United States Environmental Protection Agencies (US EPA) were investigated in this study but only 12 of them were diagnosed in water and sediment samples during the course of this study while the other 4 were below detectable limits. To assess the sensitivity of the instrument the detection limits were calculated. The calculated LOD and LOQ ranged between 0.01–0.05 and 0.03–0.71 ng/L, respectively.

30.3.1.1 Surface Water

The concentrations of the individual PAHs in Owo river and Ologe lagoon water varied between 5.88 and 43.33 ng/L and 3.34 to 35.00 ng/L respectively (Table 30.3). Owo river water (189.22 ng/L) recorded higher total PAH levels than Ologe lagoon (182.53 ng/L) suggesting discharge of anthropogenic wastes as major source of contaminants [21]. As can be seen in water samples, the highest concentration was related to benzo[ghi]perylene (6-ring PAH). According to the results, the concentra-

tion of high molecular weight (4–6 ring) polycyclic aromatic hydrocarbons (HPAHs) in water samples of Owo river and Ologe lagoon were higher than low molecular weight (2–3 ring) PAHs (LPAHs) as shown in Fig. 30.2a. The concentration (ng/L) of LPAHs in Owo river and Ologe lagoon water samples were 35.44 and 24.52 while HPAHs recorded were 153.79 and 158.01 respectively. The wastewater effluent from Agbara industrial treatment plant had the highest total PAHs of 218.02 ng/L. Therefore, the wastewater effluent from the treatment plant can be regarded as point source of PAHs contamination to the Owo river. This reasoning can be supported by Edokpayi et al. [22] who reported total PAHs in the range of BDL to 7.51 mg/L in wastewater effluent. This source was regarded as one of the contributors of PAH loadings into river sources. Therefore, wastewater treatment facilities in this study can be regarded as point source of PAHs contamination to the river.

The average total PAHs (ΣPAHs) in water from this study are comparable to the Pearl River Delta in South China (180 ng/L) [23], but higher than those in Seine River, France (20 ng/L) [24] and water in the Yellow River Delta, a newly born wetland in China (121.3 ng/L) [25], Mvudi River (0.126–7.510 ng/L) and Nzhelele River (BDL–7.805 ng/L) [22], and lower than those in Jiulong River Estuary and Western Xiamen Sea, China (17,050 ng/L) [26], Tonghui River, Beijing, China (762.3 ng/L) [27], and Lagos lagoon water, Nigeria (5730 ng/L) [28]. PAHs contamination in water may be classified into 4 degrees: low polluted 10–50 ng/L; slightly polluted 50–250 ng/L; moderately polluted 250–1000 ng/L; and highly polluted $\geq$1000 ng/L [29]. According to this classification, all the water samples in this study are slightly polluted. The average concentration of individual compounds in Owo river and Ologe lagoon water were in the order:

Fig. 30.2 Total LPAH and HPAH in water (**a**) and sediment (**b**) samples of Owo river and Ologe lagoon
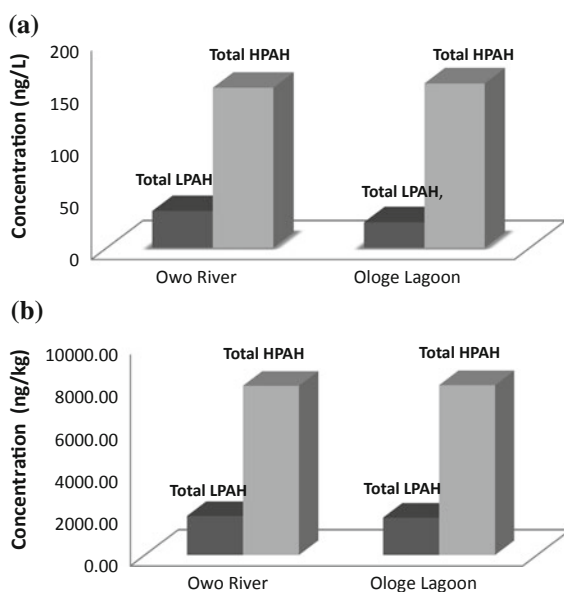
Owo river: BghiP > DahA > InP > BbF > Fl > BaP > Ace > Phe > BaA > Flu > Pyr.
Ologe lagoon: InP > BaP > BghiP > DahA > Fl > BbF > Flu > Phe > BaA > Pyr >
Ace.

30.3.1.2 Sediments

The sediment samples were expressed as dry weight (dw) as presented in Table 30.4;
the levels of PAHs determined in Owo river and Ologe lagoon sediments varied
between 230.50 to 1745 ng/kg and BDL to 2250 ng/kg respectively. The concen-
trations of PAHs were higher in the sediments of both river and lagoon than in the
water samples. This is due to the hydrophobic nature of PAHs [22]. PAHs tend to
adsorb on the surface of sediments because they are not soluble in water. Similar to
observed compositions of PAHs in surface water, HPAHs are more dominant in the
sediments than LPAHs (Fig. 30.2b). The major source of HMW PAHs can be linked
to anthropogenic activities [22]. Some HMW PAHs such as benzo[a]pyrene and flu-
oranthene are carcinogenic and mutagenic to a wide variety of organisms including
fish, birds and mammals [22]. Nasher et al. [30] reported the prevalence of HMW
PAHs in water collected around Langkawi Island in Malaysia. They attributed their
findings to anthropogenic activities such as incomplete fuel combustion and vehicle
engine emissions. Zhao et al. [31] and Okedeyi et al. [32] also reported the prevalence
of HMW PAHs in their studies around Mai Po inner deep bay of Hong Kong and
coal fired power plants around Mpumalanga, Free State and Gauteng Provinces, in
South Africa, respectively. The comparisons of Total PAHs obtained in this study
and different parts of the world are presented in Tables 30.5 and 30.6. The ΣPAHs
contamination in the sediments were categorised into four classes: low (0–100 ng/g),
moderate (100–1000 ng/g), high (1000–5000 ng/g) and very high (>5000 ng/g) [29].
Thus, the Σ PAHs contamination of sediments in this study may be assessed as
low level. The average total PAHs (Σ PAHs) in sediments for this study shows that

Table 30.5 Concentration ranges and mean values of PAHs (ng/L) in the water collected from
different rivers and lagoons worldwide

River, country	Range $\sum$ PAHs	Mean $\sum$ PAHs	Reference
Owo river, Nigeria	5.88–43.33	17.20	This study
Ologe lagoon, Nigeria	3.34–35.00	16.59	This study
Rivers in Heyuan, China	92.8–324	180	[24]
Rivers in Northern France-Belgium	BDL–6610		[34]
Wyre river, England	2.7–20		[35]
Tiber river, Italy	1.75–608	90.5	[36]
Rivers in Shanghai, China	46.5–460	113	[37]
Daliao river, China	71.1–4255	749	[38]
Maozhou river, China	13–1212	292	[39]

Table 30.6 Concentration ranges and mean values of PAHs (ng/g) in the sediment collected from different rivers and lagoons worldwide

River, country	Range $\sum$ PAHs	Mean $\sum$ PAHs	Reference
Owo river, Nigeria	0.23–1.75	0.82	This study
Ologe lagoon, Nigeria	0.26–2.25	0.88	This study
Rivers in Heyuan, China	55.7–381	186	[24]
Rivers in Northern France-Belgium	3750–22300		[34]
Huveaune river, France	572–4235	1966	[40]
Paranagua estuarine, Brazil	0.6–63.8		[41]
Tiber river, Italy	36.2–545.6	155.3	[36]
Rivers in Shanghai, China	249–36198	3328	[37]
Daliao river, China	375–11588	3700	[38]
Maozhou river, China	28–1051	458	[39]
Dongjiang river, China	100–3400	880	[42]
Erjien river, Taiwan	22–28622	737	[43]

the overall contamination level of Σ PAHs was lower than those reported for the sediments from Pearl River Delta, South China (55.7–381 ng/g) [23], Tiber River, Italy (36.2–545.6 ng/g) [33], Paranagua Estuarine, Brazil (0.6–63.8 ng/g) [34], Erjien River, Taiwan (22–28,622 ng/g) [35], Huveaune River, France (572–4235 ng/g) [36].

Correlation analysis reveals that BbF (r = 0.790, $p < 0.05$) and Fl (r = 0.888) correlated positively in the water and sediments, BghiP (r = −0.854), BaA (r = −0.823) correlated negatively but significantly in the water and sediments. Other PAHs did not show any significant correlation.

30.3.2 Identification of PAH Sources

PAHs can be used to identify the sources of pollutants [23, 37]. The sources of PAHs can either be petrogenic i.e. released from petroleum products or pyrogenic due to the combustion of biomass. Diagnostic ratios have been designed and used to distinguish the sources of PAHs due to their stability, physical and chemical attributes [22]. The most commonly used ratios for the source identification of PAHs are presented in Tables 30.3, 30.4 and 30.7.

Tables 30.3 and 30.4 shows the diagnostic ratios of the PAHs obtained in this study and their possible sources. The ratio (Low Molecular Weight PAHs)/(High Molecular Weight PAHs) gave values of <1 for all the sampling sites supporting the fact that the source of the PAHs was more likely to be due to the combustion of biomass. Also, the use of Flu/(Flu + Pyr) ratio gave values of >0.5, which further confirms a pyrogenic source. Otherwise, values of <0.4 would have implied that the source of the PAHs was due to the use of petroleum products. Burning of farmland

Table 30.7 Molecular diagnostic ratios and possible sources of PAHs in the environment

Diagnostic ratio	Petrogenic	Pyrogenic	Reference
LMW/HMW	>1.0	<1.0	[44]
Ant/(Ant + Phe)	<0.1	>0.1	[45]
Flu/(Flu + Pyr)	<0.4	≥0.5	[46]
Flu/Pyr	<1.0	>1.0	[47]
InP/(InP + BghiP)	<0.2	>0.5	[46]
BaA/228	<0.2	0.2–0.35	[43]
	Fuel combustion	Grass/coal/wood combustion	

for agriculture and refuse is a common practice around the study area. Generally, the source of PAHs in both river and lagoon systems and the wastewater treatment plants (WWTPs) can be attributed to pyrogenic activities although petrogenic contribution cannot be ruled out. Most PAHs that are persistent in environmental media are usually from pyrogenic sources rather than petrogenic sources.

30.3.3   Human Health Risk Assessment

30.3.3.1   Toxic Equivalency Factor (TEF)

Toxic equivalency factor for each PAH and calculated TEQ values are shown in Tables 30.8 and 30.9. According to the Canadian soil quality guidelines for protection of ecosystem and human health carcinogenic effects of PAH, a safe TEQcarc value should be <600 ng/g [20]. In this study, no sample was found to be above the threshold. The total TEQcarc values calculated for Owo and Ologe water samples were 49.90 ng/L with an average of 9.99 ng/L and 64.90 ng/L with an average of 13.00 ng/L respectively (Table 30.8). Among the 16 PAH congeners, DahA was the major contributor to the TEQ concentrations in Owo river water, Owo river sediment and Ologe lagoon sediment (accounting for 66.73, 57.38 and 63.74%, respectively), followed by BaP (22.65, 32.78 and 30.59%, respectively). However, BaP was the major contributor to the Ologe lagoon water (53.16%), followed by DahA (38.52%). Based on TEQ analysis, DahA and BaP are the risk pollutants in the aquatic environment.

30.3.3.2   Point Estimates

Dermal exposure assessment is considered in risk assessment when the ratio of the dermal adsorbed dose and chronic daily intake (DAD/CDI) exceeds 10% [14]. From the results shown in Table 30.10 the values of DAD/CDI ratio estimated were much higher than 10% in both adults and children. The ratio was higher in adults compared

Table 30.8 Toxic equivalency factors and BaP equivalent concentration for PAHs in water (ng/L)

PAH	No of rings	TEF[a]	Owo river	Ologe lagoon	Owo river	Ologe lagoon
			Mean	Mean	TEQi	TEQi
Nap	2	0.001	BDL	BDL	BDL	BDL
Ace	2	0.001	10.14	3.34	1.01×10^{-2}	3.34×10^{-3}
Fl	3	0.001	17.67	12.72	1.77×10^{-2}	1.27×10^{-2}
Phe	3	0.001	7.63	8.47	7.63×10^{-3}	8.47×10^{-3}
Flu	4	0.001	6.86	9.77	6.86×10^{-3}	9.77×10^{-3}
Pyr	4	0.001	5.88	4.54	5.88×10^{-3}	4.54×10^{-3}
BaA	4	0.1	7.14	8.16	0.714	0.816
BbF	5	0.1	19.27	11.08	1.93	1.11
BaP	5	1	11.30	34.46	11.3	34.5
InP	6	0.1	26.67	35.00	2.67	3.50
DahA	5	1	33.33	25.00	33.3	25
BghiP	6	0.001	43.33	30.00	4.33×10^{-2}	3.00×10^{-2}
$\sum \text{TEQ}_{\text{BaPeq}}$					50.0	65.0
$\sum \text{TEQ}_{\text{BaPeqcarc}}$					49.9	64.9
Mean $\text{TEQ}_{\text{BaPeqcarc}}$					9.99	13.00
SD $\text{TEQ}_{\text{BaPeqcarc}}$					12.3	14.00

[a]Nisbet and LaGoy [13]

to children implying that adults can have more dermal exposure to contaminants for the same concentration of the PAHs. At the concentration levels of PAHs in this study, the risk of getting cancer by adults by drinking the contaminated water over a period of 25 years is about four-in-one million (3.50×10^{-6}) and five-in-one million (4.55×10^{-6}) for Owo river and Ologe lagoon respectively while the dermal contact is about four-in-ten thousand (3.52×10^{-4}) and about five in ten thousand (4.55×10^{-4}) respectively. In both children and adults, the mean values of oral, dermal and total risk were observed to be higher than the US EPA allowable risk of one-in-one million (Table 30.10). In each exposure route, adults were found to be at higher risk levels than children by one order of magnitude. This could be due to adults having higher values of skin surface area, exposure duration and ingestion rates. As the contaminants are organic in nature, human skin cannot act as an effective barrier. Average dermal risk alone was contributing 98.88 and 98.75% (Owo river), and 99.13 and 98.79% (Ologe lagoon) of the overall risk in adults and children respectively (Table 30.10). It is highly recommended that the residents of the Owo river and Ologe lagoon do not use this water where the dermal contact is possible. Generally, an acceptable risk

Table 30.9 Toxic equivalency factors and BaP equivalent concentration for PAHs in sediment (ng/g)

PAH	No of rings	TEF[a]	Owo river	Ologe lagoon	Owo river	Ologe lagoon
			Mean	Mean	TEQi	TEQi
Nap	2	0.001	0.351	BDL	3.51×10^{-4}	
Ace	2	0.001	0.530	0.665	5.30×10^{-4}	6.65×10^{-4}
Fl	3	0.001	0.684	0.660	6.84×10^{-4}	6.60×10^{-4}
Phe	3	0.001	0.288	0.453	2.88×10^{-4}	4.53×10^{-4}
Flu	4	0.001	0.495	0.399	4.95×10^{-4}	3.99×10^{-4}
Pyr	4	0.001	0.231	0.458	2.31×10^{-4}	4.58×10^{-4}
BaA	4	0.1	0.344	0.256	3.44×10^{-2}	2.56×10^{-2}
BbF	5	0.1	1.00	0.835	0.10	8.35×10^{-2}
BaP	5	1	1.00	1.08	1.00	1.08
InP	6	0.1	1.72	1.00	0.172	0.10
DahA	5	1	1.75	2.25	1.75	2.25
BghiP	6	0.001	1.50	1.57	1.50×10^{-3}	1.57×10^{-3}
$\sum \text{TEQ}_{\text{BaPeq}}$					3.05	3.54
$\sum \text{TEQ}_{\text{BaPeqcarc}}$					3.05	3.53
Mean $\text{TEQ}_{\text{BaPeqcarc}}$					0.610	0.707
SD $\text{TEQ}_{\text{BaPeqcarc}}$					0.667	0.865

[a]Nisbet and LaGoy [13]

Table 30.10 Point estimates of incremental life time cancer risk

Owo river	DAD (mg/kg-day)	CDI (mg/kg-day)	DAD/CDI (%)	Oral risk	Dermal risk	Total risk
Adults	1.49×10^{-5}	4.79×10^{-7}	3131.5	3.50×10^{-6}	3.52×10^{-4}	3.56×10^{-4}
Children	2.70×10^{-6}	1.09×10^{-7}	2477.1	7.92×10^{-7}	6.33×10^{-5}	6.41×10^{-5}
Ologe lagoon	DAD (mg/kg-day)	CDI (mg/kg-day)	DAD/CDI (%)	Oral risk	Dermal risk	Total risk
Adults	1.94×10^{-5}	6.23×10^{-7}	3113.96	4.55×10^{-6}	4.55×10^{-4}	4.59×10^{-4}
Children	3.49×10^{-6}	1.41×10^{-7}	2617.02	1.03×10^{-6}	8.18×10^{-5}	8.28×10^{-5}

DAD Dermal adsorbed dose, *CDI* chronic daily intake

of 10^{-6} (more conservative) was set by the US EPA for comparison of actual risk. However, the values of 10^{-4} and 10^{-5} have been considered for allowable risk [38]. When a value of 10^{-4} was considered as a screening value, the risk from direct water ingestion was observed to be acceptable in both children and adults but the risk from dermal contact was acceptable for children only indicating that dermal exposure may be posing a considerable health risk to adults.

The present study shows higher dermal risk than oral in both age groups, as well as a higher overall cancer risk in adults than children. This is similar to report by Rajasekhar et al. [38] that the cancer risk is predominantly contributed (greater than 98%) by dermal exposure than the oral in both adults and children. Sarria-Villa et al. [39] found that for PAH contaminated water, risk by dermal contact was more than risk by direct water ingestion in both children and adults, and adults were at a higher risk than children. Wu et al. [40] have also shown that children are at lower risk than adults for exposure to PAH contaminated drinking water.

30.3.4   *Ecological Risk Assessment*

Ecological risk assessment is of paramount importance when developing sediment quality criteria that aimed to determine whether the sediment associated contaminants impaired the aquatic system. PAHs levels in the sediments were compared with the US National Oceanic sediment quality guidelines [41]. Table 30.11 shows the recommended ERL (effect range low) and ERM (effect range median) target values. Values above the recommended ERM values indicate the likelihood of occurrence of high negative toxic effect in that area. Mild toxic effect is expected if the PAHs concentrations range between ERL and ERM values [20]. No negative effect is expected for PAH concentrations lower than ERL values. From the results, the Σ PAHs$_{carc}$ in Owo river and Ologe lagoon sediments varied between 0.23 and 1.745 ng/g, and BDL and 2.25 ng/g respectively which were significantly less than the ERL value of Σ PAHs$_{carc}$ defined in Table 30.11. However, simultaneous and long-time exposure to a mixed of PAH compounds can contain various adverse biological effects on organisms and aquatic system. Consequently, M-ERM-Q can be used to assess the likely combined toxicity or biological risk for exposure to mix of PAHs in sediments. From the results, M-ERM-Q amounts were lower than 0.1, indicating low probability for negative biological effects in this study.

30.4   **Conclusions**

The profile of PAHs revealed that the dominant PAHs within the water and sediment samples were high molecular weight compounds. Sediment samples were more contaminated than the water samples. Wastewater from the treatment plant is regarded as a potential source of PAHs in both river and lagoon waters and sediments. Results

Table 30.11 Concentrations of PAHs (ng/g) in Owo river and Ologe lagoon sediment and toxicity guidelines

PAH	SQG		Owo river	Ologe lagoon	Owo river	Ologe lagoon
	ERL	ERM			C/ERM	C/ERM
Nap	160	2100	0.351	BDL	1.67×10^{-4}	–
Ace	16	500	0.530	0.665	1.06×10^{-3}	1.33×10^{-3}
Fl	19	540	0.684	0.660	1.27×10^{-3}	1.22×10^{-3}
Phe	240	1500	0.288	0.453	1.92×10^{-4}	3.02×10^{-4}
Flu	600	5100	0.494	0.399	9.69×10^{-5}	7.82×10^{-5}
Pyr	665	2600	0.231	0.458	8.88×10^{-5}	1.76×10^{-4}
BaA	261	1600	0.344	0.256	2.15×10^{-4}	1.60×10^{-4}
BbF	320	1880	1.000	0.835	5.32×10^{-4}	4.44×10^{-4}
BaP	430	1600	1.000	1.075	6.25×10^{-4}	6.72×10^{-4}
InP	240	NA	1.718	1.000	NA	NA
DahA	63.4	260	1.745	2.250	6.71×10^{-3}	8.65×10^{-3}
BghiP	430	1600	1.500	1.574	9.38×10^{-4}	9.84×10^{-4}
$\sum$ PAHs	3444.4	19,280	11.009	10.027		
$\sum$ PAHs$_{carc}$	1483.4	5340	6.963	6.734		
M-ERM-Q					1.19×10^{-2}	1.40×10^{-2}

from diagnostic ratios favour a pyrogenic source of PAH pollution. Human health risk assessment study for exposure to PAHs in water and sediment indicates average dermal risk contributes 98.88 and 98.75% (Owo river) and 99.13 and 98.79% (Ologe lagoon) of the overall risk in adults and children respectively. With the exception of dermal exposure posing health risk in adults, other age groups are not potentially at risk when the least conservative value of allowable risk of 10^{-4} is set as the screening criteria. Adults are at higher risk of one order of magnitude compared with children in oral and dermal exposure routes. It is found that adults are the sensitive receptors compared to the children. This finding is important since there is a general tendency to think that children are the most vulnerable due to low body weights.

References

1. Yusuf KA, Osibanjo O (2006) Trace metals in water and sediments from Ologe lagoon, southwestern Nigeria. Pak J Sci Ind Res 49:88–96
2. Sun C, Zhang J, Ma Q, Chen Y, Ju H (2017) Polycyclic aromatic hydrocarbons (PAHs) in water and sediment from a river basin: sediment–water partitioning, source identification and environmental health risk assessment. Environ Geochem Health 39:63–74

3. Yu Y, Li YX, Shen ZY, Yang ZF, Mo L, Kong YH, Lou IC (2014) Occurrence and possible sources of organochlorine pesticides (OCPs) and polychlorinated biphenyls (PCBs) along the Chao river, China. Chemosphere 114:137–141

4. Li YY, Niu JF, Shen ZY, Zhang C, Wang ZZ, He TD (2014) Spatial and seasonal distribution of organochlorine pesticides in the sediments of the Yangtze estuary. Chemosphere 114:234–238

5. Hu YD, Bai ZP, Zhang LW, Wang X, Zhang L, Yu QC (2007) Health risk assessment for traffic policemen exposed to polycyclic aromatic hydrocarbons (PAHs) in Tianjin, China. Sci Total Environ 382:240–250

6. Abdel-Aziz O, El Kosasy AM, El-Sayed Okeil SM (2014) Comparative study for determination of some polycyclic aromatic hydrocarbons "PAHs" by a new spectrophotometric method and multivariate calibration coupled with dispersive liquid–liquid extraction. Spectrochim Acta A 133:119–129

7. Aziz F, Syed JH, Malik RN, Katsoyiannis A, Mahmood A, Li J, Zhang G, Jones KC (2014) Occurrence of polycyclic aromatic hydrocarbons in the Soan river, Pakistan: insights into distribution, composition, sources and ecological risk assessment. Ecotoxicol Environ Saf 109:77–84

8. APHA, AWWA, WEF (2012) Standard methods for examination of water and wastewater, 22nd edn. American Public Health Association, Washington, USA, 1360 pp

9. US EPA (1996) US EPA Method 3540 C Rev. 3. Soxhlet extraction. Environmental Protection Agency, Washington, USA

10. Kafilzadeh F (2015) Distribution and sources of polycyclic aromatic hydrocarbons in water and sediments of the Soltan Abad river, Iran. Egypt J Aquat Res 41:227–231

11. US EPA (2014) Method 8270E (SW-846): semi volatile organic compounds by gas chromatography/mass spectrometry (GC/MS). Washington, USA

12. Yavar-Ashayeri N, Keshavarzi B, Moore F, Kersten M, Yazdi M, Lahijanzadeh AR (2018) Presence of polycyclic aromatic hydrocarbons in sediments and surface water from Shadegan wetland – Iran: a focus on source apportionment, human and ecological risk assessment and sediment-water exchange. Ecotoxicol Environ Saf 148:1054–1066

13. Nisbet ICT, LaGoy PK (1992) Toxic equivalency factors (TEFs) for polycyclic aromatic hydrocarbons (PAHs). Regul Toxicol Pharmacol 16:290–300

14. USEPA (2004) Risk assessment guidance for superfund. Human health evaluation manual (Part E, Supplemental guidance for dermal risk assessment), vol I. Washington, USA

15. US EPA (2001) Risk assessment guidance for superfund. Part A, Process for conducting probabilistic risk assessment office of emergency and remedial response, vol III. Washington, USA

16. US EPA (2016) RAIS, risk assessment information system. Toxicity profiles, RAGs a format for benzo[a]pyrene - CAS number 50328 U.S. Environmental Protection Agency, Washington, USA, EPA/635/R-16/331

17. Montuori P, Aurino S, Garzonio F, Sarnacchiaro P, Nardone A, Triassi M (2016) Distribution, sources and ecological risk assessment of polycyclic aromatic hydrocarbons in water and sediments from Tiber river and estuary, Italy. Sci Total Environ 566–567:1254–1267

18. Sun RX, Lin Q, Ke CL, Du FY, Gu YG, Cao K, Luo XJ, Mai BX (2016) Polycyclic aromatic hydrocarbons in surface sediments and marine organisms from the Daya Bay, South China. Mar Pollut Bull 103:325–332

19. Long ER, MacDonald DD, Smith SL, Calder FD (1995) Incidence of adverse biological effects within ranges of chemical concentrations in marine and estuarine sediments. Environ Manage 19:81–97

20. Long E, MacDonald D (1998) Recommended uses of empirically derived, sediment quality guidelines for marine and estuarine ecosystems. Human Ecol Risk Assess 4:1019–1039

21. Hajisamoh A (2013) Pollution levels of 16 priority PAHs in the major rivers of southern Thailand. Res Rev J Chem 2:7–11

22. Edokpayi JN, Odiyo JO, Popoola OE, Msagati TAM (2016) Determination and distribution of polycyclic aromatic hydrocarbons in rivers, sediments and wastewater effluents in Vhembe District, South Africa. Int J Environ Res Pub Health 3:387–398

23. Yu Y, Yu Z, Wang Z, Lin B, Li L, Chen X, Zhu X, Xiang M, Ma R (2018) Polycyclic aromatic hydrocarbons (PAHs) in multi-phases from the drinking water source area of the Pearl River Delta (PRD) in South China: distribution, source apportionment, and risk assessment. Environ Sci Pollut Res 25:12557–12569
24. Fernandes MB, Sicre M, Boireau A (1997) Polyaromatic hydrocarbon (PAH) distributions in the Seine river and its estuary. Mar Pollut Bull 34:857–867
25. Wang L, Yang Z, Niu J, Wang J (2009) Characterization, ecological risk assessment and source diagnostics of polycyclic aromatic hydrocarbons in water column of the Yellow River Delta, one of the most plenty biodiversity zones in the world. J Hazard Mater 169:460–465
26. Maskaoui K, Zhou JL, Hong HS, Zhang ZL (2002) Contamination by polycyclic aromatic hydrocarbons in the Jiulong river estuary and Western Xiamen Sea, China. Environ Pollut 118:109–122
27. Zhang Y, Liu M, Chen H, Hou G (2014) Source identification of polycyclic aromatic hydrocarbons in different ecological wetland components of the Qinkenpao Wetland in northeast China. Ecotoxicol Environ Saf 102:160–167
28. Adedayo A, Adeyemi D, Uyimandu JP, Chigome S, Anyakora C (2012) Evaluation of the levels of polycyclic aromatic hydrocarbons in surface and bottom waters of Lagos lagoon, Nigeria. Afr J Pharm Sci Pharm 3:58–74
29. He Y, Meng W, Xu J, Zhang Y, Guo C (2016) Spatial distribution and potential toxicity of polycyclic aromatic hydrocarbons in sediments from Liaoheriver basin, China. Environ Monit Assess 188:193
30. Nasher E, Heng LY, Zakaria Z, Surif S (2013) Assessing the ecological risk of polycyclic aromatic hydrocarbons in sediments at Langkawi Island, Malaysia. Sci World J 1–3
31. Zhao Z, Zhuang Y, Gu J (2012) Abundance, composition and vertical distribution of polycyclic aromatic hydrocarbons in sediments of the Mai Po Inner Deep Bay of Hong Kong. Ecotoxicol 21:1734–1742
32. Okedeyi OO, Nindi MM, Dube S, Awofolu OR (2013) Distribution and potential sources of polycyclic aromatic hydrocarbons in soils around coal-fired power plants in South Africa. Environ Monit Assess 185:2073–2082
33. Liu S, Liu X, Liu M, Yang B, Cheng L, Li Y, Qadeer A (2016) Levels, sources and risk assessment of PAHs in multi-phases from urbanized river network system in Shanghai. Environ Pollut 219:555–567
34. Cardoso FD, Dauner AL, Martins CC (2016) A critical and comparative appraisal of polycyclic aromatic hydrocarbons in sediments and suspended particulate material from a large South American subtropical estuary. Environ Pollut 214:219–229
35. Wang YB, Liu CW, Kao YH, Jang CS (2015) Characterization and risk assessment of PAH-contaminated river sediment by using advanced multivariate methods. Sci Total Environ 524–525:63–73
36. Kanzari F, Syakti AD, Asia L, Malleret L, Piram A, Mille G, Doumenq P (2014) Distributions and sources of persistent organic pollutants (aliphatic hydrocarbons, PAHs, PCBs and pesticides) in surface sediments of an industrialized urban river (Huveaune), France. Sci Total Environ 478:141–151
37. Yunker MB, MacDonald RW, Vingarzan R, Mitchell RH, Goyette D, Sylvestre S (2002) PAHs in the Fraser river basin: a critical appraisal of PAH ratios as indicators of PAH source and composition. Org Geochem 33:489–515
38. Rajasekhar B, Nambi IM, Govindarajan SK (2018) Human health risk assessment of ground water contaminated with petroleum PAHs using Monte Carlo simulations: a case study of an Indian metropolitan city. J Environ Manage 205:183–191
39. Sarria-Villa R, Ocampo-Duque W, Páez M, Schuhmacher M (2016) Presence of PAHs in water and sediments of the Colombian Cauca river during heavy rain episodes, and implications for risk assessment. Sci Total Environ 540:455–465
40. Wu B, Zhang Y, Zhang XX, Cheng SP (2011) Health risk assessment of polycyclic aromatic hydrocarbons in the source water and drinking water of China: quantitative analysis based on published monitoring data. Sci Total Environ 410–411:112–118

41. Us EPA (1993) Provisional guidance for quantitative risk assessment of polycyclic aromatic hydrocarbons; EPA/600/R/089. Office of Research and Development, US EPA, Washington, USA
42. US EPA (2001) Risk assessment guidance for superfund. Human health evaluation manual (Part A), vol I. Available online: http://rais.ornl.gov/documents/HHEMA
43. Rabodonirina S, Net S, Ouddane B, Merhaby D, Dumoulin D, Popescu T, Ravelonandro P (2015) Distribution of persistent organic pollutants (PAHs, Me-PAHs, PCBs) in dissolved, particulate and sedimentary phases in freshwater systems. Environ Pollut 206:38–48
44. Moeckel C, Monteith DT, Llewellyn NR, Henrys PA, Pereira MP (2013) Relationship between the concentrations of dissolved organic matter and polycyclic aromatic hydrocarbons in a typical UK upland stream. Environ Sci Technol 48:130–138
45. Zheng B, Wang L, Lei K, Nan B (2016) Distribution and ecological risk assessment of polycyclic aromatic hydrocarbons in water, suspended particulate matter and sediment from Daliao river estuary and the adjacent area, China. Chemosphere 149:91–100
46. Zhang D, Wang JJ, Ni HG, Zeng H (2017) Spatial-temporal and multimedia variations of polycyclic aromatic hydrocarbons in a highly urbanized river from South China. Sci Total Environ 581–582:621–628
47. Zhang K, Wang JZ, Liang B, Zeng EY (2011) Occurrence of polycyclic aromatic hydrocarbons in surface sediments of a highly urbanized river system with special reference to energy consumption patterns. Environ Pollut 159:1510–1515
48. Zhang W, Zhang S, Wan C, Yue D, Ye Y, Wang X (2008) Source diagnostics of polycyclic aromatic hydrocarbons in urban road runoff, dust, rain and canopy through fall. Environ Pollut 153:594–601
49. Sany SBT, Rezayi M, Hashim R, Salleh A, Mehdinia A, Safari O (2014) Polycyclic aromatic hydrocarbons in coastal sediment of Klang Strait, Malaysia: distribution pattern risk assessment and sources. PLoS ONE 9:1–14
50. Hussein RA, Al-Ghanim KA, Abd-El-Atty MM, Mohamed LA (2016) Contamination of Red Sea shrimp (*Palaemonserratus*) with polycyclic aromatic hydrocarbons: a health risk assessment study. Polish J Environ Stud 25:615–620
51. Kannan K, Kober JL, Khim JS, Szymczyk K, Falandysz J, Giesy JP (2003) Polychlorinated biphenyls, polycyclic aromatic hydrocarbons and alkyl phenols in sediments from the Odra river and its tributaries. Poland Environ Toxicol Chem 85:51–60

Chapter 31
Leaching of Cobalt from Gypsum Using Nickel Eluate

Chongo Mwenya and Melvin M. Mashingaidze

Abstract Gypsum is a waste product of the iron precipitation stage of cobalt purification in many cobalt extraction plants. Most cobalt producers either landfill the gypsum or sell it cheaply to cement manufacturers. The gypsum contains residual cobalt which can be extracted through sulphuric acid leaching but the cost of the sulphuric acid is prohibitive. Leaching using recycled acidic liquors like nickel eluate offers an economical alternative. This study investigated the technical feasibility of leaching gypsum with nickel eluate, which is an acidic waste stream from the nickel ion exchange plant at the specific cobalt producer. This study also established the optimum pH and solids concentration for nickel eluate leaching. Nickel eluate leaching tests and sulphuric acid leaching tests were conducted on a one-factor-at-a-time experimental design basis. pH and pulp densities were varied while temperature, time and agitation speed were kept constant. Cobalt recoveries from the two sets of tests were compared. In both cases the mean recoveries were ≥90%. Thus, on the basis of high cobalt recoveries, nickel eluate leaching of cobalt from gypsum is highly feasible despite a significant difference at the 5% level in cobalt recoveries from leaching with sulphuric acid. Optimum cobalt recoveries for both tests occurred at a pH of 0.5 and 50% solids. Nevertheless, it is advisable to leach at a pH of 1 and 30% solids to limit costs, corrosion of equipment and the toll on the agitators in the leaching tanks due to high pulp viscosity.

Keywords Cobalt · Leaching · Gypsum · Nickel eluate · Recoveries · Acidic liquors

C. Mwenya
Kalumbila Minerals Limited, Plot 3805, Zambia Road, Industrial Area, P. O. Box 230022, Ndola, Zambia
e-mail: chongomwenya@gmail.com

M. M. Mashingaidze (✉)
Faculty of Engineering and IT, Department of Mining and Metallurgical Engineering, University of Namibia, P. O. Box 3624, 33004 Ongwediva, Namibia
e-mail: mmashingaidze@unam.na

31.1 Introduction

The role of hydrometallurgy regarding the extraction of valuable metals from various sources has been increasing in recent years [1]. Hydrometallurgical processing, according to Ghosh and Ray [2], and Gupta [1] involves four significant stages:

1. The metal of interest is first transferred from the solid feed material into an aqueous solution by a process referred to as leaching.
2. Separation of solids and liquids (solid-liquid separation) follows leaching. Undissolved solids, referred to as leach residue, are separated from the leached solution. This is usually carried out in thickeners.
3. The metal-bearing solution, referred to as the pregnant leach solution, must then be concentrated and purified to remove impurities and increase the concentration of the valuable metal. Examples of concentration and purification unit processes include solvent extraction, ion exchange and carbon adsorption.
4. The metal must then be recovered from the purified solution in the solid state.

Common recovery processes include electrowinning and chemical precipitation.

Leaching is the most fundamental step in hydrometallurgical processing. It involves preferential dissolution of metal from a host rock (mineral), concentrate, calcine or secondary source by contacting with an active chemical solution known as a leaching reagent or lixiviant [1]. In a leaching process, attention is focused on the chemical reactions that result in the dissolution of the metallic species. The following properties of the leaching reagent are particularly important [2]:

1. It must be highly selective of the required metal, leaving the unwanted elements undissolved.
2. The leaching reagent must be relatively cheap.
3. It must have the ability to be regenerated for recycling.
4. It should not be corrosive to materials used in plant construction.

Gupta [1] identified the general conditions likely to favor dissolution, in addition to selection of a suitable leaching reagent. These may be derived from the thermodynamic data presented in the form of Pourbaix diagrams. Thermodynamic considerations are important in leaching in that they provide basic guidance in choosing the combination of reagents and their considerations so as to obtain favourable free energy changes associated with any proposed reaction. Ghosh and Ray [2] further suggest that kinetic considerations are of far greater importance than thermodynamics in hydrometallurgy. According to them on account of the relatively low temperatures of operation used, hydrometallurgical processes are generally associated with low reaction rates, unlike in pyrometallurgy where high temperatures are used and the reactions are rapid.

31.2 Leaching and Extraction

31.2.1 Leaching Agents

Ghosh and Ray [2] identified the most common leaching reagents as water, acids and bases. Dutta et al. [3] include aqueous salts to the list of common leaching reagents. In order to increase leach efficiencies, reducing and oxidizing agents are sometimes used during leaching [3]. These reagents, including reducing and oxidizing agents, are discussed in this section.

31.2.1.1 Water

Water is the cheapest leaching reagent and is non-corrosive [2]. However, it is rarely employed as a solvent because very few compounds are soluble in it. Some common compounds that dissolve in water include copper sulphate ($CuSO_4$), zinc sulphate ($ZnSO_4$) and most compounds of alkali metals. Dutta et al. [3] reported that poor grade copper sulphide ores transform slowly into water soluble sulphate under atmospheric conditions and can be recovered by simple leaching. The general equation for water solvation of metallic ions is shown in Eq. 31.1 [3]:

$$MeX_{(s)} = Me^{2+}_{(aq)} + X^{2-}_{(aq)} \tag{31.1}$$
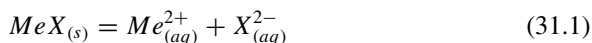
31.2.1.2 Mineral Acids

Mineral acids, chiefly sulphuric acid, are the most common leaching reagents [2]. Baba et al. [4] evaluated rutile leaching in hydrochloric acid and the findings characteristically show the impact of agitation rate, acid strength, and temperature and particle size on dissolution kinetics. Sulphuric acid (H_2SO_4) is widely used due to its low cost relative to other acids and its ability to be regenerated during electrolysis [3]. It is widely used for a variety of metal sources. These include simple and complex oxides, sulphides, selenides, tellurides, silicates, phosphates and a number of others. The simple ores are generally leached with dilute acid at ambient or elevated temperatures. The concentrated acids on the other hand, are employed for leaching of more complex refractory ores and sources [5]. Other acids used include hydrochloric acid (HCl) and nitric acid (HNO_3).

31.2.1.3 Bases and Salts

Several bases are routinely employed in many leaching operations. Common examples include sodium hydroxide (NaOH) and ammonium hydroxide (NH_4OH) [6].

NaOH is mainly used for leaching of bauxite in aluminium production. Ammonia (NH_3) is sometimes used for leaching of copper, nickel and cobalt due to their tendency to form soluble ammonia complexes. Salts are commonly used in leaching due to their complexing abilities. Examples are sodium cyanide (NaCN), sodium chloride (NaCl), calcium chloride ($CaCl_2$) and sodium carbonate (Na_2CO_3).

31.2.1.4   Oxidants

Oxidants such as pure oxygen, hydrogen peroxide (H_2O_2), ferric ion (Fe^{3+}) and chlorine gas (Cl_2) are used when reduced compounds are needed to be oxidised during leaching. Ventor and Boylett [6] studied the use of oxidation agents in uranium leaching and observed that uranium in the tetravalent state (U^{4+}) had very low solubility in acid and alkaline solutions and needed to be oxidised to the hexavalent state (U^{6+}) to become soluble. Uranium in typical uranium bearing minerals occurs in the tetravalent and hexavalent oxidation states. In acid leaching of uranium, the uranium is oxidised by ferric iron, which in turn is reduced to ferrous iron [6].

31.2.1.5   Reductants

Reductants enhance the solubility of metals, which have been solubilised to a lesser extent using only leaching reagents [7]. Examples of reducing agents include ferrous ions, sodium metabisulphite ($Na_2S_2O_5$), hydrogen peroxide and sulphur dioxide. Reducing agents such as sulphur dioxide and sodium metabisulphite have been used in the leaching of cobalt. Meshram et al. [7] observed that sodium bisulfite addition results in better recovery of cobalt and manganese by reducing them to their lower oxidation states. They also observed that cobalt dissolution increases with increasing sulphuric acid concentration from 0.5 to 3 M. Mwema et al. [8] conducted cobalt leaching laboratory tests at 40 °C and pH 4.05 in spent electrolyte with sulphur dioxide as a reductant. They observed that if present in the third oxidation state, reduction of Co^{3+} to Co^{2+} was necessary in order to dissolve it.

31.2.1.6   Miscellaneous Leaching Agents

Gupta and Mukherjee [5] comprehensively describe sundry processes of cyanide leaching, chlorine leaching, hypochlorite leaching, hypochlorous acid leaching, dichromate leaching, and electrochemical leaching. They also discuss the chemistry, kinetics and actual plant practice examples of these leaching processes. Gupta and Mukherjee [5] report that chlorine leaching of nickel and cobalt from lateritic oxide ores yields leach efficiencies approaching 100%, with limited dissolution of iron and other unwanted elements. Chlorine leaching is favoured by low temperatures because below 9 °C, chlorine at 1 atm pressure forms solid chlorine hydrate (Eq. 31.2):

$$Cl_{2(g)} + nH_2O \rightarrow Cl_2 \cdot nH_2O_{(S)} \tag{31.2}$$
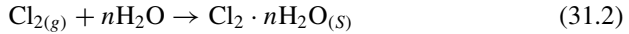
where $n = 6 - 7$. The formation of chlorine hydrate presents an opportune way of storing chlorine gas for leaching purposes.

31.2.2 Thermodynamics of Leaching

Thermodynamics are vital in leaching processes in determining the conditions of chemical equilibrium between species. The two most important parameters in leaching thermodynamics are voltage (or free energy) and pH [9]. The pH and electrical potential at specific temperature and pressure are of importance in establishing the possibility of metal dissolution. An Eh-pH diagram, commonly known as Pourbaix diagram, is an effective way of presenting the effects from oxidation-reduction potential, acid and base, complexing ligands, temperature and pressure for an aqueous system. It can be used in many scientific fields, including hydro- and electro-metallurgy, geo- and solution chemistry and corrosion science [10]. Various methods can be used to study the leaching thermodynamics of solutions. However, the Pourbaix (Eh-pH) diagram is the most widely accepted method [10]. Stuurman et al. [11] demonstrate how it can be used to predict and explain certain phase formations during cobalt leaching. The Pourbaix diagram of the cobalt-water system is illustrated in Fig. 31.1.
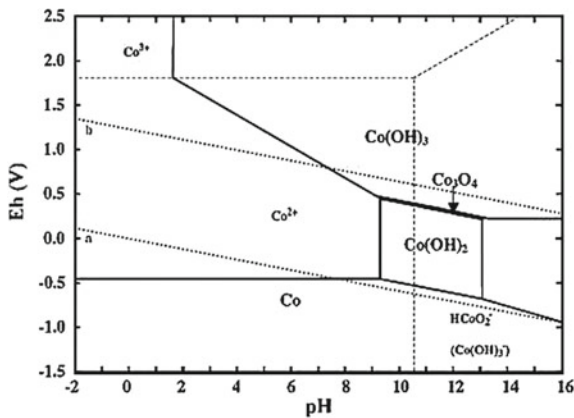

Fig. 31.1 Pourbaix diagram of cobalt-water system [12]

31.2.3 Leaching Kinetics

The study of leaching kinetics is important in improving the rate of leaching reactions, so as to make reactions cost and time effective. According to Othusitse and Muzenda [13], modelling has been used in various leaching operations to gain understanding of the process and subsequently help in decision making. The shrinking core-shrinking particle, shrinking core-constant particle and shrinking particle models are some of the earliest models developed to describe heterogeneous non-catalytic reaction kinetics. Figure 31.2 shows the shrinking particle, shrinking core-shrinking particle and shrinking core-unchanged particle models. These are the most popular models in hydrometallurgy since many leaching processes conform to kinetic models for heterogeneous solid-liquid reactions which are best described by these models [13]. Types of the shrinking core models in leaching process as identified in literature are categorized into the following types of rate controlling reactions.

Singer and Stumm [14] described leaching as a heterogeneous reaction that takes place at the interface between a solid and liquid phase and sometimes also a gaseous phase. The five main stages of leaching identified by Singer and Stumm [14] include:

1. Diffusion of reagent through the diffusion layer;
2. Adsorption of reagent on surface;
3. Reaction on the surface;
4. Desorption of product from surface;
5. Diffusion of product through the diffusion layer.

At the boundary between the two phases a diffusion layer is formed. In the case of a solid in an aqueous phase this layer consists of a stationary aqueous layer. The diffusion layer can be thinned by vigorous stirring but can never be completely
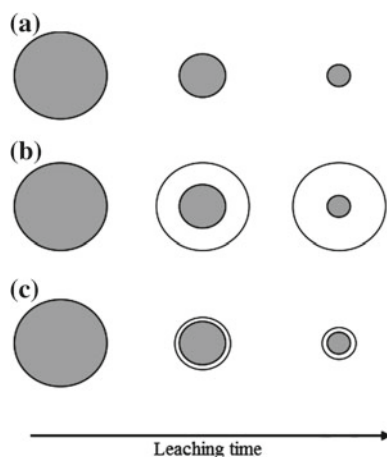

Fig. 31.2 Illustration of various mechanisms of leaching: **a** shrinking particle, **b** shrinking core-unchanging particle, **c** shrinking core-shrinking particle [13]

removed (Fig. 31.3). Typical thickness of the diffusion layer in a well stirred system is in the range of 1–10 μm. The slowest step in the leaching reaction is the rate-controlling step. Depending on which process is rate-controlling, three different types of reactions may be obtained, i.e. reaction controlled leaching, diffusion controlled leaching, and intermediate controlled leaching [14]. When the chemical reaction on the surface is much faster than the diffusion of reagent through the fluid film then the leaching becomes diffusion controlled.

Razavi-Tousi and Szpunar [16] have demonstrated that the shrinking core model can be modified for reactions where the particle grows instead of shrinking resulting in changes in diffusion distances and overall diffusion coefficient. Nonetheless, this model is very useful in the study of leaching kinetics. The leaching mechanism might become diffusion-controlled when, during the leaching, a porous product layer forms on the surface of the particle to be leached [16]. Sidborn et al. [17] modelled the bioleaching of a copper sulphide ore bed and observed that the predominant controlling step during ordinary leaching was the diffusion through the liquid film layer and explained this by the formation of a layer of elemental sulphur on the copper sulphide sites. It has been reported that the particle size, temperature, concentration (of the leaching reagent and solids) and agitation/stirring rate are among the most important variables affecting leaching kinetics [4, 8, 13–20]. In general, leaching rate increases with increased concentration of reagent and leaching temperature while extraction efficiency increases with leaching time [19]. The leaching mechanism may also change as a result of changes in the concentration of reagent. A study by Fan et al. [20] on nickel and cobalt leaching showed that the reaction rate increases rapidly at the beginning of the reaction, but slows down at the end with a decrease in reactant concentrations. Their findings show a similar trend to that reported by Takacova et al. [19].
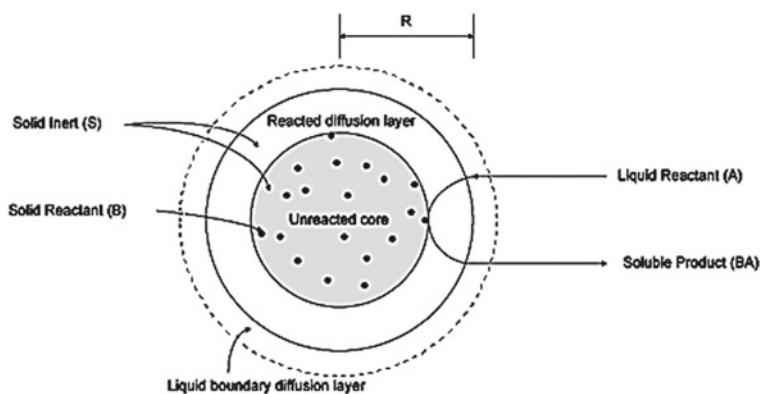

Fig. 31.3 Schematic of leaching according to the shrinking particle model [15]

31.2.4 Classification of Leaching Techniques

A number of techniques are available for the dissolution of metal values from ores and concentrates [1]. These can be separated into two all-encompassing classes: percolation leaching and agitation leaching. In percolation leaching, the ore body remains stationary and the leaching reagent is allowed to percolate up or down the body to cause dissolution. In situ leaching, heap leaching, dump leaching and vat leaching are all based on the process of percolation through a stationary ore body. Agitation leaching techniques, on the other hand, retain the finely ground ore body in suspension by agitating the slurry mechanically or pneumatically. Agitation leaching results in higher metal recoveries in a short time, but requires higher capital investment as compared with percolation leaching. The leaching operation may be performed in batch, concurrent, or countercurrent modes at slightly below atmospheric, atmospheric, or above atmospheric pressures, and at ambient or somewhat higher temperatures [1].

31.2.5 Design of Leaching Experiments

In experiments, one or more factors are deliberately changed in order to observe the effect of the changes on one or more response variables. The statistical design of experiments (DOE) is an efficient procedure for planning experiments so that the data obtained can be analyzed to yield valid and objective conclusions. The two main applications of experimental design are screening, in which the factors that influence the experiment are identified, and optimization, in which the optimal settings or conditions for an experiment can be found. Full factorial experiments are experiments that investigate the effects of two or more factors or input parameters on the output response of a process [21]. In some cases, the one-factor-at-a-time (OFAT) approach is used in leach test designs. It involves varying one factor or variable at a time while keeping others fixed. It has an advantage over full factorial design experiments in that fewer resources are required and results are obtained much faster [21]. Some researchers have shown that OFAT can be more effective than factorial designs under the following conditions [21]:

1. when the primary goal is to attain improvements in the system;
2. when experimental error is not large compared to factor effects.

However this approach has been criticized by many researchers because it does not give the interaction of different factors and can miss optimal settings of factors [21]. The 3^k approach has been the most widely used factorial design approach in leaching. In this design, k factors are considered, each at three levels. Leaching studies by Çoruh et al. [21] and Stopić et al. [22] used this kind of approach. One of the disadvantages of factorial experiments however, is that they can get large very quickly with several levels for each of several factors. Also, compared to other design

approaches the number of trials is generally more in a full factorial approach [21]. In this study, the OFAT approach was chosen since the primary goal was not to optimize cobalt leaching from the gypsum but to ascertain if similar leaching efficiencies to those from the well-established sulphuric acid leaching process were achievable with acidic waste liquor from the same processing plant.

31.2.6 Extractive Metallurgy of Cobalt

An appreciable amount of cobalt is present in most cobalt purification waste products [1–3]. Lately, several hydrometallurgical processes have been developed for cobalt recovery from these resources. These processes generally include the following major unit operations: roasting in some cases, leaching using acidic or basic lixiviants, removal of impurities (such as iron, manganese and zinc), separation and recovery processes and refining of recovered metals [1–3]. According to Chen and Ho [23], spent lithium-ion batteries are an important source of cobalt and sulphuric acid has been successfully used to extract the cobalt and other important battery metals like lithium. They conducted experiments simulating process plant extraction of cobalt i.e. leaching, solvent extraction, stripping, and chemical precipitation. A sulphuric acid strength of 2.0 M and hydrogen peroxide additions of 10% yielded optimal cobalt leaching efficiencies. In a study by Stuurman et al. [11], sulphuric acid in the presence of hydrogen peroxide as a reducing agent was able to extract about 95% copper and 80% cobalt from a copper-cobalt oxide ore. Various sources indicate that sulphuric acid is the most widely used lixiviant due to its low cost relative to other acids and ability to be regenerated during electrolysis. However, the re-use of acidic liquors provides an even cheaper alternative to leaching residue waste. Zhang and Cheng [24] report that ocean manganese nodules are a potential source of various metals such as Cu, Ni, Co and Mn. It is well known that the manganese nodules contain these metals as higher oxides or hydroxides and usually amorphous in nature. Therefore, it is essential to roast or leach the ocean manganese nodules in the presence of a reductant. Zhang and Cheng [24] also provide a schematic flowsheet of a manganese nodule pilot operation using SO_2 reductant that was designed and set up at Hindustan Zinc Limited, Udaipur, India, to recover Cu, Ni, Co, and Mn. Cobalt extraction at that pilot plant is essentially a Leach-Solvent Extraction-Electrowinning circuit i.e. Leach-SX-EW operation where sulphuric acid is the leaching agent.

Cobalt is always almost a by-product or co-product of mining for other base metals, chiefly copper, manganese iron, zinc and nickel. Large quantities of cobalt also occur in the sea floor, contained within manganese nodules and cobalt-rich crusts, although they are not economically viable with current technology and economic conditions [25]. Cobalt can either be extracted by pyrometallurgical methods or using hydrometallurgical methods. However, hydrometallurgical methods have become more popular in cobalt leaching [25]. Acid leaching is the most common leaching method for cobalt bearing mineral concentrates and ores [26]. Impurity removal processes include metal precipitation, solvent extraction and ion exchange.

Mwema et al. [8] and Seo et al. [26] studied the feasibility of using sulphuric acid in leaching cobalt. Both studies concluded that sulphuric acid could be used as a lixiviant in leaching cobalt. Seo et al. [26] further studied the use of hydrogen peroxide as a reducing agent in sulphuric acid leaching and concluded that the use of hydrogen peroxide improved the leach efficiencies. They attributed this to the reduction of acid insoluble Co^{3+} ions to acid soluble Co^{2+} ions when the reducing agent was used. Stuurman et al. [11] have also indicated that hydrometallurgical dissolution of Co^{3+} can take place only in the presence of a reducing agent. The reducing agents commonly used in the process include ferrous ions, sodium metabisulphite $(Na_2S_2O_5)$, and hydrogen peroxide. The consumption of these reducing agents is generally high, rendering the production cost of cobalt very steep. Wang and Zhou [27] have developed a hydrometallurgical process for the recovery of cobalt from a zinc plant residue. The residue contains active carbon, zinc sulphate, naphthol derivative complexes with cobalt, nickel, iron, copper, and other metals. What is evident though is that while the actual cobalt extraction process is determined by the cobalt source, leaching with an acid is common in all the studies reported herein.

31.2.7   Source of Gypsum for This Study

Gypsum, which consists mainly of calcium/iron sulphate, is a waste product of the cobalt purification circuit at the copper and cobalt producer which provided the samples of gypsum and nickel eluate. It is generated during the iron precipitation stage. The iron precipitation stage is among the various stages involved in cobalt purification and takes place in seven tanks. The feed is a raffinate solution (at a pH of 1) from the copper solvent extraction stage. The main purpose of the iron precipitation stage is to remove iron and copper by precipitation at a pH of about 3.5. The required pH is achieved by addition of quicklime (CaO). Air sparging helps in converting the ferric ions (Fe^{3+}) to ferrous ions (Fe^{2+}), an insoluble form of iron. At this stage, a reducing agent, sodium metabisulphite $(Na_2S_2O_5)$, is also added in order to further reduce Co^{3+} to Co^{2+}, an acid soluble form of cobalt. The final precipitation tank feeds a thickener from which the underflow is filtered using a drum filter. The final residue cake is the gypsum. The overflow is transferred to the zinc solvent extraction plant. About 450 metric tonnes of gypsum containing approximately 0.1% cobalt by weight are produced per day. This translates to 0.45 metric tonnes of cobalt, which if recovered could earn the company US$26,000/day at the current cobalt price compared to the US$4050/day the company is earning from gypsum sales.

31.3   Study Objectives and Hypotheses

This study investigated the technical feasibility of leaching cobalt from the gypsum with nickel eluate, which is an acidic waste stream from the nickel ion exchange plant at the cobalt producer. It is important to highlight that since both gypsum and

nickel eluate are waste streams, utilizing these two waste streams would augment the overall sustainability of the processing operations at this cobalt producer. The study objectives were to:

1. Determine the leaching efficiency (cobalt recoveries from the gypsum) when nickel eluate is used as leaching agent;
2. Compare the cobalt recoveries from leaching with nickel eluate against those obtained with sulphuric acid at similar conditions;
3. Determine the optimum pH and solids concentration for leaching cobalt with the nickel eluate.

Three hypotheses were constructed with these three objectives in consideration, viz:

H_{0_1} There is no significant difference at 95% confidence level in cobalt recoveries when either nickel eluate or sulphuric acid is the lixiviant.
H_{1_1} There is a significant difference in cobalt recoveries when nickel eluate is the lixiviant compared to when sulphuric acid is the lixiviant.
H_{0_2} There is no significant difference at 95% confidence level in cobalt recoveries between the maximum and minimum pH levels in nickel eluate leaching.
H_{1_2} There is a significant difference in cobalt recoveries between the maximum and minimum pH levels in nickel eluate leaching.
H_{0_3} There is no significant difference at 95% confidence level in cobalt recoveries between the maximum and minimum solids concentration levels in nickel eluate leaching.
H_{1_3} There is a significant difference in cobalt recoveries between the maximum and minimum solids concentration levels in nickel eluate leaching.

31.4   Materials and Methods

A one-factor-at-a-time (OFAT) experimental design approach was used for the leaching testwork. Nickel eluate leaching tests were conducted first followed by sulphuric acid leaching tests. The precipitation of iron occurs at pH 3–3.5; therefore the pH levels used were 0.5, 1 and 2. The solids concentration levels used were 30, 45 and 50% solids, because pulp densities in the plant are usually kept within these ranges for ease of pumping and agitation. The optimum pH was first determined and kept constant during the solids concentration leach tests. The recoveries obtained in the two tests were then compared. Analysis of variance (ANOVA) was used to test all the three hypotheses at a 5% significance level.

Table 31.1 Chemical composition of gypsum

Gypsum composition, %	TCo	ASCo	TCu	ASCu	TFe	ASFe
	0.10	0.09	0.031	0.023	2.62	1.29

Table 31.2 Chemical composition of nickel eluate

Nickel eluate, ppm	Cu	Co	Fe	Zn	Ni
	0.60	22.00	17.00	0.4	44

31.4.1 Materials

Instruments used comprised an atomic absorption spectrometer (AAS), electronic mass balance, pH meters, vacuum pump, mechanical agitator, drying oven, and a stop watch. Glassware and materials used included 1L beakers, filter paper, sample bags and sample bottles, burettes and pipettes, syringes, measuring cylinders and baffles. The sulphuric acid, gypsum and nickel eluate samples used in the study were provided by the cobalt producer. The initial chemical analyses of the gypsum and nickel eluate are shown in Tables 31.1 and 31.2. The 'T' prefixing the elements stands for total e.g. TCo means total cobalt, whereas 'AS' prefixing the elements stands for acid soluble.

31.4.2 Methods

Figure 31.4 illustrates the sequence of steps followed in performing the leaching experiments. The total number of trials was 36. Leaching tests were carried out using nickel eluate as the lixiviant followed by leaching tests using sulphuric acid as
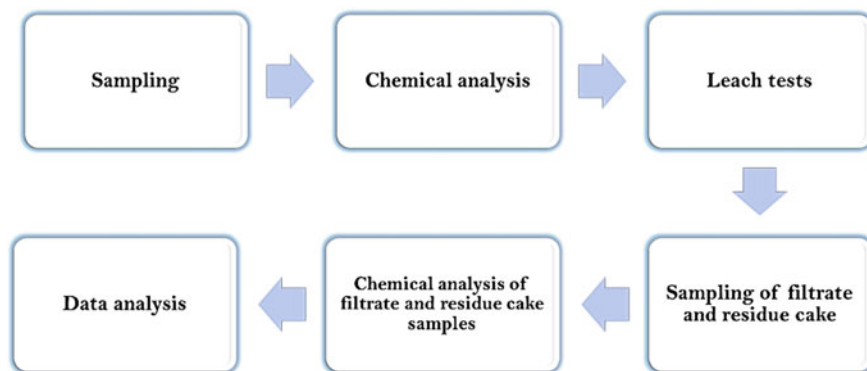

Fig. 31.4 Experimental procedure

Table 31.3 Constant leaching parameters

Parameter	Value
Terminal Leach pH	1.0
% Solids (for pH evaluation)	30.0
Initial Weight of Gypsum, g	418
Initial Volume of Water, L	1.0
Weight of Leach Residue, g	375
Filtrate Volume, ml	950
Wash Volume Collected, ml	1000
Leach Residence Time, h	3.0
Leach Temperature, °C	Ambient
Agitation Speed, rpm	600

the lixiviant. There were two replications of all the leach tests to improve reliability of the results. The pH and solids concentration were varied one at a time whereas the time, temperature and agitation speed were kept constant as portrayed in Table 31.3. There were a total of 18 trials for the nickel eluate leach tests and 18 trials for the sulphuric acid leach tests.

31.4.2.1 Leaching

This step constituted the most significant component of the procedure and the steps followed are reproduced here:

1. 100 g of gypsum were weighed and dried in the oven for 10 h. The dried sample was then weighed and the dry weight measured on the electronic mass balance. The moisture content was calculated using the formula:

$$\% \, Moisture = \frac{Wet \, gypsum \, weight - Dry \, gypsum \, weight}{Wet \, gypsum \, weight} \qquad (31.3)$$

2. A gypsum sample was measured and placed in a clamped beaker containing water and a pulp of required solids concentration was made. Equation 31.4 was used to determine how much gypsum was required for a specific solids concentration. The volume of water required was calculated from Eqs. 31.5 to 31.6:

$$Weight \, of \, gypsum = \frac{Required \, solids \, concentration, \quad \% \times 1000 g_{water}}{100 - required \, pulp \, density, \, \%}$$
$$(31.4)$$

$$Mass \, of \, water = Wet \, gypsum \, weight - Dry \, gypsum \, weight \qquad (31.5)$$

$$Volume = 1000 \text{ ml} - volume\ of\ water\ in\ gypsum \qquad (31.6)$$

3. The initial pH and temperature of the pulp were taken using the pH meter and recorded.
4. Nickel eluate was continually added to maintain the required pH level for the nickel eluate leach tests, whereas sulphuric acid was added for the sulphuric acid leach tests. The agitation speed was set at 600 rpm and the test work was carried out at room temperature. The residence time was 3 h.
5. During the tests, the temperature, pH and nickel eluate profiles were observed and recorded every 30 min.
6. After the leach tests were complete, filtration was carried out immediately. The filtrate obtained was measured in a measuring cylinder and the wet residue cake measured using the electronic mass balance. The residue cake was washed with 1000 mL of water. The wet residue cake was then dried overnight in the oven.
7. Thereafter, the dry leach residue solids were measured, sub-sampled by coning and quartering and subject to chemical analysis. Samples of the filtrate and wash were also analyzed for metals. The metals of interest were cobalt, copper, and iron. The metal recoveries after leaching, were calculated from the chemical analyses using Eq. 31.7:

$$\% \ Recovery = \frac{m_{metal\ in\ feed} - m_{metal\ in\ residue}}{m_{metal\ in\ feed}} \qquad (31.7)$$

where $m_{metal\ in\ feed}$ is the mass of metal in the feed and $m_{metal\ in\ residue}$ is the mass of metal in the residue.

31.5 Results and Analysis

31.5.1 Nickel Eluate Leach Tests

The chemical analyses of the feed solids and residue (obtained by filtration of the pulp + lixiviant mixture) are presented in Figs. 31.5, 3.6, 3.7 and 3.8. The 'T' prefixing the elements stands for total e.g. TCo means total cobalt, whereas 'AS' prefixing the elements stands for acid soluble. Metal concentrations in the filtrate and wash were higher than concentrations in the nickel eluate. This shows that substantial amounts of metal had been dissolved from the gypsum into solution. The wash for all the pH levels contained about 0.02 g/L of copper, 0.03–0.07 g/L of cobalt and 1.59–2.89 g/L of iron. This was as a result of dissolved metal entrainment in the solids during filtration. These metal concentration trends are similar to those reported [8, 11, 17, 24, 26–31].
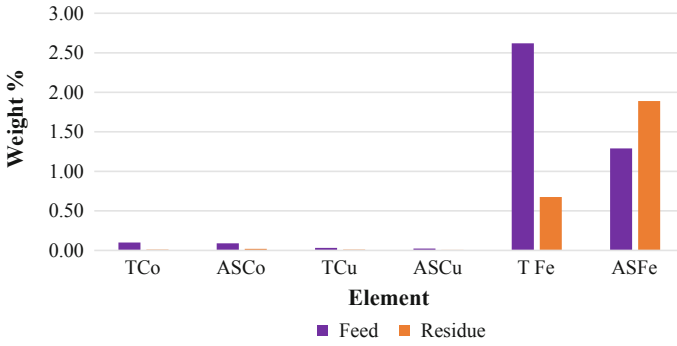
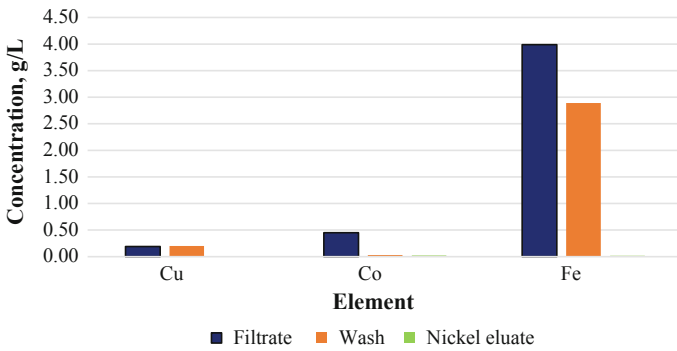**Fig. 31.5** Chemical analyses of gypsum and leach residue at pH 0.5 for nickel eluate leaching

Fig. 31.6 Chemical analyses of filtrate, wash and nickel eluate at pH 0.5 for nickel eluate leaching
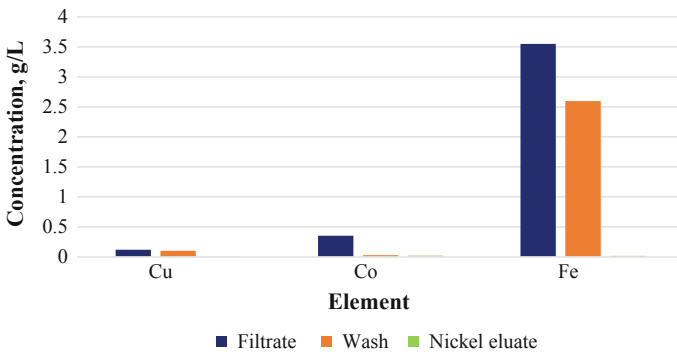

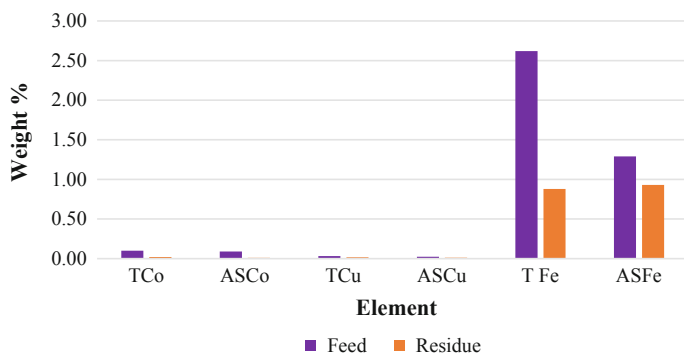**Fig. 31.7** Chemical analyses of filtrate, wash and nickel eluate at 30% solids for nickel eluate leaching

Fig. 31.8 Chemical analyses of gypsum and leach residue at 30% solids for nickel eluate leaching

At all the three solids concentration levels, the nickel eluate had less concentrations of cobalt, copper and iron than the wash and filtrate indicating that leaching of these metals had taken place. The filtrates at 30% (Fig. 31.7) and 45% solids concentration contained a higher amount of cobalt, copper and iron than the wash. However, at 50% solids concentration, the concentration of copper was lower in the filtrate than the wash. This might have been due to high entrainment of soluble copper in the residue solids during filtration.

Metal concentrations were higher in the gypsum feed than the residue because about 80–92 and 54–71% of the cobalt and iron (in the feed) respectively had been successfully leached into solution at the various solids concentration levels. This is the whole point of leaching, which is a concentration technique applied as a preparatory step for metal recovery [14]. This is portrayed in Fig. 31.8.

31.5.1.1 Temperature, PH, and Nickel Eluate Profiles

During all the nickel eluate leach tests, the initial pH was in the range 6–6.5 and the initial temperatures were about 25 °C. The temperatures marginally increased to about 26 °C during the first 10 min and gradually increased by about 2 °C at the end. Figures 31.9 and 31.10 show that the amount of nickel eluate used was inversely proportional to the pH level. Gypsum has a neutral pH, and since it has no carbonate ions, it will not neutralize acidity. The nickel eluate is in essence sulphuric acidic liquor, thus like all acids, lowering of the pH is achieved by increasing the acid dosage or concentration. In order to bring down the pH from about 7 to 0.5, incremental dosages of the nickel eluate were added until the required pH was obtained. The amount of nickel eluate used was highest at 30% solids and least at 50% solids. This can be explained by the higher water content at 30% solids than at 45 and 50%.
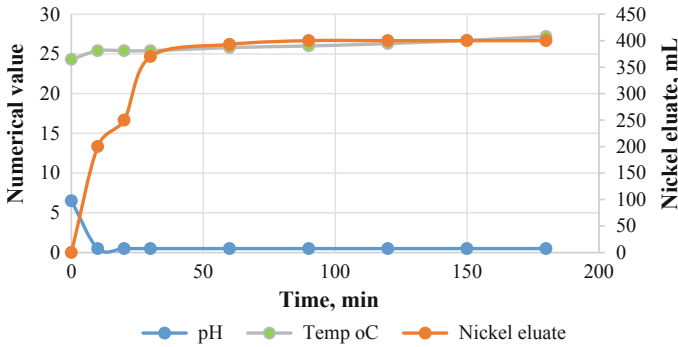
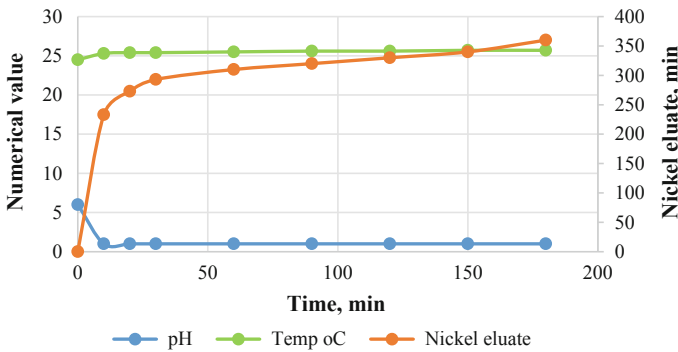**Fig. 31.9** Temperature, pH and nickel eluate profile at pH 0.5

Fig. 31.10 Temperature, pH and nickel eluate profile at 30% solids

31.5.1.2 Metal Recoveries from Leaching with Nickel Eluate

Metal recoveries were calculated using Eq. 31.7. The recoveries of cobalt and iron were inversely proportional to pH, with the highest recoveries obtained at pH 0.5 (~93% cobalt and 82% iron) as shown in Fig. 31.11. Iron is the main impurity in the gypsum as depicted in Table 31.1; therefore it was necessary to observe the iron recoveries. Low pH favours dissolution of both the cobalt and the iron since they have similar chemistry. This explains the similarity in the recovery-pH profiles in Fig. 31.11.

Cobalt and iron recoveries follow the polynomial trendline Eqs. 31.8 and 31.9 respectively.

$$\text{Co: } \% \, Recovery = 9.2147 \, \text{pH}^2 - 36.31 \, \text{pH} + 108.67 \tag{31.8}$$

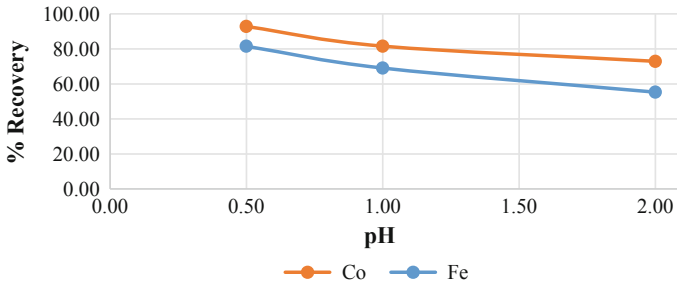$$\text{Fe: } \% \, Recovery = 7.4153 \, \text{pH}^2 - 36.014 \, \text{pH} + 97.663 \tag{31.9}$$

Fig. 31.11 % Recovery against pH for nickel eluate leaching

Similar observations were made in a study by Liu et al. [28], in which the selective leaching of cobalt and iron from cobalt white alloy under controlling potential in sulphuric solution with catalyst was carried out. In the study, the concentration of sulphuric acid was varied at levels 3.0, 3.2, 3.4, 3.8, 4.2, 4.4 and 4.8 mol/L. The results showed that the recoveries of cobalt and iron increased with increasing acid concentration. When the sulphuric acid concentration was 3.0 mol/L, the recoveries of both cobalt and iron were 75%. In that study, at the maximum acid concentration level, the recoveries were 95.01 and 95.07% for cobalt and iron respectively.

Figure 31.12 illustrates the change in metal recovery with solids concentration. The recoveries for both cobalt and iron increased with increasing solids concentration and the highest recovery obtained was at 50% solids. Equations 31.10 and 31.11 are the trendline equations for cobalt and iron respectively. Related studies by Seo et al. [26] and Liu et al. [28] similarly showed that the recovery of cobalt increased with increasing solids concentration.

$$\text{Co:} \quad \%Recovery = 0.0366w^2 + 3.5194w + 7.873 \tag{31.10}$$

$$\text{Fe:} \quad \%Recovery = 0.0306w^2 + 3.2788w + 16.142 \tag{31.11}$$

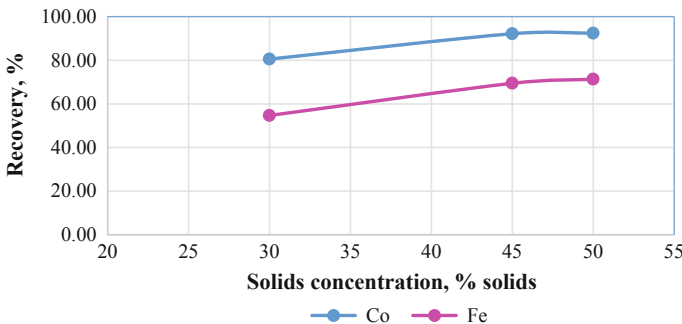where w is the % solids concentration.

Fig. 31.12 Recovery (%) against solids concentration for nickel eluate leaching

31.5.2 Sulphuric Acid Leach Tests

For all the sulphuric acid leach tests, the initial pH was in the range 6–6.5 and the initial temperatures were about 25 °C. The temperatures increased to about 40 °C during the first 10 min before slightly dropping to about 38 °C and remaining more or less constant to the end. Figure 31.13 shows that the amount of sulphuric acid used was inversely proportional to the pH level. In order to bring down the pH from about 6.5 to 0.5, incremental dosages of the sulphuric acid were added until the required pH was attained. At pH 0.5, the temperature rose from 25 °C to about 41 °C during the first 10 min. It later dropped by about 4 °C with minor fluctuations throughout the test as shown in Fig. 31.13. The same trends were observed for the rest of the tests at pH 1 and 2. Most acid was consumed at pH 1 whereas the least was consumed at pH 2, which is obviously attributable to the decreased dissolution potency of the acid at lower strength. There was little variation in sulphuric acid consumption when leaching was conducted at different solids concentration levels.

31.5.2.1 Metal Recoveries from Sulphuric Acid Leach

The graphs presented in Figs. 31.14 and 31.15 were generated in the same manner as described in Sect. 31.5.1 for nickel eluate leaching. The recoveries for cobalt and iron also increased with decreasing pH with the only exception being iron recovery at pH 2 was a negligible 0.27 percentage points lower than at pH 1. However, this is actually an important result because the lower the iron leached the better it is for subsequent cobalt extraction stages like solvent extraction, stripping, electrowinning or precipitation. The iron is an impurity requiring later separation from the cobalt. The recoveries for cobalt and iron increased with increasing solids concentration as observed for nickel eluate leaching. The maximum metal recoveries were observed at pH 0.5 and 50% solids (~94% cobalt and ~86% iron) as shown in Fig. 31.14.
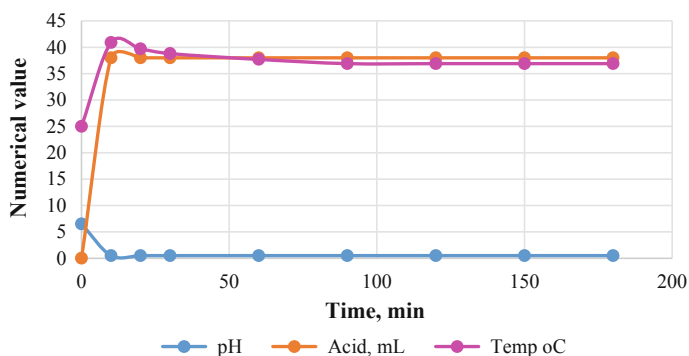

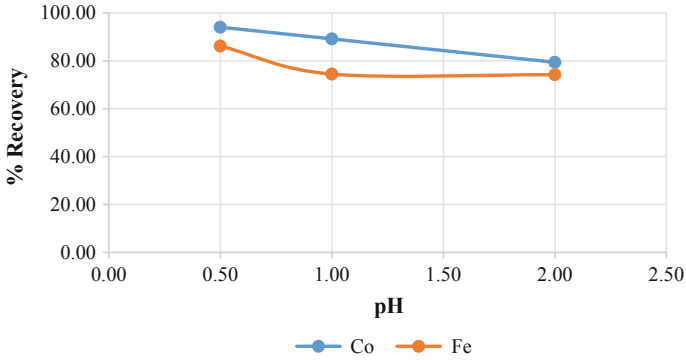**Fig. 31.13** Temperature, pH and sulphuric acid profiles at pH 0.5

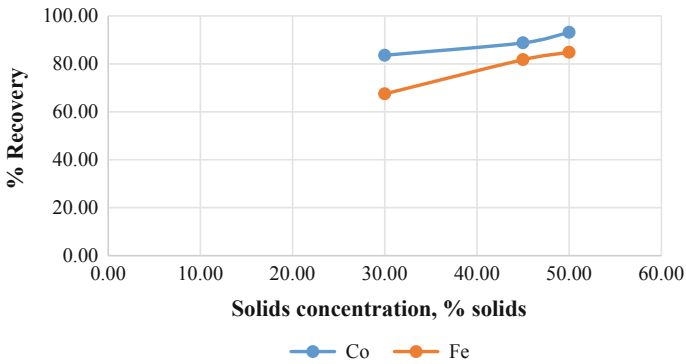**Fig. 31.14** % Recovery against pH for sulphuric acid leaching

Fig. 31.15 % Recovery against solids concentration for sulphuric acid leaching

Cobalt and iron recoveries follow the polynomial trendline Eqs. 31.12 and 31.13 respectively.

$$\text{Co:} \quad \% Recovery = -0.0216 \, \text{pH}^2 - 9.7209 \, \text{pH} + 98.916 \tag{31.12}$$

$$\text{Fe:} \quad \% \, Recovery = 15.448 \, \text{pH}^2 - 46.609 \, \text{pH} + 105.63 \tag{31.13}$$

The recoveries for both cobalt and iron increase with increasing solids concentration and the highest recovery obtained was at 50% solids. Equations 31.14 and 31.15 are the trendline equations for cobalt and iron respectively.

$$\text{Co:} \quad \% \, Recovery = 0.0266w^2 - 1.6474w + 109.12 \tag{31.14}$$

$$\text{Fe:} \quad \% \, Recovery = -0.0169w^2 + 2.2218w + 16.081 \tag{31.15}$$

where w is the % solids concentration.

Comparison of the graphs in Figs. 31.11 and 31.12 with those in Figs. 31.14 and 31.15 confirms that leaching the gypsum in nickel eluate yields similar results to leaching it in sulphuric acid. The cobalt recoveries are higher than those reported by Mwema et al. [8] who managed to extract 78% of the cobalt at pH 4.5 from a copper oxide ore using a spent electrolyte which is also an acidic liquor like the nickel eluate. Thus, cobalt leaching efficiency is supported by low pH. Seo et al. [26] who carried comparable leaching tests at 0.732 M sulphuric acid and 0.025 M hydrogen peroxide recovered 90% cobalt in 90 min. Fan et al. [20] similarly showed that cobalt recoveries exceeding 96% are possible when leaching with 40% w/w sulphuric acid at 85 °C for 5 h and an agitation speed of 250 rpm. Aaltonen et al. [30] and Moradkhani et al. [31] have also obtained above 90% cobalt recoveries when reductively leaching secondary sources of cobalt with sulphuric acid.

31.5.3 Comparison of Metal Concentrations at Optimum pH and Solids Concentration

Despite pH 0.5 giving the highest cobalt recoveries, pH 1 was selected as the optimum leaching pH because the iron recoveries are much lower than at pH 0.5 when using either leaching agent while the cobalt recoveries are still good. pH 0.5 would also result in higher plant operating costs due to usage of more sulphuric acid or nickel eluate, and more equipment corrosion problems. Optimum slurry density would be 30% solids notwithstanding 50% solids yielding higher cobalt recoveries because agitation of the pulp was observed to be more effective at 30% solids than at 50% solids. An agitation speed of 600 rpm was employed in all leach tests in the present study but some studies report much lower agitation speeds which would be ineffective for pulps with 1:1 solids to liquid ratio [20, 30]. Increasing the solids content and pH and decreasing the particle size have been detected by Klein and Laskowski [32] to increase the yield stress of mineral pulps, while also increasing the Casson viscosity. In a practical sense this would mean higher energy costs to run the mechanical agitators used in the processing plant and a shorter service life.

The cobalt concentrations (Fig. 31.16) in the nickel eluate leach solutions (filtrate and wash) were comparable to those of the sulphuric acid leach solutions (filtrate and wash). The iron concentrations on the other hand were higher in the sulphuric acid leach solutions than nickel eluate leach solutions meaning sulphuric acid tends to dissolve more iron than the nickel eluate. From Fig. 31.17, cobalt and copper concentrations in the nickel eluate leach residue were close to 0.01 wt% but below detection limits for the sulphuric acid leach residue. Iron concentrations were similar in both instances. The gypsum used in this study was sourced from a process plant that is specifically designed to extract and refine cobalt and copper. In the event that the findings of this study are implemented to recover the cobalt in the gypsum, then the cobalt-rich leach solutions will be purified through the existing process. Copper is recovered by electrowinning, and the spent electrolyte laden with cobalt is purged
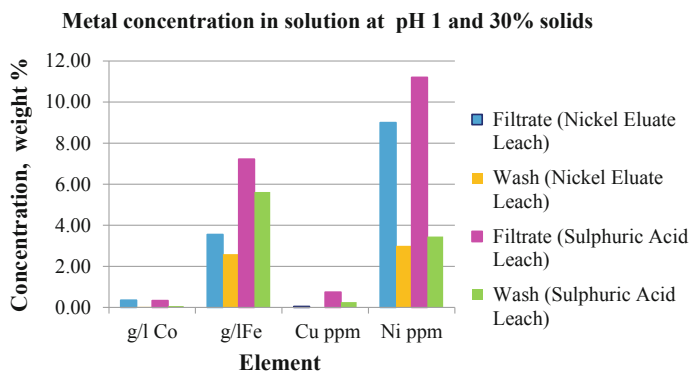
Metal concentration in solution at pH 1 and 30% solids

Fig. 31.16 Comparison of metal concentrations in nickel eluate and sulphuric acid leach solutions

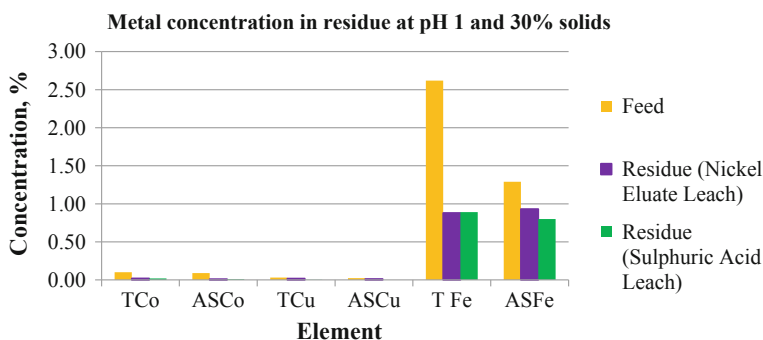**Metal concentration in residue at pH 1 and 30% solids**

Fig. 31.17 Comparison of metal concentrations in nickel eluate and sulphuric acid leach residues

of copper and iron by air sparging in the presence of quicklime generating gypsum which is separated from the cobalt-rich electrolyte by thickening and drum filtration. Successive cobalt purification stages are elution in carbon columns and then the nickel ion exchange circuit where the picolylamine chelating resin Dowex 4195 selectively extracts nickel over cobalt ions from the solution. The purified electrolyte is then pumped to the cobalt tank house for cobalt electrowinning. The nickel eluate is in fact a sulphuric acid solution used to regenerate (washing off ions trapped in active sites) the Dowex 4195 resin. Thus it is loaded with nickel and copper (see Table 31.2) among other trace metals and recycled before final disposal. Figure 31.16 illustrates that the gypsum in question is a source of nickel and copper but the fresh sulphuric acid dissolves these elements better than the nickel eluate.

Evidently from Fig. 31.16, nickel concentrations in the filtrates and wash solutions are much higher than either cobalt or copper concentrations, with sulphuric acid leaching more nickel and copper than the nickel eluate. Cobalt, copper, and nickel are important non-ferrous metals and studies by Mwema et al. [8], Fan et al. [20], Zhang and Cheng [24], Seo et al. [26], Wang and Zhou [27], Liu et al. [28],

Ma et al. [29], Aaltonen et al. [30] and Moradkhani et al. [31] all confirm the co-occurrence of these metals after leaching of the source materials, which necessitates additional separation stages to isolate and recover these metals. The overriding criterion is always production of a pregnant leach solution sufficiently concentrated to warrant profitable investment in an ion exchange, solvent extraction, precipitation or electrowinning circuit to recover the metal. These metals are usually found together in nature e.g. copper-cobalt oxide ore deposits of the Democratic Republic of Congo and Zambia [11]. Laterite ore deposits are an important source of nickel and cobalt, and these metals can be recovered pyrometallurgically or hydrometallurgically [33]. The Leach-SX-EW pilot plant described by Zhang and Cheng [24] provides a relevant case study for Cu, Ni, and Co separation and recovery. The adjacent positions of Ni and Co in the transition metal series in the periodic table result in aqueous chemical behaviour that is too similar, making separation of these two metals in aqueous solution problematic for hydrometallurgists [34].

Flett [34] discussed different Ni-Co separation techniques such as precipitation, ion exchange (Dowex M4195 resin commonly used to remove nickel from the cobalt electrolyte before electrowinning), solvent extraction (most commercial operations use the dialkyl phosphinic acid extractant, CYANEX 272), and pressure hydrogen reduction. Several Ni-Co extraction and purification flow sheets of commercial process plants have been similarly evaluated by Flett [34].

Figure 31.17 portrays that iron concentration was higher in the nickel eluate leach residue than the sulphuric acid leach residue. Liu et al. [28] who studied the effect of leachant acidity on cobalt recovery observed that cobalt, nickel, iron and copper concentrations were lower in the residue when strong sulphuric acid was used than when a weaker acid was used. Figure 31.17 confirms this observation but considered together with Fig. 31.16, these graphs demonstrate that the nickel eluate has comparable leaching potency to the sulphuric acid, with the added advantage of leaching less iron into solution.

31.5.4   One-Factor ANOVA Results

A one-way analysis of variance was generated for the cobalt recoveries obtained from the leaching tests in order to test the three hypotheses at a 5% level of significance. The results are presented in Tables 31.4, 31.5 and 31.6.

Table 31.4 Summary of one-factor ANOVA for the first hypothesis

pH	F	P-value	F critical	Decision
0.5	14.8193	0.0183	7.7086	Reject H_0
1	49.6388	0.0021	7.7086	Reject H_0
2	48.0471	0.0023	7.7086	Reject H_0

Table 31.5 One-factor ANOVA results for the second hypothesis

F	P-value	*F critical*	Decision
709.9303858	0.00001179	7.70864742	Reject H_0

Table 31.6 One-factor ANOVA results for the third hypothesis

F	P-value	*F critical*	Decision
44.318163	0.0026444	7.7086474	Reject H_0

All three hypotheses were rejected because the *F* values were greater than the *F* critical values and the *P*-values were less than α (0.05). This means the findings of the leaching tests do not support the hypotheses. Therefore pending additional test work, the findings support the three alternative hypotheses which are restated here:

H_{1_1} There is a significant difference in cobalt recoveries when nickel eluate is the lixiviant compared to when sulphuric acid is the lixiviant.

H_{1_2} There is a significant difference in cobalt recoveries between the maximum and minimum pH levels in nickel eluate leaching.

H_{1_3} There is a significant difference in cobalt recoveries between the maximum and minimum solids concentration levels in nickel eluate leaching.

Disproval of H_{0_1} makes sense considering that nickel eluate is in fact a recycled sulphuric acid solution which had been used in the nickel ion exchange plant to elute nickel from the resin, and subsequently diluted to an electrolyte for electrowinning of the nickel. Since it is continually recycled though with periodic additions of fresh sulphuric acid, it becomes contaminated (see Table 31.2) and cannot be expected to have exactly the same leaching efficiency as fresh sulphuric acid. However, the recoveries are still comparable, and the cost reductions from leaching with nickel eluate and the concomitant environmental paybacks support substituting fresh sulphuric acid with this recycled liquor. Furthermore, on the basis of metal recoveries from sulphuric acid leaching (~94% cobalt and ~86% iron) against those from nickel eluate leaching (~93% cobalt and ~82% iron), nickel eluate performs better since it dissolves less iron.

Disproval of H_{0_2} is supported by Fig. 31.11 which shows that at pH 2, cobalt recovery was 72.91% whereas it was 92.82% at pH 0.5. That is an almost 20% difference in cobalt recovery and it is very significant. Thus, low pH favours cobalt dissolution from gypsum. Azimi et al. [35] have modelled the dissolution of gypsum in $CaSO_4$–H_2SO_4–H_2O ternary systems and concluded that the addition of H_2SO_4 which lowers the pH results in a significant increase in the calcium sulphate solubility but only at ambient temperatures of 25–60 °C. This is consistent with findings of the present study where leach tests were conducted at room temperature i.e. 25 °C.

Disproval of H_{0_3} is supported by Fig. 31.12 which shows that at 30% solids, cobalt recovery was 80.54% whereas it was 92.40% at 50% solids, that is an almost 12% difference in cobalt recovery and again it is very significant. Thus, high solids content

results in high cobalt recoveries when leaching the gypsum due to the increased number of particles available but Lee et al. [36] have demonstrated that the influence of pulp density on leaching kinetics is far less pronounced than that of pH, time or temperature.

31.6 Conclusions

Peak cobalt recoveries of ~93% (nickel eluate leaching) and ~94% (sulphuric acid leaching) were obtained at pH 0.5 and 50% solids. Based on these recoveries, nickel eluate can be used as a lixiviant in extracting cobalt from gypsum. An increase in cobalt is always associated with an increase in iron recoveries. Iron will pose severe challenges later on in the purification circuit during the electrowinning stage. Optimum leaching conditions will maximize cobalt recoveries while suppressing iron recoveries. Thus, the optimum pH for cobalt leaching is 1 because the iron recoveries were much lower than at pH 0.5. Agitation of the pulp is more effective at lower solids content than at higher solids content, so 30% solids could be considered an invariable leaching parameter in related future test work. Full factorial design experiments are needed to determine the interaction effects on cobalt recoveries of the various leach parameters. Surface response methodology can then be applied to optimize cobalt recoveries. A nickel eluate leaching kinetics study can also be conducted in order to model the cobalt dissolution process and improve the reaction rates. Cobalt recoveries can be increased by the use of hydrogen peroxide, sodium metabisulphite or sulphur dioxide as reducing agents. The reducing agents reduce the insoluble Co^{3+} to soluble Co^{2+}.

References

1. Gupta CK (2006) Chemical metallurgy principles and practice. Wiley, Mumbai
2. Ghosh A, Ray HS (1991) Principles of extractive metallurgy. New Age International, New York
3. Dutta SK, Lele AB, Chokshi YB (2018) Extractive metallurgy—processes and applications. PHI, Delhi
4. Baba AA, Adekola F, Toye EE et al (2009) Dissolution kinetics and leaching of rutile ore in hydrochloric acid. J Miner Mater Charact Eng 8:787–801
5. Gupta CK, Mukherjee TK (1990) Hydrometallurgy in extraction processes, vol II. CRC Press, Bombay
6. Ventor R, Boylett M (2009) The evaluation of various oxidants used in acid leaching of uranium. Hydrometallurgy Conf 2009:445–455

7. Meshram P, Abhilash Pandey BD et al (2016) Comparison of different reductants in leaching of spent lithium ion batteries. J Miner Met Mater Soc 68:2613–2623
8. Mwema MD, Mpoyo M, Kafumbila K (2002) Use of sulphur dioxide as reducing agent in cobalt leaching at Shituru hydrometallurgical plant. J S Afr Inst Min Metall 4:1–4
9. Wadsworth ME (1987) Leaching—metals applications. In: Rousseau RW (ed) Handbook of Separation Process Technology. Wiley, New York
10. Huang HH (2016) The Eh-pH diagram and its advances. Metals 6:23
11. Stuurman S, Ndlovu S, Sibanda V (2014) Comparing the extent of the dissolution of copper-cobalt ores from the DRC Region. J S Afr Inst Min Metall 114:347–353
12. Garcia EM, Santos JS, Pereira EC et al (2008) Electrodeposition of cobalt from spent Li-ion battery cathodes by the electrochemistry quartz crystal microbalance technique. J Power Sources 185:549–553
13. Othusitse N, Muzenda E (2015) Predictive models of leaching processes: a critical review. In: 7th international conference on latest trends in engineering & technology, Pretoria. http://dx.doi.org/10.15242/IIE.E1115039
14. Singer PC, Stumm W (1970) Acidic mine drainage: the rate-determining step. Science 167:1121–1123
15. de Andrade Lima LRP (2004) A mathematical model for isothermal heap and column leaching. Braz J Chem Eng 21:435–447
16. Razavi-Tousi S, Szpunar JA (2016) Modification of the shrinking core model for hydrogen generation by reaction of aluminum particles with water. Int J Hydrogen Energ 41:87–93
17. Sidborn M, Casas J, Martínez J et al (2003) Two-dimensional dynamic model of a copper sulphide ore bed. J Hydromet 71:67–81
18. Naderi H, Abdollahy M, Mostoufi N et al (2011) Kinetics of chemical leaching of chalcopyrite from low grade copper ore: behavior of different size fractions. Int J Miner Metall Mater 18:638–645
19. Takacova Z, Havlik T, Kukurugya F et al (2016) Cobalt and lithium recovery from active mass of spent Li-ion batteries: theoretical and experimental approach. Hydrometallurgy 163:9–17
20. Fan X, Xing W, Dong H et al (2013) Factors research on the influence of leaching rate of nickel and cobalt from waste superalloys with sulfuric acid. Int J Nonferr Metall 2:63–67
21. Çoruh S, Elevli S, Geyikçi F (2012) Statistical evaluation and optimization of factors affecting the leaching performance of copper flotation waste. Sci World J 2012:758719
22. Stopić S, Friedrich B, Anastasijević N (2003) Experimental design approach regarding kinetics of high pressure leaching processes. J Metall 9:273–282
23. Chen W, Ho H (2018) Recovery of valuable metals from lithium-ion batteries NMC cathode waste materials by hydrometallurgical methods. Metals 8:321
24. Zhang W, Cheng Y (2007) Manganese metallurgy review. Part I: leaching of ores/secondary materials and recovery of electrolytic/chemical manganese dioxide. Hydrometallurgy 89:137–159
25. Hannis S, Bide T, Minks A (2009) Cobalt. Brit Geol Sur. https://www.bgs.ac.uk/mineralsuk/statistics/mineralProfiles.html. Accessed 27 Sept 2018
26. Seo SY, Choi WS, Kim MJ et al (2012) Leaching of a Cu-Co ore from Congo using sulphuric acid and hydrogen peroxide leachants. J Min Metall Sect B 49:1–7
27. Wang Y, Zhou C (2002) Hydrometallurgical process for recovery of cobalt from zinc plant residue. Hydrometallurgy 63:225–234
28. Liu W, Rao S, Wang W et al (2015) Selective leaching of cobalt and iron from cobalt white alloy in sulfuric acid solution with catalyst. Int J Miner Process 141:8–14
29. Ma L, Nie Z, Xi X (2013) Cobalt recovery from cobalt-bearing waste in sulphuric and citric acid systems. Hydrometallurgy 136:1–7
30. Aaltonen M, Peng C, Wilson BP et al (2017) Leaching of metals from spent lithium-ion batteries. Recycling 2:20
31. Moradkhani D, Sedaghat B, Khodakarami M et al (2014) Recovery of valuable metals from zinc plant residue through separation between manganese and cobalt with N-N reagent. Physicochem Probl Miner Process 50:735–746

32. Klein B, Laskowski JS (2000) Rheological measurements on settling suspensions: characterization of a cyanide leach pulp. Miner Process Extr Metall Rev 20:41–55
33. Dalvi AD, Bacon WG, Osborne RC (2004) The past and the future of nickel laterites. PDAC 2004 International Convention. http://citeseerx.ist.psu.edu/viewdoc/download?doi=10.1.1.732.7854&rep=rep1&type=pdf. Accessed 20 Dec 2018
34. Flett DS (2004) Cobalt-nickel separation in hydrometallurgy: a review. Chem Sustain Dev 12:81–91
35. Azimi G, Papangelakis VG, Dutrizac JE (2007) Modelling of calcium sulphate solubility in concentrated multi-component sulphate solutions. Fluid Phase Equilibr 260:300–315
36. Lee JY, Kumar JR, Jeon HS et al (2013) Up-gradation of MoO_3 and separation of copper, iron, zinc from roasted molybdenum ore by a leaching process. Braz J Chem Eng 30:391–397